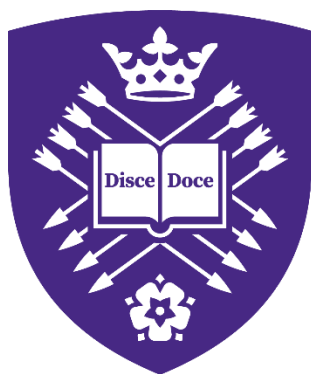


Advanced Spectroscopic Characterisation of Metal-Organic Framework Nanosheets and their use in Phosphate Sensing



University of Sheffield

Benedict Smith

200269797

A thesis submitted to the University of Sheffield in partial fulfilment of the requirements for
the Degree of Doctor of Philosophy

October 2024

The University of Sheffield

Faculty of Science

Department of Chemistry

Abstract

Understanding the relationship between material structures and optical and electronic properties is key to enabling their use in a wide range of applications. In this thesis an in-depth investigation of a class of porphyrin-based metal organic framework nanosheets (MONs) was undertaken into the effects of nanosheet stacking, aggregation, and metalation on absorption, emission, and excited state dynamics.

Concentration and centrifugation dependent aggregation of $Zn_2(TCPP)$, where TCPP is tetra(carboxyphenyl)porphyrin, was identified to cause wavelength-dependent emission quenching and increased exciton annihilation in aggregates, but also increase the excited state lifetime. Additionally, post-synthetic metalation at the porphyrin centre was investigated to introduce selective wavelength emission quenching, reduced exciton annihilation, and longer excited state lifetimes due to enhanced intersystem crossing. Specifically, avoiding aggregation and metalation with any of the metals tested is revealed to decrease the amount of exciton annihilation in these MONs. Variation in the effect different metals had is explained using electronic hybridisation theory and physical porphyrin deformation theory, providing a foundational approach to understanding the effects on these materials. The conclusions drawn from these analyses can advise the fabrication of these materials for specific optoelectronic properties required depending on application.

An ambitious experiment to 'topographically' map the emission output of $Zn_2(TCPP)$ MONs was also undertaken using a modified surface near-field optical microscopy setup to collect spectroscopic data for the analysis of single nanosheets and allow correlation with particle thickness. This proved beyond the capabilities of the setup during the research timeframe, however, successful imaging of $\sim 8 \mu m$ aggregates was achieved and there remains significant remit for optimisation and use with other materials.

Finally, application of MONs and other materials in the sensing of phosphate fertilisers for more sustainable farming were investigated. Both $Zn_2(TCPP)$ MONs and molecularly imprinted polymers (MIPs) were investigated to introduce selectivity to carbon electrodes, resulting in enhanced sensitivity and some selectivity toward phosphate over nitrate analytes.

Acknowledgements

It has been a long road to get here, and as way lead to way it wasn't always clear which direction we were going to end up in. I enjoyed every step of the journey, however, and there were always people who encouraged me towards this destination. Sheffield opened up its arms and welcomed me with good times, new experiences, and friends. This work is not mine alone but the culmination of work and effort from everyone who has been there to support me. There have been so many who have given me their time and energy either in big projects, or in the little things that mean so much. Thank you to everyone who was along for the ride. It has been a pleasure to know you all.

To **Jona Foster** and **Adrien Chauvet**, thank you for your guidance and the opportunity to come to Sheffield in the first place. Working in your groups has given me the support, encouragement and guidance which have made all the difference. From these groups, I have received enthusiastic help and friendship from many individuals.

I joined the Foster group with the ever friendly **Dave Ashworth**, **Kezia Sasitharan**, **Josh Nicks**, **Freya Cleasby**, **Mike Harris**, **Ram RR Prasad**, **Andy Jiantian Tian**, and **Amelia Wood**, and now I leave it with **Prioti Purba**, **Victor Sanyou Xu**, and **Alana Barlow**. Thank you all for your friendships, comradery, and support.

In the Chauvet group, the training and patience from **Alex Auty**, **Arthur Graf**, and **Sayantana Bhattacharya** cannot be understated, you kept your cool while I made mistakes, and while I made them again. Joining since I started, it has been a pleasure to see **Laraib Nisar** come into her own, and I look forward to seeing what she and the group go on to achieve.

For dedicating so much time, simply because I asked for your help, thank you **James Pidgeon**, **Sam Peralta**, **Iona Ivalo**, and **Martin Appleby**. With you and the other members of the ULS, I have greatly enjoyed my time playing with lasers and then thinking really hard about it. I would also like to thank **Julia Weinstein** and **Jenny Clark** for taking an interest in my work, and for your help and advice.

To **Alex Knight**, **Thomas Roseveare**, **Chester Blackburn**, **Perrine Lasserre**, **James Shipp**, **Dave Ashworth**, **Csilla Györgi** and everyone else who has helped me along the way during the technical aspects, thank you for offering help when you did. Wishing you all the best.

To **Denise Richards** and **Louise Brown-Leng**, thank you for helping me every time something needed buying, signing, sending, organising, or doing. You've both worked constantly the entire time I've known you, and I think it's well established it would all fall apart without you. Cheers for keeping it together through the chaos! To the others in the department, notably **Craig Robertson**, **Dean Liversidge**, **Deeba Zahoor**, **Dimitri Chekulaev**, **Anna Foster**, **Joe Quick**, **Simon Parker**, **Nick Smith**, and **Sharon Curl**, thanks for being friendly faces always willing to lend a hand with experiments or equipment. The man with all the smiles, **Jordan Martin**, deserves a special mention. Thanks for making the day a bit brighter every time I walk into the department.

Many highlights of my time at Sheffield have come from my experiences with the Grantham Centre for Sustainable Futures. The perspectives this scholarship has shown me and the ideas driven home have not only been invaluable and interesting but have significantly shaped my research and career interests. Adventures have ranged from Sheffield to Egypt. I am sure I will treasure those memories forever, and I know I made some firm friends along the way in **Kelli Kennedy**, **Melis Tekin**, **Nada Adham**, and **Su Natasha Binti Mohamad**. I would therefore like to thank not only **Rachel Rothman** and **Tony Ryan** as directors of the Grantham

Centre, but also **Deborah Beck** and **Jana Green**, the unsung organisers of all. It was incredible to arrive somewhere where you already knew my name and face, and I have felt welcomed ever since.

An equally fantastic experience was in my time at Parliament working between the Parliamentary Office of Science and Technology (POST) and the House of Lords Science and Technology Committee. This was such an amazing opportunity which I will take forward with me. I would therefore like to thank **Thomas Hornigold**, **Siddhant Gurung**, and **Mathew Manning** for your help and support.

Back in Sheffield, it was a pleasure to be part of the CPGS community, the department has never felt friendlier than when everyone was together sharing stories, good food, and inventing our own tea. Special thanks to **Amelia Wood**, **Ellen Wilson** for keeping me company during CHIP and getting through so many paint by numbers! A special mention to **Jasmine Catlow** for including me when I first joined and always being ready with a smile since.

To the G-floor crew, old and new, it's been laugh after laugh. Thanks to **Rob Mathews** for keeping me sane with a crossword and a chat. Thanks to **Anna Newman** for endless LARP stories, one day Xeuss will bless you with a bountiful harvest (data), and you can finally leave the shadow realm (the basement). **Jonny Gregg** and **Neil Lunt**, keep it high brow like you always do. To **Fourat Keskin**, for the easy bromance and snowmen in the park, love ya man. Thanks to all the others that have kept me company over the years: **Jenny Hughes**, **Reuben Ouanounou**, **Freya Cleasby**, **Simon Fawcett**, **Ellen Wilson**, **Xander Praet**, **Sophia van Mourik**, **Beth Ritchie**, **Millie Wood**, **Alice Rhind-Tutt**, **Courtney Thompson**, **Oleta Norvilaite**, and **Tom Jackson**. You've all been friendly faces over the years, and I wish you the best.

Nikki Mansouriborojeni, you could have fit in any of about a dozen places. Between organising conferences, events, co-editing Resonance, chairing ULS, we've done a lot together! Keep shooting for the moon, can't wait to see what you get up to.

I've changed a lot over these last few years, and only a few people have known me throughout. To my friends **Tom Fells**, **James Smith**, **Alex Bentley**, and **Leah O'brien**, who have all found their own adventures and purpose, thank you for your part in keeping me sane. Ours will be a bond forever, but we don't all have to go to the same old folks' home, do we?

To **Simon Smith**, for knowing these waters, **Carys Smith**, for her kindness, to **Olivia Smith**, for her humour, and to **Eddie**, for being a big ginger, I couldn't be here without you. Thank you for the years of love, who could have asked for a better family?

Saving the best for last, **Beth Young**. Any trial is surmountable knowing I am coming home to you, **Nala**, and **Toby**. You have been there through the highs and lows, thank you for being my port in the storm.

For some of these people, this will inevitably be goodbye, but I am glad you were a part of this chapter of my life, and I hope I made a good part of yours.

I can't wait to see what's around the corner.

Two roads diverged in a yellow wood,
And sorry I could not travel both
And be one traveler, long I stood
And looked down one as far as I could
To where it bent in the undergrowth;

Then took the other, as just as fair,
And having perhaps the better claim,
Because it was grassy and wanted wear;
Though as for that the passing there
Had worn them really about the same,

And both that morning equally lay
In leaves no step had trodden black.
Oh, I kept the first for another day!
Yet knowing how way leads on to way,
I doubted if I should ever come back.

I shall be telling this with a sigh
Somewhere ages and ages hence:
Two roads diverged in a wood, and I—
I took the one less traveled by,
And that has made all the difference.

The Road Not Taken - Robert Frost

Table of Contents

CHAPTER 1:	INTRODUCTION AND AIMS	7
Section 1.1	Introduction to Metal Organic Framework Nanosheets	7
Section 1.2	Porphyrin-based Nanosheets.....	9
Section 1.3	Fundamental Analysis of Zn ₂ (TCPP)	11
Section 1.4	Photophysical Analysis of Zn ₂ (TCPP)	15
Section 1.5	Sensing for Phosphate	20
Section 1.6	Aims	27
CHAPTER 2:	TECHNIQUES AND METHODS.....	35
Section 2.2	Optical Techniques for Photophysical Study	36
Section 2.3	Imaging the Morphology of Nanomaterials	41
Section 2.4	Fundamental Characterisation Techniques	44
Section 2.5	References.....	49
CHAPTER 3:	EFFECT OF AGGREGATION ON EXCITON DYNAMICS IN PORPHYRIN-BASED METAL ORGANIC FRAMEWORK NANOSHEETS	50
Section 3.1	Abstract.....	50
Section 3.2	Introduction	51
Section 3.3	Results and Discussion.....	52
Section 3.4	Conclusions	67
Section 3.5	Experimental	68
Section 3.6	References.....	70
Section 3.7	Supporting Information	73
CHAPTER 4:	EFFECT OF POST-SYNTHETIC METALATION ON EXCITON DYNAMICS IN PORPHYRIN-BASED METAL ORGANIC FRAMEWORK NANOSHEETS	116
Section 4.1	Abstract.....	116
Section 4.2	Introduction	117
Section 4.3	Results and Discussion.....	120
Section 4.4	Conclusions	128
Section 4.5	Experimental	130
Section 4.6	References.....	132
Section 4.7	Supporting Information	134
CHAPTER 5:	PHOTOLUMINESCENCE NANOSPECTROSCOPY OF PORPHYRIN-BASED NANOSHEETS	153
Section 5.1	Abstract.....	153
Section 5.2	Introduction	154
Section 5.3	s-SNOM of Metal Organic Framework Nanosheets	157
Section 5.4	Photoluminescence Nanospectroscopy	159
Section 5.5	Conclusions	161
Section 5.6	References.....	162
Section 5.7	Supporting Information	163
CHAPTER 6:	SENSING FOR PHOSPHATE FERTILISERS USING FUNCTIONAL NANOMATERIALS TO MODIFY GRAPHENE AND OTHER CARBON ELECTRODES	172
Section 6.1	Abstract.....	172
Section 6.2	Introduction	173
Section 6.3	Sensing using Zn ₂ (TCPP) MONs	175
Section 6.4	Sensing using Polypyrrole MIP	185
Section 6.5	Sensing using Electroactive MIP	188
Section 6.6	Conclusions	202
Section 6.7	Experimental	204
Section 6.8	References.....	207
Section 6.9	Supporting Information	210
CHAPTER 7:	CONCLUSIONS AND FUTURE OUTLOOK	231

Chapter 1: Introduction and Aims

Section 1.1 Introduction to Metal Organic Framework Nanosheets

Metal organic materials are a class of materials comprising of organic ligands coordinated to metal ions or clusters resulting in molecular architectures ranging from individual complexes, discrete cages, extended polymers, and crystalline materials (Figure 1.1).¹⁻⁷ As a class of crystalline porous materials, metal-organic frameworks (MOFs) constructed from three-dimensional networks of metal ions bridged by rigid organic linkers, offer a wide diversity in organic linker selection, metal combinations, and post-synthetic functionalisation. MOFs and their derivatives are chemically tuneable, making them especially suitable for surface interaction applications such as sensing or catalysis. High active site density and internal surface area also give them advantages over other materials.^{1,7-22}

The access of guest species to the internal surface area of MOFs is however often diffusion limited, and therefore surface interactions can be inhibited. As such, a class of MOF-based two-dimensional materials, or metal organic framework nanosheets (MONs), have become a rapidly growing focus in literature, with references to these materials first appearing in 2008 and steadily accumulating each year until >350 papers had been published by 2020.²² MONs are constructed similarly to MOFs, via rigid organic linkers coordinated to metal ions, except with minimal growth in the third dimension. MONs are established as a distinct class of hybrid nanomaterials defined as: [1] consisting of organic ligands coordinated to metal ions or clusters with continuous connectivity in two dimensions, but only non-covalent interactions between layers in the third dimension; [2] being highly anisotropic, approaching monolayer thickness; and [3] freestanding which can be isolated without support or scaffold.¹

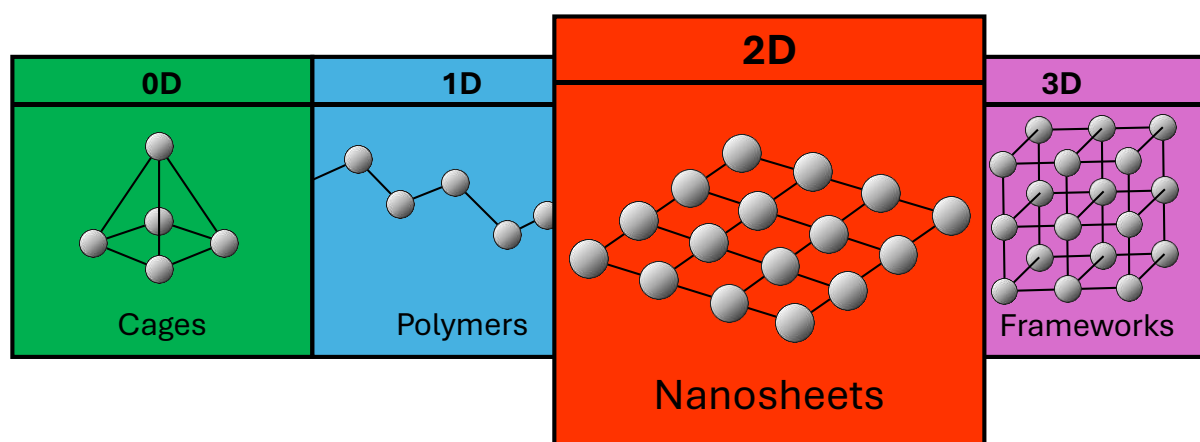


Figure 1.1 The dimensions of metal-organic chemistry, with metal ions shown as spheres, and organic linkers as rigid bridging units.

As two-dimensional materials, MONs benefit from high external surface areas.^{22,23} As such, the physical and chemical properties can be designed towards specific applications, making the opportunities represented equally diverse. Specifically, literature examples include catalysis, electronics, sensing, separation, gas storage, drug delivery, imaging, and more.^{1,5,10,22-26}

Given the reversible nature of covalent coordination bonds, metal organic structures form repeatable structures, dependant on the choice of metal and linker used.^{1,22,27} Metal centres in particular form a range of structures in metal organic nanomaterials, known as secondary building units (SBUs), which direct the topology of the extended structure (Figure 1.2). The selection of metal ions and linkers towards reliable SBUs, such as those seen in Figure 1.2, can therefore produce materials with strong in-plane interactions compared to the interlayer.

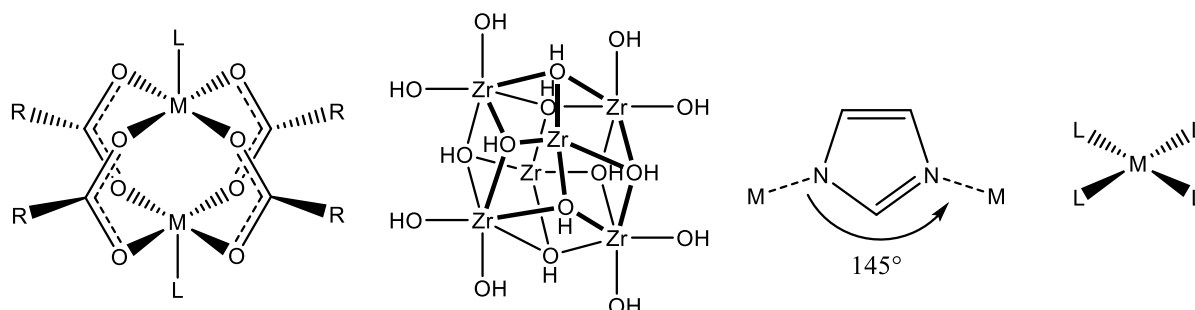


Figure 1.2 Common SBUs in MONs. (Left to right: paddlewheel, zirconium cluster, zeolitic imidazolate, and square planar).¹

The literature on the synthesis of MONs can be categorised into two broad approaches: either “top-down” exfoliation of layered MOFs, or the “bottom-up” synthesis, where conditions direct a reaction to spontaneously produce isolated nanosheets.^{1,7,23,26,28,29} The MONs produced using top-down approaches require multi-stage processing to produce materials suitable for their application (i.e., uniform thin-films), and often result in low yields.^{23,26} Chemical or physical exfoliation is required after the synthesis of bulk crystal, and dispersions may require stabilisation using a surfactant, which may affect the processing before deposition. In contrast, bottom-up methods are single-step syntheses which can be high yield, but can produce relatively thick (5 – 50 nm) nanosheets, or rely on the use of substrates or surfactants.²⁶

The synthetic approach used is effective for different metal-ligand combinations, or “systems”, and are therefore selected using several deciding factors. Namely, the chemical and physical stability of product nanosheets to vigorous top-down processing methods, solvent choices, the tendency of metal-organic products to self-assemble as monolayer nanosheets compared to bulk, or the desired scale of a process. An overview of common approaches is shown in Figure 1.3, providing bottom-up and top-down synthetic routes.¹

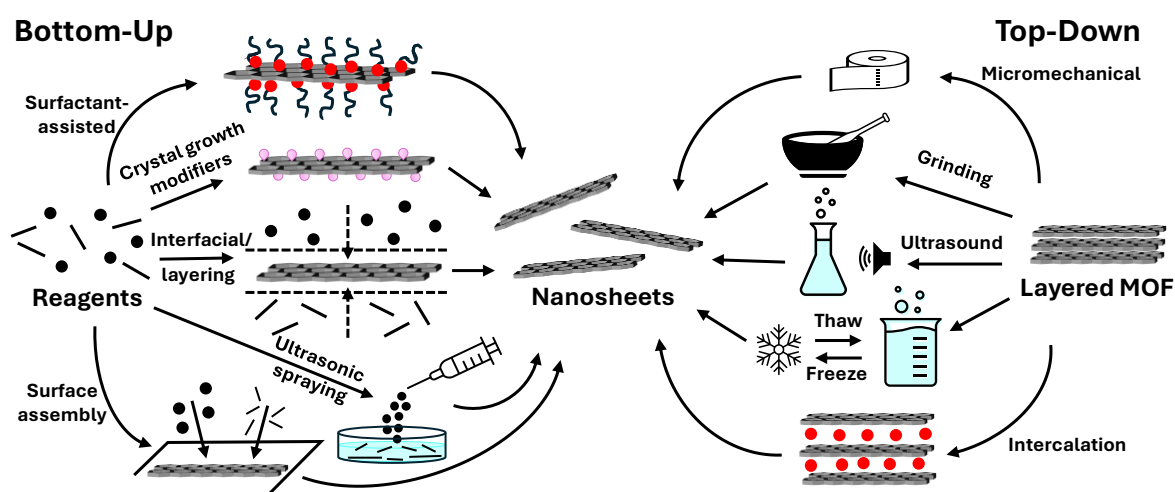


Figure 1.3 Methodologies for bottom-up and top-down synthesis routes to freestanding MONs. Reproduced from Ashworth et al.¹

Section 1.2 Porphyrin-based Nanosheets

Porphyrins are important biological molecules comprising of a tetracycle of pyrrolic units, which famously form the basis for chlorophyll (chlorins) and haemoglobin active sites (porphyrins).^{30,31} These molecules are commonly used for gas transport, catalysis, and light absorption in nature, making their synthetic counterparts popular in research, particularly surrounding their photophysical and redox properties. The macrocycle centre contains labile amine protons, the dissociation of which is highly dependent on the chemical environment, allowing chemical tunability.^{32–34} These central protons can be displaced by metal ions, which sit coordinated in the plane of the porphyrin ring (Figure 1.4).^{24,34} Metalloporphyrins are extensively studied in literature for their potential use in applications such as photothermal cancer therapy, biosensing, and optoelectronics.³⁴

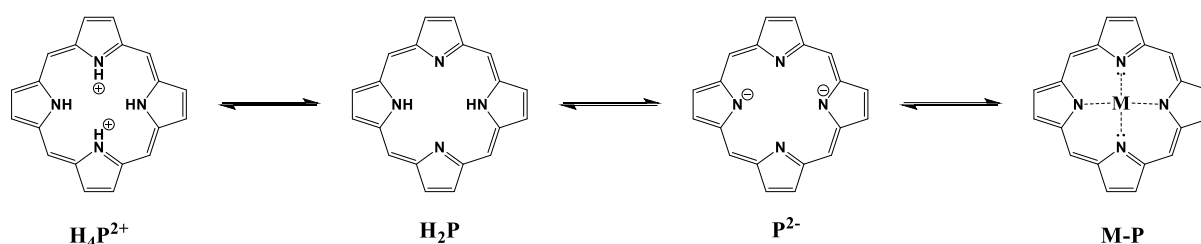


Figure 1.4 Protonation of the porphyrin macrocycle, and metalation to produce metalloporphyrin.³⁰

Notably, porphyrins are strongly absorbing in the UV-visible region, and their absorption can be tuned by adjusting the chemical structures. This electronic absorption, combined with their stability, makes them promising photosensitisers for light harvesting. Porphyrin MOFs are highlighted in the literature as good models for mimicking natural photosynthesis (e.g., highly ordered chlorophylls, which are porphyrin derivatives).^{25,35}

MONs based on tetra(carboxyphenyl)porphyrin ligands (TCPP) are amongst the earliest and most widely investigated due to their proclivity for forming high aspect ratio nanosheets due to their planar structure and high connectivity.^{33,36,37} TCPP MONs formed from zinc, copper, or zirconium metal nodes are commonly reported in literature, presenting a rich variety of structures, syntheses, and properties.^{1,6,22,36,38–41} As shown in Figure 1.5, the carboxylic acid group is deprotonated to form coordination bonds in a paddlewheel SBU, creating an extended structure in the plane of the porphyrin. The 2D porphyrin layer forms square channels, which are not interpenetrated, with dimensions of 11.8 Å.⁴² This, combined with the optoelectronic properties and accessible metal sites native to the porphyrin ligand, have led to a diverse range of applications including photocatalytic CO₂ reduction^{40,43}, solar water splitting^{44,45}, photosensitisers biomimetics, antimicrobial,⁴⁵ fluorescence sensors^{4,5,39}, therapeutics⁴¹, electro-⁴⁰ and photo-catalysis³¹, energy storage²⁹, separation²⁹, capacitors⁴⁶, antimicrobial⁴⁷, solar cells²⁹, and electronics applications.³⁶

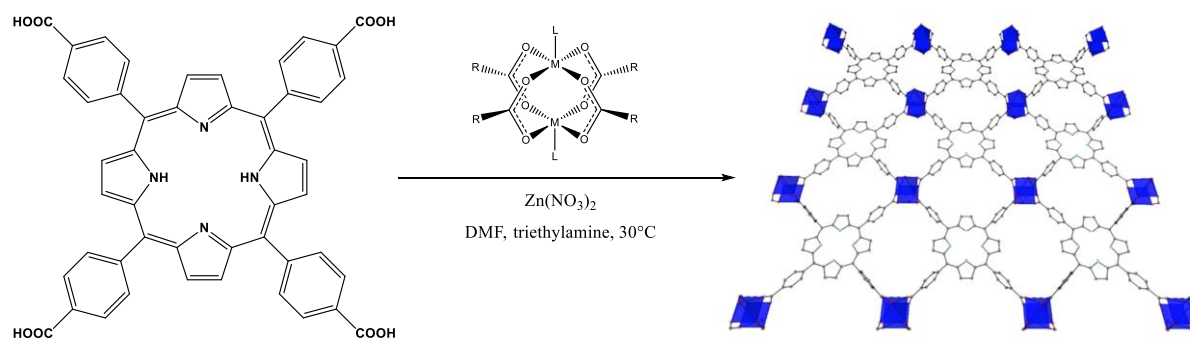


Figure 1.5 Scheme for the batch synthesis of Zn₂(TCPP) at room temperature.

The zinc-based MON produced using a TCPP linker is one of the earliest reported, first synthesised in 2009 by Choi et al. with the chemical formula $Zn_2(ZnTCPP).3H_2O.2DEF$, where DEF is axially coordinated diethylformamide and the porphyrin linker metalated during high temperature synthesis.³⁷ Most reported porphyrin MOFs are synthesised using solvothermal methods, usually with the addition of additives to direct lateral growth or inhibit stacking. These may vary in reliability, morphology of materials produced, or scalability. For example, Chen et al. report the use of 4,4'-biphenyldicarboxylic acid (BPDC) as a nucleation modulator to reduce the thickness of $Zn_2(TCPP)$ nanodisks from 5 to 0.6 μm (DMF, 150 °C, 1 hr),⁴⁵ Cao et al. used the surfactant 1-decanesulfonic acid sodium salt (DASS) to direct self-assembly using micelles (DMF + water, 25 °C, 15 days),³¹ Jon et al. also used a surfactant, polyvinylpyrrolidone (PVP) (DMF + EtOH, 80 °C, 16 hr).⁴³ This use of PVP during the synthesis of $Zn_2(TCPP)$ MONs has been popular in other literature also.⁷ Similarly, acidity regulators have been used to modify the structure produced when synthesising TCPP-based MOFs.^{45,48}

The addition of such a tetra(carboxy)porphyrin-based MON to organic solar cells was shown by Sasitharan and Foster et al. to a near doubling of their power efficiency, at the time of publishing the highest performing fullerene-based organic photovoltaic (OPV) devices in literature.^{13,36} This MON was reported as $Zn_2(ZnTCPP)(DMF)_2$, with dimethylformamide (DMF) coordinated to the paddlewheel. A following paper by Ashworth and Foster et al. dedicated to scaling the synthesis of this material describes a room temperature methodology which leads to $Zn_2(H_2TCPP)$, with no metalation at the porphyrin centre.³⁶

This variety in synthetic methods highlights the variability in the structure and morphology of the final product. The production of this porphyrin-based MON with a vacant cavity presents the opportunity for expansive study to determine the differences post-synthetically metalation might have, especially on the photophysical properties relevant to the use of these materials in optical applications.^{1,49} In particular, the study of light harvesting, and energy transfer dynamics could offer insight into how to improve these materials for use in photovoltaic technologies. This thesis therefore focuses on the photophysical investigation of $Zn_2(TCPP)$ MONs, focusing on differences in morphology and metalation.

Section 1.3 General Analysis of Zn₂(TCPP)

A variety of techniques are routinely used to characterise MONs, often relying on complementary results to identify the structure, morphology, and properties. The expected unit cell for Zn₂(TCPP) MONs is formed of one TCPP ligand and two zinc atoms, with two dimethyl formamide (DMF) groups coordinated to the axial position on the paddlewheel SBU. The crystal structure of nanomaterials are routinely characterised by X-ray diffraction (XRD) techniques, usually powder X-ray diffraction (P-XRD) for MONS. Literature for P-XRD analysis of Zn₂(TCPP) MONs is ubiquitous for fundamental characterisation. Cao et al. especially espoused the crystal structure analysis of TCPP-based metal organic nanomaterials as a foundational approach to understanding the way packing affects the photodynamics of a supramolecular porphyrin material.³¹ There is good agreement in literature that the P-XRD patterns for Zn₂(TCPP) present peaks at 8 and 18°, for the crystal orientations 002 and 004 respectively, which would represent stacked sheets. Peaks 5-8° are also common, assigned to randomly oriented sheets on the surface with 100 and 110 orientations.⁷ Cao et al. calculated a large interplanar distance of 14.6 Å in layered Zn₂(TCPP), perhaps representing a bilayer.³¹

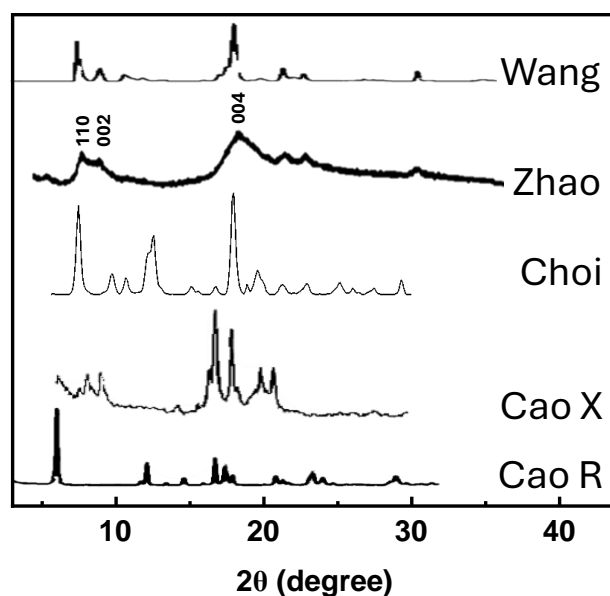


Figure 1.6 PXR D data for Zn₂(TCPP) and related materials found in literature from Cao et al.³¹, Cao X et al.⁵⁰, Choi et al.³⁷, Zhao et al.⁷, and Wang et al.⁵¹

Dynamic light scattering (DLS) is useful for size analysis of nanoparticles in suspension, although limited by the assumption that particles are spherical. Nevertheless, this is still useful for analysis of anisotropic nanosheets, particularly as a comparative technique. In literature, DLS analysis has been used to measure concentration dependant aggregation of Zn₂(TCPP) in dispersion.⁴⁷ As shown in Figure 1.7, Zhang et al. altered the concentration from 0.02 to 0.5 mg mL⁻¹ (25x), correlating with a particle size increase of 463 to 1369 nm (~3x).

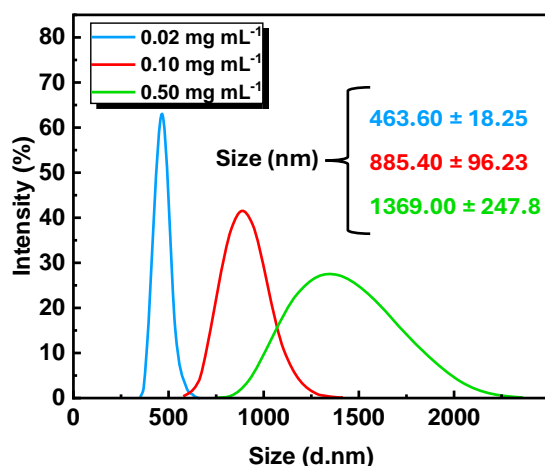


Figure 1.7 Concentration dependant aggregation measured using DLS by Zhang et al.⁴⁷ Size is reported as diameter (d) in nm, however this assumes measurement of spherical particles and is likely to be inaccurate for nanosheets.

Scanning electron microscopy (SEM) is one of the most common techniques used to study metal organic framework nanosheets, and Zn₂(TCPP) is no different. The bulk MOF usually forms layered squares 1 – 20 μm across, clearly shown by Zhao et al. and Wiśniewski et al. in Figure 1.8.^{7,40}

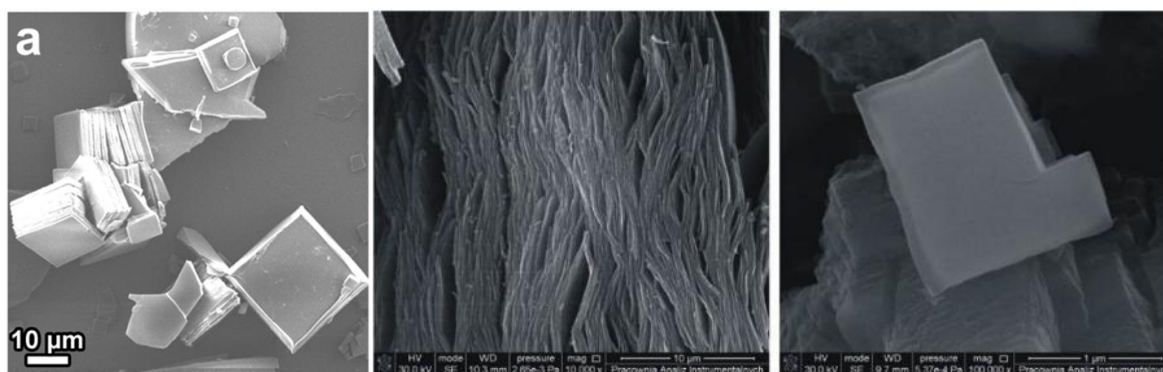


Figure 1.8 Example SEM of Zn₂(TCPP) formed by Zhao et al.⁷ (left), and Wiśniewski et al. (centre and right).⁴⁰

When synthesis is attempted to isolate nanosheets via micelles³¹ or surfactant^{7,43}, SEM is particularly useful for displaying the morphology changes visually. This is realised in the work by Jin et al., where the structure became much more diffuse and leaf-like upon the addition of PVP to the synthesis, which was varied 0 – 1000 mg (Figure 1.9).⁴³

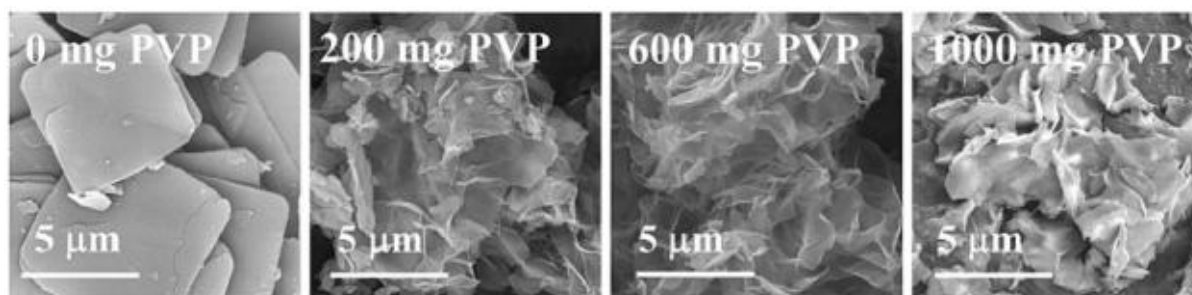


Figure 1.9 Example SEM of Zn₂(TCPP) nanosheets formed by Jin et al., with change induced by varying amounts of PVP added during synthesis.⁴³

In the analysis of $Zn_2(TCPP)$ MONs, energy dispersive spectroscopy (EDS) can be useful for confirming the distribution of elements present. As shown in Figure 1.10, EDS was used by Cao et al. to show how a $Zn_2(PdTCPP)$ MON acting as a Pt nanoparticle support had distributed palladium, but localisation of the platinum at the nanosheet edge.³¹

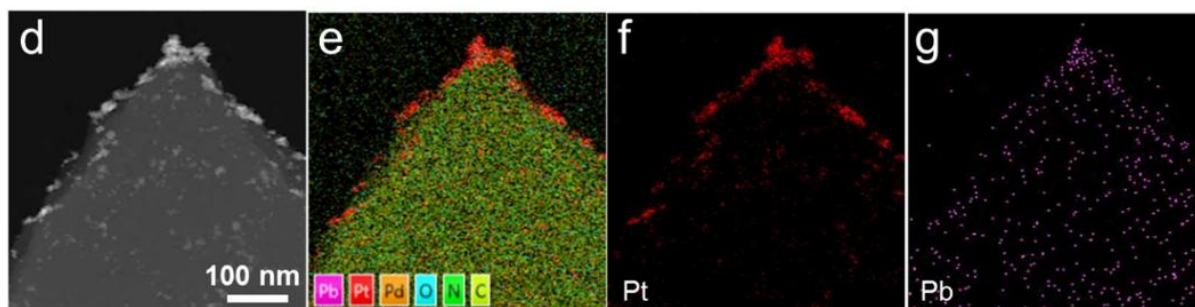


Figure 1.10 Example EDS of $Zn_2(Pd-TCPP)$ nanosheets formed by Cao et al.

For nanosheets approaching monolayer, SEM becomes limiting, and transmission electron microscopy (TEM) is often used to achieve higher resolution, with high-resolution transmission electron microscopy (HRTEM) able to image at atomic resolution. This was used by Wiśniewski et al.⁴⁰, and Cao et al.³¹ to compare theoretical extended structures with experimental patterns, and to determine interlayer distance (Figure 1.11).

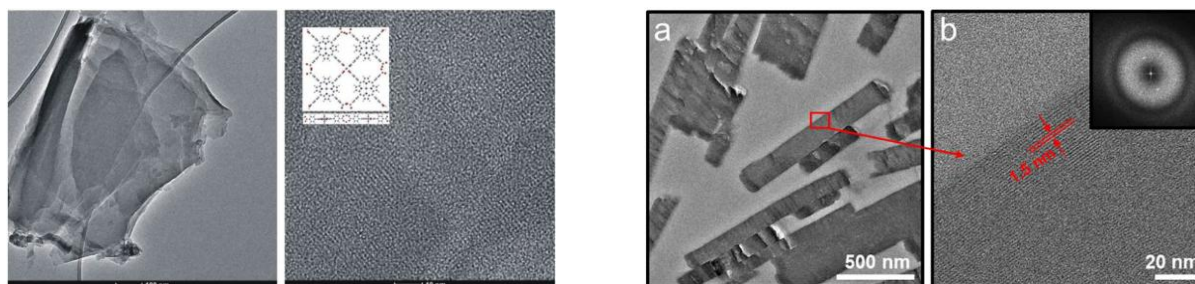


Figure 1.11 TEM and HRTEM images of $Zn_2(TCPP)$ nanosheets by Wiśniewski et al.⁴⁰ (left), and $Zn_2(Pd(TCPP))$ by Cao et al.³¹ (right).

When analysing metal organic nanomaterials, atomic force microscopy (AFM) can resolve single nanosheets, where SEM may be limited by resolution or the requirement for gold. As such, definition can be lost when analysing MONs since the particle thicknesses may be comparable to the coating, although it can still be useful for characterising layered MOF precursors. AFM is therefore useful as it allows accurate measurement of particle dimensions and allows height profiling across individual nanosheets. The drawback of AFM, is that it can only image much smaller areas ($<1 \mu\text{m}$) compared to SEM (usually 10s of μm). Thus, many AFM scans must be taken to ensure the observed morphology is representative.

Aspect ratio, defined as the width of a nanosheet divided by height, is useful for statistical analysis of nanostructures measured by AFM, as it allows definitive classification of a material as a nanosheet. Ashworth et al. defined a nanosheet as an anisotropic structure with aspect ratio of greater than 10, but most literature reports nanosheets more generally as materials with lateral dimensions $>100 \text{ nm}$ and approaching monolayer.^{1,29}

For $\text{Zn}_2(\text{TCP})$ in literature, AFM has been used not only as evidence for monolayer nanosheets, but also for statistical analysis. See example in Figure 1.12, where Zhao et al. profile multiple nanosheets across different AFM scans to plot a histogram of nanosheet thicknesses, finding an average of 7.6 nm .⁷

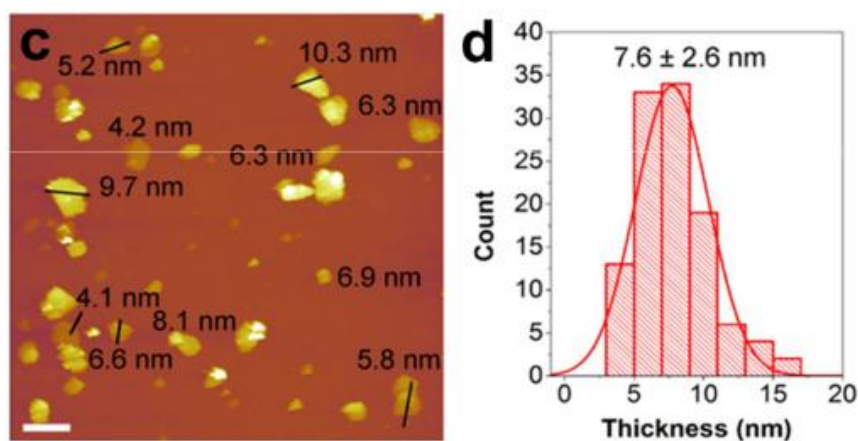


Figure 1.12 Example AFM study on $\text{Zn}_2(\text{TCP})$ MONs performed by Zhao et al.⁷

Section 1.4 Photophysical Analysis of Zn₂(TCPP)

Electronic absorption in porphyrins is well established in literature, famously characterised by Gouterman in 1961 to a standard which is still held in high regard today.³² Porphyrin spectra are characterised by Soret, or B-band, absorption ($S_0 \rightarrow S_2$) in the 415 - 430 nm region and forbidden Q-band ($S_0 \rightarrow S_1$), correspondingly less intense, at 500 - 700 nm.^{10,24,25,32,34,52-54} Electronic absorption in the aromatic porphyrins originates from $\pi \rightarrow \pi^*$ transitions.¹⁰ As outlined in the theoretical study of porphyrins by Hirao et al., the Soret and Q-bands are well modelled by one electron transitions in a four orbital system consisting of the two highest occupied π orbitals, and the two lowest unoccupied π^* orbitals.⁵⁵

The absorption spectra for porphyrins are dominated by an allowed $\pi\text{-}\pi^*$ electronic transition $S_0\text{-}S_2$, resulting in an intense peak around 400 nm known as the Soret, or B-band, absorption (Figure 1.13). The transition $S_0\text{-}S_1$ occurs via absorption in-plane across the porphyrin and is present in diprotic porphyrins (e.g., Zn₂(TCPP-H₂)) as four separate weak intensity absorptions 500-650 nm which represent pseudoparity-forbidden transitions.⁵⁵ The multiplicity of these “Q-bands” is due to the asymmetry when two protons are present in the porphyrin centre, creating two lines of symmetry x and y, each split vibrationally to create Q_x(0,0), Q_x(1,0), Q_y(0,0), and Q_y(1,0), labelled in parenthesis by the vibronic position in the upper and lower electronic states of the transition, respectively (Figure 1.13).⁵³ Since the spectroscopic absorption is directly related to symmetry, metalation at the porphyrin centre characteristically reduces the number of Q-bands from four to two as the central protons are displaced.^{32,36,53,54,56}

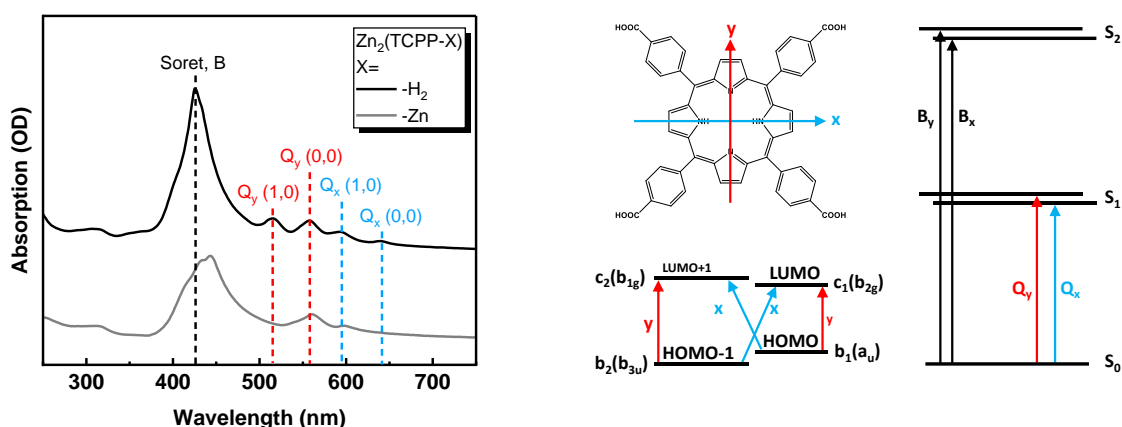


Figure 1.13 Absorption spectra of Zn₂(TCPP-X), where X = H₂ or Zn (left), and symmetry rationale behind the four Q-band absorptions in porphyrins reproduced from Valicsek et al. (right).^{32,55,56}

These electronic transitions are summarised in Figure 1.14, showing a “usual” excitation pathway from the ground state S_0 to one of two excited states S_1 and S_2 , favouring the latter. S_2 excited states would then relax by emission to the ground state (weak), or internal conversion (IC) to the S_1 state. From S_1 , electrons will either radiatively relax via red emission 600 – 700 nm or undergo intersystem crossing (ISC) to a triplet state. This ISC is the most likely fate of an S_1 excited state, with a quantum yield of 0.88. As such, the excited state lifetime of most porphyrins has a large long-lived triplet component before non-radiatively relaxing back to the ground state.^{25,34,53,54} Additionally, the agglomeration or close stacking of porphyrins enhances the rate of ISC, which explains the quenching and shorter lifetime of S_1 emission observed in porphyrin metal organic materials compared to freebase linker.

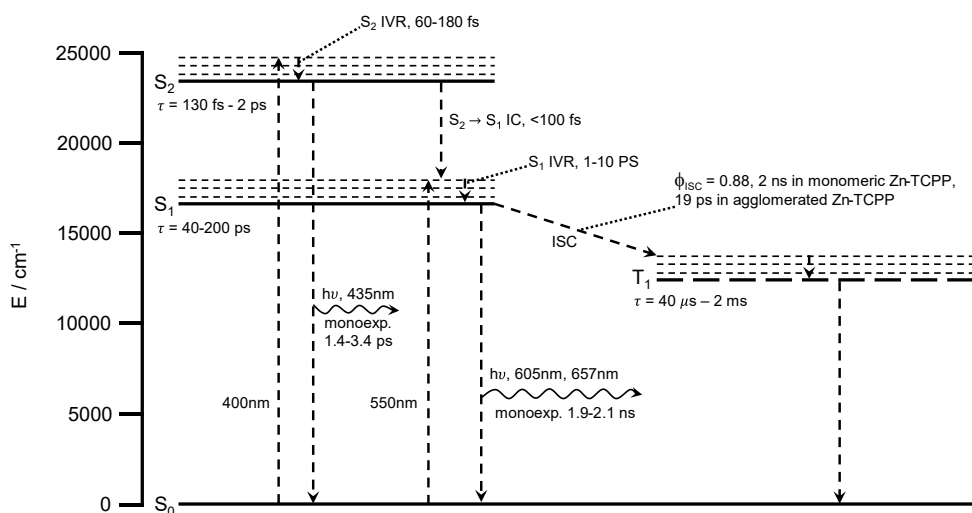


Figure 1.14 Jablonski diagram summarising data from Li et al., Haber et al., and Yu et al.^{25,34,53,54}

Examples of UV-visible spectra for $\text{Zn}_2(\text{TCPP})$, shown in Figure 1.15, demonstrate that the electronic absorption by $\text{Zn}_2(\text{TCPP})$ is similar to freebase porphyrins. Notably, Haber investigates the electronic absorption of the TCPP linker, and comparison reveals a redshifting of the Soret band from ~ 415 to ~ 425 nm in packed structures compared to freebase porphyrin. This is due to coupling from π orbital stacking, known in dyes as J-aggregation, reducing the energy gap for ($S_0 \rightarrow S_2$) transitions.^{25,34,49}

Again, comparison reported by Haber et al. of the spectrum for TCPP with absorption by $\text{Zn}_2(\text{TCPP})$ shows a reduction in the number of Q-bands from four to two upon MOF formation (Figure 1.15). Likely this is due to incidental metalation at the porphyrin centre by the high temperatures of solvothermal synthesis.

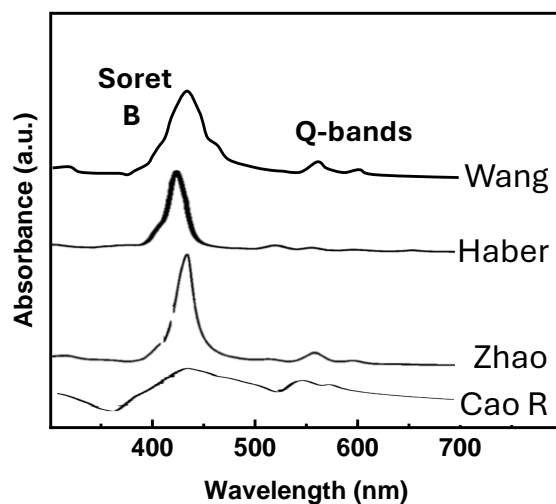


Figure 1.15 Examples of UV-visible absorption spectra for $\text{Zn}_2(\text{TCPP})$ and similar materials in literature from Cao et al.³¹, Zhao et al.⁷, and Wang et al.¹⁶ Additionally, the absorption spectrum of TCPP by Haber et al.³⁴

It is established in literature that excited porphyrins relax by red fluorescence from the S_1 state, usually with two bands at 650 and 720 nm.³⁴ Emission spectra of $\text{Zn}_2(\text{TCPP})$ in literature (Figure 1.16), similarly shows emission $S_1 \rightarrow S_0$ at 610, 650, and 720 nm, where the first two S_1 emissions are designated in literature to $Q(0,0)$, $Q(0,1)$.^{4,25,53,54} Additionally, low intensity blue emission $S_2 \rightarrow S_0$ at ~ 450 nm is sometimes reported in literature, as shown in the reported

spectra by Baskin et al., and Li et al., breaking Kasha's rule. It should also be noted that when compared with the freebase TCPP linker molecule, all emission by $Zn_2(TCPP)$ is greatly quenched.³⁸

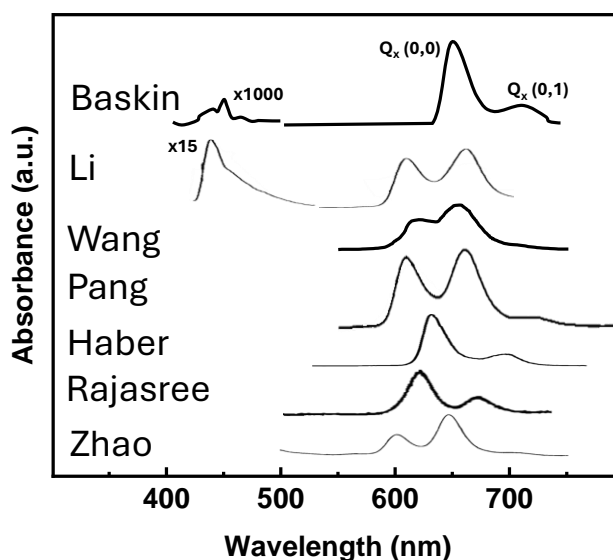


Figure 1.16 Example emission spectra of $Zn_2(TCPP)$ from literature by Zhao et al.⁷, Rajasree et al.³³, Haber et al.³⁴, Pang et al.³⁹, Wang et al.¹⁶, Li et al.²⁵, and Baskin et al. (note Baskin report on free porphyrin, not a MON).^{53,54}

Using time-correlated single-photon counting (TCSPC), Mehrzad Sajjadinezhad et al. showed the emission lifetime reduction between TCPP and $Zn_2(TCPP)$ MONs when excited at 410 nm (Figure 1.17). The emission lifetime from the S_2 excited state fitted by a monoexponential decay, and is low quantum yield compared to emission from the S_1 excited state.²⁵ Most time-resolved emission studies in literature suggest that emission from S_2 is in the order of 240 fs - 3.6 ps, with reported lifetimes of 2 ns for emission by longer lived S_1 excited states.^{25,53,54}

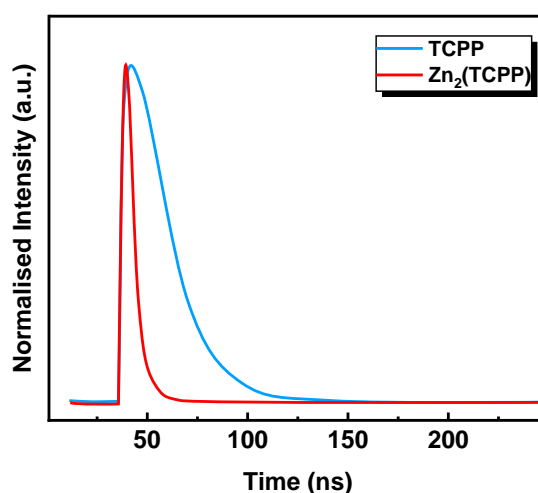


Figure 1.17 TCSPC of TCPP and $Zn_2(TCPP)$ by Mehrzad Sajjadinezhad et al.³⁸

Non-radiative processes with ultrafast lifetimes are measured in porphyrin MOFs by femtosecond transient absorption pump-probe spectroscopy. The changes in excited state spectra and lifetime upon MOF formation are well described by Li et al., shown in Figure 1.18.²⁵ Excitation at 400 nm is common due to the ease of experimentally producing this excitation wavelength and the high extinction coefficient of the Soret band. The resultant transient

absorption spectra show intense ground state bleaching at 425 nm corresponding to the Soret absorption, and a resultant excited state absorption broadly at 450 nm. Transient absorption is also observed for the Q-bands, enhanced in the MOF recorded by Li et al. to show a ground state bleach at 550 nm, and corresponding excited state absorption at 575 nm. The Soret ground state bleach redshifts according to the absorption spectrum, and the excited state absorption broadens towards lower energy as delocalisation improves in the extended π system. As seen in Figure 1.18, the kinetics of ground state bleach recovery are also affected, with the MOF experiencing less contribution from short lifetime components, and therefore taking much longer to relax. This is attributed to enhanced intersystem crossing in the MOF compared to the linker, leading to fewer S_1 excited states which may relax by emission. This matches the reduced emission observed on MOF formation and indicates electrons in a porphyrin MOF are more likely to decay via a triplet state.

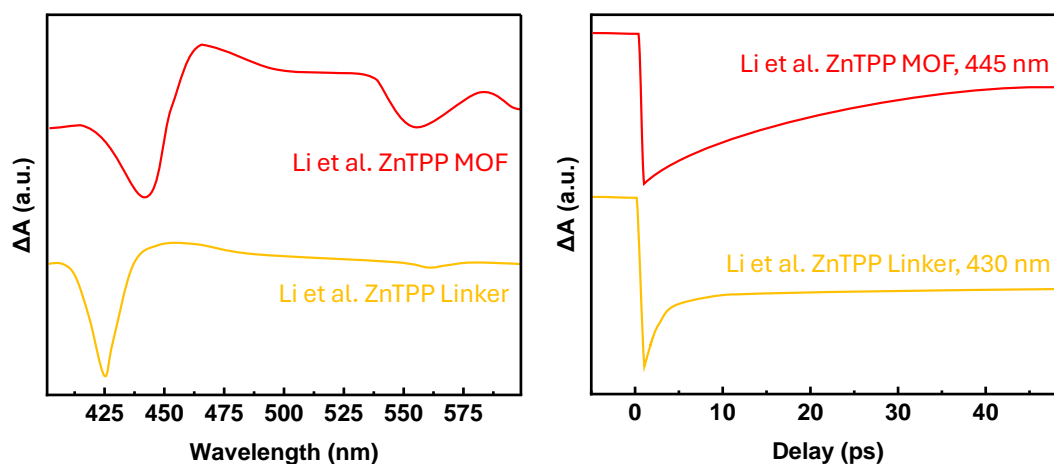


Figure 1.18 Transient absorption spectra (left) and kinetics (right) of ZnTPP linker and ZnTCPP MOF as reported by Li et al.²⁵

Bimolecular recombination of excited states, or exciton-exciton annihilation, occurs when two excited states combine to induce relaxation. Proximity, therefore, greatly effects the rate of this process, making the rate of exciton annihilation dependent on the density of excited states. This can therefore be investigated via power dependant femtosecond resolution transient absorption spectroscopy. These exciton dynamics in $\text{Cu}_2(\text{TCPP})$ were investigated by Gu et al., (summarised in Figure 1.19), where S_2 excited states relax via competitive pathways of vibrational relaxation or exciton annihilation. The rate of exciton “hopping”, inherent to the material, is the main factor which decides the amount of exciton annihilation. As such, this alternate route can reduce the emission intensity from S_1 states and offers insight into the exciton diffusion pathlength in an excited porphyrin material.

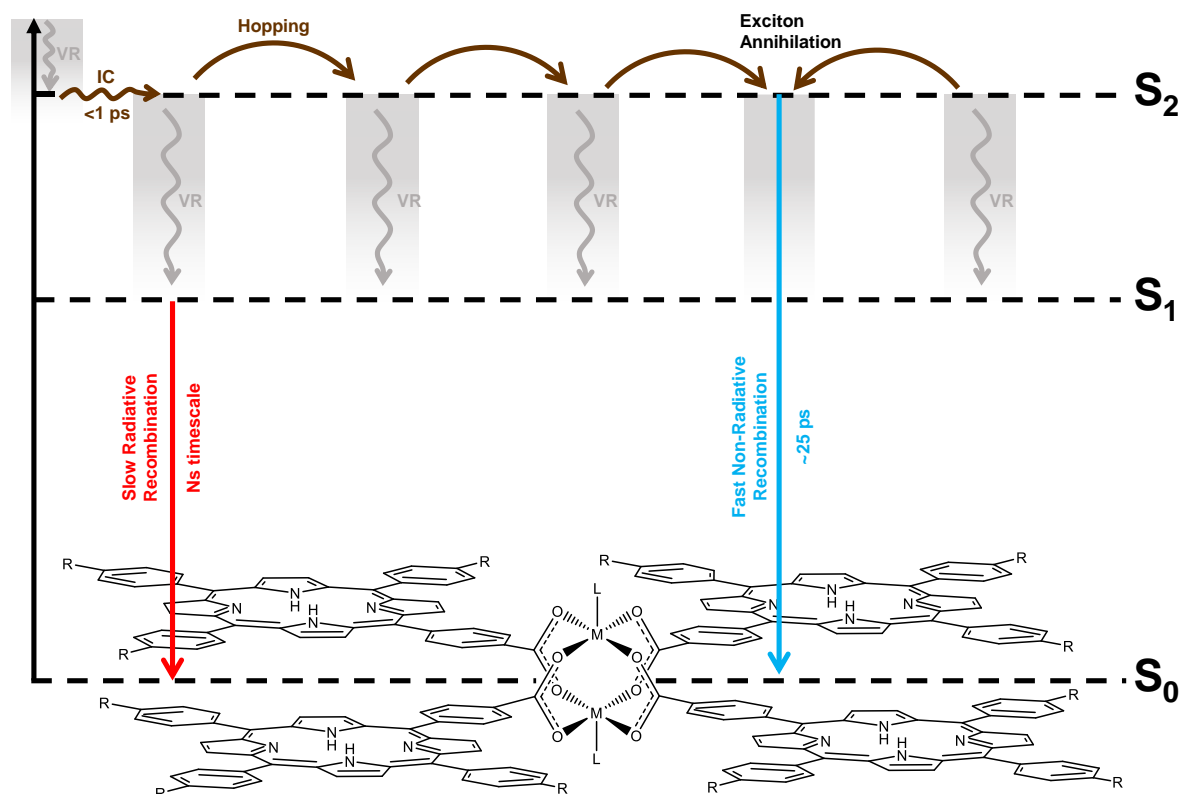


Figure 1.19 Exciton dynamics in TCPP-based MOF nanofilms reproduced from Gu et al.¹⁰

It is obvious from the literature surrounding $\text{Zn}_2(\text{TCPP})$ MONs that nanosheets with the same structure can have extreme morphological or chemical differences based on solvothermal synthesis conditions. This has included variable metalation at the porphyrin centre, amount of stacking observed within particles, or the shape of those particles between square sheets, leaves, or undefined monolayer nanosheets. Even nanosheets formed by the same synthesis diluted to different concentrations form differently sized agglomerates in suspension.

Understanding the effects these changes have on the photophysical processes in $\text{Zn}_2(\text{TCPP})$ MONs is key for identifying the optimal characteristics needed for the many and varied applications promulgated in literature. Thus, we present the opportunity for an in-depth characterisation of $\text{Zn}_2(\text{TCPP})$ via the manipulation of particle size and chemistry. This is achieved by complementary techniques, culminating in a detailed discussion surrounding the excited state dynamics of these materials.

Section 1.5 Sensing for Phosphate

Inorganic phosphate, a metabolically important nutrient to both plants and animals, is used globally to fertilise agricultural crops.⁵⁷⁻⁶⁰ Vital for physiological energy utilisation processes including photosynthesis and respiration, phosphate can greatly improve the production yield of farmland by promoting early root formation and growth, greater flowering and seed production, and improved fruit, vegetable, and grain quality.^{58,60} Other advantages of phosphate fertilisers include resistance to cold, water efficiency and early maturation of crops, reducing the energy and land requirement of food production and so can be considered a key environmental and humanitarian tool in the effort of feeding a rapidly growing human population.⁶¹ Accordingly, the global use of phosphate fertilisers has more than tripled from 4.6 Tg Yr⁻¹ in 1960 to 17.5 Tg Yr⁻¹ in 2013 (0.4 to 1.2 g m⁻² cropland Yr⁻¹).⁶¹

Phosphate species can be categorised as either inorganic, in the form of mono- or di-protic phosphoric acid, or organic, where species are monoester (83-95%), diester (4-9%), or teichoic acid, an orthophosphate diester which links sugar units (~12%).⁵⁸ Diphosphate inorganic molecules (pyrophosphates) and higher polyphosphates also exist.⁶⁰ Most phosphate fertilisers are produced by reaction of mined calcium phosphate with a strong acid.⁶² For handling, phosphoric acid is then converted to solid di- and mono- ammonium phosphate, or sometimes phosphorus pentoxide, which readily convert to phosphoric acid when exposed to water.

Detrimental effects of overuse of phosphate fertilisers can cause acidification of soil, or eutrophication in waterways exposed to run-off from fields, a process where overstimulated algae growth fatally blocks light to sub-aquatic species.^{58-60,63-66} It is therefore advantageous to monitor the concentration of phosphate in soils, allowing more appropriate fertiliser distribution.^{58,67,68} Furthermore, the capacity for sub-field phosphate monitoring allows even greater specificity for targeted spreading so quick, inexpensive, and simple analyses are desirable.

The amount of dissolved orthophosphate in groundwater (usually 0.01-0.05 mg L⁻¹ on farmland) is a good indicator of the phosphate available for plant roots.^{58,65} When fertiliser becomes 'fixed' by rapid adsorption to soil aggregate surfaces followed by diffusion into the porous matrix, it is inaccessible for uptake. Detection of only this inorganic concentration provides a facile approach to phosphate sensing as organic species may account for 50-80% of total phosphate and should not be discounted. In permanent pasture soils, organic nitrogen and sulphur components increase to equilibrium relatively quickly over 5-20 years, whereas the concentration of phosphate accumulates over time and is more varied, either associated with carbon, nitrogen and sulphur in soil humus or as independent organic phosphate compounds.⁵⁸

Diprotic orthophosphate prevails in soils <pH7, whilst monoprotic orthophosphate dominates above neutral pH. Inorganic (treated rock phosphate) is preferentially uptaken by plants when available, most easily in pHs 6.0-7.0, but in orthophosphate poor soils, plants have been proven able to dissolve organic phosphate (usually from animal manure) to form orthophosphate suitable for uptake.⁵⁸ Accounting for pH during sensing measurements therefore is important due to the varied selectivity with speciation between mono- and di-valent form.⁶⁸

Traditional analysis methods (e.g., high performance liquid chromatography, Olsen procedure) are often complex, requiring sample transport to a lab and skilled analysts, increasing the time and cost associated with mapping fertiliser, and commercial mapping services may not be

reliable.^{58,64,69,70} Optical sensing techniques can also be used to analyse soil. Raman spectroscopy is a promising example utilised in 2005 by Bogrekci et al. to develop a portable spectroscopic soil analyser.^{58,71} Whilst compact enough for on-site measurement, the sample preparation times and operator requirements prohibit full automation. Near-infrared spectroscopy has been adapted from lab equipment for in-field measurements, but experienced error margins of 27.5%, and the devices were not successfully brought to commercial use.^{58,69}

The ideal phosphate monitoring device should be compact and suitable for simple or remote operation, perhaps allowing synced detection by multiple sensors to provide a real-time data map over a large area of farmland.⁶⁴ Established techniques often require the digestion of compounds to orthophosphate to account for organic species, adding a pre-treatment step that would inhibit automated remote systems.⁵⁹ A successful technology would be long-lived, sensitive to multiple phosphate species, minimally sensitive to interferences, robust to changing weather conditions, easy to transport to remote locations, and require little maintenance. Alternative techniques to the established lab practices are therefore needed.

Luminescent or calorimetric sensing involves a change in optical or spectroscopic properties on interaction with the analyte where specific quantification can be processed using benchtop equipment.^{59,60,64,66} Three main methods of measuring phosphate concentration were identified by Mao et al. as routine colour comparison or spectrophotometer-based techniques: the vanado-molybdo-phosphoric acid, stannous chloride, and ascorbic acid methods. These can however be insensitive, unreliable, lack selectivity by emission in the presence of other anions/oxides/silicates, and rely on solvent/reagent mixing, which does not lend itself to remote/unoperated design.^{59,60}

Electrochemical sensors aim to monitor changes in electrical properties across the surface of a working electrode e.g., capacitance, resistance, or potential, when exposed to a chemical analyte. Usually this involves both a counter electrode to complete the circuit and a reference electrode which is chemically inert to interaction with the analyte, allowing comparison between the response from the reference to the working electrode.^{58,64}

Enzymes can be extremely selective, and when immobilised on a surface, can also induce electrical response, known as a biological sensor.^{58,63,66,72} Commonly, this would not involve a direct change but would stimulate the release of a product which would alter an electrical property over an electrode/electrochemical cell or a spectroscopic property e.g., in the work by Campanella et al., where the surface of raw potato contained enzymes which reacted in the presence of phosphate to generate glucose, the concentration of which could be measured by a potentiometer.⁶³ Due to the temperature dependence of enzyme activity, degradation and potential biological activity by other organisms, the long-term deployment of this kind of sensor in the field is unlikely to be successful as the environment would have significant impact on the response generated.⁷³

Soil sensors will have to contend with many other factors, including soil particle size, type, temperature conditions, and water permeation. Sensitivity should be in the ppm range for soils, and the ppb range for aqueous waste streams when monitoring agricultural runoff.⁶⁰

Compact, sensitive electrochemical devices can be fabricated which allow portable, computer-controlled operation with the potential to utilise computational techniques or transducers to improve signal, but manufacture can be complicated or sensing require reagents.^{65,68,74} Avoiding a false positive by other common macronutrients e.g., nitrate-based fertilisers ($\sim 7.4 \text{ g m}^{-2} \text{ cropland Yr}^{-1}$)⁶¹, requires high selectivity.⁶⁶ Many electrochemical sensors which run the risk of cross sensitivity to other analytes employ chemical filters e.g., ion-selective electrode (ISE) membranes (glass, polymer), to prevent access to the electrodes by imposter species and therefore avoid false positives. In soil, common anionic species such as Cl^- , NO_3^- , SO_4^{2-} , HCO_3^- are likely to be smaller and less negatively charged than phosphate anions and therefore a selective barrier is difficult to achieve without also blocking the phosphate analyte.⁷⁵ Similarly, the high hydration energy of phosphate inhibits the selectivity of ISE membranes, disallowing the use of exclusion principles for reducing cross sensitivity issues.^{58,76} Chromium, copper and manganese have also been previously identified as common interferences to phosphate sensing.⁵⁸ Commercial examples of electrochemical sensors for water measurement of macronutrients exist e.g., CleanGrow who use polyvinyl chloride based ionophores as ISE membranes.^{66,77}



Ion selective electrode (ISE) membranes with selective interaction properties for phosphate have been explored, however, the drawbacks of lifetime, response time, and requirement for pre-measurement steps are identified by Mapare et al.⁵⁸ Where ISEs have an internal electrolyte solution which is bulky, can degrade, or leak, ion-sensitive field-effect transistor (ISFETs) utilise solid-state microelectronics to be smaller and more stable, offering an alternative design.^{58,68} A field-effect transistor (FET) involves the use of a gate electrode (coated in ion-selective membrane) which controls the current between two semiconductor electrodes.^{58,65} Whilst these membrane based electrodes are promising, degradation of the membrane by mechanical peeling or chemical instability reduces the lifetime significantly and signal drift can occur without constant maintenance (e.g., washing after measurements).^{58,65} For this reason, disposable electrodes may be viable as a means to preserve sensor lifetime.^{58,72}

Cross-species interaction presents significant challenges for ion sensing due to the limits of selectivity for any given sensor.⁶⁸ Microelectronic sensor arrays provide one promising solution. These sensors cross-reference the response from many sensors, each with partial selectivity to multiple analytes. If the varying response from each sensor to each individual analyte is known, accurate concentrations of each species may be inferred.^{68,81}

When adsorption of analyte to a surface influences an electronic property e.g., potential, the response is dependent on Nernst's law. As shown in Equation 1.1, the potential across the diffusion layer (ψ_0) is proportional to the log of activity (equivalent to concentration at these ranges); as the target ion approached the surface the concentration of analyte increases ($a_1 \rightarrow a_2$), causing the measured potential change described by Equation 1.2.⁶⁸

$$\text{Equation 1.1} \quad \psi_0 = \psi_0^0 + \alpha \ln 10 \frac{kT}{zq} (\log [a]_{\text{solution}})$$

$$\text{Equation 1.2} \quad \Delta\psi_0 = \alpha \ln 10 \frac{kT}{zq} (\Delta \log [a])$$

Where ψ_0^0 is a surface potential constant, α is a dimensionless sensitivity factor between 0 and 1, k is Boltzmann's constant, T is temperature, z is the valency, and q is the electric charge.

According to Fakhri et al., in the presence of multiple ionic species the Nikolskii-Eisenman equation, a generalisation of the Nernst equation, can be applied to account for contribution

by other ionic species to the potential change (Equation 1.3).⁶⁸ Here, the coefficient K_{ij} relates to the selectivity of the i -selective sensor to interfering ion j . For N ions, by formulating an array of $1 \leq i \leq N$ ion-selective sensors where the value of K_{ij} is known for each sensor $1 \leq i \leq N$, and $1 \leq j \leq N$, the measurement of N potentials (ψ_{0i}) by each sensor allows determination of i concentration (a_i) by simultaneous solution of N nonlinear equations.

$$\text{Equation 1.3} \quad \psi_{0i} = \psi_{0i}^0 + \alpha \ln 10 \frac{k_B T}{z_i q} \log \left(a_i + \sum_{j \neq i} \left(K_{ij} a_j^{z_i/z_j} \right) \right)$$

Where ψ_{0i} is the measured potential across an i -selective membrane, ψ_{0i}^0 is a surface potential constant for the target ion i , and K_{ij} is the selectivity coefficient of the i -selective sensor towards interfering ion j .

Semiconductor bandgaps are perturbed by changes in surface potential, ψ_0 as analytes are adsorbed.⁶⁸ At constant reference potentials and bias potentials across the working electrode, the Fermi level is increased in correlation with ψ_0 according to Equation 1.4, and with the capacitive voltage division ratio approaching unity, the band-gap change is directly proportional to $\Delta\psi_0$, and therefore ion concentration.⁶⁸

$$\text{Equation 1.4} \quad \Delta E_F = q \frac{C_{\text{gate}}}{C_q + C_{\text{gate}}} \Delta V_{\text{ref}} + q \Delta \psi_0 = q \Delta \psi_0$$

Where ΔE_F is the change in Fermi level, q electric charge, C_{gate} gate capacitance, C_q electrode quantum capacitance, ΔV_{ref} change in reference potential, and $\Delta \psi_0$ the change in working electrode potential.

The Nikolskii-Eisenmann equation can therefore be applied with current as the response value (Equation 1.5), where the activity is raised to the power of the sensitivity ratio instead of the valency ratio as the membranes should be selective towards different ions, even when they have the same valency. When measuring response by sensor i from a solution of only the target ion i , the gradient of the linear plot I_i vs. $\log(a_i)$ gives the value for s_{ii} . Similarly, s_{ij} can be identified by placing sensor i in a solution of analyte j and plotting I_i vs. $\log(a_j)$ according to Equation 1.6. The current constants are related by Equation 1.7, allowing the calculation of K_{ij} by Equation 1.8.⁶⁸

$$\text{Equation 1.5} \quad I_i = I_i^0 + s_{ii} \log \left(a_i + \sum_{j \neq i} K_{ij} a_j^{s_{ij}/s_{ii}} \right)$$

$$\text{Equation 1.6} \quad I_i = I_i^0 + s_{ii} \log(K_{ij}) + s_{ij} \log(a_j) + O$$

$$\text{Equation 1.7} \quad I_{ij}^0 = I_i^0 + s_{ii} \log(K_{ij})$$

$$\text{Equation 1.8} \quad \log(K_{ij}) = \frac{I_{ij}^0 - I_i^0}{s_{ii}}$$

Where I_i is the measured current shift across sensor i , I_i^0 is the current constant, s_{ii} is the current sensitivity of sensor i for the target ion i (s_{ij} is for sensor i for target ion j), $a_{i/j}$ is considered the concentration of i/j at the surface, and K_{ij} is the selectivity coefficient of the i -selective sensor towards interfering ion j .

In the case of phosphate, where exclusion principles often fail to selectively allow adsorption, this microsensor array technique is promising. With this technique, semiconductor materials with different functionalities are needed, whilst retaining the properties that make them good electrode materials (low resistance, stable under voltage).

Detection of Phosphate by Metal Organic Nanosheets

Exploring MONs as a novel material for sensing of phosphate is based on the extensive literature identifying them as useful for sensing, especially environmental pollution monitoring of anionic contaminants, heavy metal ions, organic compounds, and gases.^{64,82} The 2D high specific external surface area, water stability, and modular chemistry of MONs makes them good candidates for selective sensing.⁸²

Fang et al. reviewed the use of metal organic frameworks for sensing of inorganic phosphate in water.⁶⁴ Luminescence sensors based on MOFs are popular, with the review identifying notable examples: Qian et al. reported the use of Tb-NTA, where NTA is nitrilotriacetate, as a luminescence sensor which was selectively quenched by PO_4^{3-} , but not impacted by F^- , Cl^- , Br^- , I^- , NO_3^- , NO_2^- , HCO_3^- , CO_3^{2-} , or SO_4^{2-} .¹⁴ Lu et al. reported the post-synthetic functionalisation of $\text{Zn}_4\text{O}(\text{BDC})_3$, where BDC is 1,4-benzodicarboxylate, with ZnO quantum dots.¹⁷ Amine-Zn interaction between the quantum dots and MOF had a quenching effect that was recovered in the presence of phosphate. The phosphate dependant fluorescence has a sensitive linear working range 0.5 – 12 μM and a detection limit of 53 nM; Zhao et al. reported a reusable Eu-BTB MOF sensor, where BTB is 1,3,5-benzenetribenzoate.⁸³ In this case, quenching by phosphate was recoverable by washing with water.

Fang et al. notes that MOFs should also be excellent candidates for electrochemical sensor surface modifiers because of their high surface area and pore volume, good absorbability, and high catalytic activity.⁶⁴ It is noteworthy, however, that MOFs have poor electrical conductivity, relatively low stability in aqueous solutions, and (usually) micron size, resulting in limited adhesion affinity between MOFs and electrode surface. MOFs are therefore commonly used to modify other functional materials that have high electrical conductivity, overcoming these limitations. As an example, Mobin et al. used Cu-BTC, where BTC is benzene-1,3,5-tricarboxylic acid, to modify reduced graphene oxide (rGO) for electrochemical measurement of nitrite.⁸⁴ This was successfully monitored via cyclic voltammetry due to the Cu-BTC@rGO oxidising the nitrite to nitrate, releasing an electron at the working electrode. The sensing range of this titration was 1-90 μM .

The use of $\text{Zn}_2(\text{T CPP})$ for sensing was considered not only due to familiarity in previous work, but also because of its stability in water, available metal centres at axial and porphyrin positions, and previous research into sensing in literature.⁸² The position of metals in the extended structure essentially makes them single-atom coordination sites, which has promising ramifications for sensing. Additionally, the porphyrin-based linker is sensitive to changes in chemical environment, especially at the porphyrin centre.

$\text{Zn}_2(\text{T CPP})$ MONs have been used as electrochemical sensor materials: Han et al. reports the use of $\text{Zn}_2(\text{T CPP})$ for sensing of S-Naproxen, an anti-inflammatory drug.⁸⁵ The work concluded that $\text{Zn}_2\text{T CPP}$ MOF outputs stronger electrochemical response than T CPP as a redox probe. This work specifically identified the problems associated with 3D MOF adhesion affinity and suggests that $\text{Zn}_2(\text{T CPP})$ MONs may also offer an advantage due to the 2D nature of porphyrin MOFs, shortening the transmission distance of ions and electrons onto the electrode surface.

Detection of Phosphate by Molecularly Imprinted Polymers

Another promising field of sensing materials is molecularly imprinted polymers (MIPs). Molecular imprinting allows for the template-assisted creation of selective recognition sites in a synthetic polymer.^{86–88} Binding to these nanomaterials is selective due to template-specific size, shape, and chemical functionality, and consequently the selectivity of these active sites is comparable to biomolecular recognition e.g., amino acids, nucleic acids, enzymes, and antibodies.⁸⁶ The benefits over biomolecules are low-cost, ease of preparation, advanced storage stability, and good specificity.⁸⁹

Canfarotta et al. outlines some of the problems with MIP synthesis, including the presence of residual template and overly complex synthetic methods.⁹⁰ To overcome these limitations, MIP nanoparticles (nanMIPs) were synthesised using a solid-phase approach. Here, template was covalently immobilised on the surface of glass beads as solid support before the polymerisation step. This ensured much greater removal of template, increasing nanoMIP affinity for target analytes.

MIPs with poor electrical conductivity have been improved by forming hybrid materials with conductive polymers.^{87,91} This can be used with electrochemical methods like cyclic voltammetry, differential pulse voltammetry, electrochemical impedance analysis, and chronoamperometry.⁸⁹ Ratautaite et al. explicitly details the method of pulsed voltage chronoamperometry, where the changes in current increase or decrease in response to the diffuse layer thickness at the surface of the working electrode.⁸⁹ Therefore, this technique is sensitive to interactions between an analyte and the electrode surface.

When discussing the use of MIPs for sensing of inorganic phosphate, literature presents some difficulty in designing small anion receptors due to the poor self-assembly between anionic template and the functional monomers, as well as the incompatibility of anions with non-polar synthesis media.⁸⁰ Despite this, success has been found sensing for organic phosphates such as pesticides e.g., Fenamiphos by Mehmandoust et al.,⁸⁶ and herbicides e.g., glyphosate by Lach et al.⁹² This latter example utilised a similar solid-phase synthesis to Canfarotta et al., forming nanoMIPs using rational selection of components via computational analysis of template with a database of monomers. The resultant nanomaterial also incorporated a ferrocene-derived monomer to imbue the nanoMIP with electroactive properties.

Additionally, precedence for MIP sensing of inorganic phosphate exists in the work by Atayi et al., where hydrogen phosphate anion imprinted polymer was synthesised via emulsion polymerisation.⁸⁰ This was achieved by polymerisation using acrylic acid and divinyl benzene as the functional monomer and cross-linker agent, respectively. The paper also details a hybrid material approach, mixing graphite, imprinted polymer, graphene, and n-eicosane. This was demonstrated to improve the efficiency compared to a MIP electrode fabricated without graphene additive. The hybrid electrode showed a dynamic linear range 10 μM – 0.1 M, with a detection limit of 5 μM .

It is posited that the sensitivity of MIP-based sensor materials for inorganic phosphate such as those produced by Atayi et al. could be improved using the solid-phase synthetic methods. This is expected to improve active site density and template affinity, and template removal from active sites. There is also scope to explore different templates with the phosphate group, to determine the active site density improvement when longer chain templates are used versus small anions. Additionally, the functionalisation using electroactive ferrocene-based monomers is of interest, as this could improve the function of nanoMIPs used in electrochemical sensors.

Screen-printed Graphene Electrodes

Due to its high surface area, high mechanical strength, and electrical conductivity, two-dimensional graphene has attracted much interest, especially in the field of electrochemical sensing.⁹³ Apart from the previous attributes, graphene is well suited as an electrode material for its improved direct electron transfer at the graphene/electrolyte interface relative to existing materials e.g., glassy carbon electrodes. Controlling the structure of graphene in order to attain these benefits, however, remains challenging, particularly reproducibly at scale.⁹³

In their 2014 paper, Randviir et al. published their paper as part of the Banks group “The fabrication, characterisation and electrochemical investigation of screen-printed graphene electrodes”.⁹³ This outlines their methodology for fabricating graphene screen-printed electrodes (G-SPEs) cheaply and reproducibly using commercially available printable graphene inks. The success of this methodology indicates graphene materials may become much more accessible to scale-production and commercialisation. The group also confirmed in their 2020 paper by Pierini et al. “Screen-printed electrochemical-based sensor for taxifolin determination in edible peanut oils” that these G-SPEs could be used as sensor electrodes.⁹⁴

It is useful to consider developments such as these in the development of sensor materials, as they have ramifications for the wholesale success of implementing novel sensing technologies. As such, in the investigations into nanomaterials for sensing, especially those that benefit from hybridisation with electrically conducting materials (i.e., graphene), these G-SPEs should be considered for inclusion into that work.

Section 1.6 Aims

The literature laid out here identifies an explicit interest by the scientific community into the application of metal organic framework nanosheets (MONs), such as $Zn_2(TCPP)$, and subsequently an interest in the photophysical applications inherent to these materials. Numerous examples exist of ultrafast spectroscopy studies comparing MONs to linker and discussing the differences, but few examples attempt to systematically and quantitatively assess the effects changes to these materials have on photophysical properties.

The synthesis of ultrathin, tunable porphyrin MONs represents an opportunity to study their photophysical properties in detail, particularly by ultrafast spectroscopic analysis. In particular, understanding and tuning the excited state dynamics in $Zn_2(TCPP)$ are of interest due to wide variety of applications of this material. This might include ways to tune the intensity or wavelengths of emission, altering excited state lifetime, tailoring the dominant relaxation pathways for excited states, or simply understanding the effect different ligand/metal combinations have on these properties. In particular, the size and thickness of MONs varies significantly with different synthesis or processing steps, so understanding the effects of these changes is important for the implementation of these materials.

As such, this thesis aims to investigate the effects of different processing/syntheses on the photophysical properties of $Zn_2(TCPP)$. To that end, **Chapter 3** explores the effect of aggregation of $Zn_2(TCPP)$ on emission, excited state lifetime, and the amount of exciton annihilation. **Chapter 4** utilises the potential of post-synthetic metalation of $Zn_2(TCPP-H_2)$ at the porphyrin centre. This chapter explores the effect of a variety of transition metals on photophysical properties of emission, excited state lifetime, and exciton annihilation. **Chapter 5** describes the process of developing a new experimental setup in collaboration with Dr Alex Knight, Department of Physics, University of Sheffield, for simultaneous measurement of photoluminescence whilst performing atomic force microscopy scans. This aims to allow mapping of emission intensity across the topological surface of nanosheets and agglomerates.

Another focus of the work here is focused on developing functional materials centred around the sensing of phosphate for applications in smart farming technologies aimed at measuring fertiliser concentration in soil. **Chapter 6**, therefore, aims to investigate MONs for the selective sensing of ammonium phosphate, exploring the possibility of differentiating between this analyte in aqueous media and ammonium nitrate, a common imposter species. Another nanomaterial, molecularly imprinted polymers, are also investigated for this application. Both nanomaterials are assessed via the electrochemical techniques cyclic voltammetry, chronopotentiometry, and chronoamperometry to determine their effectiveness for the application.

Finally, **chapter 7** will conclude this work by summarising the key outcomes and recommending future directions for research.

Section 1.7 References

1. Ashworth, D. J. & Foster, J. A. Metal-organic framework nanosheets (MONs): A new dimension in materials chemistry. *J Mater Chem A Mater* **6**, 16292–16307 (2018).
2. Zhao, X. & Miao, X. Metal–organic framework constructed by flexible ligands: A versatile platform towards efficient fluorescence sensing, adsorption separation and heterogeneous catalysis. *Coord Chem Rev* **502**, (2024).
3. Efimova, A. S. *et al.* Exfoliation of 2D Metal-Organic Frameworks: toward Advanced Scalable Materials for Optical Sensing. *Small Methods* **7**, (2023).
4. Jiang, Y. *et al.* Multifunctional Zinc Metal-Organic Framework Based on Designed H4TCPP Ligand with Aggregation-Induced Emission Effect: CO₂ Adsorption, Luminescence, and Sensing Property. *Cryst Growth Des* **17**, 2090–2096 (2017).
5. Ye, Y. *et al.* A stable pillared metal–organic framework constructed by H4TCPP ligand as luminescent sensor for selective detection of TNP and Fe³⁺ ions. *Appl Organomet Chem* **33**, (2019).
6. Sasitharan, K. *Metal-Organic Framework Nanosheets: A New Dimension in Photovoltaics Research*. (2020).
7. Zhao, M. *et al.* Ultrathin 2D Metal-Organic Framework Nanosheets. *Advanced Materials* **27**, 7372–7378 (2015).
8. Custelcean, R. & Moyer, B. A. Anion separation with metal-organic frameworks. *Eur J Inorg Chem* 1321–1340 (2007) doi:10.1002/ejic.200700018.
9. Roy, I. *et al.* Photon Upconversion in a Glowing Metal-Organic Framework. *J Am Chem Soc* **143**, 5053–5059 (2021).
10. Gu, C. *et al.* Assembled Exciton Dynamics in Porphyrin Metal-Organic Framework Nanofilms. *Nano Lett* **21**, 1102–1107 (2021).
11. Dou, X. *et al.* Nanoscale metal-organic frameworks as fluorescence sensors for food safety. *Antibiotics* **10**, (2021).
12. Bai, Y. *et al.* Zr-based metal-organic frameworks: Design, synthesis, structure, and applications. *Chem Soc Rev* **45**, 2327–2367 (2016).
13. Sasitharan, K. *et al.* Metal–organic framework nanosheets for enhanced performance of organic photovoltaic cells. *J Mater Chem A Mater* **8**, 6067–6075 (2020).
14. Xu, H. *et al.* A metal-organic framework for selectively sensing of PO₄³⁻ anion in aqueous solution. *J Alloys Compd* **509**, 2552–2554 (2011).
15. Kobayashi, Y., Jacobs, B., Allendorf, M. D. & Long, J. R. Conductivity, doping, and redox chemistry of a microporous dithiolene-based metal-organic framework. *Chemistry of Materials* **22**, 4120–4122 (2010).
16. Wang, L. *et al.* A luminescent method for detection of parathion based on zinc incorporated metal-organic framework. *Microchemical Journal* **153**, 104441 (2020).
17. Zhao, D. *et al.* Metal-organic frameworks (MOFs) combined with ZnO quantum dots as a fluorescent sensing platform for phosphate. *Sens Actuators B Chem* **197**, 50–57 (2014).

18. Nicks, J., Sasitharan, K., Prasad, R. R. R., Ashworth, D. J. & Foster, J. A. *Metal-Organic Framework Nanosheets (MONs): Promising Two-Dimensional Materials for Catalysis, Sensing, Electronics, and Separation Applications*. (2021).
19. Ma, C. *et al.* Fabrication of oriented metal-organic framework nanosheet membrane coated stainless steel meshes for highly efficient oil/water separation. *Sep Purif Technol* **229**, 115835 (2019).
20. Baghayeri, M., Ghanei-Motlagh, M., Tayebee, R., Fayazi, M. & Narenji, F. Application of graphene/zinc-based metal-organic framework nanocomposite for electrochemical sensing of As(III) in water resources. *Anal Chim Acta* **1099**, 60–67 (2020).
21. Wang, Y., Cui, H., Zhang, L. & Su, C. Y. An Acid Stable Metal-Organic Framework as an Efficient and Recyclable Catalyst for the O–H Insertion Reaction of Carboxylic Acids. *ChemCatChem* **10**, 3901–3906 (2018).
22. Nicks, J., Sasitharan, K., Prasad, R. R. R., Ashworth, D. J. & Foster, J. A. Metal–Organic Framework Nanosheets: Programmable 2D Materials for Catalysis, Sensing, Electronics, and Separation Applications. *Adv Funct Mater* **31**, (2021).
23. Makiura, R. Creation of metal–organic framework nanosheets by the Langmuir-Blodgett technique. *Coordination Chemistry Reviews* **469**, (2022).
24. Shaikh, S. M. *et al.* Light harvesting and energy transfer in a porphyrin-based metal organic framework. *Faraday Discuss* **216**, 174–190 (2019).
25. Li, X. *et al.* Ultrafast Relaxation Dynamics in Zinc Tetraphenylporphyrin Surface-Mounted Metal Organic Framework. *Journal of Physical Chemistry C* **122**, 50–61 (2018).
26. Li, F. *et al.* Large-Scale, Bottom-Up Synthesis of Binary Metal–Organic Framework Nanosheets for Efficient Water Oxidation. *Angewandte Chemie* **131**, 7125–7130 (2019).
27. Ha, J., Lee, J. H. & Moon, H. R. Alterations to secondary building units of metal-organic frameworks for the development of new functions. *Inorganic Chemistry Frontiers* **7**, 12–27 (2019).
28. Zhao, M. *et al.* Two-dimensional metal-organic framework nanosheets: Synthesis and applications. *Chemical Society Reviews* **47**, 6267–6295 (2018).
29. Duan, J., Li, Y., Pan, Y., Behera, N. & Jin, W. Metal-organic framework nanosheets: An emerging family of multifunctional 2D materials. *Coordination Chemistry Reviews* **395**, 25–45 (2019).
30. La, D. D. *et al.* Advances and prospects of porphyrin-based nanomaterials via self-assembly for photocatalytic applications in environmental treatment. *Coordination Chemistry Reviews* **463**, (2022).
31. Cao, R. *et al.* Self-Assembled Porphyrin Nanoleaves with Unique Crossed Transportation of Photogenerated Carriers to Enhance Photocatalytic Hydrogen Production. *Nano Lett* **22**, 157–163 (2022).
32. Gouterman, M. *Spectra of Porphyrins**. *JOURNAL OF MOLECULAR SPECTROSCOPY* **6** (1961).

33. Rajasree, S. S., Li, X. & Deria, P. Physical properties of porphyrin-based crystalline metal–organic frameworks. *Communications Chemistry* **4**, (2021).
34. Haber, L. H. *et al.* Efficient photoinduced energy transfer in porphyrin-based nanomaterials. *Journal of Physical Chemistry C* **124**, 24533–24541 (2020).
35. Zhang, X. *et al.* A historical perspective on porphyrin-based metal–organic frameworks and their applications. *Coord Chem Rev* **429**, 213615 (2020)
36. Ashworth, D. J. *et al.* Scalable and sustainable manufacturing of ultrathin metal–organic framework nanosheets (MONs) for solar cell applications. *Chemical Engineering Journal* **477**, (2023).
37. Choi, E. Y., Wray, C. A., Hu, C. & Choe, W. Highly tunable metal-organic frameworks with open metal centers. *CrystEngComm* **11**, 553–555 (2009).
38. Mehrzad Sajjadinezhad, S., Boivin, L., Bouarab, K. & Harvey, P. D. Photophysical properties and photonic applications of porphyrin-based MOFs. *Coordination Chemistry Reviews* **510**, (2024).
39. Pang, Y. *et al.* A novel fluorescence sensor based on Zn porphyrin MOFs for the detection of bisphenol A with highly selectivity and sensitivity. *Food Control* **132**, (2022).
40. Wiśniewski, M. & Terzyk, A. P. Non-thermal plasma-assisted catalytic CO₂ conversion over Zn-TCPP 2D catalyst. *Adsorption* **26**, 1165–1171 (2020).
41. Zhang, X. *et al.* Light-responsive Au@Zn-TCPP nanozyme functionalized with cell-penetrating peptide and antisense oligonucleotide for sensing living bacteria and synergistic therapy of diabetic wounds. *Chemical Engineering Journal* **488**, (2024).
42. Choi, E. Y., Wray, C. A., Hu, C. & Choe, W. Highly tunable metal-organic frameworks with open metal centers. *CrystEngComm* **11**, 553–555 (2009).
43. Jin, Z. *et al.* Nitrogen vacancy-induced spin polarization of ultrathin zinc porphyrin nanosheets for efficient photocatalytic CO₂ reduction. *J Colloid Interface Sci* **652**, 122–131 (2023).
44. Posligua, V. *et al.* *Engineering the Electronic and Optical Properties of 2D Porphyrin-Paddlewheel Metal-Organic Frameworks.*
45. Chen, L.-J., Zhao, X. & Yan, X.-P. Porphyrinic metal-organic frameworks for biological applications. *Advanced Sensor and Energy Materials* **2**, 100045 (2023).
46. Bai, W., Li, S., Ma, J., Cao, W. & Zheng, J. Ultrathin 2D metal-organic framework (nanosheets and nanofilms)-based: X D-2D hybrid nanostructures as biomimetic enzymes and supercapacitors. *J Mater Chem A Mater* **7**, 9086–9098 (2019).
47. Zhang, L. *et al.* 2D Porphyrinic Metal–Organic Framework Nanosheets as Multidimensional Photocatalysts for Functional Materials. *Angewandte Chemie - International Edition* **60**, 22664–22671 (2021).
48. Feng, D. *et al.* A highly stable porphyrinic zirconium metal-organic framework with shp-a topology. *J Am Chem Soc* **136**, 17714–17717 (2014).
49. Sakuma, T., Sakai, H., Araki, Y., Wada, T. & Hasobe, T. Control of local structures and photophysical properties of zinc porphyrin-based supramolecular assemblies

- structurally organized by regioselective ligand coordination. *Physical Chemistry Chemical Physics* **18**, 5453–5463 (2016).
50. Cao, X. *et al.* Design of Pd–Zn Bimetal MOF Nanosheets and MOF-Derived Pd_{3.9}Zn_{6.1}/CNS Catalyst for Selective Hydrogenation of Acetylene under Simulated Front-End Conditions. *Molecules* **27**, (2022).
 51. Wang, Q., Ke, W., Lou, H., Han, Y. & Wan, J. A novel fluorescent metal-organic framework based on porphyrin and AIE for ultra-high sensitivity and selectivity detection of Pb²⁺ ions in aqueous solution. *Dyes and Pigments* **196**, (2021).
 52. Zhao, Y. *et al.* Synthesis of porphyrin-based two-dimensional metal–organic framework nanodisk with small size and few layers. *J Mater Chem A Mater* **6**, 2828–2833 (2018).
 53. Baskin, J. S., Yu, H. Z. & Zewail, A. H. Ultrafast dynamics of porphyrins in the condensed phase: I. Free base tetraphenylporphyrin. *Journal of Physical Chemistry A* **106**, 9837–9844 (2002).
 54. Yu, H. Z., Baskin, J. S. & Zewail, A. H. Ultrafast dynamics of porphyrins in the condensed phase: II. Zinc tetraphenylporphyrin. *Journal of Physical Chemistry A* **106**, 9845–9854 (2002).
 55. Hirao, K. Theoretical study of the Q and B bands of free-base, magnesium, and zinc porphyrins, and their derivatives. *Journal of Physical Chemistry A* **103**, 1894–1904 (1999).
 56. Greco, J. A. *et al.* Two-photon spectroscopy of the Q-bands of meso -tetraphenylporphyrin and -chlorin framework derivatives. *Journal of Physical Chemistry C* **119**, 3711–3724 (2015).
 57. Pourreza, N., Sharifi, H. & Golmohammadi, H. A Green Chemosensor for Colorimetric Determination of Phosphate Ion in Soil, Bone, and Water Samples Using Curcumin Nanoparticles. *ANALYTICAL SCIENCES* **36**, 1297–1302 (2020).
 58. Mapare, S. V., Yu, P. L., Sarkar, A. & Mukhopadhyay, S. C. A Review of sensor technology for in-field phosphate monitoring. *Proceedings of the International Conference on Sensing Technology, ICST* 411–418 (2013)
 59. Wang, F. *et al.* An electrochemical microsensor based on a AuNPs-modified microband array electrode for phosphate determination in fresh water samples. *Sensors (Switzerland)* **14**, 24472–24482 (2014).
 60. Sarwar, M., Lechner, J., Naja, G. M. & Li, C. Z. Smart-phone, paper-based fluorescent sensor for ultra-low inorganic phosphate detection in environmental samples. *Microsyst Nanoeng* **5**, (2019).
 61. Lu, C. & Tian, H. Global nitrogen and phosphorus fertilizer use for agriculture production in the past half century: shifted hot spots and nutrient imbalance. *Earth Syst Sci Data* **9**, 181–192 (2017).
 62. Cheremisinoff, N. P. & Rosenfeld, P. Handbook of Pollution Prevention and Cleaner Production Vol. 2: Best Practices in the Wood and Paper Industries. *Handbook of Pollution Prevention and Cleaner Production Vol. 2: Best Practices in the Wood and Paper Industries* (2010)

63. Campanella, L., Cordatore, M., Mazzei, F., Tomassetti, M. & Volpe, G. Phosphate determination in foodstuffs using a plant tissue electrode. *Food Chem* **44**, 291–297 (1992).
64. Fang, X., Zong, B. & Mao, S. Metal–Organic Framework-Based Sensors for Environmental Contaminant Sensing. *Nanomicro Lett* **10**, 1–19 (2018).
65. Mao, S. *et al.* Ultrasensitive detection of orthophosphate ions with reduced graphene oxide/ferritin field-effect transistor sensors. *Environ Sci Nano* **4**, 856–863 (2017).
66. Berchmans, S., Issa, T. B. & Singh, P. Determination of inorganic phosphate by electroanalytical methods: A review. *Analytica Chimica Acta* **729**, 7–20 (2012).
67. Adamchuk, V. I. *et al.* Direct measurement of soil chemical properties on-the-go using ion-selective electrodes. *Comput Electron Agric* **48**, 272–294 (2005).
68. Fakhri, I. *et al.* Selective ion sensing with high resolution large area graphene field effect transistor arrays. *Nat Commun* **11**, 1–12 (2020).
69. Maleki, M. R. *et al.* Phosphorus Sensing for Fresh Soils using Visible and Near Infrared Spectroscopy. *Biosyst Eng* **95**, 425–436 (2006).
70. Rhymes, J. *et al.* Evaluating the accuracy and usefulness of commercially-available proximal soil mapping services for grassland nutrient management planning and soil health monitoring. *Precis Agric* **24**, 898–920 (2023).
71. Bogrekci, I. & Lee, W. S. Design of a portable raman sensor for phosphorus sensing in soils. *2005 ASAE Annual International Meeting* **0300**, (2005).
72. Sinfield, J. V., Fagerman, D. & Colic, O. Evaluation of sensing technologies for on-the-go detection of macro-nutrients in cultivated soils. *Comput Electron Agric* **70**, 1–18 (2010).
73. Lei, H. *et al.* Synergistic integration of Au nanoparticles, Co-MOF and MWCNT as biosensors for sensitive detection of low-concentration nitrite. *Electrochim Acta* **365**, 137375 (2021).
74. Domingo-Roca, R., Macdonald, A. R., Hannah, S. & Corrigan, D. K. Integrated multi-material portable 3D-printed platform for electrochemical detection of dopamine and glucose. *Analyst* **147**, 4598–4606 (2022).
75. Seyfferth, A. L., Henderson, M. K. & Parker, D. R. Effects of common soil anions and pH on the uptake and accumulation of perchlorate in lettuce. *Plant Soil* **302**, 139–148 (2008).
76. Epsztein, R., Shaulsky, E., Qin, M. & Elimelech, M. Activation behavior for ion permeation in ion-exchange membranes: Role of ion dehydration in selective transport. *J Memb Sci* **580**, 316–326 (2019).
77. CleanGrow. <https://www.ionselectiveelectrode.com/products/cleangrow-multi-ion-nutrient-analyzer-kit>.
78. Shannon, R. D. *et al.* Revised Effective Ionic Radii and Systematic Studies of Interatomic Distances in Halides and Chalcogenides, *Acta Crystallographica Section A*, **32** (5), 751–767 (1976)

79. Jenkins, H. D. B. & Thakur, K. P. Reappraisal of thermochemical radii for complex ions. *J Chem Educ* **56**, 576–577 (1979).
80. Alizadeh, T. & Atayi, K. Synthesis of hydrogen phosphate anion-imprinted polymer via emulsion polymerization and its use as the recognition element of graphene/graphite paste potentiometric electrode. *Mater Chem Phys* **209**, 180–187 (2018).
81. Shaw, R., Lark, R. M., Williams, A. P., Chadwick, D. R. & Jones, D. L. Characterising the within-field scale spatial variation of nitrogen in a grassland soil to inform the efficient design of in-situ nitrogen sensor networks for precision agriculture. *Agric Ecosyst Environ* **230**, 294–306 (2016).
82. Ma, T., Li, H., Ma, J. G. & Cheng, P. Application of MOF-based materials in electrochemical sensing. *Dalton Transactions* **49**, 17121–17129 (2020).
83. Xu, H., Cao, C. S. & Zhao, B. A water-stable lanthanide-organic framework as a recyclable luminescent probe for detecting pollutant phosphorus anions. *Chemical Communications* **51**, 10280–10283 (2015).
84. Saraf, M., Rajak, R. & Mobin, S. M. A fascinating multitasking Cu-MOF/rGO hybrid for high performance supercapacitors and highly sensitive and selective electrochemical nitrite sensors. *J Mater Chem A Mater* **4**, 16432–16445 (2016).
85. Han, Q. *et al.* Achieving synergistically enhanced dual-mode electrochemiluminescent and electrochemical drug sensors via a multi-effect porphyrin-based metal-organic framework. *Sens Actuators B Chem* **330**, (2021).
86. Mehmandoust, M., Erk, N., Naser, M. & Soylak, M. Molecularly imprinted polymer film loaded on the metal–organic framework with improved performance using stabilized gold-doped graphite carbon nitride nanosheets for the single-step detection of Fenamiphos. *Food Chem* **404**, (2023).
87. Des Azevedo, S. *et al.* Molecularly imprinted polymer-hybrid electrochemical sensor for the detection of β -estradiol. in *Industrial and Engineering Chemistry Research* vol. 52 13917–13923 (2013).
88. Shen, Y. *et al.* Preparation and Application Progress of Imprinted Polymers. *Polymers* vol. 15 Preprint at <https://doi.org/10.3390/polym15102344> (2023).
89. Ratautaite, V. *et al.* Molecularly imprinted polypyrrole based sensor for the detection of SARS-CoV-2 spike glycoprotein. *Electrochim Acta* **403**, (2022).
90. Canfarotta, F., Poma, A., Guerreiro, A. & Piletsky, S. Solid-phase synthesis of molecularly imprinted nanoparticles. *Nat Protoc* **11**, 443–455 (2016).
91. Lakshmi, D. *et al.* Electrochemical sensor for catechol and dopamine based on a catalytic molecularly imprinted polymer-conducting polymer hybrid recognition element. *Anal Chem* **81**, 3576–3584 (2009).
92. Lach, P. *et al.* Electroactive molecularly imprinted polymer nanoparticles for selective glyphosate determination. *Biosens Bioelectron* **236**, (2023).
93. Randviir, E. P., Brownson, D. A. C., Metters, J. P., Kadara, R. O. & Banks, C. E. The fabrication, characterisation and electrochemical investigation of screen-printed graphene electrodes. *Physical Chemistry Chemical Physics* **16**, 4598–4611 (2014).

94. Pierini, G. D. *et al.* Screen-printed electrochemical-based sensor for taxifolin determination in edible peanut oils. *Microchemical Journal* **159**, (2020).

Chapter 2:

Techniques and Methods

Section 2.1 Introduction

Given the complexities inherent with characterising metal organic framework nanosheets (MONs), there are a wide variety of techniques reported in literature. Some of these are relatively fundamental and are well known by chemical researchers from undergraduate study. Other methods require specialist theoretical knowledge or have unique experimental setups which require further introduction. This section comprises of a detailed background and theory regarding the techniques used within this thesis.

Firstly, the optical techniques for studying the photophysics of materials, such as fundamental principles of UV-visible absorption and electronic emission. Additionally, a foundational introduction to the time-resolved experiments of time-correlated single-photon counting (TCSPC), and pump-probe transient absorption (TA) spectroscopy.

Secondly, the background theory of imaging techniques for characterising the morphology of nanomaterials are described. These include scanning electron microscopy (SEM), tunnelling electron microscopy (TEM), and atomic force microscopy (AFM),

Lastly, the more fundamental techniques of elemental analysis (CHN), inductive-coupled plasma mass spectrometry (ICP-MS), powder X-ray diffraction (P-XRD), dynamic light scattering (DLS).and cyclic voltammetry (CV) are briefly introduced.

Section 2.2 Optical Techniques for Photophysical Study

UV-Visible Absorption Spectroscopy (UV-Vis)

Ultraviolet (UV) and visible light absorption by materials is an effective tool to identify discrete electronic energy levels within a molecule specific to the material. A typical experimental setup is shown in Figure 2.1, where white light is generated and passed through a monochromator to select for a wavelength. This beam is passed through the sample before hitting the detector. By scanning through discrete wavelength steps sequentially and comparing to a blank cuvette containing no sample, the absorption is measured by the drop in detection for each wavelength. In the case of a charge coupled device (CCD) detector, a diffraction grating can be used to separate the incident light beam and measure a range of wavelengths (spectrum) for each excitation wavelength scanned.

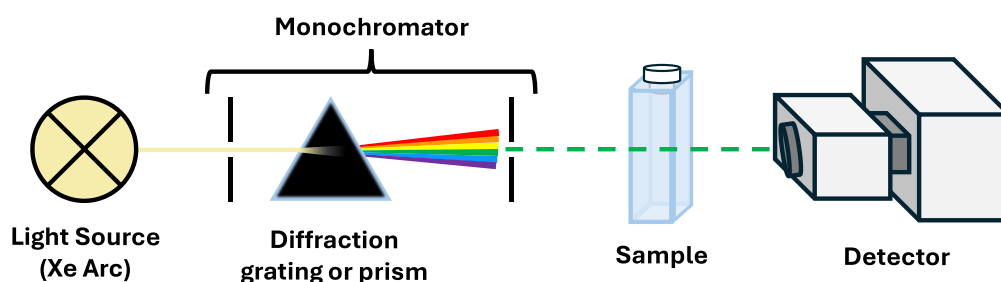


Figure 2.1 Diagram for the experimental setup of a UV-Visible absorption spectrometer.

Since the energy of a photon can be related to the wavelength of light by Equation 2.1, the wavelengths where absorption maxima are observed can be converted to the equivalent difference between electron energy levels in the material.

Equation 2.1 $E = \frac{hc}{\lambda}$ *Energy of a Photon*

Where E is the energy of a photon, h is Planck's constant (6.63×10^{-34} J s), c is the speed of light (2.998×10^8 m s^{-1}), and λ is the wavelength of light in m.

Electronic Emission Spectroscopy

Similarly to UV-visible absorption spectroscopy, the emission by a sample is also key to understanding the electronic transitions within a material. By measuring the intensity of light at 90° from an incident excitation beam, the emission spectrum from a sample can be measured (Figure 2.2).

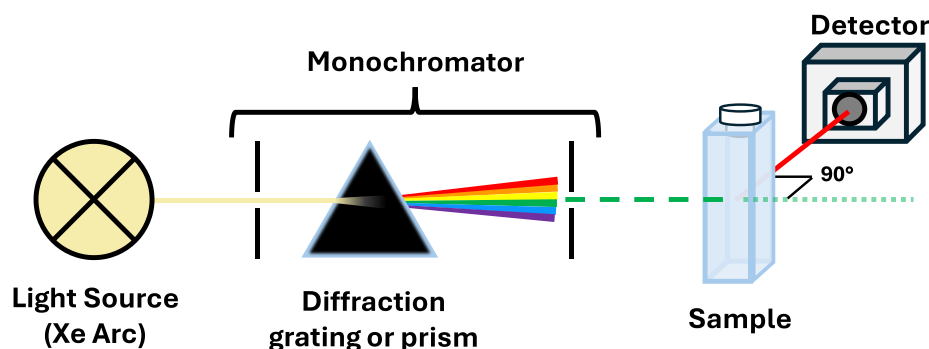


Figure 2.2 Diagram for the experimental setup of an emission spectrometer.

Time-Resolved Emission Spectroscopy

The emission lifetime of a molecule can be measured by measuring temporal snapshots of emission intensity at different points along the decay after excitation, otherwise known as time-correlated single photon counting (TCSPC). Snapshots are used instead of continuous monitoring to accurately measure over short time windows, since typical fluorescence from commonly used organic fluorophores lasts in the region of hundreds of picoseconds to tens of nanoseconds.¹ As shown in Figure 2.3, an excitation laser, with intensity tempered by a neutral density filter, is passed through a liquid sample cell, and the emitted light measured at 90°, as in steady state emission spectroscopy. The emitted light can also be filtered via a wavelength selector to observe the lifetimes associated with different energy emission events. Subsequently, the emitted light is measured by a detector, usually a charge-coupled device (CCD), which is controlled by an electronic delay system triggered by the laser pulse to take measurements at different times after excitation pulses. It should be emphasised that the photon events are recorded at high repetition rates compared to other time-resolved techniques (such as transient absorption), allowing the process to be repeated many times to create a distribution of photon emission lifetimes.

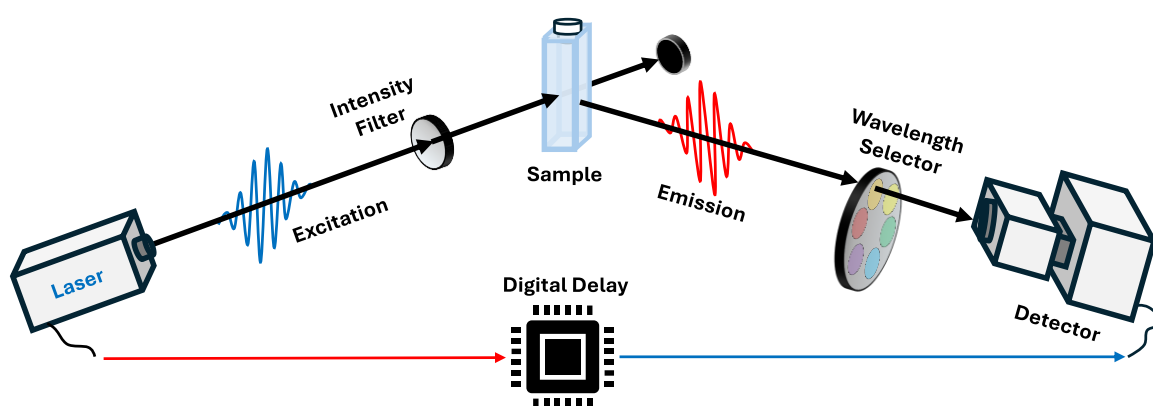


Figure 2.3 Diagram for a TCSPC setup.¹

Pump-Probe Transient Absorption (TA) Spectroscopy

The processes of light absorption and subsequent relaxation are not instant, occurring over timescales varying from atto- to pico- seconds. As such, time resolved techniques with short-time resolution are required to measure these dynamics. Where TCSPC can only reveal the lifetimes of emissive states, transient absorption (TA) spectroscopy allows the measurement of both non-emissive and emissive excited state dynamics.

Pulsed laser systems can be used to excite repeatedly a sample using a “pump” laser and coinciding its arrival at the sample using an incident “probe” laser, thus acquiring an absorption spectrum of the transient excited states present, affording the name pump-probe spectroscopy. As shown in Figure 2.4, the probe laser can then be moved temporally along points using a delay line, allowing snapshot spectra to be recorded at different intervals during the excitation-relaxation process.

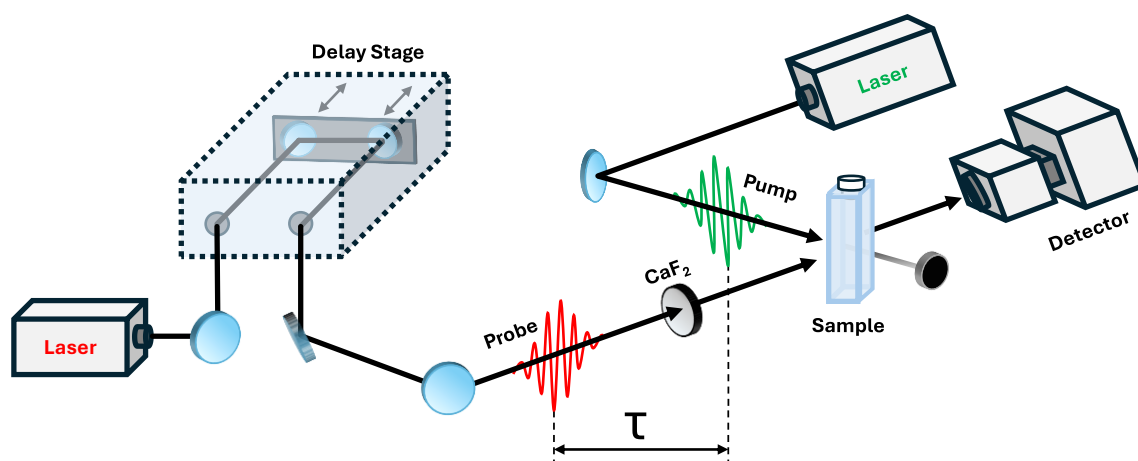


Figure 2.4 Component arrangement for pump-probe spectroscopy

When transient absorption spectra are recorded, the ground state absorption spectra are observed as negative ΔA since ground state electrons are removed by excitation to a higher electronic state. Consequently, there is a complementary positive ΔA for the new excited state formed by absorption of the white probe light by already excited molecules. As the probe beam is delayed in time, the absorption spectra of transient excited states can be measured throughout the relaxation lifetimes. The intensity at a single wavelength can then be plotted against time, and fitted with the sum of an exponential decay function such as expressed by Equation 2.2:

$$\text{Equation 2.2} \quad \Delta A(\lambda, t) = C_1(\lambda)e^{-k_1t} + C_2(\lambda)e^{-k_2t} + C_3(\lambda)e^{-k_3t} + \dots = \sum_{n=1}^n C_n(\lambda)e^{-k_n t}$$

The instrument response function (IRF) responsible for the rise and fall of detected signal can be modelled by a Gaussian function, the full width half maximum (FWHM) of which relates to an operator $\hat{\Delta}$ by Equation 2.3. The Gaussian function for the IRF can therefore be modelled by Equation 2.4.

$$\text{Equation 2.3} \quad \Delta = 2\hat{\Delta}\sqrt{\ln(2)} = 1.6651\hat{\Delta}$$

$$\text{Equation 2.4} \quad i(t) = \frac{1}{\hat{\Delta}\sqrt{2\pi}} e^{\left(-\ln(2)\left(\frac{2(t-t_0)}{\Delta}\right)^2\right)}$$

The decay must therefore be convoluted with the Gaussian function, as in the single exponential function example shown in Equation 2.5.

$$\text{Equation 2.5} \quad \Delta A(\lambda, t) = e^{-kt} e^{\left(k\left(t_0 + \frac{k\Delta^2}{2}\right)\right)} \left(1 + \text{erf}\left(\frac{t - (t_0 + k\Delta^2/2)}{\sqrt{2}\hat{\Delta}}\right)\right) A$$

Since the lifetime, τ , is the inverse of decay rate, k , leads to a fitting function similar to that described in Equation 2.6, which can be input as code in OriginPro for fitting.

$$\text{Equation 2.6} \quad \Delta A(\lambda, t) = \text{base} + \frac{\text{amp}_1}{2} e^{\left(\left(\left(\frac{\text{FWHM}}{1.6651 \times 2\tau_1}\right)^2\right) - \left(\frac{t-t_0}{\tau_1}\right) \left(1 - \text{erf}\left(\frac{\text{FWHM}}{1.6651 \times 2\tau_1} - \frac{1.6551(t-t_0)}{\text{FWHM}}\right)\right)\right)} \dots$$

The TA setup used in this work (Figure 2.5) involves an incoming pump laser of varying wavelength, selected for absorbance by the sample compound, whilst the incoming fs probe laser is set to 800 nm, subsequently used to generate a broad spectrum for absorption analysis in one of either UV, visible, or infrared regions.

A translation stage is used to delay the probe incidence time to coincide with the sample excitation, thus allowing an absorption spectrum to be taken at each step. Besides the mirrors used to direct the laser beam path, other components used in the set-up include:

- Neutral density (ND) filters - uniformly reduce the intensity of the beam across all wavelengths, used to avoid damage to the sample or the detector by oversaturation.
- White light generating crystal (WLGC) – Calcium fluoride used to generate a probe beam of relatively similar intensities at wavelengths between 400-700 nm.²
- 'Hot mirrors' selectively reflect certain wavelengths of light, allowing for example the 300-700 nm white probe beam to pass through, but reflecting the much higher intensity 800 nm laser and preventing its access to the sample/detector, where it may otherwise cause damage.
- Beam dumps – absorbing materials which reduce unsafe reflections of lasers.
- Chopper – a mechanical blade fan tuned to the frequency of the laser (~2.5 kHz) to intermittently block the pump beam and acquire probe when the sample is excited and not excited.
- Rotating polariser - The pump/probe should be polarised at 54.7°, the magic angle to reduce varying absorption effects of anisotropic molecules rotating in solution.³

The TA setup on the Helios spectrometer (HE-VIS-NIR-3200) is displayed in Figure 2.5. As pictured, the pump beam is directed through a ND filter, the chopper and polariser before passing through the sample (pinhole only used for initial alignment). After excitation, the beam finishes at a beam dump. The 800 nm probe beam is meanwhile directed through the delay stage via a double pass mirror setup, a different ND filter and the WLGC, before entering the sample after the 800 nm light is reflected into a beam dump (angled so as not to be returned along the beam path, which would otherwise damage the laser). After the sample, the probe beam is directed through another ND filter to avoid damage to/oversaturation of the detector. Several hot mirrors remove wavelengths outside the spectral range of interest before the detector.

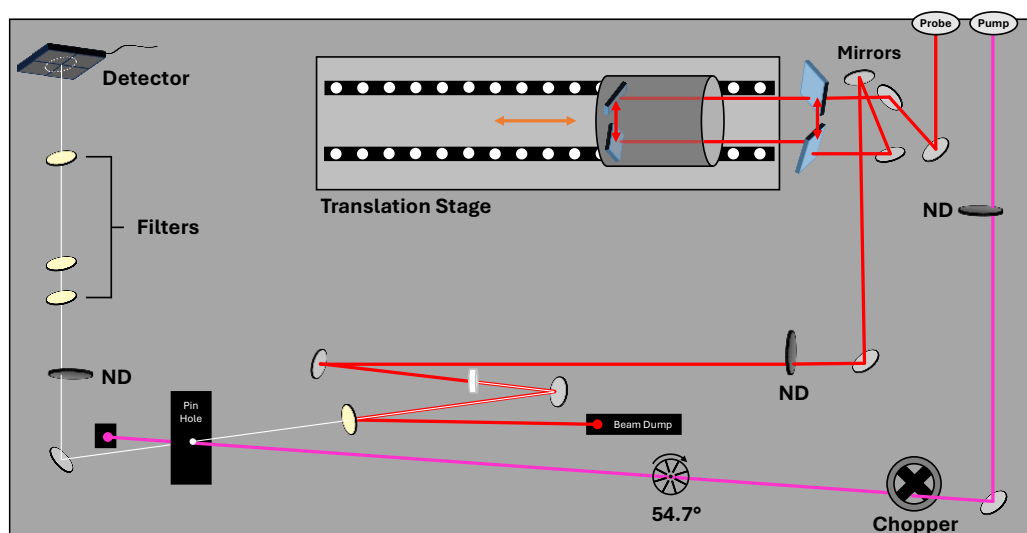


Figure 2.5 Pump-probe UV-Vis transient absorption experimental setup. ND = neutral density filter.

Due to the imperfect nature of reflection by any mirror, wavelengths of light will interact differently when passed through any optical system resulting in wavelength specific reductions in velocity across the pulse. The subsequent temporal perturbations in the data collected, known as the 'chirp' of the system. Because of this, a chirp correction including any solvent response is accounted for by collecting experimental data with pure solvent in the place of a sample. Additionally, a temporal oscillation of the electric field known as the 'coherent artifact' is also observed near time zero due to the interaction between pump and probe beams. This can be fitted using Surface Explorer software to remove from the signal.

Analysis by this method establishes the intrinsic electronic properties of materials. By knowing these, and correlating them to other desirable attributes, informed changes can be made to the material to improve those properties.

Section 2.3 Imaging the Morphology of Nanomaterials

Scanning Electron Microscopy

Scanning electron microscopy (SEM) is commonly used to image materials at resolutions below the diffraction limit (0.1 – 1000 nm). The technique directs a focused beam of electrons onto a sample surface, generating images to resolutions <1 nm up to several nanometers.⁴ Electrons in the beam interact with the sample, producing various signals which can be used to obtain information about the materials surface topography and composition. A schematic for a typical SEM setup is shown in Figure 2.6. Electrons from the source are accelerated in a vacuum toward the sample via an anode at a specific voltage (1 – 30 keV), condensed lenses reduce the beam diameter, and focused onto the sample using an objective lens to a beam diameter ranging from <1 - 20 nm. The position of the electron beam is controlled by the scan coils shown above the objective lens. The beam position is systematically moved across the surface and correlated with the electron intensity acquired by detectors e.g., secondary electrons, backscattered electrons, and characteristic X-rays.

Complementary to SEM is the technique of energy dispersive spectroscopy (EDS), which makes use of the X-rays produced when incoming electrons displace an inner shell electron in the sample. This inner shell electron is replaced by an outer shell electron, which relaxes by emitting an X-ray photon of discrete energy specific to the material. As such, EDS provides a non-destructive method of not only analysing the composition of a material, but also mapping the positioning of different elements.

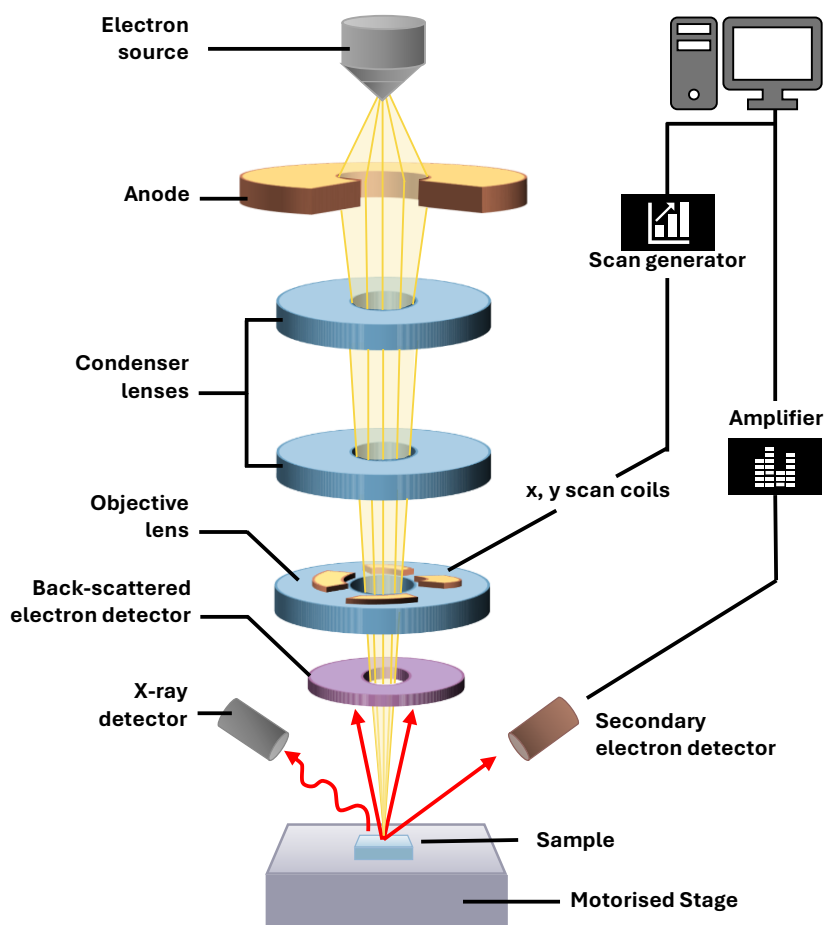


Figure 2.6 Schematic of a scanning electron microscope, reproduced from nanoscience instruments.⁴

Transmission Electron Microscopy (TEM)

Similar to SEM, transmission electron microscopy (TEM) utilises electrons to image at resolutions greater than optical microscopes. Samples are usually prepared very thin (<100 nm) to make them more transparent to electrons, and the detector is placed opposite the electron source, rather than collecting reflected electrons (Figure 2.7). The technique therefore relies on absorption of the source electrons, similar to how an optical microscope works, but able to magnify up to 50 million times. Focusing lenses and apertures throughout the microscope column are used to focus the beam on the sample, minimise distortions, and magnify the image formed onto a phosphor-based fluorescent screen.

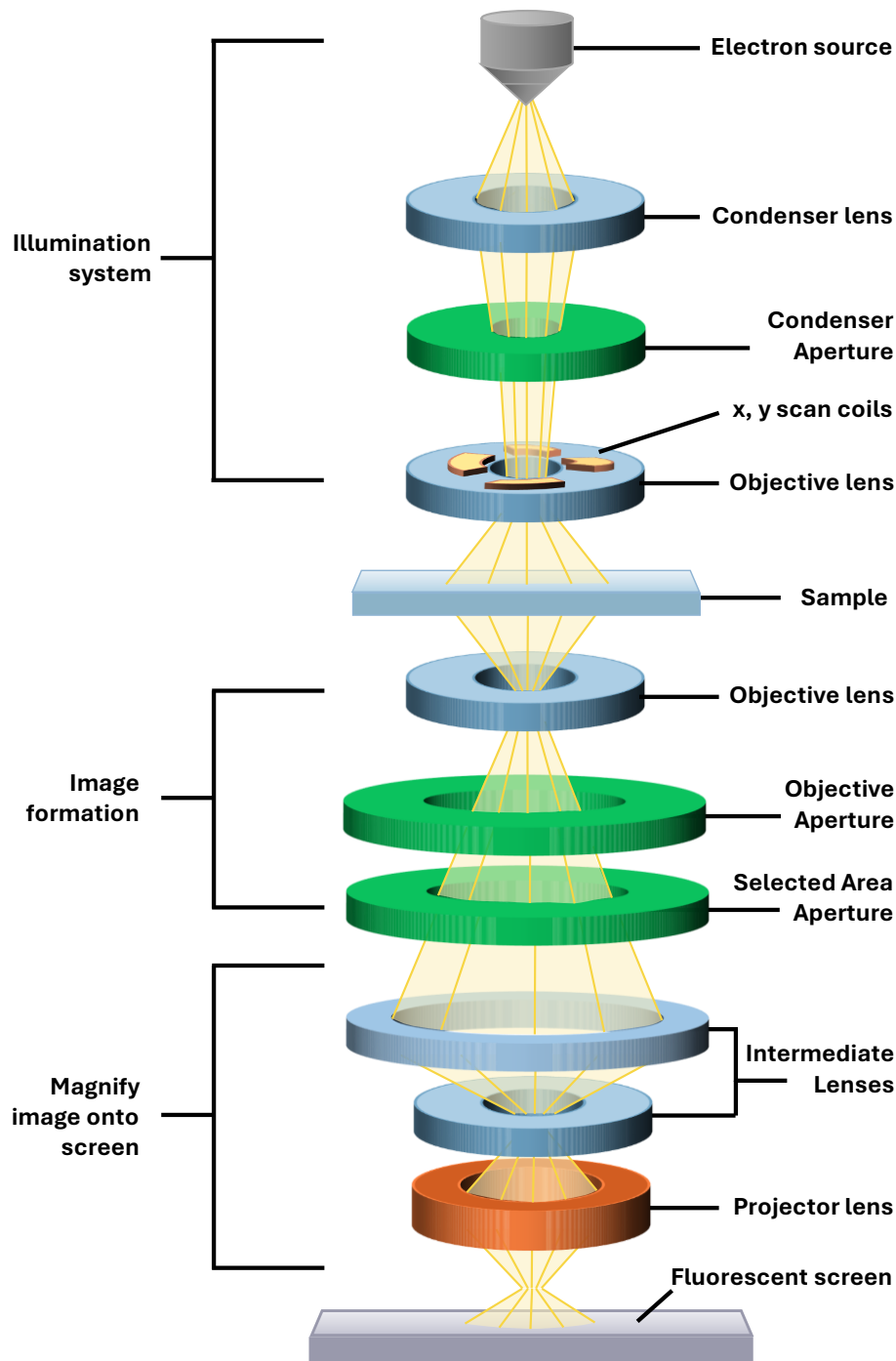


Figure 2.7 Schematic for TEM experiment setup, recreated from nanoscience.com.⁵

Atomic Force Microscopy

Atomic force microscopy (AFM) is an imaging technique for probing the surface of a material at nanometre resolution. By moving a physical probe across the surface, variations in height are either measured directly by laser incident on the cantilever tip, or inferred from the angle of reflection changing as the cantilever bends from pressure differences as the tip interacts with the sample.

Tapping mode involves a slightly different mechanism, whereby the contact between tip and sample is reduced to avoid damage to the tip or sample. Here, the tip is vibrated at near its resonance frequency, where interaction with the surface inhibits the movement. A feedback loop alters the vibration to counteract this and keep the tapping amplitude constant. The vibration frequency, therefore, allows indirect inference of the height profile across a sample.⁶

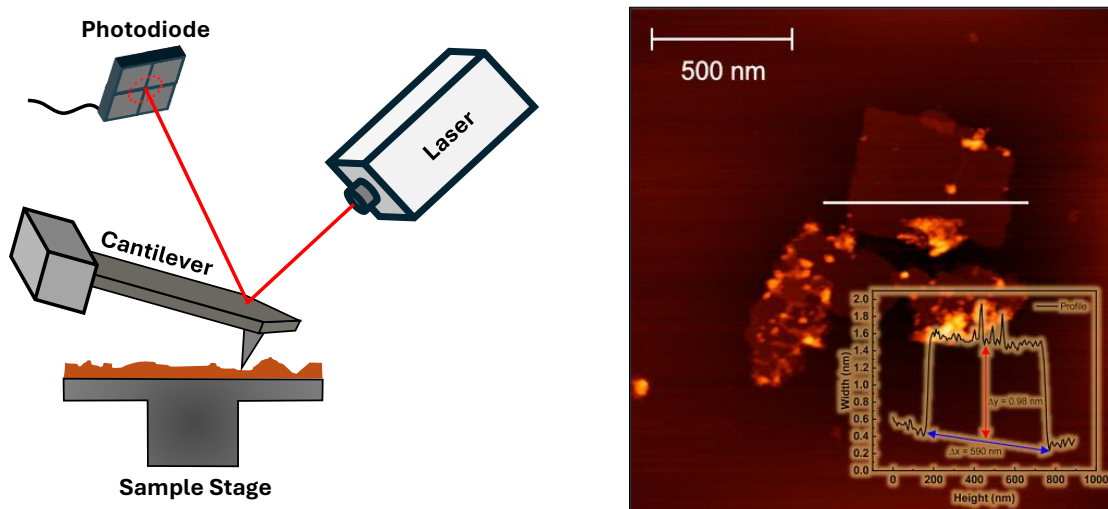


Figure 2.8 Schematic for experimental AFM setup (left), and example scan with height profile inset (right).

Section 2.4 Fundamental Characterisation Techniques

Elemental Analysis (CHN)

Used for the determination of carbon, hydrogen, nitrogen, and sulphur elemental content in samples, CHNS analysis involves the burning of a sample in the presence of oxygen to reliably produce certain species.⁷ Product gases from flash combustion at $\sim 1,800\text{ }^{\circ}\text{C}$ are passed via inert carrier gas over a heated ($600\text{ }^{\circ}\text{C}$) copper surface to remove unreacted O_2 and convert nitrous oxide products to N_2 before being passed through absorbent traps so that only N_2 , CO_2 , H_2O , and SO_2 are able to move onto the detection stage (Figure 2.9). Detection can then be carried out via thermal conductivity, gas chromatography (GC), infra-red, or other method.

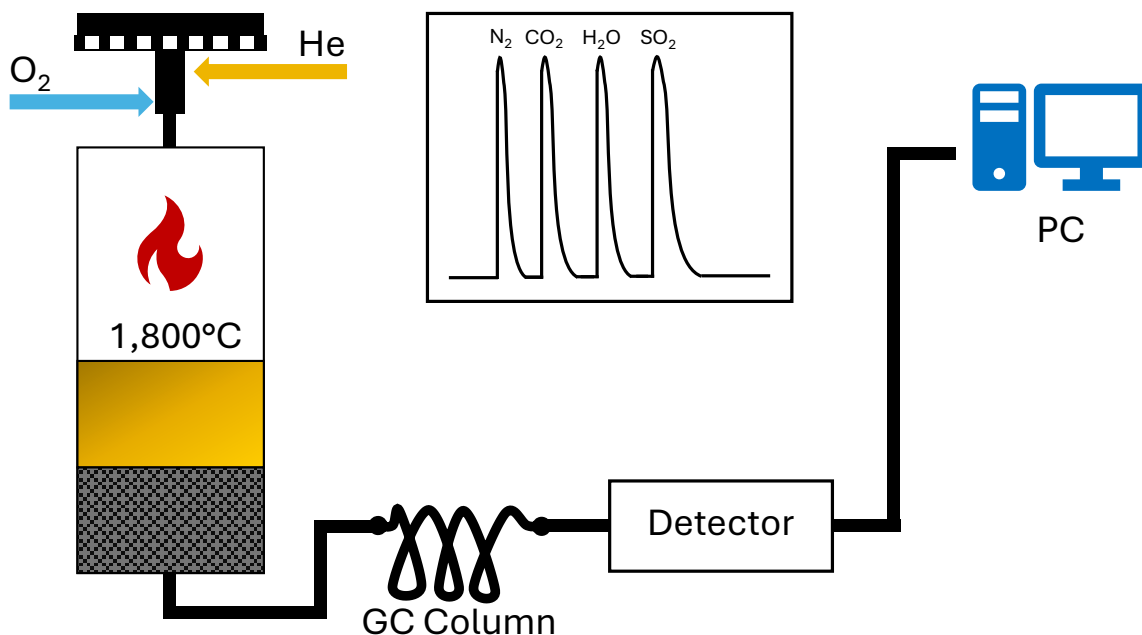


Figure 2.9 Elemental analysis experimental setup, recreated from the technical brief AMCTB no 29.⁷

Inductively Coupled Plasma Mass Spectrometry

Similarly to CHNS, inductively coupled plasma (ICP) is a powerful technique for measuring the elemental composition of a sample, utilising an argon plasma to aerosolise and ionise a liquid sample so that the components can be analysed using a secondary measurement technique, commonly optical emission spectroscopy (ICP-OES) or mass spectrometry (ICP-MS).⁸ The benefit of using this technique in combination with CHNS analysis is that ICP can provide metal concentrations in a sample to parts per million accuracy.

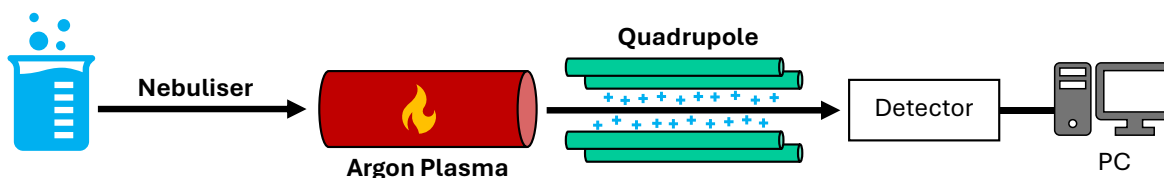


Figure 2.10 Scheme for the ICP-MS analysis.

Powder X-Ray Diffraction (PXRD)

X-ray diffraction (XRD) techniques remain the most prominent technique for analysing the crystalline structures of MONs.⁹ XRD operates on the principle that X-ray light is partially scattered when striking atoms within crystal layers.¹⁰ The setup involves a sample placed horizontally, with X-ray source and detector arranged on an angular rotation module which can change the angles of incident beam and detection respectively so that measurement over the full angular range can be achieved (Figure 2.11). A knife edge is placed close over the sample, perpendicular to the incoming X-ray beam, to reduce detection of reflected X-ray intensity (as opposed to diffracted rays from the sample).

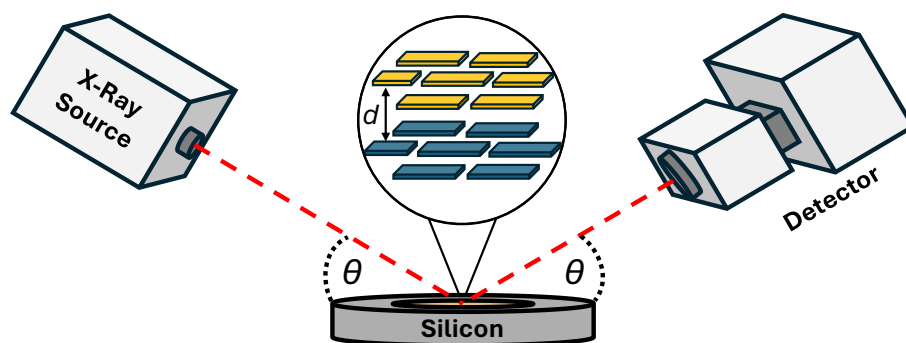


Figure 2.11 Experimental setup for PXRD analysis. X-ray source is shown incident on powder sample flattened onto silicon plate. Crystal spacing d is shown between blue bottom and yellow upper crystal layers.

The distance between layers inversely effects the angle of diffraction according to Bragg's law (Equation 2.7). A requirement of XRD is that the interlayer distance is similar to the wavelength of light used (similar to a normal diffraction grating), meaning that diffracted light between two layers constructively interfere and can be measured by the detector at certain angles. Powder X-ray diffraction (PXRD) operates on the same principles, but in cases where large enough single crystals cannot be grown, or to get a more representative measurement of a sample, the X-rays are incident on a flat powder surface, with particles in random orientations such as is likely for freestanding MON powders. By rotating the sample, multiple measurements can be taken at each angle, allowing a composite scan to be built up for the sample. This bulk measurement is more representative of a material and can be used to "fingerprint" the sample.

$$\text{Equation 2.7} \quad \sin\theta = \frac{n\lambda}{2d} \qquad \text{Bragg's Law}$$

Where θ is the angle of diffraction, n is an integer, λ is the X-ray wavelength, and d is the space between layers.

Dynamic Light Scattering (DLS)

Dynamic light scattering (DLS) is a useful technique which can infer specific properties of molecules.¹¹ The foundation of this is in the scattering by colloidal suspensions studied by Tyndall in 1868, where particles were larger than the wavelength of incident light. Following this, scattering by particles smaller than the wavelength of incident light was reported by Lord Rayleigh in 1871. In a static system, light is scattered as a function of the size and shape of macromolecules, but intensity fluctuations are observed in liquid systems due to the interference of Brownian motion, which describes diffusion of particles in a system. To infer the effects of scattering to particle size, a relationship between Brownian motion theory and the translational friction of molecules in solution is described by the Stokes-Einstein equation (Equation 2.8). Since the friction experienced by a molecule in solution is proportional to its radius and to the viscosity of the solvent surrounding the particles, the scattering of light in a known solvent system allows the determination of the diffusion coefficient of a molecule. Given the influence of heat on Brownian motion, DLS experiments must be performed at known temperature. Since the hydrodynamic radius models a hypothetical sphere, it should be noted that non-spherical bodies will have a more complex relationship with the diffusion constant, and this radius can therefore be less accurate.¹¹

Equation 2.8
$$D = \frac{k_B T}{6\pi\eta R_H}$$
 Stokes-Einstein Equation

where D is the translational diffusion coefficient ($\text{m}^2 \text{s}^{-1}$), k_B is the Boltzmann constant ($\text{m}^2 \text{kg K}^{-1} \text{s}^{-2}$), T is temperature (K), η is viscosity ($\text{Pa} \cdot \text{s}$), and R_H is the hydrodynamic radius of the molecule (m).

In a modern DLS instrument, monochromatic laser light is scattered uniformly by particles, which undergo a phenomenon known as Doppler broadening as the molecules are in continuous motion. The scattered light subsequently results in destructive and constructive phases. Intensity fluctuations are correlated with respect to time (ns – μs) to determine the rate, which can then be statistically converted to give information about the diffusion behaviour of molecules (Figure 2.12). Further details of the process are described by Stetefeld et al.¹¹

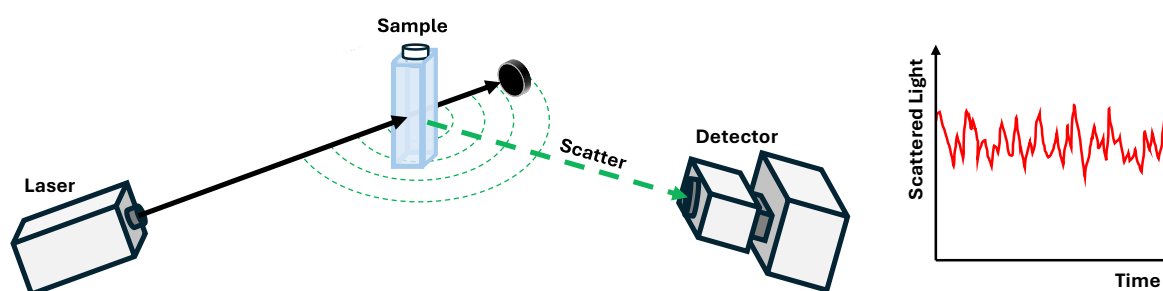


Figure 2.12 Diagram for the experimental setup of a DLS experiment.^{11,12}

Cyclic Voltammetry (CV)

In chemical reactions with electron transfer processes (i.e., REDOX), an electron moves from the HOMO of a donor molecule to the lower energy LUMO of an acceptor e.g., $\text{Fc}^+ + [\text{Co}(\text{Cp}^*)_2] \rightleftharpoons \text{Fc} + [\text{Co}(\text{Cp}^*)_2]^+$.¹³ Alternatively, the electron acceptor can be reduced electrochemically, where the energy of the applied voltage must be higher than the LUMO of the acceptor (Figure 2.13). In the example above, where $\text{Fc}^+ + e^- \rightleftharpoons \text{Fc}$, the voltage must be higher than the LUMO of Fc^+ .

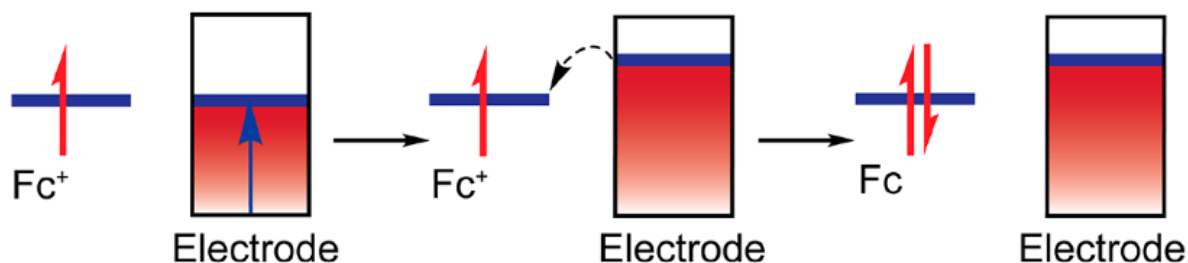


Figure 2.13 Energy levels required for an electrode to donate an electron to the LUMO of Fc^+ . Reproduced from Elgrishi et al.¹³

When an electron moves to or from an electrode, current is generated. By measuring the change in current with increasing voltage, the redox potential of any reaction occurring at the electrode surface can be measured. The cyclic voltammetry (CV) technique varies the voltage and measures the current for this purpose, first increasing voltage before returning to zero, then ramping to negative potential and then a final return to zero volts.

Figure 2.14 describes the concentration change of analyte at the electrode surface. From point A→B, the potential becomes less positive and some Fc^+ is reduced to Fc. The current increases with the flow of electrons as they are accepted, and the rate of acceptance is dependent on the voltage as it ramps. This continues until point C, the voltage at which the energy of electrons is higher than the LUMO of Fc^+ and further voltage ramping has a reduced effect. Here, the layer of newly created Fc around the electrode surface inhibits access of Fc^+ to the surface, and the response is diffusion limited. Some Fc^+ diffuses through and continues to be converted, but from point C→D the current response decreases as the Fc layer grows.

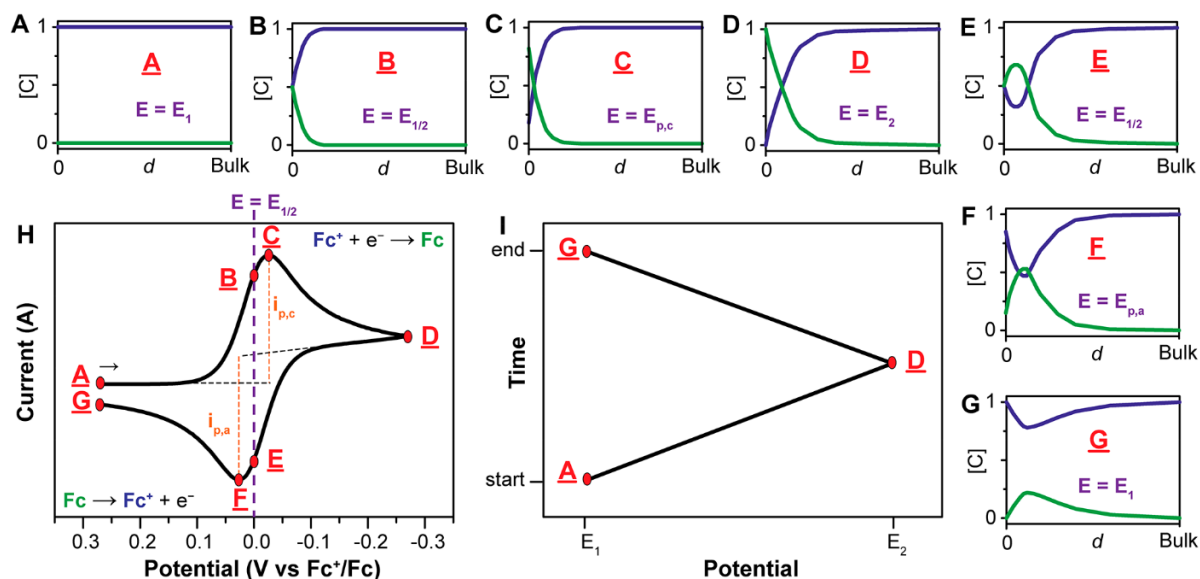


Figure 2.14 The cyclic voltammogram (H) and concentrations of Fc (green) and Fc^+ (blue) at the electrode surface at different points (A-G) throughout one voltage cycle (I). Reproduced from Elgrishi et al.¹³

At point D, the voltage peaks and begins to return to zero voltage. Here, the thick layer of Fc becomes the necessary electron donor, and the oxidation is voltage limited $D \rightarrow F$. At point F the concentration of Fc is lower than Fc^+ which has been reformed by oxidation so as the voltage continues back to positive voltage, the diffusion of Fc to the surface is limiting.

The peak separation E-F can be empirically calculated at standard temperature and pressure (STP) and compared to the Nernst predicted value of 57 mV to determine reversibility. Deviation from this indicates either a non-reversible process such as gas evolution, or degradation, or another non-Nernstian effect e.g., adsorption to the surface. When this effect is due to surface adsorption, the surface coverage can be calculated using the Randles-Sevcik equation. For free species, the peak current is linearly related to the square root of the scan rate (Equation 2.9). Repeat cyclic measurements can be used to determine the degradation of an electrode when the cycle is irregular. When analyte adsorbs to the surface, the plot of i_p vs. $v^{1/2}$ deviates from linearity and can be related by Equation 2.10, where the current response is proportional to the surface coverage by adsorbed species.

Equation 2.9
$$i_p = 0.446nFAC^0 \left(\frac{nFvD_0}{RT} \right)^{1/2}$$

Where i_p is the peak current, n is the number of electrons in the redox reaction, F is the Faraday constant, A is the electrode surface area, C^0 is the bulk concentration of analyte in mol cm^{-3} , D_0 is the diffusion coefficient in $cm^2 s^{-1}$, R is the gas constant, and T is temperature.

Equation 2.10
$$i_p = \frac{n^2 F^2}{4RT} v A \Gamma^*$$
 where Γ^* is the surface coverage in mol cm^{-2} .

The cyclic voltammetry cell uses three electrodes (Figure 2.15): the working electrode (WE) is the surface where analyte interacts, the counter electrode (CE) represents the opposite electrode in the circuit, whilst the reference electrode (RE) parallels the working electrode but is selected for inactivity to analyte to correct the current response at the WE.

Different materials are commonly used for the electrode types. The WE is commonly a glassy carbon electrode (GCE), polished to remove any adsorbed species and stable to degradation at most potentials. The counter electrode is usually platinum as this is inert to reaction with many analytes, and of a higher surface area than the WE to avoid that being a limiting factor. Reference electrodes are commonly Ag/AgCl, but other silver electrodes can be used. These will often be referenced in literature as simply Ag/Ag⁺.

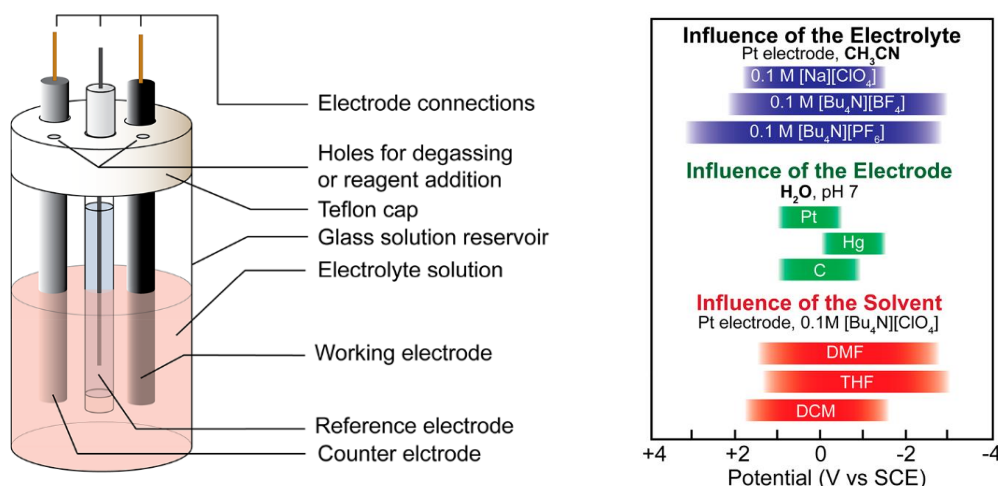


Figure 2.15 The cyclic voltammetry cell (right) with working, counter, and reference electrode, and effective potential ranges for electrolyte, electrode, and solvent selection (left). Reproduced from Elgrishi et al.¹³

Section 2.5 References

1. *The Principle of Time-Correlated Single Photon Counting*, https://www.picoquant.com/images/uploads/page/files/7253/technote_tcspsc.pdf (Accessed October 2024).
2. Li, X. *et al.* Ultrafast Relaxation Dynamics in Zinc Tetraphenylporphyrin Surface-Mounted Metal Organic Framework. *Journal of Physical Chemistry C* **122**, 50–61 (2018).
3. Li, X. *et al.* Ultrafast Relaxation Dynamics in Zinc Tetraphenylporphyrin Surface-Mounted Metal Organic Framework. *Journal of Physical Chemistry C* **122**, 50–61 (2018).
4. Nanoscope Instruments, Scanning Electron Microscopy. <https://www.nanoscience.com/techniques/scanning-electron-microscopy/>.
5. Transmission Electron Microscopy. <https://www.nanoscience.com/techniques/transmission-electron-microscopy/>.
6. Oxford Instruments: AFM Principle - How Does an Atomic Force Microscope Work? <https://afm.oxinst.com/outreach/how-does-an-afm-microscope-work>.
7. CHNS Elemental Analysers. https://www.rsc.org/images/chns-elemental-analysers-technical-brief-29_tcm18-214833.pdf (2008).
8. Thomas, R. *A Beginners Guide to ICP-MS*. www.scientificsolutions1. (2001).
9. Sasitharan, K. *Metal-Organic Framework Nanosheets: A New Dimension in Photovoltaics Research*. (2020).
10. Holder, C. F. & Schaak, R. E. Tutorial on Powder X-ray Diffraction for Characterizing Nanoscale Materials. *ACS Nano* vol. 13 7359–7365 Preprint at <https://doi.org/10.1021/acsnano.9b05157> (2019).
11. Stetefeld, J., McKenna, S. A. & Patel, T. R. Dynamic light scattering: a practical guide and applications in biomedical sciences. *Biophysical Reviews* vol. 8 409–427 Preprint at <https://doi.org/10.1007/s12551-016-0218-6> (2016).
12. The principles of dynamic light scattering. <https://wiki.anton-paar.com/en/the-principles-of-dynamic-light-scattering/>.
13. Elgrishi, N. *et al.* A Practical Beginner's Guide to Cyclic Voltammetry. *J Chem Educ* **95**, 197–206 (2018).

Chapter 3:

Effect of Aggregation on Exciton Dynamics in Porphyrin-Based Metal Organic Framework Nanosheets

Section 3.1 Abstract

Liquid exfoliation is widely used to synthesise a variety of 2D materials and is often followed by rounds of centrifugation to remove partially exfoliated material. The effect of the way suspensions of nanosheets are processed by different methods is often overlooked but can result in vastly different morphologies and aggregation behaviour. How nanoparticles aggregate can also lead to changes in their photophysical properties.

Metal organic framework nanosheets (MONs) are a class of 2D materials with tuneable chemistries making them suitable for diverse applications including sensing, catalysis, electronics, and separation. Zinc-porphyrin based nanosheets, $Zn_2(TCPP)$, were one of the first MONs to be reported, and have been used in many optical applications such as therapeutic treatments, photo-catalysis, sensing, and solar cell additives.¹ The aggregation of such materials can influence the photophysical properties, particularly emission and excited state lifetime. It is useful therefore to understand the ramifications of this and demonstrate options for specific tuning of the photophysical properties of these materials. This work therefore aims to identify the effects centrifugation has on the aggregation of $Zn_2(TCPP)$ MONs in dispersion and investigate the subsequent effect on photophysical properties of emission, excited state dynamics, and particularly exciton-exciton annihilation.

We observed that the photophysical properties of $Zn_2(TCPP)$ nanosheets changed depending on their centrifugation history, even when adjusted for concentration, indicating ramifications for their implementation in optical devices. The effect of centrifugation on the aggregation of $Zn_2(TCPP)$ MONs in suspension was investigated. Following exfoliation, the nanosheets were observed by atomic force microscopy (AFM) to be 0.5-3 nm thick, and averaging 150 nm in diameter, and subsequent post-synthetic centrifugation resulted in significant aggregation of small nanosheets, leading to particles as large as 6 μm as measured by dynamic light scattering (DLS). The concentration dependence of $Zn_2(TCPP)$ nanosheets on emission spectra shape and intensity was also investigated through Stern-Volmer modelling, with an observed aggregation dependent quenching mode of S_1 and S_2 emission bands by dynamic and static modes, respectively.

The fluence dependency of excited state lifetimes were increased proportionally by centrifugation rate, implying that the aggregate species promote exciton-exciton annihilation between particles. The exciton diffusion pathlength was calculated to decrease accordingly by 5-10x upon centrifugation.

This work highlights how centrifugation can lead to aggregation of 2D materials which can affect photophysical properties important in determining their performance in a wide range of applications. The benefit of spatially separated monolayer nanosheets is evidenced by spectroscopic techniques.

Section 3.2 Introduction

Metal organic framework nanosheets (MONs) are extended nanosheets constructed from metal ions bridged by rigid, organic linkers, with only non-covalent bonds in the 3rd dimension.^{1,2} MONs combine the high external surface area, nanoscopic dimensions and anisotropic structures of 2D materials with the diverse chemistry, tuneable structures, and intrinsic porosity of metal-organic frameworks (MOFs). Due to the range of linkers available, the properties of MONs can be tuned by modular linker substitution, or post-synthetic functionalisation to give a diverse array of chemical properties, making them exceptionally suited to many applications such as gas-storage, water purification, catalysis, drug delivery,

Ordered porphyrin MOFs such as $Zn_2(TCPP)$, where TCPP is a porphyrin derivative Tetrakis(4-carboxyphenyl)porphyrin, are highlighted in the literature as good models for mimicking natural photosynthesis (e.g., compared to ordered chlorophylls), making these systems particularly interesting for investigating excited state relaxation dynamics by ultrafast transient absorption spectroscopy.^{3,4} In particular, the bimolecular recombination of excited states, or exciton annihilation, is a process which enables the relaxation of excited states and reduces exciton transport efficiency.⁵ A paper by Sasitharan et al. revealed that $Zn_2(Zn-TCPP)$ is a useful additive in the hole transport layer of perovskite solar cells, so the study of light harvesting, and energy transfer dynamics could offer insight into improving these materials.^{6,7}

A novel method for scaling the synthesis of $Zn_2(TCPP)$ which yields a MON with a vacant porphyrin cavity was developed by Ashworth et al. (Figure 3.1).¹ MONs based on porphyrin moieties such as this are particularly attractive for photophysical study due to their optical and chemical tuneability.⁸⁻¹⁴ The inherent efficiency of porphyrins for electron transfer in electron donor-acceptor configurations makes them promising candidates for photocatalysis, sensing, solar cell, or opto-electronic device applications.⁹

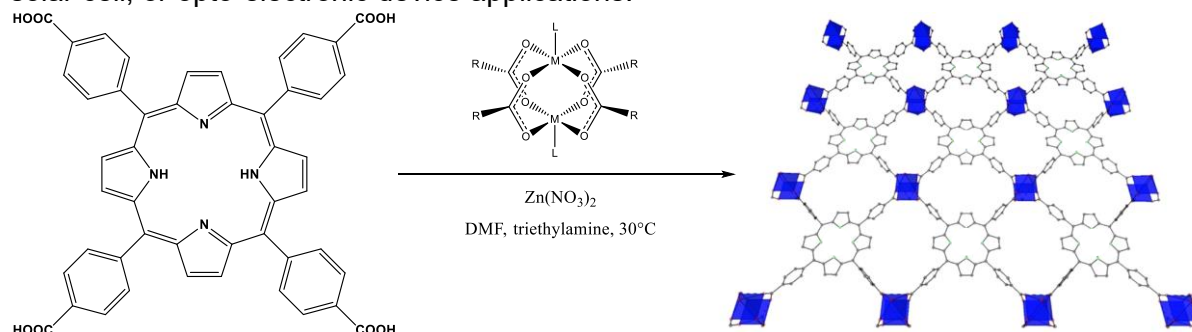


Figure 3.1 Scheme for the batch synthesis of $Zn_2(TCPP)$ at room temperature.

Synthesis conditions and post-synthetic processing methods such as centrifugation, sonication, or storage may have significant effects on nanomaterial particle size and morphology. Such effects may also result in changes to the photophysical properties of the materials. $Zn_2(TCPP)$ MONs, widely recognised material from literature, would benefit from photophysical study due to its diverse optical applications, but with a variety of reported iterations on its synthesis which may affect the material morphology and structure.¹⁵⁻¹⁹

As such, $Zn_2(TCPP)$ will be investigated to determine the effect concentration and centrifugation have on particle size distributions characterised by atomic force microscopy (AFM) and dynamic light scattering (DLS), before analysis of concentration dependence on emission by steady state and time resolved methods. Subsequently, the effects of centrifugation of $Zn_2(TCPP)$ on excited state dynamics, particularly exciton annihilation, will be characterised by the same methods, as well as ultrafast pump-probe spectroscopy to calculate the lifetime and diffusion pathlength of excitons in these materials.

Section 3.3 Results and Discussion

Zn₂(TCPP) MONs were synthesised directly via the low temperature reaction of zinc nitrate with TCPP linker in a 2:1 stoichiometric ratio in the presence of 4 molar equivalents of triethylamine, with stirring at 30 °C for 1 hr before the solids were collected and washed via centrifugation and dried giving an 80% yield. The product was analysed by powder X-ray diffraction (PXRD) to determine the crystal phase, revealing defined peaks in the PXRD pattern that indicate crystallinity in the material, matching previous literature (Figure 3.2). Ashworth et al. identified the peaks at 9° and 18° as the 002 and 004 reflections, respectively. A peak at 5.3° is ascribed to changes in interlayer distance by axial solvent exchange in a small proportion of nanosheets and is also present in previous reports, possibly due to a change in packing structure e.g., AAA to ABA.^{1,6} A simulated pattern is also shown in Figure 3.2, produced via Pawley fitting from the structure reported by Tang et al.²⁰ Experimental data match simulated peaks for the hkl coordinates 011, 002, 101, and 004.

The percentage composition of carbon, hydrogen, nitrogen, and zinc for the product formed were derived experimentally from elemental analysis and inductively coupled plasma optical emission spectroscopy (ICP-OES), shown in Figure 3.2, to compare with theoretical values for composition of Zn₂(TCPP) MONs calculated from the molecular formula Zn₂(TCPP)(DMF)₂, where DMF is a ligand coordinated via carboxylate oxygen to the axial position on the paddlewheel secondary building unit. Experimental values obtained for zinc and CHNS match the theoretical composition well, in particular finding no evidence for over metalation of zinc such as that found by Ashworth et al.¹ The loss in carbon composition, and to a lesser extent nitrogen, coupled with an increase in “other” elements could be attributed to contamination by water, with several possible structures:

- Zn₂(TCPP)(DMF)₂ = C (61 %), H (3.8 %), N (7.9 %), O (15 %), Zn (12.3 %)
- Zn₂(TCPP)(H₂O)₂ = C (60 %), H (3.2 %), N (5.9 %), O (16.8 %), Zn (13.7 %)
- Zn₂(TCPP)(DMF)₂(H₂O)₅ = C (56 %), H (4.4 %), N (7.3 %), O (21 %), Zn (11.3 %)

Based on these calculations, the elemental composition results are attributed to a general chemical structure Zn₂(TCPP)(DMF)₂ with average contamination by ~5 molar equivalents of water without substituting DMF. This does not seem to have altered the crystal structure. The extended structure can be treated as a mixture of unit cells with varying solvent stoichiometry. Future work should use thermogravimetric analysis to ascertain specific solvent content.

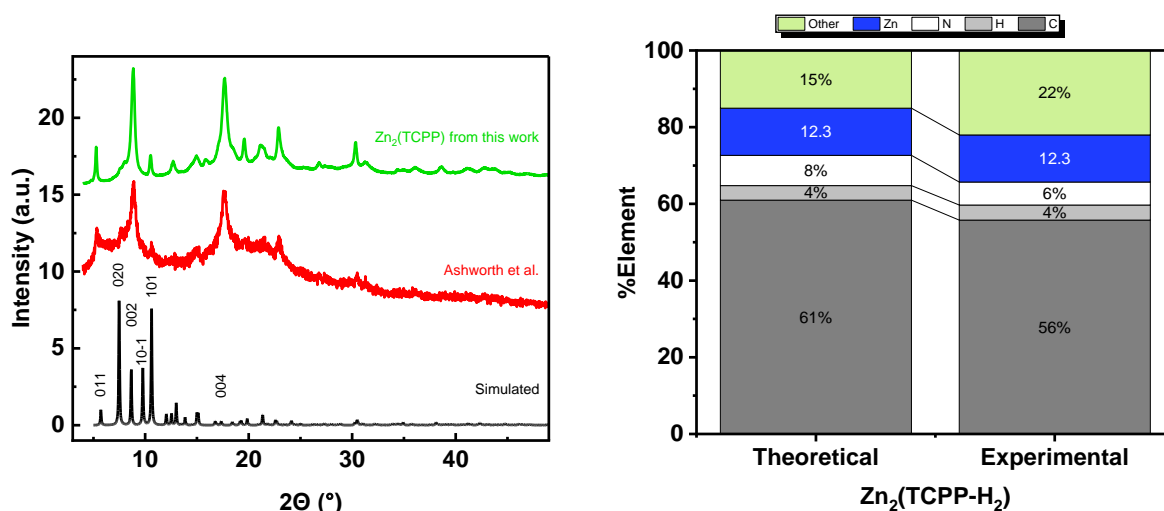


Figure 3.2 Comparison of PXRD patterns for Zn₂(TCPP) synthesised in this work, as in previous work by Ashworth et al.¹, and simulated pattern (left), and composition data of Zn₂(TCPP) measured using elemental analysis and ICP-OES, compared to theoretically calculated data (right).

To measure particle size for varying concentrations of Zn₂(TCPP) MON suspensions, dynamic light scattering (DLS) was performed. The results indicated two distinct size distributions around 500 - 2,000 nm and 3,000 - 6,000 nm, with lower concentrations tending to have smaller average size (Figure 3.3). These likely represent populations of aggregated particles rather than isolated nanosheets. Given the few data points in size distributions, and the assumption in DLS that dispersed particles are spherical, the sizes given are likely to be inaccurate for anisotropic structures such as MONs, but the distributions allow comparisons of relative sizes/populations between samples of different concentrations.

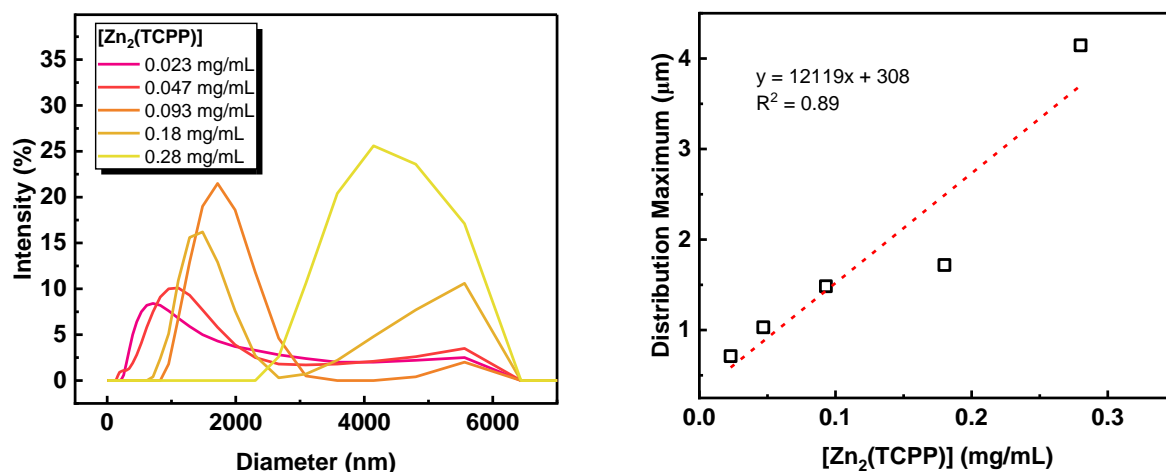


Figure 3.3 DLS population distributions for Zn₂TCPP MONs at different concentrations (left), and modal particle size plotted vs, concentration (right).

Atomic force microscopy (AFM) is routinely used as a complementary technique to DLS in the study of nanomaterials due to high angstrom resolution, allowing accurate measurement of particles with nanoscopic dimensions. It should be noted, however, that these images are only a small subset of particles dried on mica, and therefore may not be representative.

Aspect ratio, defined as the width of a nanosheet divided by height, is useful for statistical analysis of nanostructures measured by AFM, as it allows definitive classification of a material as a nanosheet. Using the definition described by Ashworth et al., a nanosheet is an anisotropic structure which is >10x wider than its thickness or height, and isolated from supports.² For the Zn₂(TCPP) produced in this work, high aspect ratio nanosheets are observed up to 600 (Figure 3.4), measured by height profiles across AFM micrographs.

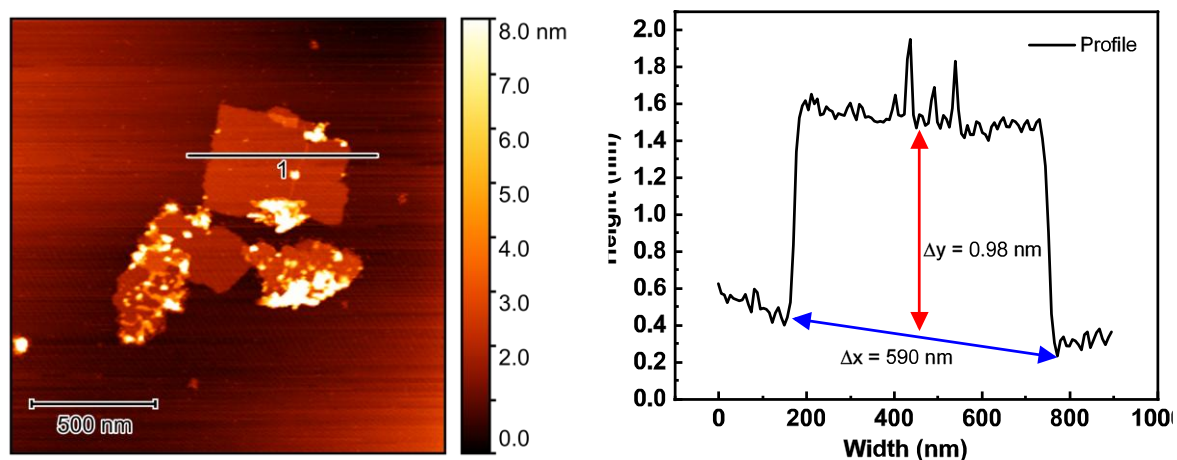


Figure 3.4 AFM micrograph and details for measurement of profile width and height

In practice, however, many isolated particles in AFM of $Zn_2(TCPP)$ are not identified as monolithic crystals but are confirmed by image analysis to consist of clusters of much smaller nanosheets (Figure 3.5). Dilution of nanosheet suspensions before dropping on hot mica is standard practice to avoid this aggregation, but samples consisting of isolated nanosheets with no aggregates are notoriously difficult to produce.² Several dilutions were tested with consolidated height/width data from over 500 height profiles taken from the AFM of $Zn_2(TCPP)$ to perform a statistical analysis of particle size distributions on the surface (Figure 3.5). Due to the presence of aggregates, these results are not representative of individual nanosheet dimensions but do show that aggregated particles 0.5-5 μm wide are common, likely responsible for the large dimensions identified in DLS. Given the height range of 1-90 nm observed, these are attributed mostly to aggregates.

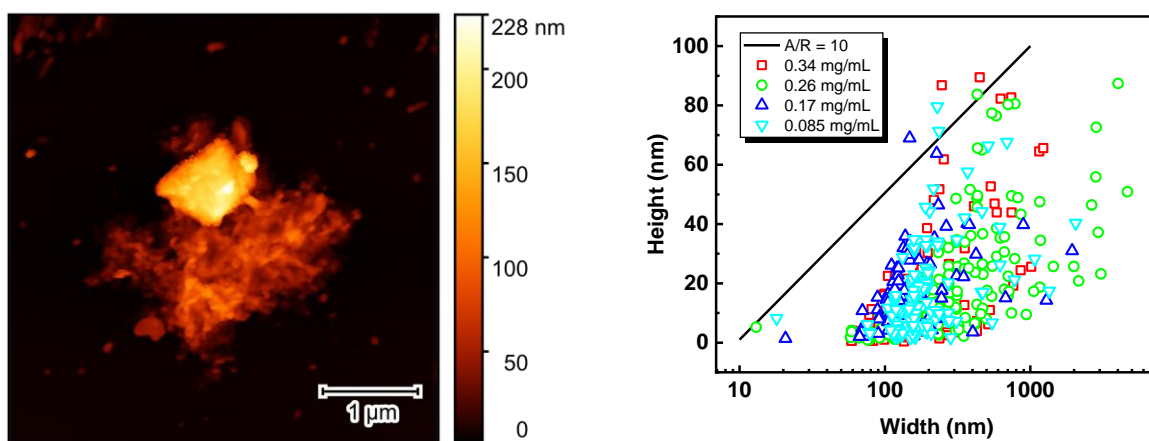


Figure 3.5 AFM micrograph of aggregates and nanosheets of $Zn_2(TCPP)$, and the height vs. width values determined from samples dried from different suspension concentrations (with aspect ratio = 10 demarcation line).

Particles with heights <3 nm are expected to be 1-4 layer nanosheets given the calculated monolayer thickness of 0.77 nm.⁶ By removing data points with thicknesses >3 nm, the isolated nanosheets approaching monolayer are shown to all have high aspect ratio, with widths between 50 – 350 nm (Figure 3.6). No concentration dependence on size of measured aggregates was observed.

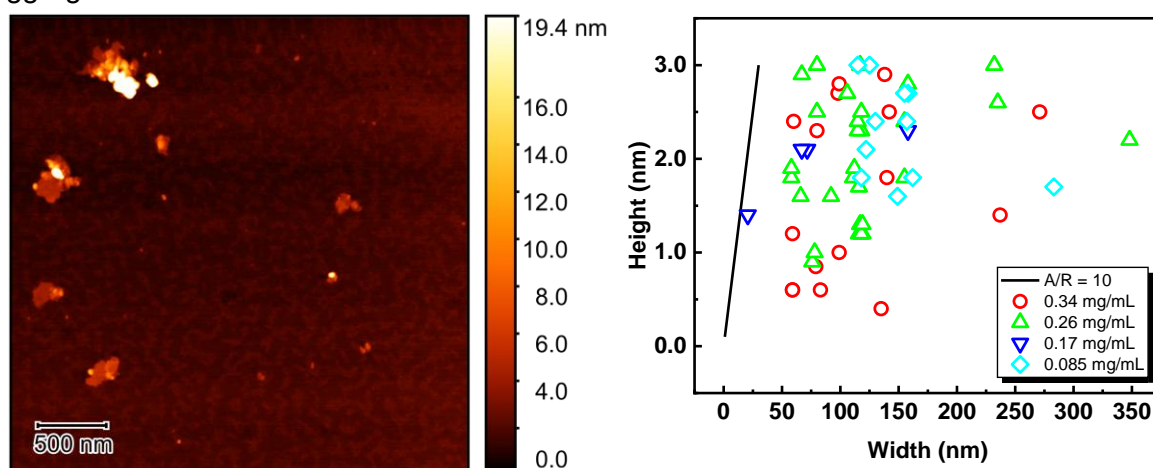


Figure 3.6 AFM with examples of monolayer $Zn_2(TCPP)$ nanosheets (left), and measured height vs width for AFM profiles of $Zn_2(TCPP)$ at different concentrations for data points where height ≤ 3 nm (right).

The ground-state electronic absorption of porphyrin moieties is well studied in literature, with predictable absorbance structures and effects when incorporated into a metal organic framework; Characteristic π - π^* Soret absorption bands are observed in the UV-visible spectrum at 417 and 425 nm for freebase TCPP and $\text{Zn}_2(\text{TCPP})$ MON respectively, indicating a redshift upon MON formation due to J-aggregation (Figure 3.7).^{1,5,9,14,21} Four Q-bands are observed in both spectra at 524, 557, 597, and 650 nm. The multiplicity of these Q-bands indicates no metalation in the porphyrin centre, as such an insertion would displace the amine protons and increase planar symmetry.^{1,21} The similarity of TCPP and TCPP MOF absorption spectra indicate little ligand-metal charge transfer in the MOF.⁵

Similarly, the emission spectra for freebase TCPP, also shown in Figure 3.7, display two emission peaks from the S_1 electronic state at 652 and 718 nm, with the former being the most intense as often seen in literature.^{8,9,14,22} Upon MON formation, the emission is greatly quenched by enhanced intersystem crossing (ISC) to a triplet state, and new weak emission bands are observed at 450, 490, 545, and 608 nm. The first two result from direct stimulated emission from the S_2 states, and the latter two assigned to emission from higher energy states corresponding to the $Q_x(0,0)$, and $Q_x(1,0)$ absorption bands.

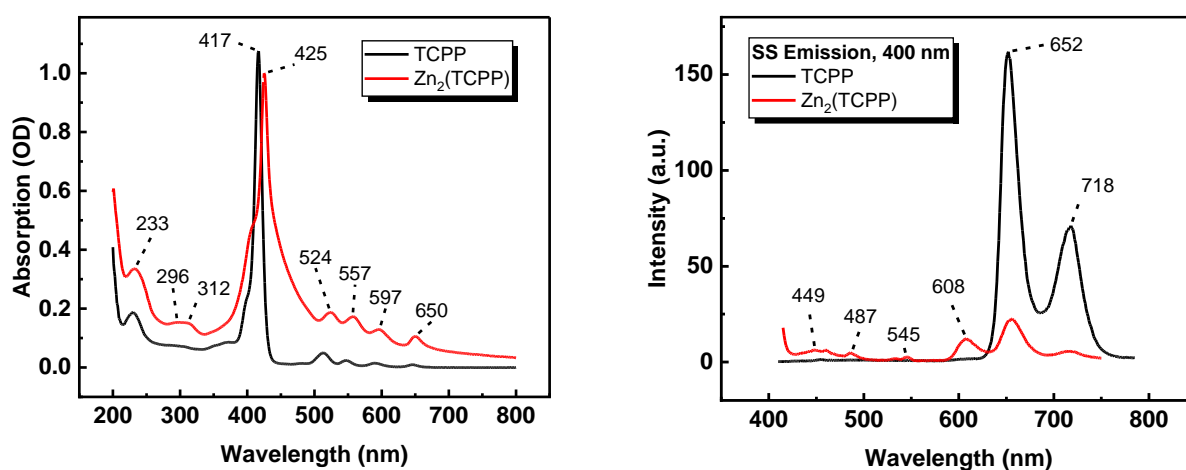


Figure 3.7 Steady state spectra comparing freebase TCPP with $\text{Zn}_2(\text{TCPP})(\text{DMF})_2$ in EtOH with absorption (left), and emission with 400 nm excitation (right).

In order to determine the effect of concentration on emission spectral shape and intensity, the emission spectra of $\text{Zn}_2(\text{TCPP})$ were measured at a range of concentrations (80 – 320 μM , see SI S3.10 for Beer-Lambert law adherence), shown in Figure 3.8. An asymmetric quenching of emission was observed where emission from the S_1 region (560 – 800 nm) undergoes greater quenching than the emission from the S_2 region due to the loss of the emission peak at 650 nm. As this 650 nm emission is a higher energy S_1 state than those responsible for emission at 720 nm, it is hypothesised this is due to enhanced intersystem crossing (ISC) between aggregates creating a quenching effect. The integration (ϕ) of these regions allows the proportion ϕ^{S_2}/ϕ^{S_1} to be calculated for each concentration and shows a linear increase in proportional S_2 emission, also shown in Figure 3.8. Reabsorption of emitted light by aggregates at higher concentrations is unlikely to be behind this observation because of the low absorption by $\text{Zn}_2(\text{TCPP})$ at wavelengths >650 nm. It is also unlikely that TCPP is being reformed at low concentrations, as the spectral shape or position of the Soret bands do not change (apart from intensity) with concentration (see SI S3.11 for normalised spectra).

A redshift in the emission maximum was observed from 448 - 464 nm with increasing concentrations of $\text{Zn}_2(\text{TCPP})$. Yue et al. ascribe this to the high extinction coefficient of the $S_0 \rightarrow S_2$ absorption, and low quantum yield of S_2 fluorescence; significant reabsorption of

emitted light leads to distortion and redshift of the emission peak. However, redshift is also associated in literature with aggregation of porphyrin moieties inducing π - π stacking, indicating another possible reason.^{22,23}

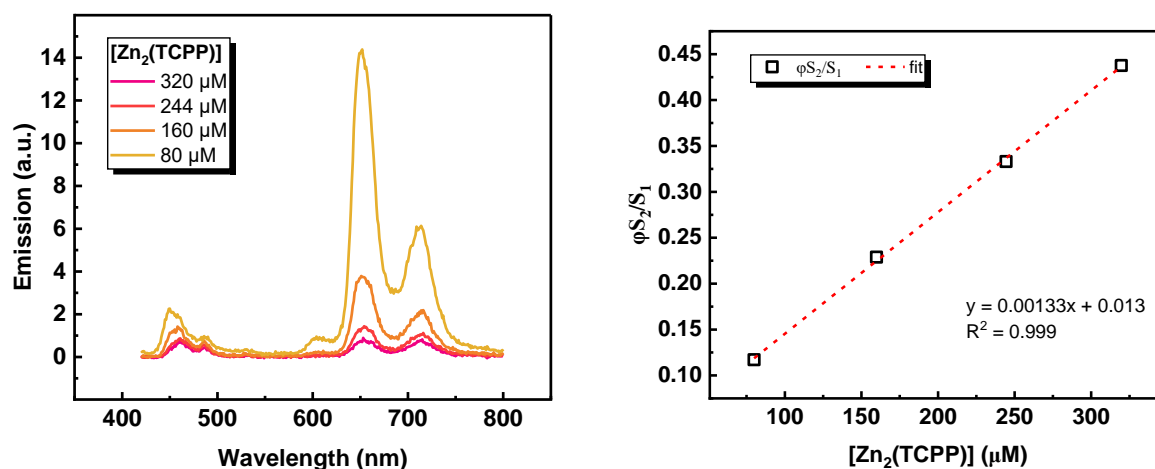


Figure 3.8 Emission spectra for different concentrations of Zn₂(TCPP) excited at 410nm in a 10 mm cell (left), and ratio of emission integrals for regions corresponding to S₂/S₁ (right).

It is conventional to use a plot to identify the Stern-Volmer constant, K_{SV} , associated with quenching mechanisms, where K_{SV} is the product of quencher rate coefficient, k_q , and the emission lifetime, τ_0 (Equation 3.1). By calculating the integral of emission bands for S₁ and S₂ separately and plotting the degree of quenching, I_f^0/I_f to concentration, K_{SV} can be established for each state (Equation 3.2).

$$\text{Equation 3.1} \quad K_{SV} = k_q \tau_0 \quad \text{Stern-Volmer Constant}^{24}$$

Where K_{SV} is the Stern-Volmer constant, k_q the quencher rate coefficient, and τ_0 the emission lifetime.

$$\text{Equation 3.2} \quad \frac{I_f^0}{I_f} \cong 1 + k_q \tau_0 \cdot [Q] \quad \text{Conventional Stern-Volmer Equation}^{24}$$

Where I_f^0 is the emission intensity with no quencher available, I_f is the variable emission intensity, k_q is the quencher rate coefficient, τ_0 is the lifetime of the emissive excited state without quencher present, and $[Q]$ is the concentration of the quencher.

As seen in Figure 3.9, the Stern-Volmer constant for S₁ quenching is much higher than that for S₂ quenching (0.0395 vs. 0.0077 μM⁻¹). The measurement of these samples by time-correlated single photon counting (TCSPC) indicate no change in emission lifetime with concentration (see SI S3.14). As such, the change in the degree of quenching must be due to an alternative, non-emissive quenching route. The fitted TCSPC data yields two emission lifetimes 1.26 and 3.88 ns. The latter was then used by Equation 3.1 to calculate the quencher rate coefficient, k_q , from the Stern-Volmer constant, K_{SV} , to be 0.01 and 0.002 μM⁻¹ ns⁻¹ for S₁ and S₂, respectively.

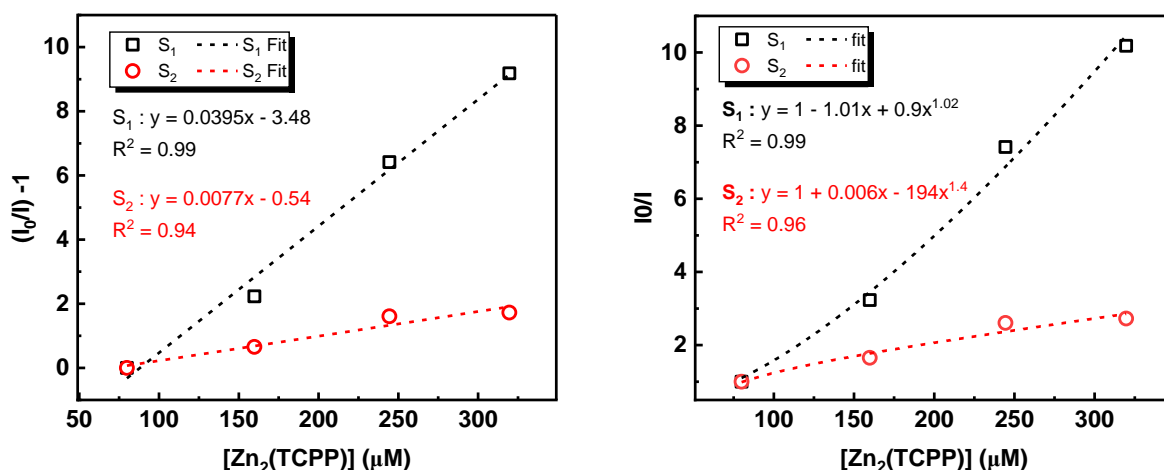


Figure 3.9 Conventional Stern-Volmer plot for S_2 and S_1 region integrals (left), and modified Stern-Volmer fitting for self-quenching (right).

Moreover, an observed positive and negative deviation, for the degree of S_1 and S_2 quenching, respectively, from the linear Stern-Volmer relationship implies some complication (Figure 3.9). Deviations from the conventional Stern-Volmer relationship may require some modification of the equation to account for other quenching mechanisms. A modified equation for a self-quenching system is used by Bae et al., Equation 3.3, to describe this relationship.^{24,25}

$$\text{Equation 3.3} \quad \frac{I_f^0}{I_f} \cong 1 + a[Q] + b[Q]^v \quad \text{Modified Stern-Volmer Equation}^{26}$$

Where I_f^0 is the emission intensity with no quencher available, I_f is the variable emission intensity, a and b are constants, $[Q]$ is the concentration of the quencher, and v is the order of quenching mechanisms involved in i.e., static/dynamic.

As seen in Figure 3.9, the S_1 and S_2 data plotted with the modified Stern-Volmer equation fits a positive, and a negative deviation respectively, indicating the potential for separate mechanisms. Positive deviation when v is greater than one implies the presence of static quenching mechanisms (i.e., non-radiative quenching within complexes or dimers) in addition to dynamic (diffusion limited) mechanisms.²⁵ As such, the positive deviation seen in the modified Stern-Volmer plot for S_1 may be due to quenching from stacked or aggregate nanosheets, although the low value for v seems to indicate only dynamic quenching mechanisms are present for S_1 excited states.

One cause of negative deviation is attributed to inaccessibility of quenchers to fluorophores due to aggregation, which is known from DLS/AFM to be present in this system. The fact that negative deviation is only present in the S_2 fitting implies that only this excited state is affected by aggregation (or is a negligible mechanism compared to the dynamic quenching in S_1). Additionally, it should be noted that the lifetime of S_2 excited states should be very short and therefore k_q could still be a large value.

It is hypothesised that only the S_2 excited state is affected by static quenching mechanisms, explaining the decreased concentration dependence, and the S_1 excited state is affected more by dynamic quenching mechanisms and therefore is more proportional with concentration. Since the population of S_1 states is directly fed by the large proportion of decaying S_2 excited states, it is therefore possible that the positive deviation of S_1 emission in the modified Stern-Volmer plot is due to reduced population in the S_1 excited state indirectly limited by the increased static quenching in the S_2 . Future work could further verify these results with greater concentration ranges/more data points.

Porphyrin excited state dynamics are extensively characterised in literature. Typically, they undergo a predictable excitation and decay pathway with excitation from the ground state S_0 to either S_1 or S_2 , where the S_2 excited state relaxes to the S_1 via rapid internal conversion before either emissive relaxation to the ground state, or intersystem crossing (ISC) to a triplet state T_1 , where it slowly decays to the ground state via the forbidden pathway.^{3,9,12,22,23}

The ultrafast transient absorption analysis of $Zn_2(TCPP)$ by pump-probe spectroscopy (Figure 3.10) reveals a much shorter-lived excited state in the MON (~4,000 ps) than the TCPP monomer (20,000 ps, SI S3.18). It is logical that there is an enhanced ISC rate in the MON vs. a TCPP molecule, also observed in literature, which is responsible for the shorter excited state lifetime and the reduced emission intensity by $Zn_2(TCPP)$ compared to TCPP.^{8,9,22,23} This model fits the observed data well so far for $Zn_2(TCPP)$, and the TA data shown in Figure 3.10, where kinetics are fitted with triple or quadruple lifetime components, with one fixed component of 3.88 ns based on the recorded fluorescence emission lifetime. To investigate the triplet state dynamics, both oxygenated and degassed $Zn_2(TCPP)$ were analysed by msTA (fitted kinetics for oxygenated and degassed can be found in SI S3.19-20) showing triplet lifetimes of 6 μ s and 20 μ s respectively, indicating quenching by oxygen of a triplet electronic state.

Negative ground-state bleach kinetics at 412 nm are observed to “lag” behind, peaking at 0.5 ps after excitation. This is in line with analysis by Li et al., who indicates that S_2 excited state is populated via a higher energy level S_2 prime (hot electronic state) responsible for the shoulder absorption at 416 nm in the steady-state.⁸ Indeed, analysis of the kinetics at 437 and 470 nm yields a <0.2 ps component consistent with the rate of S_2' to S_2 intramolecular vibrational relaxation which is not present in the fitted lifetimes for the “lagging” peaks at 412 and 532 nm.

Similarly, the 2.1 ps lifetime in the kinetics at 437 nm are consistent with the literature lifetime for emission from S_2 directly to the ground state (1.4 – 3.4 ps).^{8,9,22,23} The lifetimes 16 - 24 ps are attributed to either fast, non-radiative recombination due to the results shown for similar materials by Gu et al., or to aggregate enhanced ISC within the framework as in the works by Li, Haber, and Yu et al. which, given the distribution of aggregation observed in the materials, may suggest a distribution of rates can be expected for aggregate enhanced and non-enhanced ISC. The lifetimes between 66 - 686 ps are therefore attributed to ISC in nanoparticles of varying aggregation. Lifetimes in the ~10 ps range may be attributed to S_1 intramolecular vibrational relaxation.^{5,8,9,22,23}

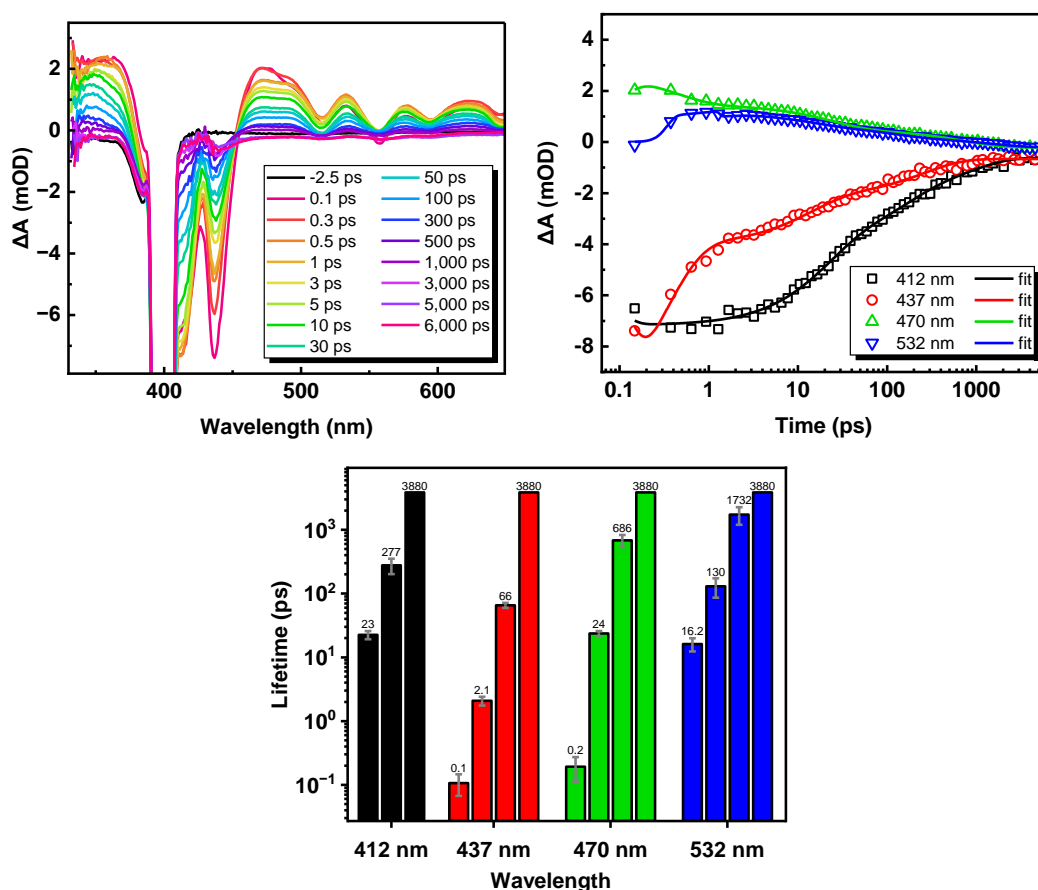


Figure 3.10 TA data for $Zn_2(TCPP)$ dispersion in ethanol with selected spectra (top left), kinetics at key wavelengths (top right), and fitted lifetimes (bottom).

To investigate the effect of centrifugation on particle size and agglomeration, the as-synthesised sample of $Zn_2(TCPP)$ was left to settle for two days in EtOH suspension before ~5 mL aliquots were diluted to 35 mL by EtOH in a 45 mL centrifuge tube and vortex mixed for 1 min to redisperse nanosheets. Prior to any post-synthetic centrifugation, 5 mL was removed from the surface of the suspension (0-2 cm depth) as a control sample labelled “Before Centrifugation”, or “Before C”, ignoring the washing steps by centrifugation in synthetic work-up. The centrifuge tube was subsequently topped back up to 35 mL by addition of 5 mL EtOH and vortex mixing for 1 min before centrifugation at 2,000 RPM for 30 mins. Once again, 5 mL was removed from the surface of the suspension and labelled “2,000 RPM” before the centrifuge tube was topped up to 35 mL by addition of 5 mL fresh EtOH. This process was similarly performed to produce samples centrifuged at 4,000, 6,000, and 8,000 RPM for 30 mins, finishing with a sample produced from the 5 mL taken after topping up for the final time and vortex mixing without further centrifugation, labelled “After Centrifugation”, or “After C” as a sample comparative to Before C (i.e., redispersed, no subsequent centrifugation). Sample concentration was measured by drying of 1 mL dispersion, before dilution to 0.2 mg mL^{-1} .

As such, a series of samples were obtained at the same concentration, which had been respectively post-synthetically centrifuged (PSC) at increasing speeds. The resultant decreasing dispersion concentrations from before dilution are listed in the SI table S3.5.

To follow the effects of PSC, dynamic light scattering (DLS) was utilised to measure the particle size distributions between samples of $Zn_2(TCPP)$ centrifuged at different speeds. A general increase in particle size is observed, with increased centrifugation speed. This was considered counterintuitive as centrifugation is typically used to remove larger particles. Given the

(overall) size change 400 nm to 800 nm between samples before PSC and after 8,000 RPM, it is apparent that large, aggregate particles are formed via this process which are loosely associated enough in dispersion to not be dense enough to be removed by centrifugation.

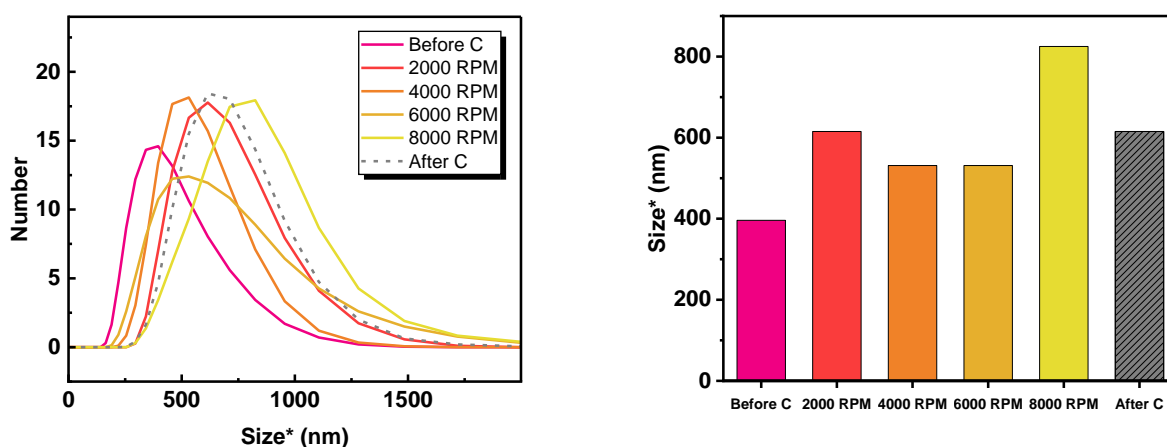


Figure 3.11 Particle size distributions of centrifuged $Zn_2(TCPP)$ as measured by DLS (left), and modal particle size from peak maxima (right). *Note that DLS assumes a spherical particle size, and therefore gives imperfect results for anisotropic nanosheets, but is still comparable for trends.

AFM analysis of PSC $Zn_2(TCPP)$ samples produced from 0.2 mg mL^{-1} suspensions offers a possible explanation to the DLS results: Samples without PSC (Before C) show isolated 50-400 nm diameter particles on the mica surface, often with high aspect ratios approaching 40. Thicknesses around 10 nm are common and there are few or no examples of large micrometre scale aggregates (Figure 3.12). Conversely, AFM analysis of 8,000 RPM PSC samples often show large multi-micrometre scale aggregates visibly made of smaller 100-300 nm diameter nanosheets.

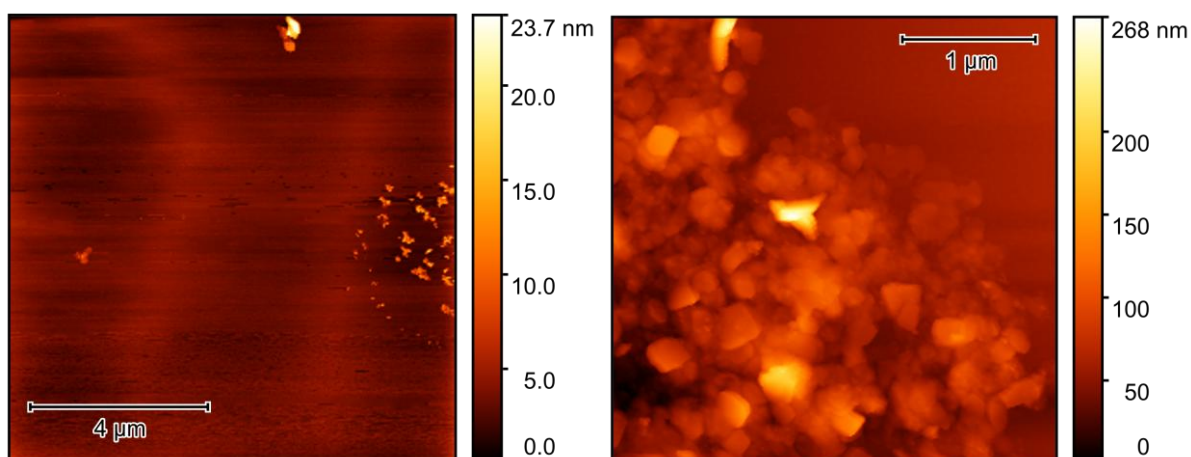


Figure 3.12 AFM of $Zn_2(TCPP)$ before PSC (left), and after 8,000 RPM PSC (right).

AFM analysis of $Zn_2(TCPP)$ samples after 8,000 rpm PSC allowed profile measurement of isolated particles around the edges of such aggregates (Figure 3.13). These show constituent particles are only slightly thicker than those before centrifugation but are notably smaller in lateral dimension after PSC. This seems good evidence that laterally wider particles are removed by PSC, but this effect is not observed in DLS analysis due to the competing effect of centrifugation driven aggregation. More results for AFM profiling can be found in the SI S3.22-26.

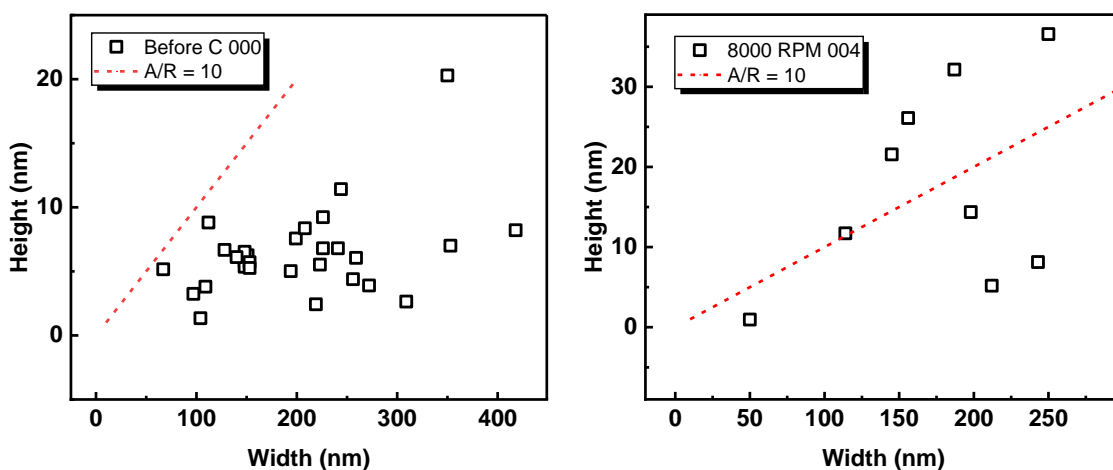


Figure 3.13 AFM of $Zn_2(TCPP)$ before PSC (left), and after 8,000 RPM PSC (right), with figures showing measured profile heights/widths plotted vs. demarcation line where aspect ratio is 10.

Comparing the intensity of UV-visible absorption peaks between samples shows an increase in the Soret absorption and central Q-band peaks with increasing centrifugation (Figure 3.14). This indicates a greater proportion of π - π^* transitions to the S_2 excited state within aggregated particles, inhibition of $Q_x(0,0)$, and increase of $Q_x(1,0)$ and $Q_y(0,0)$, and $Q_y(1,0)$ absorption in the S_1 state implying some enhancement of vibronic energy transitions.^{27,28}

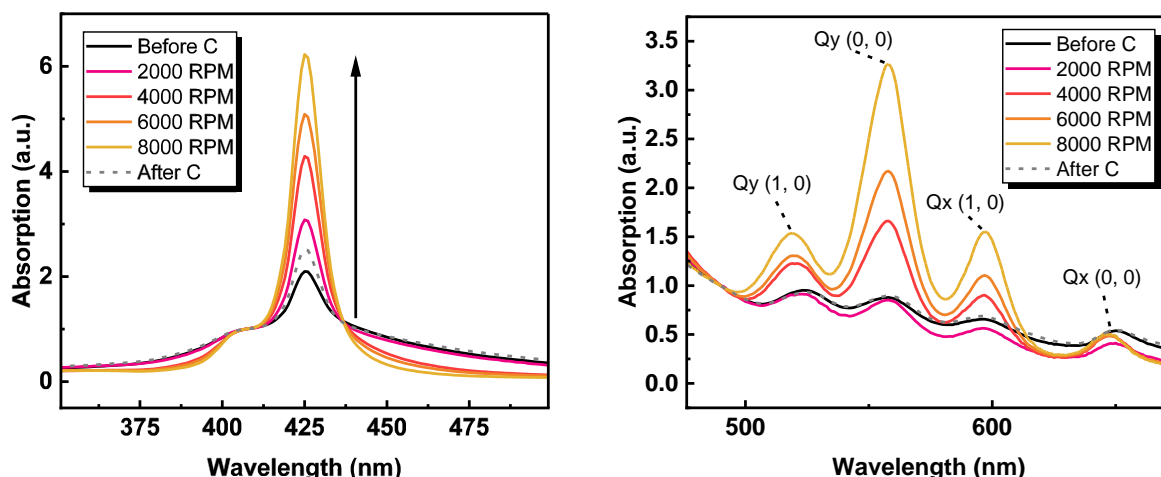


Figure 3.14 The trends of electronic absorption for $Zn_2(TCPP)$ centrifuged samples at increasing speeds 0-8,000 RPM before dilution to $4 \mu g mL^{-1}$ in ethanol. Data shows an increasing Soret absorption at 425 nm with spectra normalised at 415 nm (left), and the increase in Q bands at 557 and 597 nm in comparison to the peaks at 524 and 650 nm when normalised at 490 nm (right).

Predictably, this trend has an effect on the emission spectra for these samples, where S_1 emission is enhanced asymmetrically compared to S_2 with increasing centrifugation speed (Figure 3.15). This fits with what is expected from the Stern-Vomer analysis, since S_1 should be minimally affected by static quenching mechanisms due to aggregation. This indicates centrifugation is enhancing the population of S_1 states by reducing radiative mechanisms from S_2 . A narrowing of S_2 emission bands may indicate a reduction in π -stacking in the system, although the overall emission intensity remains similar regardless of centrifugation speed. As such, this may be evidence for decreased stacking as denser multilayer nanosheets are removed by centrifugation. It is speculated that the smaller peaks 475 – 550 nm may be due to Raman scattering contribution, which could be confirmed in future work by recording an excitation spectrum to observe the resultant shift of these peaks if true.

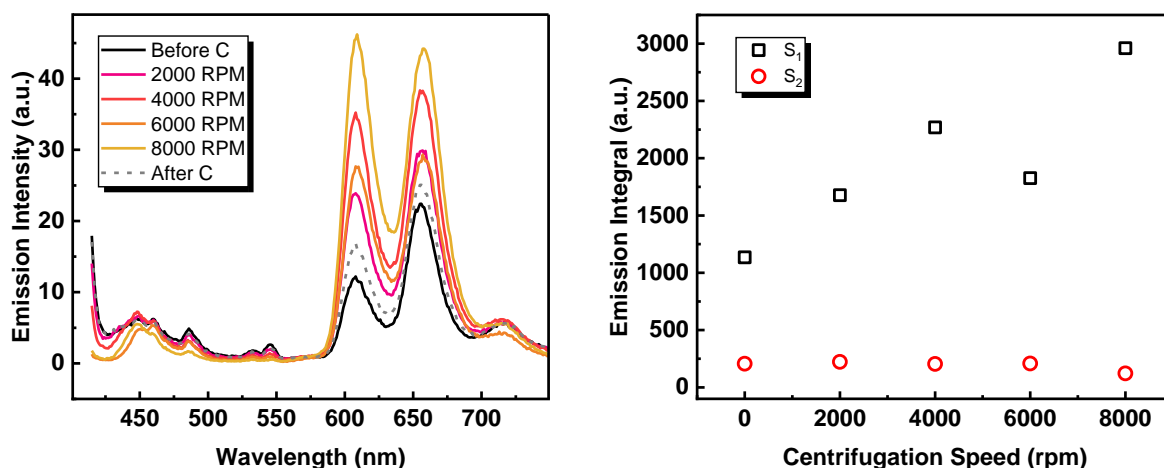


Figure 3.15 Electronic emission of centrifuged Zn₂(TCPP) samples measured after excitation at 400 nm.

TCSPC analysis reveals emission lifetimes for the samples are ~2.3 ns (Figure 3.16), less than the as-synthesised samples, but consistent with S₁ emission lifetimes in literature.^{3,9,22,23} This indicates that simply leaving the samples to settle over two days was enough for some dense particles to be removed (see SI S3.16-17 for settling rates recorded by UV-vis). The emission kinetics are unchanged by centrifugation, indicating any changes to the excited state dynamics are non-emissive (Figure 3.16). This also supports the hypothesis that centrifugation is increasing the triplet state quantum yield, as ISC kinetically competitive with fluorescence from S₁. This implies that centrifugation driven aggregation is responsible for enhancing ISC in Zn₂(TCPP).

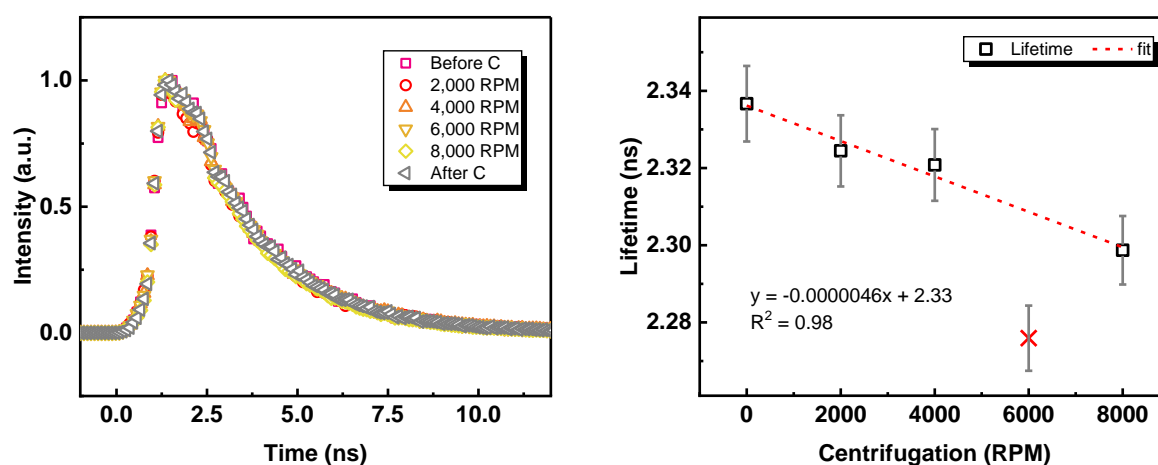


Figure 3.16 TCSPC kinetics with fitting (left) and calculated monoexponential lifetimes plotted against centrifugation speed, with data points omitted from the fit shown in red cross (right).

The transient absorption of centrifuged Zn₂(TCPP) samples were investigated using pump-probe spectroscopy to determine the power dependence of excited state lifetimes. Here, the 400 nm pump power was varied between 0.2, 0.4, 0.8, 1.0, 1.5, and 2.0 mW. Each experiment yielded time-resolved spectra with plotted kinetics chosen at key wavelengths. Methodology and results for power to fluence calculations can be found in the SI table S3.6.

The negative bleach at 440 nm is quite prominent in the Zn₂(TCPP) sample before post-synthetic centrifugation but is not obviously present in the TA spectra of the 8,000 RPM sample (Figure 3.17). This suggests the ground state Soret absorption is a convolution of a sharp peak at 425 nm and a broader, lower intensity peak at 440 nm. This latter may be from lower energy states from π -stacking in multi-layered particles. Centrifugation removing these

particles from suspension would explain the disappearance of this 440 nm ground state bleach in the centrifuged sample. As such, the accuracy of the thickness distribution measured by AFM in Figure 3.13 is called into question, suggesting this may not be representative of the sample.

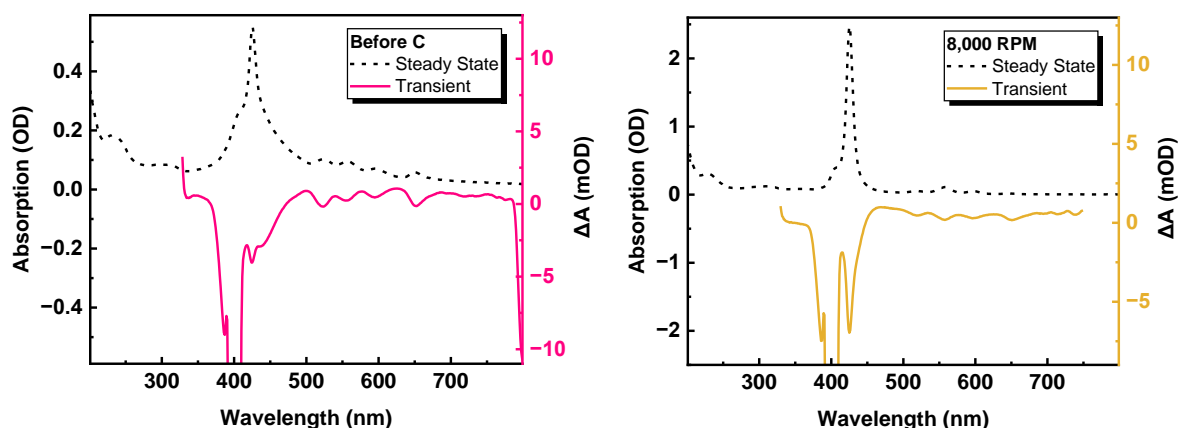


Figure 3.17 Steady state and transient absorption spectra for Zn₂(TCPP), with TA spectra 1 ps after excitation at 400 nm (2 mW) for Zn₂(TCPP) samples before centrifugation (left), and after 8,000 rpm post-synthetic centrifugation (right).

One of the processes that would lead to premature relaxation of an excited state of Zn₂(TCPP) e.g., in a solar cell, is exciton-exciton annihilation. At greater excitation laser power density, or fluence, the process of exciton-exciton annihilation is statistically more likely due to their increased proximity to each other. To assess the effect of centrifugation on exciton-exciton annihilation, a power dependence study of the kinetics at 440 nm were carried out for centrifuged Zn₂(TCPP) samples. Full data analysis for all samples can be found in the SI S3.37-48. As seen in Figure 3.18, significant power dependence is observed for all fitted lifetimes in Zn₂(TCPP) before PSC. The comparison of TA lifetimes at 440 nm for Zn₂(TCPP) shows that the diminishing proportion of negative signal at 440 nm for Zn₂(TCPP) samples centrifuged 0 – 8,000 RPM results in an increasing power dependence. These results show that PSC results in an increase in exciton-exciton annihilation for these materials. Given the particle size analysis earlier in this work, this is here hypothesised to be aggregation promoted exciton-exciton annihilation in close proximity nanosheets.

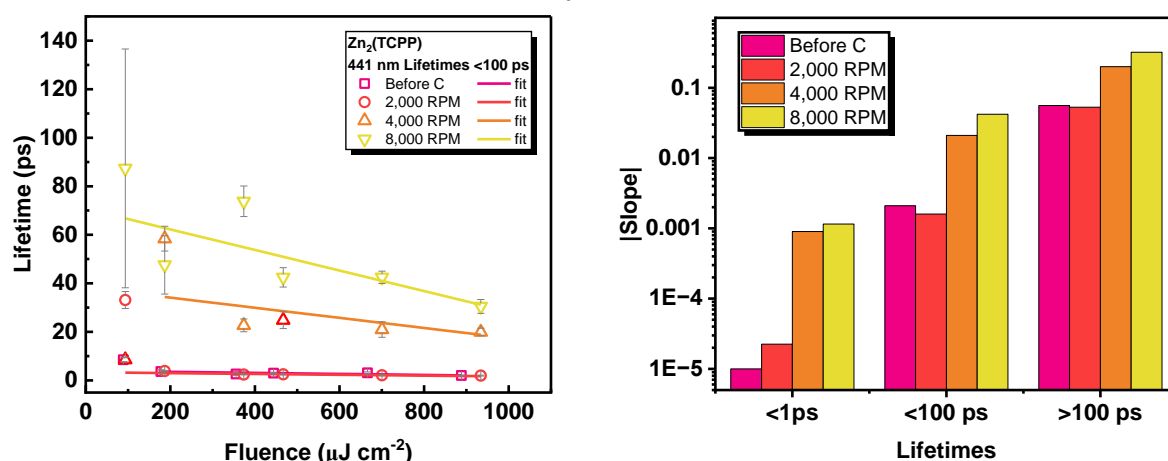


Figure 3.18 Gradients for fitting of power dependent lifetimes <100 ps calculated for TA kinetics at 441 nm for centrifuged Zn₂(TCPP) (left), and the modulus of the linear slope fitted for this relationship separated into three lifetime groups <1ps, <100 ps, and >100 ps (right).

Molecular excited states in porphyrin-based MOFs are known to efficiently migrate via hopping mechanisms to new sites before recombining via radiative or non-radiative mechanisms including exciton splitting into charge carriers.^{5,29} The Förster resonance energy transfer (FRET) process responsible for long-range exciton migration depends on the interchromophoric electronic coupling and overlap between donor fluorescence and acceptor absorption bands.⁸ In a self-quenching system such as Zn₂(TCPP), therefore, the centrifugation speed dependant increasing absorbance of the Q-band at 605 nm (Figure 3.14), and increasing emission also at 605 nm (Figure 3.15), indicates the rate of FRET transfer may be greater for PSC samples compared to before centrifugation. Additionally, since centrifugation was shown to increase particle size by aggregation (Figure 3.11, Figure 3.13), a lack of centrifugation may inhibit migration by depriving an excited MON from nearby acceptor porphyrin moieties. As FRET is typically a short-range process, this could mean centrifugation-driven aggregation increases the amount of interchromophoric transfer, leading to a greater exciton diffusion pathlength.³⁰ To investigate these effects, the method outlined by Gu et al. and Bossyani was employed for calculating annihilation coefficients and exciton diffusion pathlength from transient absorption data.^{5,31} The exciton annihilation dynamics simplified by Gu et al. are shown in Equation 3.4, where exciton density n is proportional to time delay t via a coefficient of the time-dependant annihilation rate $\gamma(t)$.

$$\text{Equation 3.4} \quad \frac{n_{(0)}}{n_{(t)}} = 1 + \gamma(t) \cdot n_{(0)} \cdot t \quad \text{Time Dependant Exciton Density}^{31}$$

Where $n_{(0)}$ is the initial exciton density, $n_{(t)}$ is the exciton density at specific delay times, $\gamma(t)$ is the time-dependant annihilation rate, and t is the delay time.

The pump laser fluence can be used to calculate values for average exciton density n by an expression combining the fluence calculation with the energy of pump wavelength and the absorption by the sample at this wavelength.³¹ As such, Equation 3.5 was used to produce a value for initial exciton density n_0 for excited state kinetics at 500 nm of Zn₂(TCPP) centrifuged at different speeds (before centrifugation, 2000 rpm, 4000 rpm, and 8000 rpm).

$$\text{Equation 3.5} \quad n_{(0)} = F_A \frac{P}{f\pi r_x r_y d} \frac{\lambda}{hc} = (1 - 10^{-A}) \frac{F_P \lambda}{d hc} \quad \text{Initial Exciton Density}^{31}$$

Where n_0 is the initial exciton density, F_A is the fraction of absorbed light at wavelength λ , P is pump power measured at the sample. f is the repetition frequency of the laser, r_x and r_y are the beam spot radii in the x and y dimensions, d is the sample thickness, λ is the pump wavelength, and h and c are Plank's constant and the speed of light respectively.

Using the Zn₂(TCPP) sample measured before PSC as an example, n_0 can therefore be calculated for each pump fluence measured. Whilst this exciton density is ostensibly correct at time zero after excitation, t_0 in following calculations is in fact set as 3 ps after excitation to remove the effects of internal conversion as suggested by Gu et al.⁵ The conversion factor β between ΔA and n_0 can be determined by ratio of the two values when performed at low fluence and early time (e.g., 170 fs), where β contains adjustment factors relating to excited state cross-section and film thickness (Equation 3.6). The conversion factor β can then be used to convert ΔA to $n_{(0)}$ at any delay time. Using the lowest fluence data point for ΔA at 163 fs, $\beta = -2.95 \times 10^{-21}$ (see SI S3.50 for details).

$$\text{Equation 3.6} \quad \Delta A_{(t)} = \beta n_{(t)} \quad \text{Finding Conversion Factor}^{31}$$

Where $\Delta A_{(t)}$ is the measured TA signal at a specific delay time, $n_{(0)}$ is the initial exciton density, and β is a conversion factor.

As such, the slope $\gamma_{(t)}$ from Equation 3.4 can be calculated by plotting $n_{(0)}/n_{(t)} - 1$ against time delay t and fitting the data using Equation 3.7, to calculate a common value for $\gamma_{(0)}$. This can then be related to the exciton diffusion coefficient D via Equation 3.8.

Equation 3.7 $\gamma_{(t)} = \gamma_{(0)}n_0t^{-1.5}$ Fitting for Initial Annihilation Rate

Where $\gamma_{(t)}$ is the time-dependant annihilation rate, $\gamma_{(0)}$ is the initial annihilation rate, n_0 is the initial exciton density, and t is the delay time.

Equation 3.8 $D = \frac{\gamma_0^2 d^2 n^2 \pi}{8}$ Calculating Diffusion Coefficient

Where $\gamma_{(0)}$ is the initial annihilation rate, d is the material's interchromophoric distance, n is the chromophore concentration in the crystal structure, and D is the exciton diffusion coefficient.

The exciton diffusion pathlength can be calculated from the diffusion dimension, diffusion coefficient and lifetime using Equation 3.9. The relationship between annihilation rate and time is dependent on the diffusion dimension, either 1D, 2D, or 3D.³¹ In this case, the data well fit a one-dimensional diffusion described by Equation 3.7, so $Z = 1$ is used in calculations.³²

Equation 3.9 $L_D = \sqrt{ZD\tau}$ Calculating Diffusion Pathlength

Where L_D is the diffusion pathlength, Z is the diffusion dimension, D is the diffusion coefficient, and τ is the lifetime of exciton hopping.

For the $Zn_2(TCPP)$ sample before post-synthetic centrifugation, the lifetime of excited states at 500 nm, τ , is calculated to be 128.8 ps, and $\gamma_{(0)}$ is calculated by fitting to be $4.36 \times 10^{-22} \text{ m}^{-3} \text{ s}^{-1.5}$ (Figure 3.19). From this, and the values for d and n , we can calculate from Equation 3.8 a value for the diffusion coefficient D . The interchromophoric distance d is assumed to be 0.77 nm due to the monolayer thickness calculated from the crystal structure, and the value for chromophore concentration is reported for a similar MOF nanofilm by Gu et al. as $n = 4 \times 10^{26} \text{ m}^{-3}$.⁵ As such, the value for D is calculated to be $7.08 \times 10^{-9} \text{ m}^2 \text{ s}^{-1}$. Following this, the one-dimensional diffusion constant z , the result for D , and the fitted lifetime of excited states, can be used in Equation 3.9 to calculate the diffusion pathlength, $L_D = 9.55 \times 10^{-10} \text{ m}$, or 0.955 nm. This was repeated to calculate exciton diffusion pathlength for $Zn_2(TCPP)$ samples centrifuged at 2,000, 4,000, and 8,000 rpm, where lifetimes were observed to decrease 124.7, 112.8, and 73.8 ps, respectively (see SI S3.50-52).

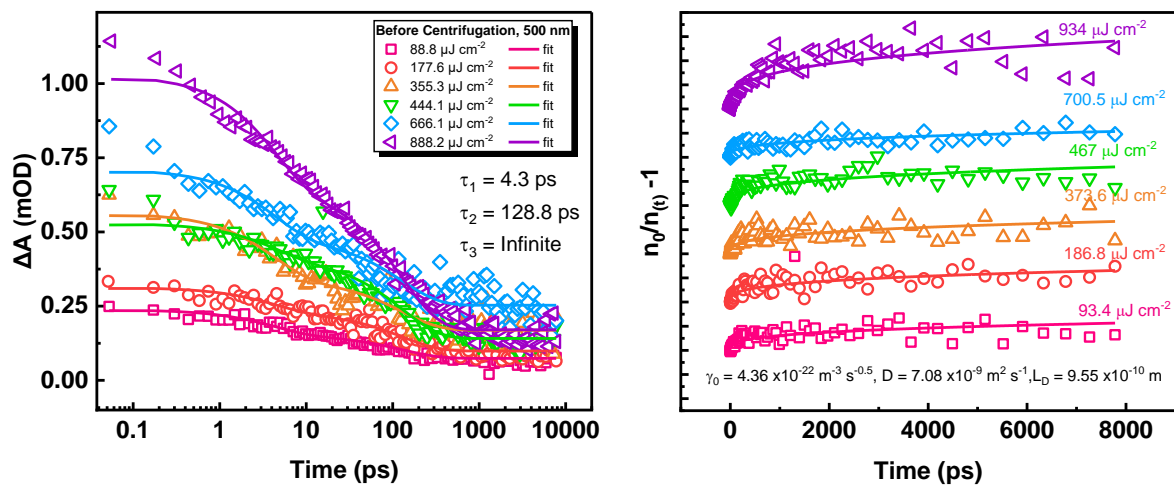


Figure 3.19 Excited state transient absorption at 500 nm for a sample of $Zn_2(TCPP)$ before post-synthetic centrifugation (Before C).

When the exciton diffusion pathlengths are compared (as in Figure 3.20), an inverse relationship with centrifugation speed is observed. Particles formed of stacked nanosheets should increase the rate of FRET transfer, increasing diffusion pathlength, yet aggregation seems to be having the inverse effect, indicating this is loose aggregation rather than layer stacking. It should be noted that all the exciton diffusion pathlengths calculated are sub-nanometre, whereas FRET transfer occurs in the 1-10 nm range. This implies that either a different process is occurring, or FRET transfer enhancing hopping rates is overcome by efficient exciton annihilation.

The question of intramolecular transfer is therefore raised, especially since the fits for 4,000 rpm and 8,000 rpm exciton graphs seem to deviate slightly compared to before C and 2,000 rpm. This may indicate less $\gamma_{(0)}$ dependence on time and could be evidence for two-dimensional (in-plane) exciton diffusion (i.e., intermolecular vs. intramolecular).³² The interlayer distance in $Zn_2(TCPP)$ is calculated to be 7.7 Å, and the unit cell porphyrin-porphyrin distance 23.6 Å. The shortest route between delocalisation rings of different porphyrin groups (i.e., porphyrin phenyl to porphyrin phenyl via the paddlewheel) is 8.14 Å. The values calculated are much smaller than a porphyrin molecule, indicating that with the exception of non-centrifuged samples, exciton diffusion is greatly limited (Figure 3.20). The values calculated for $Zn_2(TCPP)$ before centrifugation are similar to the interlayer distance in the crystal structure of $Zn_2(TCPP)$, which implies the transfer of excited states between layers, or across the paddlewheel to a neighbouring porphyrin. Multilayer particles being removed on centrifugation would reduce the likelihood of interlayer transfer and is already evidenced by the disappearance of Soret absorption at 441 nm as previously discussed, so exciton migration is ascribed to interlayer, not in-plane.

These exciton diffusion pathlength values are in direct contrast to the work on $Cu_2(TCPP)$ by Gu et al., who calculated diffusion pathlengths of up to 16 nm.⁵ Such a reduction may be an experimental error, as in this study analysis was performed on particles in solvent dispersion rather than on thin-films, or it may be a real difference between the materials. If real, this would suggest $Zn_2(TCPP)$ is a much poorer exciton transport material than $Cu_2(TCPP)$ due to a much shorter diffusion pathlength. To separate these possibilities, the experiments could be repeated with both materials to account for differences in the methodology and sample preparation.

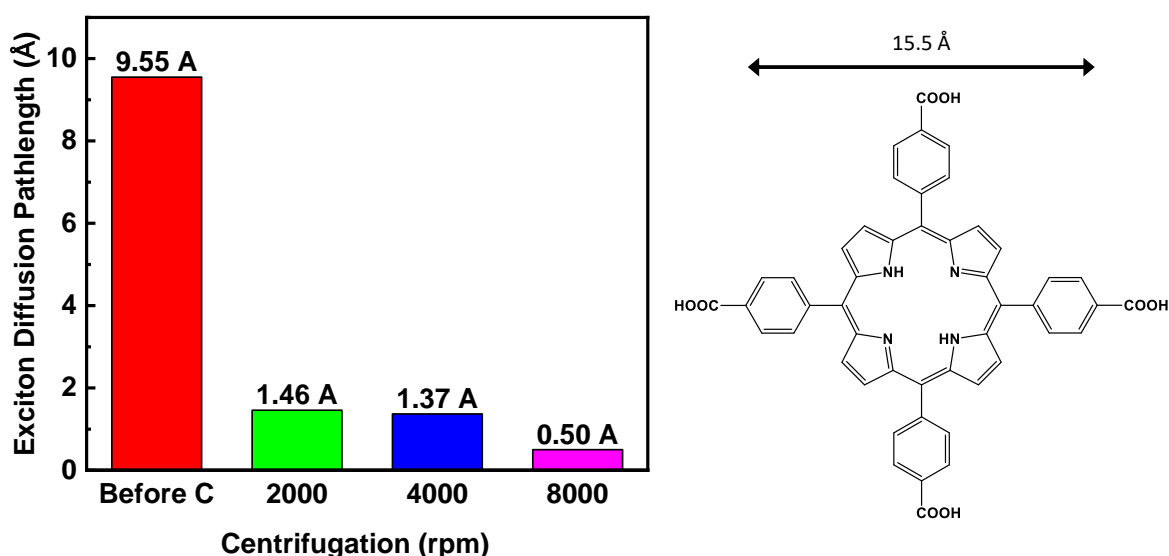


Figure 3.20 Exciton diffusion pathlength dependence on centrifugation speed.

Section 3.4 Conclusions

The advanced characterisation of $Zn_2(TCPP)$ metal organic framework nanosheets reveals that centrifugation, a common nanomaterials processing technique, can promote aggregation in suspension and in thin-films. Investigation into the effect this has on photophysical properties indicated a non-emissive quenching mechanism via exciton-exciton annihilation, which is enhanced by aggregation, indicating potential ramifications for these materials' use in optical applications such as photovoltaics or light emissive diodes (LEDs).

More specifically, a modified Stern-Volmer analysis attributed S_1 emission quenching via a non-radiative mechanism between aggregates. The exciton diffusion pathlength for $Zn_2(TCPP)$ was calculated from fundamental principles to be sub-nanometre, which compares poorly to the lengths of >10 nm reported by Gu et al. in the similarly structured $Cu_2(TCPP)$. The diffusion pathlength was shown to be significantly reduced in materials which underwent post-synthetic centrifugation, which is here ascribed to exciton annihilation in aggregated systems overcoming the expected enhanced FRET rates which would otherwise increase pathlength.

There are therefore several factors to consider regarding the behaviour of excited states and centrifugation. Firstly, centrifugation appears to have two effects: the removal of multilayer nanosheets due to their density, leaving few- or single-layer nanosheets, and stimulating the flocculation of remaining nanosheets to form loosely bound aggregates. Secondly, this results in the removal of ground state absorption at 441 nm, and the increased lifetime of excited states in centrifuged samples compared to non-centrifuged ones. The power dependence of centrifuged samples is also increased, indicating a greater amount of exciton-exciton annihilation, which explains the decreased S_2 excited state lifetime at 500 nm and the centrifugation dependant S_1 emission lifetime, which is less populated in systems with greater rates of non-radiative S_2 relaxation. Corroborating the enhancement of exciton-exciton annihilation by centrifugation is the greatly reduced exciton diffusion pathlength calculated for the samples compared to $Zn_2(TCPP)$ before centrifugation.

These results suggest that monolayer nanosheets have extended excited state lifetimes, making them more efficient transport materials than the equivalent layered MOF. Centrifugation, however, remains an inefficient technique for isolating these monolayers, as it can induce aggregation, which causes greater exciton annihilation, a process detrimental to energy transport applications. Further methods for isolating monolayer nanosheets should be explored, and the history of material processing considered in future research and well reported for greater understanding when comparing between synthetic materials.

Section 3.5 Experimental

Powder X-Ray Diffraction (PXRD)

PXRD data were collected for crystal structure determination using a Bruker D8 Advance diffractometer with a Cu K α source operating at 40 kV and 40 mA to generate $\lambda = 1.5406 \text{ \AA}$ X-rays, measurements collected using an energy dispersive LynxEye detector. Dry samples were lightly ground with a pestle and mortar and pressed onto a polished silicon flat plate using a glass slide before analysis.

Steady-State Spectroscopy

UV-visible absorption and emission spectra were recorded to determine the ground-state electronic transitions in the materials. Data were collected at room temperature, in a 1 cm quartz cell except where otherwise specified, using an Agilent Technologies Cary 50 UV-Visible spectrometer and a Cary Eclipse fluorimeter, respectively. Emission spectra were recorded in aerated solutions.

Elemental Analysis

Elemental analyses for the measurement of percentage carbon, hydrogen, and nitrogen content were obtained on an Elementar vario MICRO cube CHNS analyser equipped with a thermal conductivity detector.

Atomic Force Microscopy (AFM)

Imaging and height profiling for size determination of nanosheets was performed by AFM. Micrographs were collected using a Bruker Multimode 5 AFM operating in soft tapping mode using Bruker OTESPA-R3 cantilevers. Data were processed using Gwyddion image processing software. Samples in 15 μL EtOH were hot dropped onto freshly cleaved mica sheets heated to 90°C and allowed to dry for 5 minutes at temperature.

Inductively Coupled Plasma Optical Emission Spectroscopy (ICP-OES)

Samples were digested in 3 ml nitric acid (68%), using a Multiwave 5000 microwave digester, at 210 °C for 20 minutes. The digests were made up to 15 ml using 1% nitric acid.

Analysis was performed on SpectroGreen FMX46. Samples were diluted by 3-15x, in 1% nitric acid, as required to meet the calibration range of the instrument. A 1 ppm standard was run to correct for daily fluctuations in conditions.

The percentage zinc content was measured at the appropriate wavelength 213.856 nm.

Time-Correlated Single Photon Counting (TCSPC)

The emission lifetime for different samples were determined by time-resolved fluorescence data collected on an Edinburgh instrument mini-Tau fluorescence lifetime spectrometer and no wavelength selector. In TCSPC measurements, samples were kept in a 1 cm transparent quartz cuvette, and a NanoLED of 410 nm was used as an excitation source, with an instrument response function width of 1 ns. Kinetic traces from the TCSPC data were fit in OriginPro, using a sum of decaying exponential functions convoluted with a Gaussian function.

Pump-Probe Spectroscopy

Excited state lifetimes were analysed by UV-Visible pump-probe spectroscopy experiments performed in the Lord Porter Ultrafast Laser Laboratory (ULS), The University of Sheffield, using a Helios system (HE-VIS-NIR-3200) provided by Ultrafast Systems. A Ti:Sapphire regenerative amplifier (Spitfire ACE PA-40, Spectra-Physics) provides 800 nm pulses (40 fs

FWHM, 10 kHz, 1.2 mJ). The 400 nm pump pulses (2.5 kHz, 0.2 μ J) were generated through frequency doubling of the amplifier fundamental. The pump was focused onto the sample dispersed in solvent in a 1 mm quartz cell, with stirring, to a beam diameter of approximately 210-260 μ m. The white light probe continuum (330 – 700 nm) was generated using a CaF₂ crystal and a portion of the amplifier fundamental. The intensity of the probe light transmitted through the sample was measured using a CMOS camera, with a resolution of 1.5 nm. Prior to generation of the white light, the 800 nm pulses were passed through a computer controlled optical delay line (DDS300, Thorlabs), which provides up to 8 ns of pump-probe delay. The instrument response function is approximately 130 fs, based on the temporal duration of the coherent artifact signal from neat solvent.

Results where degradation of the sample was observable by change in UV-Visible absorption spectra were discarded. Five experimental sets were averaged to generate the data seen in this report. Pre-processing of the pump-probe data was performed using SurfaceXplorer, the software package provided by Ultrafast Systems. Kinetic traces from the pump-probe data were fit in OriginPro, using a sum of decaying exponential functions convoluted with a Gaussian function.

Materials

All solvents and reagents were purchased from commercial suppliers and used without further purification: TCPP (97%, MedChemExpress), zinc nitrate hexahydrate (98%, Acros Organics), triethylamine (High purity grade, VWR Life Science), ethanol (99.8% HPLC Grade, Fisher Chemical), and dimethylformamide (99% laboratory reagent grade, Fisher Chemical).

Synthesis of Zn₂(TCPP) MONs

The reaction of 1:2 stoichiometric tetrakis(4-carboxyphenyl)porphyrin (TCPP) and zinc nitrate hexahydrate was prepared by mixing of 200 mL TCPP (500 mg, 0.63 mmol) + triethylamine (0.25 g, 2.52 mmol) in 1:1 DMF/EtOH with 200 mL Zn(NO₃)₂·6H₂O (0.38 g, 1.26 mmol) in the same solvent with stirring for 1 hr at 30 °C. Subsequently, the products were washed three times by centrifugation at 12,000 RPM for 1 hr, each time decanting the supernatant and replacing with fresh ethanol.

Section 3.6 References

1. Ashworth, D. J. *et al.* Scalable and sustainable manufacturing of ultrathin metal–organic framework nanosheets (MONs) for solar cell applications. *Chemical Engineering Journal* **477**, (2023).
2. Ashworth, D. J. & Foster, J. A. Metal-organic framework nanosheets (MONs): A new dimension in materials chemistry. *J Mater Chem A Mater* **6**, 16292–16307 (2018).
3. Li, X. *et al.* Ultrafast Relaxation Dynamics in Zinc Tetraphenylporphyrin Surface-Mounted Metal Organic Framework. *Journal of Physical Chemistry C* **122**, 50–61 (2018).
4. Mehrzad Sajjadinezhad, S., Boivin, L., Bouarab, K. & Harvey, P. D. Photophysical properties and photonic applications of porphyrin-based MOFs. *Coordination Chemistry Reviews* **510**, (2024).
5. Gu, C. *et al.* Assembled Exciton Dynamics in Porphyrin Metal-Organic Framework Nanofilms. *Nano Lett* **21**, 1102–1107 (2021).
6. Sasitharan, K. *et al.* Metal–organic framework nanosheets for enhanced performance of organic photovoltaic cells. *J Mater Chem A Mater* **8**, 6067–6075 (2020).
7. Sasitharan, K. *et al.* Metal-Organic Framework Nanosheets as Templates to Enhance Performance in Semi-Crystalline Organic Photovoltaic Cells. *Advanced Science* **9**, (2022).
8. Rajasree, S. S., Li, X. & Deria, P. Physical properties of porphyrin-based crystalline metal–organic frameworks. *Communications Chemistry* **4**, (2021).
9. Haber, L. H. *et al.* Efficient photoinduced energy transfer in porphyrin-based nanomaterials. *Journal of Physical Chemistry C* **124**, 24533–24541 (2020).
10. Kung, C.-W. *et al.* Porphyrin-based metal–organic framework thin films for electrochemical nitrite detection. *Electrochem Commun* **58**, 51–56 (2015).
11. Zhang, X. *et al.* A historical perspective on porphyrin-based metal–organic frameworks and their applications. *Coord Chem Rev* **429**, 213615 (2020)
12. Shaikh, S. M. *et al.* Light harvesting and energy transfer in a porphyrin-based metal organic framework. *Faraday Discuss* **216**, 174–190 (2019).
13. Shaikh, S. M. *et al.* Light harvesting and energy transfer in a porphyrin-based metal organic framework. *Faraday Discuss* **216**, 174–190 (2019).
14. Zhao, Y. *et al.* Synthesis of porphyrin-based two-dimensional metal–organic framework nanodisk with small size and few layers. *J Mater Chem A Mater* **6**, 2828–2833 (2018).
15. Chen, L.-J., Zhao, X. & Yan, X.-P. Porphyrinic metal-organic frameworks for biological applications. *Advanced Sensor and Energy Materials* **2**, 100045 (2023).
16. Pang, Y. *et al.* A novel fluorescence sensor based on Zn porphyrin MOFs for the detection of bisphenol A with highly selectivity and sensitivity. *Food Control* **132**, (2022).
17. Jin, Z. *et al.* Nitrogen vacancy-induced spin polarization of ultrathin zinc porphyrin nanosheets for efficient photocatalytic CO₂ reduction. *J Colloid Interface Sci* **652**, 122–131 (2023).

18. Zhao, M. *et al.* Ultrathin 2D Metal-Organic Framework Nanosheets. *Advanced Materials* **27**, 7372–7378 (2015).
19. Wang, F. *et al.* An electrochemical microsensor based on a AuNPs-modified microband array electrode for phosphate determination in fresh water samples. *Sensors (Switzerland)* **14**, 24472–24482 (2014).
20. Zhu, Z. H. *et al.* Porphyrin-Based Two-Dimensional Layered Metal-Organic Framework with Sono-/Photocatalytic Activity for Water Decontamination. *ACS Nano* **16**, 1346–1357 (2022).
21. Sakuma, T., Sakai, H., Araki, Y., Wada, T. & Hasobe, T. Control of local structures and photophysical properties of zinc porphyrin-based supramolecular assemblies structurally organized by regioselective ligand coordination. *Physical Chemistry Chemical Physics* **18**, 5453–5463 (2016).
22. Baskin, J. S., Yu, H. Z. & Zewail, A. H. Ultrafast dynamics of porphyrins in the condensed phase: I. Free base tetraphenylporphyrin. *Journal of Physical Chemistry A* **106**, 9837–9844 (2002).
23. Yu, H. Z., Baskin, J. S. & Zewail, A. H. Ultrafast dynamics of porphyrins in the condensed phase: II. Zinc tetraphenylporphyrin. *Journal of Physical Chemistry A* **106**, 9845–9854 (2002).
24. Gehlen, M. H. The centenary of the Stern-Volmer equation of fluorescence quenching: From the single line plot to the SV quenching map. *Journal of Photochemistry and Photobiology C: Photochemistry Reviews* **42**, (2020).
25. Lakowicz, J. R. *Principles of Fluorescence Spectroscopy*. (Springer, 2006).
26. Bae, W., Yoon, T. Y. & Jeong, C. Direct evaluation of self-quenching behavior of fluorophores at high concentrations using an evanescent field. *PLoS One* **16**, (2021).
27. Stradomska, A. & Knoester, J. Shape of the Q band in the absorption spectra of porphyrin nanotubes: Vibronic coupling or exciton effects? *Journal of Chemical Physics* **133**, (2010).
28. Lopes, J. M. S. *et al.* Novel insights on the vibronic transitions in free base meso-tetrapyrrolyl porphyrin. *Spectrochim Acta A Mol Biomol Spectrosc* **209**, 274–279 (2019).
29. Rajasree, S. S., Li, X. & Deria, P. Physical properties of porphyrin-based crystalline metal–organic frameworks. *Communications Chemistry* **4**, (2021).
30. Hedley, G. J., Ruseckas, A. & Samuel, I. D. W. Light harvesting for organic photovoltaics. *Chemical Reviews* **117**, 796–837 (2017).
31. Bossanyi, D. *Triplet-Pair States in Exciton Fission and Fusion*. (2022).
32. Spano, F. C. & Silva, C. H- and J-aggregate behavior in polymeric semiconductors. *Annu Rev Phys Chem* **65**, 477–500 (2014).

Section 3.7 Chapter 3 Supporting Information

In literature, electronic absorption in porphyrins is identified as the characteristic Soret ($S_0 \rightarrow S_2$) in the 415-430nm region, and forbidden Q-band ($S_0 \rightarrow S_1$), correspondingly less intense, at 500-700nm.^{1,3-8} Electronic absorption in highly aromatic porphyrins originates from $\pi \rightarrow \pi^*$ transitions.¹ As outlined in the theoretical study of porphyrins by Hirao et al., the Soret and Q-bands are well modelled by one electron transitions in a four orbital system consisting of the two highest occupied π orbitals, and the two lowest unoccupied π^* orbitals.⁹ Due to symmetry rules, the porphyrin which is unmetalated at the centre should produce four Q-bands. Upon metalation at the centre, the amine protons are removed, and another plane of symmetry is formed (D_{4h}). Thus, only two Q-bands would be observed in the absorption spectrum of a metalated porphyrin centre.⁵

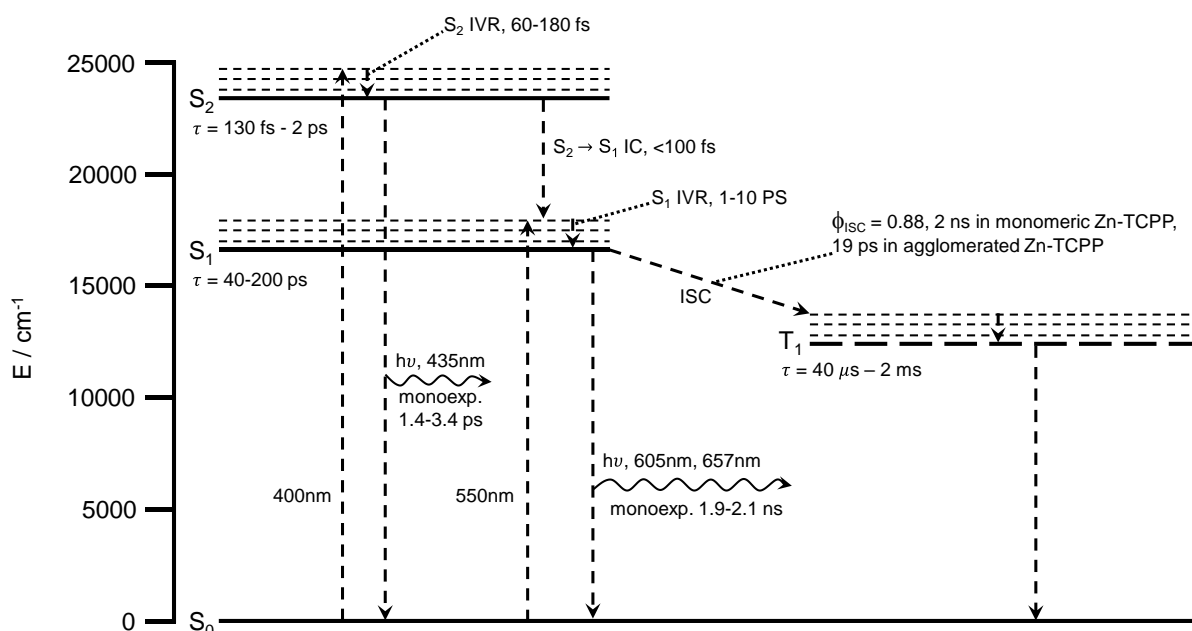


Figure S3.1 Jablonski diagram summarising data from Li et al., Haber et al., and Yu et al.

Quenching is expected when comparing a MOF to free linker.^{1,3} This effect is suggested to be coincident with redshift from J-aggregation, where coupling between stacked π -electron systems creates excitonic states at a lower energy than the free molecule.^{3,5,10} Emission spectra of porphyrin MOFs clearly show $S_2 \rightarrow S_0$ at $\sim 450 \text{ nm}$, and $S_1 \rightarrow S_0$ at 610, 650, and 720 nm, where the first two S_1 emissions are designated in literature to $Q_{(0,0)}$, $Q_{(0,1)}$.^{3,6,7} The emission from the S_2 ES is monoexponential, and low quantum yield compared to emission from the S_1 ES.³ Time-resolved emission studies in literature suggest that emission from S_2 is in the order of 240fs-3.6ps, with commonly reported lifetimes of 2ns for the emission by longer lived S_1 electrons.^{3,6,7}

Table S3.1 Summary of key findings from literature on ultrafast spectroscopy of porphyrins, where single molecules are identified as “monomeric”.

Material	Assigned	Lifetime	Details	Ref.
Monomeric TPP(Zn) + Zn-TPP(Zn) MOF	S ₁ →S ₀ Emission	1.9-2.1ns	Metalloporphyrin, various polarity solvent. In Zn-TPP, quenching from S ₁ -S ₁ and S ₂ -S ₂ intramolecular Forster energy transfer and charge transfer in both S ₂ and S ₁ . High quantum yield of intersystem crossing in metal porphyrins. S ₂ →S ₁ IC is much faster in metal free porphyrins (<50fs). In surface mounted MOF, quenching of both S ₂ and S ₁ states is observed due to spectral overlap of absorption-emission (incoherent and quantum coherent energy transfer and redistribution).	Li et al. ³
	S ₂ →S ₀ Emission	1.4-3.4ps		
	S ₂ →S ₁ IC	<100fs		
	S ₁ -solvent VR	1-10ps		
	S ₂ IVR	60-180fs		
	τ _{S₁}	40-200ps		
	τ _{S₂}	130fs-1ps		
	τ _{T₁}	40μs-1.5ms		
Monomeric TCPP(Zn)	S ₁ →T ₁ ISC	2ns	Shorter lifetime τ ₁ attributed to intermolecular energy transfer redistribution between nearby TCPP molecules (π-π) at both S ₂ and S ₁ of agglomerates. Excited state dynamics significantly faster in metalated porphyrins, aggregated or not. S ₁ vibrational relaxation is polarity dependent.	Haber et al. ¹
	S ₁ →S ₀ IVR	58ps		
	S ₂ →S ₁ IC	1ps		
	π-π	1.2ns		
Agglomerate TCPP	S ₁ →T ₁ ISC	3ns		
Agglomerated TCPP(Zn)	π-π	19ps		
	S ₁ →T ₁ ISC	74ps		
Monomeric TPP(Zn)	S ₂ →S ₀ Emission	1.45ps	Peaks in S ₁ fluorescence measured at 596nm for Q(0,0), 645nm for Q(0,1), and 560nm for Q(1,0). Reported relative fluorescence yield φ ^{S₂} /φ ^{S₁} = 0.012. The reported lifetime of T ₁ measured at room temperature in outgassed solvents falls between 1-2ms. S ₂ decay is dependent on solvent (1.43ps in benzene to 1.9ps in CH ₂ Cl ₂).	Yu et al. ^{6,7}
	S ₁ Emission τ ₁	1.15ps		
	S ₁ Emission τ ₂	12ps		
	S ₁ Emission τ ₃	1.7ns		
	Emission @560nm	25ps		
TCPP	S ₁ →S ₁	2ps	TA kinetics assigned to solvent induced processes causing vibrational reorganisation of exciton energy in the S ₁ state, vibrational relaxation of S ₁ , and fluorescence.	Shaikh et al. ²
	S ₁ →S ₀	57ps		
	S ₁ →S ₀	>1ns		
Zr ₆ -TCPP	S ₁ →S ₁	5ps		
	S ₁ →S ₀	115ps		
	S ₁ →S ₀	>1ns		

Table S3.2 Elemental analysis of 97% pure TCPP from MedChemTronica

Element	Expected	Experimental
%C	72.91	67.08
%H	3.82	4.063
%N	7.09	6.71
%S	0	0.015

The elemental analysis of $Zn_2(TCPP-H_2)$ product is displayed in Table S3.3, where the formal chemical structure is expected to be $Zn_2(TCPP-H_2)(DMF)_2$, resulting in a molecular formula $Zn_2C_{54}H_{40}N_6O_{10}$. A slight contamination by ethanol is expected to be the cause of deviation from expected value in the results due to ligand exchange/incomplete drying.

Table S3.3 Elemental analysis of $Zn_2(TCPP-H_2)(DMF)_2$

Element	Expected	Experimental	Deviation
%C	60.97	55.77	-8.5%
%H	3.79	3.944	+4.1%
%N	7.90	5.97	-2.44%
%S	0	0.115	-

Elemental ratios predicted by Chemdraw:

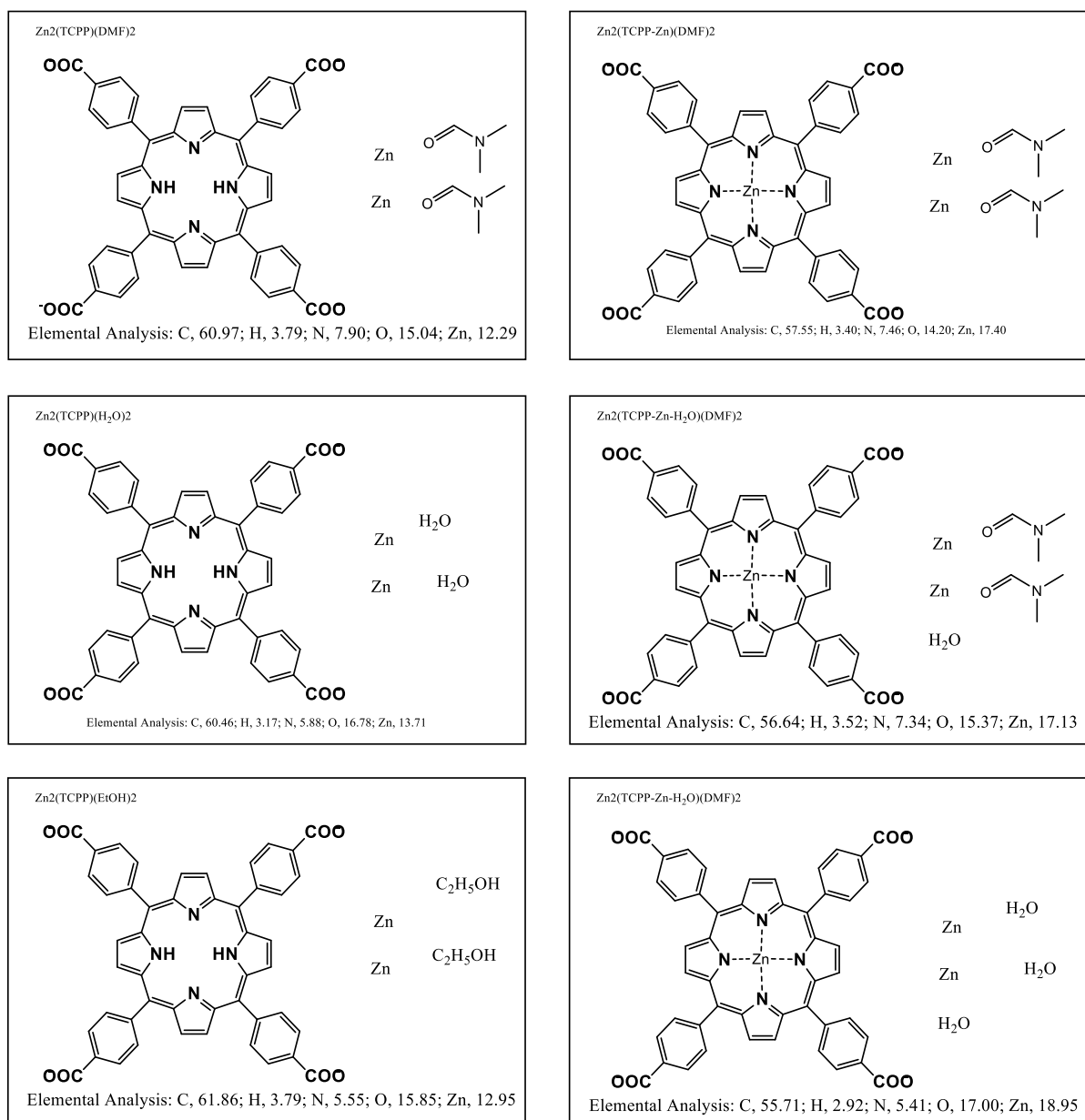


Figure S3.2 Theoretical elemental composition of Zn₂(TCPP-X)(Y)₂ derivatives

The PXRD patterns are compared with patterns recorded for the previous work unpublished in the group (Sasitharan, chlorobenzene), and simulated patterns, as shown in Figure S3.3. As shown by the vertical marker lines, the major peaks poorly match both predicted and previous experiment. The peak at 5° is a noteworthy difference that should be compared to TCPP and Zn(NO₃)₂ PXRD data.

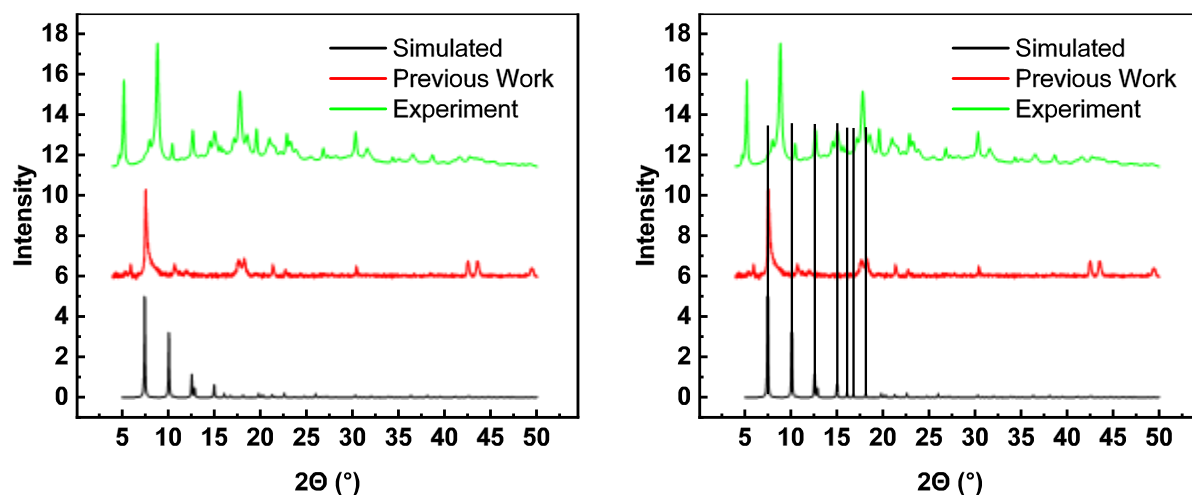


Figure S3.3 PXRD patterns for product of Zn₂(TCPP) batch synthesis with comparison to previous work by Ashworth et al. and simulated pattern. Figure on the right is the same data displayed with marker lines.

After washing with DMF, the PXRD patterns are compared with patterns recorded for the previous work (Sasitharan, chlorobenzene), and simulated patterns, as shown in Figure S3.4. As shown, the peak at 5.3° is still present here, indicating that this is unlikely to be from unreacted TCPP or impurity, but instead is part of the crystal structure.

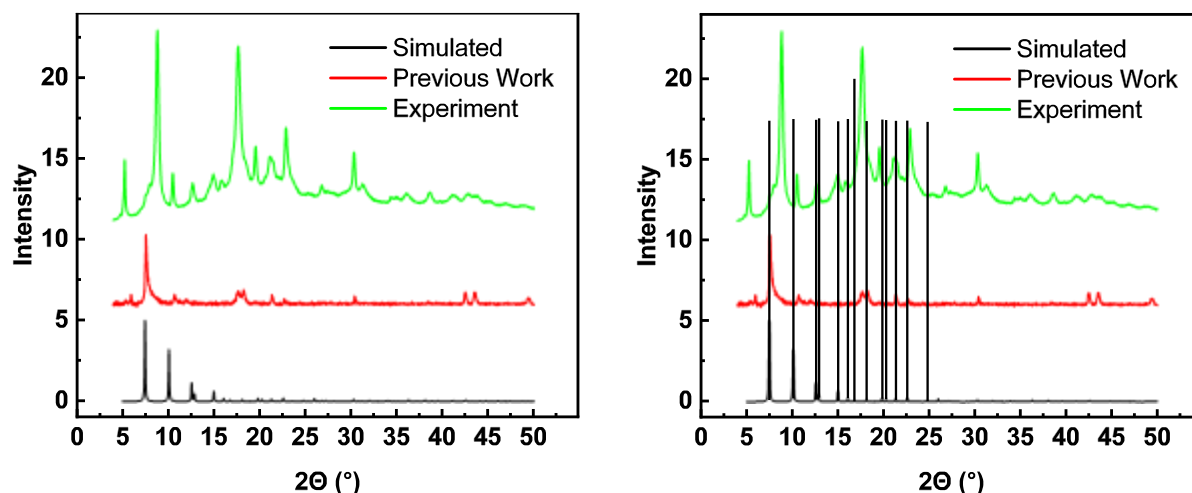


Figure S3.4 PXRD patterns for product of Zn₂(TCPP) batch synthesis

As seen in Figure S3.5, sharp peaks have been observed in previous work at 5.3, 7.5, 8.8, 10.7, 18.0, 19.3, 21.3, 22.7, and 30.3 °. The formation of monolayer nanosheets versus bulk MOF is observed in this previous work to have little difference on peak position for these materials. Differences in product thickness therefore need not be considered in the analysis of these results.

The increase in crystallinity (more intense, sharper peaks) is likely because less material is monolayer. A preferred orientation for the "previous work" is why there are fewer peaks and largely only those associated with in-layer interactions (002, 004 etc.). There are some peaks at 43° which are artifacts of the knife edge.

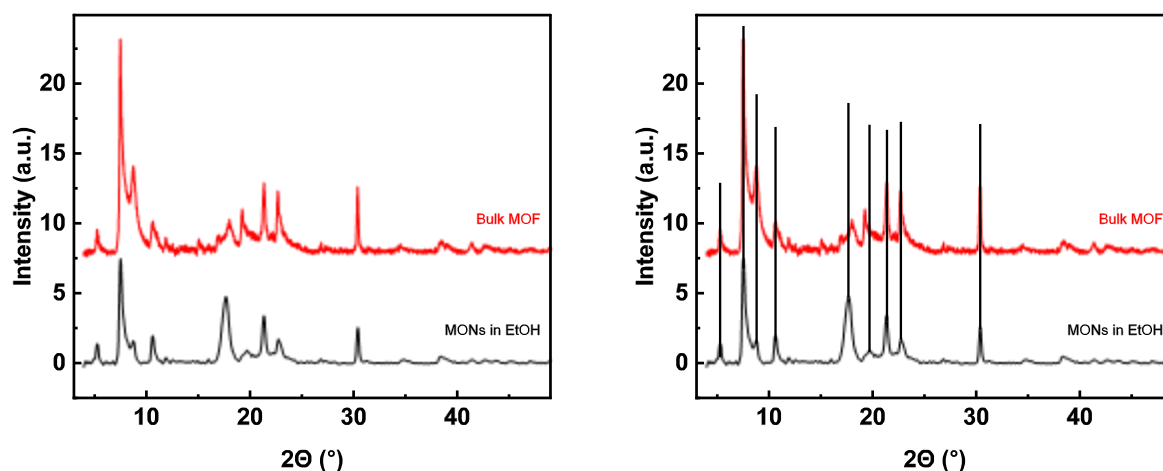


Figure S3.5 XRD patterns collected by Sasitharan et al. for comparison of $Zn_2(TCPP)$ in the bulk phase, and MONs centrifuged in EtOH.

On review of previous work by Sasitharan et al., several studies determining the effects of solvent changes during washing indicate the patterns seen in Figure S3.3. may not be a uniform representation of expected XRD data (though it should be noted that these patterns do match the simulated data well). Nevertheless, comparison of XRD pattern in Figure S3.6 with those studied under ethanol washing (as in this work), shows the common peak at 8.8° which is not predicted in the simulated pattern between both batch produced $Zn_2(TCPP)$, and the previous work by Sasitharan et al.

The method of powder pattern simulation native to Mercury was used to predict the patterns expected for $Zn_2(TCPP)(DMF)_2$, $Zn_2(TCPP(H_2O)_2)(DMF)_2$, and $Zn_2(TCPP-Zn)(DMF)_2$.

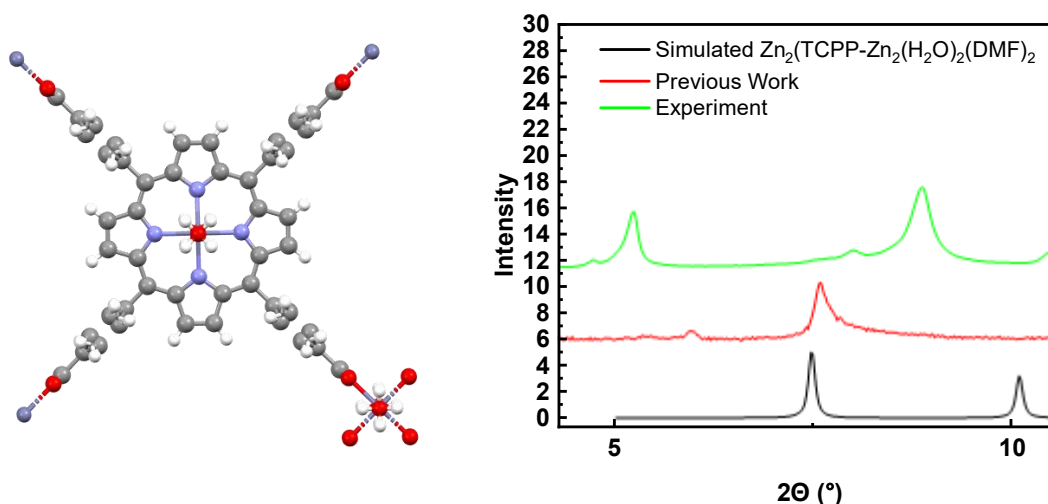


Figure S3.6 Simulated XRD pattern for $Zn_2(TCPP-Zn(H_2O)_2)(H_2O)$

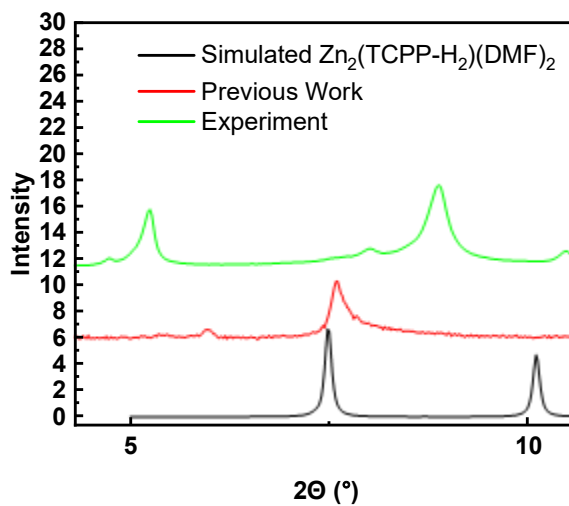
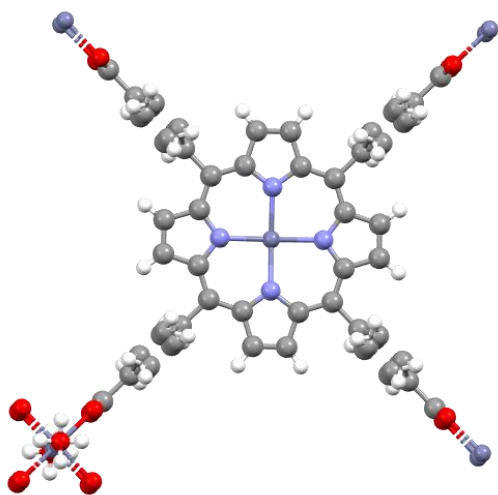


Figure S3.7 Simulated pxrd pattern for $Zn_2(TCPP-Zn)(H_2O)_2$

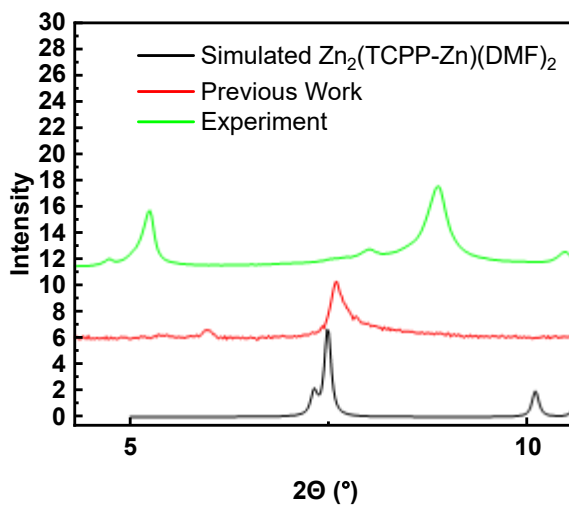
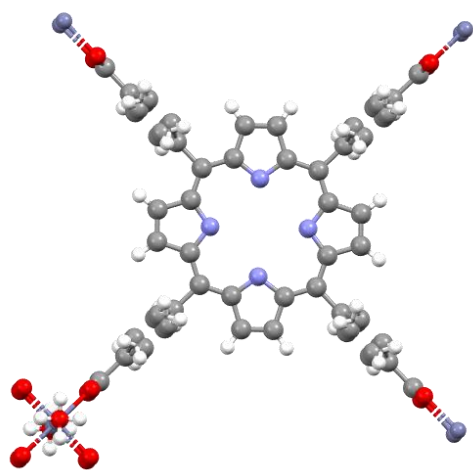


Figure S3.8 Simulated pxrd pattern for $Zn_2(TCPP-H_2)$

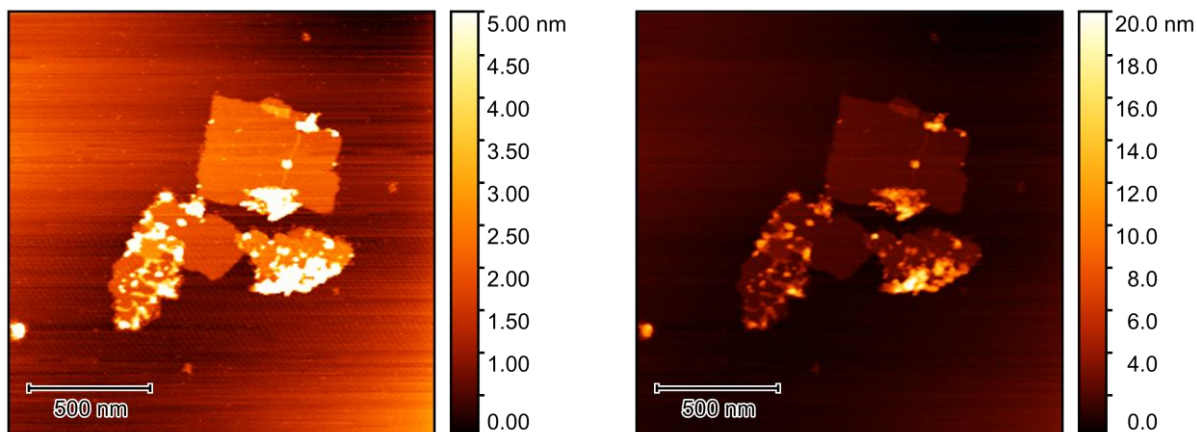


Figure S3.9 AFM micrograph from figure 4 with y-axis adjusted to show thicker particulates

Zn₂(TCPP) follows the Beer-Lambert law well between 0 – 1.5 μM, with an extinction coefficient of $\epsilon = 1.3 \mu\text{M}^{-1} \text{cm}^{-1}$

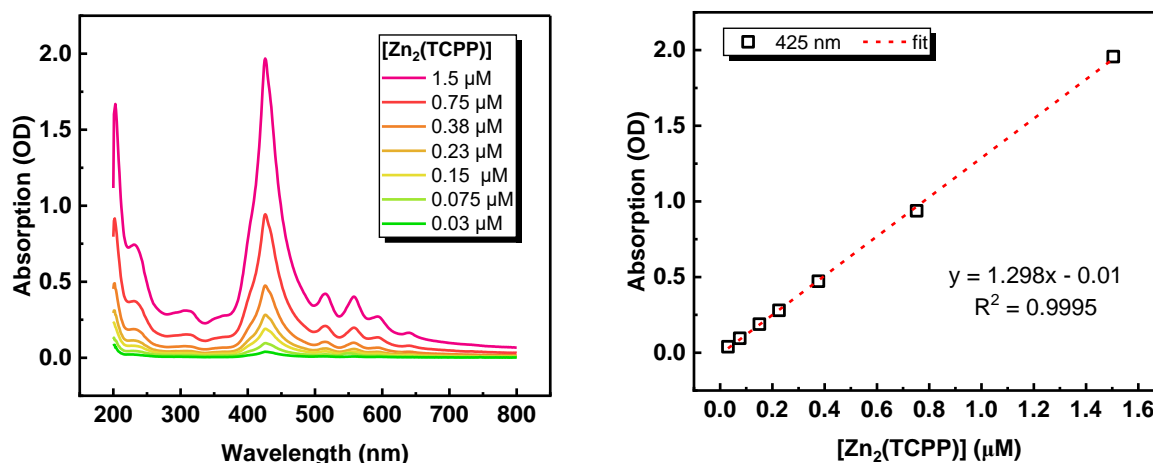


Figure S3.10 Electronic absorption spectra for different concentrations of Zn₂(TCPP) in a 10 mm cell (left), with absorption intensity at 425 nm plotted against concentration with linear fit (right).

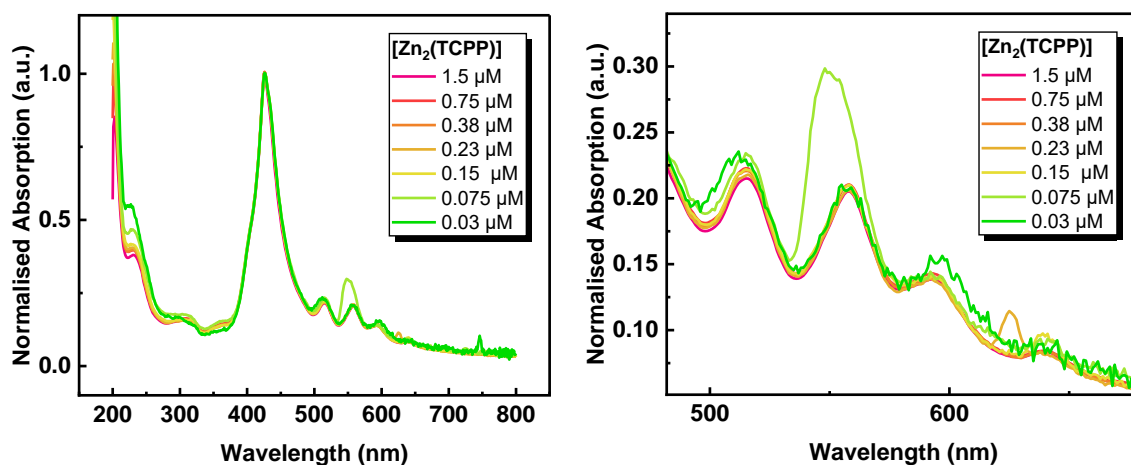


Figure S3.11 Electronic absorption spectra for different concentrations of Zn₂(TCPP) in a 10 mm cell (left), with absorption intensity at 425 nm plotted against concentration with linear fit (right). Normalised against Soret maxima intensity.

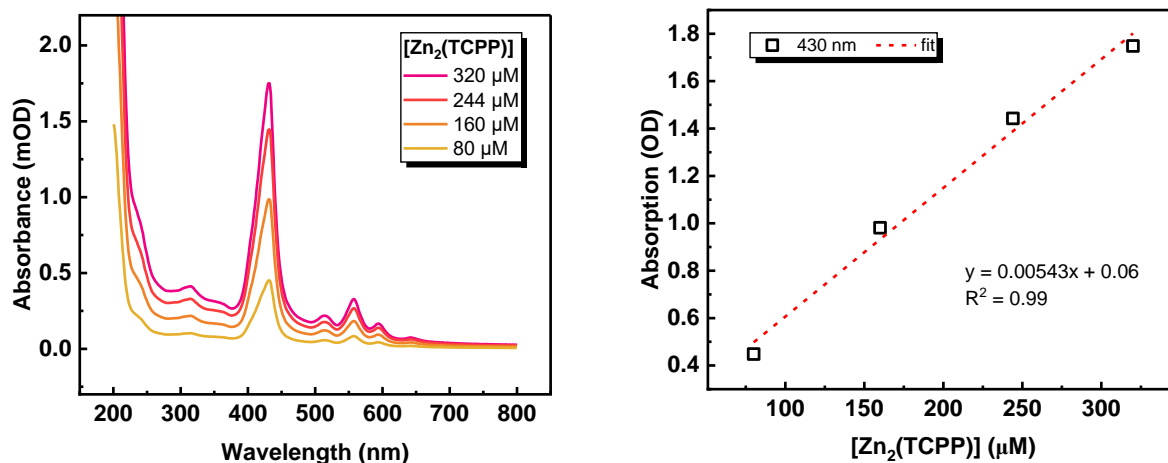


Figure S3.12 Electronic absorption spectra for different concentrations of Zn₂(TCPP) in a 1 mm cell (left), with linear fit of absorption intensity at 425 nm vs concentration (right).

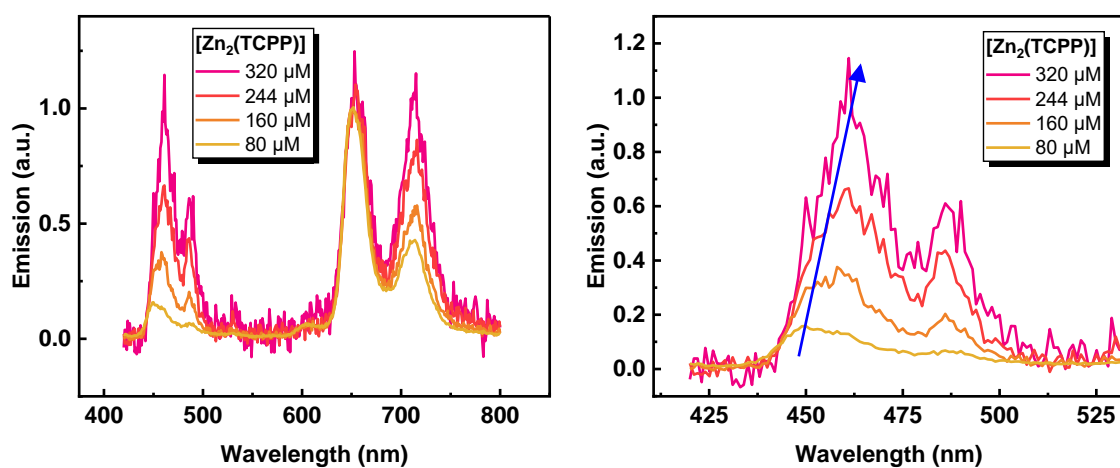


Figure S3.13 Electronic emission spectra for different concentrations of Zn₂(TCPP) MONs, normalised by the emission intensity at 651 nm.

TCSPC results are attributed to S_1 emission, shown in figure 10.^{3,9,10} Fitting suggests common ~ 1 ns and ~ 4 ns lifetimes in all samples (table 2). The indifference of Zn-TCPP emission lifetime to concentration implies that no other radiative or non-radiative processes are contributing to S_1 depopulation upon aggregation.

Gu et al. observed a reduced emission lifetime on formation of TCPP MOF, ascribing this change to the introduction of a competing non-radiative process in the assembled system also identified in the current work (table 3).¹ Similarly, Sakuma et al. identifies a 2.1 ns lifetime with a monoexponential decay and observes a shorter average lifetime in aggregated TCPP.⁶ The decrease in overall intensity observed as concentration increases indicates a less populated S_1 state. Without a rate change to indicate an alternate S_1 relaxation route, the alternate decay must occur from S_2 .

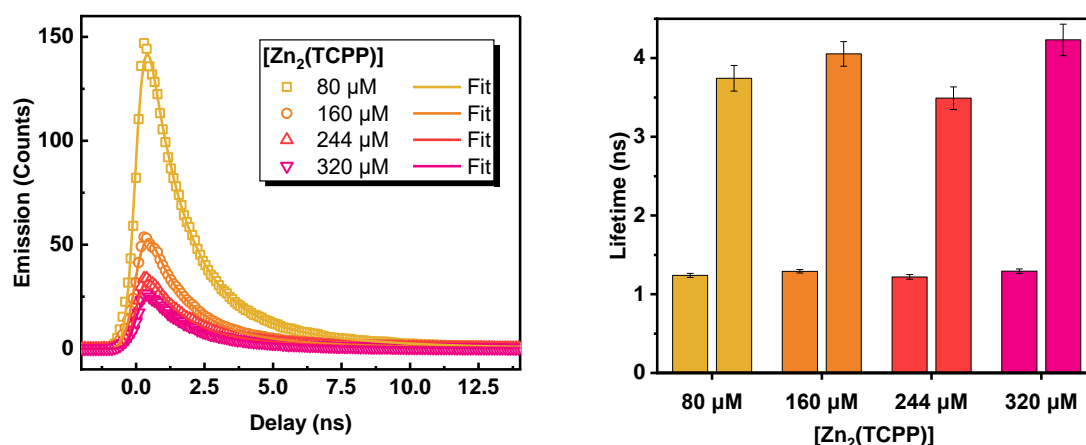


Figure S3.14 TCSPC decay curves as collected (left) and lifetimes from fitting (right).

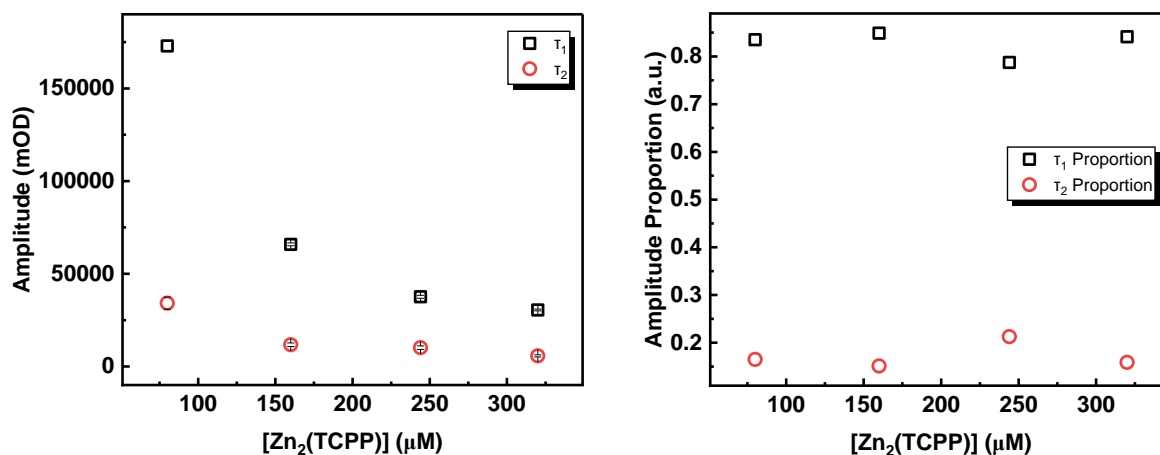


Figure S3.15 Comparison of fitted lifetime amplitudes for TCSPC of Zn₂(TCPP) (left), and proportion of total amplitude (right).

In order to determine the rate of dispersed particles settling out of suspension, a kinetic UV-visible absorption experiment was performed to measure the absorbance over four days (Figure S3.16). Spectra were collected every 30 mins for 96 hours (condensed here for simplicity). Peak at 426 nm selected for single wavelength kinetics (Figure S3.17) shows a general decrease from 0.938 OD to 0.825 OD over the four days, indicating that the drop out of suspension in ethanol is not expected to have a significant effect on absorption intensity over experiments which take 15-60 minutes.

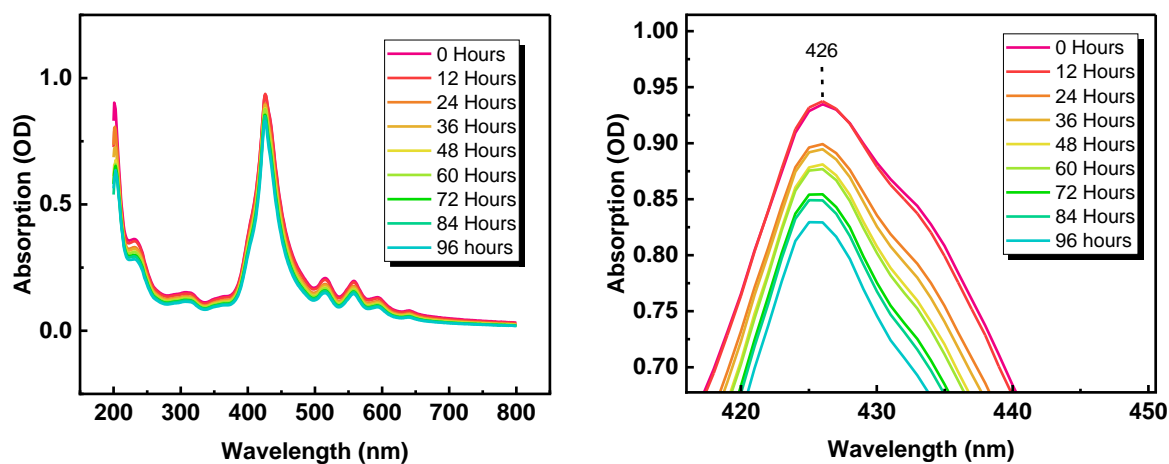


Figure S3.16 UV-Vis spectra (left) for $Zn_2(TCPP)$ produced by batch synthesis from 97% pure TCPP, and zoomed peak at 426 nm (right).

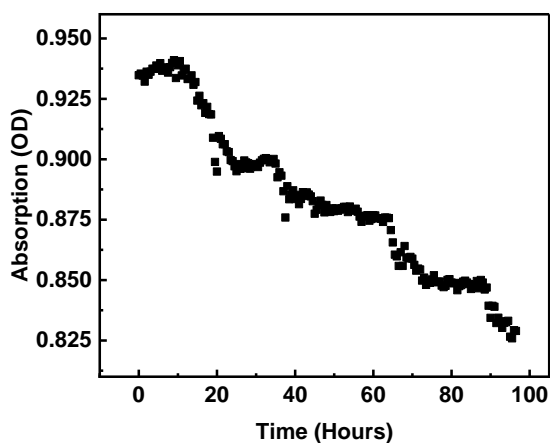


Figure S3.17 Kinetics for absorption at 426 nm for $Zn_2(TCPP)$ produced by batch synthesis from 97% pure TCPP. Steps in trend are caused by day/night temperature fluctuations.

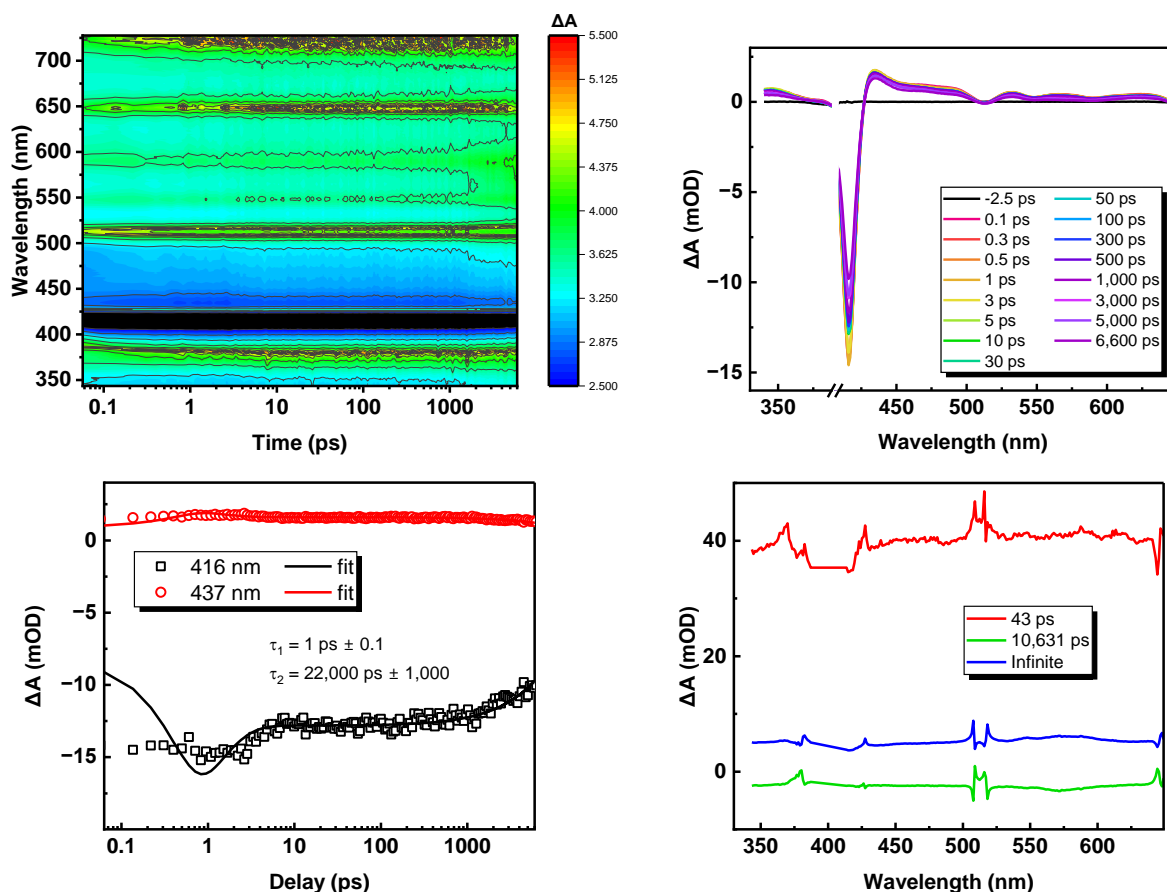


Figure S3.18 TA data for freebase TCPP solution in ethanol with heatmap (top left), selected spectra (top right), kinetics (bottom left), and decay associated spectra (bottom right)

A long-time TA setup was used to investigate the presence of triplet state in the excited Zn-TCPP MONs. With 355 nm excitation, the absorption spectra show no negative signal at either 425 or 450 nm as it is too fast decaying for the resolution of the setup but retains similar ES features: a broad absorption starting above 435 nm with a maximum absorption at 464 nm and a shoulder at 530 nm. Further GSB features at 559 nm and 600 nm are complemented by ES absorption at 581 nm and >610 nm. Global fit of the kinetic data shows a 6 μ s lifetime.

Comparison with degassed Zn-TCPP sample showed minimal spectral changes, however the kinetics show an increased 20 μ s lifetime on removal of triplet quenching oxygen (figure 15c). This evidences that the long lifetimes are due to the excited T_1 state, and it is not expected that decay from the triplet state is emissive.^{9,10} The 2 ns ISC $S_1 \rightarrow T_1$ component identified in the same work, and mentioned above, is now observable as a 2.2 ns (0.0022 μ s), indicating that it is the major S_1 decay component in the deoxygenated system.^{9,10}

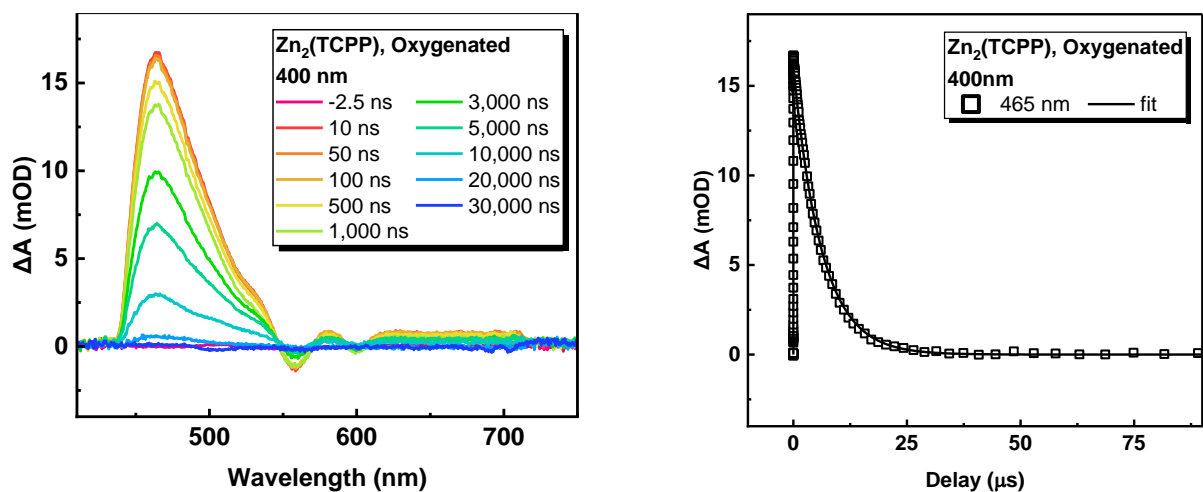


Figure S3.19 TA spectra (left) and kinetics (right) for oxygenated Zn₂(TCPP) with global fit across three wavelengths.

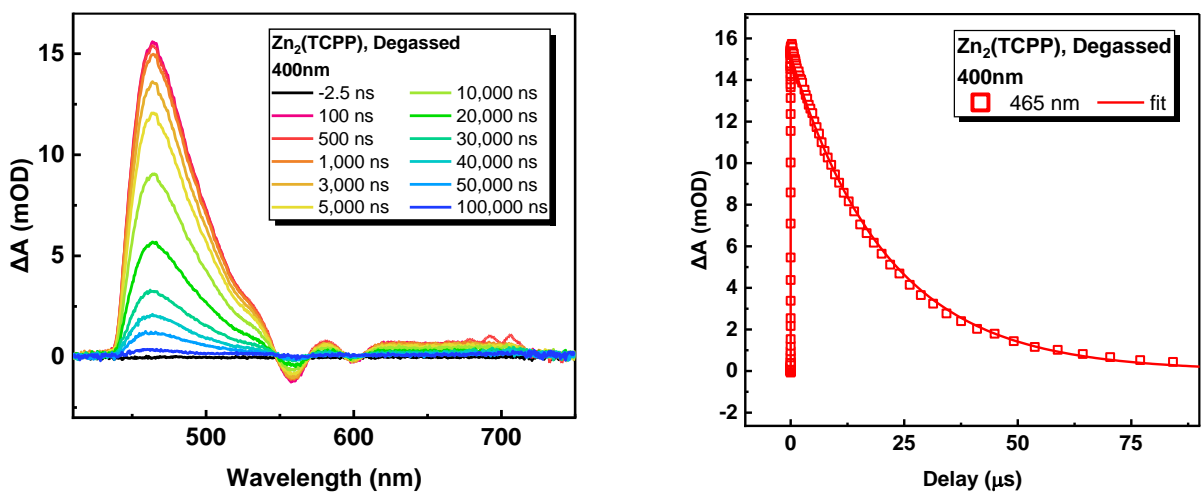


Figure S3.20 TA spectra (left) and kinetics (right) for degassed Zn₂(TCPP) with global fit across three wavelengths.

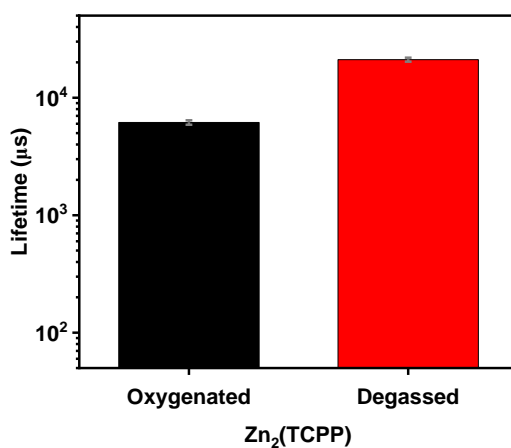


Figure S3.21 Bar graph comparing lifetimes for oxygenated and degassed Zn₂(TCPP) using fitting results from msTA.

During centrifugation, larger particles should be preferentially removed at lower speeds compared to smaller ones. This is true for both laterally larger nanosheets, and multi-layer nanosheets compared to monolayer, ignoring the assumed negligible effects of liquid resistance, which would otherwise adversely affect the sedimentation of highly anisotropic particles compared to lower surface area to volume ratio particles.

Table S3.4 Sample preparation for centrifugation of Zn₂(TCPP)

	Empty Vial	Dried Vial	Concentration / mg mL ⁻¹
Before C	1784.8	1787.5	2.7
2,000 rpm	1756.1	1757.3	1.2
4,000 rpm	1749.4	1750.3	0.9
6,000 rpm	1653.0	1653.2	0.2
8,000 rpm	1733.6	1733.8	0.2
After C	1739.4	1740.6	1.2

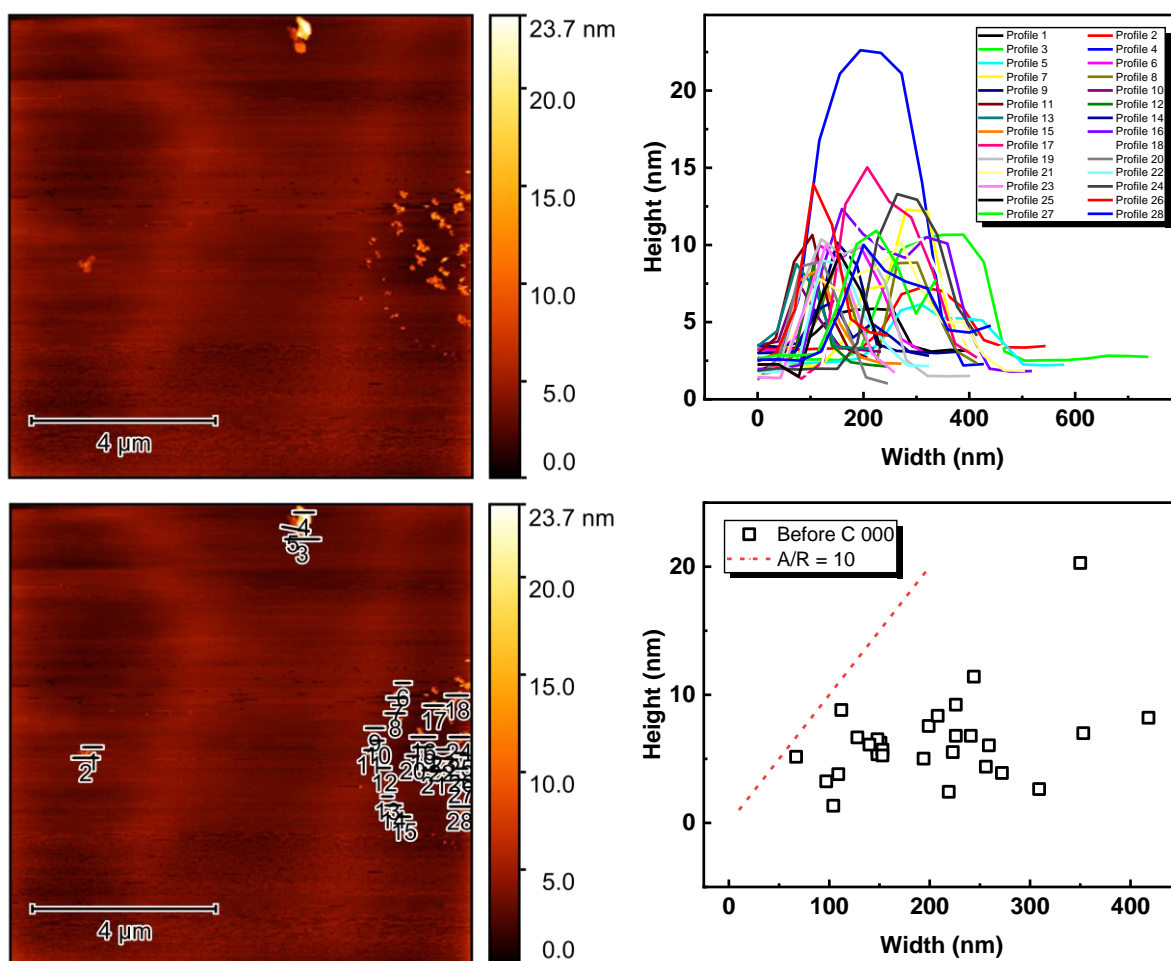


Figure S3.22 Before C 0.2mg mL⁻¹ profiles for sample 000 AFM data, Average Roughness: 3.33 nm.

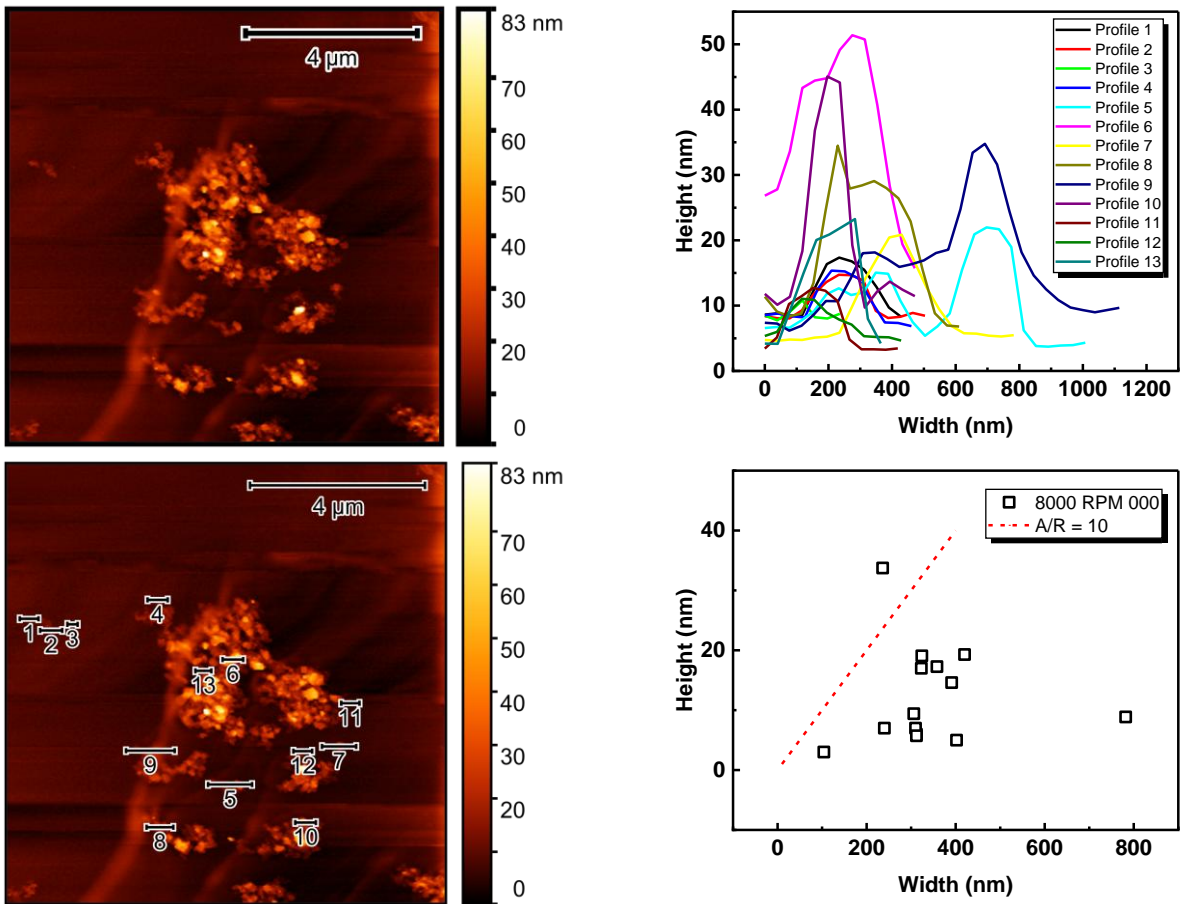


Figure S3.23 8000 RPM 0.2mg mL^{-1} profiles for sample 000 AFM data, Average Roughness: 8.56 nm.

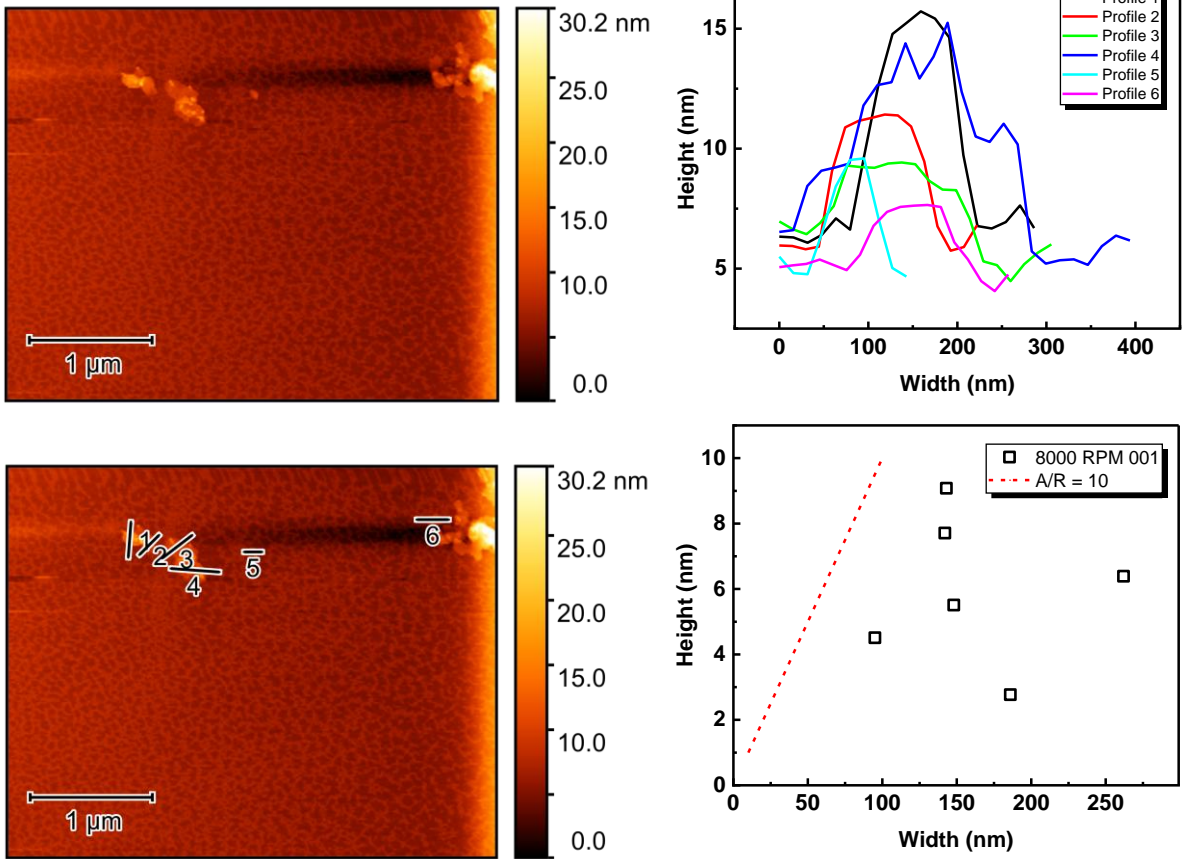


Figure S3.24 8000 RPM 0.2mg mL⁻¹ profiles of sample 001 AFM data, Average Roughness: 3.49 nm.

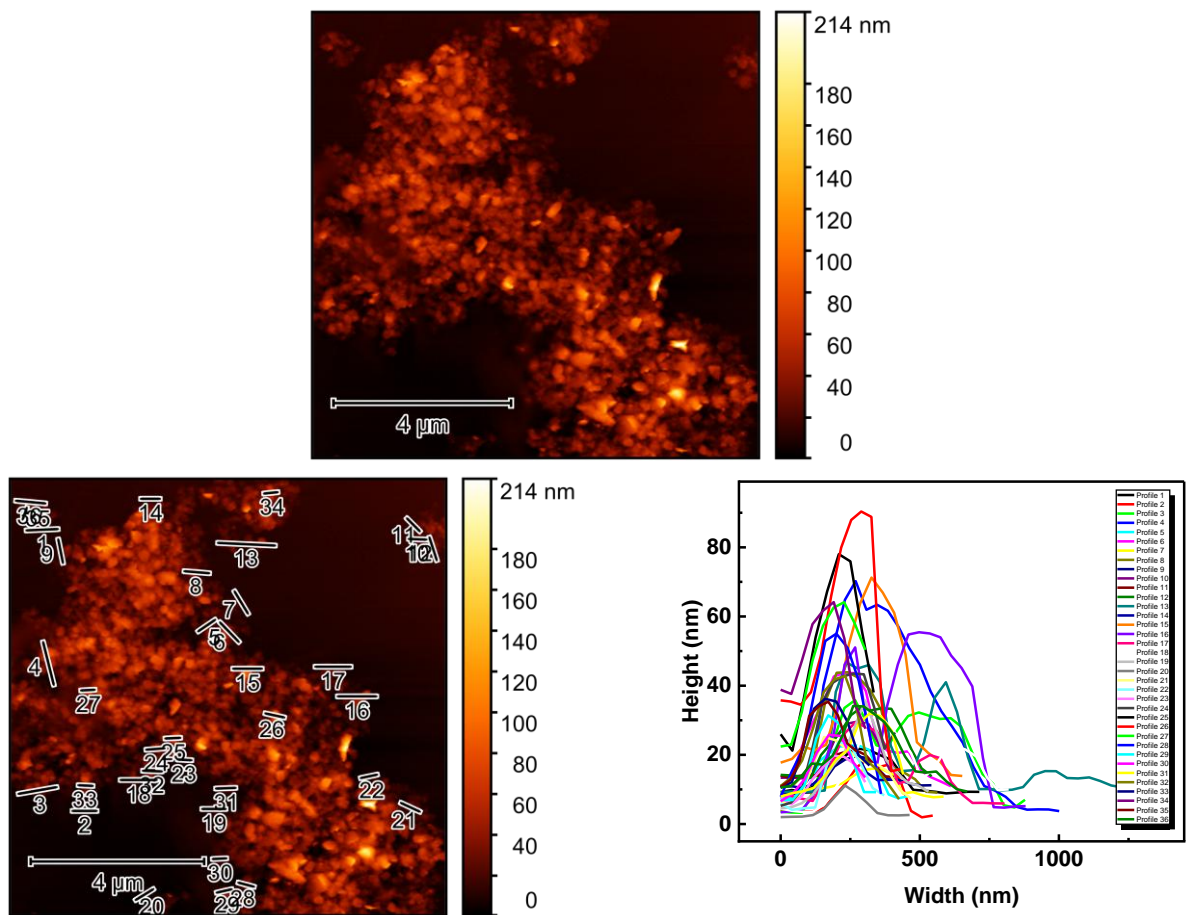


Figure S3.25 8000 RPM 0.2mg mL⁻¹ profiles for sample 003 AFM data, Average Roughness: 20.4 nm.

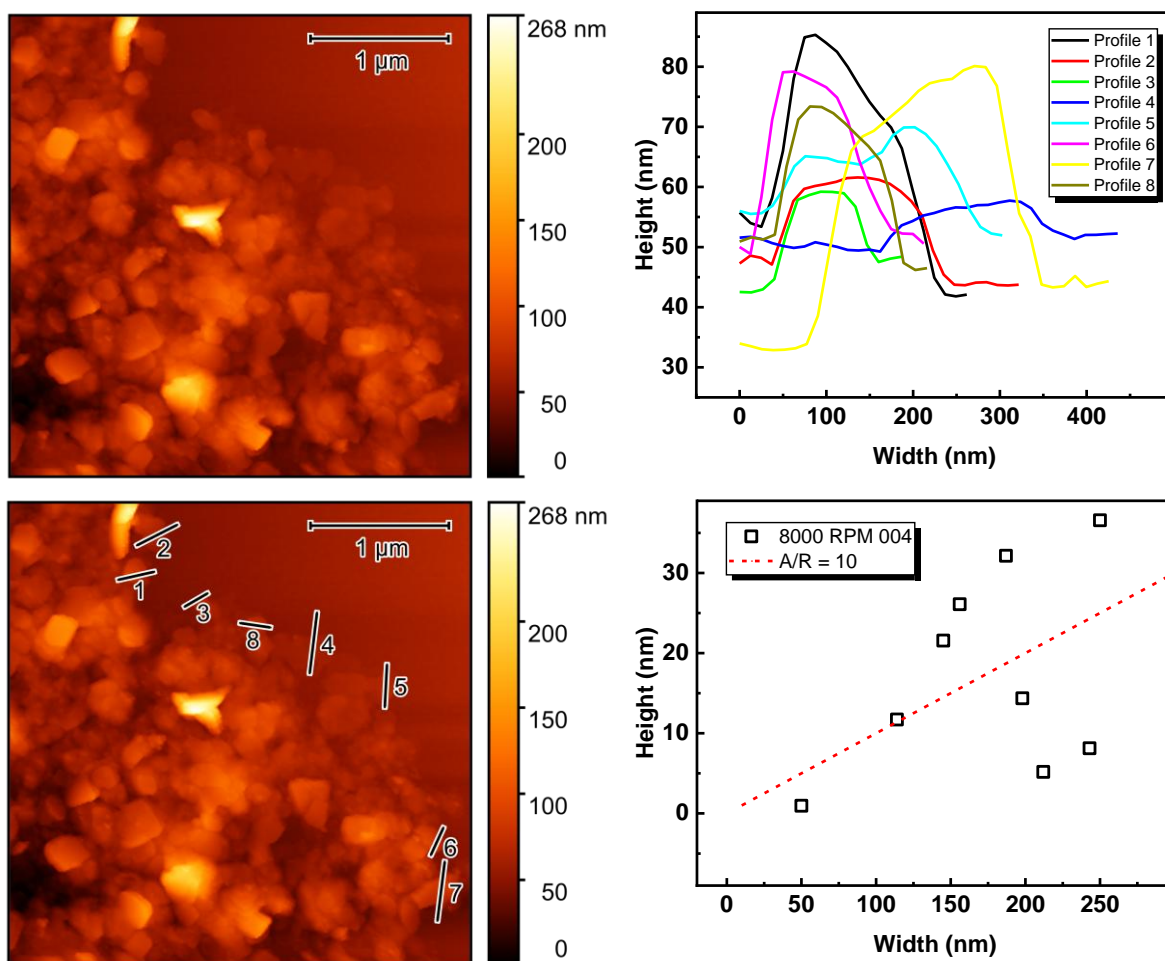


Figure S3.26 8000 RPM 0.2 mg mL^{-1} profiles for sample 004 AFM data, Average Roughness: 61.8 nm.

The steady state absorption of centrifuged $\text{Zn}_2(\text{TCPP})$ samples was measured when dispersions were all diluted to 0.02 mg mL^{-1} .

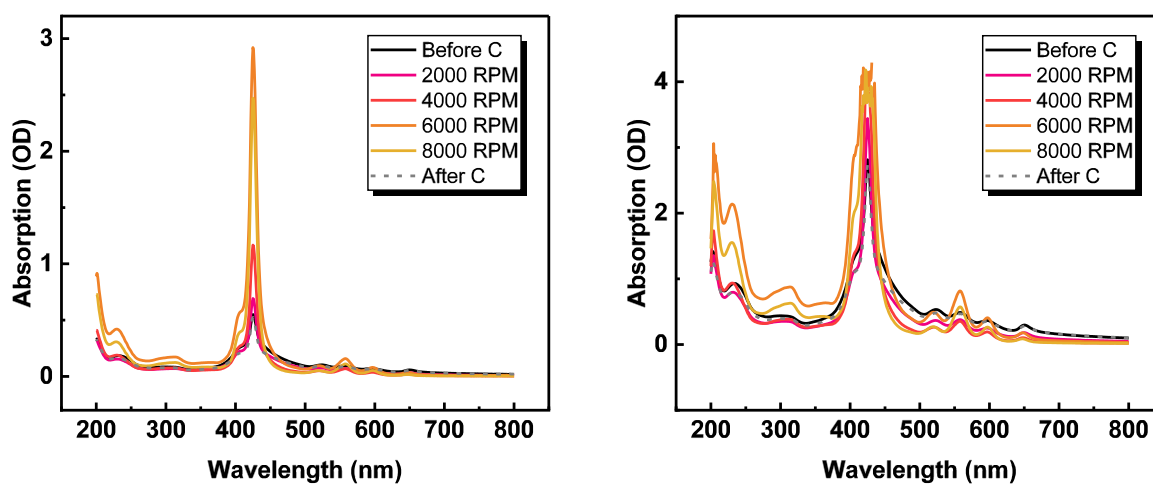


Figure S3.27 Electronic absorption of $4\text{ }\mu\text{g mL}^{-1}$ (left) and 0.02 mg mL^{-1} (right) dispersions of $\text{Zn}_2(\text{TCPP})$ in a 10 mm cuvette.

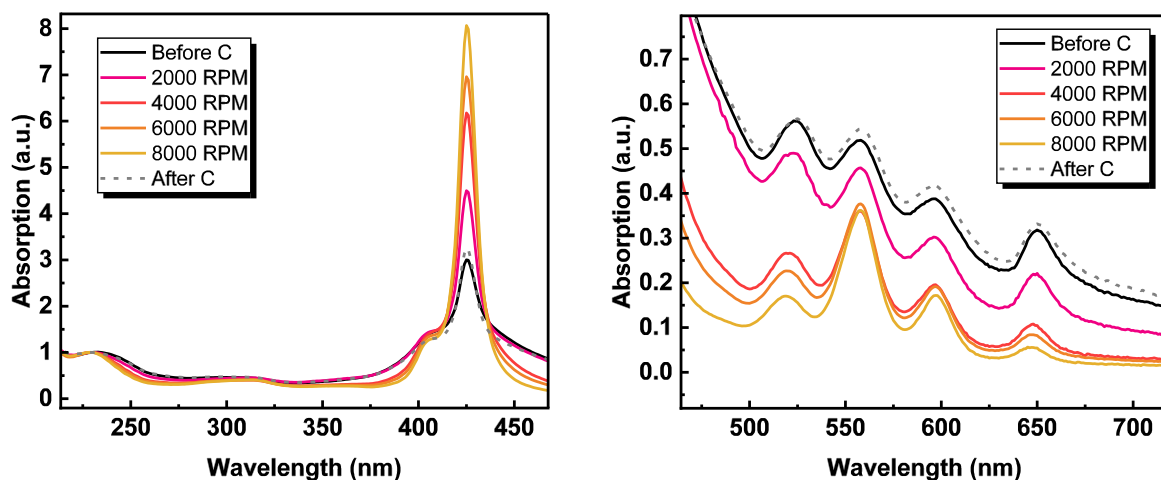


Figure S3.28 Electronic absorption of centrifuged $Zn_2(TCPP)$ samples normalised by the intensity at 230 nm. Spectra are separated into absorption 200-460 nm (left), and 460-740 nm (right)

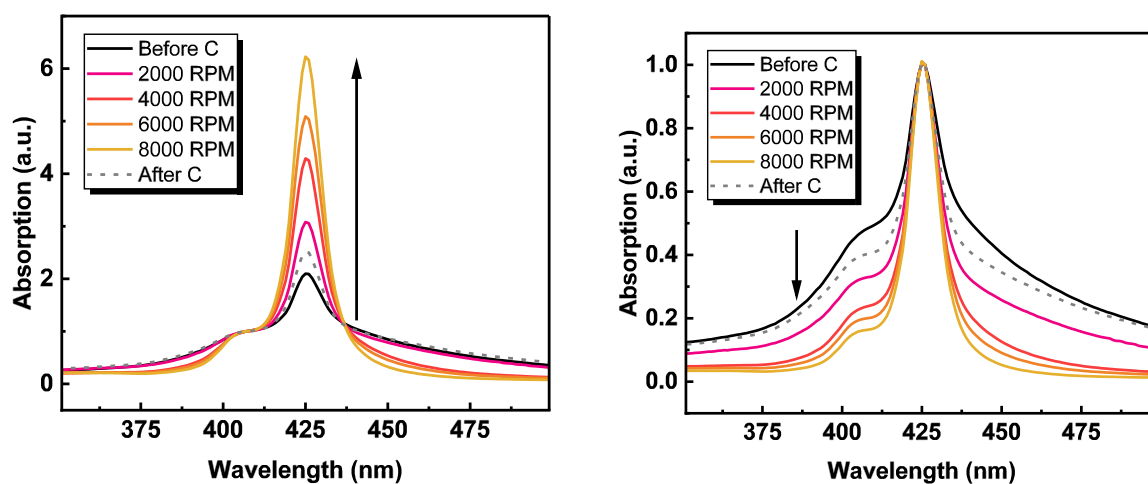


Figure S3.29 Electronic absorption normalised at 415 nm (left), and 425 nm (right)

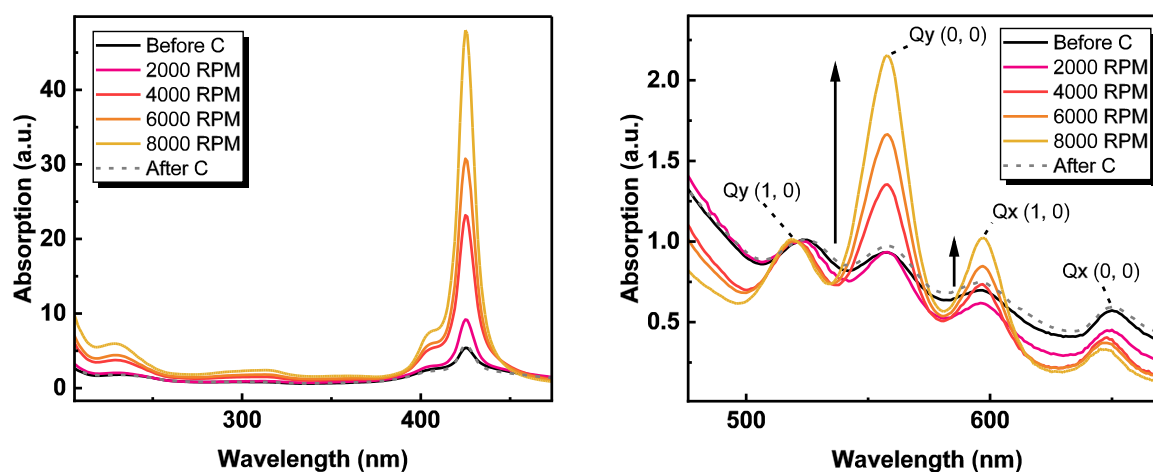


Figure S3.30 Electronic absorption of centrifuged $Zn_2(TCPP)$ samples normalised by the intensity at 521 nm with absorption 210-470 nm (left) and zoomed in to Q bands 470-670 nm (right).

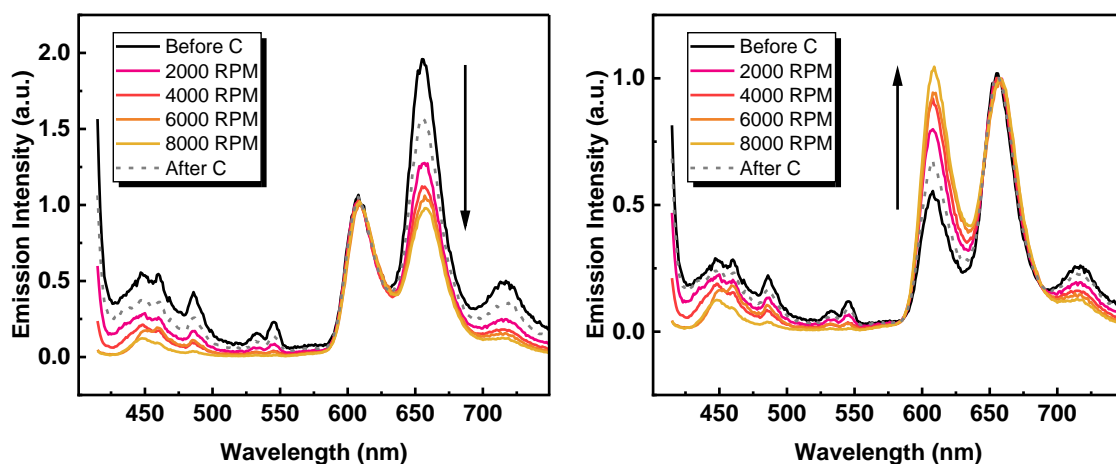


Figure S3.31 Electronic emission of cc $Zn_2(TCPP)$ samples measured after excitation at 400 nm. Spectra are shown normalised by intensity at 608 nm (left), and 652 nm (right).

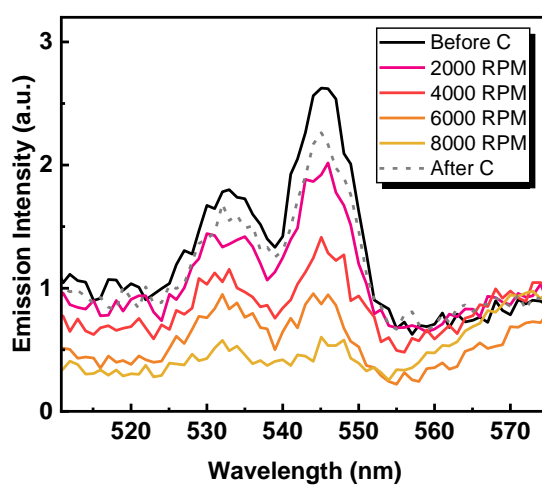


Figure S3.32 Electronic emission of cc $Zn_2(TCPP)$ samples measured after excitation at 400 nm. Cropped to show peak at 545 nm.

The transient absorption of centrifuged Zn₂(TCPP) samples were investigated using pump-probe spectroscopy to determine the power dependence of excited state lifetimes.

Power varied between 0.2 and 2 mW using excitation beam with major ellipsoid diameter 620.77 μm and minor ellipsoid diameter 542.63 μm. Pump fluence (energy density per surface area) can be calculated using Equation S3.1. where the unit of pump fluence is usually reported in μJ cm⁻², P is measured pump power, f is the pump rate (for Helios, $f = 5000 \text{ Hz}$, a is the pump ellipse major *radius*, and b is the pump ellipse minor *radius* (note beam spot measurement outputs diameters). Therefore, using the equation, tested pump fluences were 15, 30, 60, 76, 91, 106, and 151 μJ cm⁻². P was converted to Watts and multiplied by 1,000,000, and a and b were divided by (2 × 10,000) to convert to radii in cm.

Equation S3.1 $Pump\ Fluence = P \div (f \times \pi \times a \times b)$

The pump fluences for each day were calculated, as seen in Table S3.7.

Table S3.5 Pump power to fluence conversions for each day of TA measurement

Power / mW	Fluence Day 1 / μJ cm ⁻²	Fluence Day 2 / μJ cm ⁻²
0.2	88.8	93.4
0.4	177.6	186.8
0.8	355.3	373.6
1.0	444.1	467.0
1.5	666.1	700.5
2.0	888.2	934.0

The experiments were carried out over three days, and therefore the measured powers will equate to variable fluences based on the pump spot dimensions at the sample, the profiles of which were measured each day.

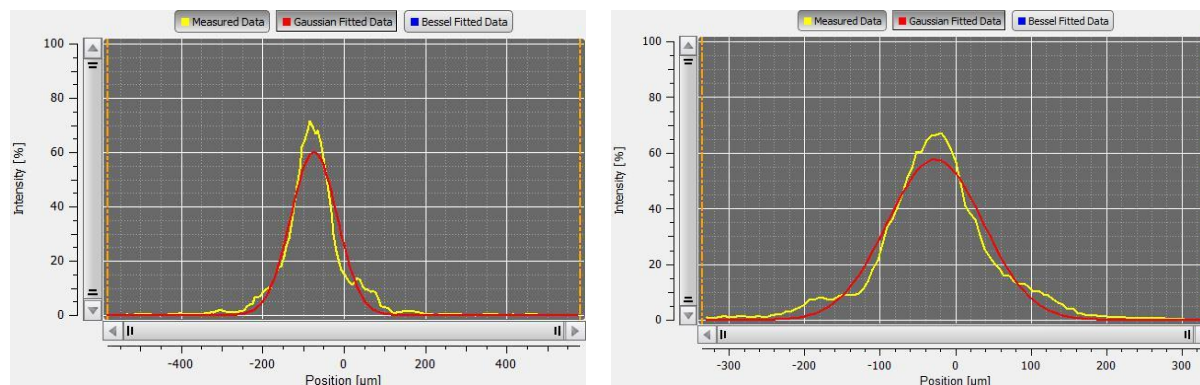


Figure S3.33 Profiles x (left), and y (right) with fitted Gaussian curves for pump beam spot on day 1.

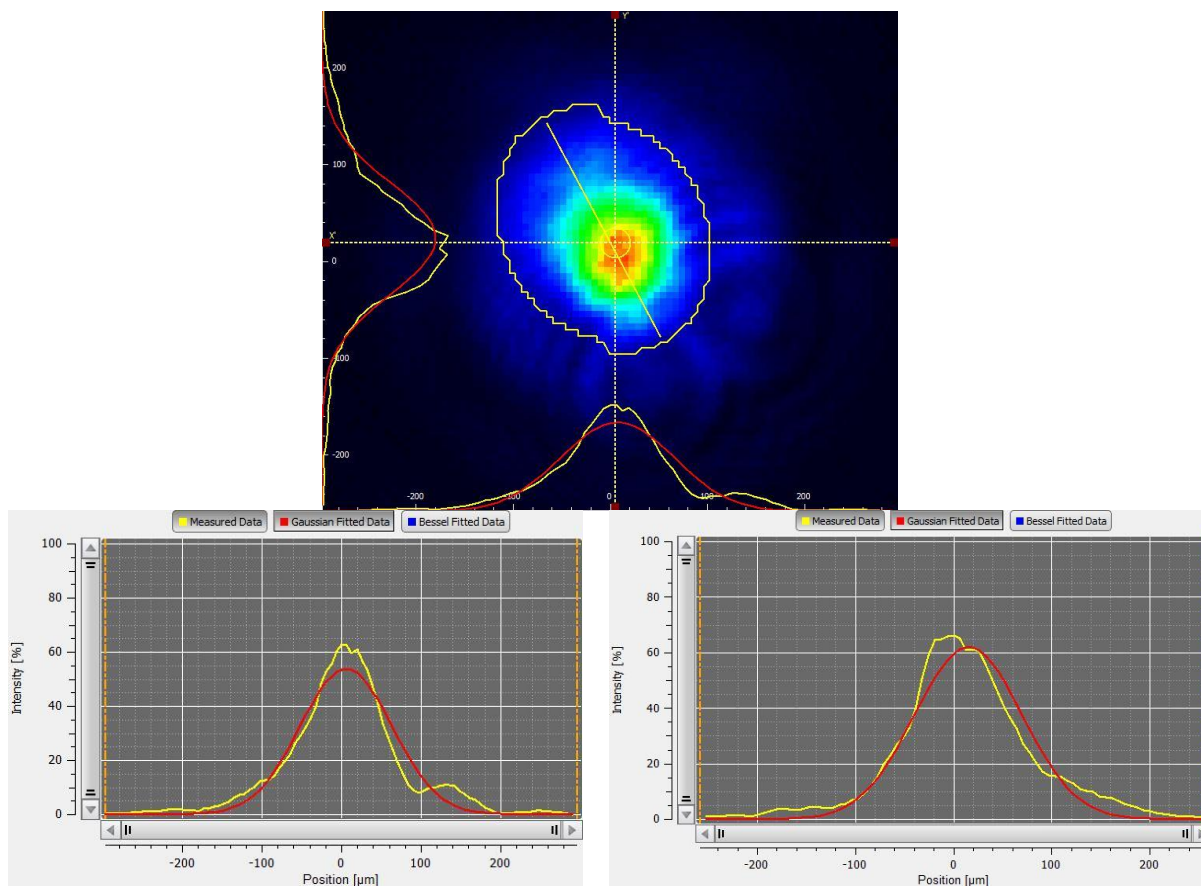


Figure S3.34 Pump spot image (top), and profiles x (bottom left), and y (bottom right) with fitted Gaussian curves for pump beam spot on day 2.

Table S3.6 Calculated pump spot dimensions for each day of TA measurements from beam profiles.

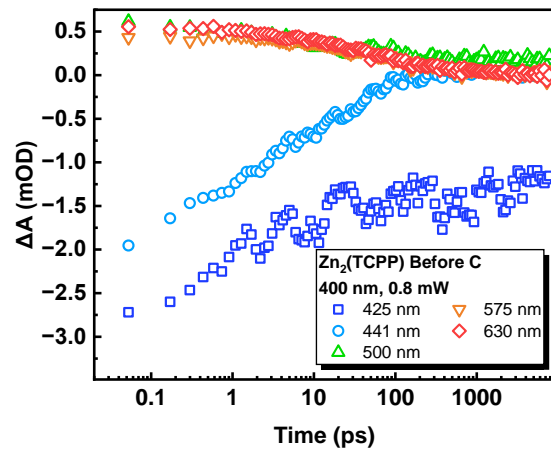
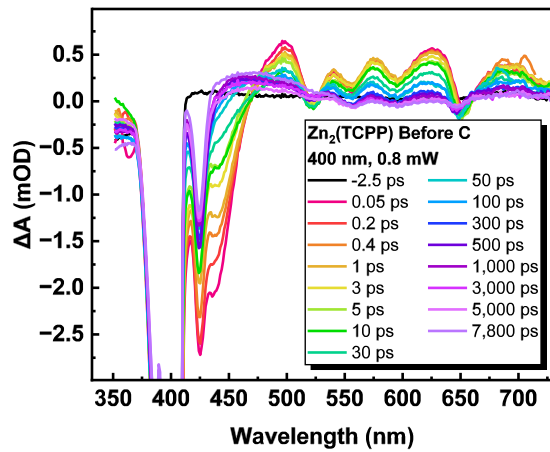
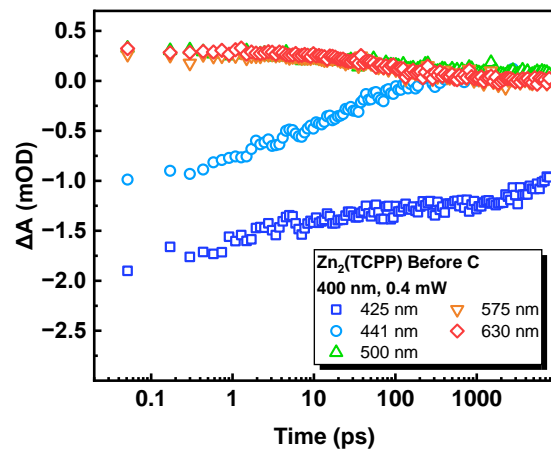
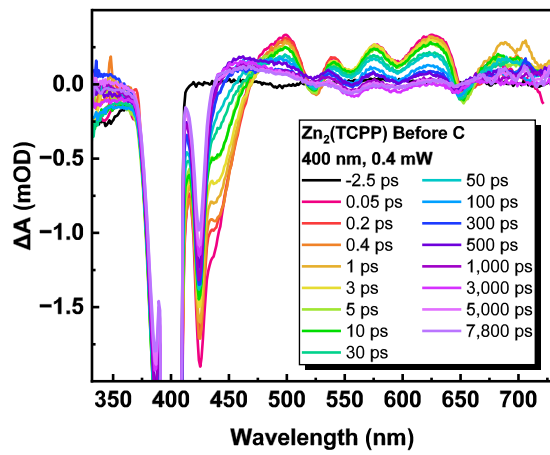
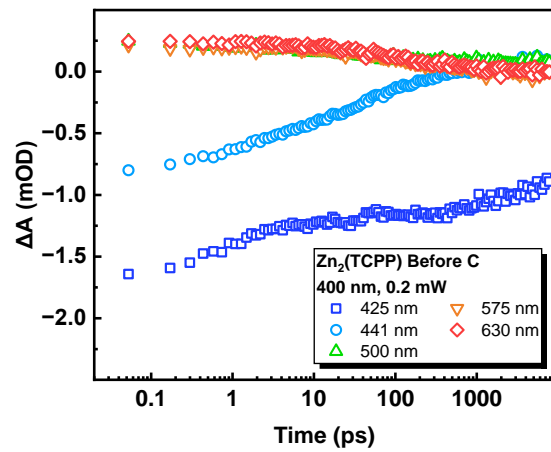
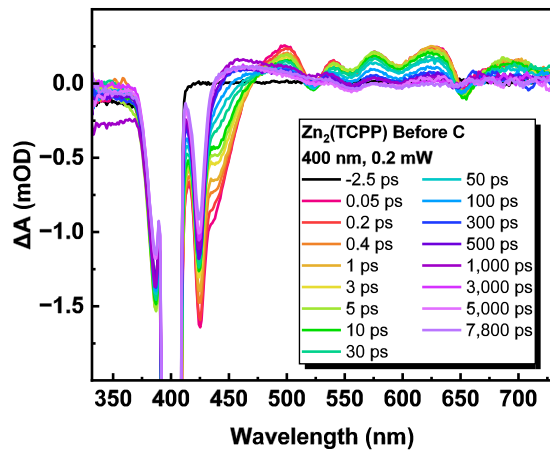
Day	Minor Ellipsoid / μm	Major Ellipsoid / μm
1	225.29	254.53
2	218.37	249.72

The pump fluences for each day were calculated using the method as seen in Table S3.7.

Table S3.7 Pump power to fluence conversions for each day of TA measurement

Power / mW	Fluence Day 1 / $\mu\text{J cm}^{-2}$	Fluence Day 2 / $\mu\text{J cm}^{-2}$
0.2	88.8	93.4
0.4	177.6	186.8
0.8	355.3	373.6
1.0	444.1	467.0
1.5	666.1	700.5
2.0	888.2	934.0

Here, the 400 nm pump power was varied between 0.2, 0.4, 0.8, 1.0, 1.5, and 2.0 mW (Day 1, see Table S3.7).



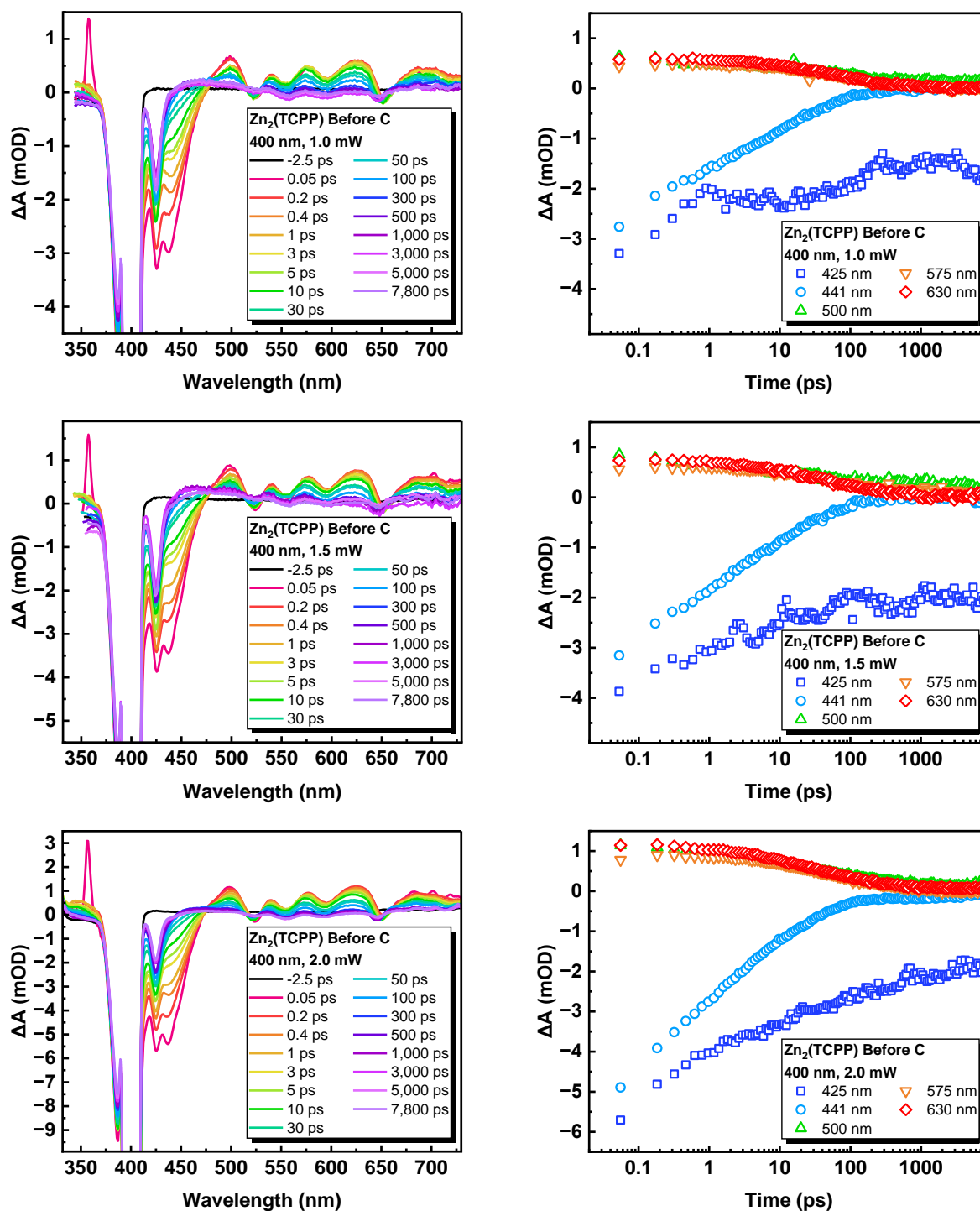


Figure S3.35 TA Spectra and kinetics at key wavelengths for $Zn_2(TCPP)$ before post-synthetic centrifugation with pump powers at 0.2, 0.4, 0.8, 1.0, 1.5, and 2.0 mW.

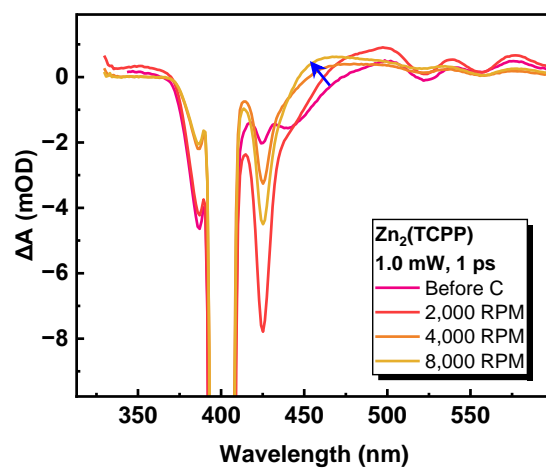


Figure S3.36 TA spectral changes for Zn₂(TCPP) 1 ps after excitation at 400 nm with 1 mW pump power. Arrow indicates loss of ground state bleach leading to recovery of excited state absorption positive ΔA.

Power Dependence of TA Kinetics of Zn₂(TCPP) Before Centrifugation at 425 nm

The kinetics of transient absorbance at 425 nm for Zn₂(TCPP) before post-synthetic centrifugation (Before C), are plotted in Figure S3.37. The 400 nm excitation beam was recorded at powers 0.2, 0.4, 0.8, 1.0, 1.5, and 2.0 mW, and are converted to fluence in the Day 1 column of Table S3.7.

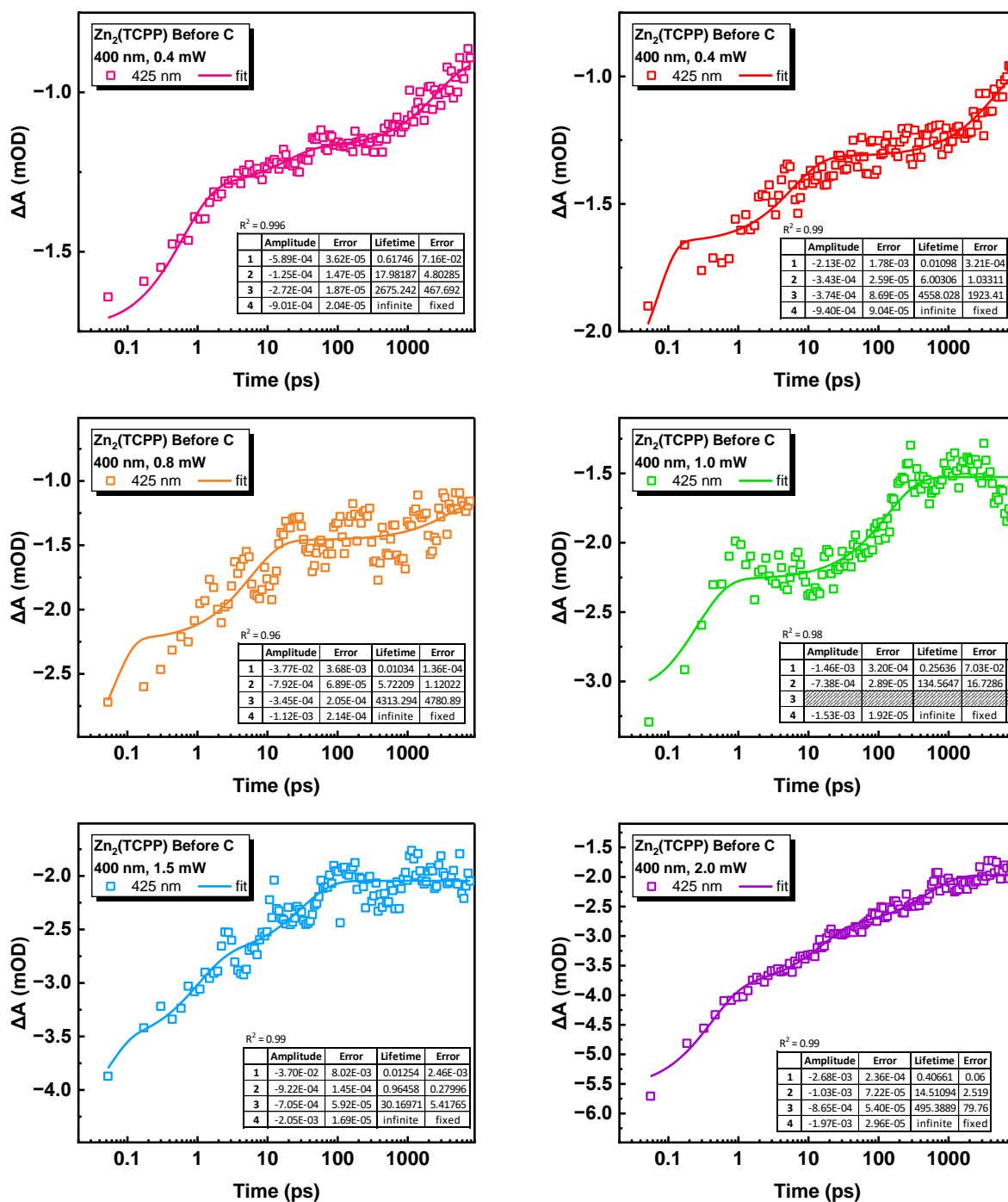


Figure S3.37 Transient absorption kinetics at 425 nm for Zn₂(TCPP) Before C with 400 nm excitation power of 0.2, 0.4, 0.8, 1.0, 1.5, and 2.0 mW.

Power Dependence of TA Kinetics of Zn₂(TCPP) Before Centrifugation at 441 nm

The kinetics of transient absorbance at 441 nm for Zn₂(TCPP) before post-synthetic centrifugation (Before C), are plotted in Figure S3.38. The 400 nm excitation beam was recorded at powers 0.2, 0.4, 0.8, 1.0, 1.5, and 2.0 mW, and are converted to fluence in the Day 1 column of Table S3.7.

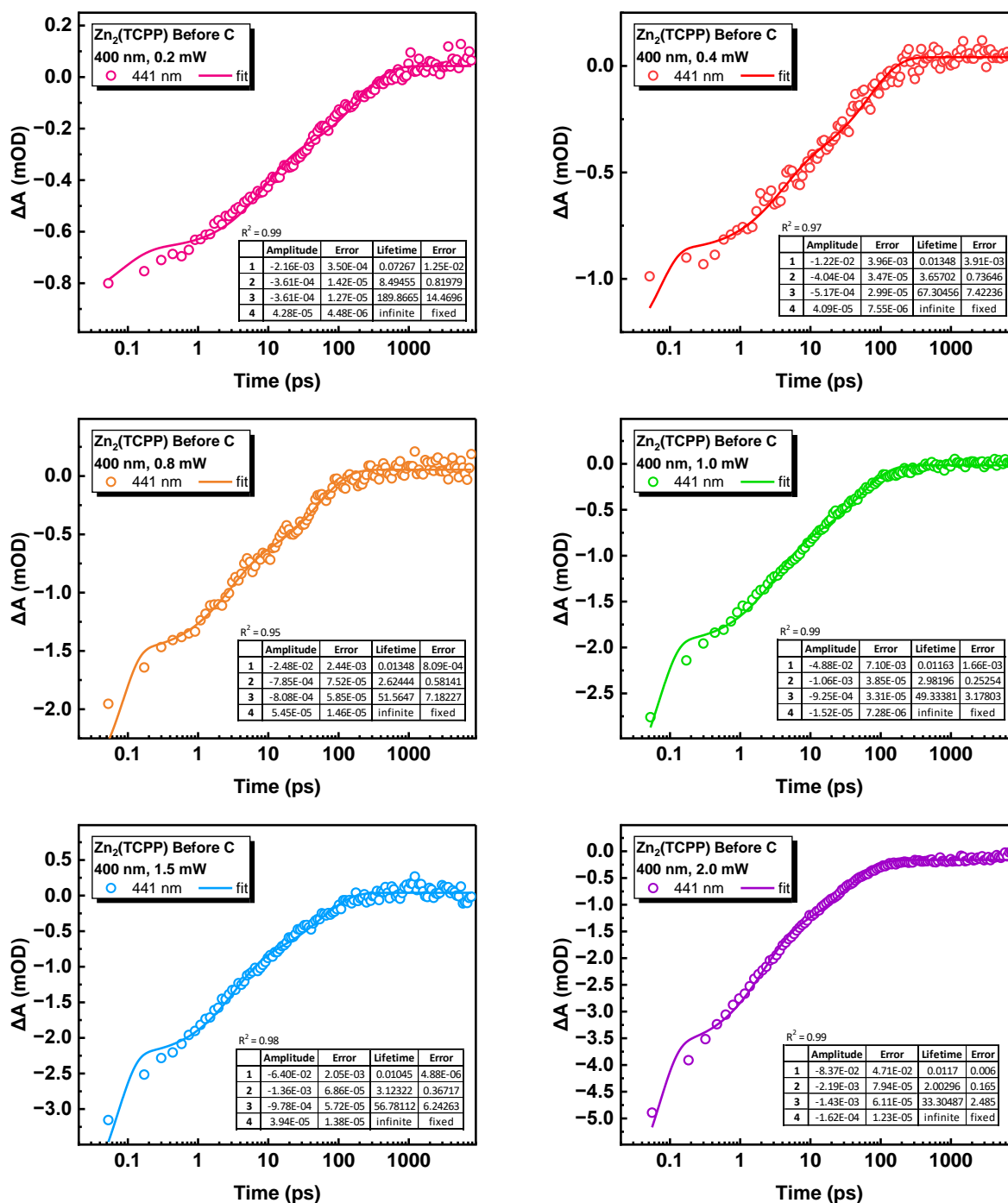


Figure S3.38 Transient absorption kinetics at 441 nm for Zn₂(TCPP) Before C with 400 nm excitation power of 0.2, 0.4, 0.8, 1.0, 1.5, and 2.0 mW.

The normalised TA kinetics at 441 nm for Zn₂(TCPP) before post-synthetic centrifugation are overlaid in Figure S3.39.

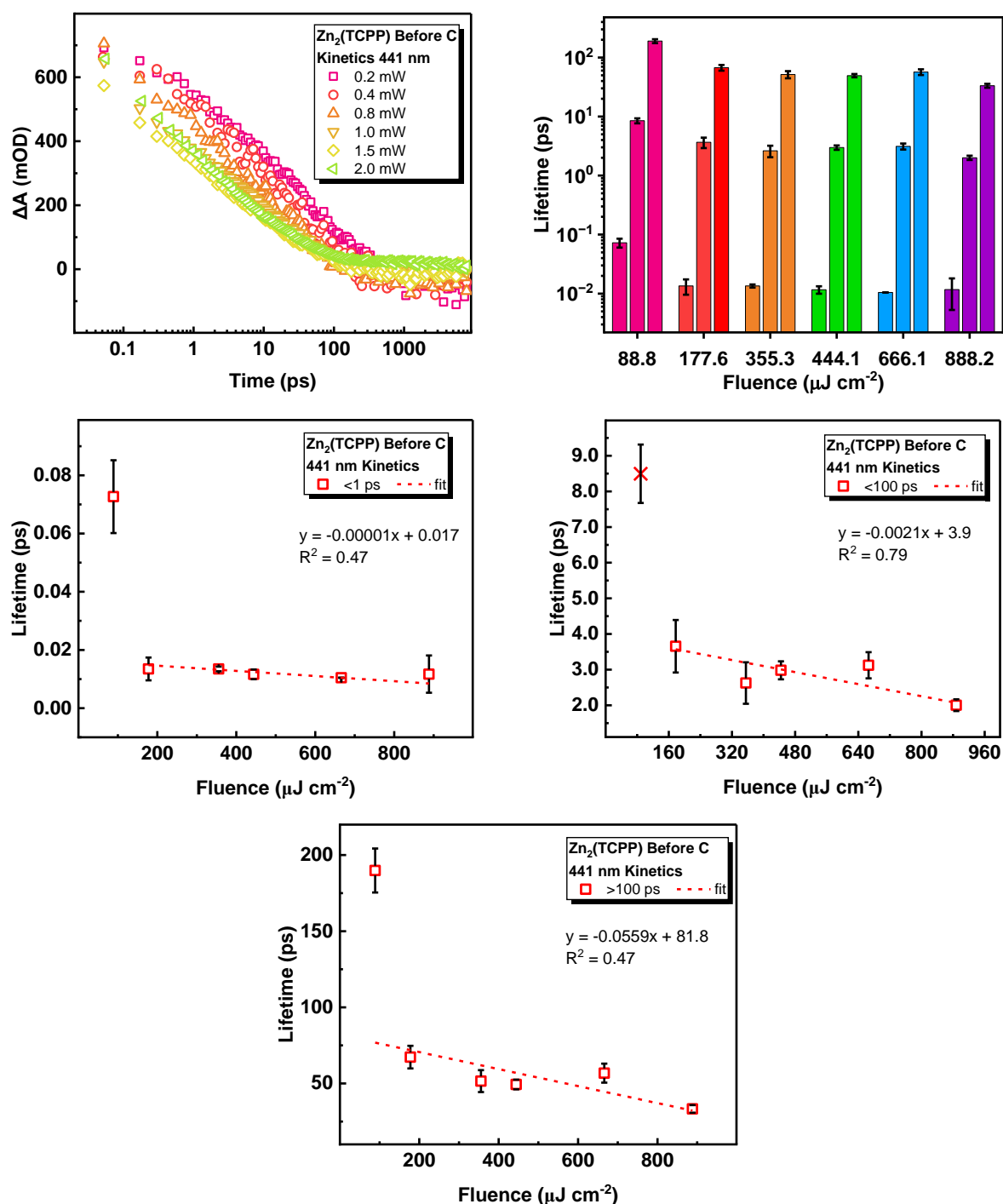
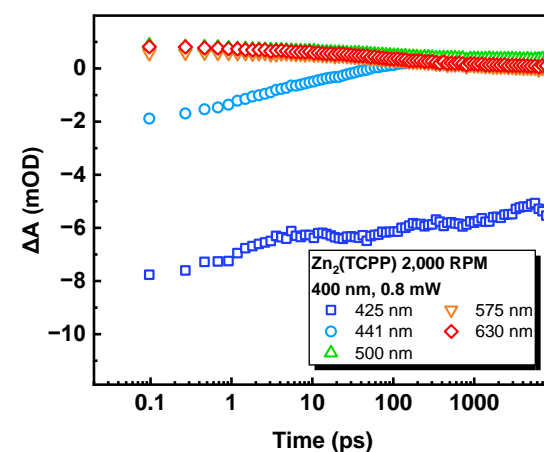
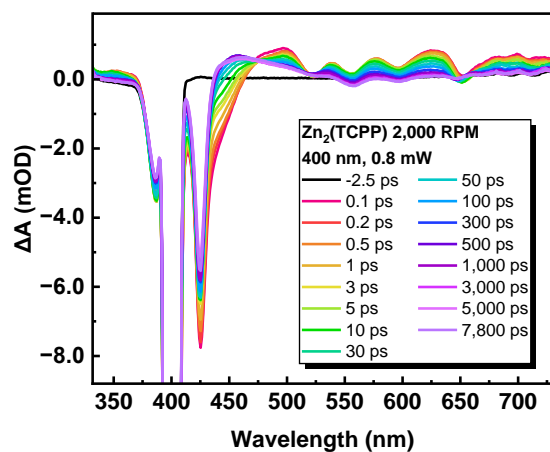
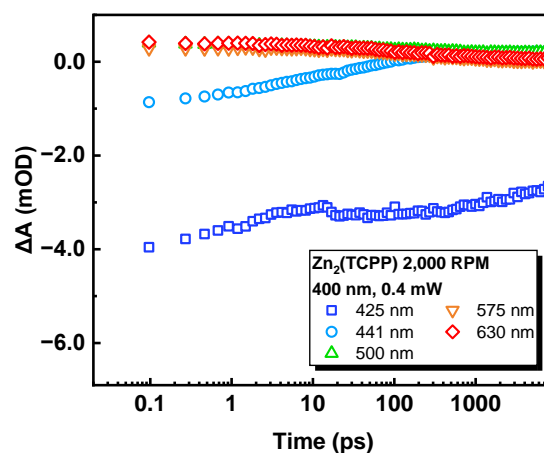
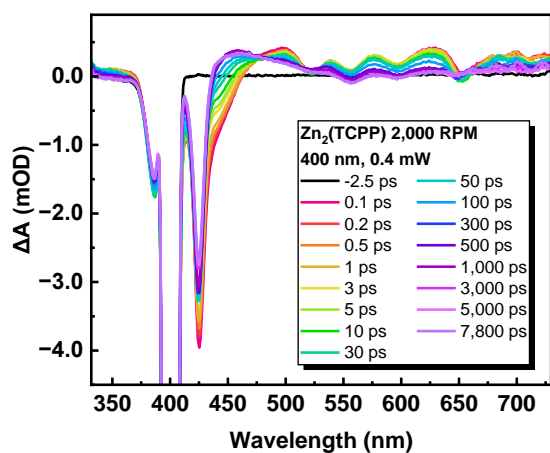
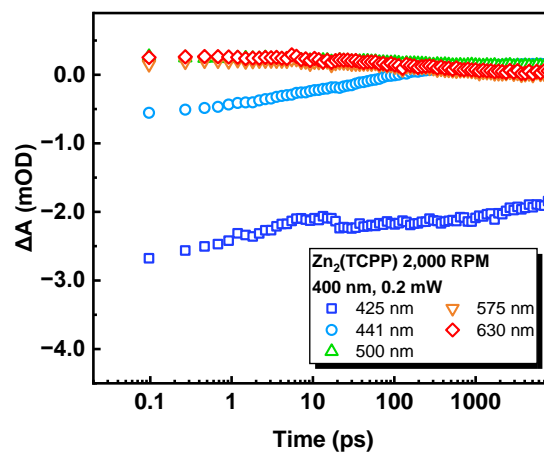
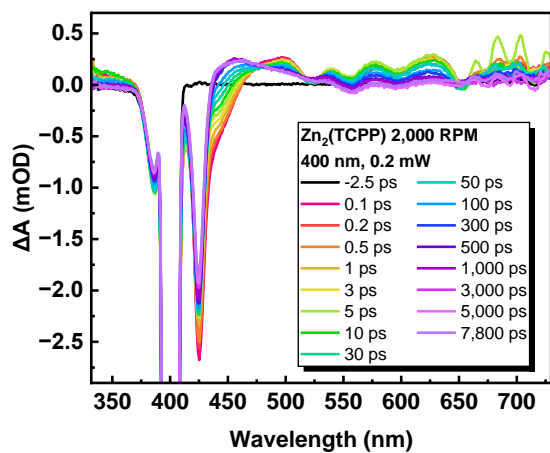


Figure S3.39 Normalised TA kinetics at 441 nm for Zn₂(TCPP) before post-synthetic centrifugation (top left), lifetimes compared by each power (top right), and the power dependence of lifetimes less than 1 ps (middle left), between 1-100 ps (middle right), and greater than 100 ps (bottom middle).

TA Power Dependence of Zn₂(TCPP) Samples After 2,000 RPM Post-Synthetic Centrifugation

Here, the 400 nm pump power was varied between 0.2, 0.4, 0.8, 1.0, 1.5, and 2.0 mW (Day 1, see Table S3.7).



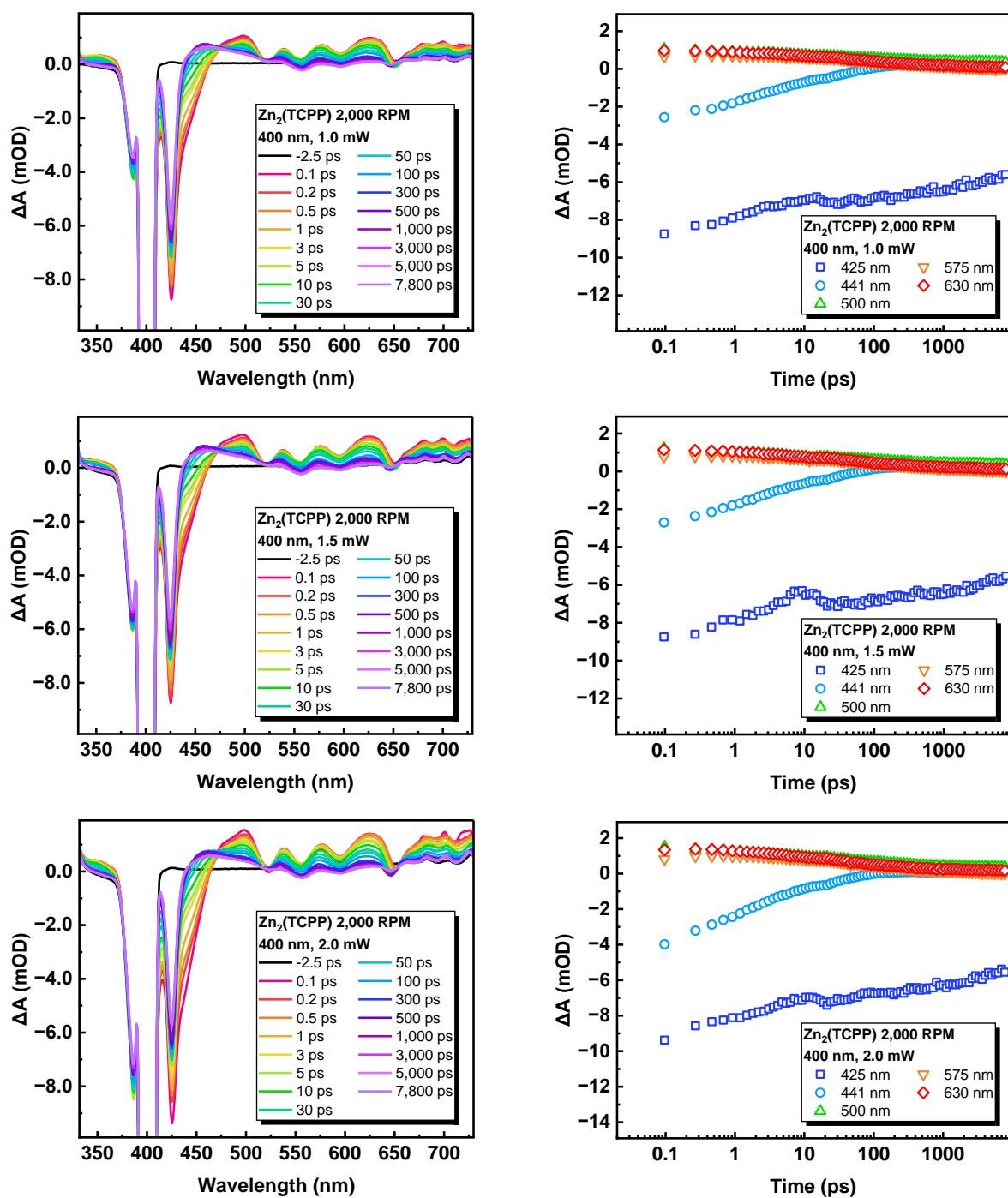


Figure S3.40 TA Spectra and kinetics at key wavelengths for Zn₂(TCPP) after 2,000 RPM post-synthetic centrifugation with pump powers at 0.2, 0.4, 0.8, 1.0, 1.5, and 2.0 mW.

Power Dependence of TA Kinetics at 441 nm of Zn₂(TCPP) After 2,000 RPM Centrifugation

The kinetics of transient absorbance at 441 nm for Zn₂(TCPP) before post-synthetic centrifugation (Before C), are plotted in Figure S3.41. The 400 nm excitation beam was recorded at powers 0.2, 0.4, 0.8, 1.0, 1.5, and 2.0 mW, and are converted to fluence in the Day 2 column of Table S3.7.

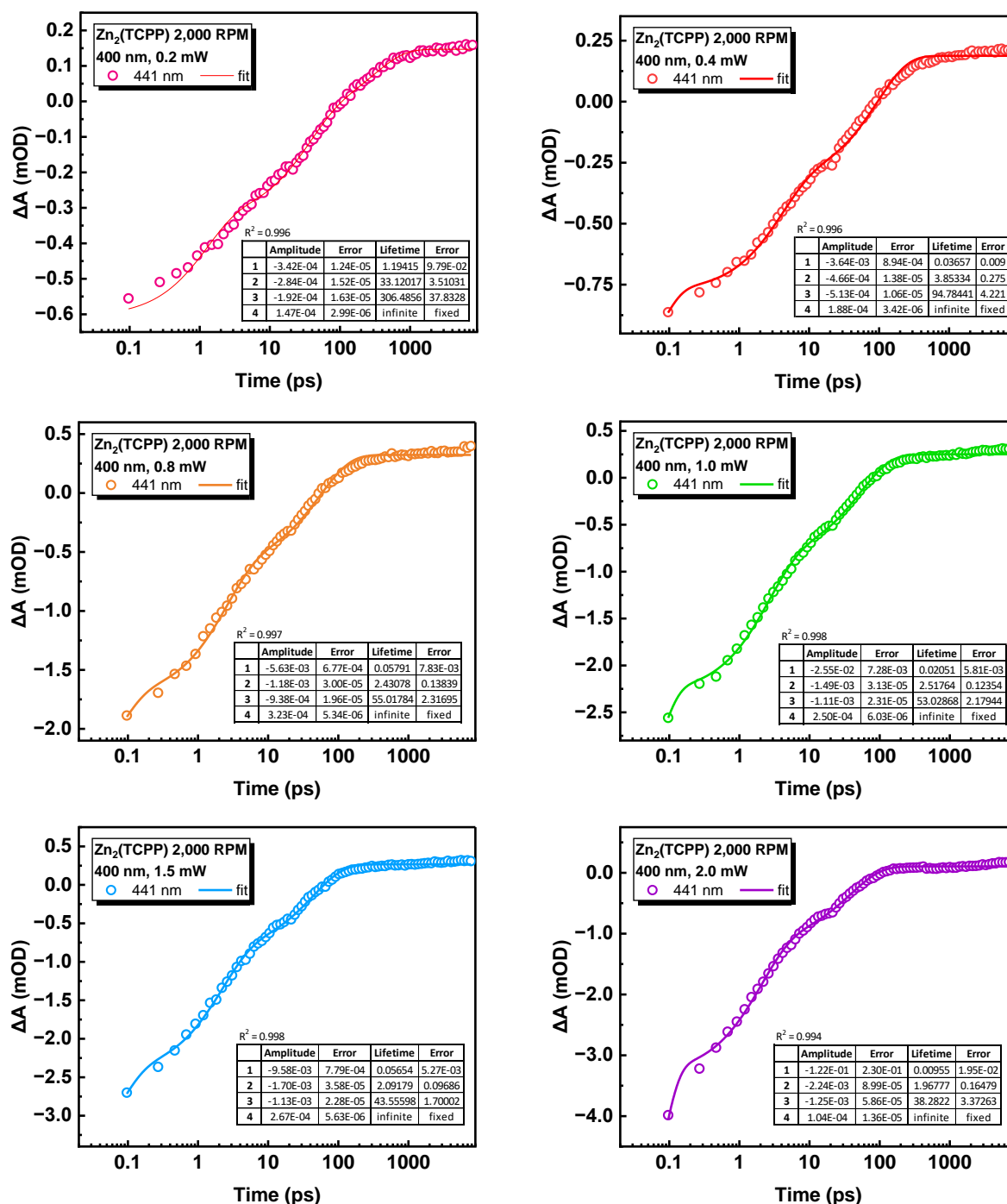


Figure S3.41 Transient absorption kinetics at 441 nm for Zn₂(TCPP) after PSC at 2,000 RPM with 400 nm excitation power of 0.2, 0.4, 0.8, 1.0, 1.5, and 2.0 mW.

The normalised TA kinetics at 441 nm for Zn₂(TCPP) after 2,000 RPM post-synthetic centrifugation are overlaid in Figure S3.42. It should be noted that the data points at 93.4 $\mu\text{J cm}^{-2}$ and 467 $\mu\text{J cm}^{-2}$ are masked so as to not influence the fit due to their anomalous nature (carried forward to all graphs for consistency).

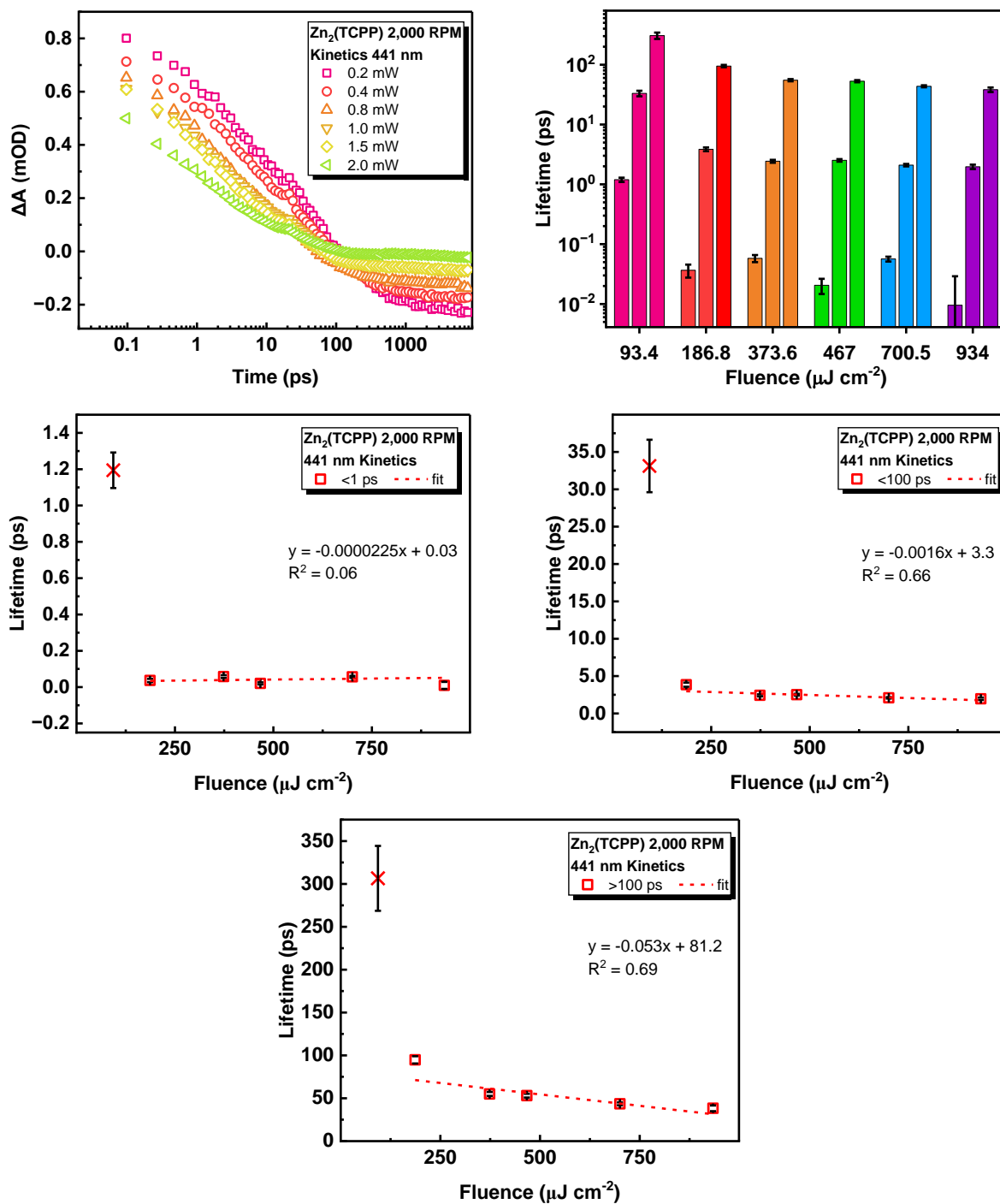
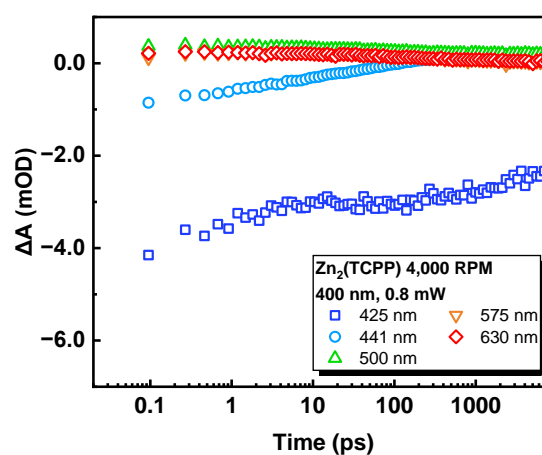
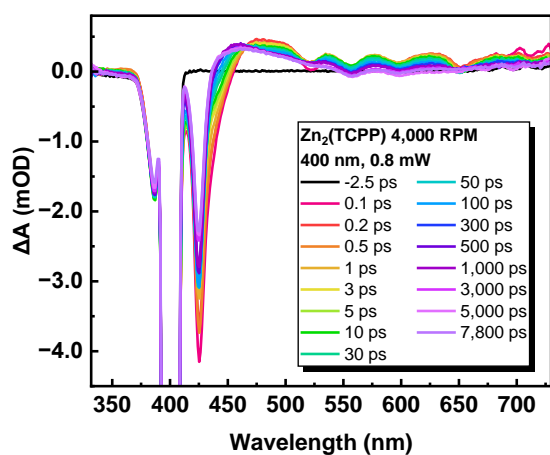
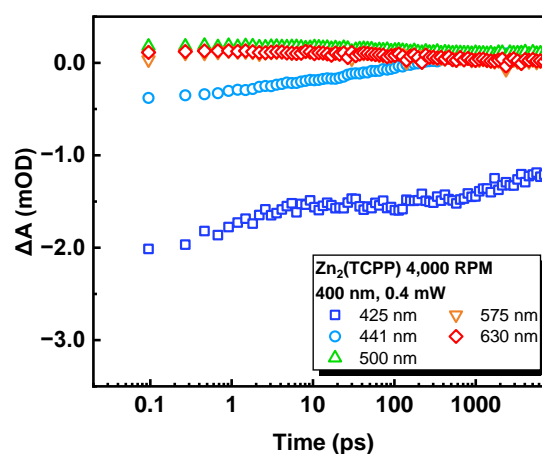
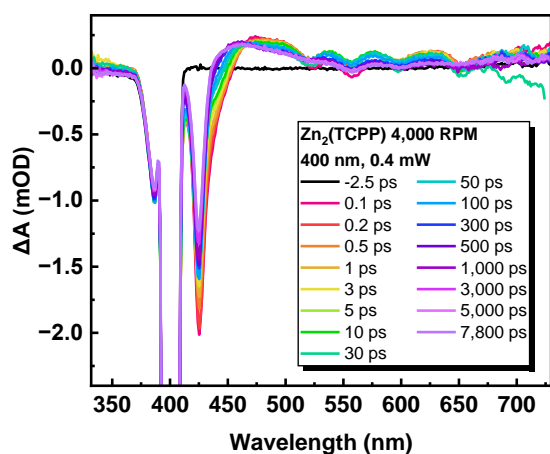
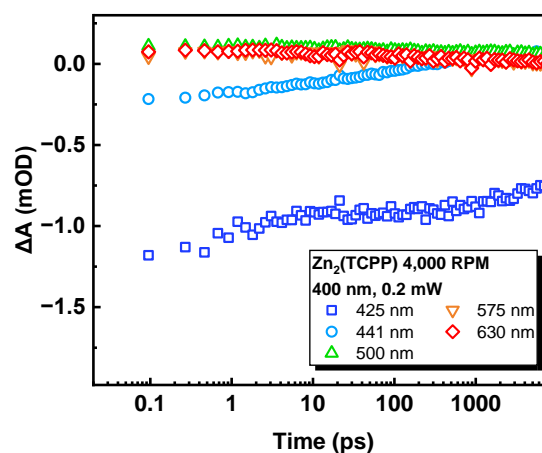
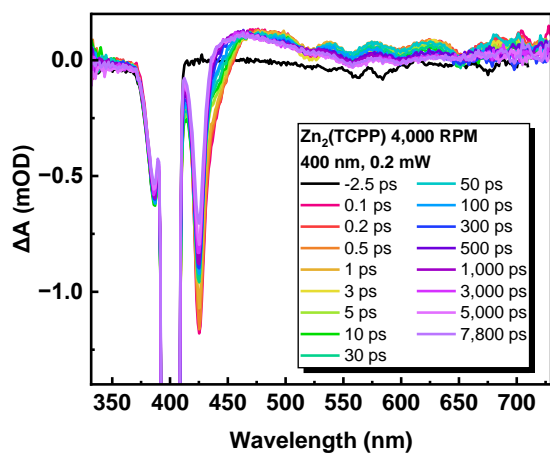


Figure S3.42 Normalised TA kinetics at 441 nm for Zn₂(TCPP) after 2,000 RPM PSC

TA Power Dependence of Zn₂(TCPP) Samples After 4,000 RPM Post-Synthetic Centrifugation

Here, the 400 nm pump power was varied between 0.2, 0.4, 0.8, 1.0, 1.5, and 2.0 mW (Day 2, see Table S3.7).



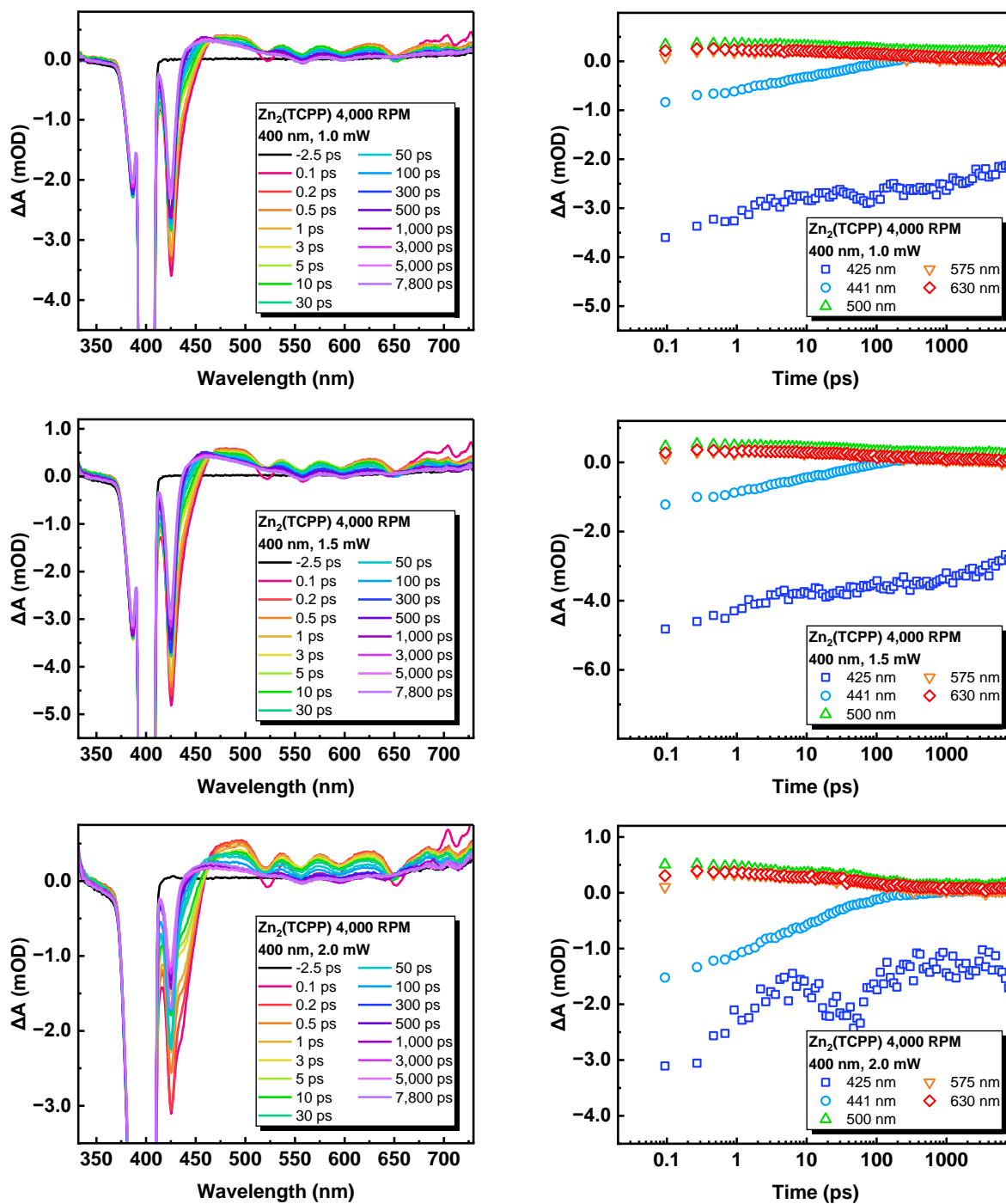


Figure S3.43 TA Spectra and kinetics at key wavelengths for $Zn_2(TCPP)$ after 4,000 RPM post-synthetic centrifugation with pump powers at 0.2, 0.4, 0.8, 1.0, 1.5, and 2.0 mW.

Power Dependence of TA Kinetics at 441 nm of Zn₂(TCPP) After 4,000 RPM Centrifugation

The kinetics of transient absorbance at 441 nm for Zn₂(TCPP) after post-synthetic centrifugation at 4,000 rpm are plotted in Figure S3.44. The 400 nm excitation beam was recorded at powers 0.2, 0.4, 0.8, 1.0, 1.5, and 2.0 mW, and are converted to fluence in the Day 2 column of Table S3.7.

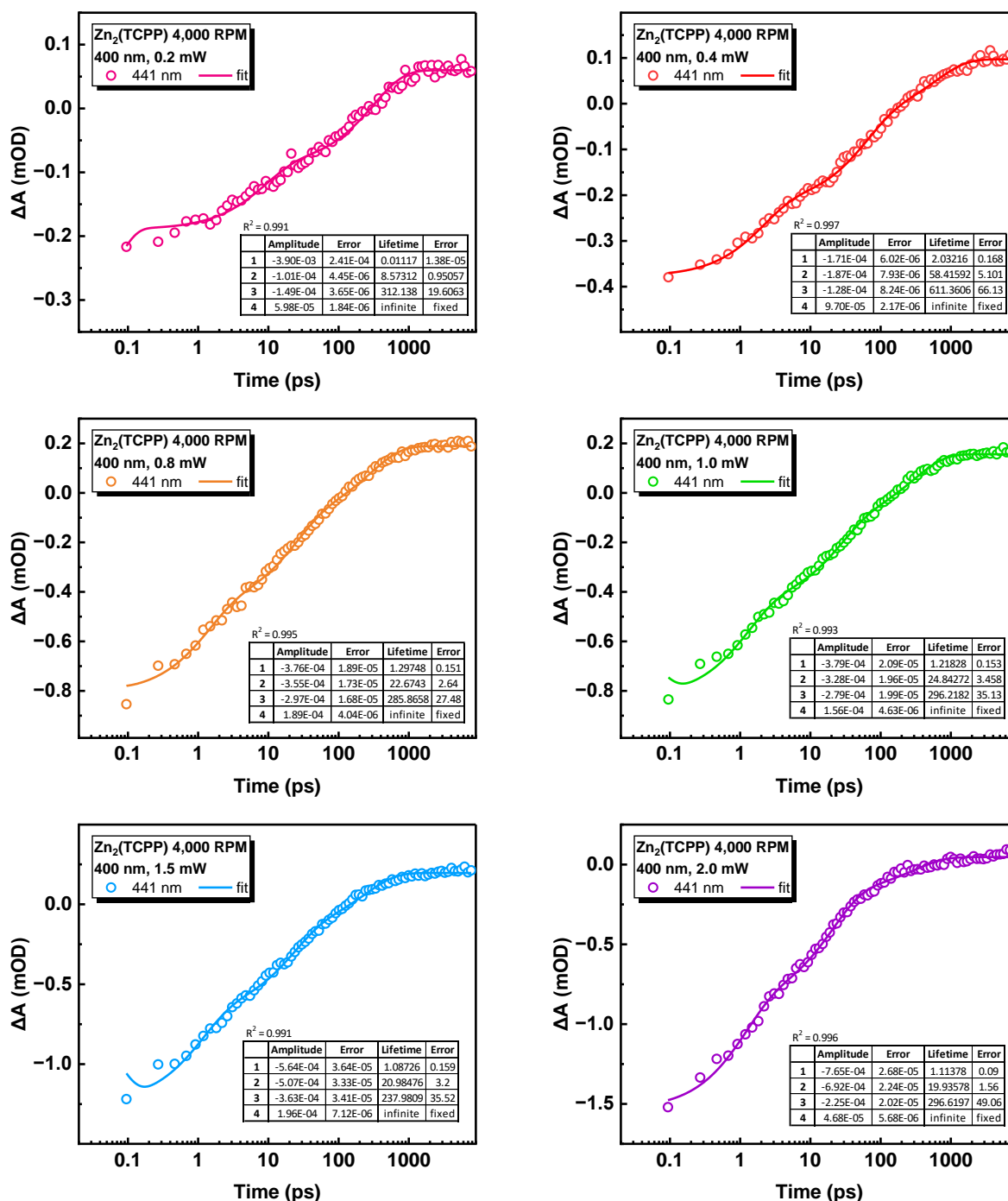


Figure S3.44 Transient absorption kinetics at 441 nm for Zn₂(TCPP) after post-synthetic centrifugation at 4,000 rpm with 400 nm excitation power of 0.2, 0.4, 0.8, 1.0, 1.5, and 2.0 mW.

The normalised TA kinetics at 441 nm for Zn₂(TCPP) after 4,000 RPM post-synthetic centrifugation are overlaid in Figure S3.45. It should be noted that the data points at 93.4 $\mu\text{J cm}^{-2}$ and 467 $\mu\text{J cm}^{-2}$ are masked so as to not influence the fit due to their anomalous nature (carried forward to all graphs for consistency).

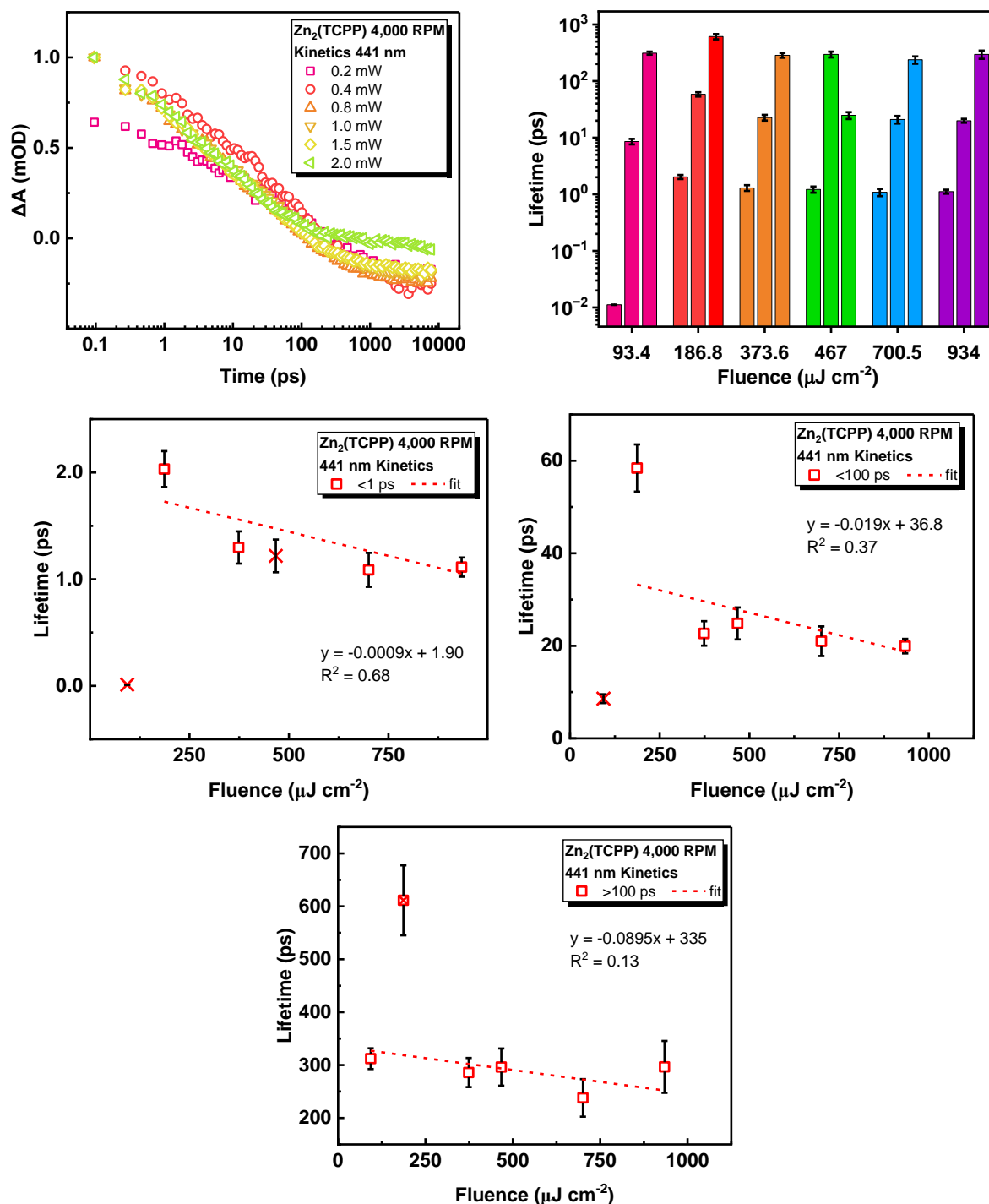
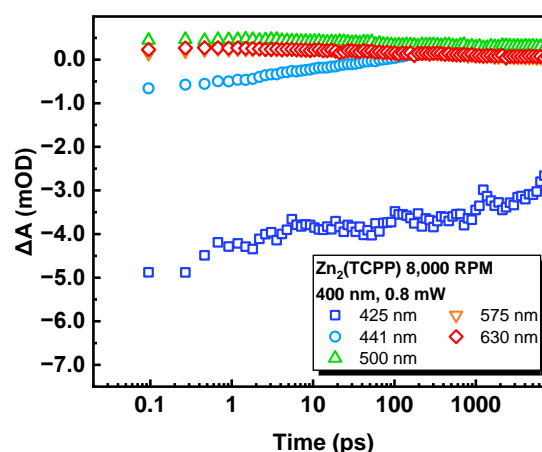
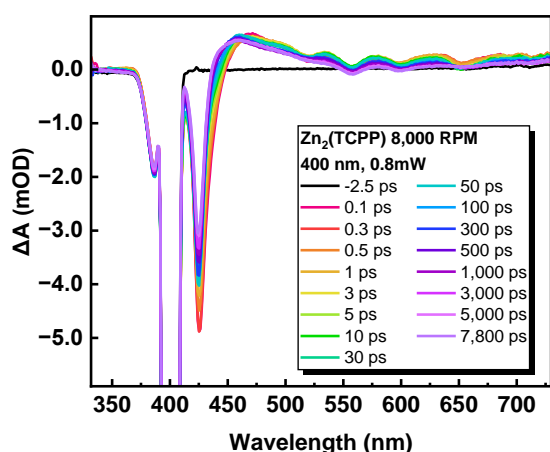
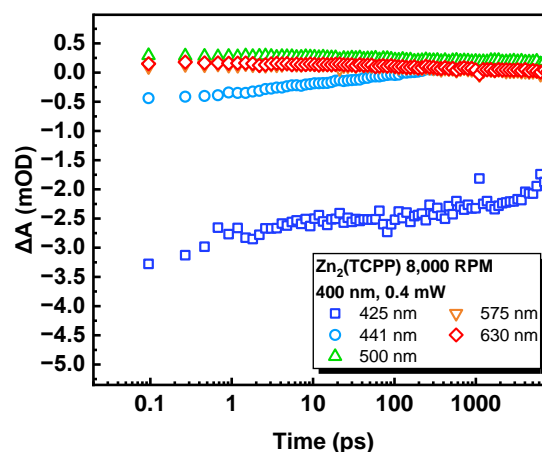
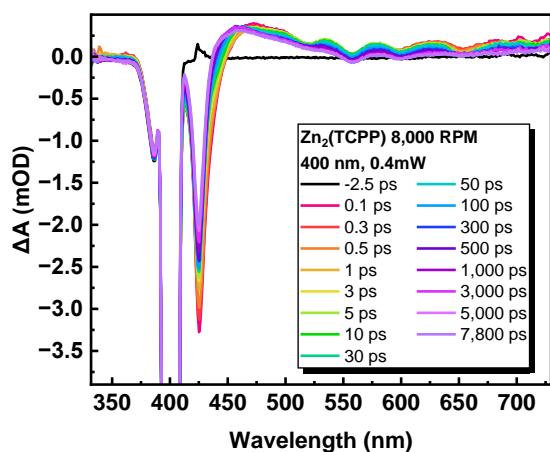
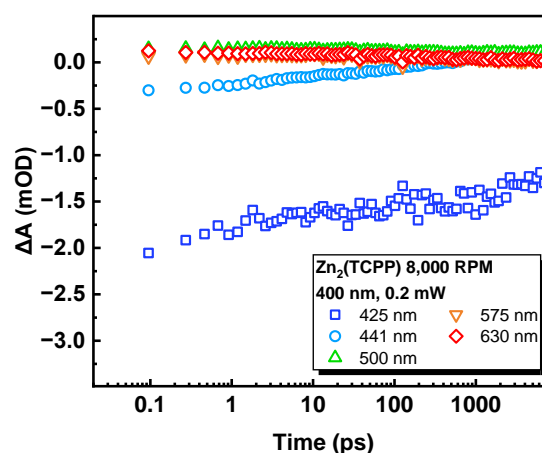
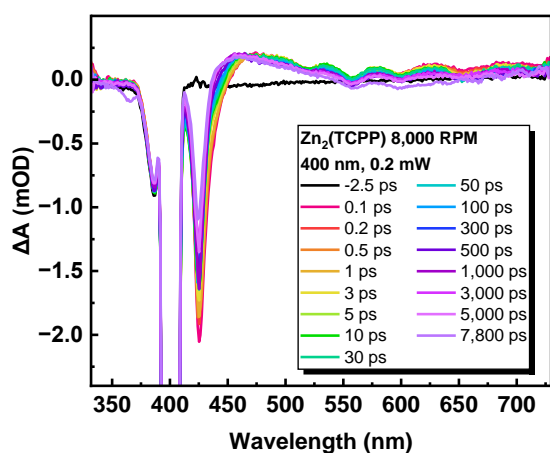


Figure S3.45 Normalised TA kinetics at 441 nm for Zn₂(TCPP) after 4,000 rpm post-synthetic centrifugation

TA Power Dependence of Zn₂(TCPP) Samples After 8,000 RPM Post-Synthetic Centrifugation

Here, the 400 nm pump power was varied between 0.2, 0.4, 0.8, 1.0, 1.5, and 2.0 mW (Day 2, see Table S3.7).



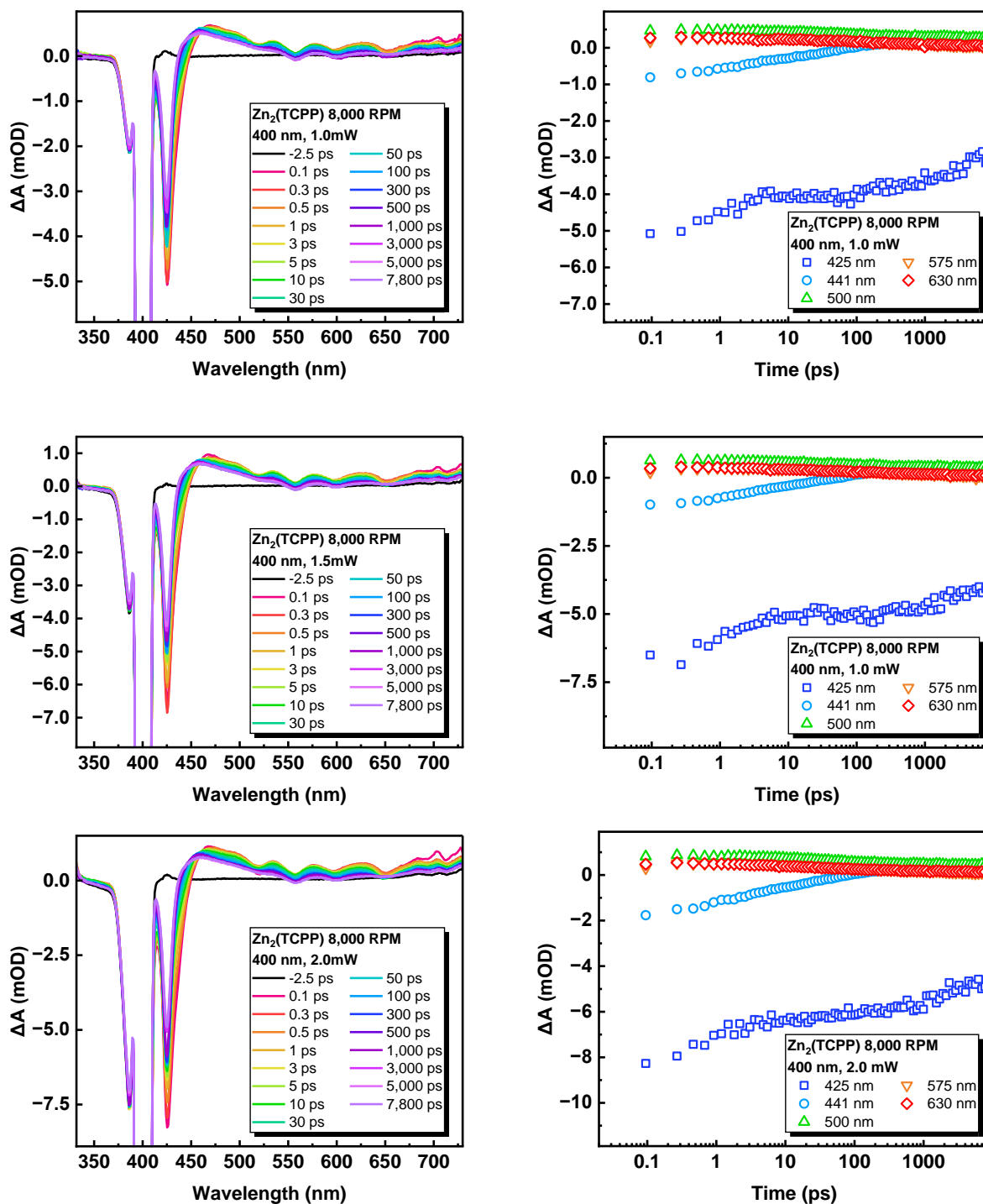


Figure S3.46 TA Spectra and kinetics at key wavelengths for $Zn_2(TCPP)$ after 8,000 RPM post-synthetic centrifugation with pump powers at 0.2, 0.4, 0.8, 1.0, 1.5, and 2.0 mW.

Power Dependence of TA Kinetics at 441 nm of Zn₂(TCPP) After 8,000 RPM Centrifugation

The kinetics of transient absorbance at 441 nm for Zn₂(TCPP) after 8,000 rpm post-synthetic centrifugation are plotted in Figure S3.47. The 400 nm excitation beam was recorded at powers 0.2, 0.4, 0.8, 1.0, 1.5, and 2.0 mW, and are converted to fluence in the Day 2 column of Table S3.7.

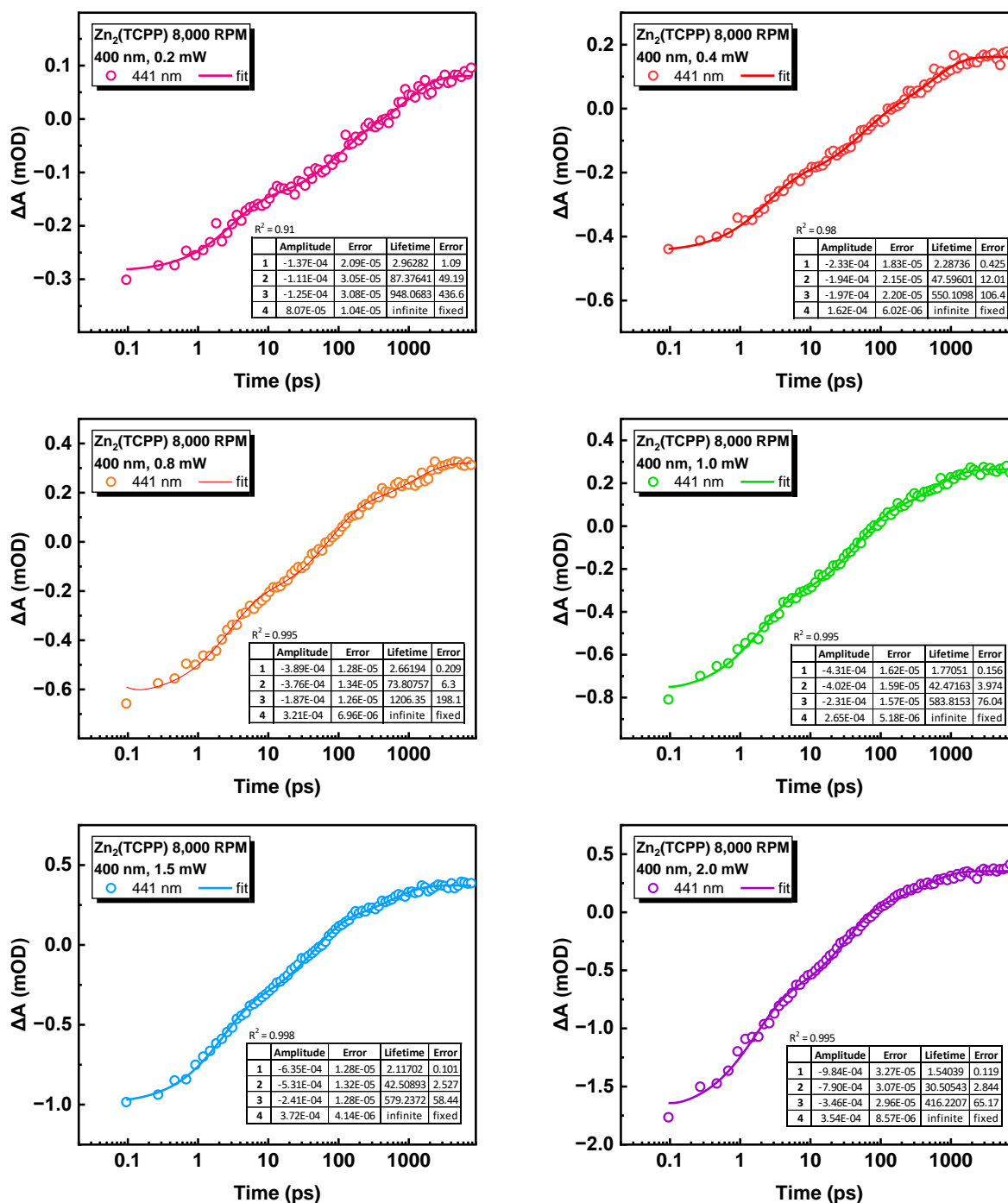


Figure S3.47 Transient absorption kinetics at 441 nm for Zn₂(TCPP) after 8,000 rpm centrifugation with 400 nm excitation power of 0.2, 0.4, 0.8, 1.0, 1.5, and 2.0 mW.

The normalised TA kinetics at 441 nm for Zn₂(TCPP) after 8,000 RPM post-synthetic centrifugation are overlaid in Figure S3.48.

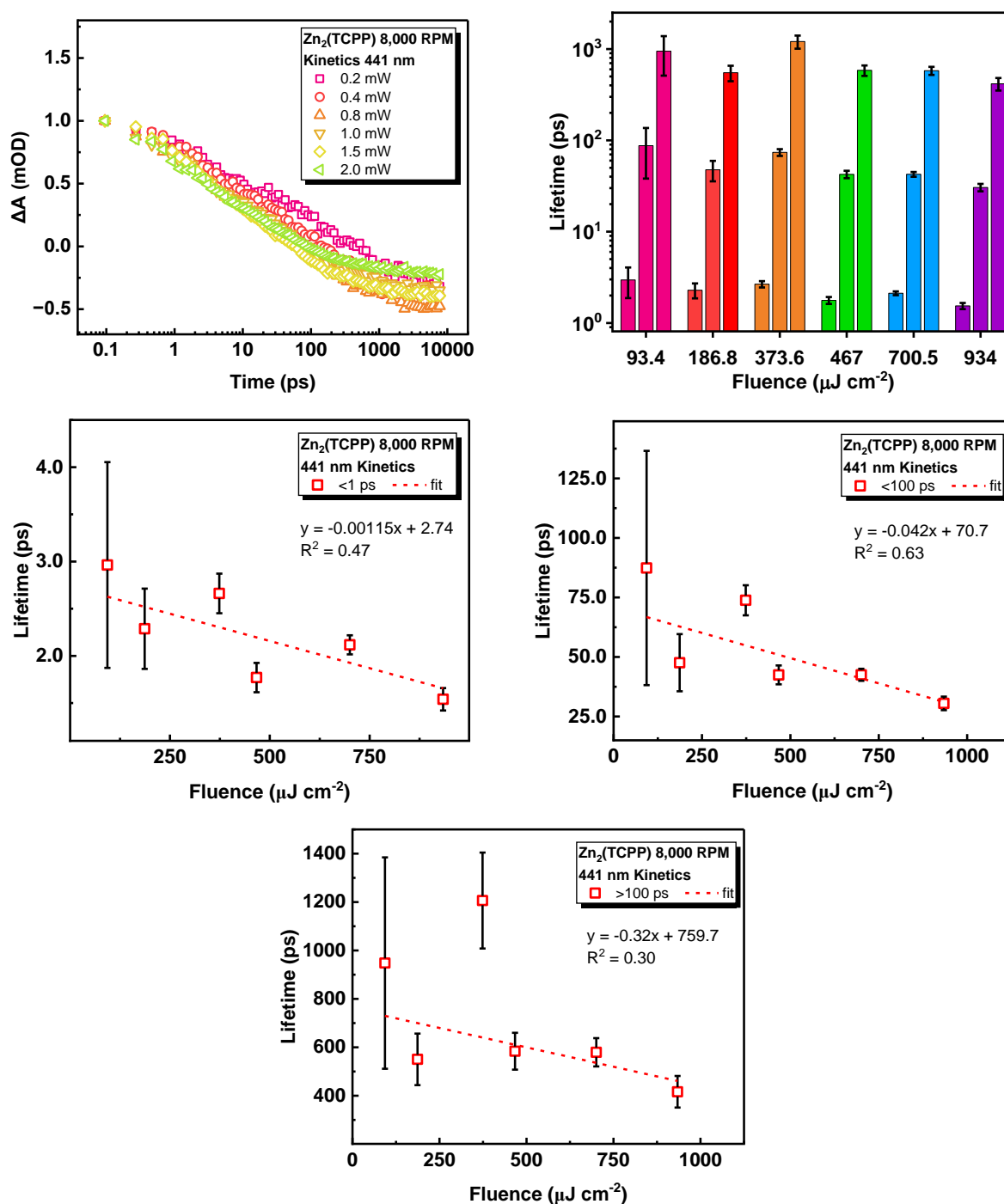


Figure S3.48 Normalised TA kinetics at 441 nm for Zn₂(TCPP) before post-synthetic centrifugation (top left), lifetimes compared by each power (top right), and the power dependence of lifetimes less than 1 ps (middle left), between 1-100 ps (middle right), and greater than 100 ps (bottom middle).

Comparing the Fluence Dependence of TA Lifetimes for Zn₂(TCPP)

The comparison of fluence dependence of TA lifetimes for Zn₂(TCPP) without post-synthetic centrifugation and with 8,000 RPM post-synthetic centrifugation. The error for the low fluence 8,000 rpm data point is due to poor signal to noise in a sample with low peak intensity at 441 nm.

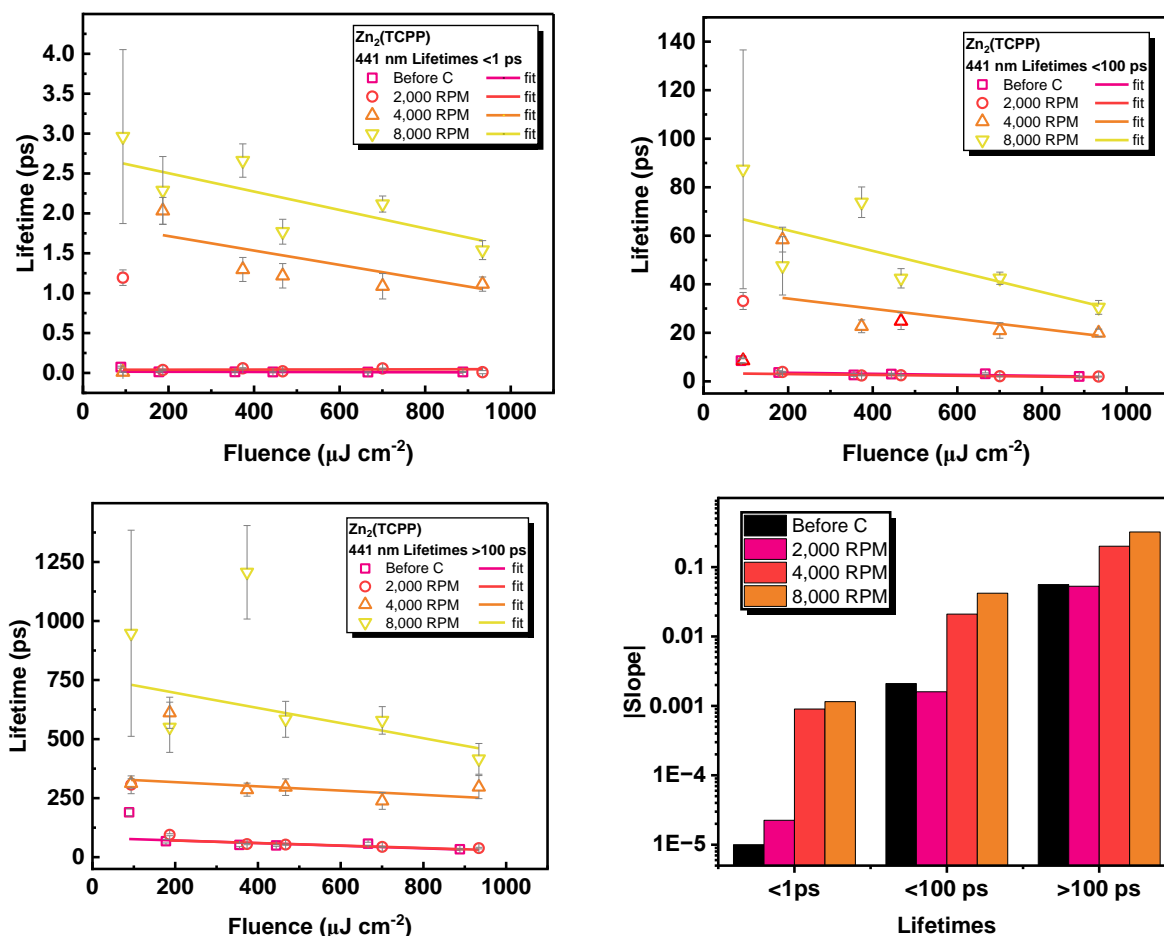


Figure S3.49 Lifetime fluence dependence graphs for Zn₂(TCPP) comparing samples before post synthetic centrifugation and after PSC at 8,000 RPM. Relationships are separated by lifetimes <1 ps (top left), <100 ps (top right), and >100 ps (bottom left). The slopes for each graph are compared in a bar chart (bottom right).

Exciton Diffusion calculations

In the case of the 2,000 rpm sample, τ is calculated to be 124.7 ps, and $\gamma_{(0)}$ to be $6.77 \times 10^{-23} \text{ m}^{-3} \text{ s}^{-1.5}$ (Figure S3.50). The value for D is calculated as $1.71 \times 10^{-10} \text{ m}^2 \text{ s}^{-1}$. Following this, the diffusion pathlength is therefore calculated as $L_D = 1.46 \times 10^{-10} \text{ m}$, or 0.146 nm.

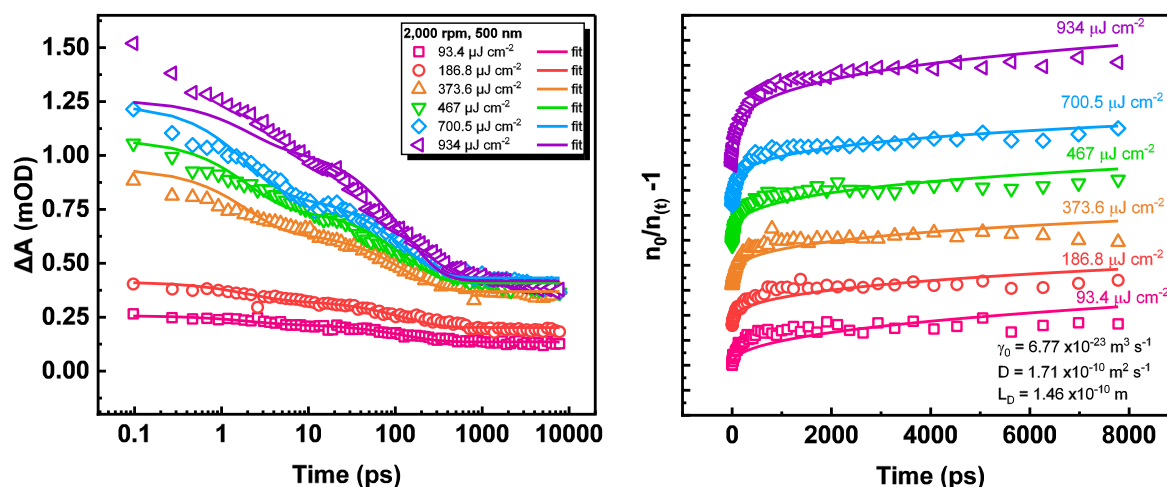


Figure S3.50 Excited state transient absorption at 500 nm for a sample of $\text{Zn}_2(\text{TCPP})$ after post-synthetic centrifugation at 2,000 rpm.

In the case of the 4,000 rpm sample, τ is calculated to be 112.8 ps, and $\gamma_{(0)}$ to be $6.66 \times 10^{-23} \text{ m}^{-3} \text{ s}^{-1.5}$ (Figure S3.51). The value for D is calculated as $1.65 \times 10^{-10} \text{ m}^2 \text{ s}^{-1}$. Following this, the diffusion pathlength is therefore calculated as $L_D = 1.37 \times 10^{-10} \text{ m}$, or 0.137 nm.

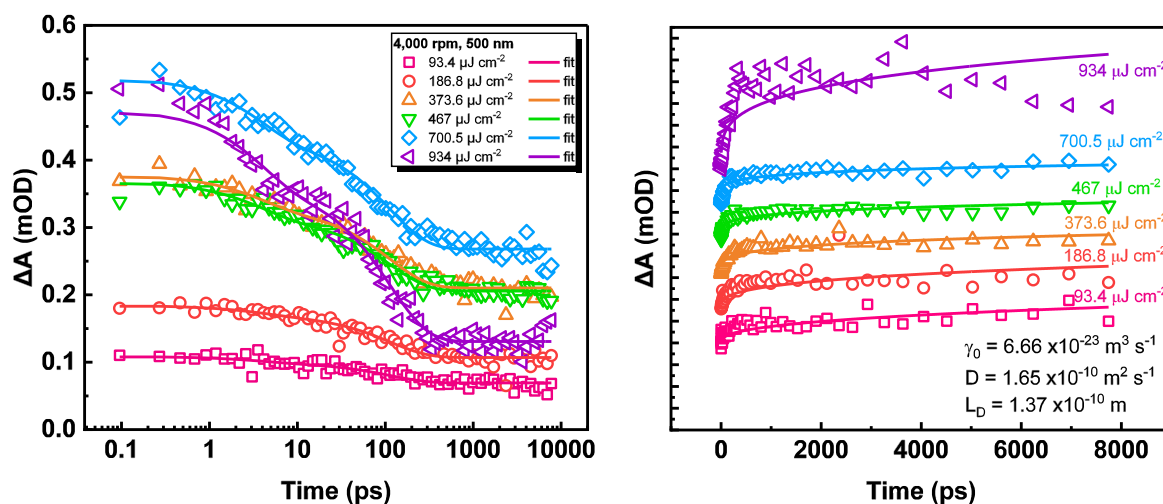


Figure S3.51 Excited state transient absorption at 500 nm for a sample of $\text{Zn}_2(\text{TCPP})$ after post-synthetic centrifugation at 4,000 rpm.

In the case of the 8,000 rpm sample, τ is calculated to be 73.8 ps, and $\gamma_{(0)}$ to be $2.99 \times 10^{-23} \text{ m}^{-3} \text{ s}^{-1.5}$ (Figure S3.52). The value for D is calculated as $3.34 \times 10^{-11} \text{ m}^2 \text{ s}^{-1}$. Following this, the diffusion pathlength is therefore calculated as $L_D = 4.96 \times 10^{-11} \text{ m}$, or 0.050 nm.

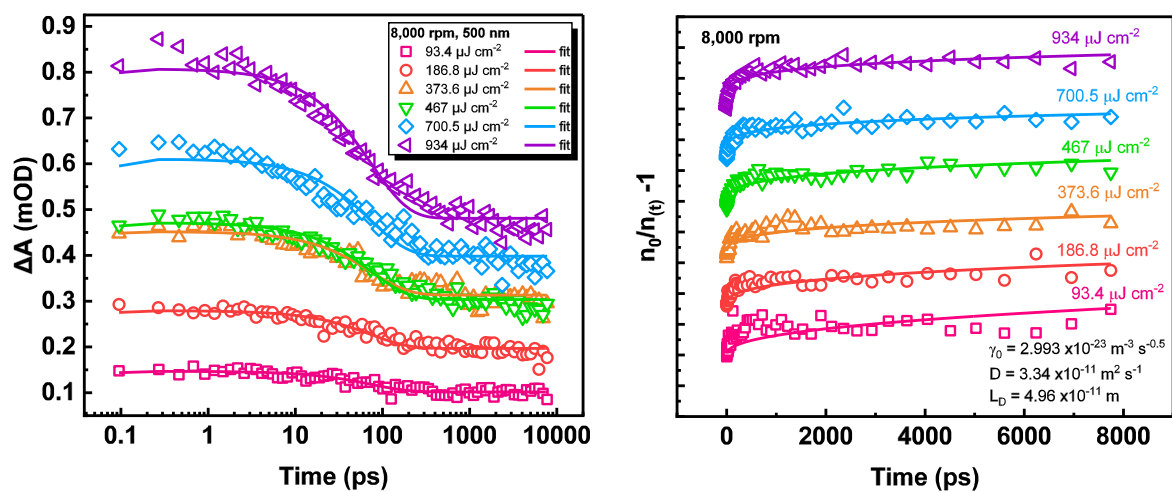


Figure S3.52 Excited state transient absorption at 500 nm for a sample of $\text{Zn}_2(\text{TCPP})$ after post-synthetic centrifugation at 8,000 rpm.

Chapter 4:

Effect of Post-Synthetic Metalation on Exciton Dynamics in Porphyrin-Based Metal Organic Framework Nanosheets

Section 4.1 Abstract

In this chapter, the effect of different metal ions on the photophysical properties of porphyrin-based metal organic nanosheets were investigated. The central cavity of $Zn_2(TCPP-H_2)$ was post-synthetically metalated with Co, Ni, Cu, Zn, and Cd before analysis by steady state and time-resolved spectroscopy techniques to understand the effect of cavity metal on excited state lifetime. The photophysical properties of metalloporphyrins are well understood in literature, and the prevalent theories are applied to understand the effect on these systems.

Steady-state and time-resolved spectroscopy techniques were used to measure the electronic dynamics within the materials, allowing insight into the photophysical processes affected by the post-synthetic metalation. Namely, the tuning of emission output, excited state lifetimes, and inhibition of exciton-exciton annihilation. Short, excited state lifetimes (60-100 ps) were introduced by metalation, with the exception of copper and cadmium, which had increased lifetimes due to emission quenching and poor spin-orbit coupling, respectively. This culminated in a power dependence study which showed metalation significantly reduced exciton annihilation compared to $Zn_2(TCPP-H_2)$, leading to generally greater intersystem crossing to triplet states in metalated samples.

Comparison of results with theoretical literature indicated a distortion effect on the porphyrin moiety by metal insertion, with in-plane metals cobalt and nickel identified as the most potent modifiers for reducing the fluence dependence of the material.

Section 4.2 Introduction

Porphyrins can accept metal ions into their central cavity via coordination to the lone pairs on pyrrole nitrogen atoms, forming metalloporphyrins.¹ This capacity is reflected in the vast number of essential roles played by metalloporphyrins in nature, notably magnesium chlorin in chlorophyll, iron protoporphyrin in haemoglobin, myoglobin, cytochromes, and a variety of enzymes important for biological function.¹ Porphyrin-based metal organic framework nanosheets (MONs) with the chemical formula $Zn_2(TCPP)(DMF)_2$, where TCPP is the ligand meso-tetra(4-carboxyphenyl)porphine, are used for many applications ranging from therapeutic treatments, electro- and photo- catalysis, biological sensing, energy storage, separation, and electronics.¹⁻³ The possibility of metalation at the porphyrin centre, therefore, allowing the synthesis of bimetallic MONs, presents an opportunity for tuning the chemical structure. Understanding the effects of metalloporphyrin-based $Zn_2(TCPP-M)$ MONs, where M is an inserted metal, compared to $Zn_2(TCPP-H_2)$, with a vacant porphyrin cavity, is important for predicting the effects on photophysical properties such as absorption, emission, and excited state dynamics.

The high temperature synthesis of $Zn_2(TCPP)$ MONs often results in metalation of the central cavity of the TCPP porphyrin. In the recent paper by Ashworth et al., a low temperature synthesis was reported which allowed for the scaled-up production of $Zn_2(TCPP-H_2)$, where the central cavity is vacant. The authors also demonstrated that the central cavity could be post-synthetically metalated by a range of different metals including Co, Ni, Cu, Zn and Cd (Figure 4.1).⁴ The nanomaterials $Zn_2(TCPP-H_2)$ and $Zn_2(TCPP-Zn)$ were successfully used to enhance organic solar cell efficiency, though limited characterisation of the effect of the different metal ions on the photophysical properties of the nanosheets was reported. This presents an opportunity not only to rationalise the differences observed between metalloporphyrin-based $Zn_2(TCPP-M)$ and unmetalated $Zn_2(TCPP-H_2)$, but also to investigate the effects of different metals at the centre. Thus, this work aims to understand the photophysical tuning of these materials by post-synthetic metalation and provide rationale for improving their use in optical applications.⁵

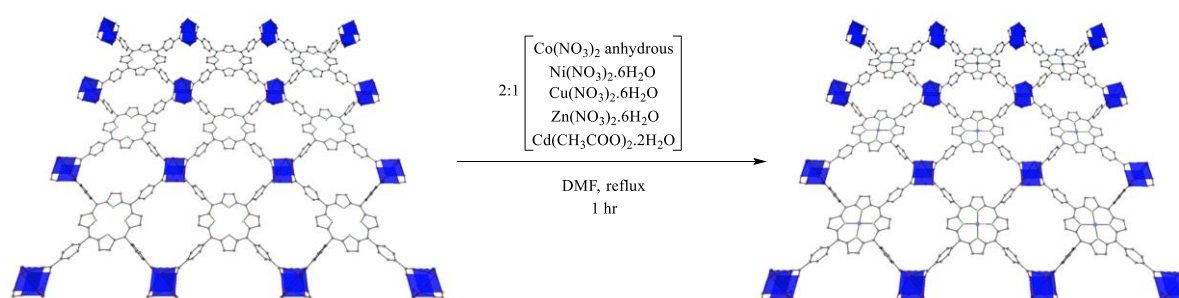


Figure 4.1 Scheme for the post-synthetic metalation (PSM) of $Zn_2(TCPP)$.

The absorption spectra for porphyrins are dominated by an allowed $\pi-\pi^*$ electronic transition S_0-S_2 , resulting in an intense peak around 400 nm known as the Soret, or B-band, absorption (Figure 4.2). The transition S_0-S_1 occurs via absorption in-plane across the porphyrin and is present in diprotic porphyrins (e.g., $Zn_2(TCPP-H_2)$) as four separate weak intensity absorptions 500-650 nm which represent pseudoparity-forbidden transitions.⁶ The multiplicity of these “Q-bands” is due to the asymmetry when two protons are present in the porphyrin centre, creating two lines of symmetry x and y, each split vibrationally to create $Q_x(0,0)$, $Q_x(1,0)$, $Q_y(0,0)$, and $Q_y(1,0)$, labelled in parenthesis by the vibronic position in the upper and lower electronic states of the transition, respectively (Figure 4.2).⁷ Since the spectroscopic absorption is directly related to symmetry, metalation at the porphyrin centre characteristically reduces the number of Q-bands from four to two as the central protons are displaced.^{4,5,7-9}

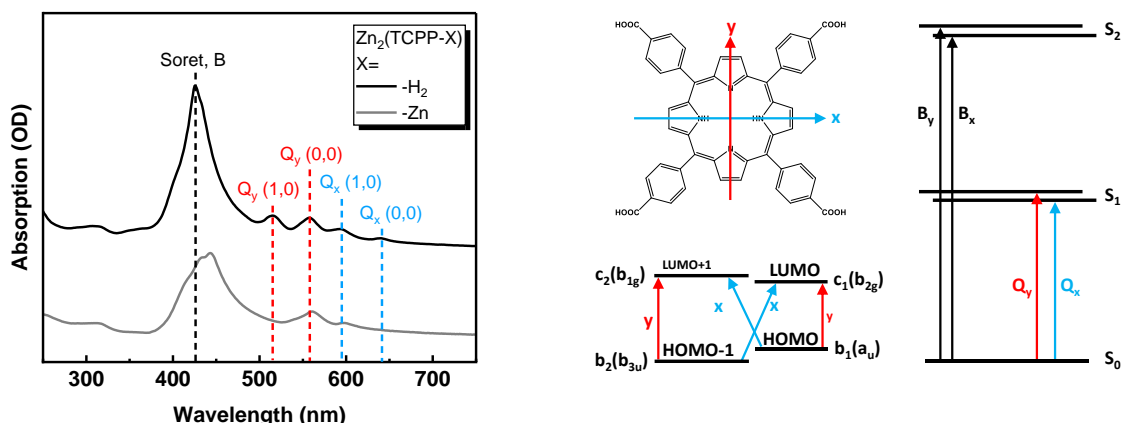


Figure 4.2 Absorption spectra of $Zn_2(TCPP-X)$, where $X = H_2$ or Zn (left), and symmetry rationale behind the four Q-band absorptions in porphyrins reproduced from Valicsek et al. (right).^{6,8,9}

Deprotonation of the central pyrrolic nitrogen extends delocalisation of the lone electron pairs and results in a redshift of Soret absorption, but the effects on absorption spectra are heavily dependent on the metal ion used.¹ Specifically, a distortion of planarity experienced by a metalloporphyrin is heavily dependent on metal ion size. Where metal ions have a radius >75 - 90 pm, or does not prefer a square-planar configuration, dome deformation can take place (e.g., cadmium). This involves the metal centre sitting out-of-plane to the porphyrin, where the metal orbitals can stabilise the porphyrin lowest unoccupied molecular π^* orbitals (LUMOs), thus causing a redshift to lower energy absorption (Figure 4.3).^{1,10}

Alternatively, metal ions with small ionic radius (e.g., top row transition metals) will form too short metal-nitrogen bonds ($\ll 2$ Å), resulting in the contraction of porphyrin cavity and ruffled distortion with the metal centre in-plane. The effect of this deformation may be enhanced in phenyl substituted porphyrins, such as TCPP, when the twisting of substituent bonds brings phenyl groups from perpendicular to closer to the porphyrin plane and further enhancing delocalisation. Consequently, the stabilisation of the HOMO by this blue shifts the Soret absorption of in-plane metalloporphyrins.^{1,10}

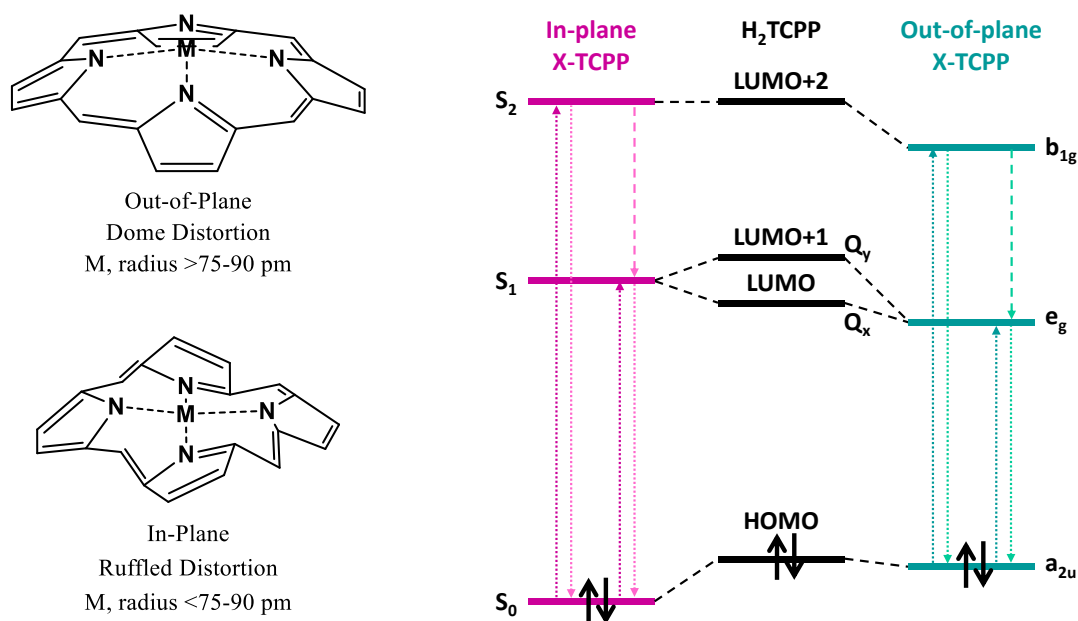


Figure 4.3 Distortion types for metalloporphyrins with central metal ions, M , of different sizes (left) with simplified energy level diagram describing the effects of central porphyrin species (X) reproduced from the paper by Valicsek et al. (right).¹

Liao et al. show computationally how metallic d orbitals interact with the S_2 LUMO in metalloporphyrins, where a $d_{x^2-y^2}$ orbital mixing with a b_{1g} MO trends down in energy as the central metal ion is varied across the series Fe-Zn.¹⁰ Valicsek et al. categorise metalloporphyrins by central ion position and lability of the metal-porphyrin complex, drawing a general correlation between large, labile, out-of-plane metals, and smaller, less labile, in-plane metals.¹ The metalloporphyrin lability series is thus reported as $Cd^{2+} > Mg^{2+} > Mn^{2+} > Fe^{2+} > Zn^{2+} \gg Co^{2+} > Cu^{2+} > Ni^{2+}$, with Cd defined as an out-of-plane metalloporphyrin, Cu and Ni as in-plane metalloporphyrins, and Zn as a borderline case. The preference of Cu and Ni for square planar configurations are highlighted as reasons for their in-plane nature.^{1,10}

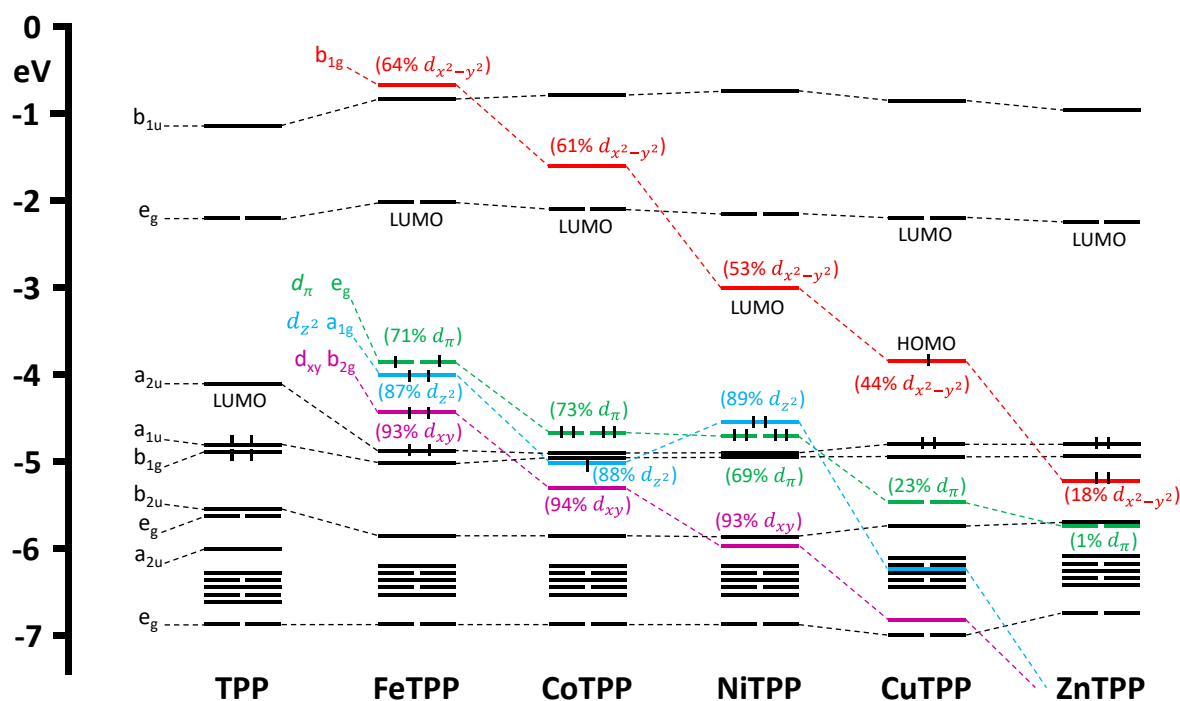


Figure 4.4 Calculated electronic orbitals of metalloporphyrins reproduced from the paper by Liao et al.¹⁰

This work aims to apply these principles to understanding the photophysical properties of $Zn_2(TCPP)$, where the nanosheets have been post-synthetically metalated to identify exciton dynamics and rationalise the changes from unmodified material. This will involve the synthesis of $Zn_2(TCPP-X)$, where $X = H_2, Co, Ni, Cu, Zn,$ or Cd , and subsequent steady-state and time resolved spectroscopic analysis to identify changes in emission, excited state lifetime, and other dynamics such as amount of exciton-exciton emission. This work will contribute to the understanding of how the existing understanding of metalloporphyrin photophysics translates to metal organic nanomaterials, applying the two theories of metal-ligand electronic hybridisation and physical porphyrin deformation to the observed changes in photophysical properties and rationalise the selection of metal ions for tuning $Zn_2(TCPP)$ MONs.

Section 4.3 Results and Discussion

$Zn_2(TCPP)(DMF)_2$ MONs were synthesised by the low temperature synthesis described in chapter 3 which were characterised to have a vacant central porphyrin cavity. Suspensions of these MONs were separately metalated by reflux in a DMF solution of two equivalents of metal salt for 1 hr, before washing three times in ethanol by centrifugation. Some sample was dried for use in characterisation and the rest left in ethanol suspension for spectroscopic analysis.

Powder x-ray diffraction (PXRD) was performed to identify any changes to the crystal structure of the MON during metalation (Figure 4.5). The patterns are compared to the simulated data for $Zn_2(TCPP)$ and $Zn_2(TCPP-Zn)$, recreated from the structural data generated by Tang et al.¹¹, and Ashworth et al.⁴, respectively. The peak at 8.9° seen in the pattern for $Zn_2(TCPP-H_2)$ is observed to be lost upon post-synthetic metalation with all metals used. This is coincident with a new peak at 7.3° seen in all the post-synthetically metalated samples. These changes are consistent with peaks in the simulated pattern and are evidence for a simultaneous rise in 020 and loss of 002 phases. According to Braggs law, this is consistent with a larger interlayer distance, d , in the post-synthetically metalated samples (calculated values for d shown in Figure 4.5). The shift to lower angle is most pronounced for the cadmium metalated sample, indicating a greater change in interlayer distance.

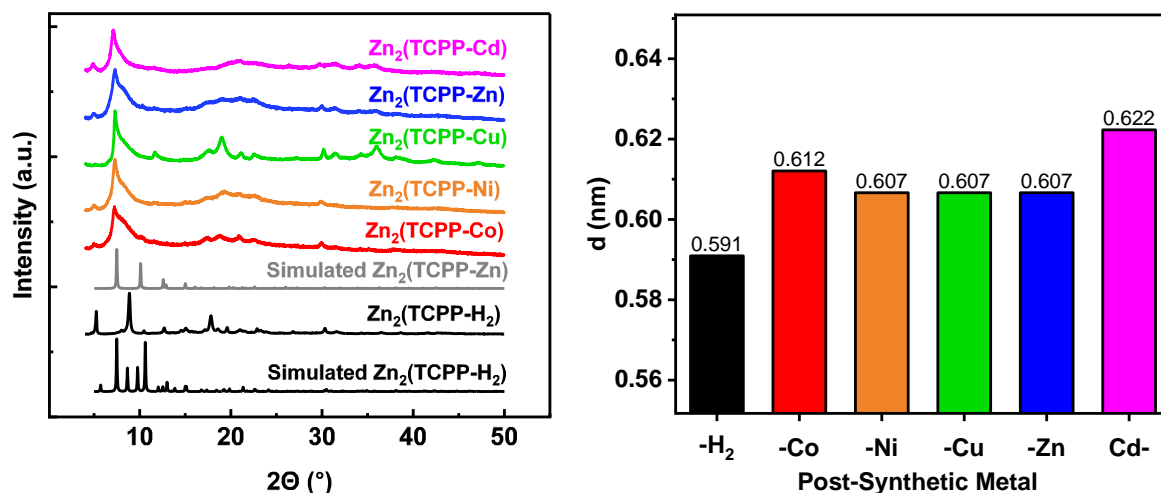


Figure 4.5 Powder X-ray diffraction patterns (left), and ICP-OES and elemental analysis results (right) for $Zn_2(TCPP-X)$ samples where X = H₂, Co, Ni, Cu, Zn, and Cd.

Inductively coupled plasma optical emission spectroscopy (ICP-OES) and elemental analysis were performed in tandem to establish the metal content of post-synthetically metalated (PSM) $Zn_2(TCPP)$ (Figure 4.6). As with the non-post-synthetically metalated version discussed in Chapter 3, the formula which gave the best match with experimental data included around six additional water molecules per formula unit. The water is present in the reaction due to the use of hydrated metal salts and may be co-ordinated to free metal-sites or present within the pores or inter-layer spaces of the MOF.

According to the new chemical formulae described in Figure 4.6, the percentage content of these metals should be Co = 4.37%, Ni = 4.47%, Cu = 4.82%, Zn = 14.87%, and Cd = 7.91%. Assuming the paddlewheel zinc accounts for 9-10% of $Zn_2(TCPP-Zn)$, the amount of zinc coordinated to the porphyrin centre should be 5-6%. Using the values for the percentage of each metal measured by ICP-OES, the proportion of metalated porphyrin can be calculated as Co (3%) = 0.68, Ni (3%) = 0.67, Cu (14%) = 2.9, Zn (17%) = 0.5, and Cd (14%) = 1.8, respectively. The values for copper and cadmium metalated samples are therefore greatly overrepresented, which may be evidence for unremoved metal salt or paddlewheel

substitution. Since the measured values for percentage zinc in all samples is similar to theoretical values for paddlewheel zinc, the overrepresentation of other metals is therefore ascribed to metal salts poorly removed by washing in ethanol.

The metalation reaction followed a protocol outlined in the work by Ashworth et al., who attributed similar over representation of metals to metalation of peripheral carboxylate groups, or substitution with zinc in the paddlewheel structure.¹² The values for copper and cadmium are too high for these to be a likely explanation, so latent metal salt remains the most likely cause. These data were collected rather later than PXRD and spectroscopic data which indicated successful metalation had occurred, and optimising the metalation by varying time, temperature, or metal ions may have delayed the project disadvantageously. For these reasons further analysis was conducted on all samples, with the caveat that metal salt contamination could affect the photodynamics.

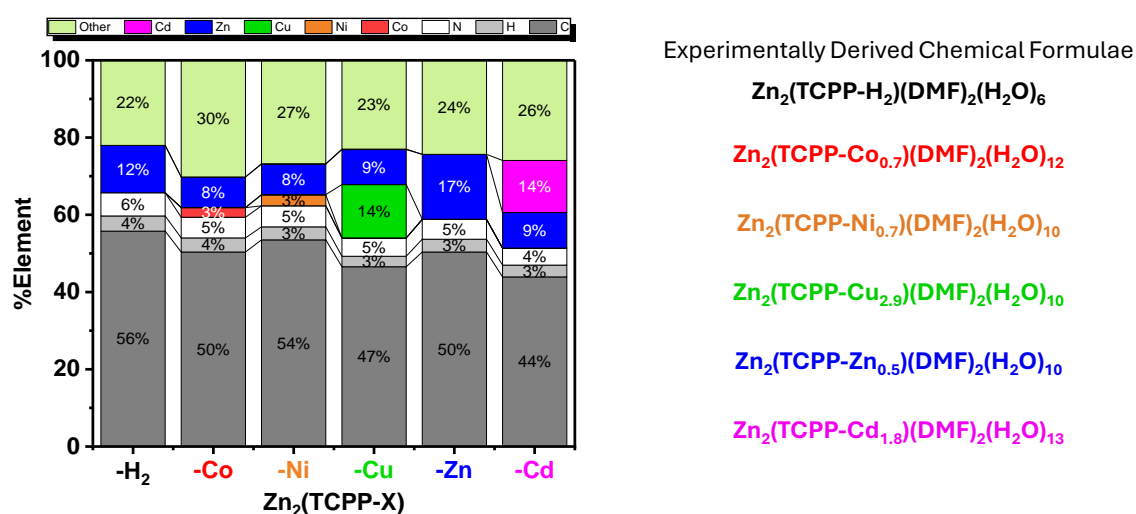


Figure 4.6 ICP-OES and elemental analysis results (left), and possible chemical formula with water contamination (right) for $Zn_2(TCPP-X)$ samples where $X = H_2, Co, Ni, Cu, Zn,$ and Cd .

The absorption spectra for all $Zn_2(TCPP-X)$ samples were recorded by UV-visible spectroscopy to identify the changes from $Zn_2(TCPP-H_2)$ upon metalation and characterise the metalation at the porphyrin centre via the shifting of absorption and reduction in the number of Q-bands. Specifically, these spectra are analysed for red shifted absorption in the case of out-of-plane metals, and blue shifted absorption in the case of in-plane metals.

As seen in Figure 4.7, all $Zn_2(TCPP-X)$ sampled showed several characteristic Soret absorptions 400-500 nm, with a common peak at 426 nm in all samples. A low intensity, broad shoulder is seen in most samples at ~ 410 nm, and a red shifted Soret absorption at 436, 444, and 436 nm observed in copper, zinc, and cadmium metalated samples respectively. These redshifted peaks are ascribed to an out-of-plane metal coordination. Contrastingly, the Co and Ni metalated samples showed much narrower Soret peaks, which may represent a removal of low energy absorption which is normally convoluted with the 425 nm peak. Indeed, the shoulder at 410 nm seems more pronounced in these samples compared to others, indicating there may be red shifted absorption here. It should be noted that according to Liao et al.¹⁰, cobalt and nickel metalloporphyrins have metal-porphyrin orbital mixing resulting in a vacant $d_{x^2-y^2}$ orbital acting as a low energy Soret LUMO, as well as a higher energy d_{π} HOMO in copper metalloporphyrins (Figure 4.4). Where the theory reported by Valicsek et al.¹ predicts a blue shift by in-plane deformation, this reduction in HOMO-LUMO gap may result in a red shifted absorption. Since no definitive shift is observed in Figure 4.7 for cobalt and nickel

metalated samples, it is possible these effects counter each other somewhat, masking the expected outcome.

It is also possible that these cobalt and nickel samples were not successfully metalated, so analysis of the Q-bands is required. It is well understood that the number of Q-bands in an absorption spectrum is reduced from four to two upon metalation at the porphyrin centre.^{1,9,10,13} As shown in Figure 4.7, most metalated samples show a reduction in outer Q-band absorption peaks at 520 and 645 nm, indicating successful metalation at the porphyrin centre.

Notably, the Co sample retains its four Q-bands, although the Q_y (1,0) and Q_x (0,0) peaks have redshifted by 10 nm independently of the Q_y (0,0) and Q_x (1,0) peaks for the same material. As reported by Chen et al.¹⁴, it is possible that cobalt can substitute the paddlewheel zinc to produce $ZnCo(TCPP)$ frameworks. This would explain how cobalt becomes present in the system without the expected loss of the number of Q-absorption bands however there is no comparative drop in the zinc content according to ICP-OES, and no obvious change in the crystal structure according to PXRD. As such, it is more likely that the presence of cobalt is due to unremoved cobalt nitrate from the post-synthetic metalation.

Another issue arises from the redshifting of the outer Q-bands in the $Zn_2(TCPP-Co)$ absorption spectrum. As cobalt is one of the least labile metals, and has small ionic radius, it would be expected from the deformation theory proposed by Valicsek et al.¹ to sit in-plane in the porphyrin centre, thus blue shifting Q-bands due to the stabilisation of the HOMO (see Figure 4.3).^{1,10}

From these data we can conclude confidently that metalation has occurred at the porphyrin centre in nickel, copper, zinc, and cadmium samples. The Soret red shifts are in-line with the theory of porphyrin deformation from planarity by out-of-plane metalloporphyrins, but the in-plane metals are better explained by electronic theory. Finally, the spectrum for the $Zn_2(TCPP-Co)$ sample shows poor evidence for metalation by cobalt.

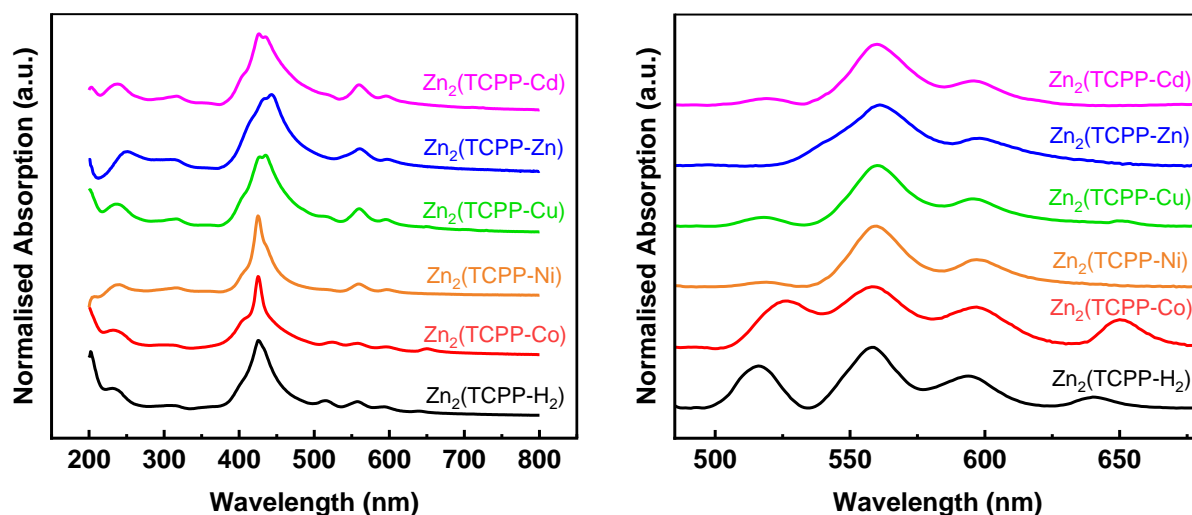


Figure 4.7 UV-visible absorption for $Zn_2(TCPP-X)$ where $X = H_2, Co, Ni, Cu, Zn,$ or Cd with full range of wavelengths tested 200 – 800 nm (left) and cropped to show Q-bands 485 – 680 nm (right).

Metalloporphyrin emission spectra separated by two processes S_2-S_0 (400-500 nm) and S_1-S_0 (550-750 nm) are well documented, with the emission from the S_1 state being the strongest due to Kasha's rule.^{1,9,10,13,15–17} Indeed, emission from the S_2 state is not observed in the linker TCPP molecule and is only measurable in the MON structure.¹⁵ The overall quenching of emission observed in metalloporphyrins compared to protonated porphyrins is attributed to spin-orbit coupling enhancing intersystem crossing (ISC) S_1-T_1 , removing excited electrons from potentially fluorescent S_1 states (ISC rate 12 ns in TPP, 2 ns in $Zn-TCPP$).^{5,7,18}

The total emission integral (Figure 4.8) for the $Zn_2(TCPP-X)$ samples increase as follows: Cu (142) < Ni (397) < Cd (445) < Co (528) < Zn (737) << H_2 (1190) integrated counts. The $Zn_2(TCPP-Cu)$ species is identified as an outlier due to the complete S_1 quenching observed. This is due to its paramagnetism (see Figure 4.4) combined with its in-plane metal ion position allowing spin-orbit coupling to enhance ISC to the point where no S_1 fluorescence is detectable.^{10,19}

Valicsek speculated that lower energy emission bands may be created by the extension of delocalisation in the S_1 excited state by the twisting of aryl substituents from perpendicular orientation relative to the porphyrin plane.¹ It should be noted, therefore, that the S_1 emission at 715 nm is quenched in the $Zn_2(TCPP-Cd)$, where the dome distortion by a large out-of-plane cadmium ion would inhibit such phenyl twisting (Figure 4.8). Similarly, the stabilising effect of out-of-plane metalation on the S_1 energy levels discussed in the introduction (Figure 4.3) explains the redshift of Q_x emission in $Zn_2(TCPP-Cd)$, which is not seen in the smaller, more in-plane metalloporphyrin samples.^{1,20}

Finally, another noteworthy observation is the increase of S_2 emission for Co, Ni, and Zn metalated samples compared to $Zn_2(TCPP-H_2)$, even whilst the S_1 emission is quenched. This is attributed to the increased rigidity of in-plane metalloporphyrins (in contrast to the out-of-plane $Zn_2(TCPP-Cd)$ sample, where the S_2 emission integral is unchanged from $Zn_2(TCPP-H_2)$ at 201).¹

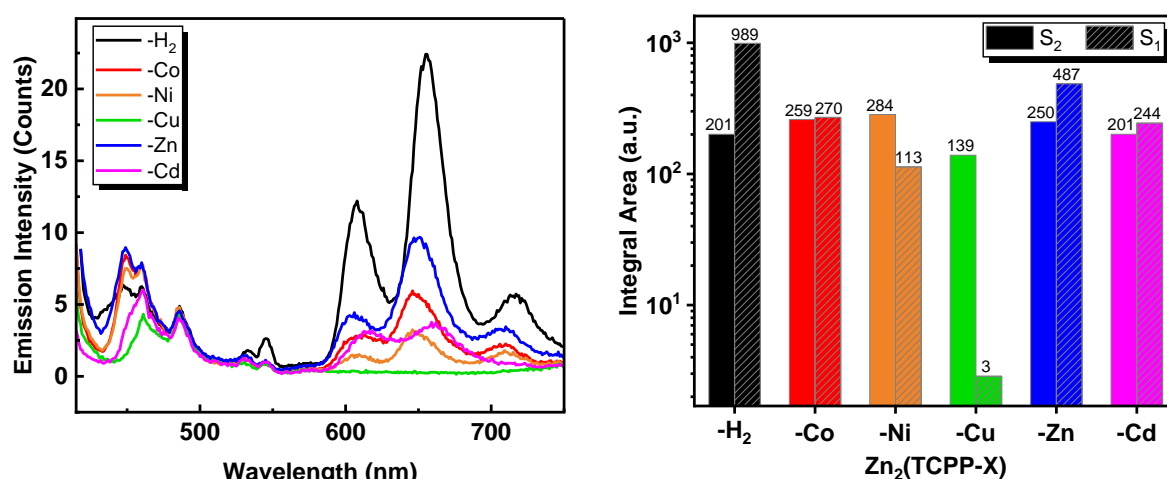


Figure 4.8 Emission spectra for $Zn_2(TCPP-X)$, where $X = H_2, Co, Ni, Cu, Zn,$ and Cd (left), with peak integrations for S_2 and S_1 regions respectively (right).

Time-correlated single photon counting (TCSPC) across the visible spectrum shows that all metalloporphyrin MONs have emission lifetimes an order of magnitude shorter than $Zn_2(TCPP-H_2)$, ascribed to enhanced intersystem crossing from the S_1 state, which would otherwise fluoresce (Figure 4.9). Given the very short lifetimes reported in literature for S_2 fluorescence in porphyrins (up to a few ps), the lifetimes calculated from TCSPC fitting are attributed to S_1 emission.¹ Even though the $Zn_2(TCPP-Co)$ sample was identified as having the least metal content (3% by ICP-OES), it has a great effect on fluorescence lifetime.

The number of unpaired d-electrons is responsible for varying amounts of spin-orbit coupling enhanced ISC (and therefore fluorescence lifetime reduction).¹⁰ This explains the alternation in observed behaviour across the trend with -Co metalloporphyrin (quenched, d^7), -Ni (less quenched, d^8), -Cu (quenched, d^9), and -Zn (unquenched, d^{10}). Generally, as seen in Figure 4.9, the experimental results fit this trend. Yet again, however, $Zn_2(TCPP-Cu)$ has an unexpectedly high lifetime, especially since the system is paramagnetic and should have the

most enhanced ISC.²¹ It should be noted that the instrument response function (IRF) of this experiment is <1 ns, so these differences may not be significant.

To conclude, metalation has a selective quenching effect on S₁ excited states regardless of metal ion inserted, however, specific differences are observed in the cases of copper and cadmium metalated Zn₂(TCPP) due to electronic and deformation effects, respectively.

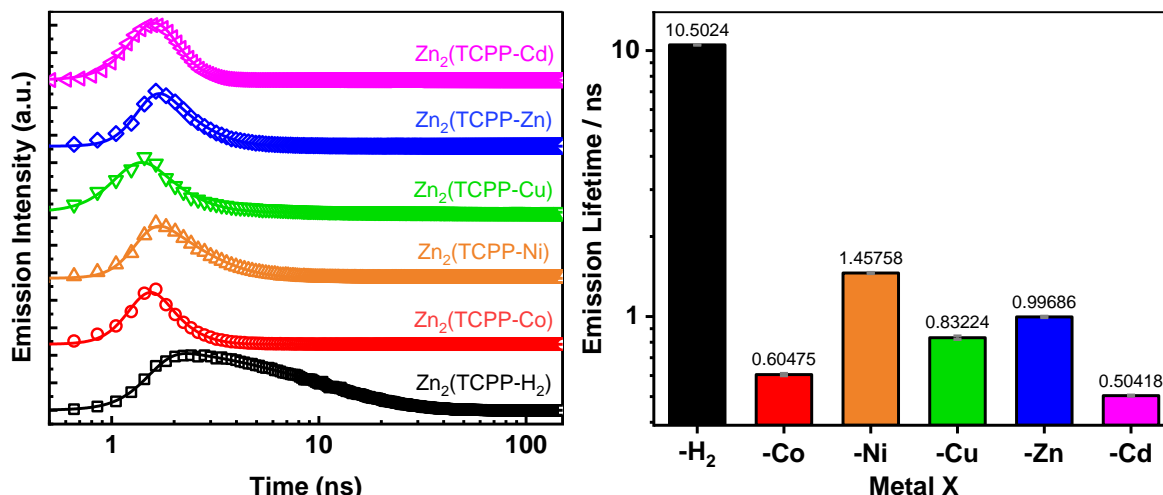


Figure 4.9 TCSPC kinetics (left) and fitted lifetimes (right) for Zn₂(TCPP-X) dispersions in ethanol where X = H₂, Co, Ni, Cu, Zn, or Cd. Excitation wavelength = 410 nm. Emission recorded without wavelength filter.

The transient absorption spectra for Zn₂(TCPP-X) samples were measured by pump-probe spectroscopy to investigate their excited state dynamics (Figure 4.10). The characteristic ground-state bleach (GSB) peaks were observed in most samples at 425-445 nm, with the negative peak at 436 nm for the Zn₂(TCPP-H₂) sample redshifted in metalloporphyrin MONs to >440 nm, as expected based on either dome or ruffled distortion. The GSB is perturbed most obviously in Zn₂(TCPP-H₂) and Zn₂(TCPP-Co) samples by an excited state absorbance ~430 nm which is not intense or long-lived enough to produce positive signal. This is ascribed to multiple Soret states responsible for GSB peaks in this region, with the short lived S₂' a higher energy S₂ state, rapidly decaying to the S₂ state before following the normal relaxation route.^{5,7} Accordingly, the GSB at 445 nm peaked at early time (~0.05 ps), whilst the GSB at 425 nm did not reach a maximum until 10 ps after excitation due to the convolution with positive signal.

Interestingly, a GSB at 425 nm which is quenched in most of the metalloporphyrin MONs is restored in the Zn₂(TCPP-Cd) sample. Given the size and poor charge density of the central Cd ion, and the subsequent out-of-plane nature of this ion, it is likely that little to no metalloporphyrin orbital mixing can take place, returning the unaffected porphyrin excited state. Similarly, distortion of the substituent phenyl groups from planarity by dome distortion could be increasing the energy of this transition.

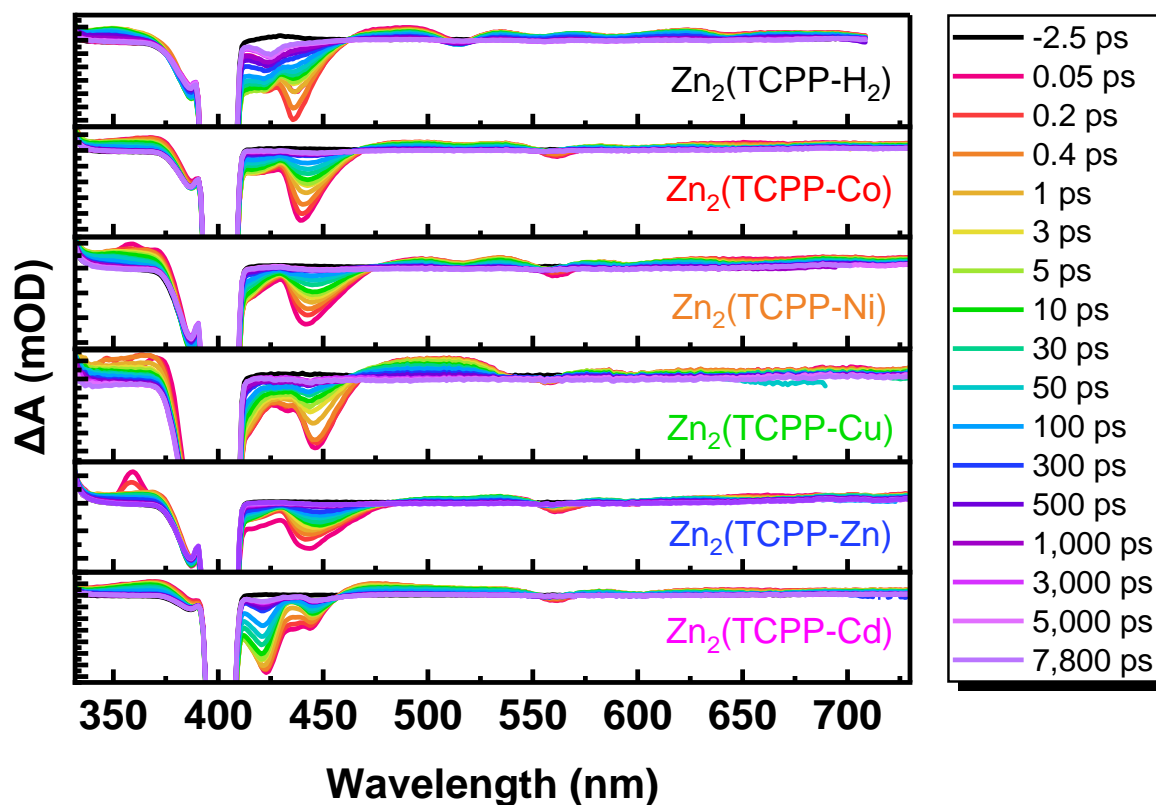


Figure 4.10 TA spectra for $Zn_2(TCPP-X)$ dispersions in ethanol where $X = H_2, Co, Ni, Cu, Zn,$ or Cd . Excitation wavelength = 400 nm, 1 mW. Selected spectra are taken at -2.5 ps delay (black), and at regular intervals 0.05– 7,900 ps (pink to purple).

As shown in Figure 4.11, fitting of the kinetics at ~ 440 nm (436 nm for $Zn_2(TCPP-H_2)$), corroborates these observations, showing similar early dynamics for all samples' lifetimes < 1 ps (lifetimes ~ 0.01 ps are likely to be due to IRF, which for this instrument is 150 fs, and the transitions $S_2'-S_2$ is likely to be ultrafast femtosecond lifetimes, so are not expected to be observed here). Samples diverge at $\sim 1-10$ ps, where all samples maintain a 60-120 ps lifetime, but $Zn_2(TCPP-H_2)$, and $Zn_2(TCPP-Cd)$ retain long lived components 742 and 1104 ps respectively, and $Zn_2(TCPP-Cu)$ has a fast 4 ps lifetime.

Despite the expected heavy atom effect, the long-lived component in $Zn_2(TCPP-Cd)$ is evidence for poor spin-orbit coupling in this system, requiring slow ISC dynamics, again, ascribed to poor orbital overlap with diffuse Cd metal orbitals sitting out of the plane of the porphyrin.

The fast 4 ps lifetime observed for the $Zn_2(TCPP-Cu)$ sample is reported in literature to be of similar order lifetimes to S_2 emission.^{5,7,22} The lack of S_1 emission observed in Figure 4.8 may indicate poor internal conversion within this system, leading to a lack of S_1 population entirely. Given the extended 142 ps lifetime seen for $Zn_2(TCPP-Cu)$ compared to ~ 90 ps observed for other systems, it is suggested that the uniquely populated HOMO of the copper metalloporphyrin (Figure 4.4) may lead to an alternative relaxation route. This fits with the unique enhanced intersystem crossing from singlet to triplet excited states in copper metalloporphyrins via a ligand-to-metal charge transfer reported by McGarry et al.²³

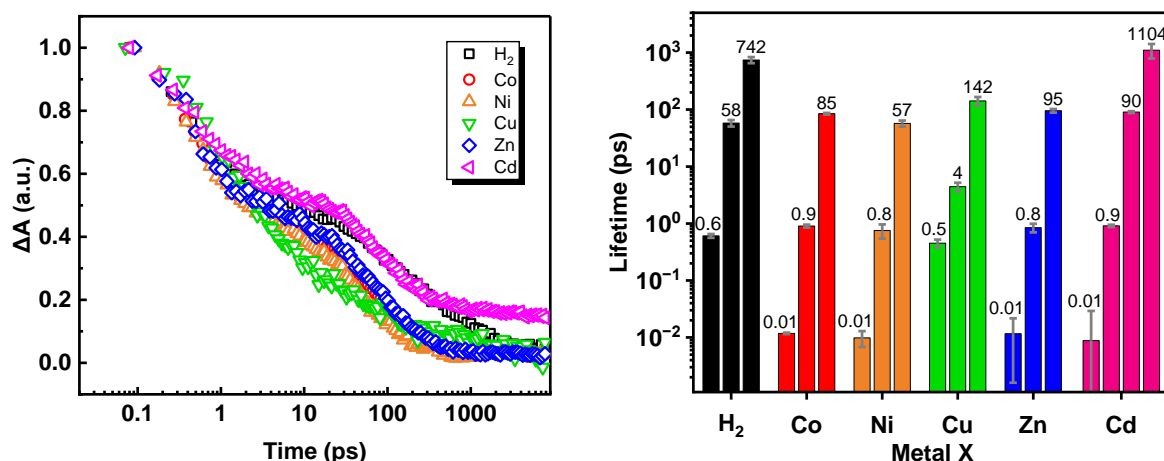


Figure 4.11 Normalised TA kinetics at ~ 440 nm for $Zn_2(TCPP-X)$ dispersions in ethanol (left) where $X = H_2, Co, Ni, Cu, Zn,$ or Cd . Excitation wavelength = 400 nm, 1 mW. Calculated excited state lifetimes from fitting of kinetics (right).

Excited state lifetime dependence on the fluence (power density) of the excitation beam indicates the presence of exciton-exciton annihilation in a sample because the excitons are generated in closer proximity to each other at higher fluences. Given that exciton-exciton annihilation is expected to occur from the S_2 excited state, a power dependence study was conducted to determine the effect of metalation on these dynamics.¹³ As shown in Figure 4.12, all samples were observed to have fitted lifetimes for TA kinetics at 440 nm which decreased with greater fluences (energy per unit area). The linear fitting of these dependence plots shows that the most exciton-exciton annihilation occurs in the $Zn_2(TCPP-H_2)$ sample, since the slope of this dependence is the highest. Analysing the trends between metalloporphyrin MON power dependence is difficult due to the compounded errors of measurement, non-linear kinetics fitting, and linear fluence dependence fitting, however, a generally increasing trend is observed $Co \rightarrow Cu/Zn \rightarrow Cd$. Since these trends don't match the emission lifetime trends reported in Figure 4.9, it is likely this is a non-emissive process as reported by Gu et al.¹³ It should also be noted that the fitting of power dependent lifetimes measured for $Zn_2(TCPP-Cu)$ has a high error due to the disparity in lifetimes observed in TA kinetics, and cannot be treated as significant.

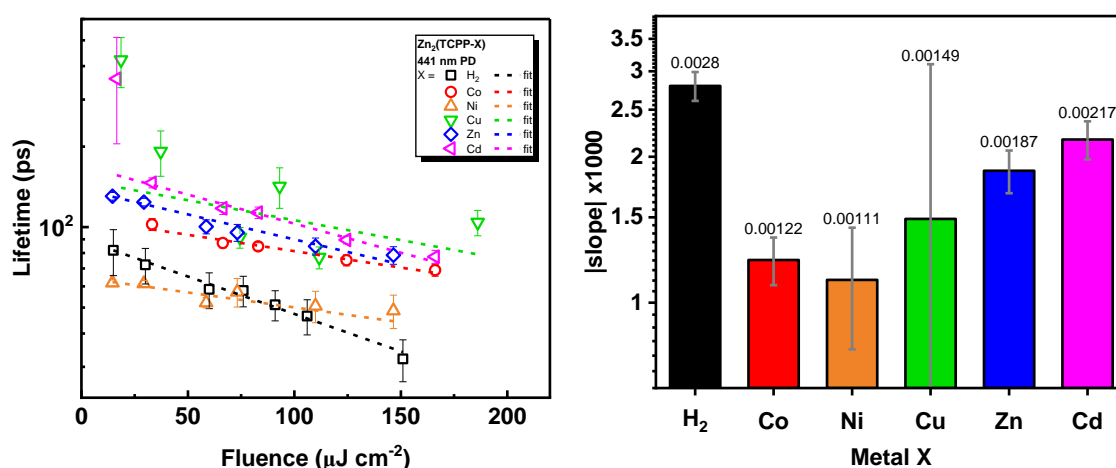


Figure 4.12 Fluence dependent lifetimes (largest component) for $Zn_2(TCPP-X)$, where $X = H_2, Co, Ni, Cu,$ or Zn , derived from TA kinetics at 441 nm (left), and magnitude of the slopes for these fluence dependencies for each PSM material (right).

Metal $d_{x^2-y^2}$ orbital mixing should be decreasing across the period, as Co and Ni are in-plane metalloporphyrins, Zn is a borderline case, and Cd is an out-of-plane metal centre. Electron-

phonon coupling is a vibrational relaxation process S_2-S_1 which competes with exciton hopping over the predominant S_2 relaxation routes.¹³ Since greater exciton hopping rates increase the likelihood of exciton interactions, it is proposed that the increase in fluence dependency across the metal centres tested can be ascribed to decreasing delocalisation across the period Co-Zn, as the ruffle-distortion caused by in-plane metal centres decreases and phenyl groups in the TCPP ligand become more perpendicular. Additionally, the out-of-plane Cd metalloporphyrin also fits this hypothesis, since delocalisation is at a minimum in the dome distorted porphyrin.¹

The effect of metalation is obvious on the photophysical properties of Zn_2 (TCPP) MONs, with variations specific to the metal used. Not only can the emission wavelengths be tuned by selective quenching of the red bands, but distinct excited state dynamics between metal choices. The excited state lifetime of Zn_2 (TCPP-X) is highly dependent on metal choice, as well as the amount of exciton annihilation. These results are therefore a useful guide for modifying Zn_2 (TCPP) MONs for desired properties. For example, it can be concluded that Zn_2 (TCPP) based materials that would benefit from long excited state lifetimes should be metalated to avoid exciton-exciton annihilation, particularly by either cobalt or cadmium. Future work should focus on establishing materials without any possibility of uninserted metal salt which might be responsible.

Section 4.4 Conclusions

The metal organic framework nanosheet (MON) $Zn_2(TCPP-H_2)$ was successfully post-synthetically metalated by a series of transition metals according to a literature protocol. Metal presence in the samples was confirmed by ICP-OES and elemental analysis, and the insertion into the porphyrin centre by spectroscopic analysis of the Q-bands. With the exception of cobalt, all of nickel, copper, zinc, and cadmium are identified as successfully inserted. Some over metalation is observed, likely due to metal salt present, but this is observed to not affect the crystal structure of the $Zn_2(TCPP)$ MONs according to PXRD.

These samples were then investigated spectroscopically for expected changes in photophysical properties based on molecular metalloporphyrins in literature. The steady-state absorption of these materials behaved similarly to discrete molecular metalloporphyrins in solution, with the Soret absorption band red-shifted, and changes in the number and intensity of Q-bands due to symmetry changes in the porphyrin. Given these similarities, two hypotheses for changes observed in molecular metalloporphyrins are applied to explain the variable characteristics observed in $Zn_2(TCPP)$ MONs when metalated by different metals: an electronic hybridisation of metal-porphyrin orbitals, and a physical deformation of the porphyrin from planarity by coordinated metals.

It was established that the emission output of $Zn_2(TCPP)$ MONs can be tuned across the UV-visible wavelengths by post-synthetic metalation (PSM) of the porphyrin cavity to quench red emission wavelengths. The emission spectra follow varied quenching mechanisms compared to the unmetalated $Zn_2(TCPP-H_2)$, with the copper metalated sample particularly experiencing complete quenching of S_1 emission. Different metals had quenching effects regardless of percentage metal content, with in-plane metals poorly quenching S_1 , and enhancing emission from S_2 excited states. Copper metalation resulted in complete quenching of S_1 emission, which is expected from molecular metalloporphyrin literature. The emission lifetime of $Zn_2(TCPP)$ MONs is significantly reduced by metalation using all the metals investigated, including cobalt. This indicates the presence of metals may be enough to inhibit S_1 emission without necessarily being inserted into the porphyrin, or else partial coordination without loss of symmetry. Emission lifetime measured by time-correlated single photon counting (TCSPC) revealed a decrease from ~ 10 ns in $Zn_2(TCPP-H_2)$ to ~ 1 ns in all metalated MONs despite some only being minimally metalated, suggesting low metal content is required for this change.

The transient absorption spectra of $Zn_2(TCPP-X)$ samples showed similar ground state bleach broadening and redshift compared to $Zn_2(TCPP-H_2)$ as the steady-state absorption analysis. This was particularly pronounced in the $Zn_2(TCPP-Cd)$ sample, which is expected to cause the most pronounced porphyrin deformation from planarity due to its size. This is reflected in the transient absorption kinetics at 440 nm, which show generally shorter lifetimes 60-100 ps for samples metalated with copper, nickel, or zinc compared to $Zn_2(TCPP-H_2)$, which has a longer-lived component of 742 ps. Copper and cadmium metalated samples are exceptions to this, with $Zn_2(TCPP-Cu)$ being fitted with significant S_2 emission component of 4 ps, and a longer 142 ps lifetime. $Zn_2(TCPP-Cd)$ has a much longer-lived component than other samples, with a fitted lifetime of 1104 ps. Most of these effects are ascribed to the metals enhancing intersystem crossing, which is particularly effective in copper due to its ability for ligand-to-metal charge transfer, and cadmium due to its large mass. The power dependence of excited state lifetimes was reduced in all post-synthetically metalated MONs compared to $Zn_2(TCPP-H_2)$, and it is clear from the extended lifetimes observed for cobalt, copper, zinc, and cadmium, that these materials remain in excited states for much longer than the other materials tested.

The overall impact of this work is that the direct comparison of metalloporphyrin-based MONs spectroscopically allowed the two theories of electronic hybridisation and porphyrin deformation to be applied. These are used to rationalise the observed outcomes and act as a predictor for other metals which might be tested. This can be applied to light harvesting materials, which might favour metals which sit out-of-plane to the porphyrin, such as cadmium, introducing long-lived excited states. In contrast, in-plane metals, such as cobalt and nickel, reduced the fluence dependence of the material, indicating their suitability for inhibiting exciton annihilation in transport materials.

There is significant remit for further research of these materials, specifically into varying the amounts of each metal needed to induce the observed changes, more efficient removal of suspected metal salts from the structure, and incorporation of differently metalated samples into optical devices e.g., solar cells, to evidence the benefits of metalation in an application.

Section 4.5 Experimental

Powder X-Ray Diffraction (PXRD)

PXRD data were collected for crystal structure determination using a Bruker D8 Advance diffractometer with a Cu K α source operating at 40 kV and 40 mA to generate $\lambda = 1.5406 \text{ \AA}$ X-rays, measurements collected using an energy dispersive LynxEye detector. Dry samples were lightly ground with a pestle and mortar and pressed onto a polished silicon flat plate using a glass slide before analysis.

Steady-State Spectroscopy

UV-visible absorption and emission spectra were recorded to determine the ground-state electronic transitions in the materials. Data were collected at room temperature, in a 1 cm quartz cell except where otherwise specified, using an Agilent Technologies Cary 50 UV-Visible spectrometer and a Cary Eclipse fluorimeter, respectively. Emission spectra were recorded in aerated solutions.

Elemental Analysis

Elemental analyses for the measurement of percentage carbon, hydrogen, and nitrogen content were obtained on an Elementar vario MICRO cube CHNS analyser equipped with a thermal conductivity detector.

Atomic Force Microscopy (AFM)

Imaging and height profiling for size determination of nanosheets was performed by AFM. Micrographs were collected using a Bruker Multimode 5 AFM operating in soft tapping mode using Bruker OTESPA-R3 cantilevers. Data were processed using Gwyddion image processing software. Samples in 15 μL EtOH were hot dropped onto freshly cleaved mica sheets heated to 90°C and allowed to dry for 5 minutes at temperature.

Inductively Coupled Plasma Optical Emission Spectroscopy

Samples were digested in 3 ml nitric acid (68%), using a Multiwave 5000 microwave digester, at 210°C for 20 minutes. The digests were made up to 15 ml using 1% nitric acid.

Analysis was performed on SpectroGreen FMX46. Samples were diluted by 3-15x, in 1% nitric acid, as required to meet the calibration range of the instrument. A 1 ppm standard was run to correct for daily fluctuations in conditions.

The percentage metal content was measured at the appropriate wavelengths for Co (228.616 nm), Ni (231.604 nm), Cu (324.754 nm), Zn (213.856 nm), and Cd (214.438 nm).

Time-Correlated Single Photon Counting (TCSPC)

The emission lifetime for different samples were determined by time-resolved fluorescence data collected on an Edinburgh instrument mini-tau fluorescence lifetime spectrometer and no wavelength selector. In TCSPC measurements, samples were kept in a 1 cm transparent quartz cuvette, and a NanoLED of 410 nm was used as an excitation source, with an instrument response function width of 1 ns. Kinetic traces from the TCSPC data were fit in OriginPro, using a sum of decaying exponential functions convoluted with a Gaussian function.

Pump-Probe Spectroscopy

Excited state lifetimes were analysed by UV-Visible pump-probe spectroscopy experiments performed in the Lord Porter Ultrafast Laser Laboratory (ULS), The University of Sheffield, using a Helios system (HE-VIS-NIR-3200) provided by Ultrafast Systems. A Ti:Sapphire regenerative amplifier (Spitfire ACE PA-40, Spectra-Physics) provides 800nm pulses (40 fs FWHM, 10 kHz, 1.2 mJ). The 400 nm pump pulses (2.5 kHz, 0.2 μJ) were generated through frequency doubling of the amplifier's fundamental. The pump was focused onto the sample

dispersed in solvent in a 1 mm quartz cell, with stirring, to a beam diameter of approximately 210-260 μm . The white light probe continuum (330 – 700nm) was generated by focusing a portion of the fundamental onto a CaF_2 crystal. The intensity of the probe light transmitted through the sample was measured using a CMOS camera, with a resolution of 1.5 nm. Prior to generation of the white light, the 800 nm pulses were passed through a computer controlled optical delay line (DDS300, Thorlabs), which provides up to 8 ns of pump-probe delay. The instrument response function is approximately 130 fs, based on the temporal duration of the coherent artifact signal from neat solvent.

Results where degradation of the sample was observable by change in UV-Visible absorption spectra were discarded. Five experimental sets were averaged to generate the data seen in this report. Pre-processing of the pump-probe data was performed using SurfaceXplorer, the software package provided by Ultrafast Systems. Kinetic traces from the pump-probe data were fit in OriginPro, using a sum of decaying exponential functions convoluted with a Gaussian function.

Materials

All solvents and reagents were purchased from commercial suppliers and used without further purification: TCPP (97%, MedChemExpress), zinc nitrate hexahydrate (98%, Acros Organics), triethylamine (High purity grade, VWR Life Science), ethanol (99.8 HPLC Grade, Fisher Chemical), dimethylformamide (99% laboratory reagent grade, Fisher Chemical), copper nitrate trihydrate (Sigma Aldrich), nickel nitrate hexahydrate (Merck Life Science Limited), cobalt nitrate (Technical grade, VWR International), and cadmium acetate dihydrate (98%, Alfa Aesar).

Synthesis of $\text{Zn}_2(\text{TCPP-H}_2)(\text{DMF})_2$

The synthesis of $\text{Zn}_2(\text{TCPP})$ is as described in Chapter 3 of this thesis, repeated below:

The reaction of 1:2 stoichiometric tetrakis(4-carboxyphenyl)porphyrin (TCPP) and zinc nitrate hexahydrate was prepared by mixing of 200 mL TCPP (500 mg, 0.63 mmol) + triethylamine (0.25 g, 2.52 mmol) in 1:1 DCM/EtOH with 200 mL $\text{Zn}(\text{NO}_3)_2 \cdot 6\text{H}_2\text{O}$ (0.38 g, 2.53 mmol) in the same solvent with stirring for 1 hr at 30 °C. Subsequently, the products were washed three times by centrifugation at 12,000 RPM for 1 hr, each time decanting the supernatant and replacing with fresh ethanol.

Post-Synthetic Metalation

2 mL dispersions of 12 mg mL^{-1} $\text{Zn}_2(\text{TCPP-H}_2)$ in EtOH were diluted to 10 mL by DMF and heated to reflux before addition of 2 molar equivalents metal salt dissolved in 10 mL DMF. Samples were heated at reflux for 2 hours before cooling and centrifugation at 10,000 RPM for 1 hr to remove solids. Supernatant was decanted and replaced with fresh ethanol and vortex mixed for 1 min before another centrifugation at the same speed for another hour. This ethanol washing step was performed three times before final dispersion in minimum ethanol and diluted to concentrations suitable for spectroscopic measurements. A portion of the resultant product was dried in air at 30°C overnight for solid sample testing by PXRD, ICP-OES, and elemental analysis.

The metal salts added were $\text{Zn}(\text{NO}_3)_2 \cdot 6\text{H}_2\text{O}$, $\text{Cu}(\text{NO}_3)_2 \cdot 3\text{H}_2\text{O}$, $\text{Ni}(\text{NO}_3)_2 \cdot 6\text{H}_2\text{O}$, $\text{Co}(\text{NO}_3)_2$ anhydrous, and $\text{Cd}(\text{CH}_3\text{COO})_2 \cdot 2\text{H}_2\text{O}$. More information on specific molar amounts can be found in the SI Table S4.1.

Section 4.6 References

1. Valicsek, Z. & Horváth, O. Application of the electronic spectra of porphyrins for analytical purposes: The effects of metal ions and structural distortions. *Microchemical Journal* **107**, 47–62 (2013).
2. Rajasree, S. S., Li, X. & Deria, P. Physical properties of porphyrin-based crystalline metal–organic frameworks. *Communications Chemistry* vol. 4 Preprint at <https://doi.org/10.1038/s42004-021-00484-4> (2021).
3. Mehrzad Sajjadinezhad, S., Boivin, L., Bouarab, K. & Harvey, P. D. Photophysical properties and photonic applications of porphyrin-based MOFs. *Coordination Chemistry Reviews* vol. 510 Preprint at <https://doi.org/10.1016/j.ccr.2024.215794> (2024).
4. Ashworth, D. J. *et al.* Scalable and sustainable manufacturing of ultrathin metal–organic framework nanosheets (MONs) for solar cell applications. *Chemical Engineering Journal* **477**, (2023).
5. Yu, H. Z., Baskin, J. S. & Zewail, A. H. Ultrafast dynamics of porphyrins in the condensed phase: II. Zinc tetraphenylporphyrin. *Journal of Physical Chemistry A* **106**, 9845–9854 (2002).
6. Hirao, K. Theoretical study of the Q and B bands of free-base, magnesium, and zinc porphyrins, and their derivatives. *Journal of Physical Chemistry A* **103**, 1894–1904 (1999).
7. Baskin, J. S., Yu, H. Z. & Zewail, A. H. Ultrafast dynamics of porphyrins in the condensed phase: I. Free base tetraphenylporphyrin. *Journal of Physical Chemistry A* **106**, 9837–9844 (2002).
8. Gouterman, M. *Spectra of Porphyrins**. *JOURNAL OF MOLECULAR SPECTROSCOPY* vol. 6 (1961).
9. Greco, J. A. *et al.* Two-photon spectroscopy of the Q-bands of meso -tetraphenylporphyrin and -chlorin framework derivatives. *Journal of Physical Chemistry C* **119**, 3711–3724 (2015).
10. Liao, M. S. & Scheiner, S. Electronic structure and bonding in metal porphyrins, metal = Fe, Co, Ni, Cu, Zn. *Journal of Chemical Physics* **117**, 205–219 (2002).
11. Zhu, Z. H. *et al.* Porphyrin-Based Two-Dimensional Layered Metal-Organic Framework with Sono-/Photocatalytic Activity for Water Decontamination. *ACS Nano* **16**, 1346–1357 (2022).
12. Borges-Martínez, M., Montenegro-Pohlhammer, N. & Cárdenas-Jirón, G. The bimetallic and the anchoring group effects on both optical and charge transport properties of hexaphyrin amethyrin. *New Journal of Chemistry* **45**, 6521–6534 (2021).
13. Gu, C. *et al.* Assembled Exciton Dynamics in Porphyrin Metal-Organic Framework Nanofilms. *Nano Lett* **21**, 1102–1107 (2021).
14. Chen, L.-J., Zhao, X. & Yan, X.-P. Porphyrinic metal-organic frameworks for biological applications. *Advanced Sensor and Energy Materials* **2**, 100045 (2023).
15. Benedict Smith. *Exciton Dynamics in Porphyrin-Based Metal Organic Framework Nanosheets Part I: Effect of Agglomeration [Unpublished]*. (2024).

16. Lopes, J. M. S. *et al.* Novel insights on the vibronic transitions in free base meso-tetrapyrrolyl porphyrin. *Spectrochim Acta A Mol Biomol Spectrosc* **209**, 274–279 (2019).
17. Stradomska, A. & Knoester, J. Shape of the Q band in the absorption spectra of porphyrin nanotubes: Vibronic coupling or exciton effects? *Journal of Chemical Physics* **133**, (2010).
18. Scoditti, S., Chiodo, F., Mazzone, G., Richeter, S. & Sicilia, E. Porphyrins and Metalloporphyrins Combined with N-heterocyclic Carbene (NHC) Gold(I) Complexes for Photodynamic Therapy Application. What Is the Weight of the Heavy Atom Effect? *Molecules* **27**, (2022).
19. Szintay, G. & Horváth, A. *Five-Coordinate Complex Formation and Luminescence Quenching Study of Copper(II) Porphyrins*. *Inorganica Chimica Acta* vol. 324 www.elsevier.com/locate/ica (2001).
20. Mchiri, C. *et al.* Insights into the new cadmium(II) metalloporphyrin Synthesis, X-ray crystal structure, Hirshfeld surface analysis, photophysical and cyclic voltammetry characterization of the (morpholine)(meso-tetra(para-chlorophenyl)porphyrinato)cadmium(II) Insights into the New Cadmium(II) Metalloporphyrin: Synthesis, X-ray Crystal Structure, Hirshfeld surface analysis, Photophysical and Cyclic voltammetry Characterization of the (Morpholine){(meso-tetra(para-chlorophenyl)porphyrinato)cadmium(II)}. *Polyhedron* **171**, 10–19 (2019).
21. Skoog, D. A., Holler, F. J. & Crouch, S. R. *Principles of Instrumental Analysis*.
22. Haber, L. H. *et al.* Efficient photoinduced energy transfer in porphyrin-based nanomaterials. *Journal of Physical Chemistry C* **124**, 24533–24541 (2020).
23. McGarry, R. J., Varvarezos, L., Pryce, M. T. & Long, C. Excited-State Dynamics Leading Either to Triplet Formation or Coordinative Expansion following Photolysis of Cu(II)-Porphyrins: A DFT, TD-DFT, Luminescence and Femtosecond Time-Resolved Absorbance Study. *Molecules* **28**, (2023).

Section 4.7 Chapter 4 Supporting Information

For reference, the Mw of materials is recorded here as:

- TCPP = 792.77 g mol⁻¹
- Zn₂(TCPP-H₂)(DMF)₂ = 1063.71 g mol⁻¹
- TEA = 101.19 g mol⁻¹

Post-Synthetic Metalation

Table S4.1 Calculated amounts of metal salts required for reflux.

Metal Salt	M _w / g mol ⁻¹	Moles / mmol	Mass / mg
Zn(NO ₃) ₂ ·6H ₂ O	297.46	0.05	13.4
Cu(NO ₃) ₂ ·3H ₂ O	241.60	0.05	12.1
Ni(NO ₃) ₂ ·6H ₂ O	290.79	0.05	14.5
Co(NO ₃) ₂	291.03	0.05	14.6
Cd(CH ₃ COO) ₂ ·2H ₂ O	266.54	0.05	13.3

Powder X-ray diffraction

Values for the interlayer distance *d* were calculated from the 002 and 020 peak positions in the PXRD of Zn₂(TCPP-X) using Bragg's law, with the assumption that *n* = 1.

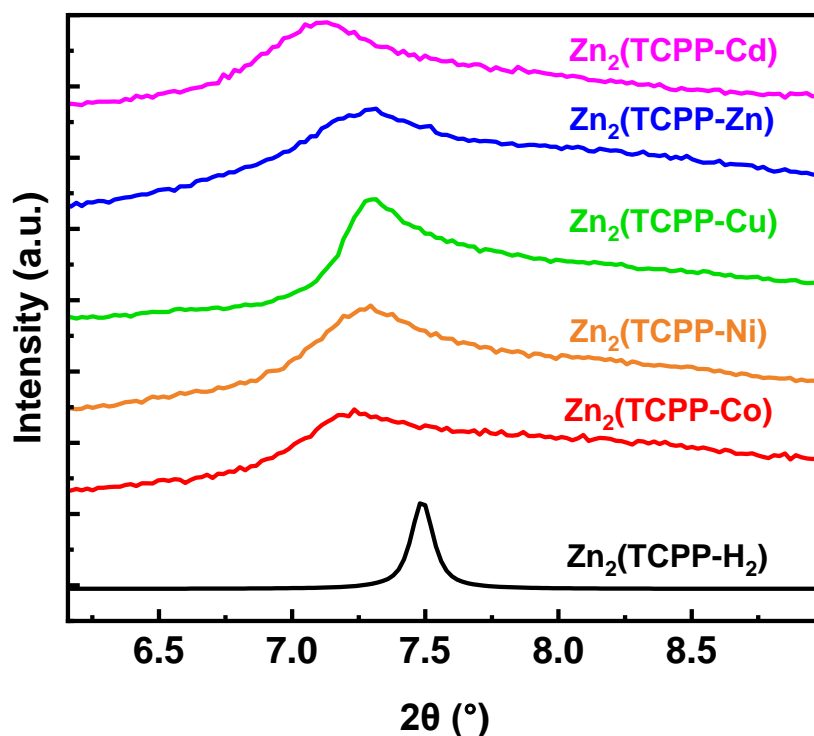
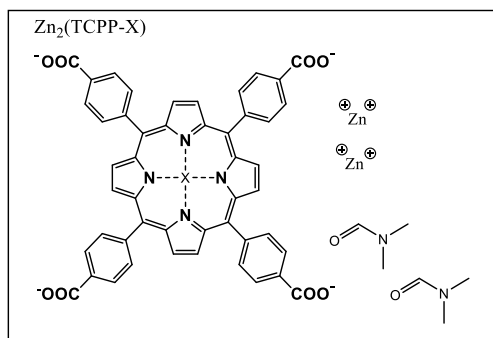
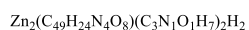


Figure S2.1 Powder X-ray diffraction of Zn₂(TCPP-X), where X = H₂, Co, Ni, Cu, Zn, or Cd. Zoomed to show peak at 7-7.5°.

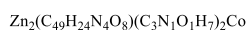
Elemental Analysis



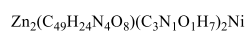
Theoretical Chemical Formula



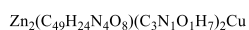
Elemental Analysis: C, 61.41; H, 3.75; N, 7.81; O, 14.87; Zn, 12.16



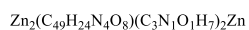
Elemental Analysis: C, 58.32; H, 3.38; Co, 5.20; N, 7.42; O, 14.13; Zn, 11.54



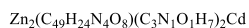
Elemental Analysis: C, 58.34; H, 3.38; N, 7.42; Ni, 5.18; O, 14.13; Zn, 11.55



Elemental Analysis: C, 58.09; H, 3.37; Cu, 5.59; N, 7.39; O, 14.07; Zn, 11.50

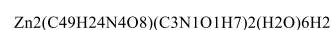


Elemental Analysis: C, 57.99; H, 3.36; N, 7.38; O, 14.05; Zn, 17.22



Elemental Analysis: C, 55.69; H, 3.23; Cd, 9.48; N, 7.09; O, 13.49; Zn, 11.02

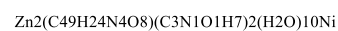
Contaminated Chemical Formula



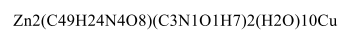
Elemental Analysis: C, 55.80; H, 4.43; N, 7.10; O, 21.62; Zn, 11.05



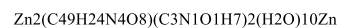
Elemental Analysis: C, 48.98; H, 4.63; Co, 4.37; N, 6.23; O, 26.10; Zn, 9.69



Elemental Analysis: C, 50.33; H, 4.45; Ni, 6.40; N, 4.47; O, 24.38; Zn, 9.96



Elemental Analysis: C, 50.14; H, 4.44; Cu, 4.82; N, 6.38; O, 24.29; Zn, 9.93



Elemental Analysis: C, 50.08; H, 4.43; N, 6.37; O, 24.26; Zn, 14.87



Elemental Analysis: C, 46.51; H, 4.54; Cd, 7.91; N, 5.92; O, 25.91; Zn, 9.21

Figure S2.2 Elemental composition of $\text{Zn}_2(\text{TCPP-X})$, with theoretical amounts (left), and with speculated contamination by water (right).

Steady-State Emission Spectroscopy

Individual emission spectra baselined and integrated using native origin Pro tools are shown in Figure S2.3. 2 mL dispersions are dried and weighing to measure concentrations in mg mL^{-1} as $\text{H}_2 = 0.2$, $\text{Co} = 0.05$, $\text{Ni} = 0.044$, $\text{Cu} = 0.064$, $\text{Zn} = 0.05$. and $\text{Cd} = 0.048 \text{ mg mL}^{-1}$.

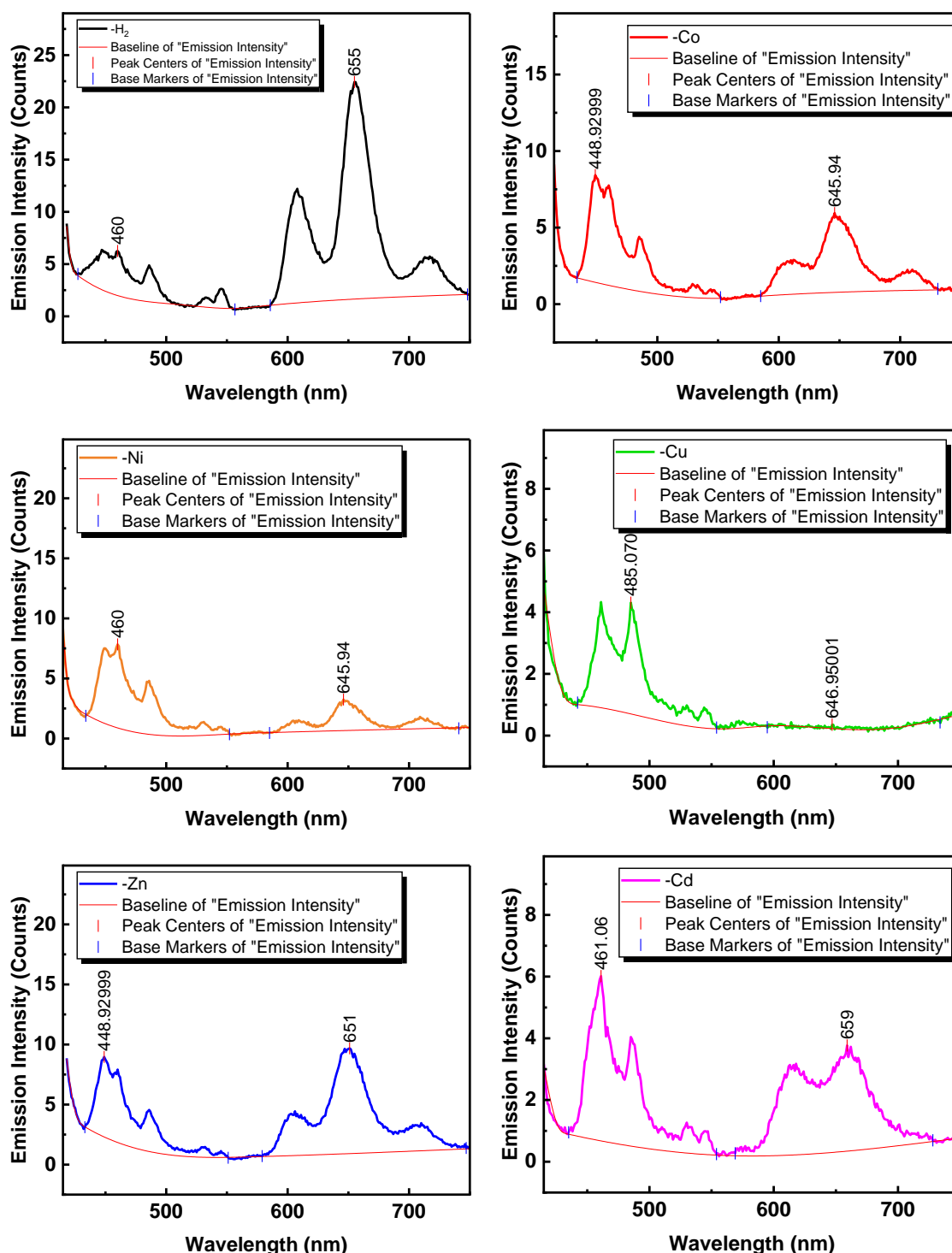


Figure S2.3 Emission spectra of $\text{Zn}_2(\text{TCPP})$ dispersions in EtOH with excitation at 400 nm.

Transient Absorption

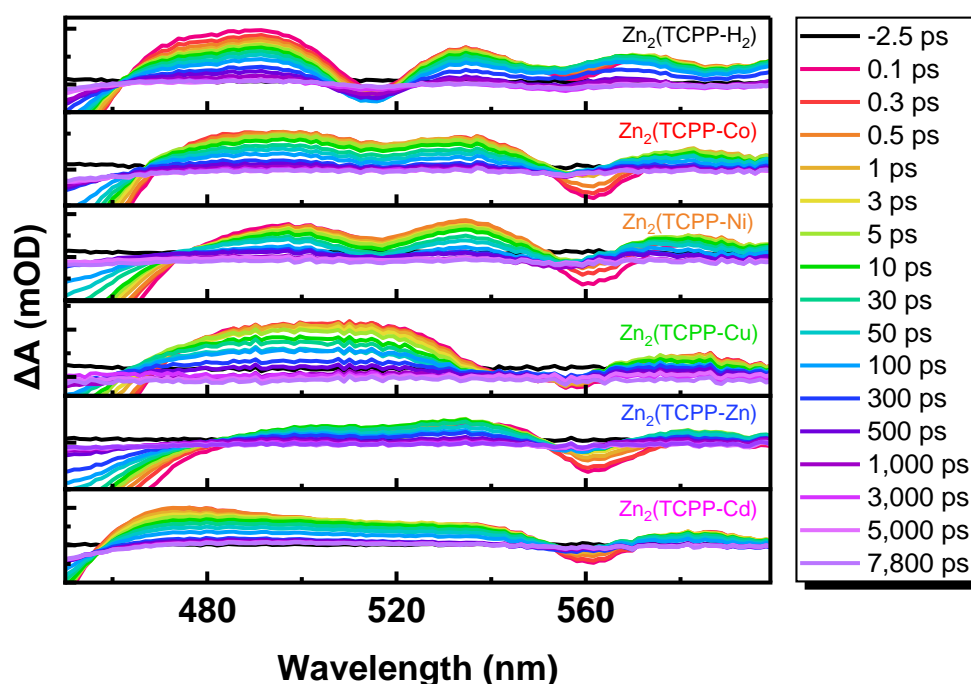


Figure S2.4 TA spectra for $Zn_2(TCPP-X)$, where $X = H_2, Co, Ni, Cu, Zn,$ or Cd , cropped to 450 – 600 nm to show the ESA from S_1 .

Power Dependence

Power varied between 0.2 and 2 mW using excitation beam with major ellipsoid diameter 685.48 μm and minor ellipsoid diameter 447.40 μm (these dimensions are also applicable to $Zn_2(TCPP-Cd)$ TA calculations). Pump fluence (energy density per surface area) can be calculated using Equation S4.1 where the unit of pump fluence is usually reported in $\mu J cm^{-2}$, P is measured pump power, f is the pump rate (for Helios, $f = 5000 Hz$, a is the pump ellipse major *radius*, and b is the pump ellipse minor *radius* (note beam spot measurement outputs diameters)).

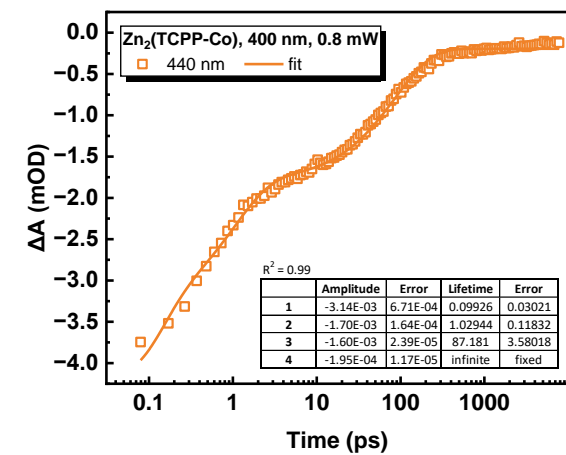
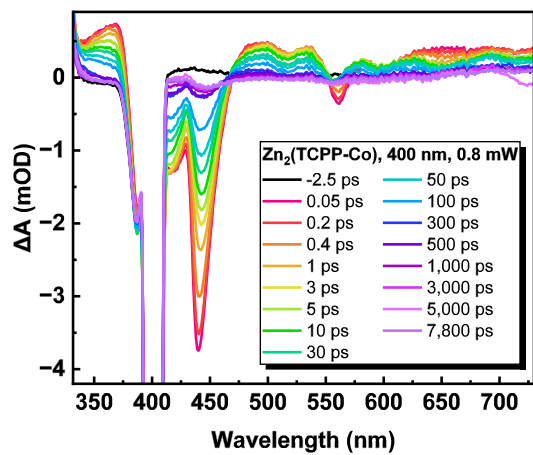
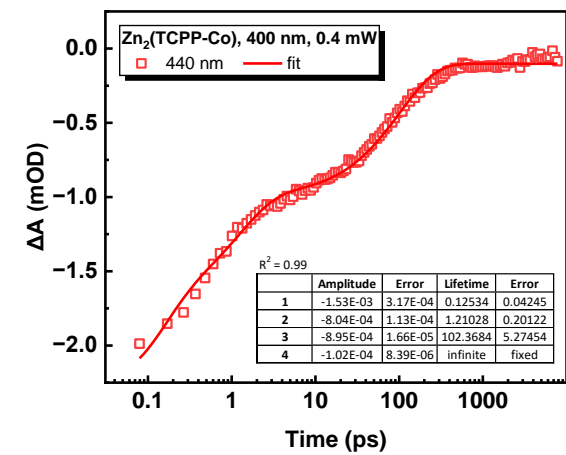
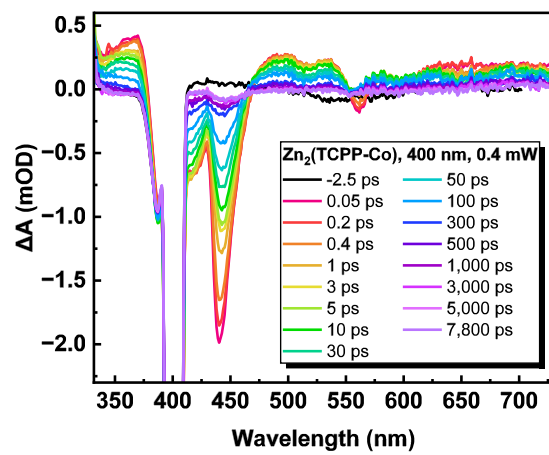
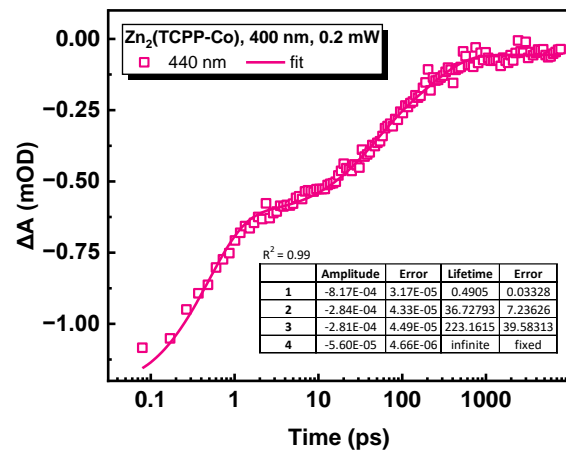
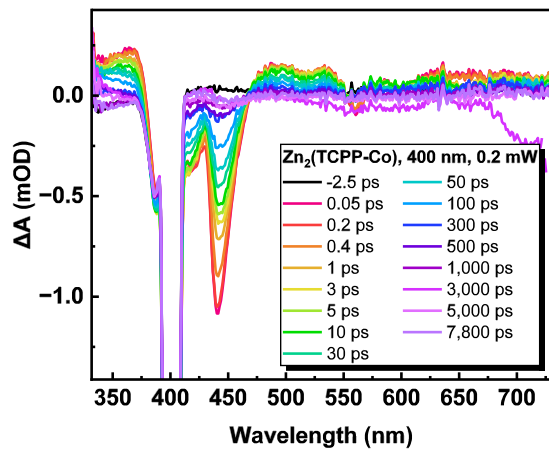
Equation S4.1 $Pump\ Fluence = P \div (f \times \pi \times a \times b)$

Therefore, using the equation, tested pump fluences can be converted as in 15, 30, 60, 76, 91, 106, and 151 $\mu J cm^{-2}$. P was converted to Watts and multiplied by 1,000,000, and a and b were divided by $(2 \times 10,000)$ to convert to radii in cm.

Table S4.2 Pump power to fluence conversion for TA of $Zn_2(TCPP-Co)$ and $Zn_2(TCPP-Cd)$

Power / mW	Fluence / $\mu J cm^{-2}$
0.2	16.6
0.4	33.2
0.8	66.4
1.0	83.0
1.5	124.5
2.0	166.1

TA Power Dependence of Zn₂(TCPP-Co)



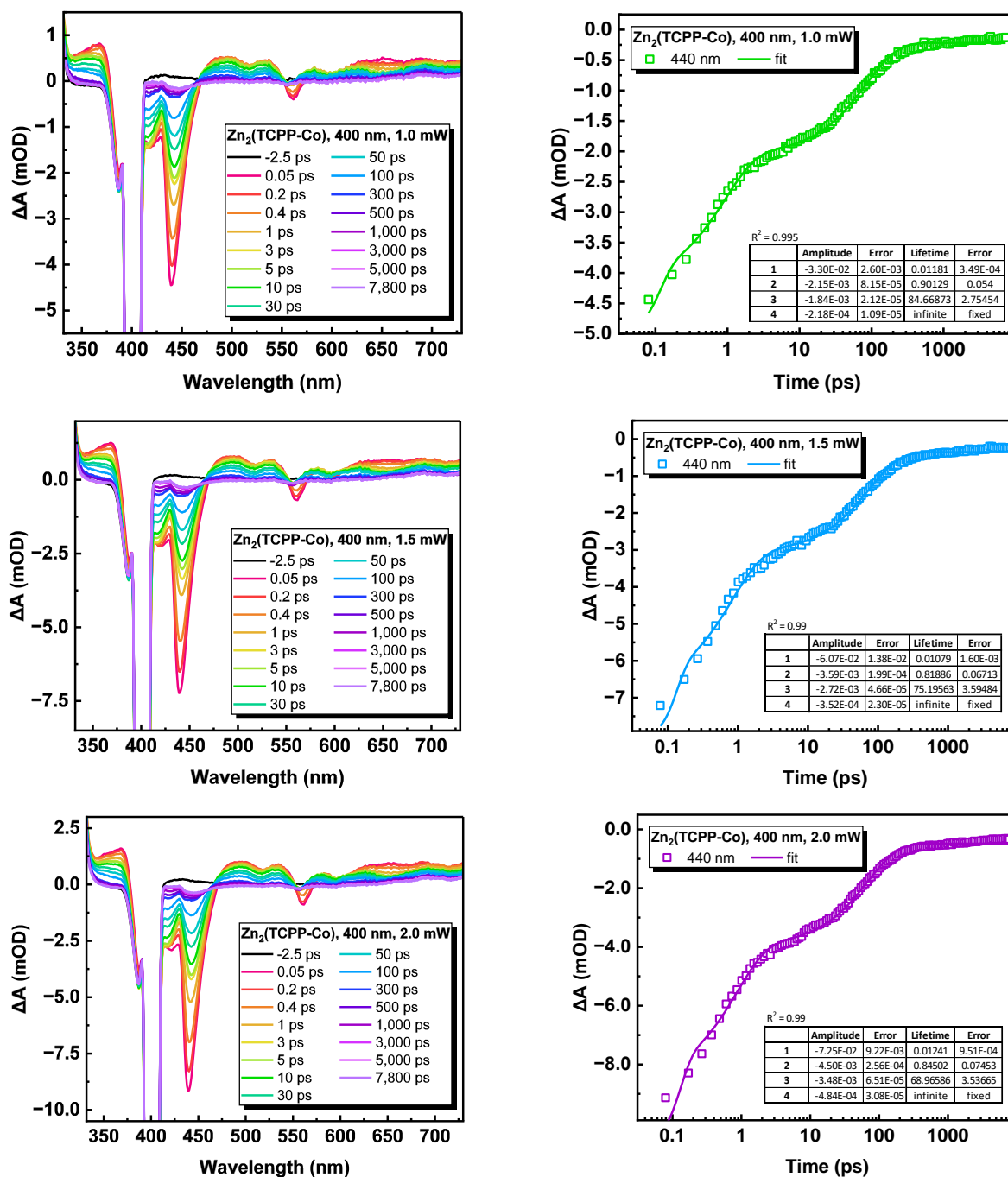


Figure S2.5 Transient absorption spectra (left) and kinetics at 440 nm (right) for Zn₂(TCPP-Co) with 400nm excitation power of 0.2, 0.4, 0.8, 1.0, 1.5, and 2.0 mW.

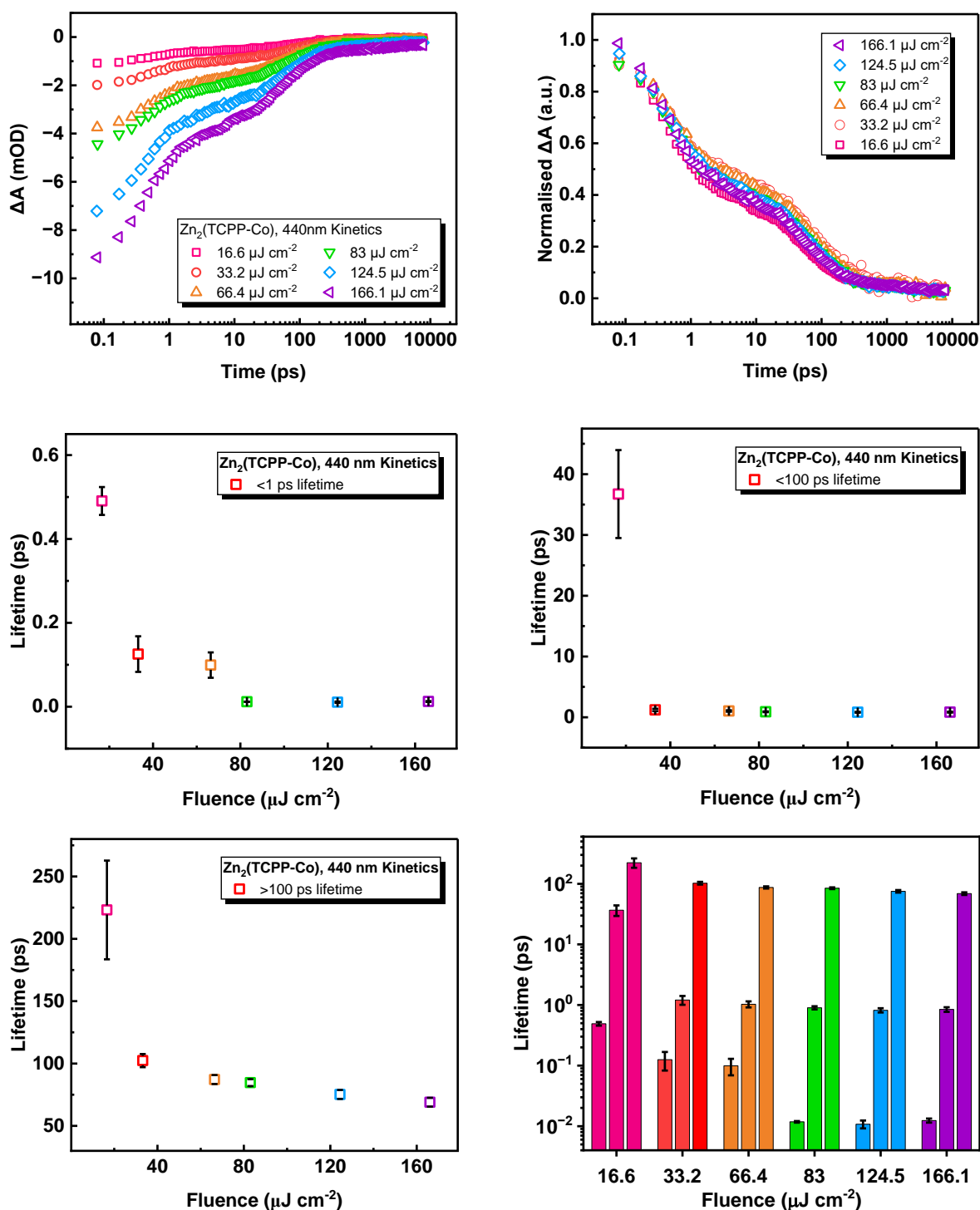
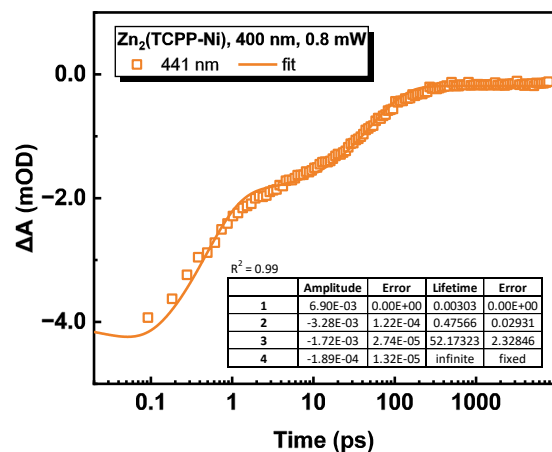
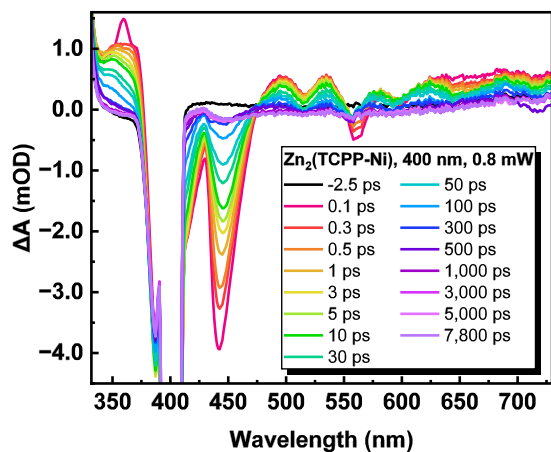
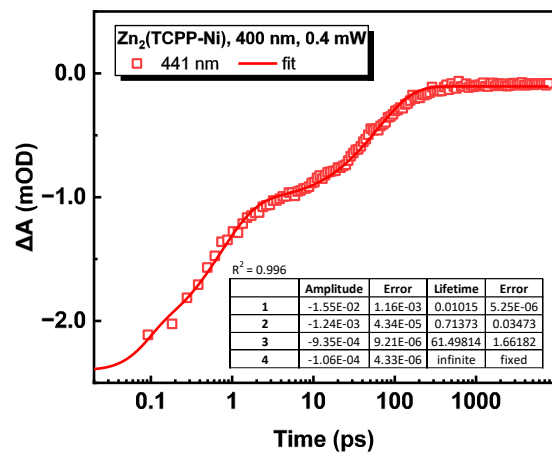
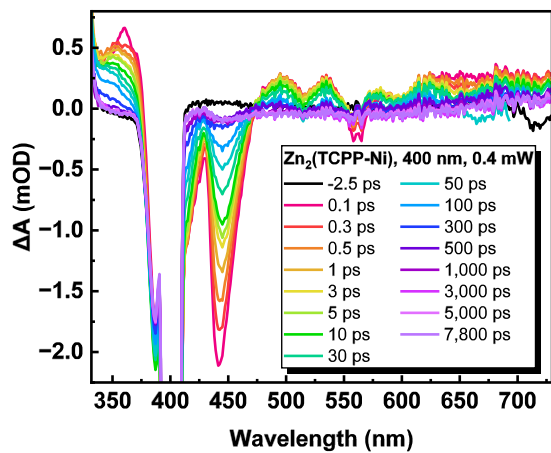
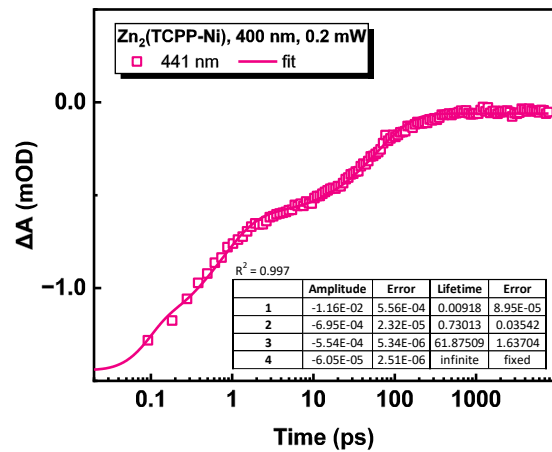
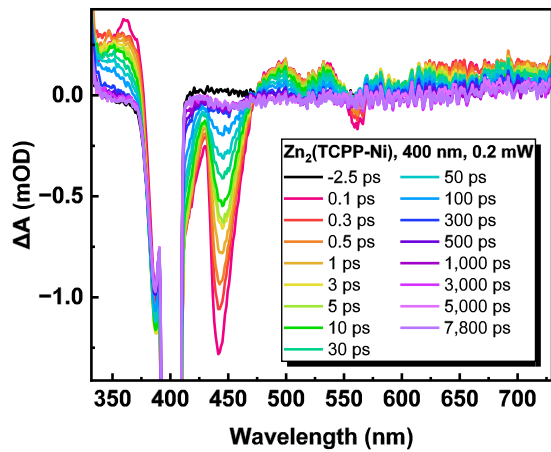


Figure S2.6 TA kinetics at 441 nm for $Zn_2(TCPP-Co)$ in EtOH excited by different fluences at 400 nm. Kinetics are plotted as recorded in mOD (top left), normalised by most negative value (top right). Calculated lifetimes τ_1 , τ_2 , and τ_3 produced from fitting of these kinetics are plotted against fluence (middle left, middle right, and bottom left respectively). A bar chart of all lifetimes calculated for each fluence (bottom right).

TA Power Dependence of Zn₂(TCPP-Ni)



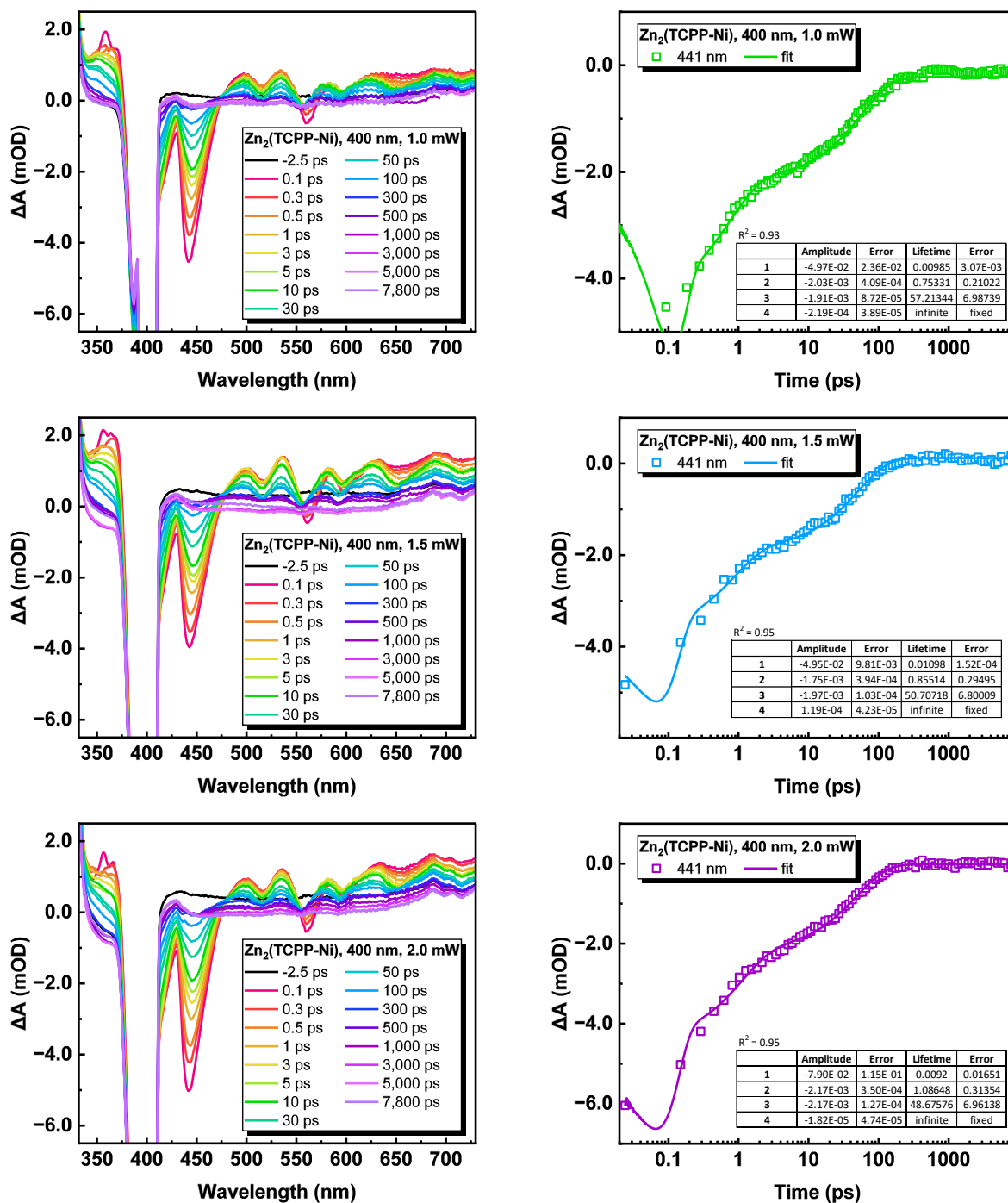


Figure S2.7 Transient absorption spectra (left) and kinetics at 440 nm for Zn₂(TCPP-Ni) with 400nm excitation power of 2.0 mW.

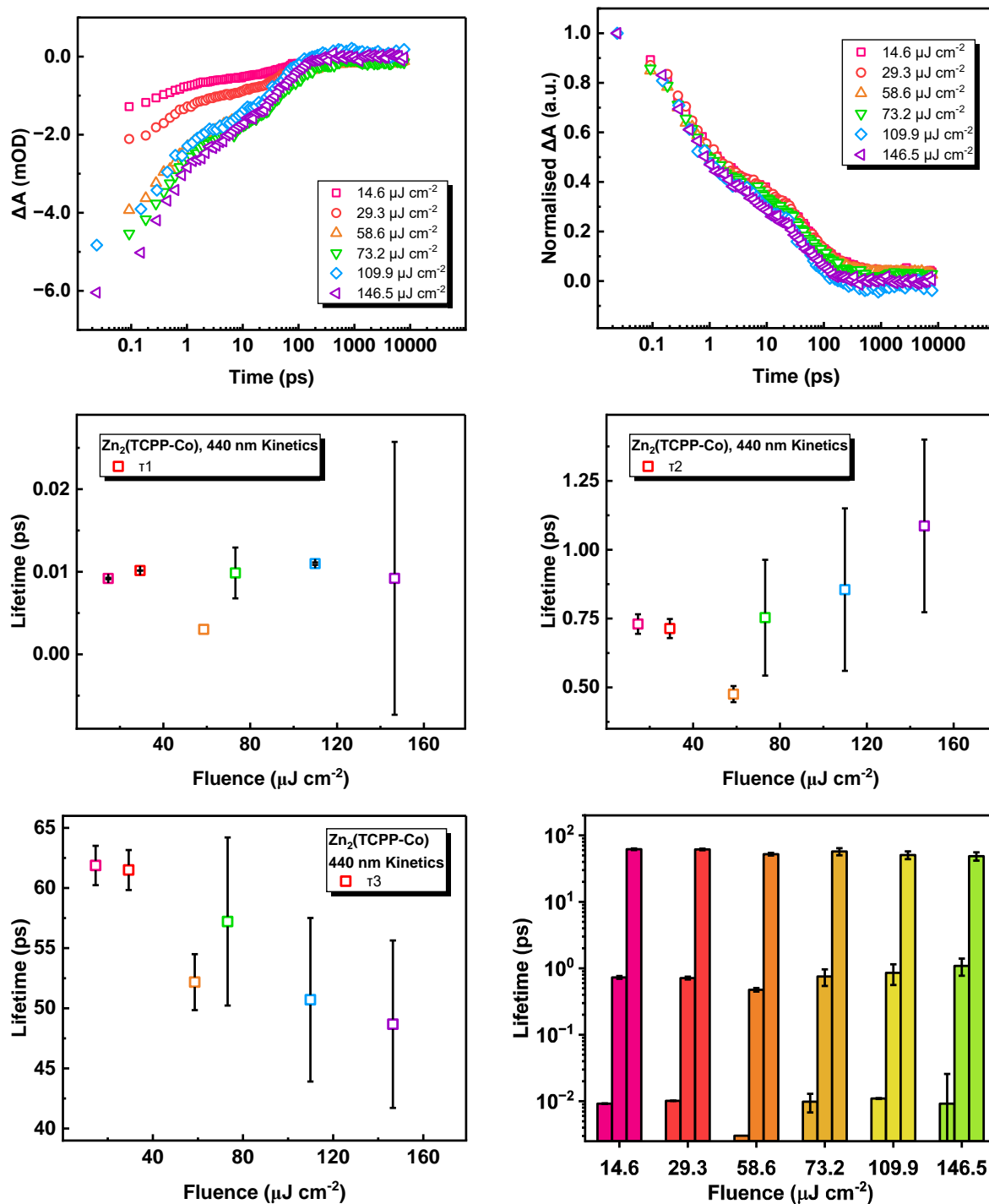
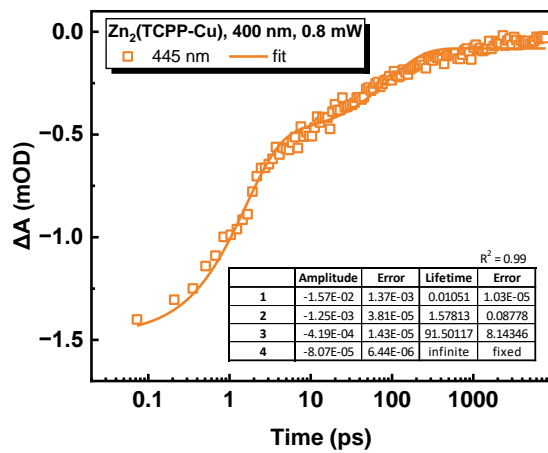
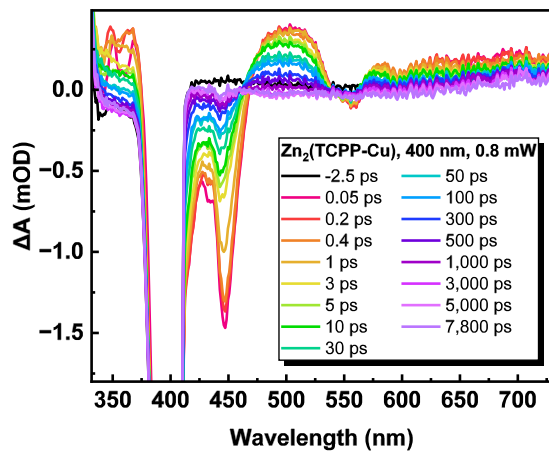
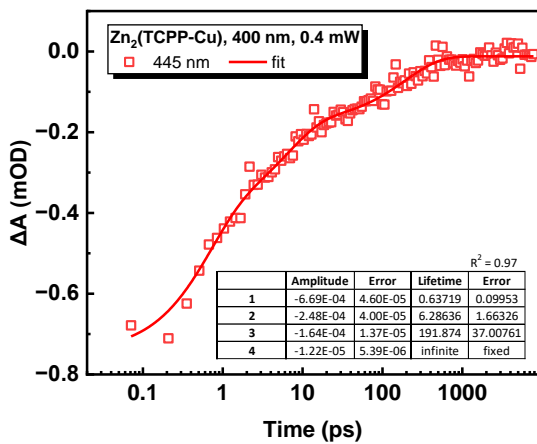
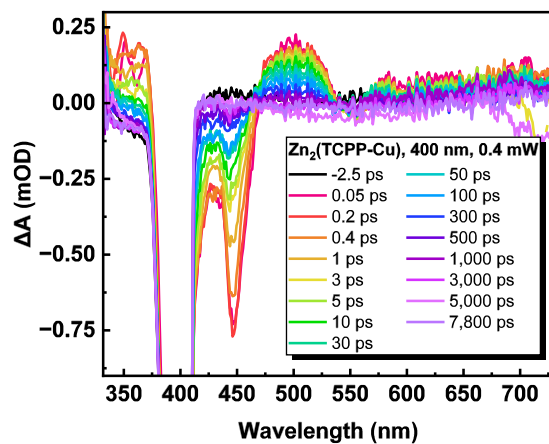
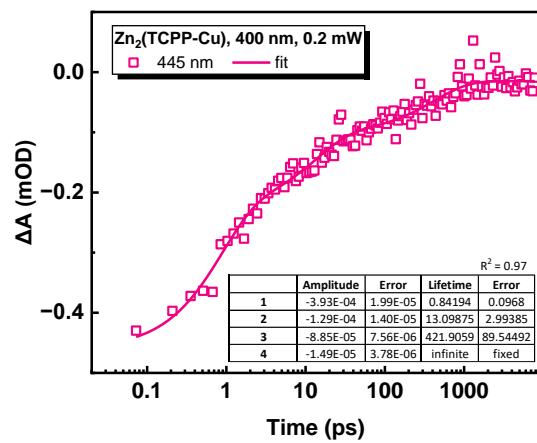
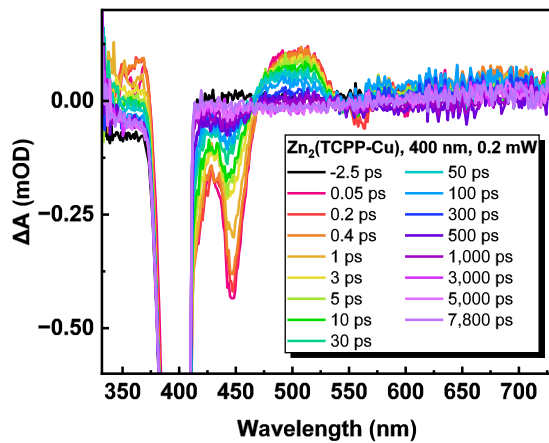


Figure S2.8 TA kinetics at 441 nm for $Zn_2(TCPP-Ni)$ in EtOH excited by different fluences at 400 nm. Kinetics are plotted as recorded in mOD (top left), normalised by most negative value (top right). Calculated lifetimes τ_1 , τ_2 , and τ_3 produced from fitting of these kinetics are plotted against fluence (middle left, middle right, and bottom left respectively). A bar chart of all lifetimes calculated for each fluence (bottom right).

TA Power Dependence of Zn₂(TCPP-Cu)



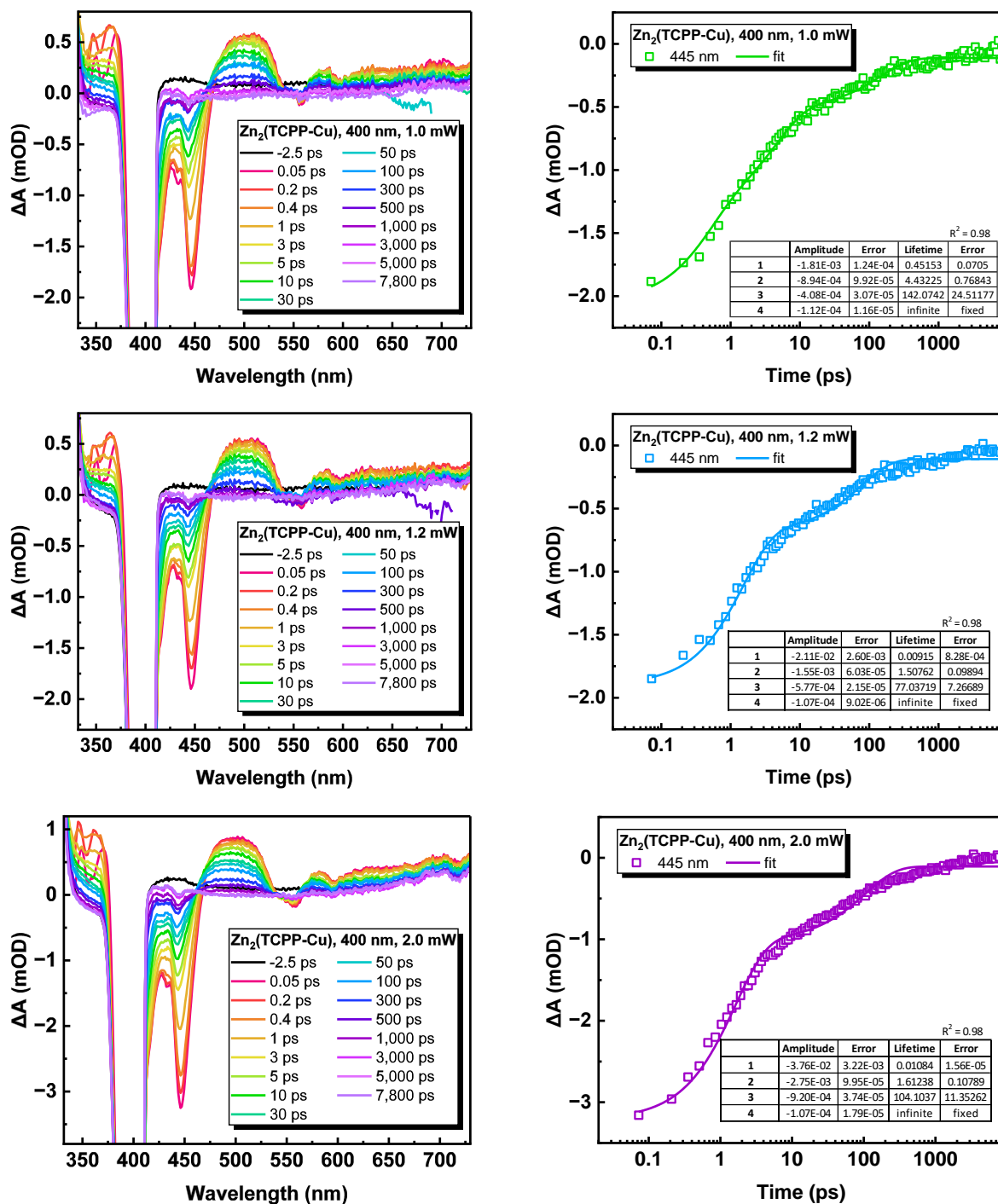


Figure S2.9 Transient absorption spectra (left) and kinetics at 440 nm for Zn₂(TCPP-Cu) with 400nm excitation power of 2.0 mW.

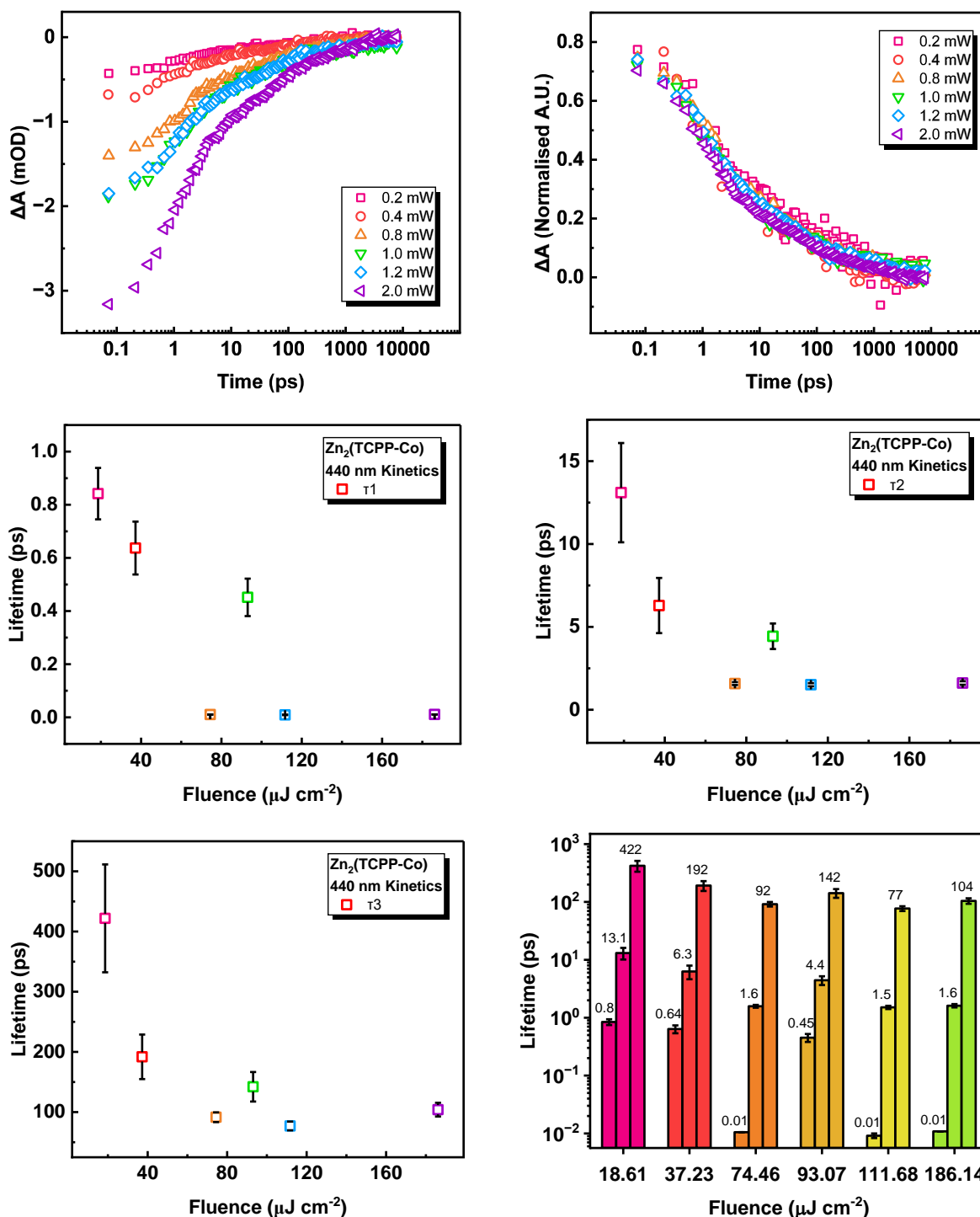
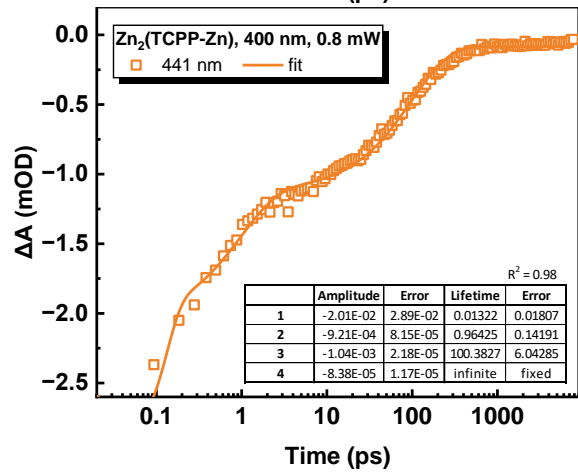
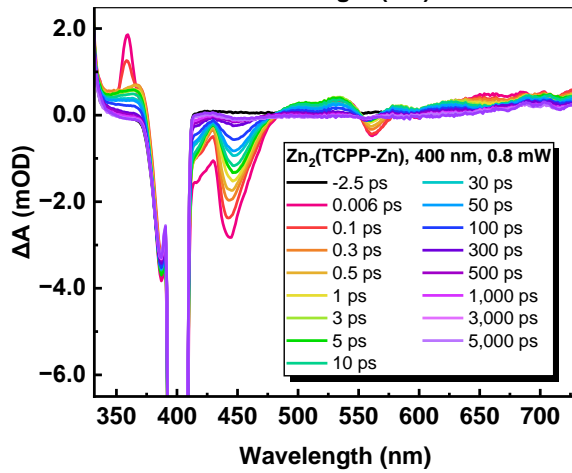
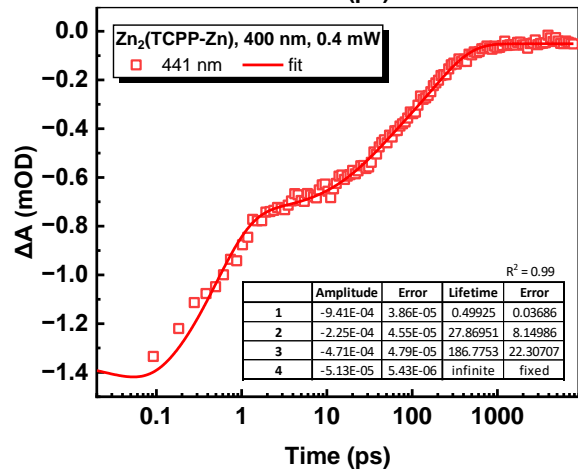
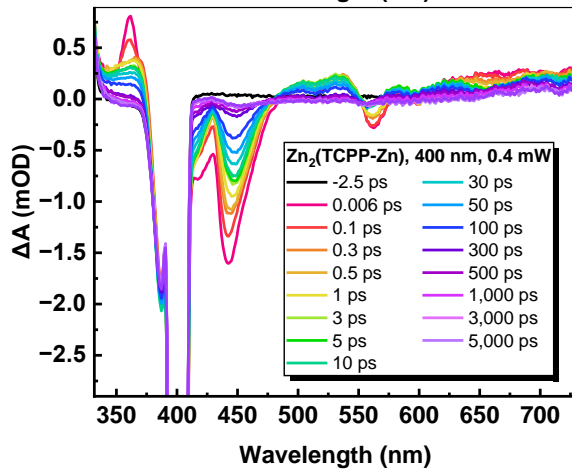
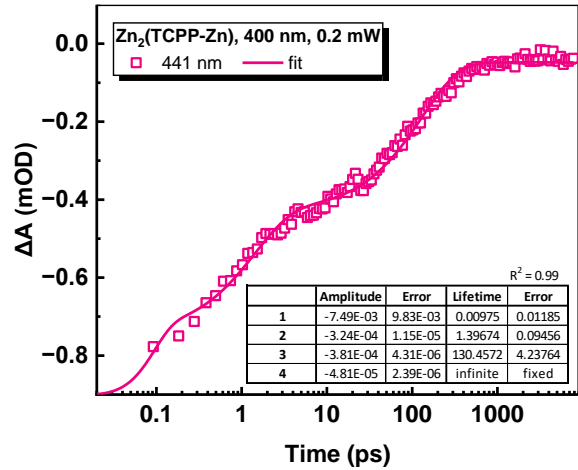
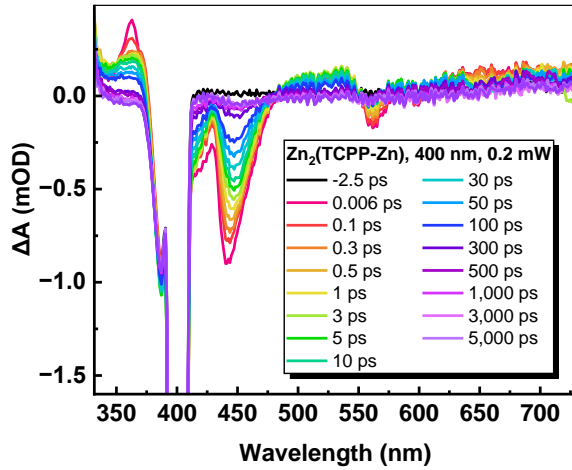


Figure S2.10 TA kinetics at 441 nm for $Zn_2(TCPP-Cu)$ in EtOH excited by different fluences at 400 nm. Kinetics are plotted as recorded in mOD (top left), normalised by most negative value (top right). Calculated lifetimes τ_1 , τ_2 , and τ_3 produced from fitting of these kinetics are plotted against fluence (middle left, middle right, and bottom left respectively). A bar chart of all lifetimes calculated for each fluence (bottom right).

TA Power Dependence of Zn₂(TCPP-Zn)



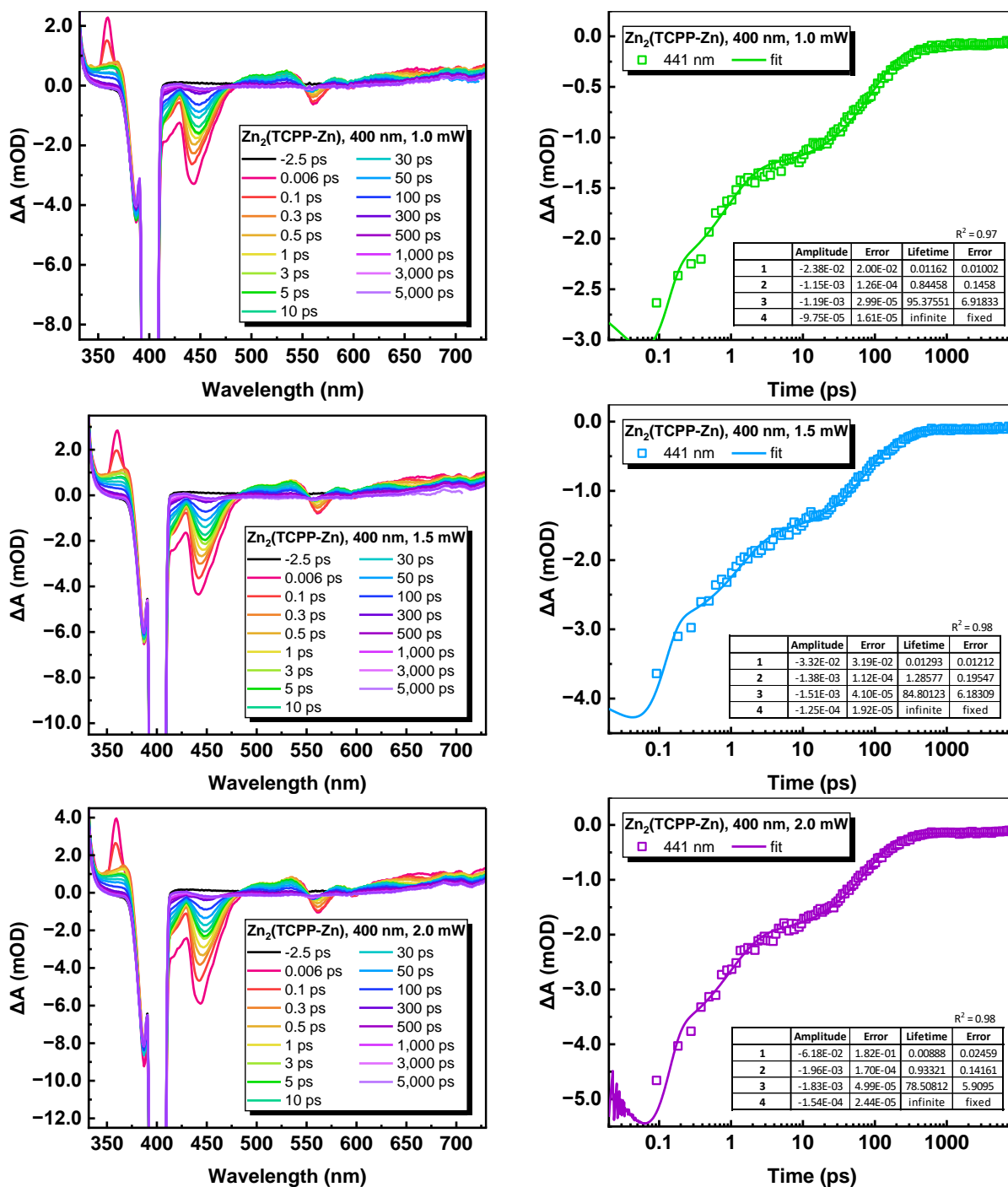


Figure S2.11 Transient absorption spectra (left) and kinetics at 440 nm for Zn₂(TCPP-Zn) with 400nm excitation power of 2.0 mW.

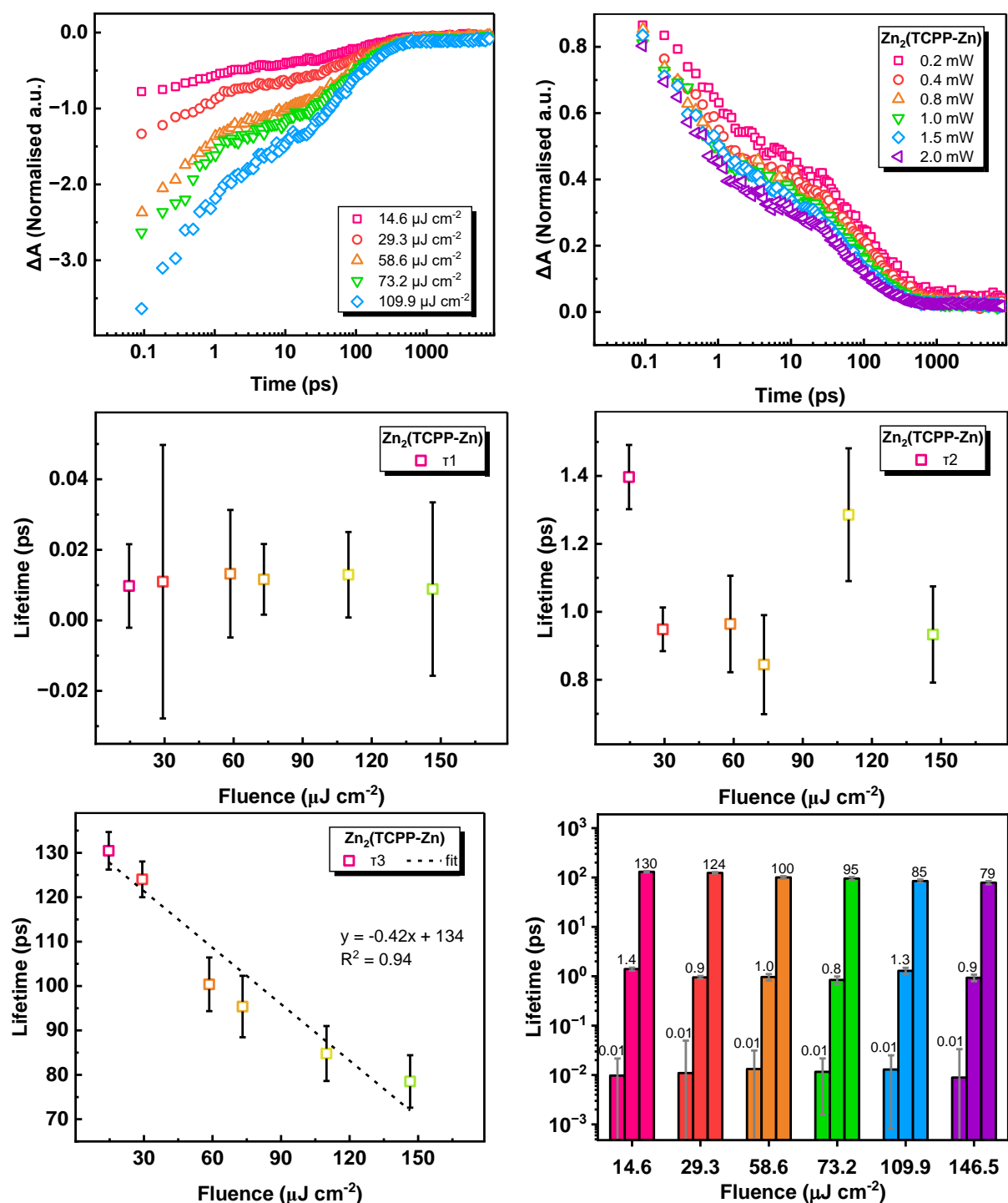
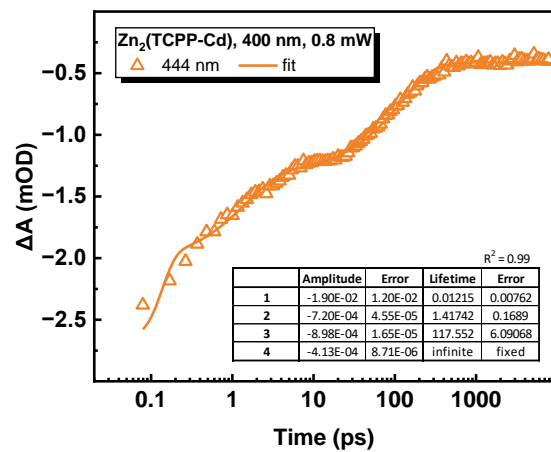
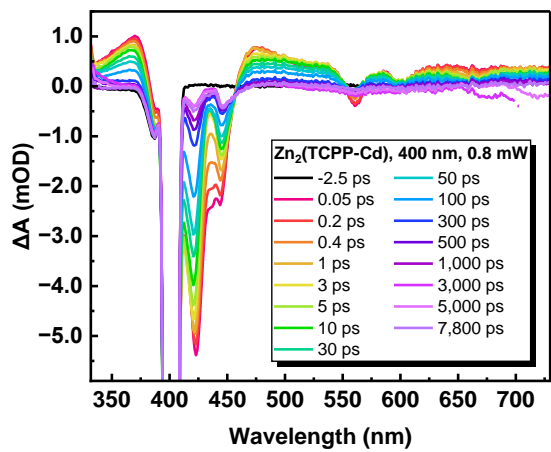
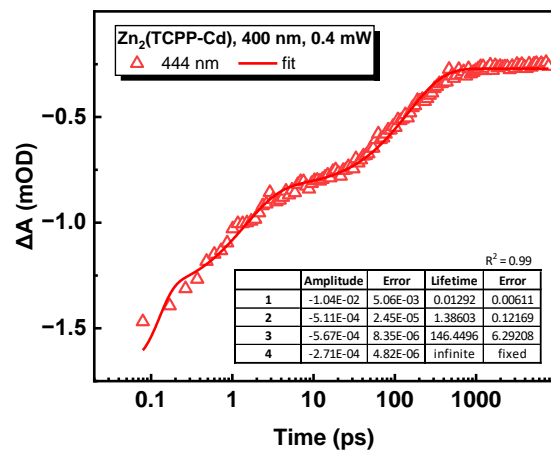
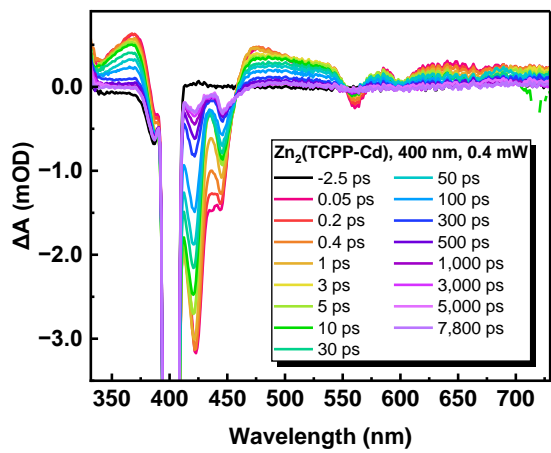
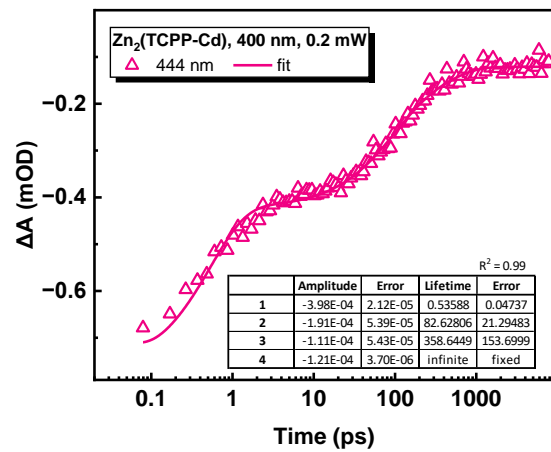
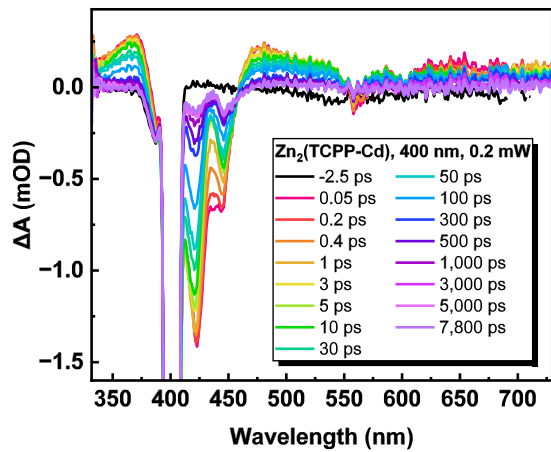


Figure S2.12 TA kinetics at 441 nm for $Zn_2(TCPP-Cu)$ in EtOH excited by different fluences at 400 nm. Kinetics are plotted as recorded in MOD (top left), normalised by most negative value (top right). Calculated lifetimes τ_1 , τ_2 , and τ_3 produced from fitting of these kinetics are plotted against fluence (middle left, middle right, and bottom left respectively). A bar chart of all lifetimes calculated for each fluence (bottom right).

TA Power Dependence of Zn₂(TCPP-Cd)



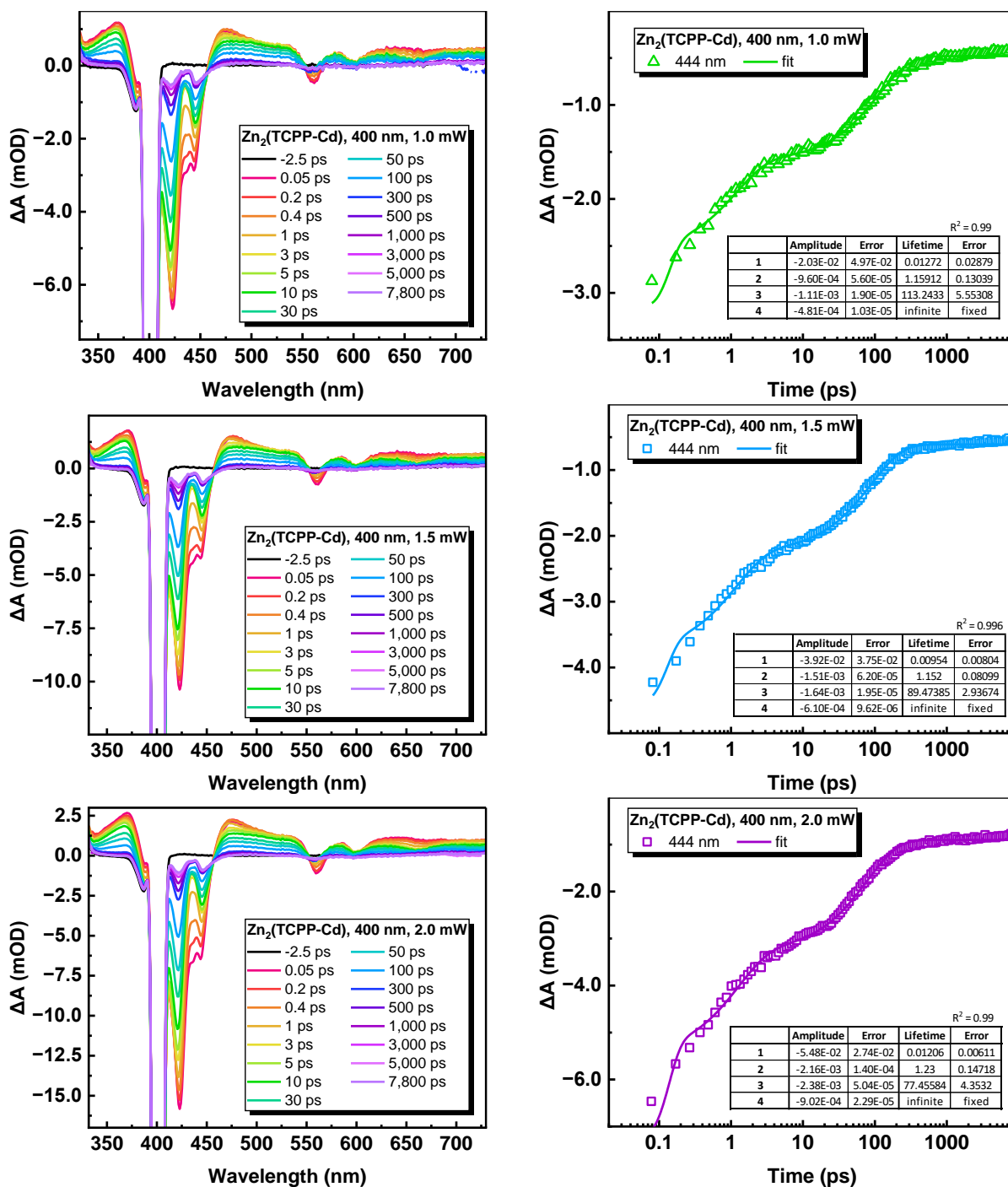


Figure S2.13 Transient absorption spectra (left) and kinetics at 440 nm for Zn₂(TCPP-Cd) with 400nm excitation power of 2.0 mW.

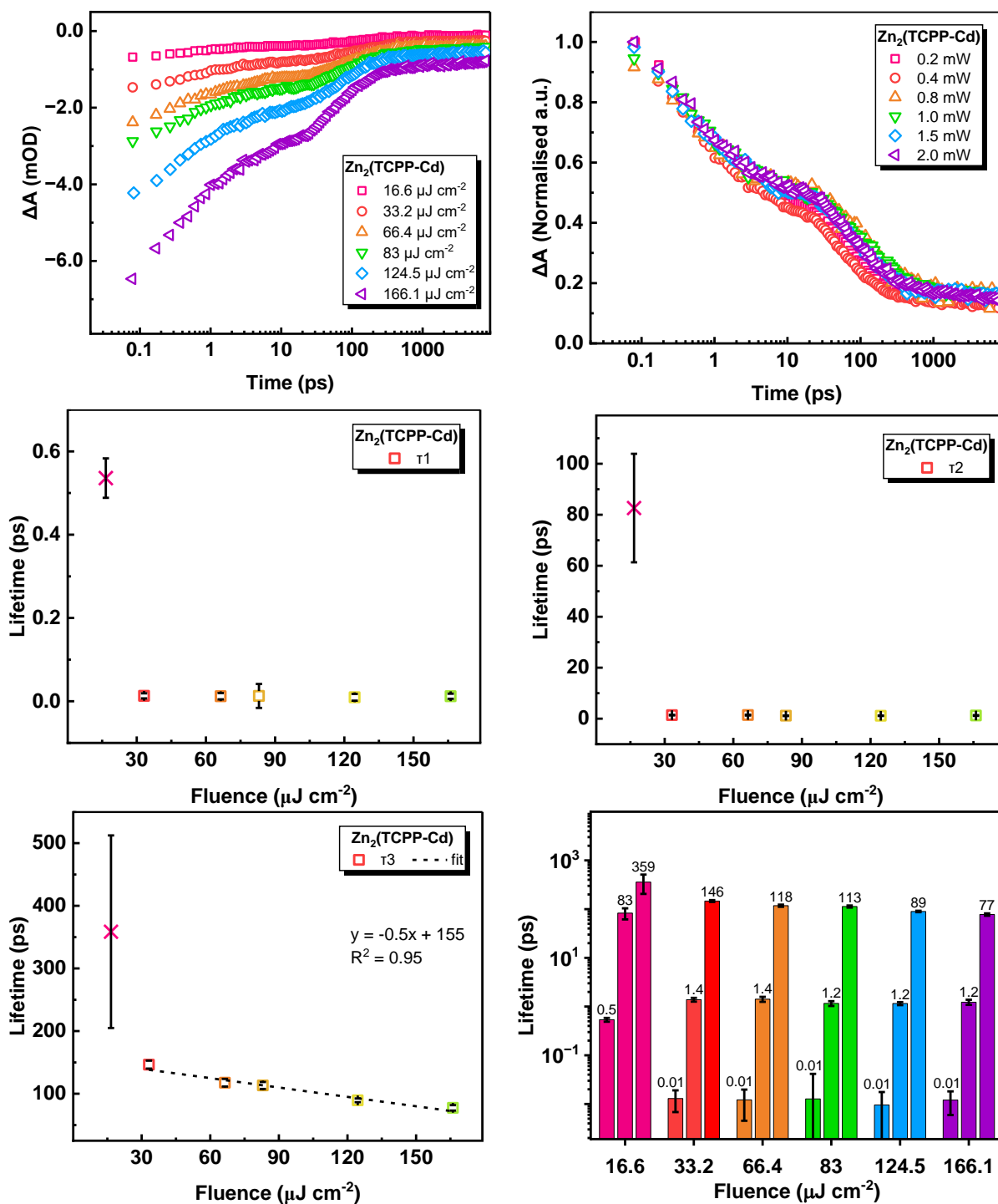


Figure S2.14 TA kinetics at 441 nm for $Zn_2(TCPP-Cd)$ in EtOH excited by different fluences at 400 nm. Kinetics are plotted as recorded in mOD (top left), normalised by most negative value (top right). Calculated lifetimes τ_1 , τ_2 , and τ_3 produced from fitting of these kinetics are plotted against fluence (middle left, middle right, and bottom left respectively). A bar chart of all lifetimes calculated for each fluence (bottom right).

Chapter 5:

Photoluminescence Nanospectroscopy of Porphyrin-based Nanosheets

Section 5.1 Abstract

Many 2D materials show thickness dependent photophysical properties but directly correlating nanomaterial structures with absorption, emission, or other properties remains a challenge. Partly this is due to poor size determination of anisotropic nanoparticles in dispersion. For example, dynamic light scattering (DLS) is difficult because modelling assumes samples are spherical particles. Surface near-field optical microscopy (SNOM) offers the opportunity to combine two measurements, measuring photophysical properties in-situ to size measurements, and directly mapping them to observed morphology.

Work towards overcoming the seemingly mutually exclusive techniques of anisotropic size determination and photophysical characterisation, particularly emission measurements, is performed by the modification of the scanning near-field optical microscopy (SNOM) suite in the Physics Department at the University of Sheffield. Emission-based 2D mapping of metal organic framework nanosheets (MONs) was achieved with 3.3 μm resolution using a 400 nm laser incident on a silicon tip during an atomic force microscopy (AFM) experiment. This allowed concurrent data measurement of emission intensity collected from parabolic mirror and height profiling data. The data was intended to correlate the thickness of individual MON nanosheets <200 nm diameter and 1-3 nm thickness, however the resolution required for this outcome proved to be beyond the limits of the setup. The achieved resolution however allowed the good resolution emission imaging of several large agglomerates (8 μm dimensions).

This study therefore provides a foundational capability for measuring combined size determination and emission intensity, with promising applications for a variety of materials.

Section 5.2 Introduction

Previous chapters have discussed a dichotomy when correlating photophysical properties of nanosheet materials to particle size or morphology. Particle size determination is most commonly measured in liquid dispersion using dynamic light scattering (DLS) but measuring anisotropic nanosheet size via DLS is notoriously hard due to the modelling assumption that particles are spherical. Measuring the size and dimensions of anisotropic nanomaterials is therefore more commonly achieved using methods such as atomic force microscopy (AFM), where particles are deposited onto a surface.

Most photophysical measurements are optimised for liquid samples (dilute, long absorption pathlength) due to the issues of scattering or non-uniformity of films/solids. There is also a high technical difficulty barrier with aligning optical measurements to the area of deposited samples which have been measured by AFM. This prohibits comparison between optical measurements and particle size measurements as they are most commonly acquired from different sample forms (optical: liquid cell, size: deposited particles). There is therefore difficulty obtaining quantitative analysis correlating spectroscopic properties with size.

In scattering scanning near-field optical microscopy (s-SNOM), incident light is directed onto the tip of a metal-coated AFM cantilever, generating near-field excitation, or plasmons, in the metal surface. These near-field excitations consist of a highly confined electromagnetic field, which is used to probe the sample surface.¹ As the AFM tip approaches contact with the sample, the near-field excitations interact with surface atoms according to the dielectric response of the sample material. This dielectric response is effected by the presence of electronic, vibrational, or phonon resonances pertaining to the material within a ~ 20 nm distance of the AFM tip (and hence limiting the resolution here). Further incoming light is scattered off the interaction region between the tip and the sample, thereby carrying information regarding the dielectric response of the sample back to a detector, where the data is processed. By scanning the changes in absorbance in scattered light in the near-field during an AFM measurement, the spectral changes due to these properties can be spatially mapped in tandem with height measurements.

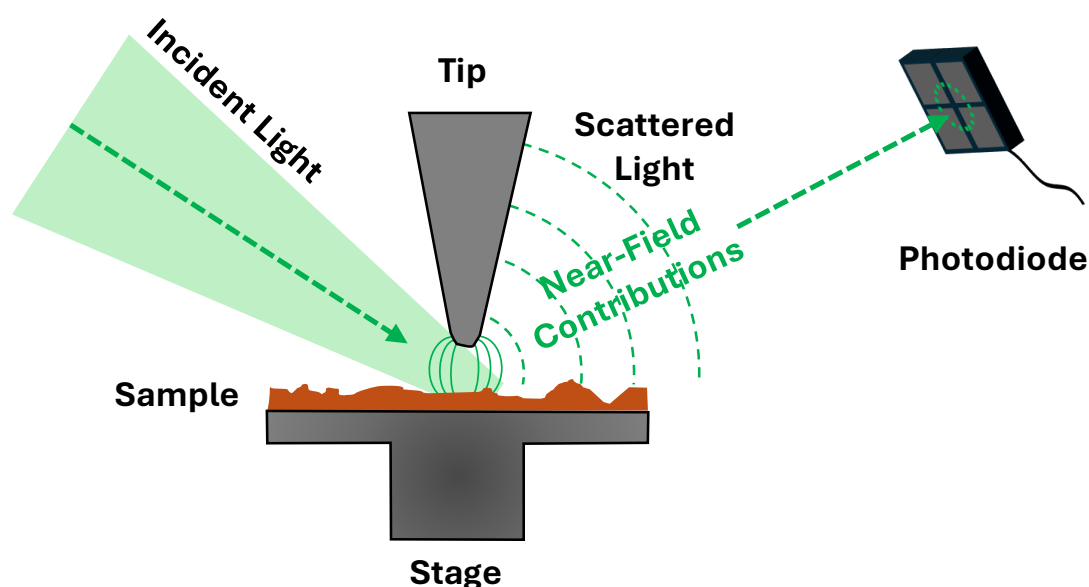


Figure 5.1 Diagram showing scattering scanning near-field optical microscopy (s-SNOM) setup.

To our knowledge, there are no previous examples of s-SNOM being used to characterise metal organic framework nanosheets. Only one related investigation of a 3D metal organic framework (MOF) by the Tan group in the study of zeolitic imidazolate frameworks (ZIF-8).^{2,3} In this study, Tan et al. used s-SNOM to study the insertion of rhodamine B (RhB) as a guest in ZIF-8 (Figure 5.2). Here, they showed a scan of RhB and ZIF-8 mixed, compared with the RhB@ZIF-8, where RhB is a guest. As shown, the vibrational absorption spectra of the RhB@ZIF-8 contain peaks from each of the two components and are shown by AFM to be a single particle.

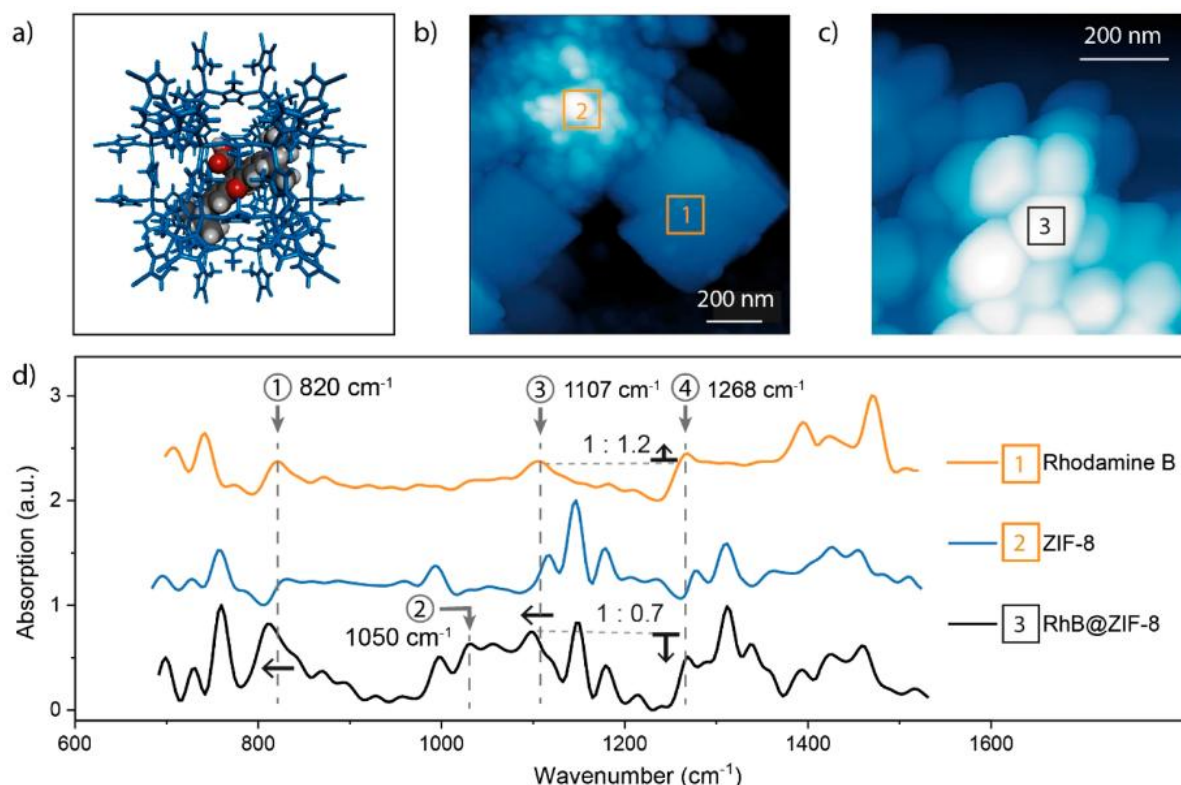


Figure 5.2 (a) Schematic representation of the RhB@ZIF-8 composite, depicting a RhB guest molecule being encapsulated in the pore of the ZIF-8 host framework (in blue). (b) AFM image of the as-synthesized sample containing two distinctive phases, i.e., (1) RhB and (2) ZIF-8, showing the positions where IR spectra were recorded. (c) AFM image of a single-phase sample of ZIF-8 nanocrystals adsorbing RhB. (d) nanoFTIR spectra determined at the designated locations on the AFM image. Reproduced from Tan et al.³

Smith et al. recorded fluorescence anisotropy microscopy (FAM) images of a polymer after annealing at different temperatures to identify the changes in absorption transition dipoles within resultant thin-films. The polymer, poly[4-(octyloxy)-9,9-diphenylfluoren-2,7-diyl]-co-[5-(octyloxy)-9,9-diphenylfluoren-2,7-diyl] (PODPF) was also mapped by time-resolved emission microscopy (TREM) to determine the effect of different anisotropic orientations on emission lifetime. As shown in Figure 5.3, these techniques in tandem offered a unique opportunity to compare the two properties, identifying significant correlation.⁴

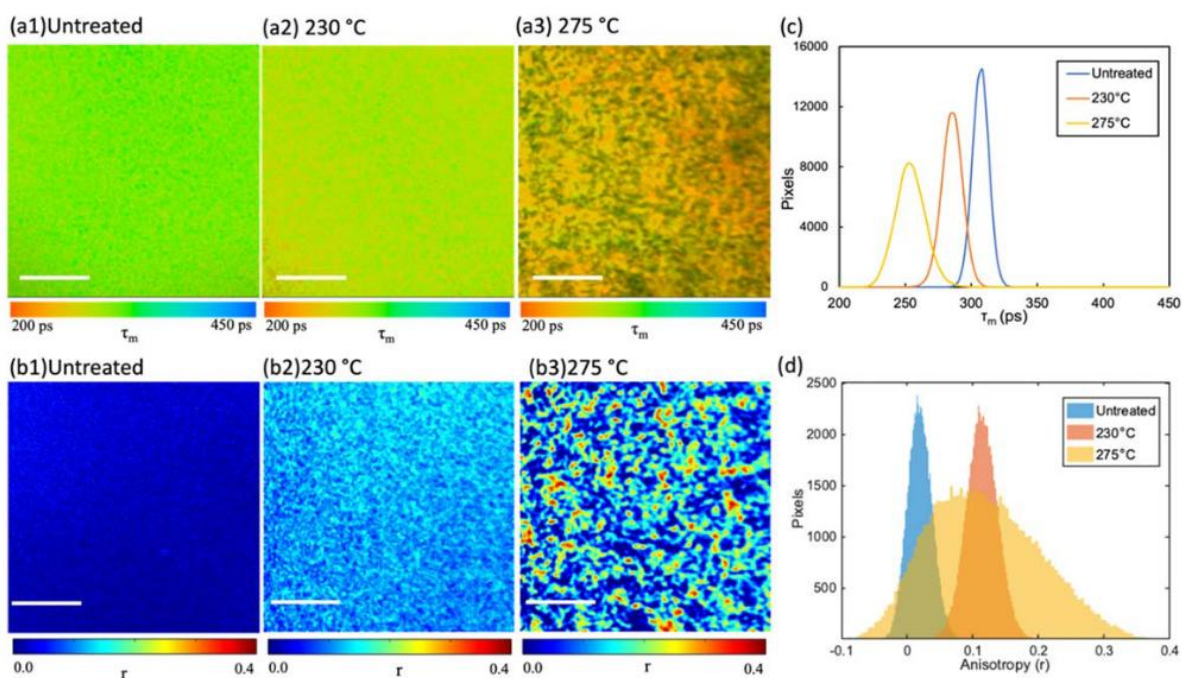


Figure 5.3 TREM (a) and FAM (b) images of PODPF films before annealing (a1, b1) and after annealing at 230 °C (a2, b2), and 275 °C (a3, b3). (c) and (d) are distribution diagrams for the average fluorescence decay time and fluorescence anisotropy of films annealed at different temperature, respectively. Scale bar: 10 μ m. Figure reproduced from Smith et al.⁴

These examples show how useful mapping techniques such as this can be. In this chapter, we explore the capability of an s-SNOM setup for characterising metal organic framework nanosheets (MONs) and detail the process of designing a new experimental setup to measure the photoluminescence (PL) of MONs when excited by a low power laser in tandem with atomic force microscopy (AFM) measurements. $Zn_2(TCPP)$ MONs were chosen because of our ongoing interest into their photophysical properties including fluorescence. The effect of agglomeration on spectroscopic properties has been explored in earlier chapters, with some interesting results regarding the quenching mechanisms observed in solution with agglomerates. The aim of this chapter, therefore, is to assess the capability of s-SNOM to analyse $Zn_2(TCPP)$ monolayer and agglomerate particles with the end goal of correlating parameters such as nanosheet thickness with emission intensity.

Section 5.3 Surface Nearfield Optical Microscopy of Metal Organic Framework Nanosheets

Zn₂(TCPP) was synthesised as reported in previous chapters and measured on the s-SNOM setup in the Near-Field Optical Imaging and Spectroscopy Centre in the Department of Physics at the University of Sheffield with the help of Dr Alex Knight in Professor Tartakovskii's research group. Atomic force microscopy (AFM) of Zn₂(TCPP) on mica was used to isolate an area with identifiable features so repeat scans on the same area could be performed. The mica scar in the area shown in Figure 5.4 is such a feature, surrounded by both agglomerate particles and high aspect ratio nanosheets.

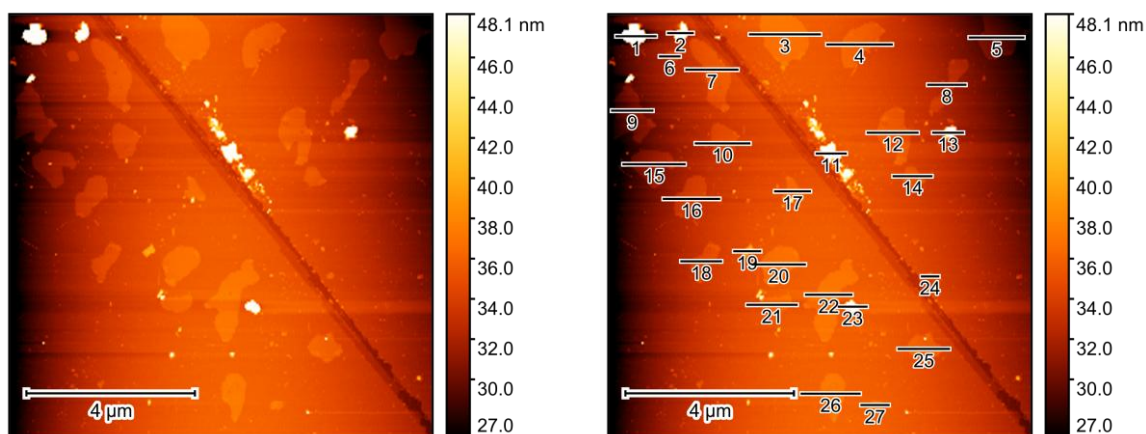


Figure 5.4 AFM data showing a) 10µm micrographs for sample C and b) profiles

As seen in Figure 5.5, height profiles gathered from this AFM show nanosheets mostly approaching monolayer (0.7 – 2.5 nm), with widths ranging from 200 – 1200 nm. The agglomerates observed reaching thicknesses of around 50 nm. This was chosen to allow a variety of represented morphologies be studied by s-SNOM.

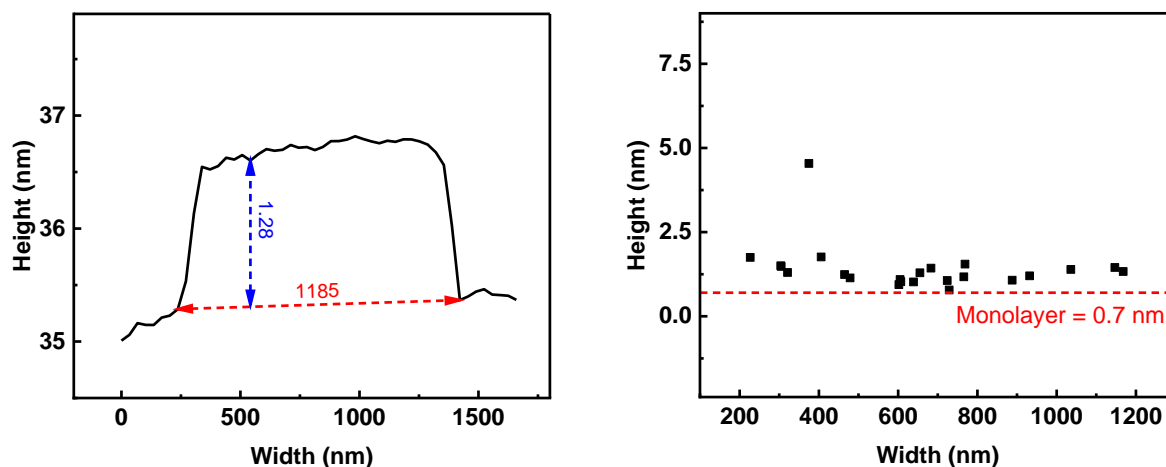


Figure 5.5 Example height profile measurement (left), and distribution of height/width measurements for the profiles in Figure 5.4 (right).

s-SNOM measurements were recorded to determine what, if any, differences in absorption could be identified between agglomerates and high aspect ratio nanosheets. Optical data were collected using a 650 nm excitation laser which is suitably absorbing by the Q-band absorption of Zn₂(TCPP), discussed in earlier chapters.

Figure 5.6 shows some examples of output data from s-SNOM over the same sample area as the AFM in Figure 5.4, with amplitude and phase data for the same scan shown. The light scattered and collected at the detector is processed so that the amplitude and phase of the signal wave are recorded relative to a reference signal. These data are useful to report separately because amplitude data is akin to the reflectivity of the sample, whilst the phase is more representative of the optical absorption by the sample at the excitation wavelength. Data is also recorded with different demodulation orders. Demodulation relates to the harmonic of the tapping frequency the optical data is recorded at. Higher demodulation orders have less background influence, and are more surface-sensitive, but generally suffer from more noise. As can be seen in the graph labelled O2A, several agglomerates are well defined, probably due to a scattering effect by the particles themselves. This is evidenced by the 'ripple' effect observed around these particles, where the light scattered around particles is also incident on the AFM tip so that depending on the distance of the agglomerate from the tip, the two light sources (i.e., the incident excitation beam on the tip, and the light scattered by particles back onto the tip) interfere constructively or destructively, resulting in the ripple pattern. The nanosheets, however, do not appear to give any signal. For a more in-depth analysis, further demodulation orders should be considered since they are less likely to be background influenced, but these figures serve to highlight that even at low demodulation, there is not enough material depth in nanosheet samples to be observed by this setup. Efforts to improve the sensitivity of the measurement by increasing laser power were abandoned due to observed degradation of the sample via AFM.

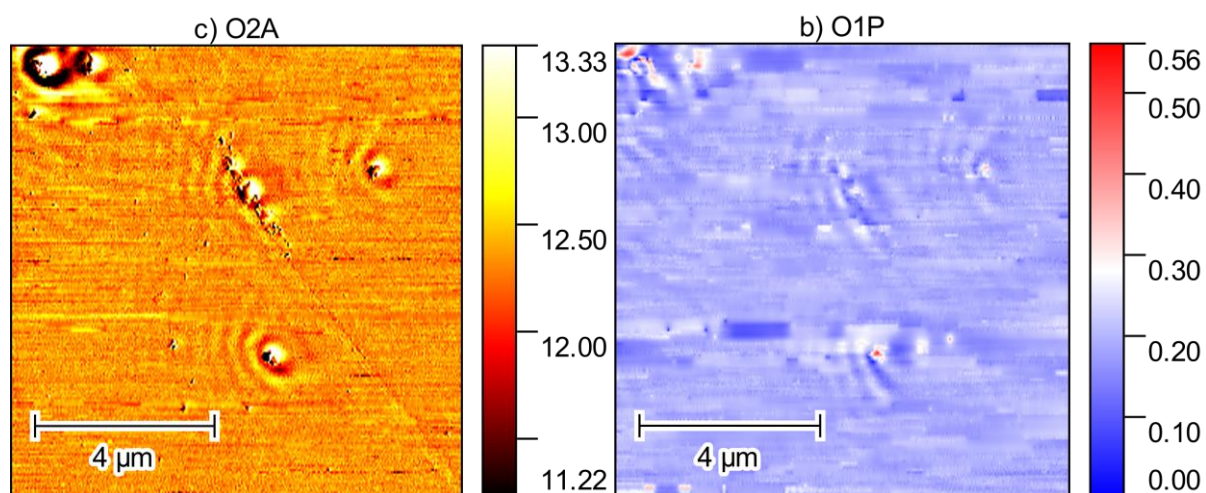


Figure 5.6 S-SNOM data for Zn-TCPP showing amplitude data with 2nd demodulation order O2A (left), and phase data with 1st demodulation order O1P (right).

Section 5.4 Photoluminescence NanoSpectroscopy

Previous chapters investigated the quenching effect of aggregation on photoluminescence (PL). The s-SNOM setup was modified to measure photoluminescence output focused onto a detector. Tip-incident lasers were used to excite the sample and measure emission spectra in-situ during an AFM scan. It should be noted that the resolution of these PL measurements was not tip-enhanced.

Samples of $Zn_2(TCPP)$ were deposited on mica and an area scouted by AFM before collecting PL data at different locations on the surface. As shown in Figure 5.7, intense PL was observed at 550 – 900 nm when the tip (and beam) was aligned onto an agglomerate. This was centred around 650 nm, with identifiable peaks at 620 and 720 nm. No emission was observed when the tip was moved to the edge of the mica substrate, however, when directed between agglomerates to areas which had no identifiable material via AFM, some PL was still observed. This was attributed to the excitation laser being scattered by the transparent, layered mica, causing incident light to hit agglomerates when not directly aligned to them.

The substrate was therefore exchanged for silicon and the samples re-measured. The amount of background scattering when measuring between agglomerates on silicon was much lower than for mica. However, some PL could still be detected when the acquisition time was increased to 60 s, indicating some scattering from the silicon surface still takes place.

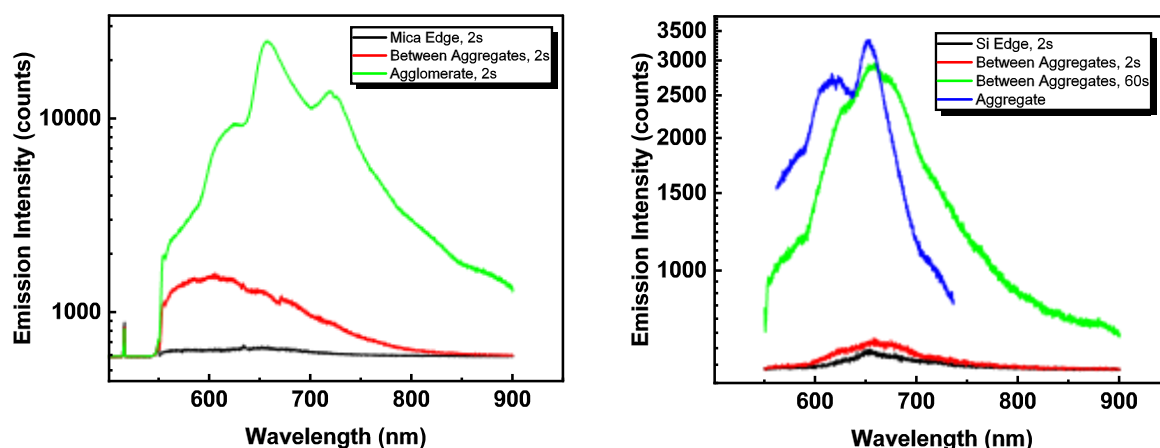


Figure 5.7 PL measurements from PL microscopy showing emission spectra for $Zn_2(TCPP)$ samples on mica (left), and silicon (right).

Since this measurement was not tip-enhanced, the expected resolution was much lower than AFM. As resolution was limited by beam spot size ($\sim 3.3 \mu\text{m}$), the problem of laser intensity arises. For example, a usual laser power on this setup would be 0.2 mW. This translates to $6,000,000 \text{ W m}^{-2}$, whilst the transient absorption setup used to measure the dispersion samples in previous chapters are on the order of 800 W m^{-2} . Given these high fluences, very short acquisition times were required in order to avoid damaging the sample.

By matching the spectra acquisition rate to the AFM scanning rate, a spectrum was acquired for each pixel of an AFM scan, allowing the spatial mapping of PL coincidentally with height measurements. Figure 5.8 shows the results of such a measurement recorded for an agglomerate of $Zn_2(TCPP)$ which is approximately $8 \mu\text{m}$ wide, and 150 nm thick at its highest point. Comparing the two graphs it can be visually determined that height generally correlates to PL intensity, although the shape of the particle is slightly different between the two. As a preliminary use of this setup, this is a reasonably successful reproduction. Longer experiments and improvements in data processing will also allow for more accurate spatial plotting of the PL data recorded. As for quantitatively assessing the PL output as a function of particle

thickness, this method cannot yet resolve individual nanosheets, so directly relating thickness by number of layers to PL intensity is not yet possible.

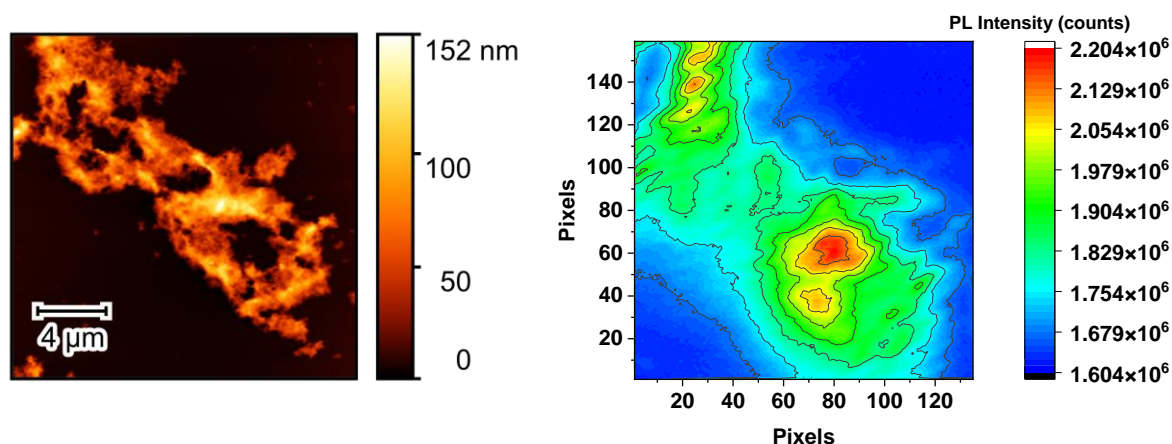


Figure 5.8 Concurrent PL acquisition and AFM scan of $Zn_2(TCPP)$ agglomerate on silicon with AFM data (left), and PL mapping (right).

Due to the resolution limit for the current setup (non-tip-enhanced PL measurement) it was not possible to measure the PL output of individual nanosheets. Not only can the shape of a nanosheet not be identified in the PL mapping scans (which would allow confirmation of PL output position), but contamination by surface scattering PL from agglomerates or nearby nanosheets is likely to overwhelm signal from individual nanosheets.

Consequently, an experiment was conducted to measure a single PL spectrum over the area of an entire AFM scan ($10 \mu m^2$). Since the beam spot of the excitation laser is measured at $\sim 3.3 \mu m$ diameter, AFM measurements were recorded for $10 \mu m^2$ areas, and the tip position aligned to the centre of the resultant micrograph before a 5 min scan (100 ms exposure, 300 frames averaged) of the PL output were recorded. Five sample areas (01, 02, 03, 04, 05) were randomly selected from different parts of the sample of $Zn_2(TCPP)$ on silicon. Sample areas 03 and 05 are shown in Figure 5.9 as an example of the differences in material coverage.

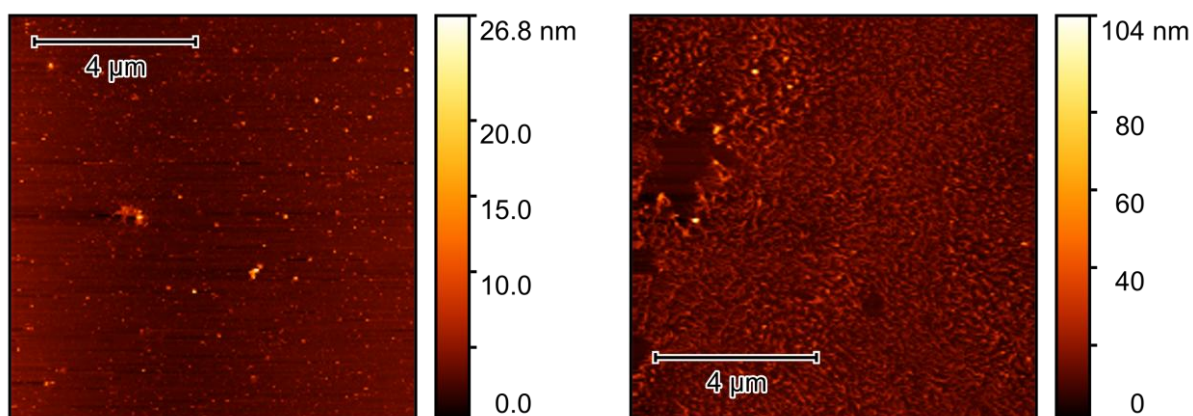


Figure 5.9 AFM scanning areas 03 (left), and 05 (right) of $Zn_2(TCPP)$ on silicon illustrating regions with low, and high loadings, respectively.

The spectra recorded for these areas are shown in Figure 5.10. Even with a 5 min acquisition time, most of the spectra lack definitive peaks due to the small amount of material present. Using the Gwyddion software statistical analysis tool, the average roughness of each AFM scan was calculated as a proxy for the amount of material present. The integrated area under baselined spectra were plotted against the mean roughness to determine the correlation, if any, between these parameters. As shown in Figure 5.10, right, there is a trend towards higher

area with greater roughness. It should be noted that area 01 is omitted in the fit based on an artifact in the AFM (see SI), anomalous spectral shape, and consequent anomalous data point.

Roughness is limited as an assessment of the average height of nanoparticles in an area, making this a fairly weak argument regarding the correlation between MON thickness and emission intensity, however, this may be a foundation for similar but better optimised experiments in the future. For example, sample areas with mainly monolayer, bilayer, or multilayer nanosheets could be found which could be scanned for more significant results.

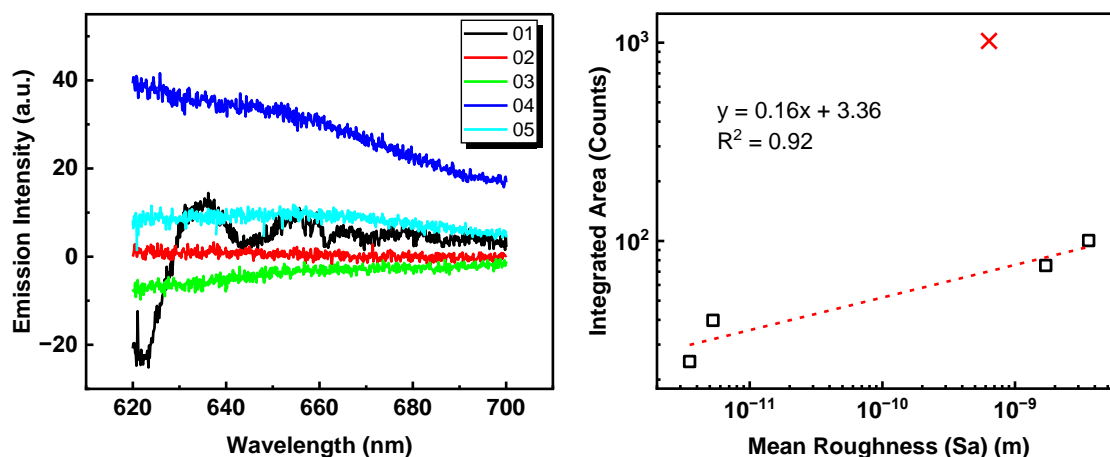


Figure 5.10 PL-AFM Spectra Baselined by their associated blank silicon measurements (left), and integration values plotted against mean roughness (right) for areas 01-05 between 620-700 nm. Data points marked with a cross are masked from the fitting.

Section 5.5 Conclusions

The metal organic framework nanosheet $Zn_2(TCPP)$ was investigated by s-SNOM to determine if it was possible to map absorption according to the morphology and thickness of isolated nanosheets. The experiment concluded that whilst the optical absorption of agglomerate clusters of material could be measured, the nanosheets approaching monolayer could not be resolved.

The s-SNOM setup was modified to perform tip-incident photoluminescence nanospectroscopy with the aim of spatially mapping photoluminescence output. The experiment produced an emission map resolving an $Zn_2(TCPP)$ agglomerate particle of 8 μm size which visually approximated the height mapped AFM graph of the same particle. Whilst a basic positive correlation was observed, this resolution is too poor for quantitative analysis of single nanosheet photoluminescence output but may be possible with optimisation/tip-enhanced measurements.

To explore the possibility of future experiments without improvements in resolution, an experiment was undertaken as proof of concept which recorded an emission spectrum approximately central to an AFM scan, which was subsequently performed. A tentative correlation was made between average statistical roughness from the AFM image and the emission intensity.

This work describes a foundation for experiments such as those described, which may be expanded on in the future.

Section 5.6 References

1. Wang, L. & Xu, X. G. Scattering-type scanning near-field optical microscopy with reconstruction of vertical interaction. *Nat Commun* **6**, (2015).
2. Möslein, A. F., Donà, L., Civalleri, B. & Tan, J. C. Defect Engineering in Metal-Organic Framework Nanocrystals: Implications for Mechanical Properties and Performance. *ACS Appl Nano Mater* **5**, 6398–6409 (2022).
3. Möslein, A. F., Gutiérrez, M., Cohen, B. & Tan, J. C. Near-Field Infrared Nanospectroscopy Reveals Guest Confinement in Metal-Organic Framework Single Crystals. *Nano Lett* **20**, 7446–7454 (2020).
4. Xu, Y., Sun, L., Ghiggino, K. P. & Smith, T. A. Resolving conjugated polymer film morphology with polarised transmission and time-resolved emission microscopy. *Methods Appl Fluoresc* **12**, (2024).

Section 5.7 Chapter 5 Supporting Information

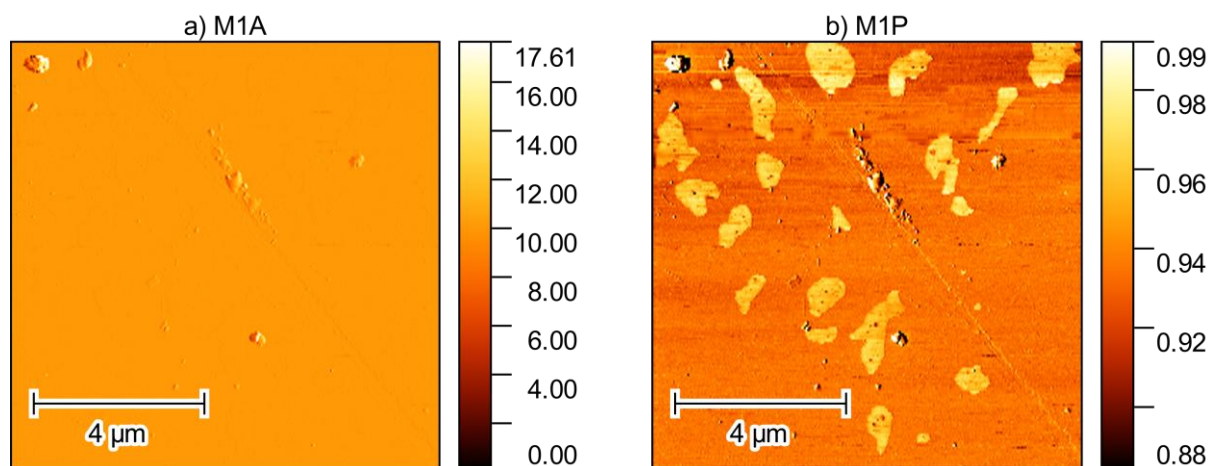


Figure S5.1 AFM Phase data with a) M1A and b) M1P

The PL is not enhanced by SNOM, so resolution should be $\sim 400\text{nm}$ rather than the SNOM enhanced absorption resolution of $\sim 20\text{nm}$. There is however still scope for an experiment where single particle emission is observed and thickness correlated to output, and also aggregate measurements taken over areas with many particles, where the average thickness can be measured by AFM and correlated the PL output per unit area.

Initial experiments involved optimisation of the system, so the laser was aligned onto an area of mica without optically visible MON present (no evidence in AFM either) to measure the baseline PL. Normal operating practice (NOP) in the SNOM experiments do not involve turning off room lights as laser systems are enclosed in dark boxes, but as seen in figure 24a, there is significant impact from the room lights on detected light. Iterative experiments measuring detected lights included turning off the main source lights, laser sources, and blocking the exit of the sample stage can be seen in figure 24b. These identified further detected light at 840nm as laser artefact, and at 560nm as bleed from an LED component in the camera used to monitor the sample stage during experimental setup.

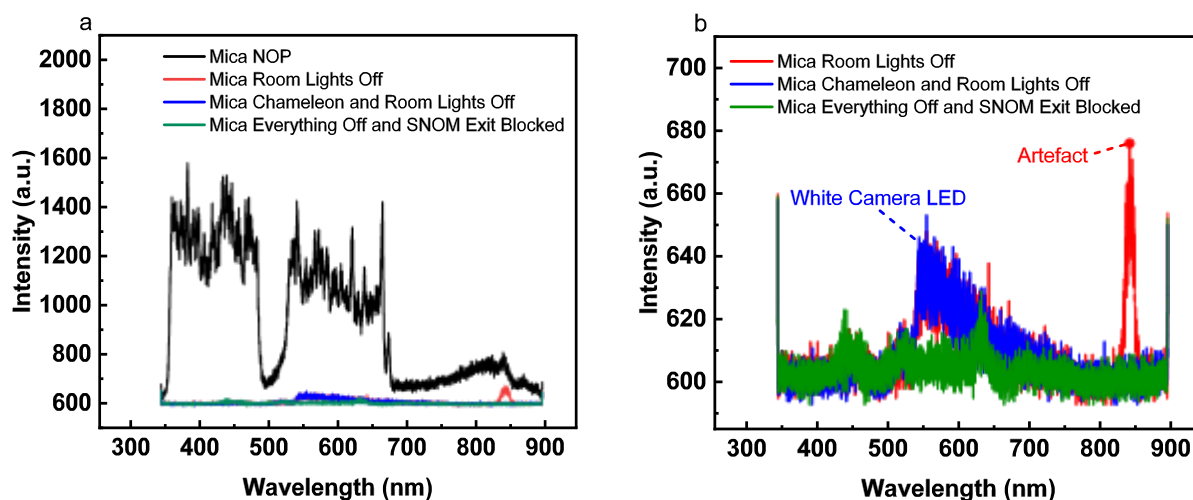


Figure S5.2 Photoluminescence output spectra measured on the surface of mica as baseline. a) Measurements under NOP conditions and below, and b) more stringent conditions turning off room lights, laser components, and blocking detector from SNOM sample stage.

Photoluminescence spectra appear centred at 550nm and are significantly greater than light contamination observed from room lights. The stage exit filter at 500nm is obviously cutting off part of the peak and should be replaced with a lower wavelength filter in future experiments.

The position of this emission is particularly interesting as the emission in dispersion is at 650 and 750nm, which are not observed here. It is possible we are observing red-shifted emission from S_2 , which occurs at 450nm in dispersion and is usually low intensity.

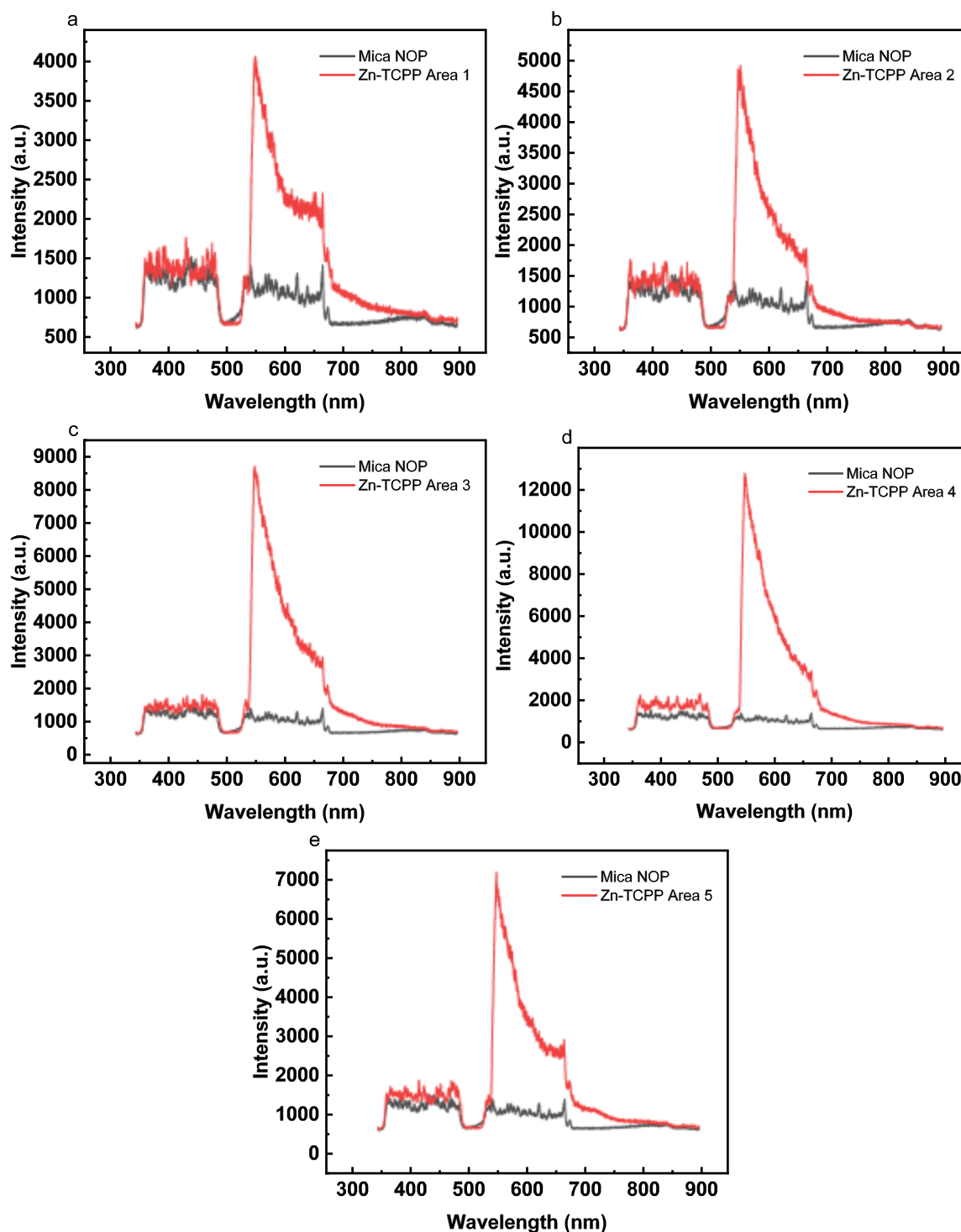


Figure S5.3 Photoluminescence spectra for Zn-TCPP on mica using the SNOM setup on different areas of samples 1-5 (a-e).

The PLS setup is realigned to move the PL beam up by 2cm. The issue of minimum periscope size being 4 cm was resolved by moving the beam up 4 cm with a periscope and then moving the detector up 2cm as well.

PL output is recorded as spectrum (beam aligned to tip) every 100ms with the number of scans taken to overlap with simultaneous AFM scan (figure 26). Data is processed by MATLAB code which takes the sum of all spectral data points as intensity of PL (z axis). 3D viewing of data shows a hump around central particle, but suspected alignment issues and beam size problems.

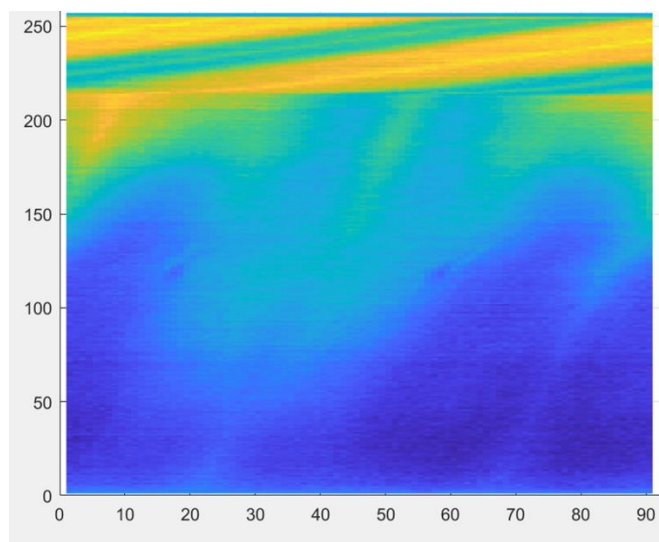


Figure S5.4 MATLAB processed data for PL output over 20 μ m scan. Axes are in pixels scanned.

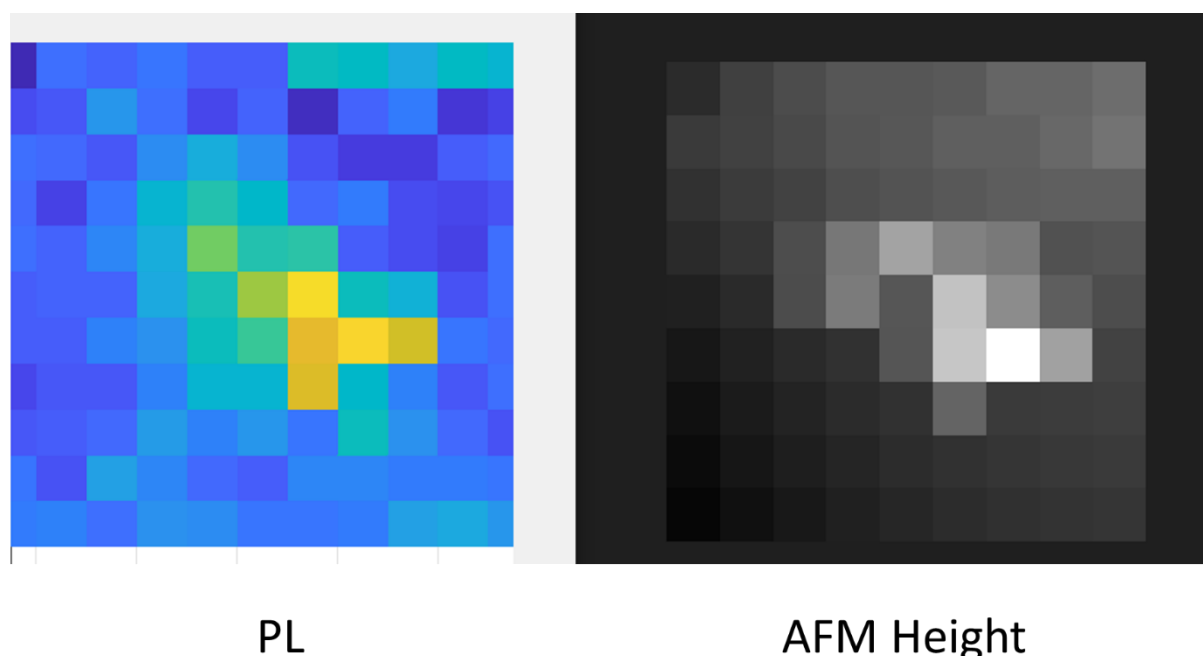


Figure S5.5 Low-resolution initial PL-AFM experiment on Zn₂(TCPP) cluster (30 μ m).

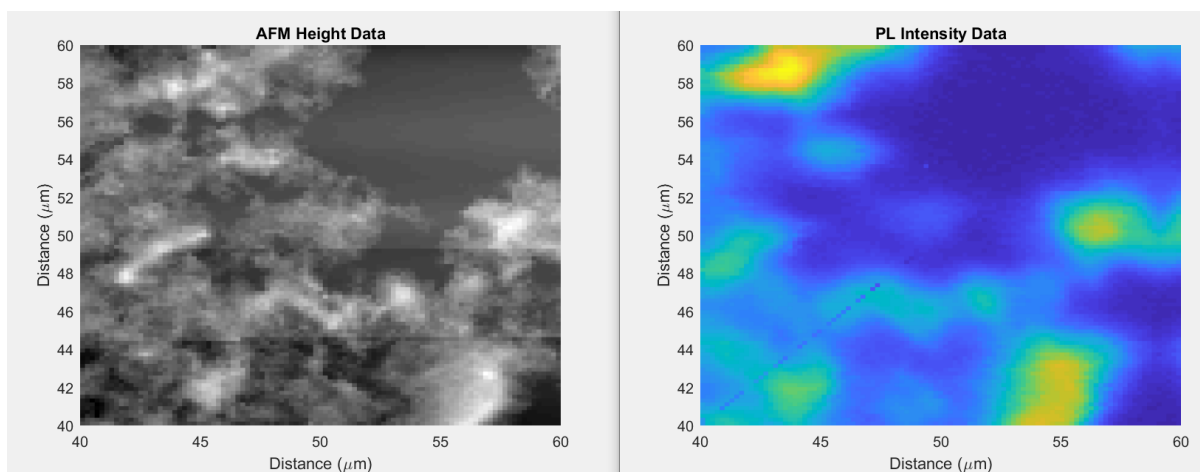


Figure S5.6 PL-AFM mapping of $Zn_2(TCPP)$ agglomerate

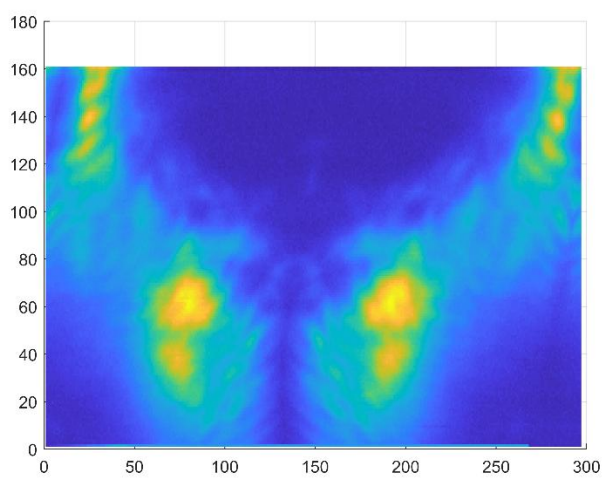


Figure S5.7 Mirroring effect from double scan

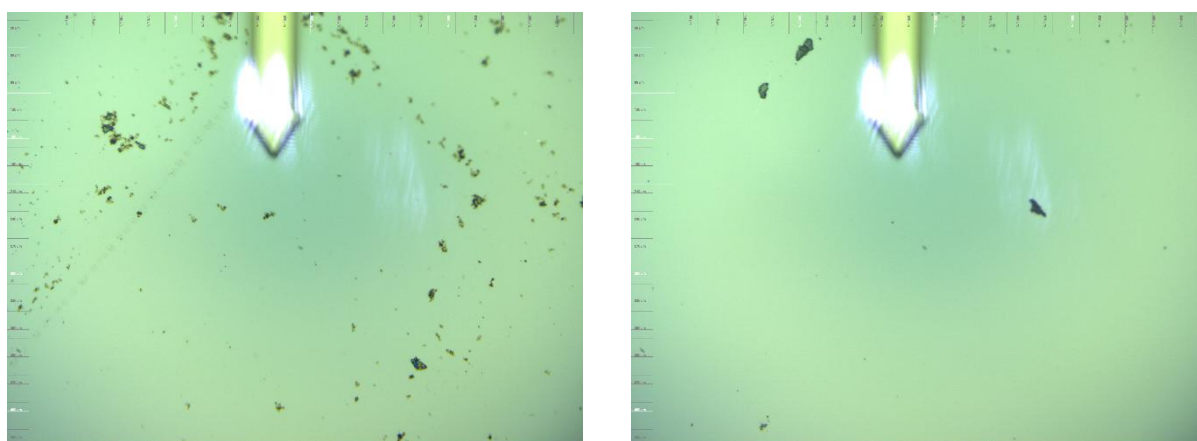


Figure S5.8 Scan 01 Optical microscope positioning of tip for concurrent PL and AFM measurements. Images are for dilute $Zn_2(TCPP)$ sample (left), and blank silicon background (right).

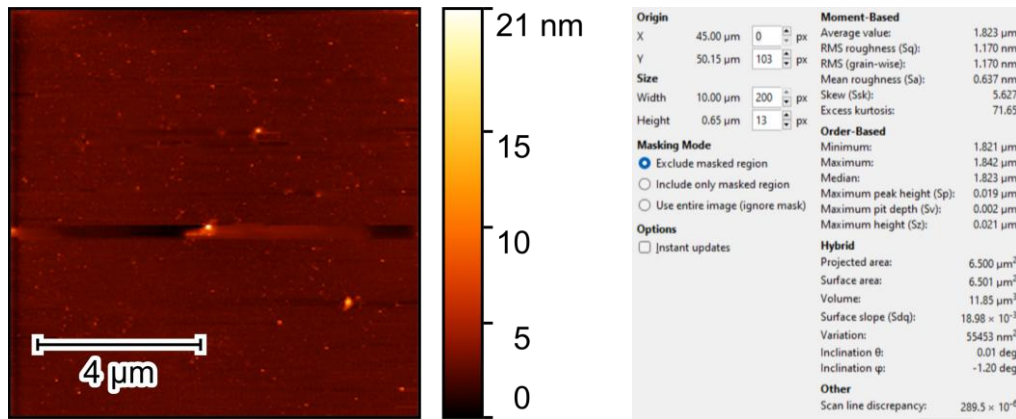


Figure S5.9 Scan 01 AFM micrograph (left) and Gwyddion statistical analysis of entire image excluding scar across centre (see Figure S5.10).

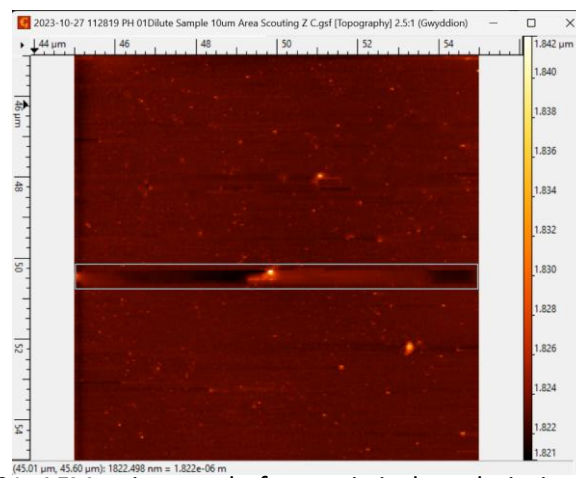
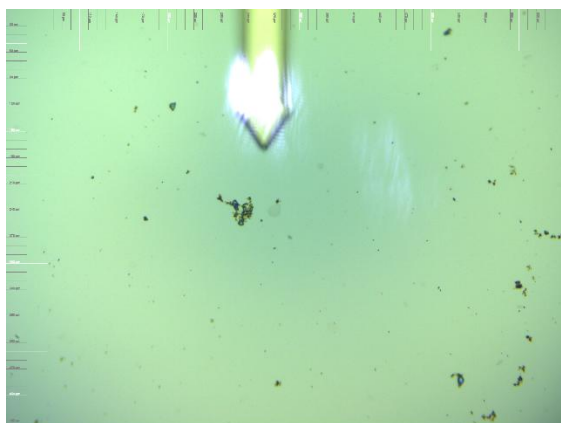


Figure S5.10 Scan 01 AFM micrograph for statistical analysis in Figure S5.9 with excluded masked region.



Origin		Moment-Based	
X	45.00 μm	Average value:	3.67 nm
Y	45.00 μm	RMS roughness (Sq):	866.4 μm
Size		RMS (grain-wise):	866.4 μm
Width	10.00 μm	Mean roughness (Sa):	352.9 μm
Height	10.00 μm	Skew (Ssk):	32.00
		Excess kurtosis:	1.719×10^3
Masking Mode		Order-Based	
<input type="radio"/> Exclude masked region <input type="radio"/> Include only masked region <input checked="" type="radio"/> Use entire image (ignore mask)		Minimum:	0.00 nm
Options		Maximum:	60.65 nm
<input type="checkbox"/> Instant updates		Median:	3.69 nm
		Maximum peak height (Sp):	56.98 nm
		Maximum pit depth (Sv):	3.67 nm
		Maximum height (Sz):	60.65 nm
Hybrid		Projected area:	$100.0 \mu\text{m}^2$
		Surface area:	$100.0 \mu\text{m}^2$
		Volume:	$0.3670 \mu\text{m}^3$
		Surface slope (Sdq):	22.58×10^{-3}
		Variation:	$0.8653 \mu\text{m}^2$
		Inclination θ :	0.00 deg
		Inclination ϕ :	-3.17 deg
Other		Scan line discrepancy:	0.1833

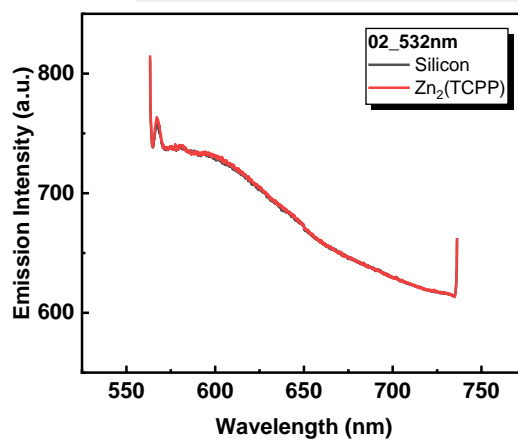
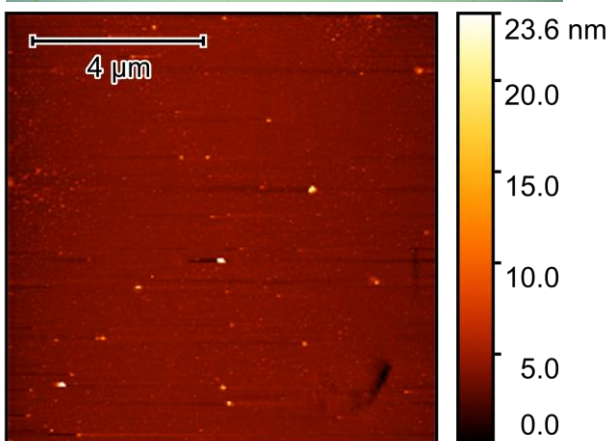
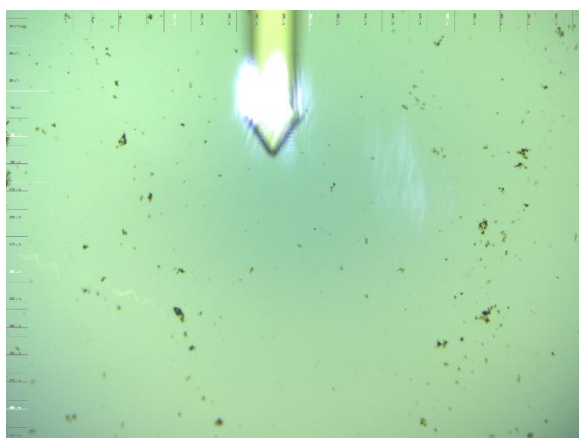


Figure S5.11 Scan 02 PL-AFM data for $\text{Zn}_2(\text{TCPP})$



Origin		Moment-Based	
X	45.00 μm	Average value:	2.87 nm
Y	45.00 μm	RMS roughness (Sq):	910.4 μm
Size		RMS (grain-wise):	910.4 μm
Width	10.00 μm	Mean roughness (Sa):	528.9 μm
Height	10.00 μm	Skew (Ssk):	6.228
		Excess kurtosis:	82.08
Masking Mode		Order-Based	
<input type="radio"/> Exclude masked region <input type="radio"/> Include only masked region <input checked="" type="radio"/> Use entire image (ignore mask)		Minimum:	0.00 nm
Options		Maximum:	27.03 nm
<input type="checkbox"/> Instant updates		Median:	2.73 nm
		Maximum peak height (Sp):	24.17 nm
		Maximum pit depth (Sv):	2.87 nm
		Maximum height (Sz):	27.03 nm
Hybrid		Projected area:	$100.0 \mu\text{m}^2$
		Surface area:	$100.0 \mu\text{m}^2$
		Volume:	$0.2866 \mu\text{m}^3$
		Surface slope (Sdq):	26.16×10^{-3}
		Variation:	$1.389 \mu\text{m}^2$
		Inclination θ :	0.01 deg
		Inclination ϕ :	0.13 deg
Other		Scan line discrepancy:	0.2709

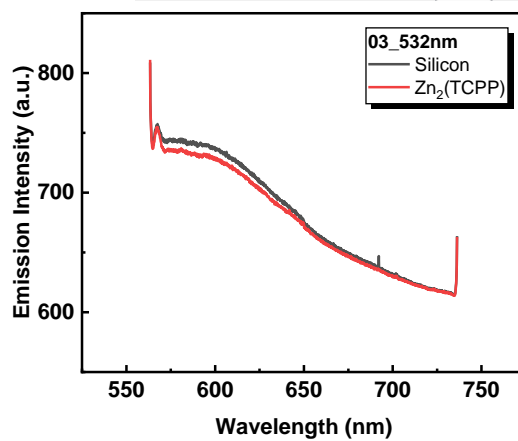
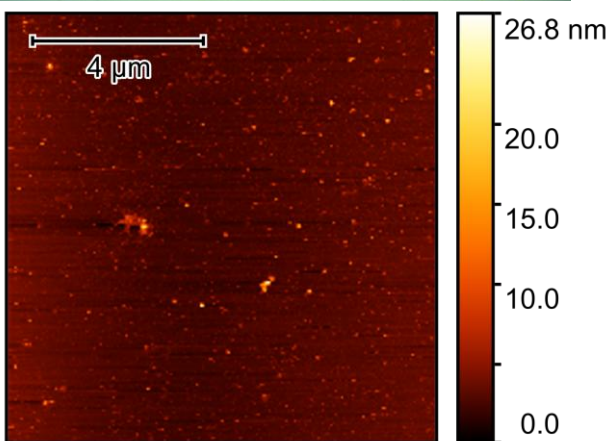


Figure S5.12 Scan 03 PL-AFM of $\text{Zn}_2(\text{TCPP})$

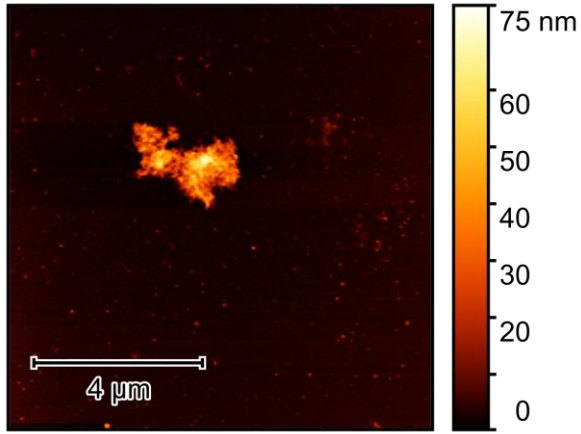
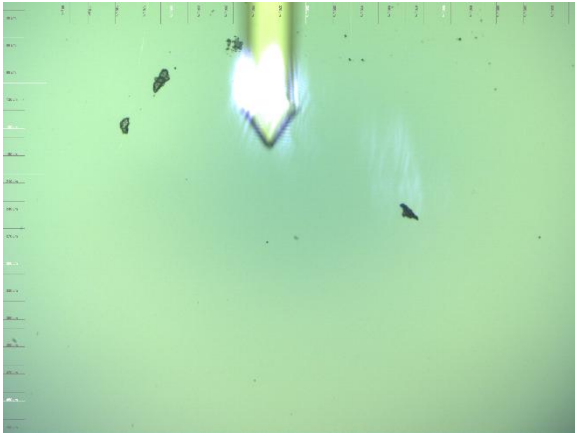
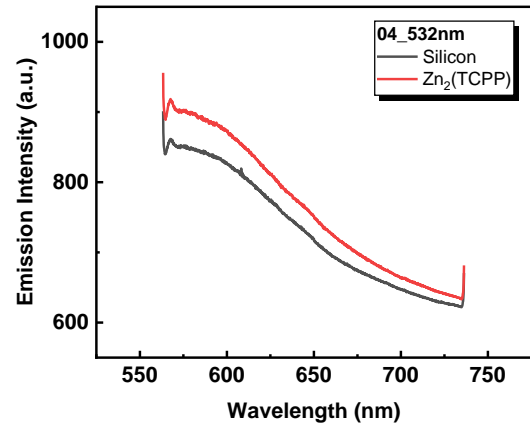
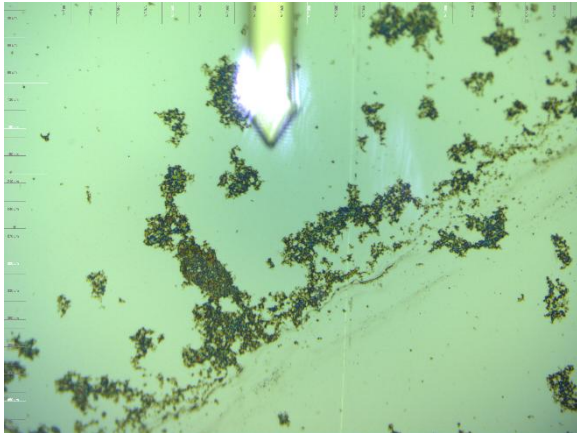


Figure S5.13 Scan 04 PL-AFM of Zn₂(TCPP)

Origin		Moment-Based	
X	45.00 μm	Average value:	3.45 nm
Y	45.00 μm	RMS roughness (Sq):	4.982 nm
		RMS (grain-wise):	4.982 nm
		Mean roughness (Sa):	1.705 nm
Size		Skew (Ssk):	7.042
Width	10.00 μm	Excess kurtosis:	56.16
Height	10.00 μm		
		Order-Based	
		Minimum:	0.00 nm
		Maximum:	75.27 nm
		Median:	2.59 nm
		Maximum peak height (Sp):	71.82 nm
		Maximum pit depth (Sp):	3.45 nm
		Maximum height (Sz):	75.27 nm
		Hybrid	
		Projected area:	100.0 μm^2
		Surface area:	100.1 μm^2
		Volume:	0.3452 μm^3
		Surface slope (Sdq):	0.05250
		Variation:	1.904 μm^2
		Inclination θ :	0.01 deg
		Inclination ϕ :	63.66 deg
		Other	
		Scan line discrepancy:	0.2375





Origin		Moment-Based	
X	38.34 μm	Average value:	11.8 nm
Y	43.60 μm	RMS roughness (Sq):	4.974 nm
Size		RMS (grain-wise):	4.974 nm
Width	10.00 μm	Mean roughness (Sa):	3.591 nm
Height	10.00 μm	Skew (Ssk):	2.672
		Excess kurtosis:	21.01
Masking Mode		Order-Based	
<input type="radio"/> Exclude masked region <input type="radio"/> Include only masked region <input checked="" type="radio"/> Use entire image (ignore mask)		Minimum:	0.0 nm
<input type="checkbox"/> Instant updates		Maximum:	104.8 nm
		Median:	10.7 nm
		Maximum peak height (Sp):	92.9 nm
		Maximum pit depth (Sp):	11.8 nm
		Maximum height (Sz):	104.8 nm
Options		Hybrid	
		Projected area:	100.0 μm^2
		Surface area:	100.9 μm^2
		Volume:	1.184 μm^3
		Surface slope (Sdq):	0.1506
		Variation:	11.77 μm^2
		Inclination θ :	0.00 deg
		Inclination ϕ :	-24.14 deg
Other		Scan line discrepancy:	0.3655

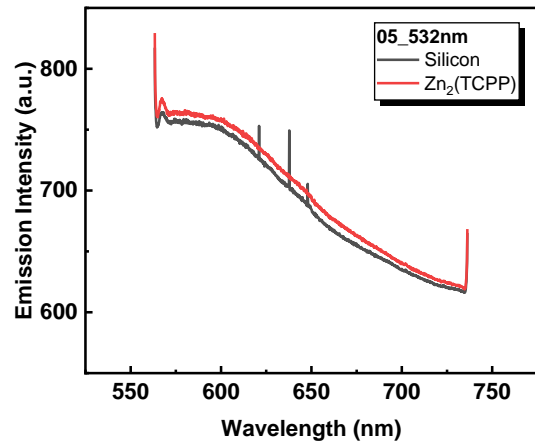
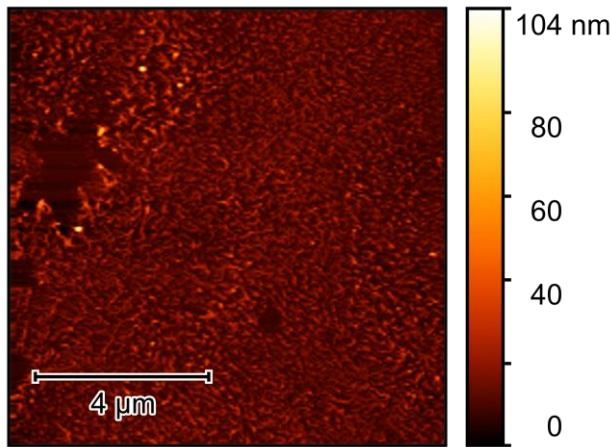


Figure S5.14 Scan 05 PL-AFM of Zn₂(TCPP)

A(X1)	B(X2)	C(X3)	D(X4)	E(X5)	F(X6)	G(X7)	H(Y7)
	Average Va	RMS Roug	RMS (Grain	Mean Roug	Variation	Variation	Integrated
	m	m	m	m	μm^2	m^2	
	Average Va	RMS rough	RMS (Grain	Mean Roug	Variation		
1	1.823E-6	1.17E-9	1.17E-9	6.37E-10	0.00555	5.543E-14	1019.932
2	3.67E-9	8.664E-12	8.664E-12	3.529E-12	0.8653	8.6E-13	24.64339
3	2.87E-9	9.104E-12	9.104E-12	5.289E-12	1.383	1.383E-12	39.73724
4	3.45E-9	4.982E-9	4.982E-9	1.705E-9	1.904	1.904E-12	75.17035
5	1.18E-8	4.974E-9	4.974E-9	3.591E-9	11.77	1.177E-11	100.41855

Figure S5.15 Statistics values from AFM data and integration area calculated for each area 01-05 after baselining to endpoints.

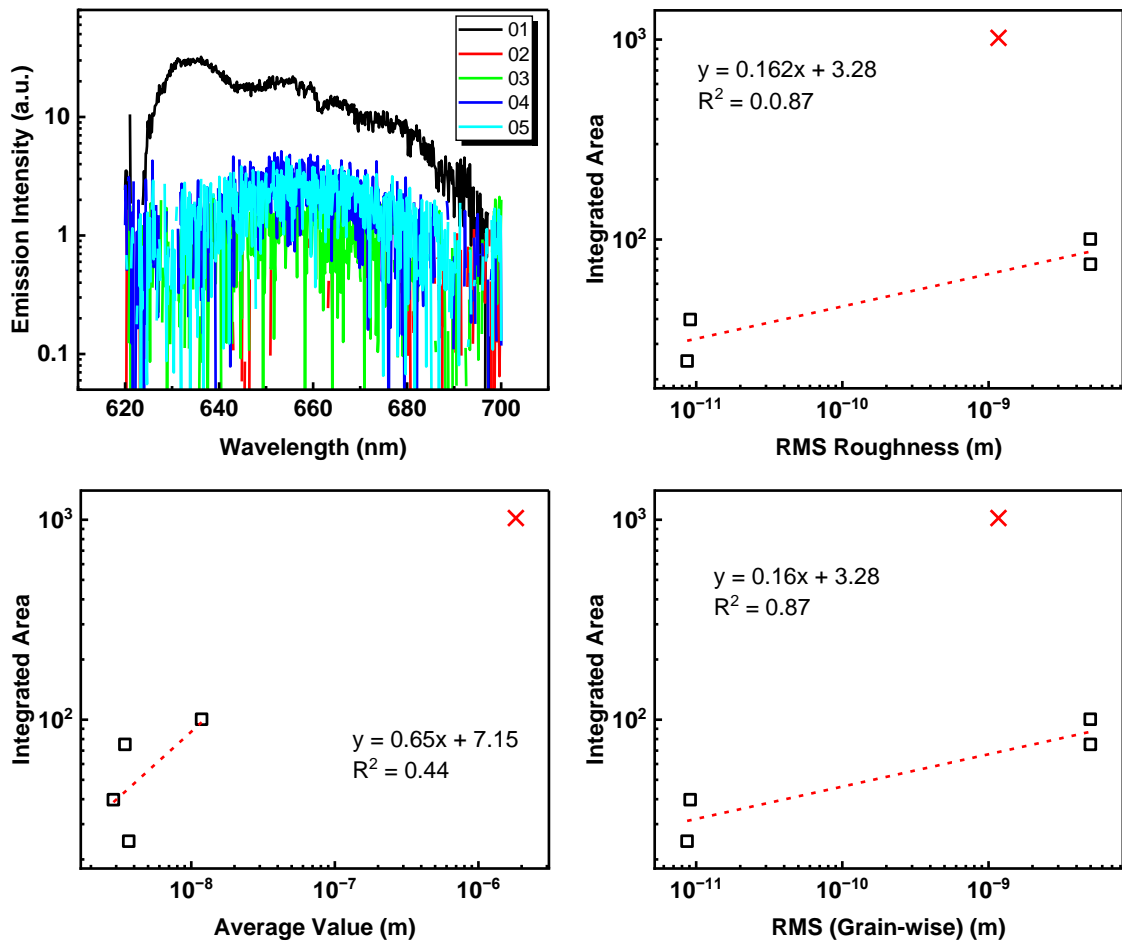


Figure S5.16 Baselined spectra for $Zn_2(TCPP)$ samples (top left), plotted integrated area of spectra vs. RMS roughness (top right), average value (bottom left), and RMS (grainwise) (bottom right)

Chapter 6:

Sensing for Phosphate Fertilisers using Functional Nanomaterials to Modify Graphene and other Carbon Electrodes

Section 6.1 Abstract

The detection and measurement of fertiliser species in soil is essential for reducing the use of critical materials and preventing loss of growth agents to the marine environment, which would cause ecological damage in the form of eutrophication. Developing sensors which can identify concentrations of specific fertilisers (phosphate, nitrate, potassium) without interference from others is key to the success of the technology as it allows specific distribution of each component. Phosphate specificity, however, proves to be problematic due to the size of this analyte preventing the use of size exclusion for selectivity.

High sensitivity can be achieved using carbon or graphene-based sensors, but other components are required to provide selectivity. Three distinct routes to adding selectivity for phosphate to graphene-based electrodes were therefore investigated. Firstly, a metal organic framework nanosheet (MON) was synthesised with the chemical structure $Zn_2(TCPP)(DMF)_2$, where TCPP = Tetrakis (4-carboxyphenyl) porphyrin and DMF = dimethylformamide. This was characterised spectroscopically and investigated as a modifier material in carbon electrodes. Secondly, a molecularly imprinted polymer (MIP) layer of polypyrrole was electropolymerized onto a graphene screen-printed electrode (G-SPE) surface. Lastly, an intrinsically electroactive crosslinked polymer nanoMIP was attached to either a G-SPE surface or a glassy carbon electrode surface via methods of drop casting, covalent attachment, or encapsulation in a polymer layer.

An electrochemical method, pulsed-voltage chronoamperometry, was employed in both MON and MIP modified electrode experiments to sense for ammonium phosphate. This involved the development of a novel data processing programme using code generated by ChatGPT.

The most promising technology identified in this work is established as the glassy carbon electrode (GCE) modified using electroactive MIPs encapsulated by a non-imprinted N-phenylethylene diamine methacrylamide (NPEDMA) polymer, which resulted in a high signal range correlation in ammonium phosphate concentrations $>10 \text{ mM} - 1 \text{ M}$. It was therefore concluded that this latter system had the most potential for future research.

Section 6.2 Introduction

Phosphate is widely used in agricultural fertiliser due to its essential role as a macronutrient for many biological processes, enhancing crop yield. Accessible sources of phosphate are finite, and phosphorus is designated as a critical element with resources mined from rock expected to be exhausted in the next 50-100 years based on current and projected usage.¹⁻³ Contrasting with this limited supply, overuse of fertilisers means that wastewater runoff from agricultural land has an increasingly detrimental effect on the environment via the process of eutrophication.^{2,3} This process involves the deoxygenation of waterways by overstimulated growth of algae, and the subsequent threat to marine life and associated ecosystems. Last year, it was reported that only 40-60% of agricultural phosphate was utilised by plants, with the remainder leached into the marine environment.⁴

The technology of real-time, remotely operated, in-situ sensors for accurate and selective measurement of fertiliser is highlighted in political and scientific discussions as a key tool in curtailing the environmental impact of agriculture via monitoring of nitrate, phosphate, and potassium content in soils.^{3,5-9} A variety of colorimetric sensors are available which aim to reduce the cost and time required for laboratory-based testing of soil samples, but these usually require specialist equipment or skilled hands-on processing, which does not promote uptake by farmers.² Electrochemical sensors are a popular candidate for a successful technology, able to record measurements with high resolution and the potential for digital readouts, simplifying the interpretation of results via wireless or continuous monitoring systems. This is in line with a research project funded by UKRI entitled "Signals in the Soil", which aims to deliver sustainable, resilient, and functional soils by using advances in sensor systems and modelling to transform existing capabilities in understanding the dynamic near-surface of soils.¹⁰

Two-dimensional materials are popular for sensing applications due to their increased sensitivity from high surface area. Graphene is particularly prevalent in electrochemical research for its enhanced electrical properties of low charge transfer resistance, large potential window, and environmental stability.² However, the adoption of this material in sensing is limited by the lack of selectivity of the carbon surface, and the cost of high-quality large-scale, reproducible graphene manufacturing. The latter issue has been improved in recent years due to the availability of relatively inexpensive graphene inks allowing the use of established mass market processes to be used in the manufacturing of graphene electrodes, particularly inkjet or screen-printing.¹¹

The emerging field of metal organic framework nanosheets (MONs) combines the two-dimensional nature of graphene with the tunability and modular chemistry of metal organic frameworks, a class of porous material constructed from rigid organic linkers bridging metal centres.¹² These materials have found success in recent years in sensing applications due to their high external specific surface area, and the possibility for the selectivity of these materials to be tailored via their tunable chemistry.¹³ Analytes of interest have varied from metal ions, dyes, anionic pollutants, and biological samples.¹⁴⁻²²

In particular, the porphyrin-based MON, $Zn_2(TCPP)$, where TCPP = tetrakis (4-carboxyphenyl) porphyrin, has been extensively studied as a sensing material due to its ease of synthesis, and photophysical properties sensitive to the chemical environment.^{13,14,16,21,23-25} Given the success of $Zn_2(TCPP)$ as a sensing modifier, this chapter investigates its use for the modification of graphene electrodes, for the purpose of increasing their electrochemical sensitivity to phosphate in aqueous media.

Another avenue is of interest due to the work by Atayi et al., which investigates the formation of hydrogen phosphate anion imprinted molecularly imprinted polymers (MIPs).²⁶ MIPs are an especially promising technology for sensing applications, where biomimetic nanoparticles are designed to have a high selective affinity for analytes by the self-assembled formation of crosslinked polymer matrices around a template molecule, which can then be removed to expose a chemically and structurally specific cavity, equivalent to a biological recognition site e.g., in an enzyme.²⁷ These materials improve on the high selectivity of biological sensing materials, with the advantages of long-term stability and improved operating temperature, pH, and pressure ranges.

Sensing of inorganic phosphate using MIPs is reportedly difficult due to the poor interaction between functional monomers and small anions.²⁶ Literature by Canfarotta et al.²⁸, Ratautaite et al.²⁹, and Lach et al.³⁰ outline advancements in nanoMIP formation by solid-phase synthesis, hybridisation of MIPs with graphene, and electroactive monomer selection, respectively. Combined, these three techniques represent an opportunity to advance the sensitivity and selectivity of MIPs for phosphate sensing.

An inexpensive screen-printed graphene electrode (G-SPE) produced in collaboration with Professor Craig Banks, Manchester Metropolitan University (MMU), was used for much of the work to explore the possibility of producing these at scale for mass market. This thesis chapter explores the use of both MONs and MIPs as sensing elements for detecting phosphate within carbon-based electrochemical sensors. This would be achieved by the fabrication of materials for the modification of carbon-based electrodes such as these G-SPEs, exploring several methods for modification. The chapter firstly characterises the $Zn_2(TCPP)$ MONs spectroscopically to determine the effects of chemical environment changes, before exploring electrochemical methods of sensing such as cyclic voltammetry, chronopotentiometry, or chronoamperometry. Two phosphate-templated MIPs will then be synthesised and characterised electrochemically for their selectivity to phosphate, with several binding methods to the carbon support investigated.

Section 6.3 Sensing using Zn₂(TCPP) MONs

Spectroscopy

The synthesis and spectroscopy of Zn₂(TCPP) MONs with changes to morphology or structure is discussed in previous chapters, but little has been covered regarding the effects of external chemical environment on the optical properties of these materials. Investigating the effects of changes in chemical environment to the spectroscopic properties of Zn₂(TCPP) MONs is key to identifying possible methods of detection, as well as helping to understand the mechanisms of interaction between Zn₂(TCPP) and analyte.

Phosphoric acid was used to investigate Zn₂(TCPP) in dispersion to identify the effect on the spectroscopic properties of the MON. The phosphate species present vary at different acidity, so the interaction of phosphate with Zn₂(TCPP) across a range of concentrations is of interest.³ A suspension of Zn₂(TCPP) was acidified with different concentrations of phosphoric acid and the pH measured. The colour gradient observed ranged from purple to green with increasing concentrations of phosphoric acid, as shown in figure 2.

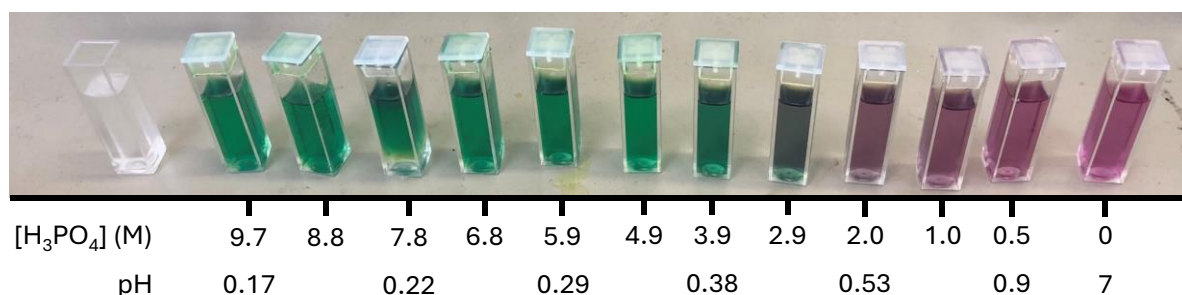


Figure 6.1 Colour change for Zn₂(TCPP) at different concentrations of H₃PO₄.

The colour change can be explained by UV-visible spectroscopic analysis of the Soret absorption band at ~425 nm by Zn₂(TCPP), responsible for the electronic transition S₀-S₂. This absorption is redshifted in the freebase linker in solution compared to the Zn₂(TCPP) MON in suspension due to the j-aggregation of dye moieties held in close proximity.³¹⁻³³ Upon acidification, further redshift can be observed due to the protonation of the porphyrin centre of the structure as seen in Figure 6.3, where proton repulsion within the cavity distorts the porphyrin moiety from planarity (discussed more fully in chapter 3).³⁴

The position of the Soret band can therefore provide information about the porphyrin, so an electronic absorption measurement was carried out by UV-visible spectroscopy of Zn₂(TCPP) samples, shown in Figure 6.2. Here, suspended Zn₂(TCPP) nanosheets were diluted using ethanol/acidified water mixtures to retain constant ethanol/water content, whilst increasing H₃PO₄ concentration. The position of the Soret peak at 0M H₃PO₄ is initially at 425 nm but reduces in wavelength upon acidification 2-3M so that the entire absorption is at 416 nm, suggesting complete digestion to the TCPP linker. Upon further acidification, an absorption at 440 nm is observed to be increasing with acid concentration, suggesting an increasing proportion of H₂TCPP is being protonated to H₄TCPP.

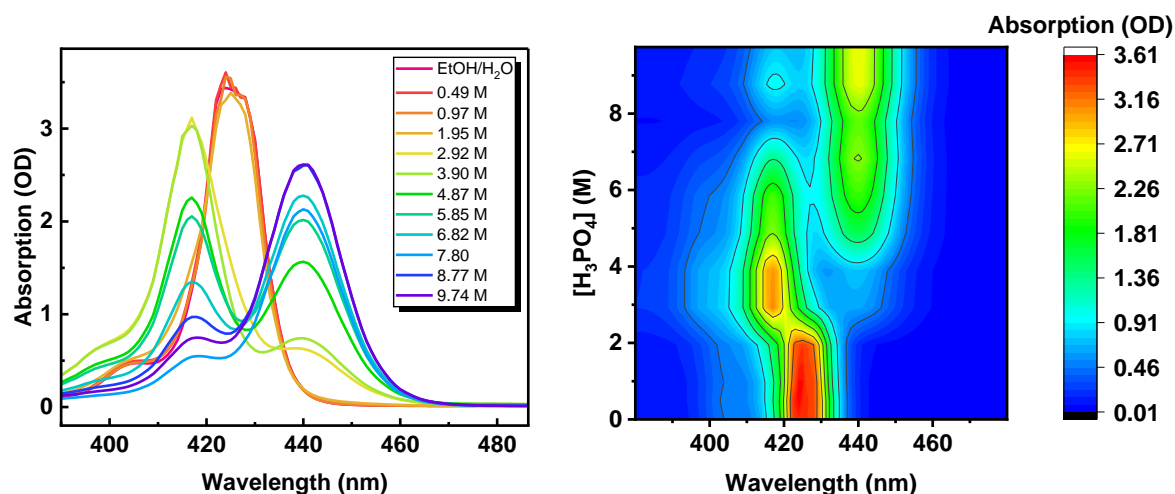


Figure 6.2 Soret band electronic absorption changes with increasing concentration of H_3PO_4 .

The effect of pH on Soret absorption position can be related to the different structures shown in Figure 6.3. At $<2 \text{ M H}_3\text{PO}_4$, $\text{Zn}_2(\text{TCPP})$ is stable as a MON with two central porphyrin protons. Above $2 \text{ M H}_3\text{PO}_4$, the MON is protonated at the carboxylic acid groups, digesting the nanosheet and reforming freebase H_2TCPP linker with two central protons. Above $5 \text{ M H}_3\text{PO}_4$ the central porphyrin cavity of TCPP is protonated to form H_4TCPP .

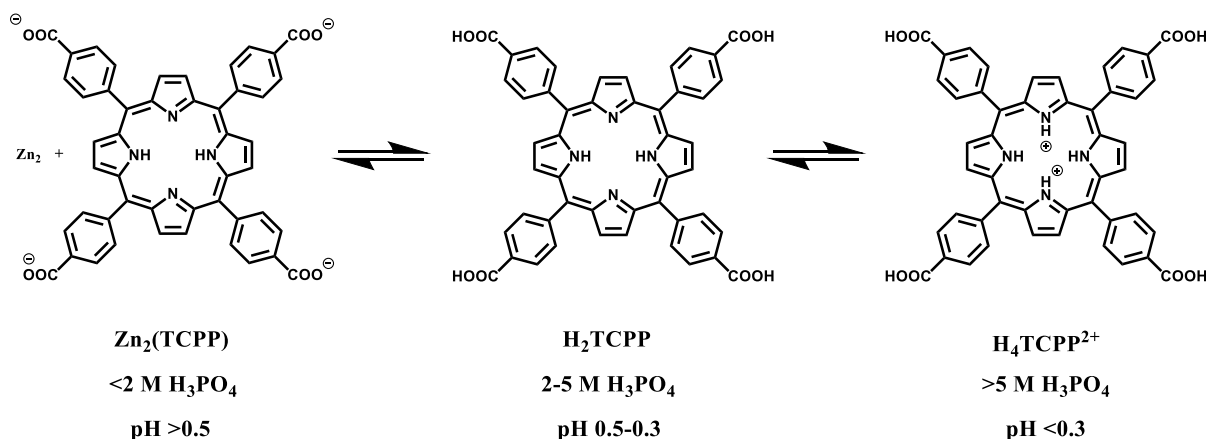


Figure 6.3 Possible protonation structures of the TCPP moiety.^{31,34}

The changes in protonation can also be tracked in the position and intensity of the Q-bands, responsible for electronic transitions from the ground state to the singlet S_1 , the number of which are determined by the symmetry across the porphyrin centre.^{33,35} Briefly, a bi-protonated H_2 porphyrin centre has two planes of symmetry across the central cavity in the x and y direction, each responsible for a different extinction coefficient. The S_1 state is therefore split into two S_1 absorptions x and y, known conventionally as Q_x , and Q_y . Excitation from the vibrationally excited ground state allows further splitting of each peak to yield the paired absorptions $\text{Q}_x(0,0)$ and $\text{Q}_x(1,0)$, and $\text{Q}_y(0,0)$ and $\text{Q}_y(1,0)$.

The Q-band absorption spectra in the region 460-750 nm is shown for the H_3PO_4 titration onto $\text{Zn}_2(\text{TCPP})$ in Figure 6.4. At pH 0, where $\text{Zn}_2(\text{TCPP})$ is stable, there are two major absorbances at 555 and 595 nm, due to the $\text{Q}_y(0,0)$ and $\text{Q}_x(1,0)$ bands respectively. Upon acidification to $3 \text{ M H}_3\text{PO}_4$, a dramatic shift to low intensity is observed for the central bands, and the satellite peaks for $\text{Q}_y(1,0)$ at 520 nm and $\text{Q}_x(0,0)$ at 645 nm are increased in intensity as the TCPP is reformed. The $\text{Q}_y(1,0)$ peak, however, is lost as acidification continues, since the proportion of H_4 Porphyrin is increasing with pH and $\text{Q}_x(0,0)$ character becomes dominant.

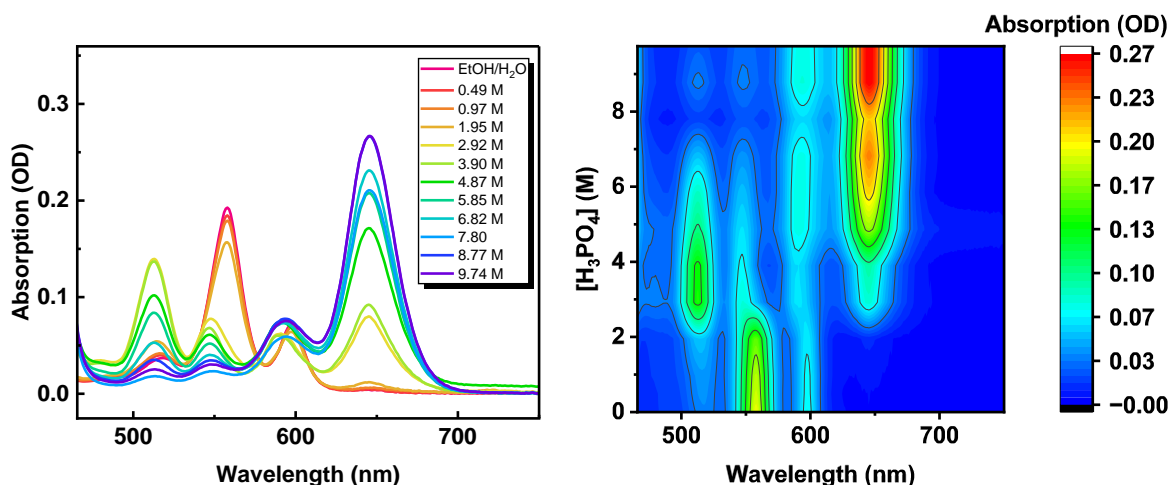


Figure 6.4 Electronic absorption Q-band changes for $Zn_2(TCPP)$ with increasing H_3PO_4 concentration.

A titration of H_3PO_4 concentrations <5 mM was used to determine the effect on emission intensity of $Zn_2(TCPP)$. Between 0.1-0.2 mM H_3PO_4 an increase in emission from S_1 (580-750 nm) is observed. S_1 emission from free TCPP linker is characterised by two very intense peaks 650 nm and 750 nm which are not seen increasing in this case. Given this and the stability of the MON at concentrations of phosphoric acid <2 M determined via the absorption experiment, it can be assumed that this is not due to acid degradation $Zn_2(TCPP) \rightarrow H_2TCPP$. This suggests a quenching mechanism that exists in $Zn_2(TCPP)$ is being removed. As such, the explanation for this change is probably also due to chemical environment changes at the porphyrin centre, possibly from partial metalation at the porphyrin centre leftover from synthesis which is being removed (similarly discussed in chapter 4)

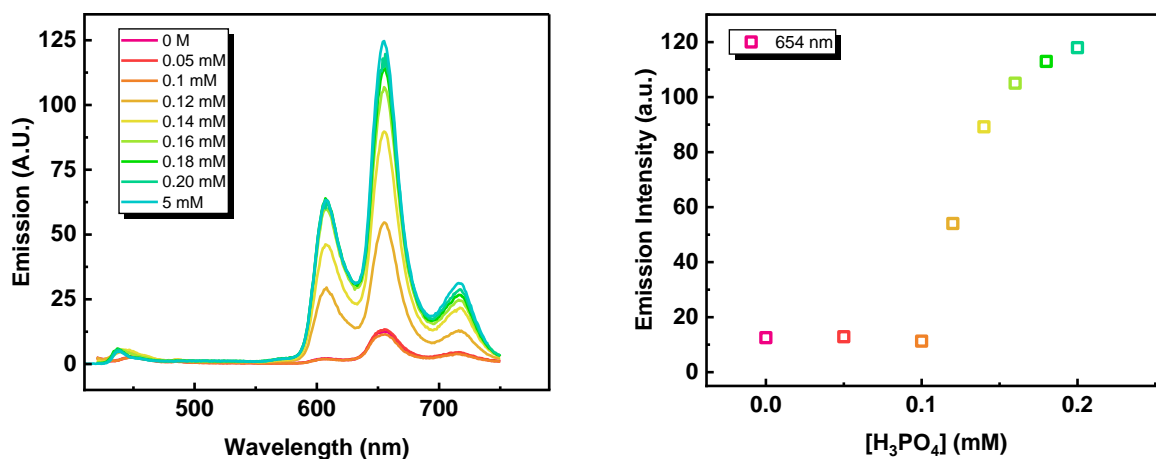


Figure 6.5 Emission spectra of $Zn_2(TCPP)$ with changing H_3PO_4 concentration (left), and emission intensity at 654 nm (right).

The sensitivity to pH of $Zn_2(TCPP)$ allows it to be used as a colorimetric or emission-based sensor for phosphoric acid, with a workable sensing range 0.1 to 0.2 mM. This is quite constrained compared to the expected ranges observed in soil (typically nanomolar to micromolar), and there are more effective means of measuring pH available.^{3,14,36} Methods which measure the concentration based on anion interactions are required for the specificity needed in soil measurement applications, and also a colorimetric sensor is not ideal for remote or automated measurements. As such, electrochemical sensing was pursued as a technique of interest in further studies.

Electrochemical Sensing

In collaboration with Professor Craig Banks at Manchester Metropolitan University, graphene screen printed electrodes (G-SPEs) were modified during the printing process to contain $Zn_2(TCPP)$ throughout the working electrode layer. These $Zn_2(TCPP)$ -G-SPEs were formed as batch produced, three electrode units containing modified graphene working electrode, graphene counter electrode, and an Ag/AgCl reference electrode (Figure 6.6). Existing three-electrode G-SPEs were modified by screen-printing a new layer over the working electrode using graphene ink mixed with dry $Zn_2(TCPP)$.

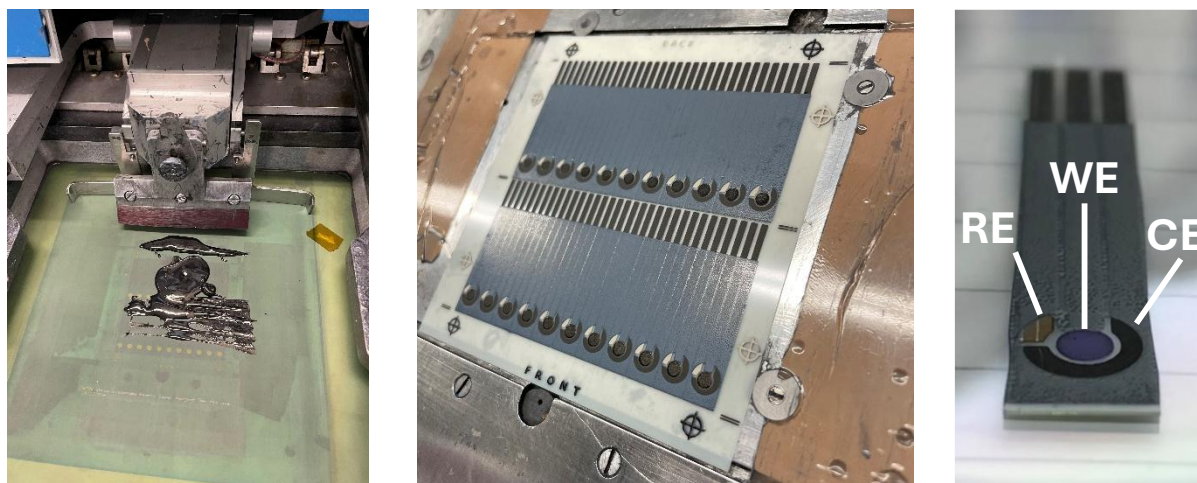


Figure 6.6 Screen printing of graphene SPEs with doctor blade printing setup (left), printed electrodes during drying (middle), and labelled SPE (right) with working electrode (WE), reference electrode (RE), and counter electrode (CE).

To investigate the morphology of graphene and $Zn_2(TCPP)$ modified G-SPEs, scanning electron microscopy (SEM) was employed to image the working electrode surface. As seen in Figure 6.7, $Zn_2(TCPP)$ -G-SPEs show a rougher surface than in the unmodified sample, with energy dispersive spectroscopy (EDS) identifying the presence of 0.6% zinc on the surface. This implies a successful modification of G-SPEs by $Zn_2(TCPP)$. The dispersion of zinc on the surface measured by EDS is non-uniform, indicating some aggregation during the printing process.

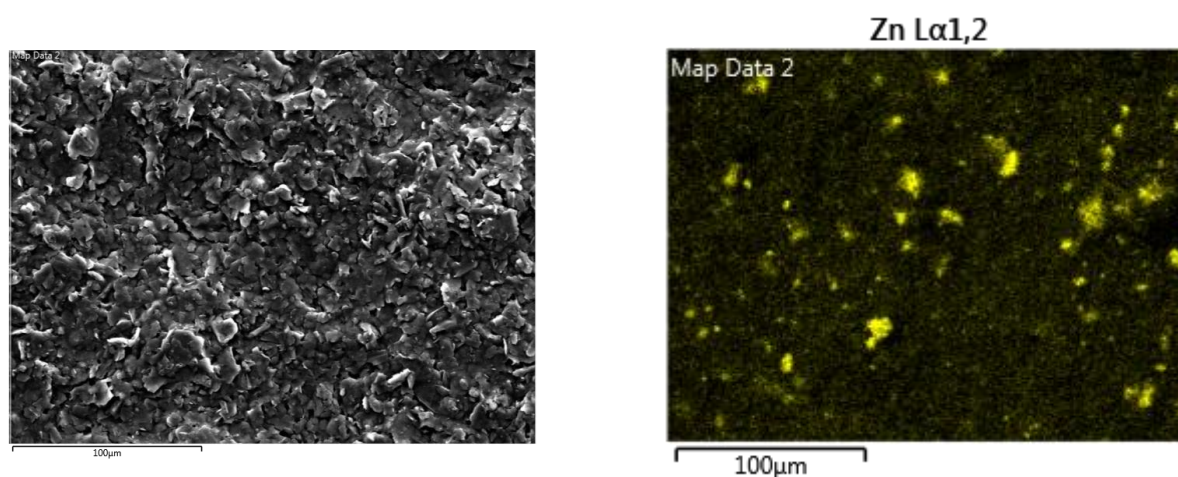


Figure 6.7 Scanning electron micrographs of $Zn_2(TCPP)$ -G-SPEs with normal (left), and energy dispersive spectroscopy filter for zinc (right).

Cyclic Voltammetry

Cyclic voltammetry can be a valuable technique for measuring the electrochemical redox reactions occurring in a cell. To determine the effect of repeat scans using the same electrode, the same $Zn_2(TCPP)$ -G-SPE was used to repeat a CV scan 100 times in 0.1 M phosphate buffered saline (PBS) and 0.5 M KCl (Figure 6.8). Significant redox activity was observed in the first scan, with two oxidation peaks at 0.6 and 0.8 V, and a single comparable reduction peak at 0.54 V, which are likely to be occurring on the Zn^{2+} ions in the metal organic structure. Additionally, a large reduction peak is observed at -0.72 V, which is assigned to water splitting as it has no equivalent oxidation peak. A significant drop-off in signal intensity was observed with subsequent scans, with oxidation peaks disappearing after only 25 scans. It can therefore be concluded that adding $Zn_2(TCPP)$ to graphene ink before screen-printing can introduce redox activity, although this is not stable and peak intensity reductions indicate some degradation of the electrode.

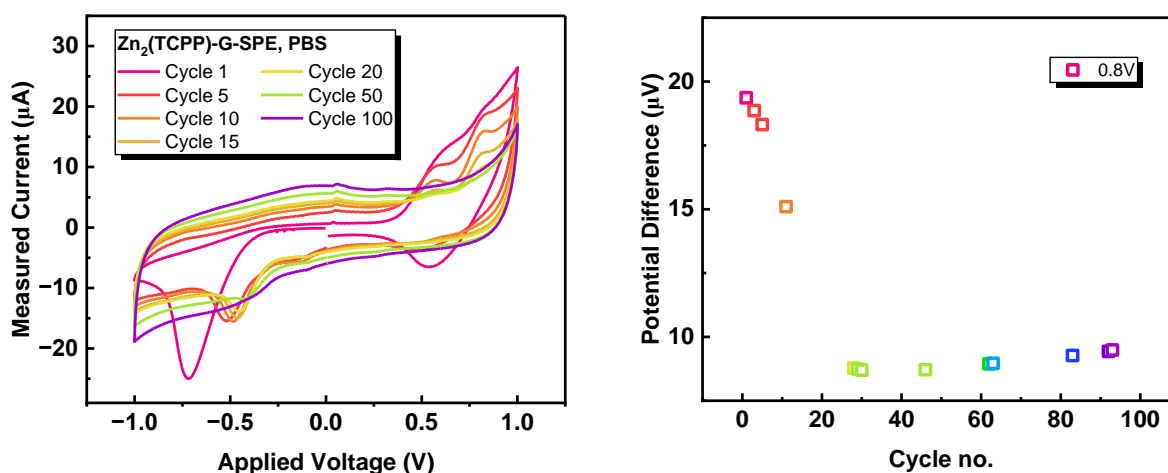


Figure 6.8 Cyclic voltammetry cycle testing for $Zn_2(TCPP)$ -G-SPEs at 0.1 V s^{-1} .

To identify any changes upon addition of ammonium phosphate to redox activity recorded using G-SPEs and a fresh $Zn_2(TCPP)$ -G-SPEs, cyclic voltammograms (CVs) were recorded using each electrode in different concentrations of ammonium phosphate, with no electrolyte (Figure 6.9). No redox peaks were observed when bare graphene electrodes were used, consistent with the absence of any redox active species. Meanwhile, the $Zn_2(TCPP)$ -G-SPEs consistently showed current ranges $\pm 40 \mu\text{A}$, whereas the G-SPEs showed ranges $\pm 2 \mu\text{A}$, although this may just be variation in the electrodes from the production processes.

The intensity changes due to phosphate concentration for the G-SPE measurements are likely due to increasing concentration of ammonium phosphate salt in the cell, which without electrolyte will have a large effect on cell conductivity. Electrodes containing $Zn_2(TCPP)$ showed redox activity even in DI water, with an oxidation peak at 0.55 V and a complementary reduction peak at 0.38 V (Figure 6.9). Measurements were taken as five repeat scans, and it was commonly observed that subsequent scans showed decreasing redox intensity. The redox peak intensity of the $Zn_2(TCPP)$ -G-SPE CVs could not be determined to change with ammonium phosphate concentration, and the position of the redox peaks does not correlate with ammonium phosphate concentration.

It is concluded that cyclic voltammetry is unsuitable for ammonium phosphate sensing as the degradation from redox reactions are too damaging to the electrodes, which cannot withstand multiple measurements. There is potential for an application of single-use electrodes, but this would require consistent signal between different G-SPEs at the point of printing.

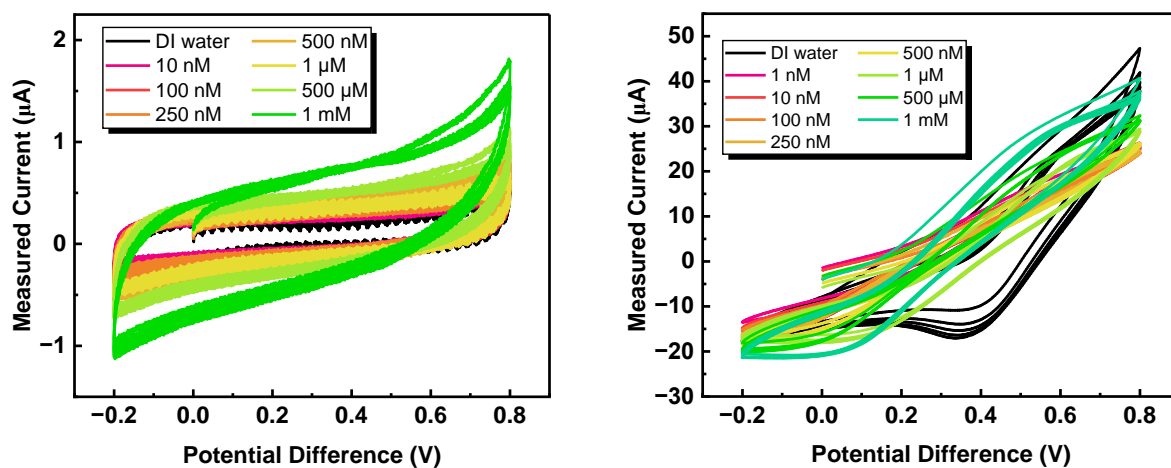


Figure 6.9 Cyclic voltammograms comparing ammonium phosphate titrations using G-SPE (left), and Zn₂(TCPP)-G-SPE (right).

Chronopotentiometry

Chronopotentiometry, the measurement of voltage over time, was previously used by Atayari et al. to electrochemically sense for phosphate.²⁶ To test this technique as a sensor using the G-SPE and Zn₂(TCPP)-G-SPEs, chronopotentiometry was performed over 10 mins in different concentration solutions of ammonium phosphate (no electrolyte). The recorded voltage reached equilibrium during this time, with the final voltage proving to be reliably dependant on analyte concentration (Figure 6.10-Figure 6.11).

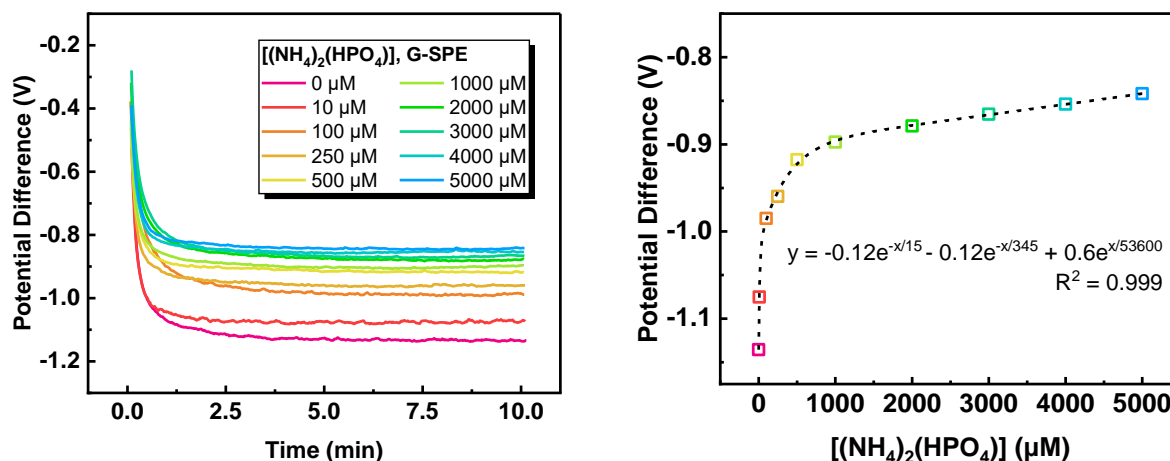


Figure 6.10 Chronopotentiometry over 10s of aqueous ammonium phosphate solutions using a G-SPE (left), and final voltages plotted against ammonium phosphate concentration (right).

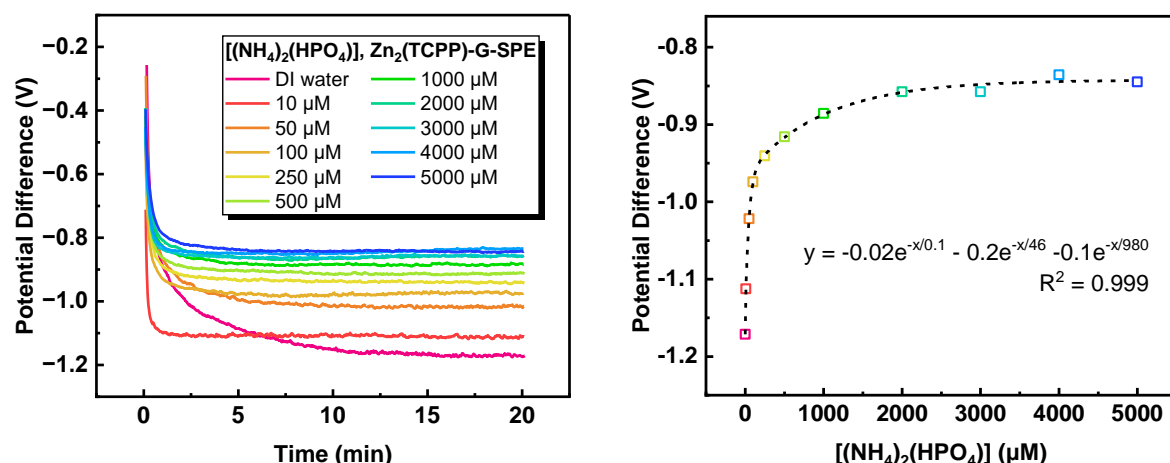


Figure 6.11 Chronopotentiometry over 20s of aqueous ammonium phosphate solutions using a bulk modified Zn₂(TCPP)-G-SPE (left), and final voltages plotted against ammonium phosphate concentration (right).

Plotting these results together (Figure 6.12) showed no difference between the chronopotentiometry results for the unmodified or modified electrodes, indicating no enhancement of selectivity by Zn₂(TCPP). Similar experiments were performed for ammonium nitrate and phosphoric acid titrations (see SI for chronopotentiometric graphs). Also shown in Figure 6.12 are the endpoint voltages for different concentrations of ammonium phosphate, ammonium nitrate, and phosphoric acid. The relationship between signal and ammonium phosphate concentration had twice the gradient of the relationship between signal and ammonium nitrate concentration, whilst no significant relationship between signal and phosphoric acid concentration was observed (Figure 6.12). It was therefore concluded that the observed changes in signal were due to changes in ammonium ion concentration (ammonium phosphate has two ammonium ions per phosphate, whilst ammonium nitrate has only one, and phosphoric acid has none).

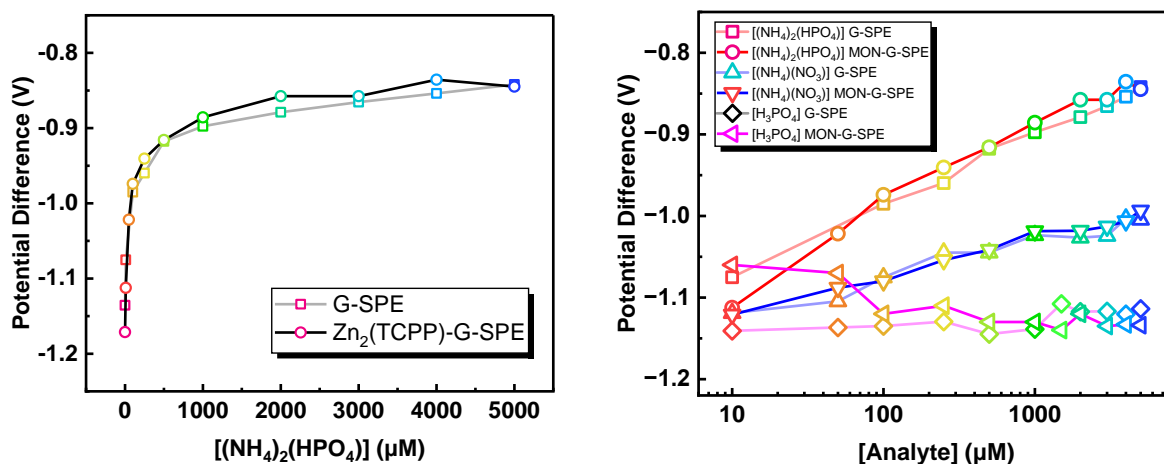


Figure 6.12 Chronopotentiometry results for different aqueous ammonium phosphate solutions comparing different electrodes (left), and chronopotentiometry results for different aqueous ammonium phosphate, ammonium nitrate, and phosphoric acid solutions comparing different electrodes.

To explore the possibility of other analytes, similar chronopotentiometry experiments were performed using 5 mM concentrations of various other analytes ranging from other salts to amino acids: water, ammonium phosphate, ammonium nitrate, potassium carbonate, potassium chloride, magnesium sulphate, sodium sulphate, sodium hydrogen carbonate, L-arginine, L-histidine, L-proline, L-Serine, L-Threonine, and L-Valine (Figure 6.13). No selectivity was observed by $Zn_2(TCPP)$ -G-SPEs compared to unmodified G-SPEs for any of these.

This technique was therefore determined as not suitable for phosphate/nitrate sensing applications, or for any of the other analytes tested as it did not meet the selectivity requirements.

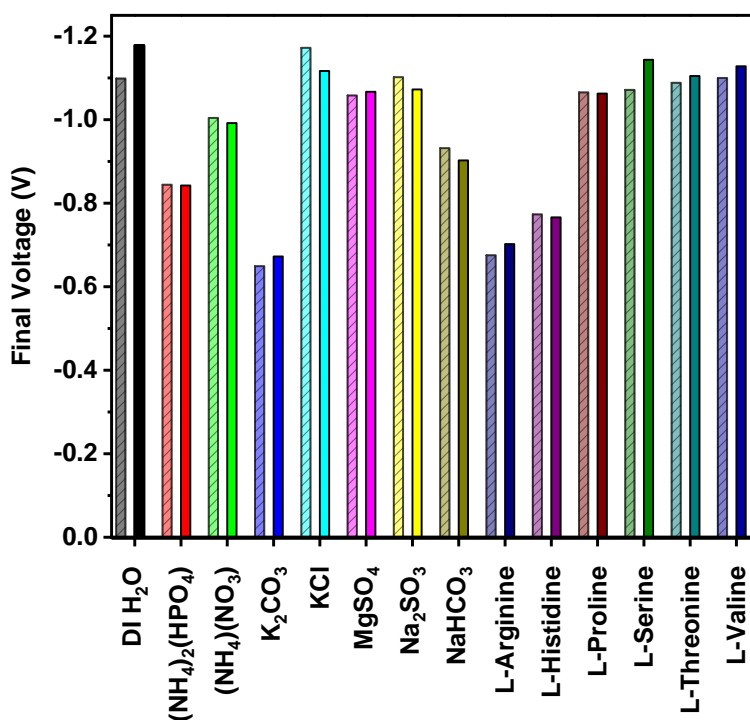


Figure 6.13 Chronopotentiometry results for a variety of 5mM analytes in aqueous solution. Measurements taken using G-SPEs are shown with hashed line pattern, whilst corresponding measurements taken using $Zn_2(TCPP)$ -G-SPEs are shown in solid colour.

Pulsed voltage chronoamperometry

A pulsed-voltage chronoamperometric technique was used by Ratautaite et al. for the detection of SARS-CoV-2 spike protein.²⁹ The magnitude of the difference in current between chronoamperometric measurements with voltage applied and with no voltage applied are expected to decrease with analyte concentration as redox sites on the working electrode are blocked. To determine the effectiveness of this technique for sensing for phosphate, $Zn_2(TCPP)$ -G-SPEs were used to measure different concentrations of ammonium phosphate in DI water. As shown in Figure 6.14, a 0.6 V potential difference was applied 10x for 5 s, with intermittent 5 s “rest” time at 0 V. The final current after each 5 s pulse is defined as I_1 , and the current 5 s after 0 V were applied as I_2 . The difference ΔI between these values was averaged over the 10 pulses for each concentration of ammonium phosphate. These data were processed using python code generated using ChatGPT and compared to manually graphed data, as outlined in the SI page 229.

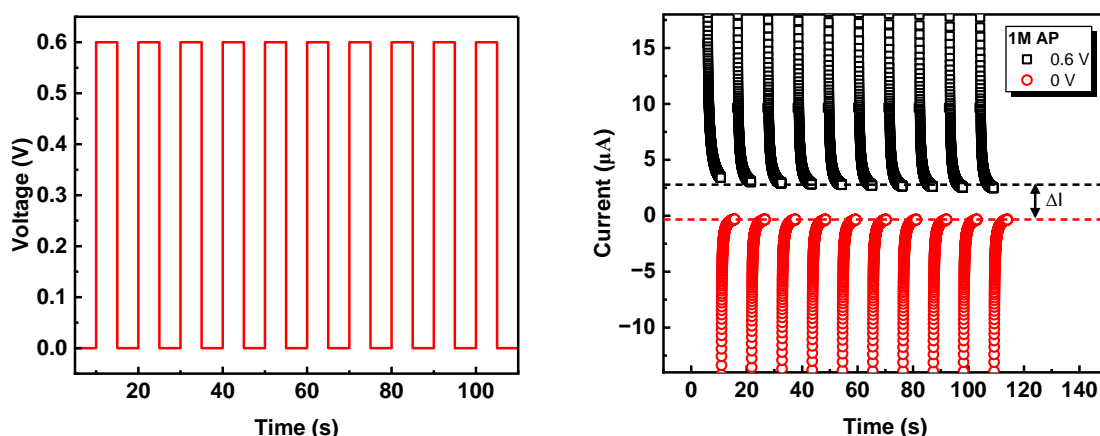


Figure 6.14 Voltage profile during pulsed-voltage chronoamperometric measurements (left), and example data using $Zn_2(TCPP)$ -G-SPE in 1M ammonium phosphate (right).

As shown in Figure 6.15, pulsed-voltage chronoamperometric measurements recorded using the G-SPE are indifferent to ammonium phosphate concentration, whereas $Zn_2(TCPP)$ -G-SPEs have a weakly negative correlation between 1 pM and 100 μ M ammonium phosphate, and a much stronger negative correlation between 100 μ M and 3 mM. Above 3 mM, the data do not follow the negative trend, becoming a positive relationship 10 mM to 1 M. When compared to measurements in ammonium nitrate, $Zn_2(TCPP)$ -G-SPEs show similar trends, albeit with nitrate forming a slightly more negative profile compared to phosphate.

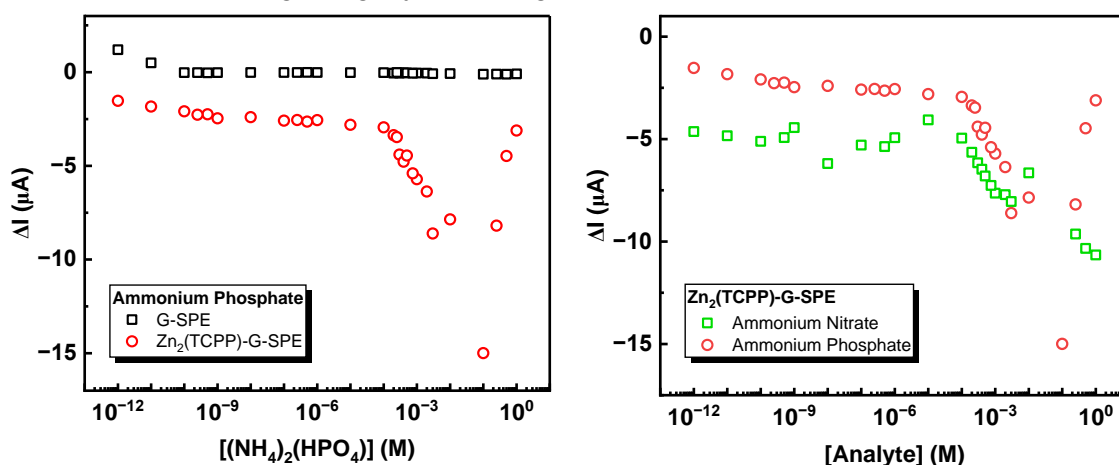


Figure 6.15 Pulsed-voltage chronoamperometric results for different concentrations of analyte. Graphs compare measurement of different concentrations of ammonium phosphate by G-SPE and $Zn_2(TCPP)$ -G-SPE (left), and measurement of ammonium nitrate compared to ammonium phosphate by $Zn_2(TCPP)$ -G-SPE (right).

In conclusion, the pulsed-voltage chronoamperometry technique seems to be the most suited to analyte measurements. Following this, it is likely that the use of $Zn_2(TCPP)$ as an additive in G-SPEs is beneficial to their use as sensors of phosphate via enhancing the sensitivity, but at present have minimal if any selectivity towards phosphate compared to nitrate. The response to analyte does not need to be radically different for effective selectivity when used in conjunction with other electrode, as described in the Introduction. Further experiments could therefore employ the $Zn_2(TCPP)$ -G-SPEs in array sensors to identify the effectiveness of that technique. Having identified the suitability of nanosheets to be added to G-SPEs in this way, future work may also be undertaken to explore more selective nanosheets or different analytes.

Section 6.4 Sensing using Polypyrrole MIP

Molecularly imprinted polymers (MIPs) offer the opportunity to synthesise high surface area materials with inherent selectivity for an analyte. This is achieved by forming a polymer around a template analyte, before removing the template to leave behind cavities which are specific to that analyte in size and shape (physical) or functionality (chemical).²⁹ The chemical or physical recognition of these MIPs rivals the selectivity and sensitivity of antibody-based biosensors, without the limitations in operating conditions or the high cost of production that these devices have.²⁹

Templated polypyrrole MIP was synthesised using an electropolymerisation deposition technique, based on a protocol developed by Ratautaite et al., who used platinum electrodes functionalised with a polypyrrole-based MIP to sense for SARS-CoV-2 spike glycoprotein.²⁹ Given the differently sized analytes in the previous work and this work, the performance of selectivity by these materials must be tested with care. In this work, graphene screen printed electrode (G-SPE) surfaces were modified using pulsed voltage electropolymerisation of polypyrrole (ppy) in the presence of ammonium phosphate as template (Figure 6.16). The MIP synthesis was performed in the presence of 200 mM ammonium phosphate in line with the literature protocol.²⁹ A similar protocol was followed without the presence of ammonium phosphate to synthesise a non-imprinted polymer (NIP) for comparison measurements. The MIP and NIP modified G-SPEs are henceforth referred to as “ppy MIP-G-SPEs”, and “ppy NIP-G-SPEs”, respectively. Preliminary studies followed the Ratautaite et al. method which used phosphate-buffered saline (PBS) to stabilise the pH during electropolymerisation and during measurement. Initial experiments with both ppy MIP-G-SPEs and ppy NIP-G-SPEs synthesised and measured in the presence of PBS showed no correlation, likely due to the excess of phosphate present in the buffer. Polymers synthesised in PBS were therefore subsequently used in sensing experiments without PBS present. Later, a further adaptation was made to the protocol to resynthesise polymers without PBS, and measure without PBS also. These three experiments are discussed in detail below.

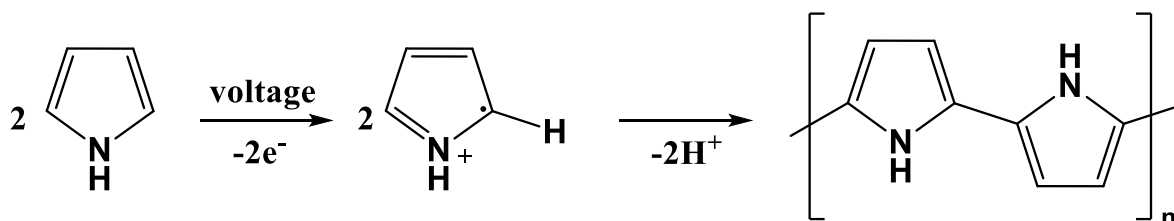


Figure 6.16 Synthesis scheme for the electropolymerisation of pyrrole. Applied twenty 0.95 V pulses for 2 s, each followed by 10 s at 0 V in an aqueous solution of 0.5 M pyrrole. Additives to the cell were 274 mM NaCl and 200 mM ammonium phosphate in the case of MIPs.

For detection measurements, pulsed-voltage chronoamperometry was used. A 0.6 V potential difference was applied 20x for 2s, with intermittent “rest” time at 0 V. The difference ΔI was recorded for different concentrations of ammonium phosphate in 0.3 M NaCl solution.

Results for measurements by ppy MIP-G-SPE and ppy NIP-G-SPE with ammonium phosphate in PBS solutions are shown in figure SI section 5. These data showed little correlation between signal and ammonium phosphate concentration, likely due to competitive cavity filling by the phosphate-based buffer. The method was therefore adapted to only include NaCl as an electrolyte. For these experiments, a good variation in signal intensity was seen for ammonium phosphate concentrations 0-10 mM, with a positive correlation tailing off around 5 mM (Figure 6.17). These were the first pulsed-voltage chronoamperometry experiments to be performed, and the data were analysed by graphing individual measurements, which can be found in the SI pg 218).

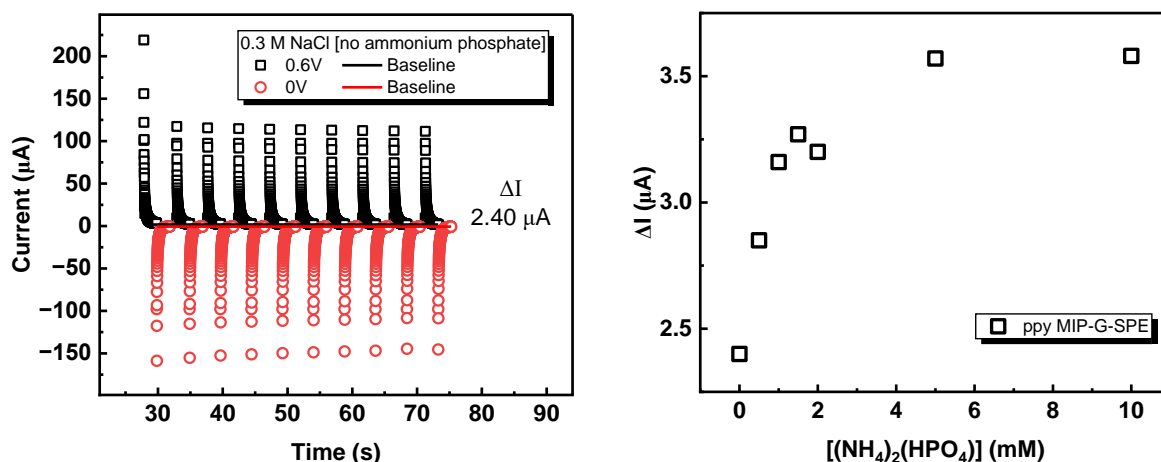


Figure 6.17 Pulsed voltage chronoamperometry measurements ppy MIP-G-SPE in 0.3 M NaCl (left), and subsequent ΔI signal plotted against ammonium phosphate concentration (right).

To expedite data analysis, a python-based code was written with the aid of chat GPT and used to process the data. This method, fully outlined in the SI section 8, interprets ΔI from the average of the last data point in each of the twenty chronoamperometric curves. Processing the data from Figure 6.17 using this code compared to the manual graphing method shows reasonable similarity between manual and coded data, although there is a systematic error where the signal is routinely higher ΔI in the code analysed compared to the manually graphed data (Figure 6.18). Likely, this difference comes from the coded method identifying the last data point in a curve, whereas manually graphed data are fitted with an exponential curve to identify an average asymptote value. Additionally, there is greater difference in intensity for low concentration values. Despite these problems, the time taken to graph individual measurements would have been prohibitive to further experiments, so the interpretation of pulsed-voltage chronoamperometric data was henceforth automated by this code.

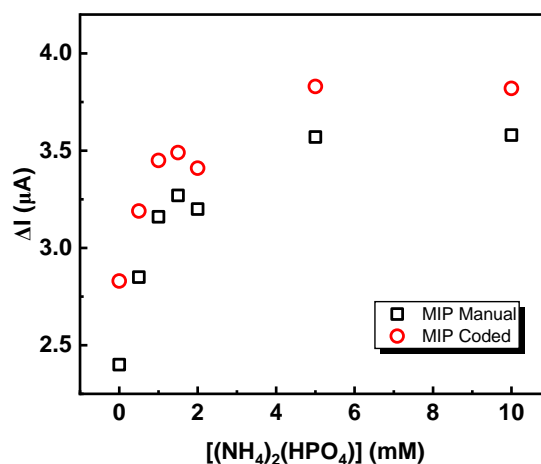


Figure 6.18 Comparison of the chronoamperometry results produced manually with results produced from coded analysis method.

Given the adverse competition effect PBS had on the sensing by ppy MIP-G-SPEs, the electrodes were resynthesised without PBS in the electropolymerisation solution, and the four electrodes were compared via ammonium phosphate titration, which was also without PBS (Figure 6.19). When the pulsed-voltage chronoamperometry measurements in ammonium phosphate concentrations using ppy MIP-G-SPE produced using PBS were compared to its companion electrode ppy NIP-G-SPE (Figure 6.19, left), the signal seen for the ppy NIP-G-SPE was much higher intensity than the ppy MIP-G-SPE, templated with ammonium

phosphate. When ppy MIP-G-SPE and ppy NIP-G-SPE were produced without PBS in the electropolymerisation (Figure 6.19, right), the signal intensities are greatly enhanced for measurements using ppy MIP-G-SPE, almost matching that of the ppy NIP-G-SPE. Since the signal from the ppy MIP-G-SPE is consistently lower than that for the ppy NIP-G-SPE, and this disparity increases with ammonium phosphate concentration, it is reasonable to conclude that this effect is due to irreversible filling of cavity sites by ammonium phosphate.

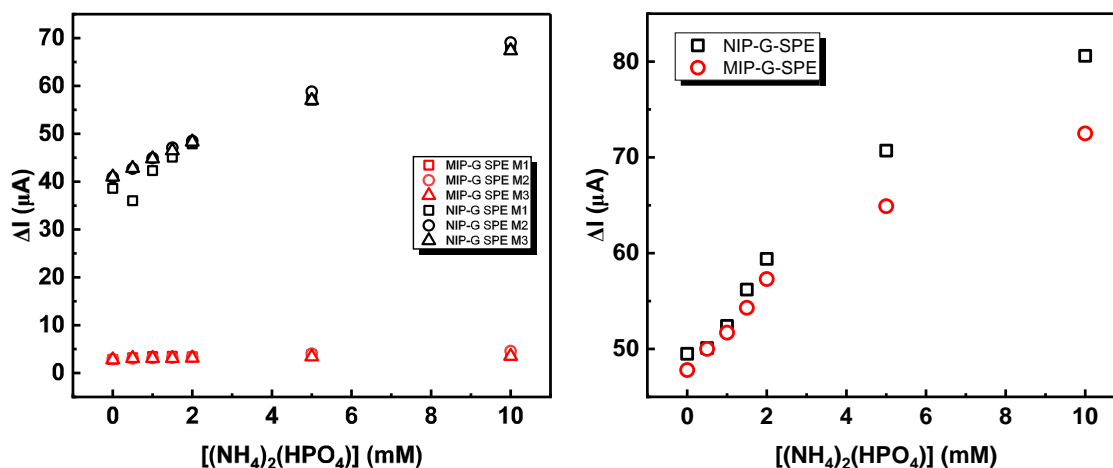


Figure 6.19 Chronopotentiometry results for ammonium phosphate titration using MIP-G-SPEs, and NIP-G-SPEs in aqueous 0.3 M NaCl solutions, where the ppy synthesis was done in the presence of PBS (left) and without PBS (right).

These data contrast with the results reported by Ratautaite et al., who observed a negative linear correlation with analyte concentration.²⁹ This may be due to the ionic analyte playing the role of electrolyte in this experiment, whereas Ratautaite et al. were sensing for a glycoprotein which could not fill this purpose. As such, where selective binding of analyte is expected to block surface sites and inhibit access to the surface by electrolyte, thus reducing signal, in the case of the ammonium phosphate sensor we do not see this relationship because the increasing concentration of ions overcomes the negative effect of binding.

This explains the sensing behaviour seen in Figure 6.19, where PBS used in the electropolymerisation is presumably remaining bound to the ppy MIP cavity, and thus inhibiting the signal intensity. When PBS is removed from the electropolymerisation, the signal intensity returns, with both MIP- and NIP- modified G-SPEs displaying similar positive Δ correlation with ammonium phosphate concentration. In this, there is a negative deviation in the measurement by the MIP-G-SPE compared to NIP-G-SPE, suggesting a successful (if minor) templating of polypyrrole by ammonium phosphate.

In conclusion, the positive correlation observed for measurements using both molecularly imprinted and non-imprinted ppy MIP-G-SPEs was not expected based on the literature for MIP sensing, which suggests a negative correlation with analyte concentration. However, the positive trend measured by the imprinted electrode was curtailed compared to the non-imprinted electrode indicating some selectivity towards phosphate. This deviation is small, presumably because the signal was too weak to overcome the positive relationship due to increasing conductivity from the analyte acting as electrolyte.

Section 6.5 Sensing using Electroactive MIP

To enhance the stability and response of the molecularly imprinted polymer for phosphate, a multi-component, crosslinked polymer with intrinsic electroactivity was designed. Ferrocenyl methyl methacrylate (FcMMA) was added as a monomer in the polymer matrix to add the redox activity of the ferrocene groups into the material. Additionally, the method described by Canfarotta et al. utilising a solid phase stabilised template was employed for this synthesis, as well as using PEG-4-phosphate as a low steric hindrance template during polymerisation to improve the density and availability of active binding sites.²⁸

The electroactive MIP synthesis is described more fully in Figure 6.20, showing the glass bead with carboxy-PEG₄-phosphate template coordinated to the surface. Added functional monomers self-assemble around the phosphate group via electrostatic interactions, and then fixed in place by UV polymerisation with crosslinkers (including electroactive monomer FcMMA). Washing breaks apart the polymer-template matrix to yield MIP nanoparticles with vacant active sites. It should be noted that the self-assembly of functional monomers and the addition of crosslinker monomers is a single step in the synthesis but have been separated here for clarity. The resultant electroactive MIPs were used to functionalise G-SPEs via several methods, which are discussed in the following subsections: Drop casting, covalent bonding, or encapsulation in a conductive polymer.

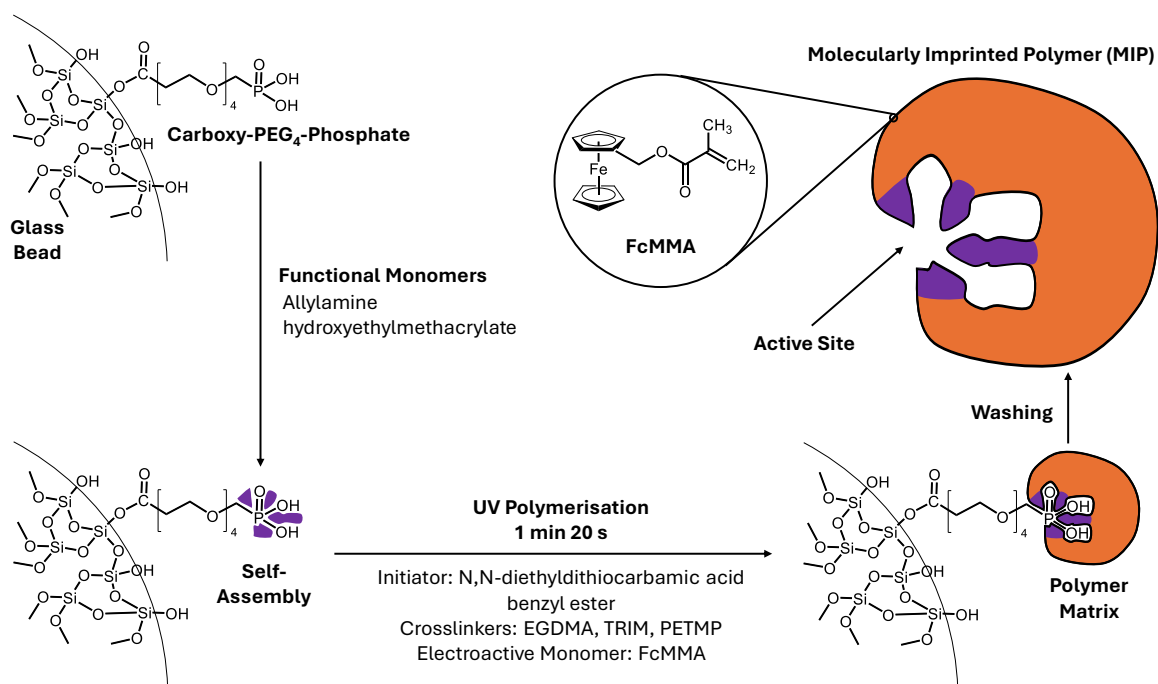


Figure 6.20 Synthesis scheme for electroactive MIPs.

Drop casting MIPs onto G-SPEs

Graphene screen-printed electrodes (G-SPEs) were functionalised via the room temperature drop casting of 15 μL electroactive MIPs (61.2 mg mL^{-1}) in ethanol suspension to form drop cast MIP-G-SPEs. The first electrode modified this way is henceforth referred to as drop cast MIP-G-SPE E1, and the second electrode formed as a repeat referred to as drop cast MIP-G-SPE E2, and so forth. Cyclic voltammogram (CV) measurements using drop cast MIP-G-SPE E1 in 0.1 M KCl and DI water, (Figure 6.21) showed the introduction of a new oxidation peak at 0.38 V, and reduction peak at -0.18 V corresponding to the expected peaks for ferrocene. These were not observed for the bare G-SPEs in 0.1 M KCl. This ferrocene activity evidences the presence of electroactive MIP on the SPE surface.

Upon addition of 3 mM ammonium phosphate (AP), a shift of redox peaks to higher voltage is observed, with diminished intensities for both peaks (Figure 6.21). This was attributed to the binding of ammonium phosphate to the surface of the MIP blocking access to ferrocene moieties. Another effect of ammonium phosphate on CV shape is the crossing over of the voltammogram trace with itself at -0.4 V (indicative of an irreversible change in the cell which we attribute to high affinity phosphate binding).

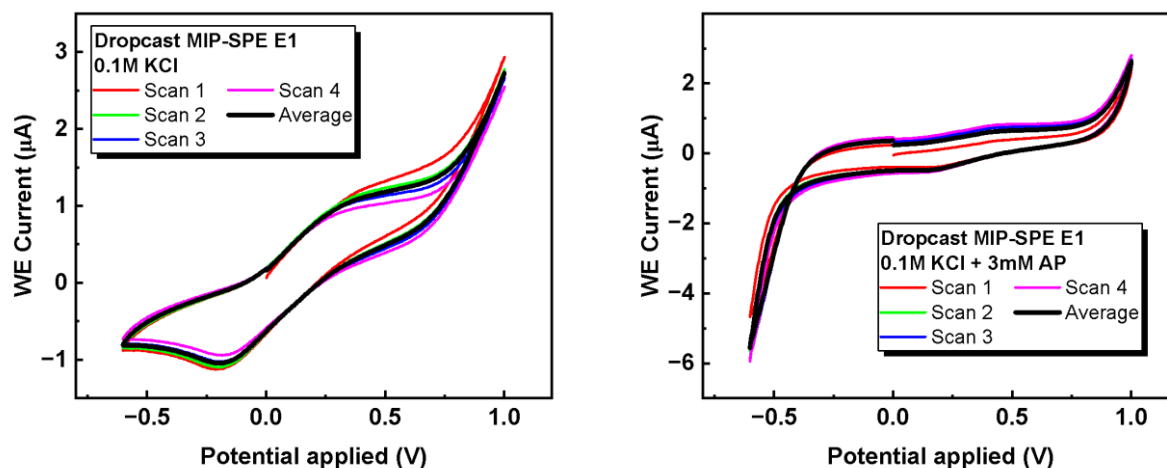


Figure 6.21 CVs of drop cast MIP-SPE E1 measured -0.6 V to 1 V in 0.1 M $\text{KCl}_{(aq)}$ (left) and 0.1 M $\text{KCl}_{(aq)}$ + 3mM ammonium phosphate (right).

A second electrode, drop cast MIP-G-SPE E2, was fabricated in the same way as E1. It was used to perform CV scans at voltages between -0.2 V to 0.8 V in 0.1 M KCl, and -0.4 V to 0.8 V in 0.1 M KCl + 3 mM ammonium phosphate. This reduced voltage window was used to avoid the irreversible process at voltage less than -0.4 V which might be responsible for electrode degradation. The cyclic voltammogram recorded using drop cast MIP-G-SPE E2 again showed good ferrocene character, this time with an increase in oxidation (0.38 V) and reduction (-0.1 V) intensity in the presence of ammonium phosphate (Figure 6.22).

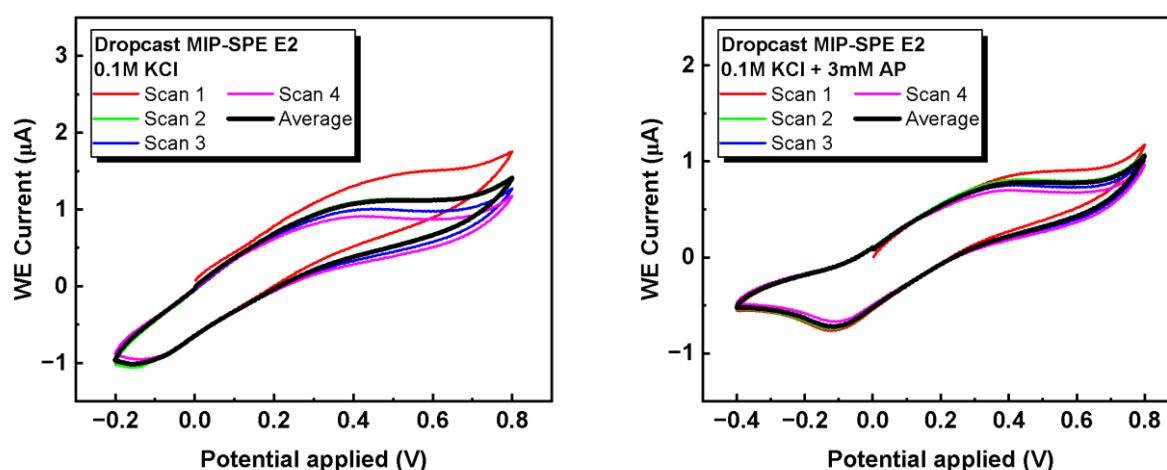


Figure 6.22 CVs of drop cast MIP-G-SPE E2 measured -0.2 V to 0.8 V in 0.1 M $\text{KCl}_{(aq)}$ (left) and in 0.1 M $\text{KCl}_{(aq)}$ + 3mM ammonium phosphate (right).

After dipping in DI water 10 times to wash the surface, the same electrode drop cast MIP-G-SPE E2 was used to perform another CV scan of 0.1 M $\text{KCl}_{(aq)}$ solution from -0.2 to 0.8 V to judge the repeatability between measurements and the effectiveness of electrode washing steps. The CV scans for this repeat blank measurement are shown in Figure 6.23 (left). When compared with the previous two measurements (Figure 6.23, right), it is observed that the oxidation peak at 0.38 V is not recovered after exposure to AP, indicating poor removal of

ammonium phosphate from binding sites. Additionally, the reduction peak was perturbed to 0.2 V, making the “baseline” voltammogram in 0.1 M KCl non-reproducible.

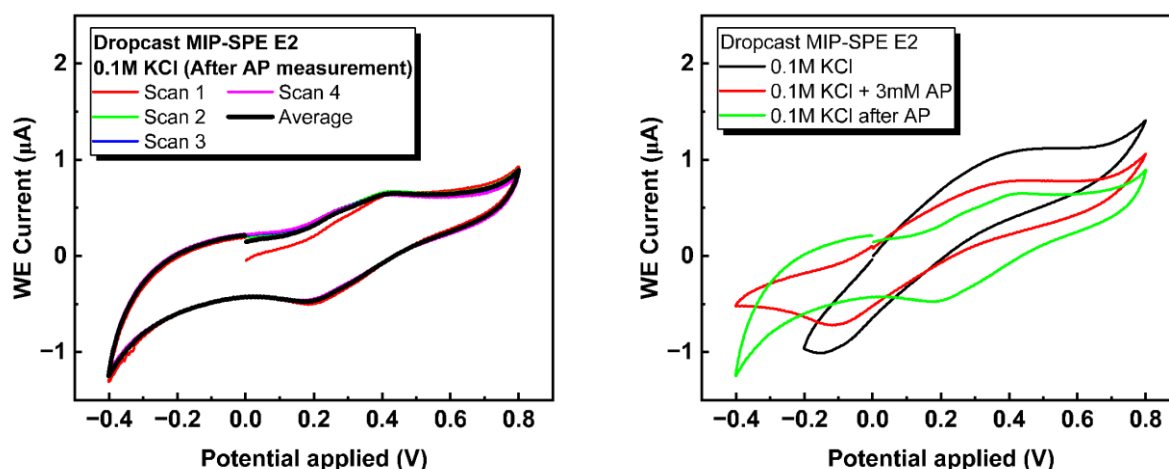


Figure 6.23 CVs using drop cast MIP-SPE E2 in 0.1M KCl recorded after the measurements in Figure 7 (left), and all three averaged CVs plotted together for comparison (right).

Pulsed voltage chronoamperometry measurements were recorded as a low voltage alternative to CV, as it was hypothesised this would reduce degradation. The initial measurements recorded in DI water only with pulses at 0.38 V before increasing AP concentration indicated a negative trend as expected from literature and CV measurements (Figure 6.24). After one sweep from 0 to 3 mM AP however, measurements from 3 to 0 mM produces a minimal correlation trend, indicating degradation of the drop cast layer or graphene electrode.

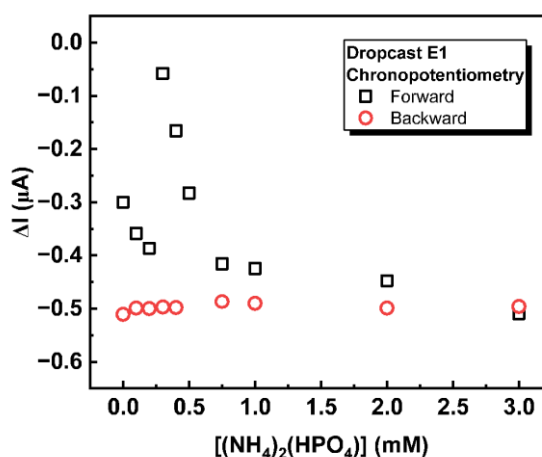


Figure 6.24 Pulsed-voltage chronoamperometry at 0.38 V using drop cast MIP-G-SPE E1 in aqueous ammonium phosphate solutions.

In conclusion, ferrocene methyl methacrylate-based polymers are a good way to introduce inherent redox activity to an electrode surface, which is useful for remote sensing as it doesn't require an electroactive marker additive. Adding ammonium phosphate to the system had a significant effect on CVs, showing a reduction in redox peak intensity. Evidence for degradation of the electrode at voltages less than -0.4 V was observed, and also a likely irreversible binding of phosphate meant the recorded CVs were not repeatable with the same electrode. Low voltage pulsed-voltage chronoamperometry had little effect on the repeatability of measurements, indicating that the drop cast electrodes are too unstable for repeat measurements. Future experiments may utilise this method as single-use electrodes for measurement, although it is doubtful this method can reliably produce thin-films of repeatable thickness and morphology.

Covalently Binding MIPs onto G-SPEs

In an attempt to improve the stability of MIPs on the G-SPE, a method by Gautam et al. was adapted which covalently linked the MIPs to the graphene surface. MIPs were bound to the graphene surface via a glycine bridge to fabricate “covalent MIP-G-SPEs” using the following method adapted from Gautam et al.³⁷ Unmodified G-SPEs were incubated in aqueous glycine solution (100 mM) for 1 hr, before activation with 20 mM) 1-ethyl-3-(3-dimethylaminopropyl) carbodiimide and N-hydroxysuccinimide (EDC/NHS) for 1 hr, and incubation in aqueous nanoMIP dispersion for a further 1 hr. As described in Figure 6.25, glycine bound to the carbon surface reacts with EDC/NHS to form a cyclic leaving group which can be displaced by an amine functionalised MIP.

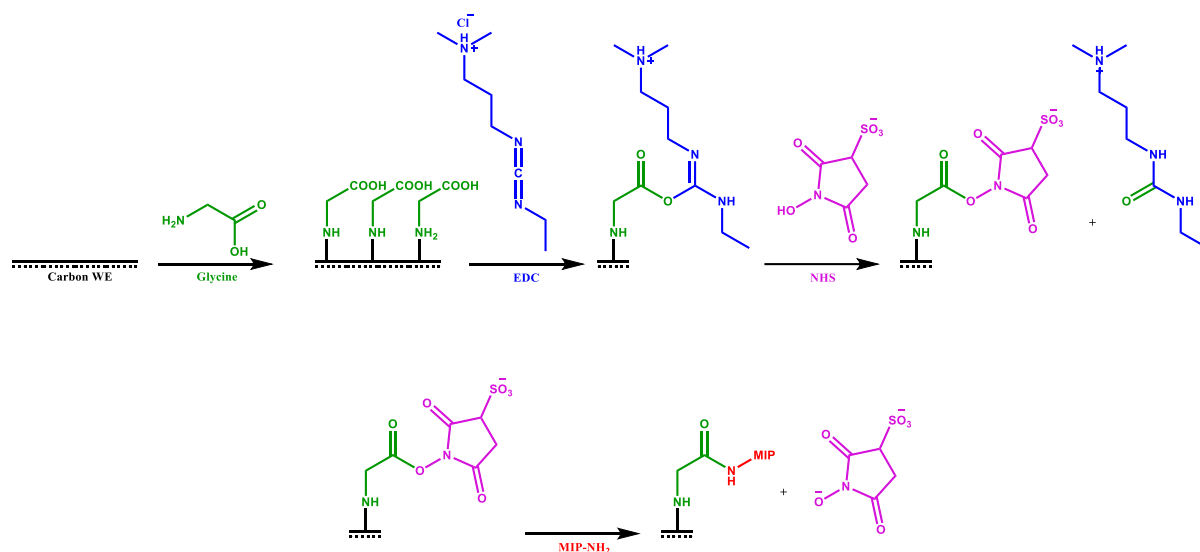


Figure 6.25 Steps for the fabrication of covalent MIP-G-SPEs via glycine linkage.³⁷

Cyclic voltammetry in 0.5 M KCl + 5 mM ferrocyanide was performed comparing the unmodified G-SPE and G-SPE after only the glycine incubation step (Figure 6.26). A reduction in redox peak was observed indicating successful binding of glycine to the carbon surface.

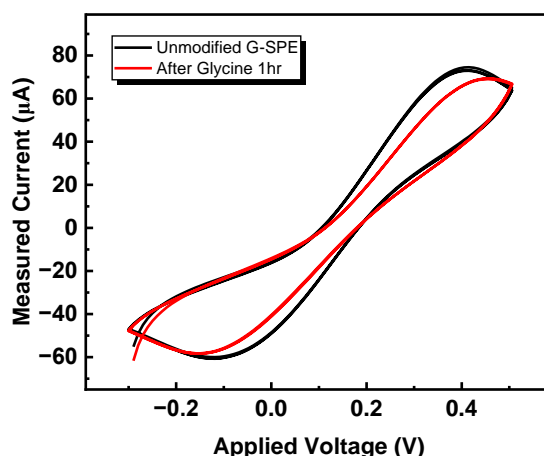


Figure 6.26 Change in CV after incubation of G-SPEs in 100 mM glycine at for 1 hr.

The covalent MIP-G-SPE was used to measure CVs in samples with no analyte, 3 mM ammonium phosphate, and 3 mM ammonium nitrate (each with the addition of 0.1 M KCl_{aq}) to determine the differences in redox character (Figure 6.27). In KCl only, the covalent MIP-G-SPE showed inherent ferrocene character, with oxidation peaks at 0.2 and 0.38 V, and reduction peaks at 0 and 0.25 V, evidence of the presence of MIPs on the surface of the

electrode. Oxidation peak intensity is heavily reduced on introduction of 3 mM AP to the cell, with complete removal of the reduction peak at 0 V and no change to the reduction peak at 0.2 V (Figure 6.27, top right). Addition of ammonium nitrate in 0.1 M KCl to the cell instead of ammonium phosphate further reduced the intensity of all peaks, including the reduction peak at 0.2 V (Figure 6.27, bottom left). This behaviour may be indicative of either non-reversible phosphate binding, non-selectivity allowing ammonium nitrate binding, or general degradation of the covalent MIP-G-SPE over the three sequential scans.

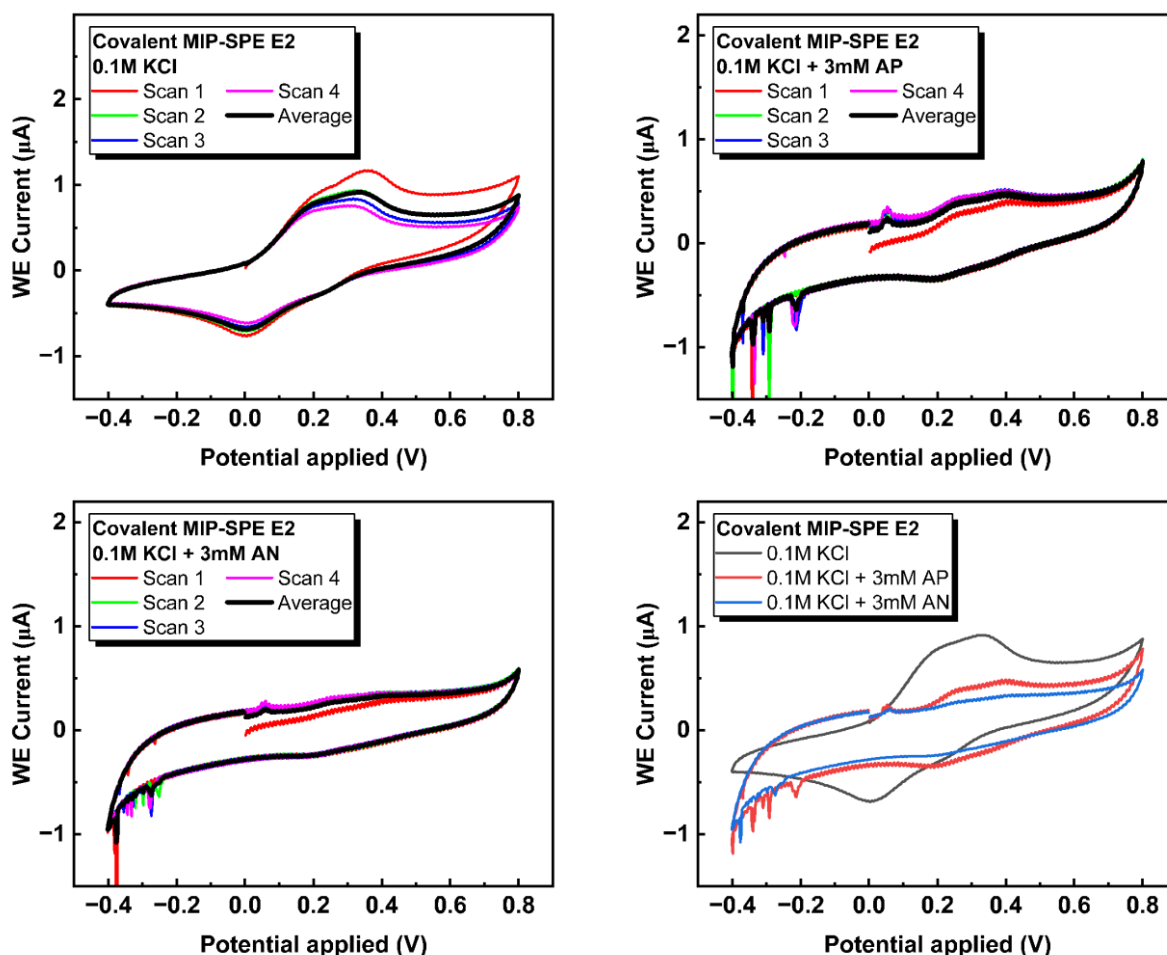


Figure 6.27 CVs of covalently attached MIP on the surface of G-SPE E2 measured -0.4 V to 0.8 V in 0.1 M $\text{KCl}_{(\text{aq})}$ (top left), in 0.1 M $\text{KCl}_{(\text{aq})}$ + 3mM ammonium phosphate (AP, top right), in 0.1 M $\text{KCl}_{(\text{aq})}$ + 3 mM ammonium nitrate (AN, bottom left), and averages for each CV experiment plotted together (bottom right).

To examine the possibility of covalent MIP-G-SPEs for sensing of phosphate in samples without electrolyte, CV measurements were undertaken. Over the course of CV experiments in only DI water (no electrolyte), with water washing between measurements, no ferrocene character was observed (Figure 6.28).

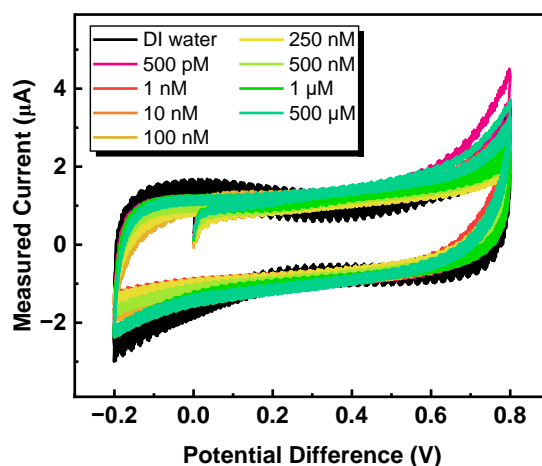


Figure 6.28 CV recorded using covalent MIP-G-SPE for ammonium phosphate concentrations in water.

Pulsed voltage chronopotentiometry was employed as an alternative sensing method, with covalent MIP-G-SPE in aqueous solutions of ammonium phosphate. Experimental methods for pulsed-voltage chronoamperometry are largely similar to previous experiments (10 pairs of on and off pulses), although voltage was sometimes varied. If not otherwise stated, data analysis was performed using the coded method described previously.

When measured with voltage pulses of 0.2 V, the current differences showed good negative correlation with a range of ~ 1.5 -0.2 μA when the concentration of AP in DI water was varied 0-0.5 mM (Figure 6.29). The signal, ΔI , became close to zero above 0.5 mM, and could not be recovered by reducing the concentration of AP. Again, it is unclear if this drop in signal is due to irreversible blocking of cavity binding sites by AP or decrease of electroactive activity by degradation of electrode.

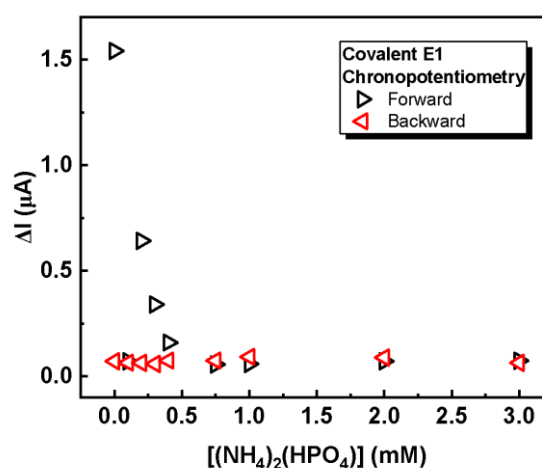


Figure 6.29 Pulsed-voltage chronopotentiometry at 0.2 V using covalent MIP-SPE with AP titration.

To determine if this issue was due to irreversible binding of phosphate to the MIP, several washing techniques were tested to determine whether the repeatability of pulsed voltage chronoamperometry measurements could be improved. As such, a pulsed-voltage chronoamperometry experiment with AP titration was conducted using the covalent MIP-G-SPE with 0.38 V pulses to measure concentrations of ammonium phosphate washing the same covalent MIP-G-SPE electrode between measurements with either water, acidified methanol, or surfactants glycine and Tween 20 (Figure 6.30). Washing was performed by dipping ten times in the specified solution, before rinsing with DI water.

Pulsed-voltage chronoamperometric measurements for covalent MIP-G-SPE in different ammonium phosphate solutions are shown in Figure 6.30. Data points described by the “initial” legend describe measurements taken with increasing concentrations of ammonium phosphate. The “return” descriptor refers to the immediate repeat measurement of the highest concentration ammonium phosphate solution, before measuring decreasing concentrations of ammonium phosphate. The “third” descriptor refers to repeat measurements of the increasing concentrations.

For the measurements with water washing, a strong positive relationship between ammonium phosphate concentration and signal intensity ΔI was observed, with changes plateauing at 1 mM ammonium phosphate in DI water (Figure 6.30, left). This trend is lost at ammonium phosphate concentrations >10 mM (active sensing range of $1.75 \mu\text{A}$), and reversal of the titration back to lower concentrations did not produce concordant values (Figure 6.30, right). This non-repeatability would suggest either degradation at 0.38 V or irreversible binding of ammonium phosphate.

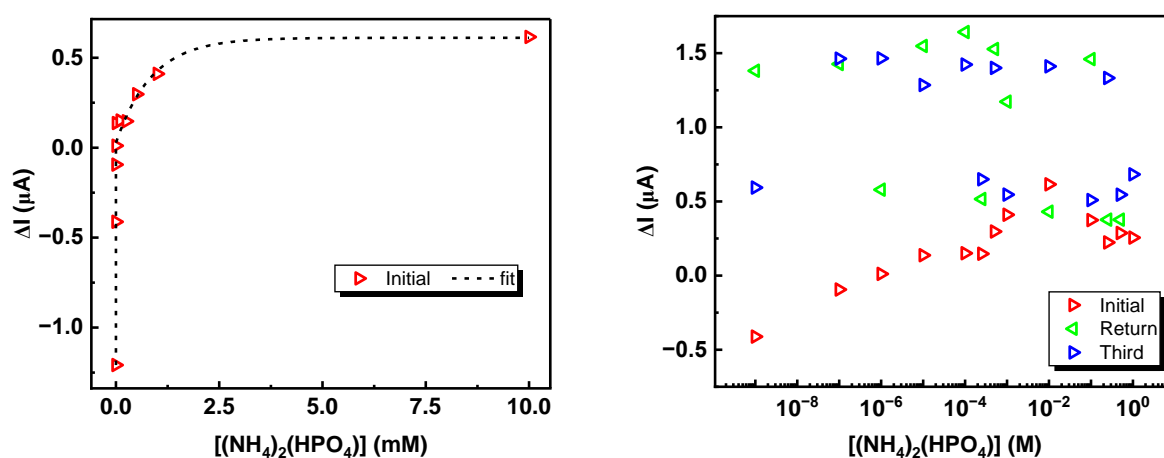


Figure 6.30 Pulsed-voltage chronoamperometry experiment at 0.38 V measuring the titration of aqueous ammonium phosphate concentrations with water washing of the covalent MIP-G-SPE between measurements.

For the measurements with acidified methanol washing (3% acetic acid), the measured current difference ΔI for the first data point (1 nM) is much higher than for the water washed electrode (0.8 vs. $-0.45 \mu\text{A}$), indicating a removal of some template (Figure 6.31). The ΔI increase with initial ammonium phosphate concentration increase is a similar trend to electrodes washed in water, plateauing at $3.4 \mu\text{A}$ (Figure 6.31, left). The resultant ΔI active sensing range of $2.6 \mu\text{A}$ is 1.5 times that observed with water washing. This relationship seems to be only true for ammonium phosphate concentrations <0.1 mM however, with a large increase in signal observed above 0.1 mM ammonium phosphate, up to $40 \mu\text{A}$ (Figure 6.31, right). Between 0.1 mM and 1 M, a negative trend is observed, which fits the expectation of electroactive MIP sensing from literature.²⁹ This trend is followed reasonably closely on the return titration with decreasing concentration but is constant at ammonium phosphate concentrations <0.1 mM, indicating the changes below this concentration are irreversible. This may suggest that up to 0.1 mM AP is required to saturate the highest affinity binding sites in the MIP, from which template cannot be removed, whereas the remaining sites are more labile and allow washing out with the acidified methanol.

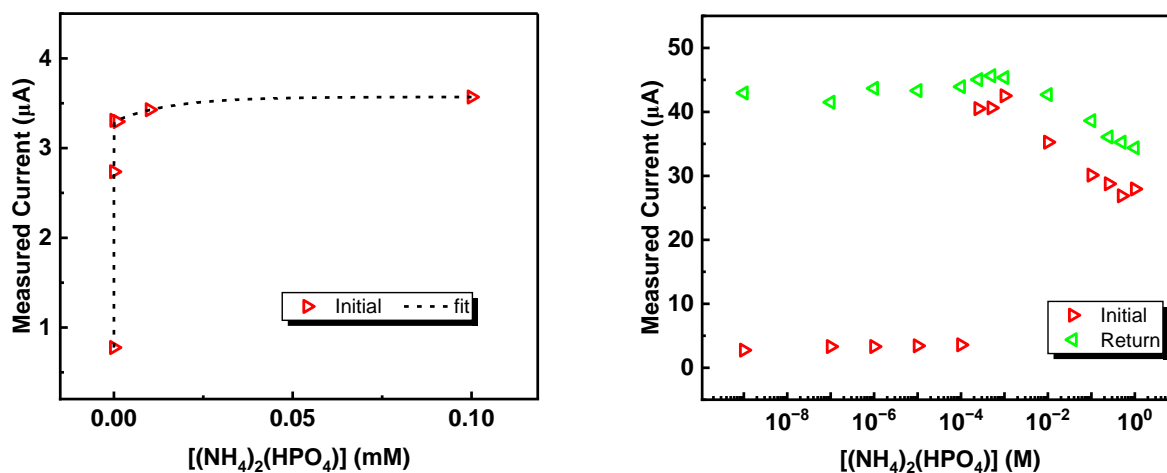


Figure 6.31 Pulsed-voltage chronoamperometry experiment measuring aqueous ammonium phosphate concentrations with acidified methanol washing of the covalent MIP-G-SPE between measurements. Initial relationship up to 0.1 mM (left), and entire concentration range nanomolar to molar for both forward and backward measurements (right).

In order to test a more aggressive cleaning regime, the covalent MIP-G-SPE was washed with glycine and Tween 20 (a sorbitol-derived non-ionic surfactant) between measurements. Pulsed-voltage chronoamperometric measurements on different ammonium phosphate concentrations with this washing did not show clear correlation (Figure 6.32). It was decided that this method is either damaging the electrode's ability to sense phosphate, or this particular electrode had been used too many times and had degraded.

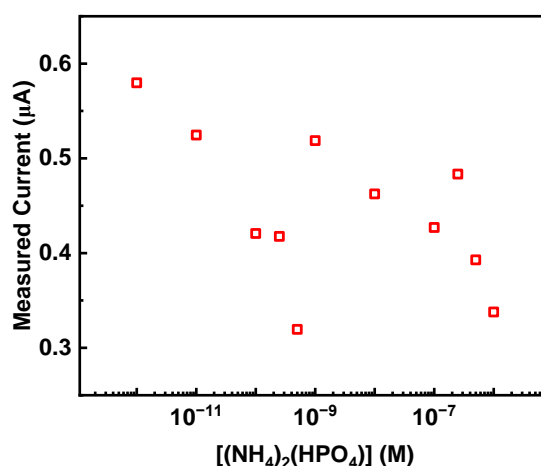


Figure 6.32 Chronoamperometry experiment measuring the titration of aqueous ammonium phosphate concentrations with glycine/tween washing of the covalent MIP-G-SPE between measurements.

Given the apparent degradation between measurements (either due to poor washing, or due to unstable thin-films), multiple covalent MIP-G-SPEs were synthesised as single-use electrodes to compare their activity to ammonium phosphate via pulsed-voltage chronoamperometry. Firstly, all of the 15 covalent MIP-G-SPEs, prepared by a batch method, were used to measure the chronoamperometric response in DI water only (Figure 6.33). These produced relatively varied responses ranging from 0-0.3 μA . It is possible this could be from variation in MIP coating, but considering each G-SPE was subjected to the same covalent linkage conditions, this diversity was attributed to variations in graphene ink deposition during SPE fabrication.

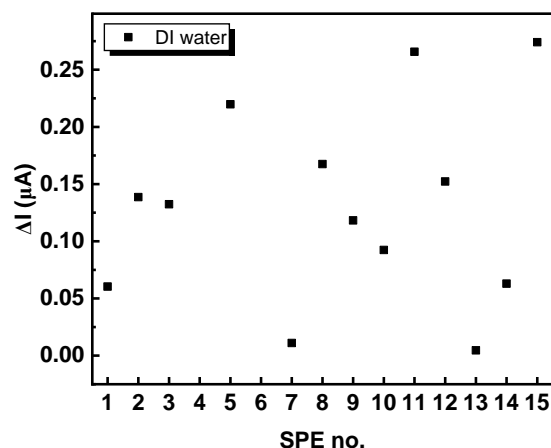


Figure 6.33 Chronoamperometry experiment measuring the titration of aqueous ammonium phosphate concentrations with measurements taken using a fresh covalent MIP-G-SPE electrode 1-15 for each data point. Measurements shown were taken in DI water.

The fifteen covalent MIP-G-SPEs were used to measure three repeats of five different ammonium phosphate concentrations with a fresh electrode used for each measurement. The resultant data are shown in Figure 6.34. All data points have reduced from their corresponding DI water result, with a $\sim 0.5 \mu\text{A}$ spread in the data and no significant correlation with AP concentration. Given the large variation observed in Figure 6.33, the data for each electrode were normalised in the plot with respect to their corresponding measured value in DI water (Figure 6.34, right). This technique also provides a poor correlation, indicating that the variation between different electrodes cannot simply be baselined for calibration.

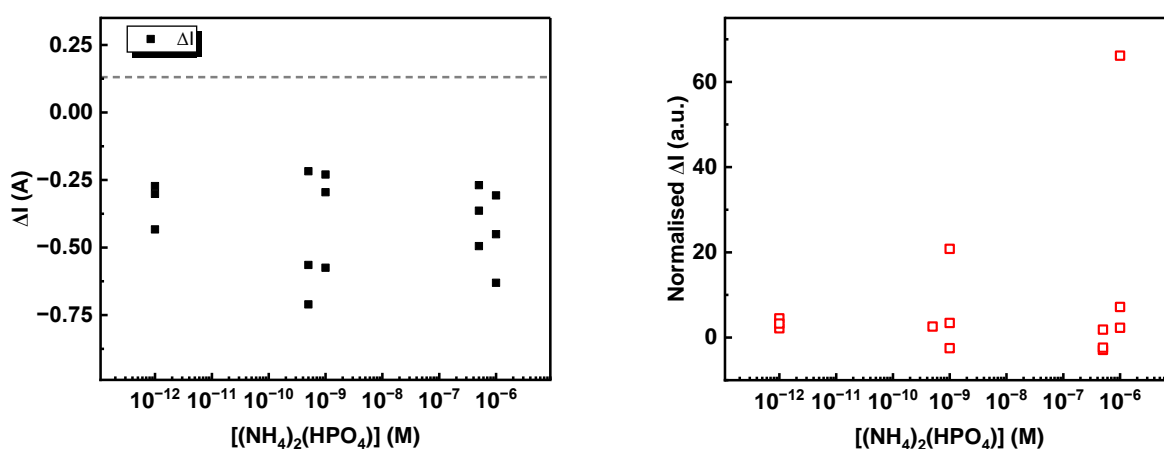


Figure 6.34 Chronoamperometry experiment measuring the titration of aqueous ammonium phosphate concentrations with measurements taken using a fresh covalent MIP-G-SPE electrode 1-15 for each data point. Measurements were taken in ammonium phosphate stock solutions, shown with average DI water signal demarcation line (left). Finally, these data are plotted with each ammonium phosphate measurement normalised by each electrodes signal in DI water (right).

In conclusion, covalent bonding by the method described effectively attached MIPs to the graphene surface. CVs in the presence of ammonium phosphate were observed to have decreased redox peak intensity, but ammonium nitrate measurements also gave reduced intensity. After three measurements, all ferrocene character was removed regardless of analyte, indicating either degradation of the electrode or saturation of the surface with irreversibly bound analyte. CVs of a fresh electrode in DI water with no electrolyte showed no ferrocene character, so pulsed-voltage chronoamperometry was utilised as a low voltage method.

Pulsed-voltage chronoamperometry results indicate an initial positive trend with increasing ammonium phosphate concentration, and repeatability can be improved by washing between measurements with acidified methanol. This experiment showed an initial rise in ΔI 0 – 0.1 mM, and strong negative correlation 0.1 mM – 1 M which matches what is expected from literature. Repeat measurements performed with decreasing concentrations of ammonium phosphate were concordant until 0.1 mM was reached. Thus, it was determined that there are two distinct binding sites on the surface: high affinity, and low affinity, with the high affinity site saturated at 0.1 mM ammonium phosphate. The possibility of covalent MIP-G-SPEs used as single-use electrodes was ruled out by mixed results caused by variations in printing process.

Encapsulating MIPs onto G-SPEs using NPEDMA

Encapsulating MIPs in a non-templated polymer has previously been reported as a method for attaching MIPs to an electrode surface. Electropolymerised N-phenylethylene diamine methacrylamide (NPEDMA) is popular in literature for this purpose, with the reported benefit of improved electrical conductivity between MIPs and the electrode surface, and increased stability.^{38,39} Here, NPEDMA was electropolymerised on G-SPEs to form a layer on the working electrode (Figure 6.35). By performing the electropolymerisation in a dispersion of electroactive MIPs (containing FcMMA), the encapsulation of these by the polymer was attempted to fix the MIPs to the G-SPE surface and form NPEDMA MIP-G-SPEs.

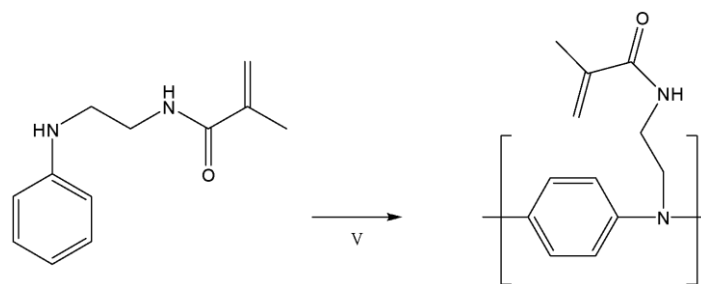


Figure 6.35 NPEDMA Polymerisation Scheme.

CVs recorded using the NPEDMA MIP-G-SPEs show poor ferrocene behaviour when measuring in 0.1 M KCl, whereas the peaks at -0.35 V and 0.38 V are readily seen upon measurement in 3 mM ammonium phosphate (Figure 6.36). This behaviour is not observed when measuring in 3 mM ammonium nitrate, although baselining of the peaks reveals a low intensity oxidation peak at 0.38 V in this solution. This behaviour is not as expected, since phosphate binding to exposed MIPs on the surface should block ferrocene moieties from interacting, thus reducing redox character. Based on these results, it is hypothesised that electroactive MIPs were successfully encapsulated on the surface but blocked from electrochemical interaction by NPEDMA. As CV experiments were performed, degradation at high voltages removed NPEDMA to expose electroactive MIPs, so redox character could be observed. As experiments continued, this character was removed as further degradation occurred. Consequently, it cannot be said with confidence that any changes shown in Figure 6.36 were due to changing phosphate interaction.

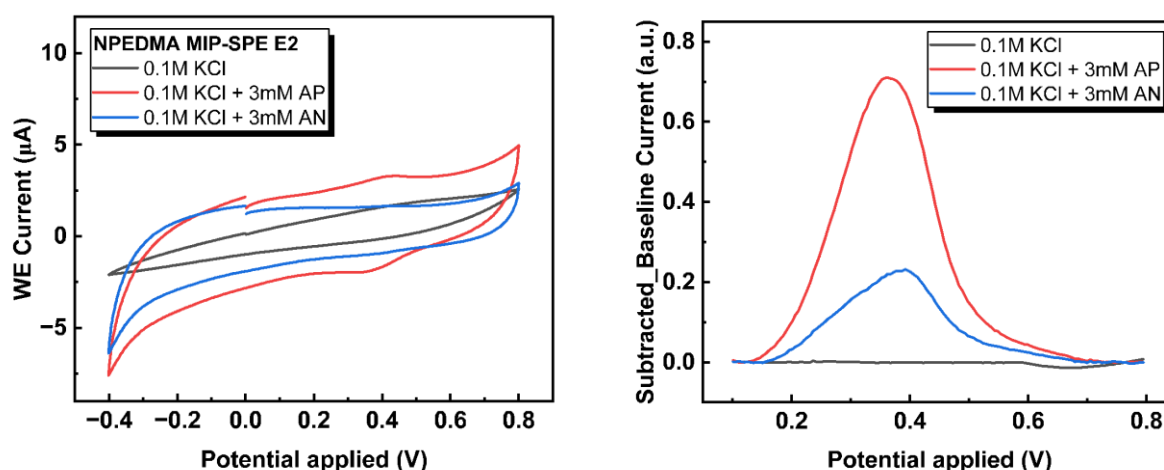


Figure 6.36 Cyclic voltammograms recorded using NPEDMA MIP-G-SPE in 0.1 M KCl, 0.1 M KCl + 3 mM ammonium phosphate (AP), and 0.1 M KCl + 3 mM ammonium nitrate (AN). CVs are averages of 5 scans for each measurement.

When no KCl was added as an electrolyte, CVs measured using NPEDMA MIP-G-SPE electrodes do not have any ferrocene character, at any concentration of ammonium phosphate (see SI S6.28-29). As such, pulsed-voltage chronoamperometry with water washing between measurements was used as an alternative method to measure the signal for different concentrations of ammonium phosphate (Figure 6.37). The positive correlation observed is possibly due to increasing analyte concentration acting as an electrolyte. Although this is a clear trend, the effect is not expected to be enhanced by the MIP, and therefore probably lacks selectivity. Additionally, the reversed titration of AP has a reduced gradient, indicating loss of functionality between experiments, assigned to irreversible binding of ammonium phosphate.

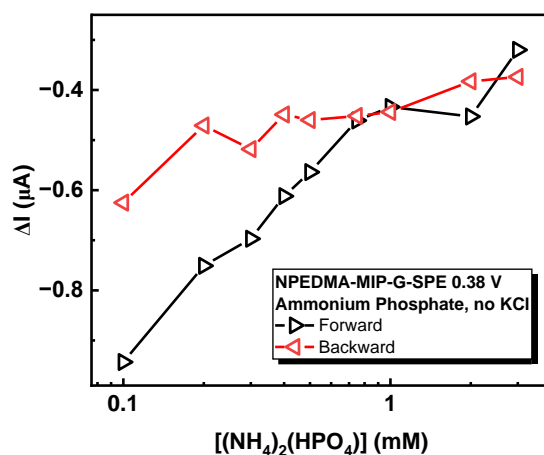


Figure 6.37 Pulsed-voltage chronoamperometry with different concentrations of ammonium phosphate using NPEDMA-MIP-G-SPE without KCl.

A pulsed-voltage chronoamperometry experiment using NPEDMA MIP-G-SPE with acidified methanol and water washing was performed measuring different concentrations of ammonium phosphate. A positive correlation of ΔI to analyte concentration was observed for the initial rise 0 to 1 mM, with a good current range 0-25 μA (Figure 6.38, left). At concentrations above 1 mM, the gradient abruptly reverses to cause a negative correlation. Possibly this is the MIP related negative gradient overcoming the positive changes seen by addition of extra analyte acting as electrolyte. Repeat measurements do not follow the initial data well, indicating changes in electrode activity.

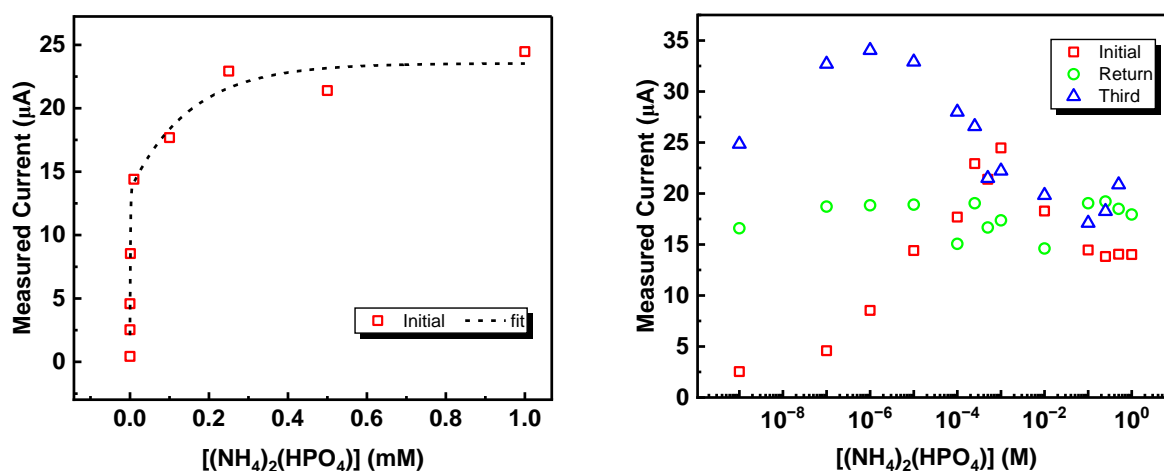


Figure 6.38 A pulsed-voltage chronoamperometry experiment recorded using NPEDMA MIP-G-SPE measuring concentrations of aqueous ammonium phosphate with acid/water washing. Cropped data for the first titration 0 – 1 mM are shown (left), and three repeats are shown in the concentration range 0 – 1 M (right).

In conclusion, NPEDMA can successfully bind electroactive MIPs to G-SPE surface as evidenced by ferrocene character in CVs. The redox peaks in CVs cannot be proven to be affected by phosphate or nitrate concentration, and these redox peaks disappear after only three CV measurements, indicating significant degradation of the sensor. Pulsed-voltage chronopotentiometry showed a positive correlation between measured current and phosphate concentration, but when washed with water between measurements the data were not repeatable. Acidified methanol and water washes were used in a repeat experiment to remove more tightly bound analyte, showing positive correlation 0 – 1 mM, and negative correlation 1 mM – 1 M. Despite a good correlation in the initial measurements, these data were also not repeatable.

Encapsulating MIPs onto GCEs using NPEDMA

Given the lack of repeatability for pulsed-voltage chronoamperometric measurements in screen-printed graphene electrodes (G-SPEs), it is unlikely that the positive correlation of signal ΔI with ammonium phosphate concentration is wholly due to the analyte acting as electrolyte in the experiments without KCl. One possible explanation is degradation of the electrode, which would explain the results where after the first measurement, the signal remains relatively constant at high ΔI .

To determine if the non-repeatability observed when using modified G-SPEs is due to degradation of the electrode material or the NPEDMA thin-film, a glassy carbon electrode (GCE) with electrodeposited NPEDMA encapsulated MIP as described in SPE sections was used to measure electrochemical response via pulsed-voltage chronoamperometry. The modified working electrode, designated as NPEDMA MIP-GCE, was used to record data during ammonium phosphate and ammonium nitrate titrations against an Ag/AgCl reference electrode, and a platinum wire counter electrode. Data were collected with three repeats.

As shown in Figure 6.39, the data are far more consistent between runs, with a much larger ΔI signal range than the screen-printed electrode results (-30 to 250 μA). At low concentrations of ammonium phosphate, signal is relatively consistent around 0 μA , decreasing at concentrations >0.1 mM to -25 μA . At concentrations >10 mM, a rapid increase in signal is observed, up to 250 μA at 1 M ammonium phosphate. Ammonium nitrate follows a similar relationship, with slight differences in intensity and rate of negative decrease in signal between 0.1 to 3 mM (as shown by the cropped data in Figure 6.39, right). Fitting of the negative trending data show these follow an exponential decay, with the exponent factor for phosphate 1.5 times more than for nitrate ($1/0.00077 > 1/0.00116$).

In the paper by Ratautaite et al., an inverse linear correlation of ΔI is expected with analyte concentration, whereas the ammonium phosphate sensor in this work shows a negative exponential trend (Figure 6.39).²⁹ Possibly this is due to convolution with the positive correlation seen at higher concentrations, and could be corrected for with an unmodified GCE measurement. Thus, we can conclude that analyte binding to the MIP is producing a demonstrable signal in the sensor in the concentration range 0.1 to 3 mM (Figure 6.39, right). The more negative signal change observed for ammonium phosphate indicates a greater binding of this analyte compared to ammonium nitrate, evidencing specificity.

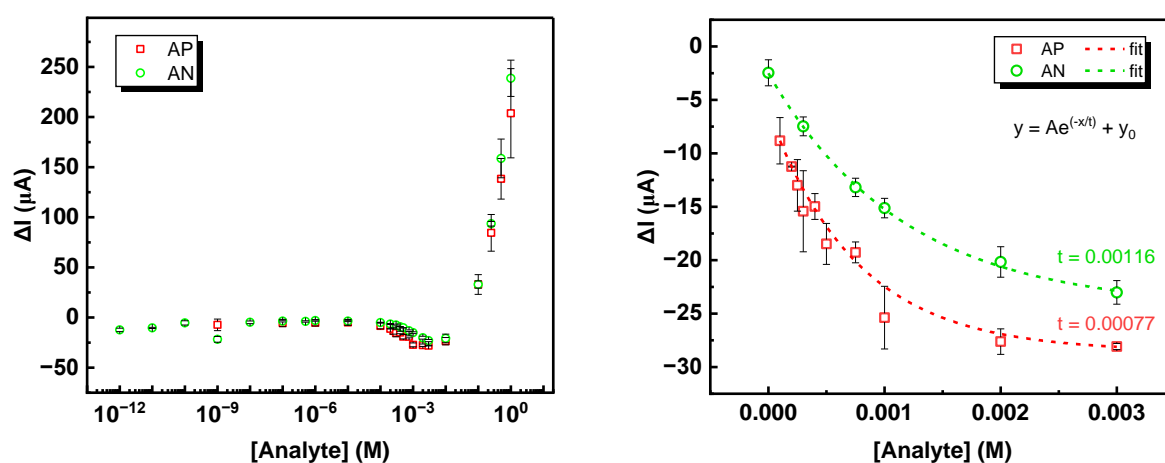


Figure 6.39 Pulsed-voltage chronoamperometry experiment measuring different concentrations of aqueous ammonium phosphate with water washing of the NPEDMA MIP-GCE between measurements. Full experimental concentration range (left), and cropped data to show negative relationship 0.1 to 3 mM (right).

Section 6.6 Conclusions

Three distinct methods for modifying carbon-based electrodes have been investigated for their use for sensing of ammonium phosphate with the aim of improving selectivity. Sensing was tested via cyclic voltammetry, chronopotentiometry, and a pulsed-voltage chronoamperometry technique. Experiments utilised a graphene screen-printed electrode (G-SPE) due to their inexpensiveness compared to the usually researched glassy carbon electrode (GCE).

The first investigation involved zinc porphyrin-based metal organic framework nanosheets ($Zn_2(TCPP)$ MONs). These were first characterised by optical methods to show the ways they are highly sensitive to changes in the chemical environment, especially pH. Specifically, this was the changing position of the Soret absorption band from 425 to 416 nm as acidity increases. This occurs as $Zn_2(TCPP)$ is digested by acid at 2 M H_3PO_4 , or pH 0.5, to form freebase H_2TCPP . At lower pH (5 M, pH 0.3), a peak at 440 nm is observed relating to H_4TCPP . At pH >0.5, where $Zn_2(TCPP)$ is stable to digestion, a change in emission intensity is observed relating to protonation at the porphyrin centre displacing latent metal ions.

The modification of screen-printed graphene electrodes (G-SPEs) with $Zn_2(TCPP)$ MONs has been proven to introduce redox activity inherent to the electrode. This activity is unstable, with redox peaks disappearing after 20 CV cycles. Chronopotentiometry using $Zn_2(TCPP)$ -G-SPEs proved to be sensitive technique for measuring the concentration of either ammonium phosphate or ammonium nitrate, but it was determined the selectivity was for ammonium ions rather than anionic analytes. Pulsed-voltage chronoamperometry was utilised to good effect, with $Zn_2(TCPP)$ providing sensitivity to ammonium phosphate in the concentration range 100 μM to 3 mM where unmodified G-SPE had none. The sensitivity of $Zn_2(TCPP)$ -G-SPE to ammonium nitrate was similar, so selectivity is likely poor but provides a good foundation for electrochemical sensing with hybrid MON/graphene materials in future.

Secondly, a molecularly imprinted polymer (MIP) based on polypyrrole was fabricated by electropolymerisation in the presence of ammonium phosphate onto a G-SPE. Pulsed-voltage chronoamperometry was used to measure different concentrations of ammonium phosphate. Results were interpreted using code-based data analysis to expedite processing. The positive correlation observed for measurements by both molecularly imprinted and non-imprinted ppy MIP-G-SPEs was not expected based on the literature for MIP sensing, which suggests a negative correlation with analyte concentration. However, the positive trend measured by the imprinted electrode was curtailed compared to the non-imprinted electrode and the system was concluded to have the potential for selectivity towards phosphate, but the observable signal was too weak to overcome the positive relationship due to increasing conductivity from the analyte acting as electrolyte.

Thirdly, another MIP was synthesised using a solid phase, less sterically hindered template technique, with inherent electroactivity from incorporation of ferrocenylmethyl methacrylate (FcMMA) in the polymeric structure. The resultant MIP was used to functionalise G-SPEs via drop casting, covalent bonding, or encapsulation in a conductive polymer (NPEDMA, non-imprinted). Each of these were assessed for effectiveness in sensing for ammonium phosphate by electrochemical methods.

All three attachment methods introduced ferrocene electroactivity character into cyclic voltammograms, indicating the presence of MIPs on the working electrode surface. This character, however, was observed to disappear after 2-3 measurements. This poor repeatability of peaks in all tested electrodes indicated degradation of either electrodes or MIP attachment. The low-voltage sensing method of pulsed-voltage chronoamperometry was investigated for each deposition technique.

Deposition of MIPs directly onto G-SPE proved to have poor MIP-surface cohesion and data were poorly correlative and non-repeatable. The covalently bonded MIP-G-SPEs showed good initial correlation with ammonium phosphate concentration, but poor repeatability due to irreversible binding of analyte. In this case, several washing techniques were explored, determining an optimal regime of acidified methanol before water rinsing. Bulk production of these electrodes proved to be non-correlative, indicating that the variation between G-SPEs before modification is too great for comparison. Finally, the NPEDMA encapsulated MIP-G-SPEs also showed correlation with this method but could not repeatably be measured even with acidified washing steps.

Given the lack of repeatability for measurements taken with modified G-SPEs, a glassy carbon electrode (GCE) was also modified using NPEDMA/MIPs. It was concluded that analyte binding to the MIP is producing a demonstrable signal in the sensor in the concentration range 0.1 to 3 mM, with the more negative signal change observed for ammonium phosphate compared to ammonium nitrate indicating a greater specificity to phosphate. Future work should focus on this system for its greater sensitivity and selectivity, possibly exploring an improved sensing concentration range via baselining to a non-modified GCE.

Section 6.7 Experimental

Steady-State Spectroscopy

UV-visible absorption and emission spectra were recorded to determine the ground-state electronic transitions in the materials. Data were collected at room temperature, in a 1 cm quartz cell except where otherwise specified, using an Agilent Technologies Cary 50 UV-Visible spectrometer and a Cary Eclipse fluorimeter, respectively. Emission spectra were recorded in aerated solutions.

Cyclic Voltammetry (CV)

Cyclic voltammograms were measured using a Metrohm Autolab PGSTAT100 potentiostat, in a three-electrode cell. Unless specified to be using the screen-printed three-electrode G-SPEs, the reference, working, and counter electrodes were Ag/AgCl (0.1 mol dm^{-3}), glassy-carbon and platinum wire, respectively. All measurements were carried out in water with 0.1M KCl as supporting electrolyte unless otherwise specified.

Synthesis of $\text{Zn}_2(\text{TCPP})$

The synthesis of $\text{Zn}_2(\text{TCPP})$ was the same as that reported in chapter 3 for batch synthesis of MONs unmetalated at the porphyrin centre. The synthetic method is repeated below for clarity, and characterisation can be found in chapter 3.

The reaction of 1:2 stoichiometric tetrakis(4-carboxyphenyl)porphyrin (TCPP) and zinc nitrate hexahydrate was prepared by mixing of 200 mL TCPP (500 mg, 0.63 mmol) + triethylamine (0.25 g, 2.52 mmol) in 1:1 DCM/EtOH with 200 mL $\text{Zn}(\text{NO}_3)_2 \cdot 6\text{H}_2\text{O}$ (0.38 g, 1.26 mmol) in the same solvent with stirring for 1 hr at 30 °C. Subsequently, the products were washed three times by centrifugation at 12,000 RPM for 1 hr, each time decanting the supernatant and replacing with fresh ethanol.

SPE fabrication

The fabrication of graphene screen-printed electrodes (G-SPEs) and MON modified graphene screen-printed electrodes ($\text{Zn}_2(\text{TCPP})$ -G-SPEs) was performed with the aid of expertise and equipment from the Banks group at Manchester Metropolitan University according to the protocol outlined in the paper by Randviir et al.¹¹

A carbon ink was screen printed onto a polyester backing material to form the substructure for working, counter, and reference electrodes. This carbon ink layer was cured at 60 °C in a fan oven for 30 mins before overlaying a screen-printed Ag/AgCl paste, which was subsequently also cured as before. Next, 1.33 g dry $\text{Zn}_2(\text{TCPP})$ was added to 50 mL graphene ink (15-17 % carbon solid) and screen printed over the working electrode of the SPE. Finally, a dielectric paste was printed over the electrode to cover the connections and separate active electrode areas. The dry ink thickness is estimated by Randviir et al, to be 4-11 μm , and the electrodes are stated as single-use due to the reduced functionality observed after use.¹¹

Polypyrrole electrochemical deposition

The method outlined by Ratautaite et al. was used to electrochemically deposit polypyrrole. A sequence of twenty 0.95 V voltage pulses for 2 s, each followed by 10 s at 0 V in an aqueous solution of 0.5 M pyrrole, 274 mM NaCl, and 0.2 M ammonium phosphate.²⁹ In the case of non-imprinted polymer electrodes, this was carried out without the ammonium phosphate template. One set of experiments used 0.2 M phosphate buffer saline during the polypyrrole electropolymerisation, and another without any buffer (specified in text). After

electropolymerisation, the template was removed by immersion in 0.05 M H₂SO₄ for 10 mins followed by washing in DI water.

Synthesis of Electroactive Molecularly Imprinted Polymers (MIPs)

30 g of glass beads were boiled in 24 mL aqueous solution NaOH (4 M) for 15 mins at 100 °C before filtering and washing firstly with DI water and secondly with acetone. Beads were then dried at 65 °C for 2 hours before redispersing in 12 mL toluene and the addition of 360 μ L APTMS. Solution was purged with nitrogen for 5 mins before oven incubation at 65 °C for 24 hours.

Activated beads were filtered and washed with acetone (600 mL), and methanol (200 mL) before oven drying at 65 °C for 1 hour. Beads were then incubated for 1 hour in a solution of NHS (150 mg), EDC (600 mg), and PEG-4-PO₄ template (9 mg) in 15 mL aqueous PBS. Template-bound beads were then filtered and washed sequentially with DI water, and finally methanol.

The polymerisation mixture was prepared by dissolution of allylamine (0.228 g, 3.99 mmol), hydroxyethyl methacrylate (0.781 g, 24.9 mmol), FcMeMMA (0.150 g, 0.48 mmol), EGDMA (3.24 g, 16.3 mmol), and TRIM (3.24 g, 9.6 mmol), PETMP (0.18 g, 0.37 mmol), N,N-diethyldithiocarbamic acid benzyl ester (0.70 g, 3.31 mmol) in 11 mL DMF. This mixture was purged with nitrogen for 10 mins before adding to the template-glass beads and exposed to UV for 1 min 20 s using a CL-1000 Ultraviolet Crosslinker. The product was chilled at 0 °C for 10 mins and gravity filtered, washing four times with 60 mL DMF at 0 °C, then three times with 60 mL DMF/EtOH (50:50), followed by triple washing with 60 mL EtOH at 0 °C and a final wash with hot EtOH (60 °C) to remove high affinity MIPs.

Electropolymerisation of NPEDMA

2.44 mM stock solution of monomer prepared by dissolving 30 mg NPEDMA in 2 mL acetonitrile. 320 μ L aliquot of this solution taken and diluted to 10 mL by addition of 9.18 mL of water and 500 μ L 0.5 M H₂SO₄. Polymerisation performed by 10 CV scans between -0.2 V and +1 V with a scan rate of 50 mV s⁻¹.

Materials

Materials for Zn₂(TCPP) synthesis are as reported in Chapter 3.

All solvents and reagents were purchased from commercial suppliers and used without further purification: TCPP (97%, MedChemExpress), zinc nitrate hexahydrate (98%, Acros Organics), triethylamine (High purity grade, VWR Life Science), ethanol (99.8 HPLC Grade, Fisher Chemical), dimethylformamide (99% laboratory reagent grade, Fisher Chemical), copper acetate anhydrous (99%, thermos scientific), cadmium acetate dihydrate (98%, Alfa Aesar), cobalt acetate tetrahydrate (reagent grade, Honeywell), nickel acetate tetrahydrate (98%, Alfa Aesar), copper nitrate trihydrate (Sigma Aldrich), ammonium nitrate (99.4%, VWR Chemicals), ammonium phosphate dibasic (fluorochem), acetaminophen (99.0%, Sigma Aldrich), L-Valine (99%, Alfa Aesar), L-Histidine (99%, Sigma Aldrich), L-Serine (99%, Sigma Aldrich), L-Threonine (98%, Alfa Aesar), L-Proline (99%, Alfa Aesar), L-Alanine (98%, Sigma Aldrich), Caffeine (99%, thermos scientific), potassium hydroxide (85% min, Alfa Aesar), sodium chloride (99.5%, Fisher Chemical), potassium chloride (99%, Sigma Aldrich), phosphate-buffered saline (E&O Laboratories Limited), Pyrrole (98%, Aldrich), glass beads (Sigma-Aldrich cat. no. 59200-U), sulphuric acid (95%, Fisher Scientific Limited), sodium hydroxide (98%, Fisher Scientific), acetone (laboratory reagent grade, Fisher Chemical), toluene (99.8%, Fisher Chemical), (3-aminopropyl)trimethoxysilane (APTMS, 97%; Sigma-Aldrich), hydroxyethyl methacrylate (99%, Sigma Aldrich), ferrocenylmethyl methacrylate (FcMeMMA),

95%, Sigma Aldrich), ethylene glycol dimethacrylate (EGDMA; 98%, Sigma-Aldrich), trimethylolpropane trimethacrylate (TRIM, technical grade, Sigma-Aldrich), pentaerythritol tetrakis(3-mercaptopropionate) (PETMP, >95%, Sigma-Aldrich), N,N-diethyldithiocarbamic acid benzyl ester (Insight Biotechnology), N-(3-Dimethylaminopropyl)-N'-ethylcarbodiimide hydrochloride (EDC, ≥98.0%, Sigma-Aldrich), N-Hydroxysuccinimide (NHS, 98%, Sigma-Aldrich), carboxy-PEG4-phosphonic acid (98%, BroadPharm), and allylamine (98%, Sigma Aldrich).

Materials for SPE fabrication as reported by Banks et al.¹¹ Carbon ink: (Product Code: Vor-inkS103; Vorbeck Materials Ltd, USA), Ag/AgCl paste: (Product Code: C2040308D2; Gwent Electronic Materials Ltd, UK), Dielectric paste: (Product Code: D2070423D5; Gwent Electronic Materials Ltd, UK).

Section 6.8 References

1. Cordell, D. & White, S. Life's bottleneck: Sustaining the world's phosphorus for a food secure future. *Annual Review of Environment and Resources* **39** 161–188 (2014).
2. Nagaraja, T., Krishnamoorthy, R., Asif Raihan, K. M., Lacroix, B. & Das, S. R. Microplotter-Printed Graphene-Based Electrochemical Sensor for Detecting Phosphates. *ACS Appl Nano Mater* **6**, 20288–20297 (2023).
3. Mapare, S. V., Yu, P. L., Sarkar, A. & Mukhopadhyay, S. C. A Review of sensor technology for in-field phosphate monitoring. *Proceedings of the International Conference on Sensing Technology, ICST* 411–418 (2013).
4. Akinnowo, S. O. Eutrophication: Causes, consequences, physical, chemical and biological techniques for mitigation strategies. *Environmental Challenges* **12** 100733 (2023).
5. Richardson, K. *By Krishna Moorthy via Unsplash Transformation Labs Ideas for Fast-Tracking Research into Societal Transformation*. (2024).
6. Pourreza, N., Sharifi, H. & Golmohammadi, H. A Green Chemosensor for Colorimetric Determination of Phosphate Ion in Soil, Bone, and Water Samples Using Curcumin Nanoparticles. *ANALYTICAL SCIENCES* **36**, 1297–1302 (2020).
7. Wang, F. *et al.* An electrochemical microsensor based on a AuNPs-modified microband array electrode for phosphate determination in fresh water samples. *Sensors (Switzerland)* **14**, 24472–24482 (2014).
8. Sarwar, M., Leichner, J., Naja, G. M. & Li, C. Z. Smart-phone, paper-based fluorescent sensor for ultra-low inorganic phosphate detection in environmental samples. *Microsyst Nanoeng* **5**, (2019).
9. Lu, C. & Tian, H. Global nitrogen and phosphorus fertilizer use for agriculture production in the past half century: shifted hot spots and nutrient imbalance. *Earth Syst Sci Data* **9**, 181–192 (2017).
10. UKRI Signals in the Soil. <https://www.ukri.org/what-we-do/browse-our-areas-of-investment-and-support/signals-in-the-soil/>.
11. Randviir, E. P., Brownson, D. A. C., Metters, J. P., Kadara, R. O. & Banks, C. E. The fabrication, characterisation and electrochemical investigation of screen-printed graphene electrodes. *Physical Chemistry Chemical Physics* **16**, 4598–4611 (2014).
12. Ashworth, D. J. & Foster, J. A. Metal-organic framework nanosheets (MONs): A new dimension in materials chemistry. *J Mater Chem A Mater* **6**, 16292–16307 (2018).
13. Nicks, J., Sasitharan, K., Prasad, R. R. R., Ashworth, D. J. & Foster, J. A. Metal–Organic Framework Nanosheets: Programmable 2D Materials for Catalysis, Sensing, Electronics, and Separation Applications. *Adv Funct Mater* **31**, (2021).
14. Fang, X., Zong, B. & Mao, S. Metal–Organic Framework-Based Sensors for Environmental Contaminant Sensing. *Nanomicro Lett* **10**, 1–19 (2018).
15. Saraf, M., Rajak, R. & Mobin, S. M. A fascinating multitasking Cu-MOF/rGO hybrid for high performance supercapacitors and highly sensitive and selective electrochemical nitrite sensors. *J Mater Chem A Mater* **4**, 16432–16445 (2016).

16. Zhao, X. & Miao, X. Metal–organic framework constructed by flexible ligands: A versatile platform towards efficient fluorescence sensing, adsorption separation and heterogeneous catalysis. *Coord Chem Rev* **502**, (2024).
17. Xu, H., Cao, C. S. & Zhao, B. A water-stable lanthanide-organic framework as a recyclable luminescent probe for detecting pollutant phosphorus anions. *Chemical Communications* **51**, 10280–10283 (2015).
18. Dou, X. *et al.* Nanoscale metal-organic frameworks as fluorescence sensors for food safety. *Antibiotics* **10**, (2021).
19. Zhao, D. *et al.* Metal-organic frameworks (MOFs) combined with ZnO quantum dots as a fluorescent sensing platform for phosphate. *Sens Actuators B Chem* **197**, 50–57 (2014).
20. Wang, L. *et al.* A luminescent method for detection of parathion based on zinc incorporated metal-organic framework. *Microchemical Journal* **153**, 104441 (2020).
21. Liu, Y. *et al.* A porphyrin-based metal-organic framework Al-TCPP for highly selective sensing of copper ions with exceptional low limit of detection. *J Environ Chem Eng* **11**, (2023).
22. Xu, H. *et al.* A metal-organic framework for selectively sensing of PO₄³⁻ anion in aqueous solution. *J Alloys Compd* **509**, 2552–2554 (2011).
23. Burger, T. *et al.* Luminescent Porphyrinic Metal-Organic Frameworks for Oxygen Sensing: Correlation of Nanostructure and Sensitivity. *ACS Appl Nano Mater* **6**, 248–260 (2023).
24. Pang, Y. *et al.* A novel fluorescence sensor based on Zn porphyrin MOFs for the detection of bisphenol A with highly selectivity and sensitivity. *Food Control* **132**, (2022).
25. Ma, T., Li, H., Ma, J. G. & Cheng, P. Application of MOF-based materials in electrochemical sensing. *Dalton Transactions* **49**, 17121–17129 (2020).
26. Alizadeh, T. & Atayi, K. Synthesis of hydrogen phosphate anion-imprinted polymer via emulsion polymerization and its use as the recognition element of graphene/graphite paste potentiometric electrode. *Mater Chem Phys* **209**, 180–187 (2018).
27. Sullivan, M. V. *et al.* Hybrid aptamer-molecularly imprinted polymer (AptaMIP) nanoparticles selective for the antibiotic moxifloxacin. *Polym Chem* **12**, 4394–4405 (2021).
28. Canfarotta, F., Poma, A., Guerreiro, A. & Piletsky, S. Solid-phase synthesis of molecularly imprinted nanoparticles. *Nat Protoc* **11**, 443–455 (2016).
29. Ratautaite, V. *et al.* Molecularly imprinted polypyrrole based sensor for the detection of SARS-CoV-2 spike glycoprotein. *Electrochim Acta* **403**, (2022).
30. Lach, P. *et al.* Electroactive molecularly imprinted polymer nanoparticles for selective glyphosate determination. *Biosens Bioelectron* **236**, (2023).
31. Rajasree, S. S., Li, X. & Deria, P. Physical properties of porphyrin-based crystalline metal–organic frameworks. *Communications Chemistry* **4**, 47 (2021).
32. Benedict Smith. *Exciton Dynamics in Porphyrin-Based Metal Organic Framework Nanosheets Part I: Effect of Agglomeration [Unpublished]*. (2024).

33. Baskin, J. S., Yu, H. Z. & Zewail, A. H. Ultrafast dynamics of porphyrins in the condensed phase: I. Free base tetraphenylporphyrin. *Journal of Physical Chemistry A* **106**, 9837–9844 (2002).
34. Valicsek, Z. & Horváth, O. Application of the electronic spectra of porphyrins for analytical purposes: The effects of metal ions and structural distortions. *Microchemical Journal* **107**, 47–62 (2013).
35. Yu, H. Z., Baskin, J. S. & Zewail, A. H. Ultrafast dynamics of porphyrins in the condensed phase: II. Zinc tetraphenylporphyrin. *Journal of Physical Chemistry A* **106**, 9845–9854 (2002).
36. Mao, S. *et al.* Ultrasensitive detection of orthophosphate ions with reduced graphene oxide/ferritin field-effect transistor sensors. *Environ Sci Nano* **4**, 856–863 (2017).
37. Gautam, R. P. & Barile, C. J. Preparation and Electron-Transfer Properties of Self-Assembled Monolayers of Ferrocene on Carbon Electrodes. *Journal of Physical Chemistry C* **125**, 8177–8184 (2021).
38. Des Azevedo, S. *et al.* Molecularly imprinted polymer-hybrid electrochemical sensor for the detection of β -estradiol. in *Industrial and Engineering Chemistry Research* vol. 52 13917–13923 (2013).
39. Lakshmi, D. *et al.* Electrochemical sensor for catechol and dopamine based on a catalytic molecularly imprinted polymer-conducting polymer hybrid recognition element. *Anal Chem* **81**, 3576–3584 (2009).

Section 6.9 Chapter 6 Supporting Information

Spectroscopy

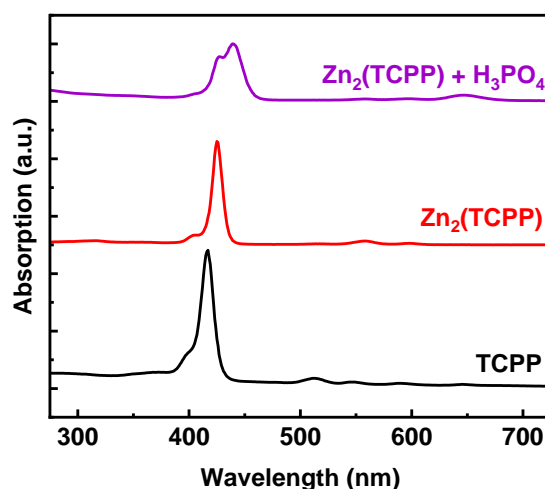


Figure S6.1 Comparison of absorption spectra for TCPP linker, $Zn_2(TCPP)$, and $Zn_2(TCPP) + 1M H_3PO_4$.

Given the lack of spectral response $< 2 M H_3PO_4$, the UV-visible absorption of metalloporphyrin-based MONs $Zn_2(TCPP-Cu)$, and $Zn_2(TCPP-Zn)$ were tested in the presence of $0.056 M H_3PO_4$ and found to have significant changes even at this low concentration (Figure S6.2). The metalation at the porphyrin centre removes a plane of symmetry, reducing the Q-bands to two transitions. The redshift of the Soret from $425 nm$ to form two peaks at 425 and $440 nm$ indicates the metalated porphyrins are being distorted by addition of the metal (ruffled distortion, chapter 3) to improve delocalisation and stabilise the porphyrin orbitals. Note that upon addition of phosphoric acid, the copper metalated sample shows a reduced contribution of the absorbance at $440 nm$ due to metalation, whilst the zinc metalated sample shows an increase in absorbance at $440 nm$. This seemingly opposing behaviour may indicate different interactions with the additive phosphoric acid.

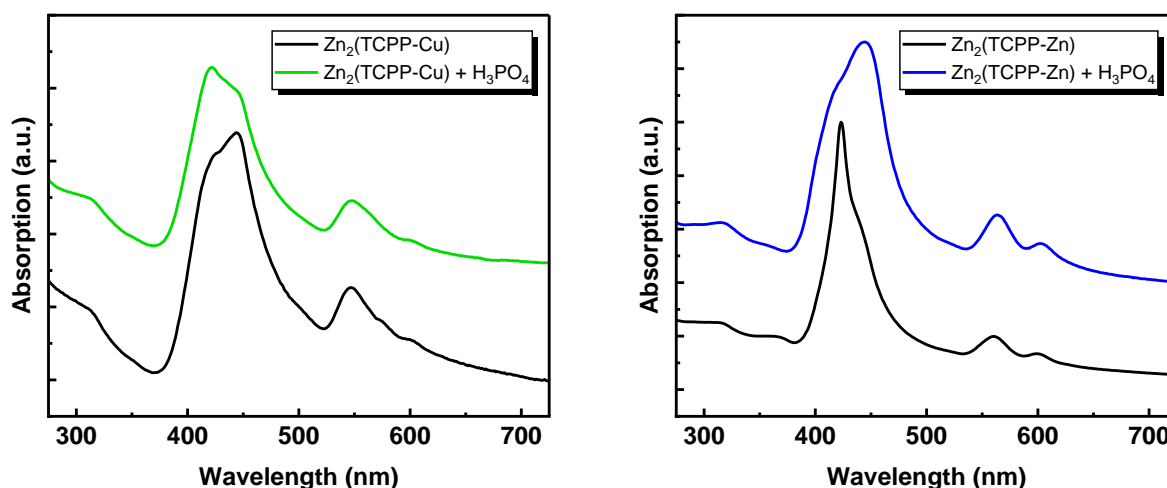


Figure S6.2 Absorption spectra for $Zn_2(TCPP-X)$, where $X = Cu$ (left), and Zn (right), comparing the effect of $1M$ phosphoric acid.

Addition of 8 mM ammonium nitrate leads to minor spectral changes in $Zn_2(TCPP-Cu)$ and $Zn_2(TCPP-Zn)$, mostly showing a reduction in red side of Soret absorption and increase in blue side, with $Zn_2(TCPP-Cu)$ showing a blue-shift of the Q_y absorption band (Figure S6.3).

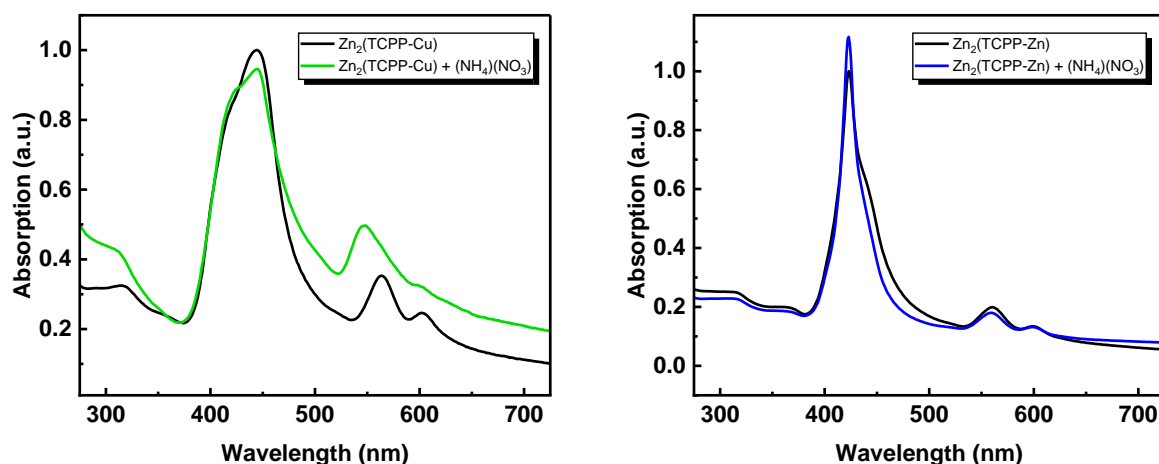


Figure S6.3 UV-visible absorption spectra for $Zn_2(TCPP-X)$, where $X = Cu$ (left), and Zn (right), with and without the addition of 8mM ammonium nitrate.

Emission lifetime decreases upon addition of phosphoric acid, the opposite of what would be expected for removal of metal ions. Note 0.1 ns component is an order of magnitude shorter than the instrument response function (1 ns).

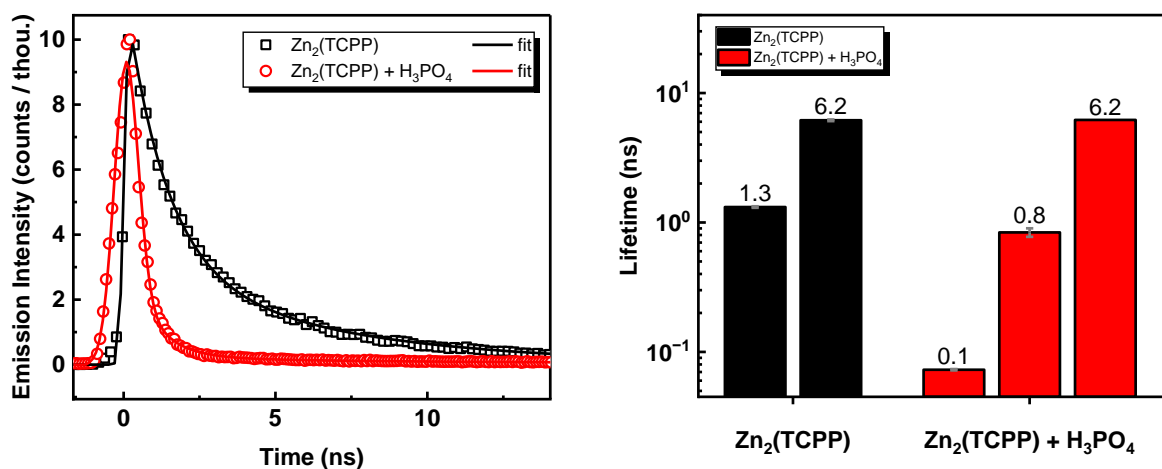


Figure S6.4 TCSPC kinetics (left) and fitted lifetimes (right) for $Zn_2(TCPP)$ with and without addition of 1M H_3PO_4 .

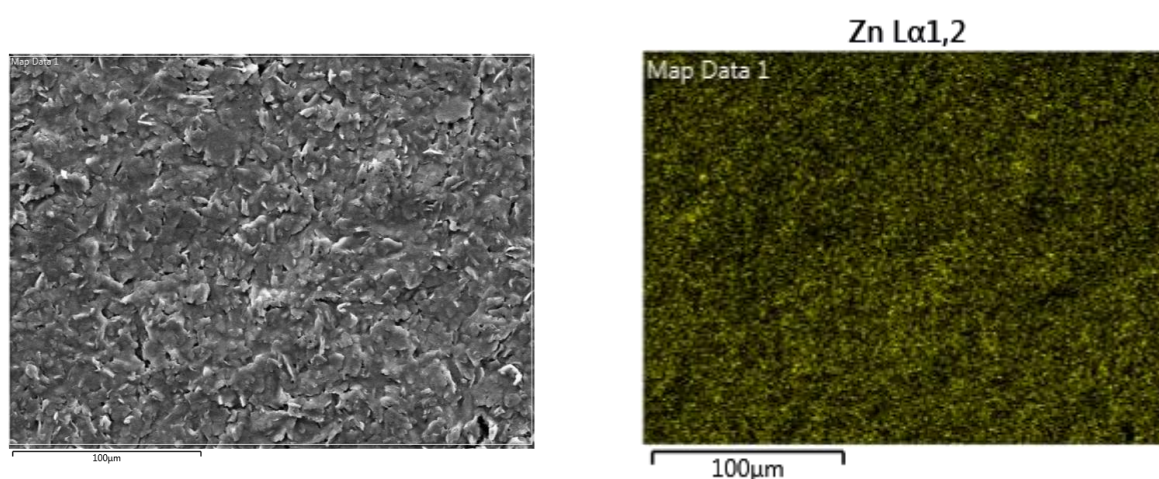


Figure S6.5 Scanning electron micrographs of unmodified G-SPEs with normal (left), and energy dispersive spectroscopy filter for zinc (right).

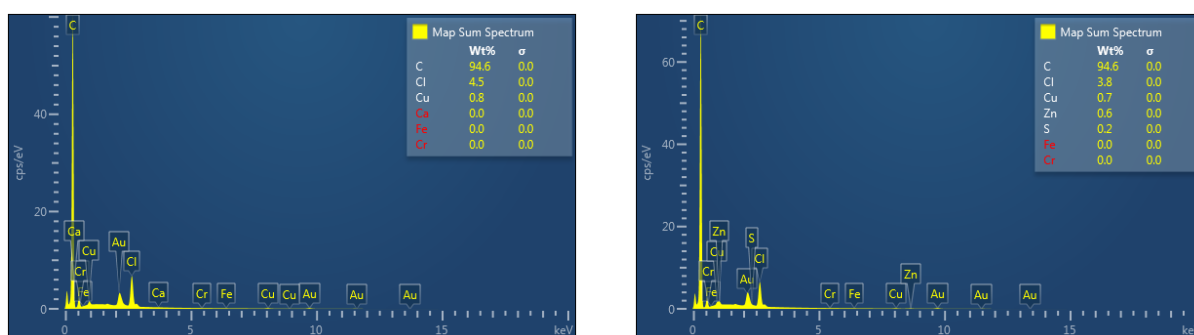


Figure S6.6 EDS results for unmodified G-SPEs (left), and $Zn_2(TCPP)$ -G-SPEs (right).

Initial G-SPE testing

Three G-SPEs tested by CV in 5 mM ferrocyanide with 0.5 M KCl (Figure 31) show minimal variation in voltammogram intensity e.g., the oxidation peak varies between 0.37-0.39 V for ferrocyanide, and peak intensity has a variation of 6% ($\sim 3.7 \mu A$ vs. total peak intensity $\sim 62 \mu A$).

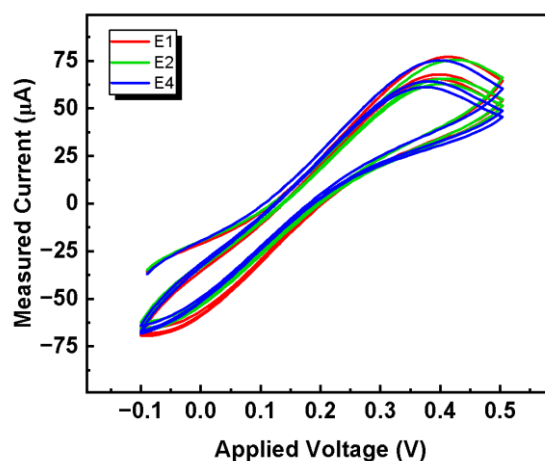


Figure S6.7 CV scans for three different unmodified G-SPEs to compare variation.

Cleaning Preparation for G-SPEs

The electrodes were prepared by washing and cleaning steps suggested by Wei et al. and analysed by cyclic voltammetry (CV) in 5 mM ferrocyanide and 0.5 M KCl to determine the effect on their performance before any preparation, after washing with IPA, after incubating in 0.5 M NaOH, after anodising in 0.5 M NaOH, and after exposure to ozone for 1 and 2 hours respectively.¹⁹

The preparation steps tested show obviously improved performance (greater intensity, more defined peaks) for almost all washing steps (Figure S6.8). Specifically, the IPA washes and ozone exposure had the greatest effect, with a combined IPA wash and ozone exposure for 2 hours recommended for all future electrode prep.

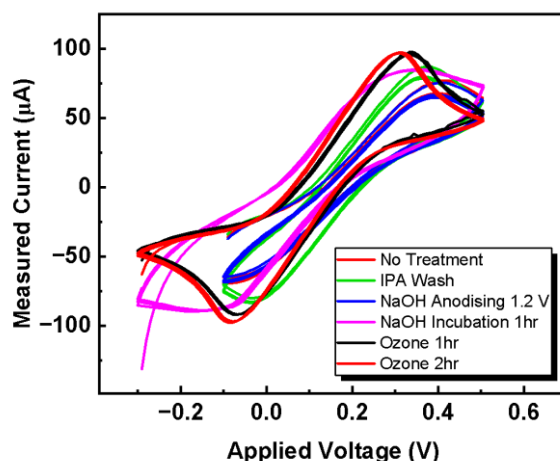


Figure S6.8 CV scans comparing electrodes prepared by IPA wash, NaOH anodising at 1.2 V, NaOH incubation 1 hr, and ozone exposure for 1 and 2 hours.

Scan rate analysis of G-SPEs

A scan rate analysis was performed for $Zn_2(TCPP)$ -G-SPEs in 0.5 M KCl to determine the optimal rate and to identify characteristics of the CV profile. A distinct oxidation peak was identified at 0.1 to 0.5 V, and a corresponding reduction peak at -0.5 to -0.75 V (without redox probe e.g., ferrocene). The rate 0.1 V s^{-1} is selected as optimal for CV.

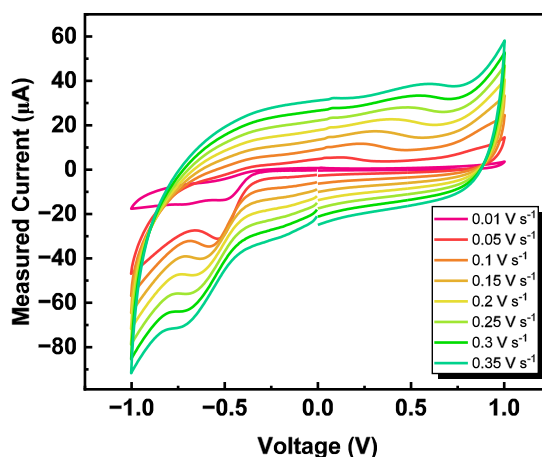


Figure S6.9 Scan rate analysis of $Zn_2(TCPP)$ -G-SPEs by cyclic voltammetry.

Multiple cycle testing of $Zn_2(TCPP)$ -G-SPEs

The same $Zn_2(TCPP)$ -G-SPE was used to repeat a CV scan 100 times in 0.1 M phosphate buffered saline (PBS) and 0.5 M KCl to determine the degradation caused by CV experiments. A significant drop-off in signal intensity was observed immediately, with oxidation peaks disappearing after only 25 scans.

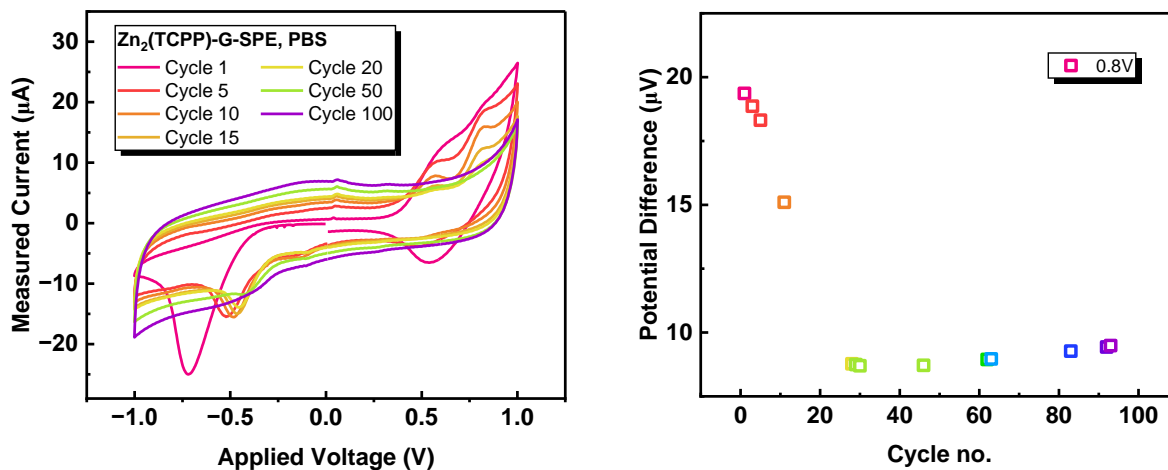


Figure S6.10 Cyclic voltammetry cycle testing for $Zn_2(TCPP)$ -G-SPEs at $0.1 V s^{-1}$.

Cyclic voltammetry ammonium phosphate sensing with $Zn_2(TCPP)$ -G-SPEs

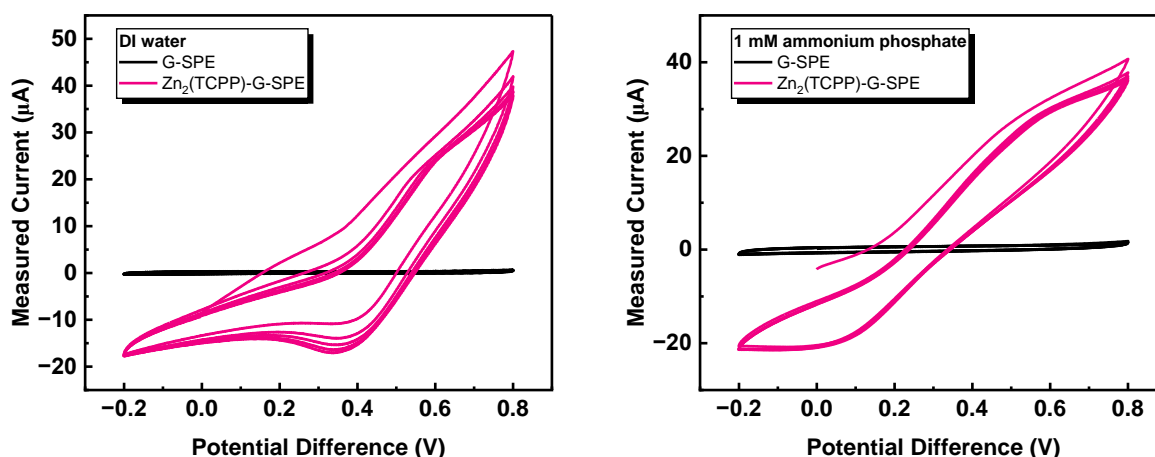


Figure S6.11 Cyclic voltammograms comparing G-SPEs and $Zn_2(TCPP)$ -G-SPEs in DI water (left), and 1 mM ammonium phosphate solution (right).

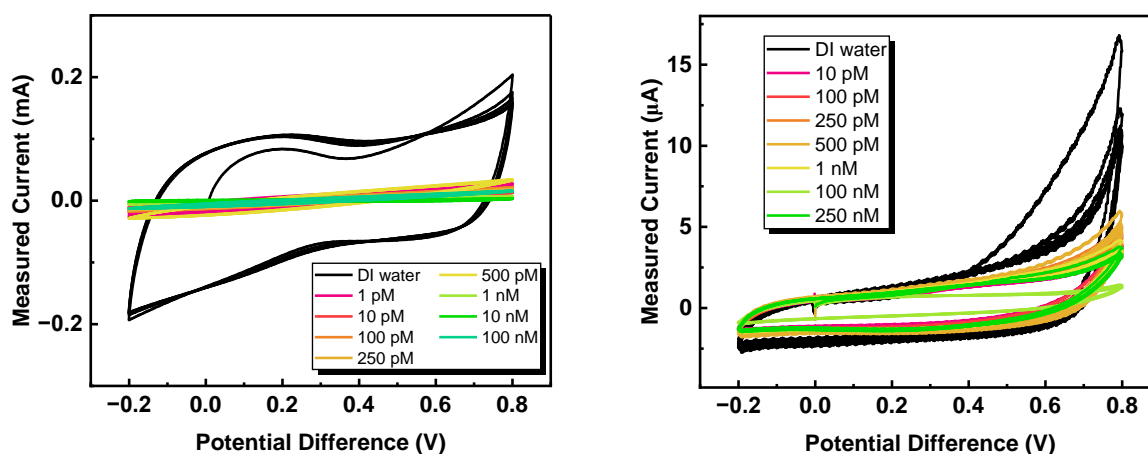


Figure S6.12 CV recorded using NPEDMA MIP-GCE (left), and NPEDMA MIP-Au-SPE (right) for ammonium phosphate titration in water.

Sensing using a multimeter with $Zn_2(TCPP)$ -G-SPEs

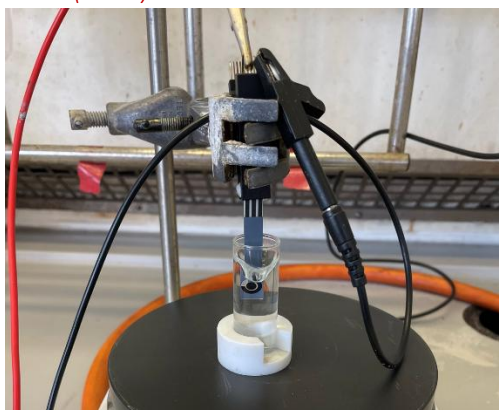


Figure S6.13 Electrode setup for SPE experiments measured using a multimeter.

Due to the degrading effect the CV technique has on the SPEs, specialist equipment, and poor correlation observed between ammonium phosphate concentration, a less taxing technique was required for analysis. By recording the voltage across a $Zn_2(TCPP)$ -G-SPE in ammonium phosphate using a multimeter, the change over time for 20 mins was measured for various ammonium phosphate concentrations (Figure S6.14). The measurements tended to different values over time, with the measurement taken after 5 mins for each sample mostly correlating with concentration. This method however, was not specific enough for sensing and was discarded for the more accurate potentiostat measurements.

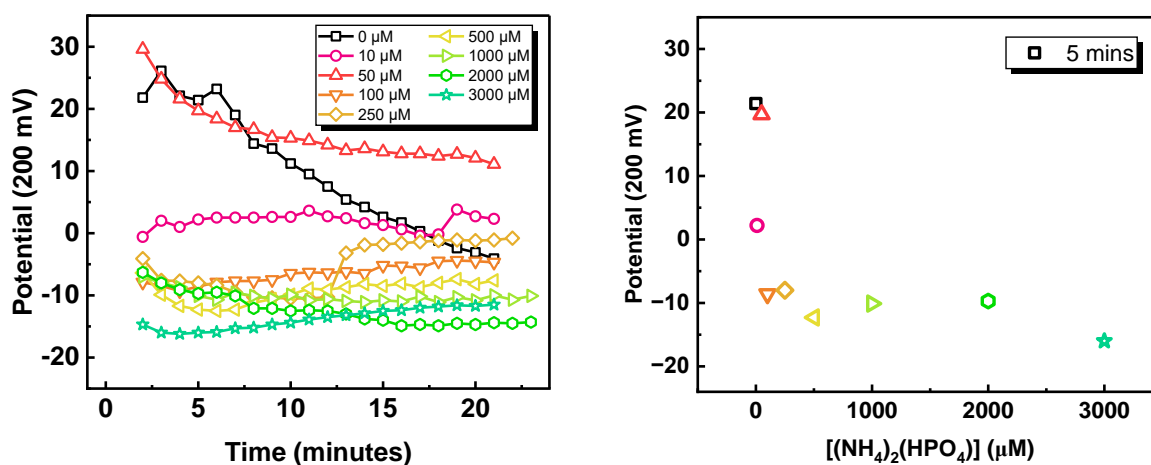


Figure S6.14 Multimeter readings for $Zn_2(TCPP)$ -G-SPEs in aqueous solutions of ammonium phosphate. Plots show data recorded over 25 minutes (left) and the potential after 5 minutes plotted against concentration of ammonium phosphate (right).

Chronopotentiometry measurements for Zn₂(TCPP)-G-SPEs and G-SPEs

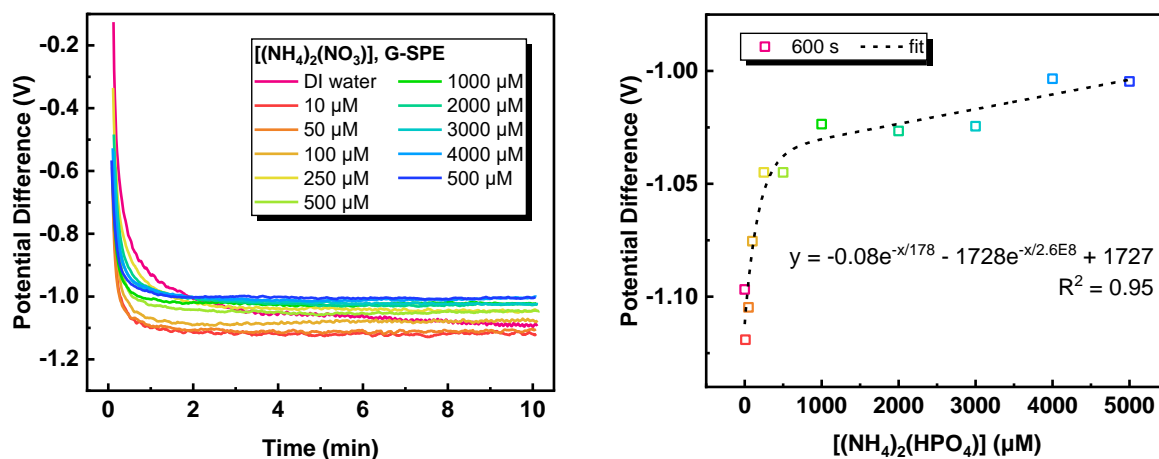


Figure S6.15 Chronopotentiometry over 1 mins for aqueous ammonium nitrate solutions using a G-SPE (left), and final voltages plotted against ammonium phosphate concentration (right).

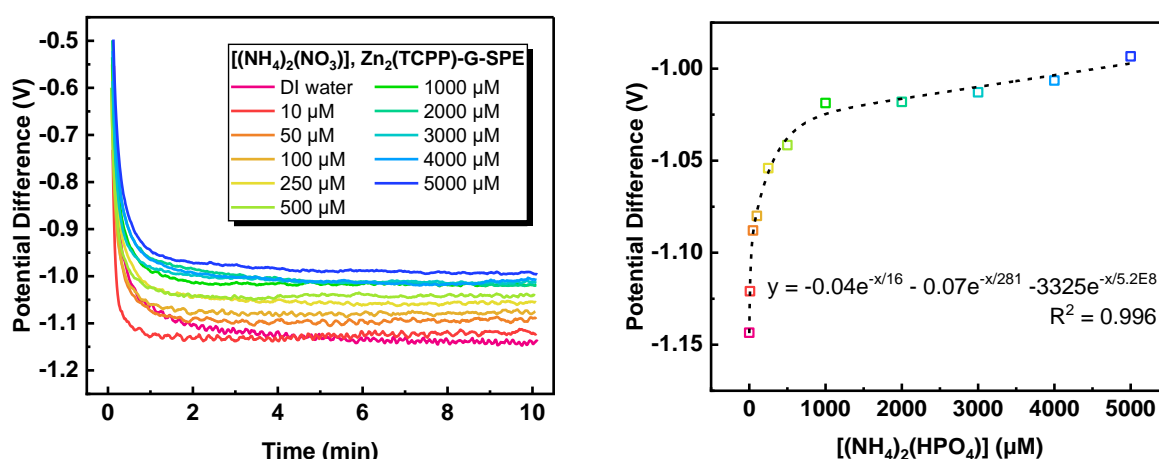


Figure S6.16 Chronopotentiometry over 20s of aqueous ammonium nitrate solutions using a bulk modified $Zn_2(TCPP)$ -G-SPE (left), and final voltages plotted against ammonium phosphate concentration (right).

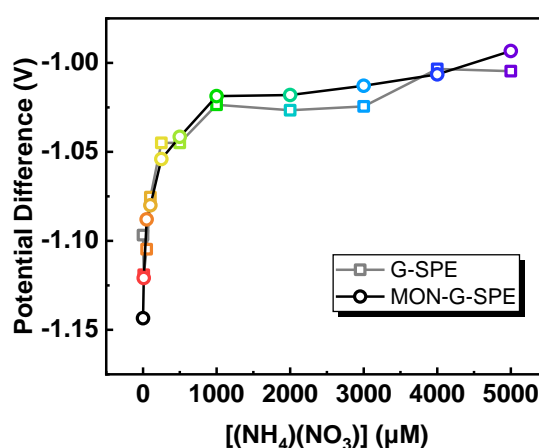


Figure S6.17 Chronopotentiometry results for different aqueous ammonium nitrate solutions comparing different electrodes.

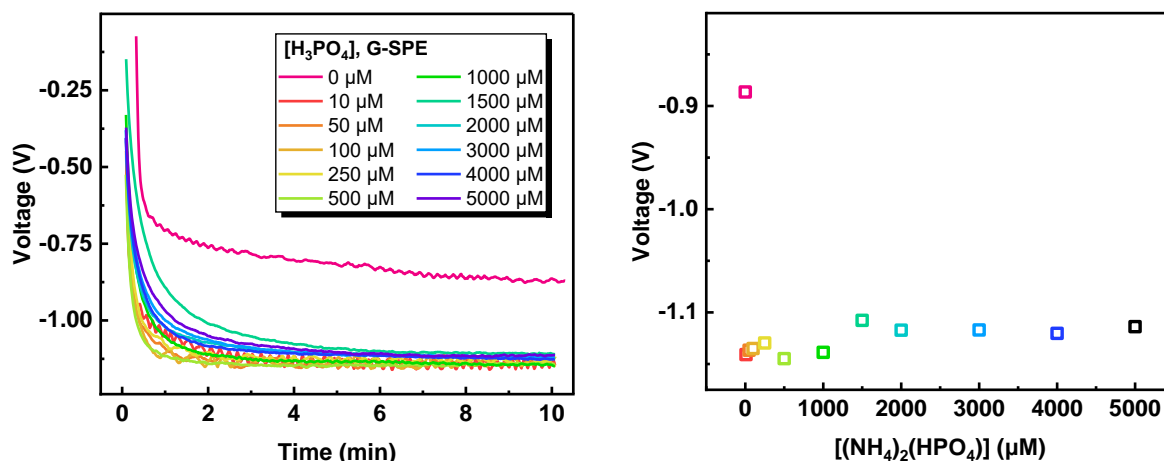


Figure S6.18 Chronopotentiometry over 10s of aqueous phosphoric acid solutions using a G-SPE (left), and final voltages plotted against ammonium phosphate concentration (right).

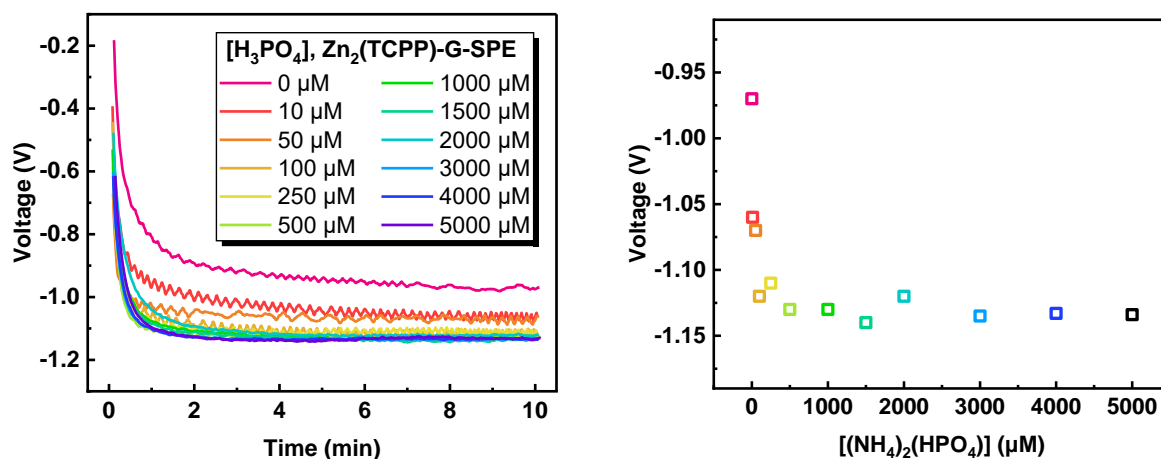


Figure S6.19 Chronopotentiometry over 10s of aqueous phosphoric acid solutions using a bulk modified $Zn_2(TCPP)$ -G-SPE (left), and final voltages plotted against ammonium phosphate concentration (right).

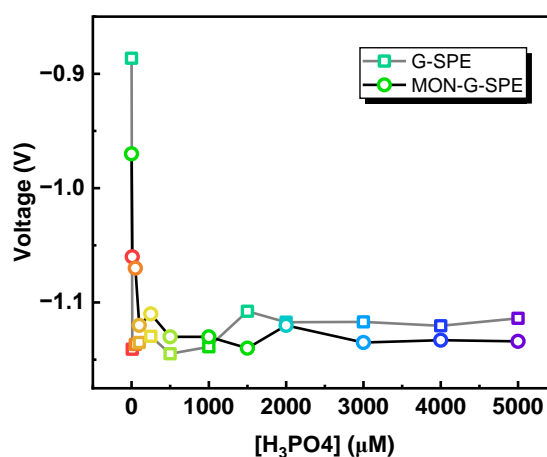


Figure S6.20 Chronopotentiometry results for different aqueous phosphoric acid solutions comparing different electrodes.

Polypyrrole MIP sensing

Measurements made in solutions with PBS

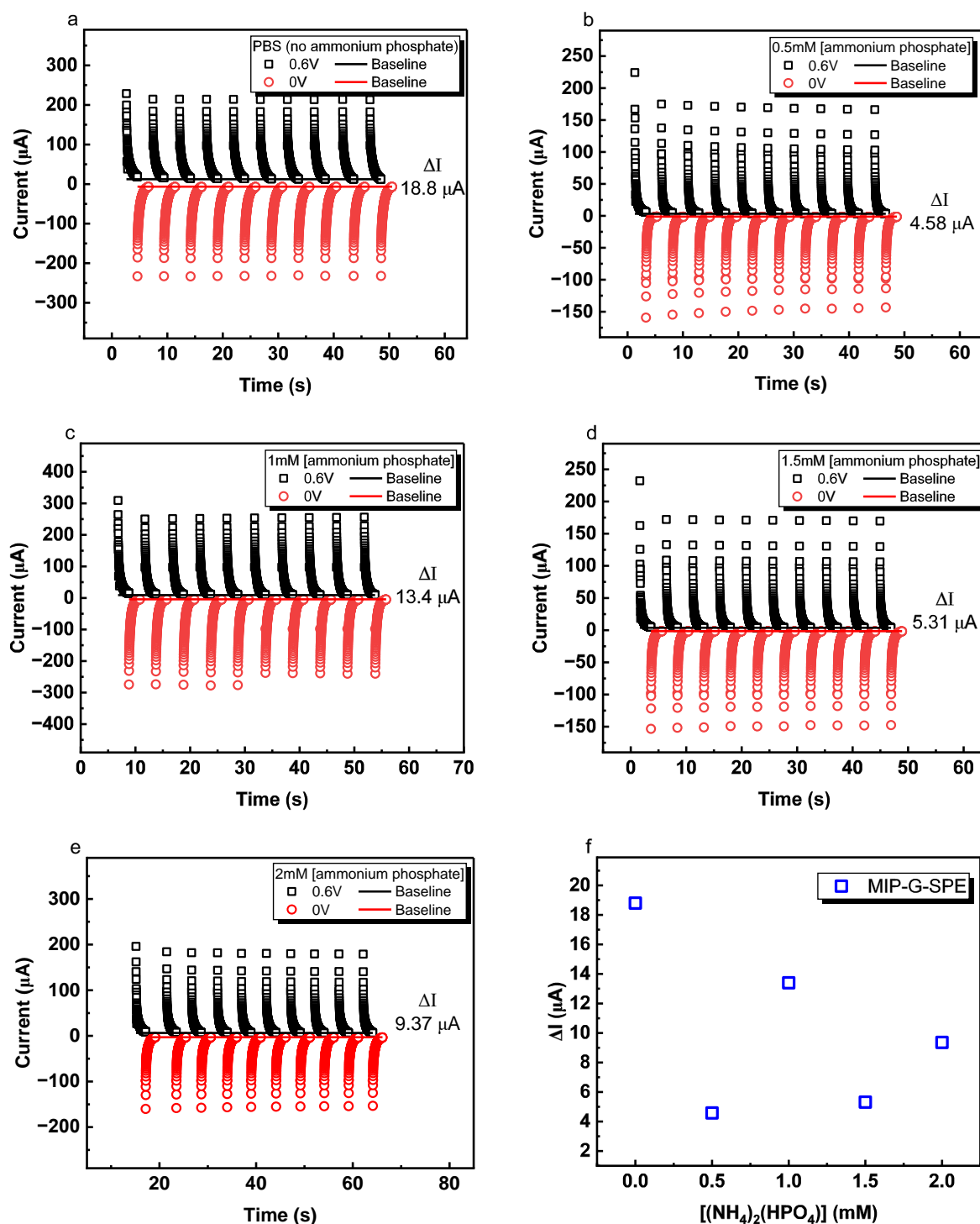


Figure S6.21 Pulsed voltage chronoamperometry using G SPE MIP (AP) in PBS solution with a) 0 mM, b) 0.5 mM, c) 1 mM, d) 1.5 mM, and e) 2 mM AP, with f) ΔI plotted against each concentration of AP.

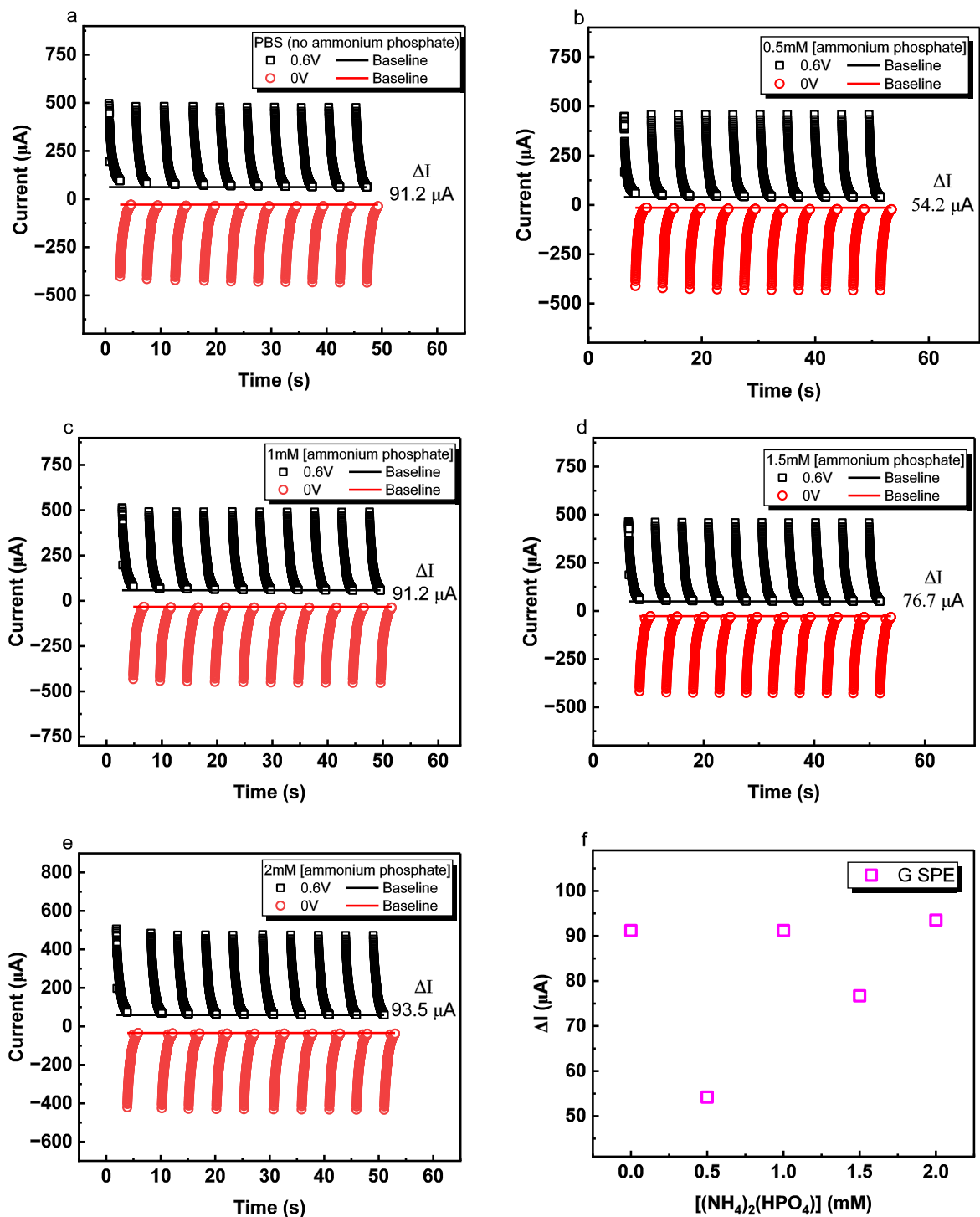


Figure S6.22 Pulsed voltage chronoamperometry using G SPE NIP in PBS solution with a) 0 mM, b) 0.5 mM, c) 1 mM, d) 1.5 mM, and e) 2 mM AP, with f) ΔI plotted against each concentration of AP.

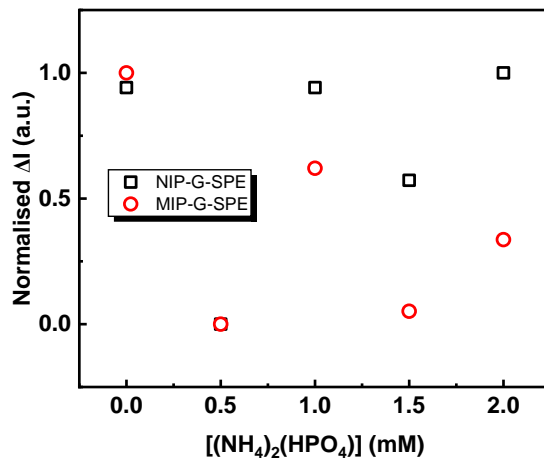
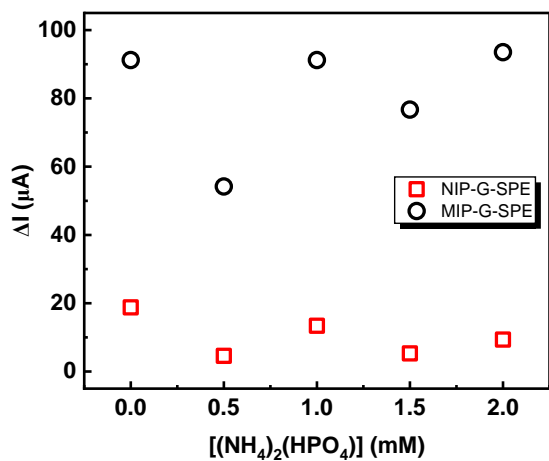
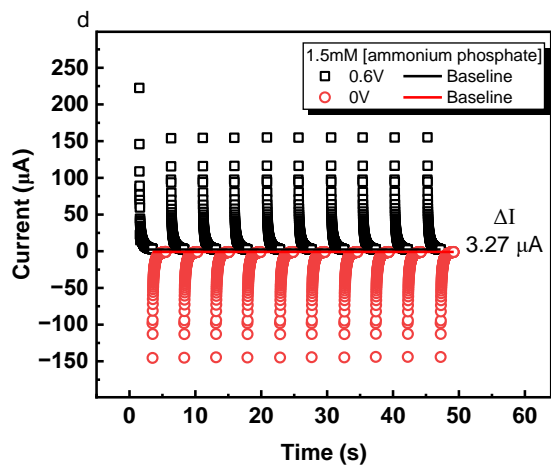
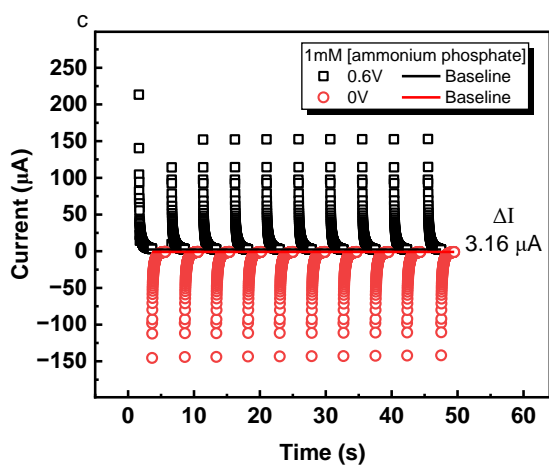
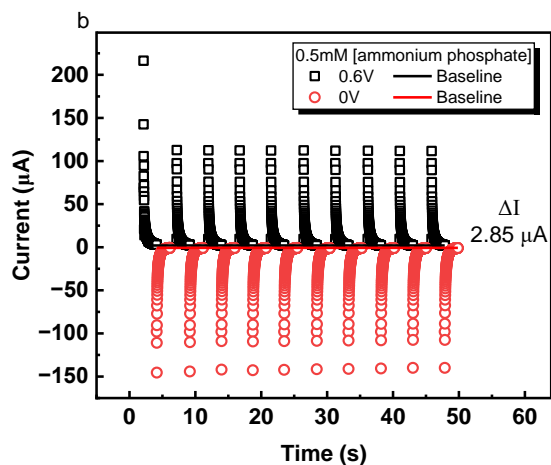
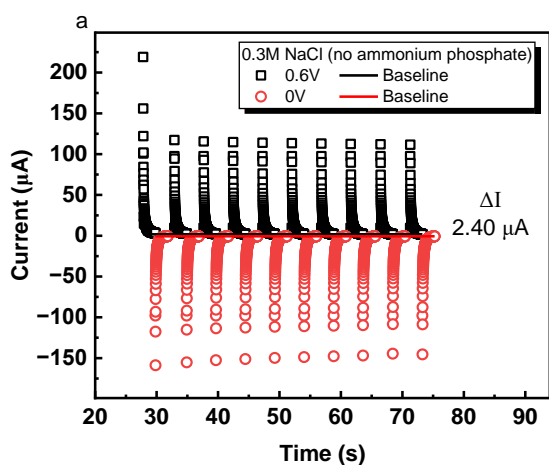


Figure S6.23 Chronoamperometry results plotted against concentration of ammonium phosphate in 20mM PBS solution.

Measuring ammonium phosphate concentration without PBS



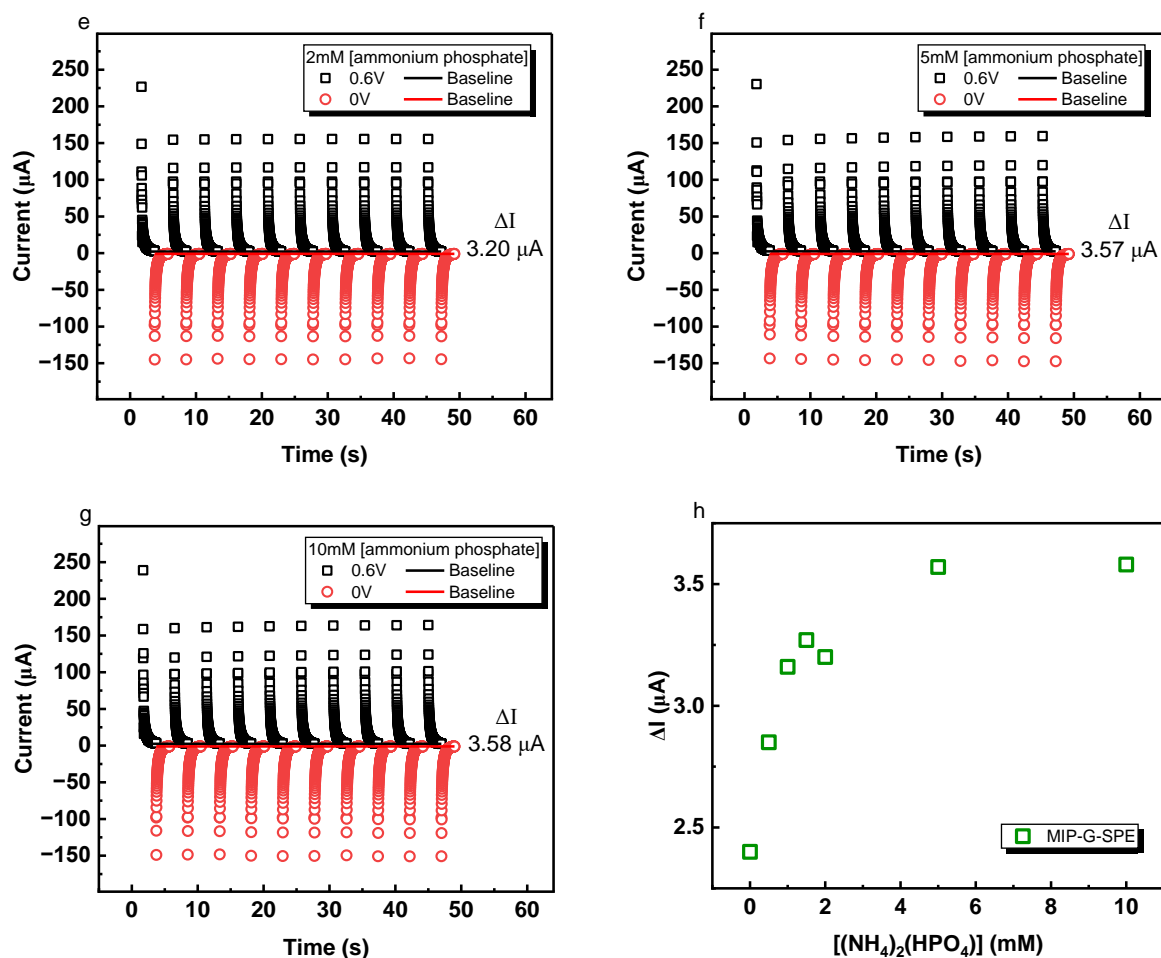


Figure S6.24 Chronoamperometry results for ammonium phosphate titration using polypyrrole MIP-G-SPE in aqueous 0.3 M NaCl solutions.

Comparison of ppy MIPs versus Zn₂(TCPP)-G-SPEs for AP titration

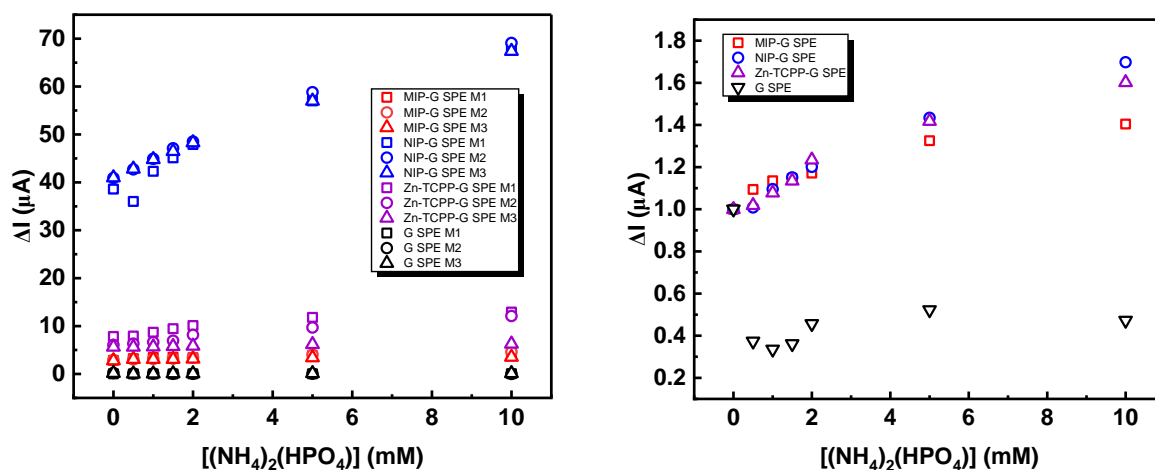


Figure S6.25 Chronoamperometry results for ammonium phosphate titration in 0.3 M NaCl solution comparing MIP-G-SPE, NIP-G-SPE, Zn₂(TCPP)-G-SPE, and unmodified G-SPE.

Electroactive MIP sensing

Covalent

After the incubation step in glycine, the Glycine-G-SPE was tested using CV -0.6 to 0.6 V (Figure 14) to determine the affinity, if any, of this material on the electrode. A small oxidation peak is observed at 0.11 V, indicating this should be discounted as phosphate signal in further experiments.

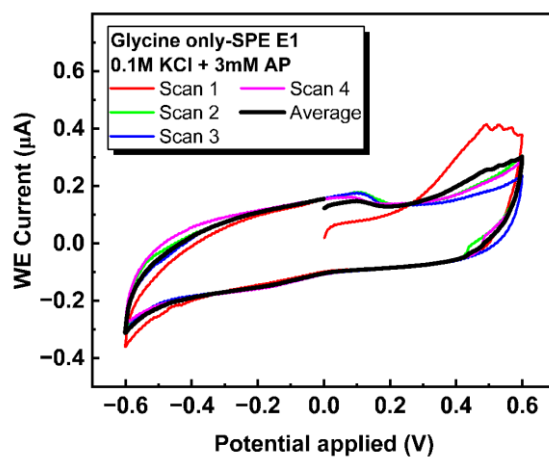


Figure S6.26 CV recorded for glycine incubated G-SPE (without MIP) from -0.6 to 0.6 V.

After glycine incubation and EDC/NHS treatment, the electrode E1 was produced by dropcasting a dispersion of MIPs onto the G-SPE WE surface.

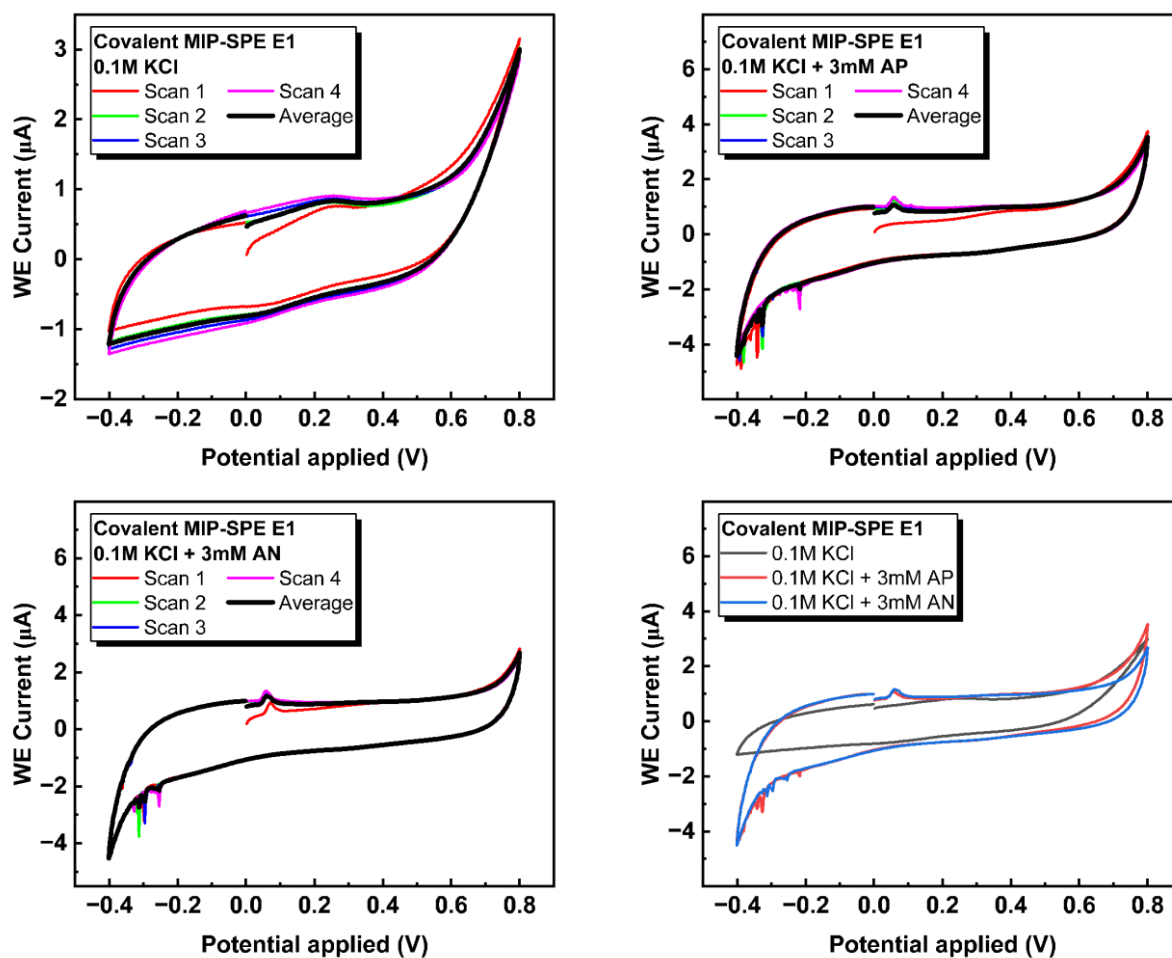


Figure S6.27 CVs of covalently attached MIP on the surface of G-SPE E1 measured -0.4 V to 0.8 V in 0.1 M $\text{KCl}_{(\text{aq})}$ (top left), in 0.1 M $\text{KCl}_{(\text{aq})}$ + 3mM ammonium phosphate (top right), in 0.1 M $\text{KCl}_{(\text{aq})}$ + 3mM ammonium nitrate (bottom left), and averages for each CV experiment plotted together (bottom right).

NPEDMA

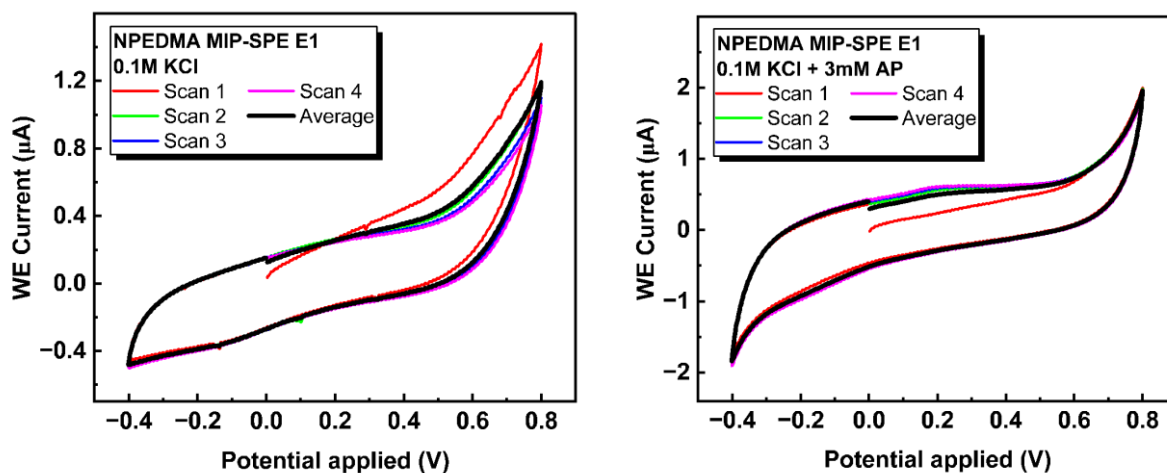


Figure S6.28 CVs of NPEDMA encapsulated MIP-SPE E1 measured -0.4 V to 0.8 V in 0.1 M KCl_(aq) (left) and in 0.1 M KCl_(aq) + 3mM ammonium phosphate (right).

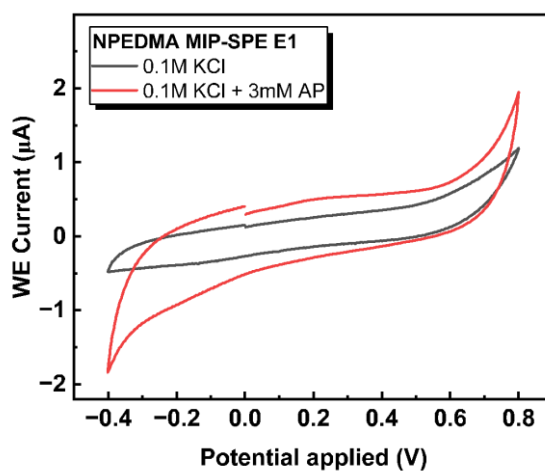


Figure S6.29 Averaged CVs recorded using NPEDMA MIP-SPE E1 in 0.1M KCl solution and 0.1M KCl + 3mM ammonium phosphate solution plotted together using data from Figure 9 for comparison.

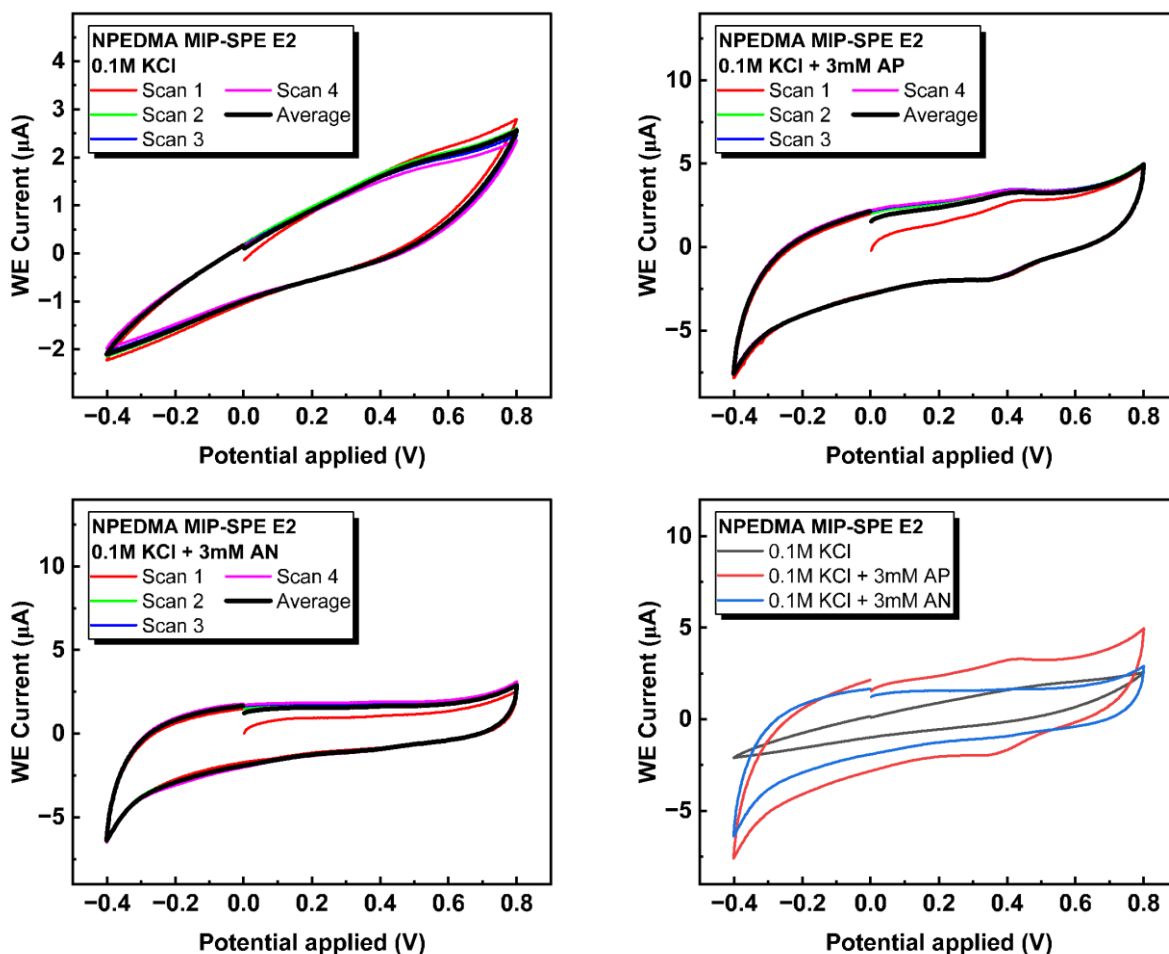


Figure S6.30 CVs of NPEDMA encapsulated MIP-SPE E2 measured -0.4 V to 0.8 V in 0.1 M KCl_(aq) (top left), in 0.1 M KCl_(aq) + 3mM ammonium phosphate (top right), in 0.1 M KCl_(aq) + 3mM ammonium nitrate (bottom left), and the averaged voltammograms from all three plotted together for comparison (bottom right).

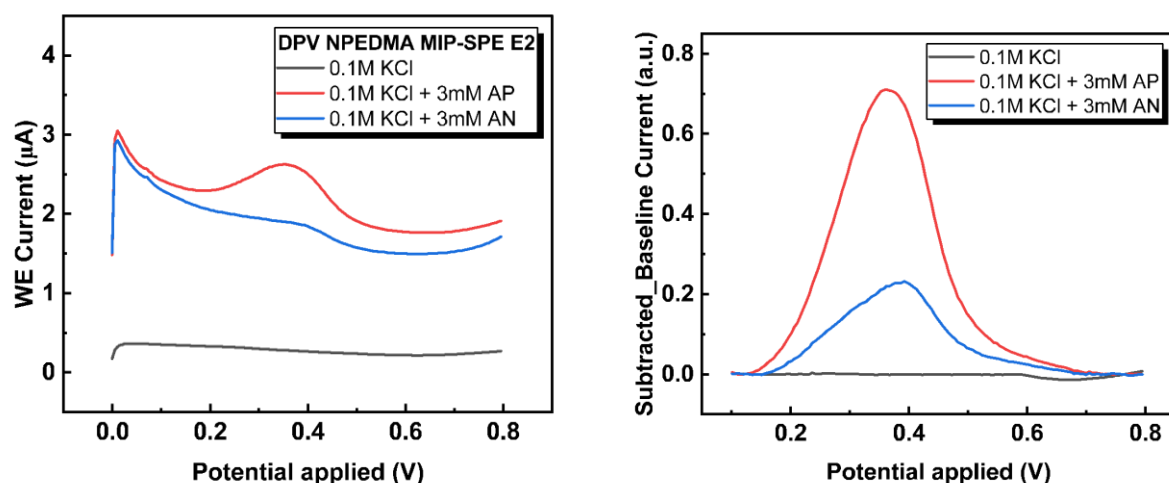


Figure S6.31 DPV scans recorded using NPEDMA MIP-SPE E2 measured 0 V to 0.8 V (left), and the same scans baselined.

An electrode produced using only electropolymerized NPEDMA on G-SPE was produced (E3) as a control to confirm the encapsulating polymer has no intrinsic affinity for phosphate. Without MIP present during the electropolymerisation (or measurement), the oxidation peak at 0.4 V was not observed (Figure 13). It should be noted that a reduction peak at ~ -0.25 V was observed in the

sample without phosphate, so no signal can be confirmed to be from phosphate without a concentration dependent change.

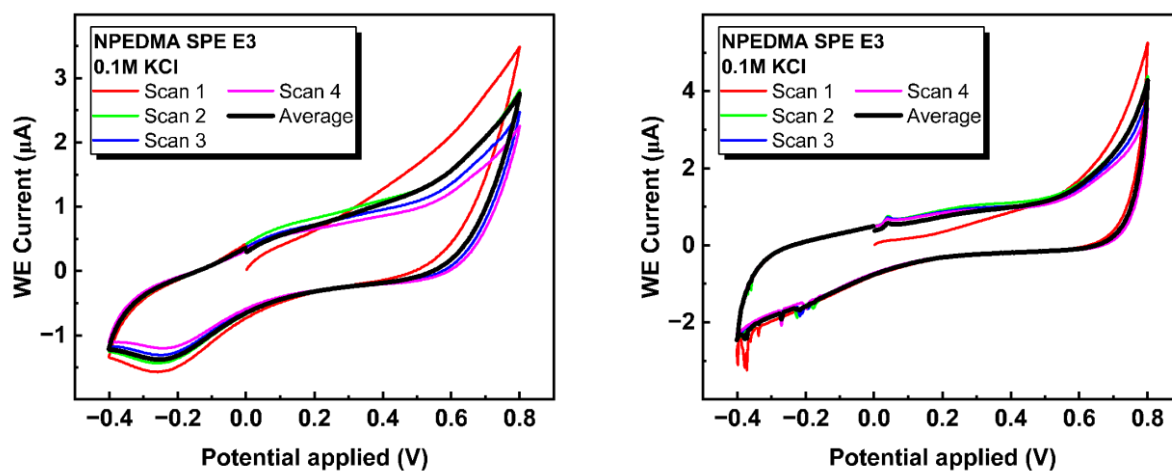


Figure S6.32 CVs of NPEDMA electropolymerized on the surface of G-SPE E3 measured -0.4 V to 0.8 V in 0.1 M KCl_(aq) (left), and in 0.1 M KCl_(aq) + 3mM ammonium phosphate (right).

When titrations of ammonium phosphate are performed without KCl electrolyte, the ferrocene character is not observed in the cyclic voltammograms (Figure S6.33).

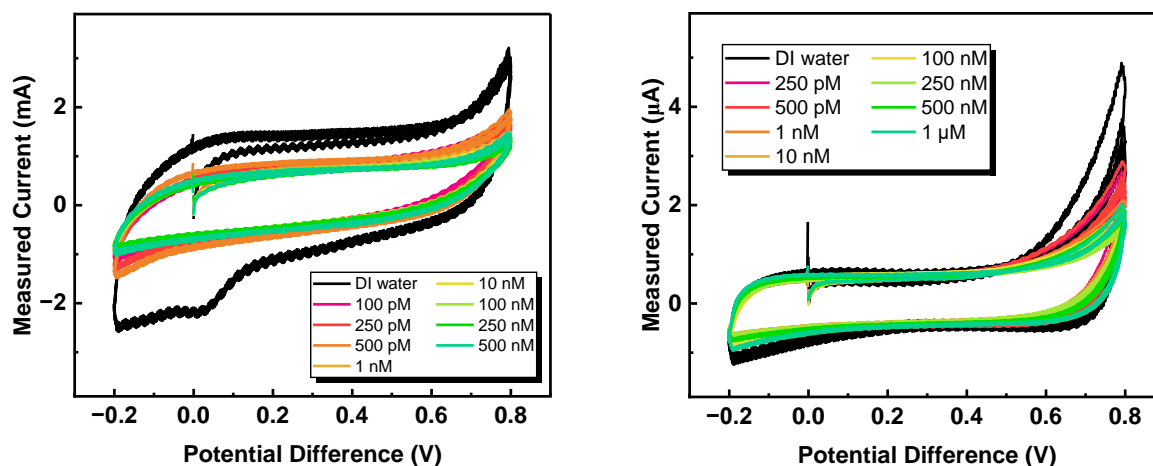


Figure S6.33 CV recorded using NPEDMA MIP-G-SPE E2 (left), and NPEDMA MIP-G-SPE E4 (right) for ammonium phosphate titration in water.

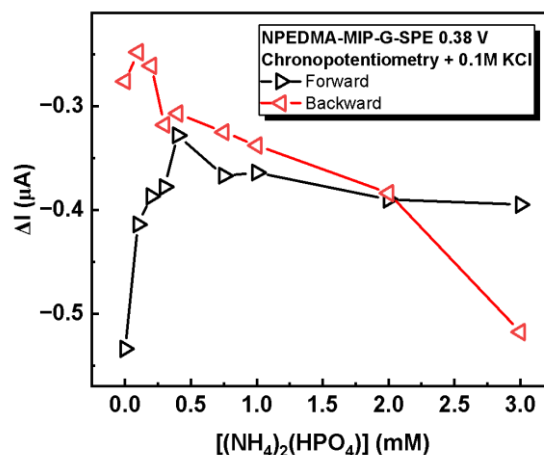


Figure S6.34 Chronoamperometry at 0.38 V using NPEDMA-MIP-G-SPE

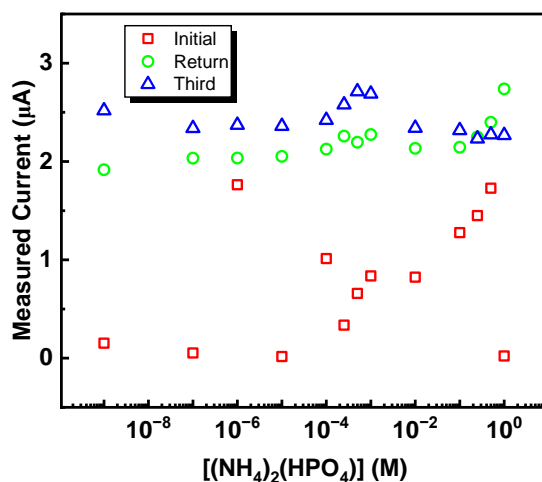


Figure S6.35 Chronoamperometry experiment measuring the titration of aqueous ammonium phosphate concentrations with water washing of the NPEDMA MIP-G-SPE between measurements.

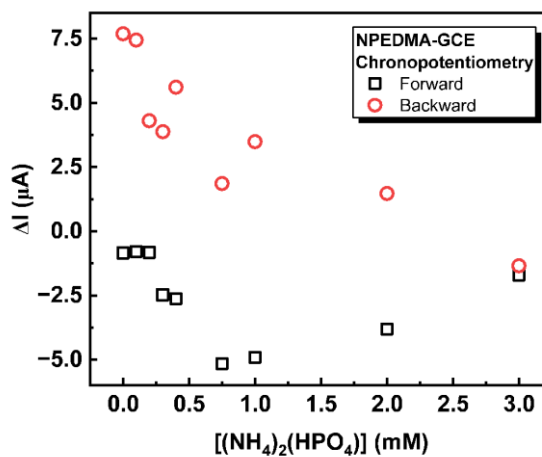


Figure S6.36 Pulsed-voltage chronoamperometry at 0.2 V using NPEDMA-MIP-GCE over ten scans.

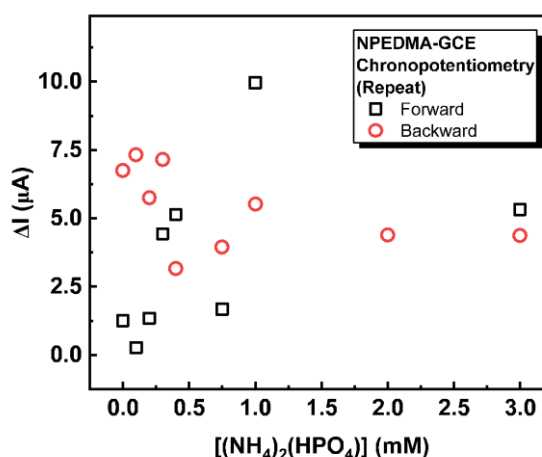


Figure S6.37 Pulsed-voltage chronoamperometry repeat at 0.2 V using NPEDMA-MIP-GCE over ten scans.

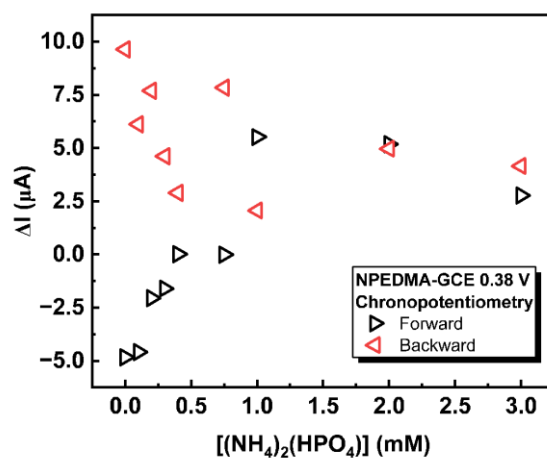


Figure S6.38 Chronopotentiometry at 0.38 V using NPEDMA-MIP-GCE over ten scans.

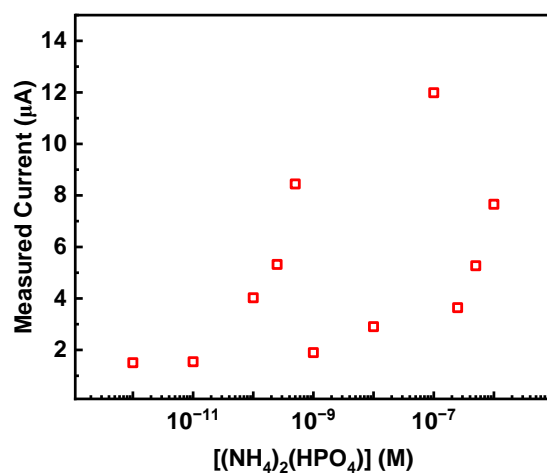


Figure S6.39 Chronoamperometry experiment measuring the titration of aqueous ammonium phosphate concentrations with glycine/water washing of the NPEDMA MIP-GCE between measurements.

Data processing for pulsed voltage chronoamperometry produces unnecessary graphs and is time consuming. Python code is written with the aid of ChatGPT to convert data from potentiostat to csv files, then to process data for sensing.

First, we need to convert the files exported after the experiment from excel (xlsx) to comma separated value (CSV):

```
import pandas as pd
import os

# Specify the directory containing the XLSX files
xlsx_dir = r'Folder where data is stored'

# Loop over all XLSX files in the directory
for xlsx_path in os.listdir(xlsx_dir):
    if xlsx_path.endswith('.xlsx'):
        # Load data into a pandas DataFrame
        print(f>Loading file: {xlsx_path}")
        df = pd.read_excel(os.path.join(xlsx_dir, xlsx_path),
engine='openpyxl')

        # Save data to a CSV file
        csv_path = os.path.join(xlsx_dir,
os.path.splitext(xlsx_path)[0] + '.csv')
        df.to_csv(csv_path, index=False)
        print(f>Saved file: {csv_path}")
```

Then we can take the ten csv files, each containing 4 columns where column A is the time during the “on” pulse of 0.6 V, column B is the current measured during the “on” pulse, column C is the time during the “off” pulse, and column D is the current measured during the “off” pulse.

Since the “on” pulse tends to a minimum (positive value), and the “off” pulse tends to a maximum (negative value), the difference between these can be calculated and reported in a csv file “results.csv”.

The coded analysis method was performed on the MIP measurements 1-3 and compared to the manual method (graphing and fitting in OriginPro).

```
import os
import pandas as pd
import glob

# Specify the output file name
output_file = "results.csv"

# Specify the directory containing the CSV files
csv_dir = r'G:\shortcut-targets-by-id\1x17LCiiM6S-
Q01rvJpjflrXk3rvbbiu2\Ben Smith FG\Lab-book\BJS-Proj14-Molecular
imprinted polymers for sensing\23.04.17 NaCl AP sensing repeats\Zn-
TCPP-G SPE\Measurement 3\10mM'
# Initialize lists to store the on and off values for each pulse
on_min_vals = []
off_max_vals = []
```

```

# Loop over all CSV files in the directory
for csv_path in glob.glob(csv_dir + '/*.csv'):

    # Load data into a pandas DataFrame
    print(f"Loading file: {csv_path}")
    df = pd.read_csv(csv_path)

    # Find the minimum value in column 2 and append it to the
    on_min_vals list
    if 'Column 2' in df.columns:
        on_min_vals.append(df['Column 2'].min())

    # Find the maximum value in column 4 and append it to the
    off_max_vals list
    if 'Column 4' in df.columns:
        off_max_vals.append(df['Column 4'].max())

# Calculate the average minimum "on" value and maximum "off" value
if len(on_min_vals) > 0:
    on_min_avg = sum(on_min_vals) / len(on_min_vals)
    print(f"Average minimum 'on' value: {on_min_avg}")
else:
    print("No 'Column 2' data found in CSV files")

if len(off_max_vals) > 0:
    off_max_avg = sum(off_max_vals) / len(off_max_vals)
    print(f"Average maximum 'off' value: {off_max_avg}")
else:
    print("No 'Column 4' data found in CSV files")

# Save results to a CSV file in the same directory as the input CSV
files
output_path = os.path.join(csv_dir, output_file)
results_dict = {'Average minimum on value': [on_min_avg],
                'Average maximum off value': [off_max_avg],
                'Difference': [off_max_avg - on_min_avg]}
results_df = pd.DataFrame(results_dict)
results_df.to_csv(output_path, index=False)
print(f"Results saved to {output_path}")

```

Chapter 7:

Conclusions and Future Outlook

Understanding the relationship between a material's structure and its optical and electronic properties is key to enabling its use in a wide range of applications, including sensing. In this thesis I have undertaken an in-depth investigation into the effects of nanosheet stacking, aggregation, and metalation on the optoelectronic properties of a class of porphyrin-based metal organic framework nanosheets (MONs). I have also investigated the application of MONs and other materials in the sensing of phosphate-based fertilisers for sustainable farming. In this overall conclusion, key lessons from across the thesis will be considered and opportunities for future work identified.

The focus of this thesis is a series of porphyrin-based MONs consisting of zinc in a paddlewheel secondary building unit linked by tetra(carboxyphenyl)porphyrin (TCPP) ligands. These $Zn_2(\text{TCPP})$ MONs are well established in literature, and the synthesis of these has previously been reported within the group. Nonetheless, attempts to resynthesise this material as standalone monolayer nanosheets were problematic, with issues arising due to nanosheet aggregation. Efforts to optimise the synthesis have shown that the effect of dispersion concentration and the history of MON processing e.g., settling time or centrifugation, can have a large effect on the distribution of nanosheet dimensions.

These priorities are collected in the aims of **chapters 3 and 4** to form a rational basis for choosing physical properties in these MONs which result in desired optoelectronic interactions. For example, porphyrins are good natural light harvesters which have been used in solar cells, so their efficiency could be improved by broadening the range of the solar spectrum which they can absorb, configuring their bandgaps to better align with other component materials, or inhibiting processes that lead to reduced electron/hole transport.

Chapter 3 established a relationship between the concentration of $Zn_2(\text{TCPP})$ in dispersion and particle size. The aggregates formed at high concentrations were shown by Stern-Volmer analysis to undergo two self-quenching routes from S_1 and S_2 states, via dynamic and static mechanisms, respectively. This therefore presents an opportunity to avoid such aggregation in applications which require emission. In the same chapter, post-synthetic centrifugation, a common processing technique used to remove multilayer MOFs from nanosheet suspensions, were shown to induce aggregation in suspension. Since the S_1 emission was quenched by a concentration dependent mechanism (dynamic), but the S_2 emission is quenched by an aggregation dependant mechanism (static), the red emission is enhanced by centrifugation at higher speeds 2,000-8,000 rpm. This represents an interesting way to tune the colour of emission.

A transient absorption measurement identified that centrifugation decreased the presence of a low energy S_2 excited state due to the removal of π -stacked particles. Higher centrifugation speeds increased the overall lifetime of excited states, likely due to quenched emission from S_2 no longer competing with the route to long-lived triplet states. A power dependence study, however, indicated that the amount of exciton-exciton annihilation increased in centrifuged samples. Calculations for the exciton diffusion pathlength revealed extremely short values 0.5-10 Å, which indicated rapid annihilation in centrifuged samples. Only the uncentrifuged samples exhibited diffusion pathlengths long enough for intermolecular transfer, indicating interlayer interactions can be responsible for exciton-exciton annihilation.

This chapter, therefore, concludes that post-synthetic centrifugation can greatly effect the excited state dynamics of $Zn_2(TCPP)$ MONs, and provides a framework for identifying these changes in future work or with similar materials. It may be useful when utilising these materials in solar cells for electron/hole transport, for example, to choose lower centrifugation speeds that remove multilayer particles without enhancing exciton-exciton annihilation.

There is significant remit for further testing of these outcomes, either in more extensive or iterative material design e.g., pillared $Zn_2(TCPP)$, different MONs, or post-synthetically modified linkers. Additionally, the outcomes advising different methods should be tested by incorporating these materials into devices for optical applications e.g., solar cells.

Chapter 4 investigated the post-synthetic metalation of $Zn_2(TCPP)$ MONs to form materials with the chemical structure $Zn_2(TCPP-X)$, where $X = H_2, Co, Ni, Cu, Zn, \text{ or } Cd$. This chapter aims to translate the breadth of understanding shown in literature about metalloporphyrins and apply it to these porphyrin-based MONs. There are two complementary theories regarding the changes in absorption and emission observed in metalloporphyrins: the first is based on distortion of planarity due to metalation, and the second on computationally modelled changes in electronic populations due to hybridisation of delocalised porphyrin electron rings with metal orbitals, respectively.

Both theories are used to explain the observed results of absorption and emission testing of $Zn_2(TCPP-X)$, with the planarity distortion most obvious in the cadmium metalated sample. Short, excited state lifetimes (60-100 ps) were introduced by metalation, with the exception of copper and cadmium, which had increased lifetimes due to emission quenching and poor spin-orbit coupling, respectively. This culminated in a power dependence study which showed metalation significantly reduced exciton annihilation compared to $Zn_2(TCPP-H_2)$, leading to generally greater intersystem crossing to triplet states in metalated samples.

Not only does this chapter present some experimental evidence for the theories described but presents an opportunity to tailor the spectroscopic properties of $Zn_2(TCPP)$ by metalation. The emission intensity, for example, can be modulated by the inclusion of copper, or the exciton deactivation in transport materials reduced by inclusion of cadmium. At the least, this work provides a framework for understanding differences which might arise when incorporating these materials into devices for optoelectronic applications e.g., solar cells.

Chapter 5 aimed to correlate the size of individual nanosheets with their optical properties by combining spectroscopic and atomic force microscopy measurements. The metal organic framework nanosheet $Zn_2(TCPP)$ was investigated by s-SNOM to determine if it was possible to map absorption according to the morphology and thickness of isolated nanosheets. It was concluded that whilst the optical absorption of aggregate clusters of material could be measured, the nanosheets approaching monolayer could not be resolved. This indicates there is not enough material in a <1 nm nanosheet for the s-SNOM measurement.

To explore another option, the s-SNOM setup was modified to perform tip-incident photoluminescence nanospectroscopy with the aim of spatially mapping photoluminescence output, thus allowing direct correlation of emission intensity with particle height/thickness. The experiment yielded an emission map of a $Zn_2(TCPP)$ agglomerate particle of $8 \mu m$ size which visually approximated the height mapped atomic force microscopy graph of the same particle. This resolution is too poor for quantitative analysis of single nanosheet photoluminescence output but demonstrated the viability of the technique. It also may be possible with optimisation/tip-enhanced measurements to resolve the individual nanosheets in future.

To explore the possibility of future experiments without improvements in resolution, an experiment was undertaken as proof of concept which recorded an atomic force microscopy scan, during which a 3.3 μm excitation beam approximately central to the scan was used to record the emission spectrum. A tentative positive correlation was made between average statistical roughness from the AFM image and the emission intensity, which is largely representative of the amount of material present. It was concluded that this would be more useful quantitative analysis if samples were prepared with more isolated nanoparticles of discrete size differences to be properly effective in future analyses. Therefore, the future of this work would involve preparation of discretely synthesised single, double, or triple layer nanosheets to properly identify the effect layering of these nanomaterials has, but this currently remains a significant challenge.

Chapter 6 aims to develop the selectivity of smart materials for sensing phosphate fertilisers in soil for more sustainable farming. Specifically, it was established in this work that high sensitivity can be achieved using carbon or graphene-based sensors, but other components are required to provide selectivity. Three distinct routes to adding selectivity for phosphate to graphene-based electrodes were therefore investigated. Firstly, $\text{Zn}_2(\text{TCP})$ was characterised spectroscopically and investigated as a modifier material in carbon electrodes. Secondly, a molecularly imprinted polymer (MIP) layer of polypyrrole was electropolymerized onto a graphene screen-printed electrode (G-SPE) surface. Lastly, an intrinsically electroactive crosslinked polymer nanoparticle MIP was investigated by attachment to either a G-SPE surface or a glassy carbon electrode surface via methods of drop casting, covalent attachment, or encapsulation in a polymer layer.

This work successfully developed a methodology for incorporating $\text{Zn}_2(\text{TCP})$ MONs into graphene inks for screen printing electrodes, showing some inherent redox character, and electrochemical response in the presence of ammonium phosphate and ammonium nitrate. A range of different electrochemical sensing methods were investigated, of which pulsed voltage chronoamperometry proved the most promising due to its low electrode degradation risk and demonstrated sensitivity. The lack of selectivity by $\text{Zn}_2(\text{TCP})$ modified electrodes for phosphate over nitrate ultimately limit their potential for applications in soil sensing. It may, therefore, be of interest to pursue MON-modified electrodes fabricated by this method for sensing using a range of alternative MON systems which could enhance the selectivity.

Given the challenges of using MONs for sensing applications, a promising alternative was explored in molecularly imprinted polymers (MIPs) which have previously been reported to display high selectivity for phosphate. Firstly, a polypyrrole-based MIP was fabricated by electropolymerisation in the presence of ammonium phosphate onto a G-SPE. Pulsed-voltage chronoamperometry was used to measure different concentrations of ammonium phosphate in deionised water, however it was concluded that the analyte was also acting as electrolyte leading to a positive correlation counter to the negative correlation expected from literature. The positive trend measured by the imprinted electrode was slightly different compared to the non-imprinted electrode, but any observable signal was too weak. It was concluded that the electroactive response by the MIP should be enhanced somehow.

To this aim, another MIP was synthesised using a solid phase, less sterically hindered template technique, with inherent electroactivity from incorporation of ferrocenylmethyl methacrylate (FcMMA) in the polymeric structure. The resultant MIP was used to functionalise G-SPEs via drop casting, covalent bonding, or encapsulation in a conductive polymer (NPEDMA, non-imprinted). Each of these were assessed for effectiveness in sensing for ammonium phosphate by electrochemical methods, particularly pulsed voltage chronoamperometry, employed in both MON and MIP modified electrode experiments. This

involved the development of a novel data processing programme using code generated with the aid of ChatGPT, and tested against a manual graphing of experimental data. The repeatability of phosphate sensing by modified G-SPEs was quite poor, so the alternative binding methods aimed to improve this, with modest success.

Given the instability of G-SPEs during electrochemical measurements, a glassy carbon electrode was modified by electroactive MIP encapsulated in NPEDMA to remove the inherent instability of the G-SPEs. With this electrode it was concluded that analyte binding to the MIP produced a demonstrable signal in the sensor in the concentration range 0.1 to 3 mM, with the more negative signal change observed for ammonium phosphate compared to ammonium nitrate indicating a greater specificity to phosphate. Future work should focus on this system for its greater sensitivity and selectivity, possibly exploring an improved sensing concentration range via baselining to a non-modified GCE.

The investigation into materials for sensing of phosphate fertilisers identified several possible options for enhancing the selectivity of graphene or carbon-based electrodes. A pulsed-voltage chronoamperometry technique was established to be accurate for sensing of small anion analytes, with a less labour-intensive data processing method developed. There remains significant testing to confirm the aptitude of these materials in soil-samples, as well as the longevity of these materials when incorporated into sensing devices.

Overall, we anticipate that the new insights gained into the photophysical properties and sensing behaviour of this important class of MONs will aid the development of new systems that will support optoelectronic and sustainable technologies in the future. The analysis in this work forms a good foundation for future work, and I look forward to seeing the possibilities grow.